EVALUATING THE MAGMATIC HISTORY, MAGMATIC SOURCE FERTILITY, AND METAL CONTRIBUTIONS TO GOLD-BEARING HYDROTHERMAL SYSTEMS, MOOSHLA INTRUSIVE COMPLEX, DOYON-BOUSQUET-LARONDE MINING CAMP, ABITIBI GREENSTONE BELT, QUEBEC

By

Kevin John Neyedley

A thesis submitted to Saint Mary's University, Halifax, Nova Scotia in partial fulfillment of the requirements for the degree of Doctor of Philosophy in Applied Science

December, 2024, Halifax, Nova Scotia

Approved: Dr. Jacob Hanley
Supervisor
Department of Geology
Saint Mary's University

Approved: Dr. Patrick Mercier-Langevin
Supervisory Committee
Geological Survey of Canada

Approved: Dr. Stephen Piercey
Supervisory Committee
Department of Earth Sciences
Memorial University

Approved: Dr. Daniel Kontak
Supervisory Committee
Harquail School of Earth Sciences
Laurentian University

Approved: Dr. Robert Singer
Supervisory Committee
Department of Chemistry
Saint Mary’s University

Approved: Dr. Alan Galley
External Examiner
Malleus Consulting Inc.

Date: December 17, 2024

ABSTRACT

Evaluating the magmatic history, magmatic source fertility, and metal contributions to gold-bearing hydrothermal systems, Mooshla Intrusive Complex, Doyon-Bousquet-LaRonde mining camp, Abitibi greenstone belt, Quebec

By: Kevin John Neyedley

The Mooshla Intrusive Complex is an Archean polyphase tonalite-trondhjemite-quartz diorite-gabbroic magmatic body located in the Doyon-Bousquet-LaRonde mining camp of the Abitibi greenstone belt, Québec, Canada. The complex is spatially and temporally associated with numerous gold-rich volcanogenic massive sulfide, epizonal intrusion-related Au ± Cu, and shear zone-hosted orogenic gold and/or remobilized volcanogenic massive sulfide deposits. The intrusive complex has been characterized by numerous methods including high-precision U-Pb geochronology, accessory mineral trace element composition (i.e., zircon, titanite, anhydrite, quartz), silicate melt inclusions, and isotopic analyses. This provides a comprehensive study on the melt and pressure-temperature-time evolution of the magmatic system and potential influence the system had in supplying metals to the gold deposits. Additionally, two gold deposits hosted in the Mooshla Intrusive Complex have been studied to document the ore mineralogy and trace element and isotopic characteristics that aid in identifying a magmatic fluid source for these systems.

December 17, 2024

ACKNOWLEDGEMENTS

I would like to thank Dr. Jacob Hanley for his continual guidance over the years to provide me with everything I needed to succeed. As well as giving me time and space to work independently on this project to make mistakes, correct those mistakes, develop my own ideas, and letting me explore any rabbit whole we both would venture down. Dr. Patrick Mercier-Langevin provided an exceptional amount of knowledge, time in the field, and support throughout the project and always gave me the reminder that every project has an end and not every question can be answered. I appreciated the constructive comments and criticisms of the supervisory committee that helped evolve this project along the way.

Valuable time in the field during was lent by numerous people at IAMGOLD (Westwood operations) and Agnico Eagle (LaRonde operations). Especially, David Yergeau and David Pitre for answering many questions about the local geology and spending time in the field. Allan Galley and his plethora of knowledge was of immense value in the field and continually throughout the project.

Support from many people at SMU helped in numerous ways throughout the project, whether it be in a scientific or non-scientific form. The Hanley group of students at SMU over the years here have all contributed to this project in one way or another. In particular, Dan Meagher, where we spent weeks in Noranda together collecting rocks and discussing them at Le Trèfle Noir.

The late Trevor MacHattie from the Nova Scotia Geological Survey provided me with the opportunity to work with him and expose me to the geology of Nova Scotia during the PhD Internship associated with this program. The opportunity led me to my role with the survey now and could not be more grateful to him. Our trip to Nevada will always be a highlight of our time together.

My high school geography teacher, Mr. Richard Humphrey, sparked my interest in geology in grade 10 at Glenlawn Collegiate. Finally, of course, my parents and brother, thank you for your endless support through the years and letting me do whatever I want in life.

TABLE OF CONTENTS

LIST OF FIGURES

In Chapter 2

In Chapter 3

In Chapter 4

LIST OF TABLES

In Chapter 2

In Chapter 3

In Chapter 4

LIST OF ELECTRONIC APPENDICES

In Chapter 2

Supplementary Table 2.1: Zircon trace element chemistry determined by LA-ICP-MS

Supplementary Table 2.2: Zircon $\delta^{18}O$ composition

Supplementary Table 2.3: Zircon U-Pb CA-TIMS isotopic data

Supplementary Table 2.4: Titanite EMPA chemistry

Supplementary Table 2.5: Titanite LAICPMS chemistry

Supplementary Table 2.6: Ti-in-quartz concentrations

Supplementary Table 2.7: EARTHTIME 2000 Ma solution U-Pb CA-TIMS isotopic data

Supplementary Table 2.8: Average concentrations of zircon 91500 determined by LA-ICP-MS

In Chapter 3

Supplementary Table 3.1: Sample Locations and Lithology

Supplementary Table 3.2: Anhydrite trace element chemistry determined by LA-ICP-MS

Supplementary Table 3.3: Anhydrite $\delta^{34}S$ and $\delta^{18}O$ isotope compositions

Supplementary Table 3.4: Silicate melt inclusion zircon host compositions

Supplementary Table 3.5: Zircon-hosted silicate melt inclusion compositions determined by LA-ICP-MS

Supplementary Table 3.6: Zircon-hosted silicate melt inclusion compositions determined by SEM-EDS and EPMA

Supplementary Table 3.7: Quartz-hosted silicate melt inclusion compositions determined by LA-ICP-MS

Supplementary Table 3.8: Maximum concentrations of metals in sulfide inclusions hosted in quartz and zircon

In Chapter 4

Supplementary Table 4.1: Chlorite chemistry determined by EPMA

Supplementary Table 4.2: Sphalerite and pyrrhotite chemistry determined by EPMA

Supplementary Table 4.3: Pyrite sulfur isotope and trace element compositions from sample 18KN03

Supplementary Table 4.4: Pyrrhotite sulfur isotope and trace element compositions from sample 18KN03

Supplementary Table 4.5: Pyrite sulfur isotope and trace element compositions from sample 18KN09

Supplementary Table 4.6: Sulfur isotope composition of pyrite and pyrrhotite from the Doyon deposit

Supplementary Table 4.7: Pyrite sulfur isotope for sample 18KN07

Chapter 1: Introduction to Thesis

1.1 BACKGROUND AND RESEARCH PROBLEMS

The Mooshla Intrusive Complex (MIC) is an Archean polyphase magmatic body located in the Doyon-Bousquet-LaRonde (DBL) mining camp of the Abitibi greenstone belt (AGB), Québec. The DBL camp is hosted in the 2704–2695 Ma Blake River Group (BRG), consisting primarily of tholeiitic to transitional mafic volcanic rocks and transitional to calc-alkaline intermediate to felsic volcanic rocks (BRG; Lafrance et al., 2005; McNicoll et al., 2014). Together with the BRG volcanics, the MIC is spatially and temporally associated with numerous gold-rich volcanogenic massive sulfide (VMS; e.g., LaRonde Penna and Bousquet 2-Dumagami), epizonal intrusion-related Au ± Cu (e.g., Doyon), and shear zone-hosted orogenic gold and/or remobilized VMS mineralization (e.g., Mouska and Mic Mac) deposits. Historic gold production by the end of 2019 for the entire DBL camp totaled 107.48 Mt with an average grade of 4.85 g/t Au equating to a total of 521 t (16.8 Moz) of Au (Mercier-Langevin et al., 2021). Combining past production, current reserves, and estimated resources, the total Au budget of the camp is roughly 894 t (28.7 Moz) of Au, making it one of the most important precious metal districts in the AGB.

Previous studies (e.g., Valliant & Hutchinson, 1982; Gosselin, 1998; Mercier-Langevin, 2007a, b, c; Galley & Lafrance, 2014; Yergeau, 2022a, b) have highlighted a possible genetic link between the MIC and Au deposits in the area based on geochronology, mapping/field relations, petrography, and lithogeochemistry. However, direct evidence such as the age of mineralization itself (e.g., Endako porphyry, Selby and Creaser, 2001; Jogran porphyry, Perelló et al., 2020; Côté porphyry-type, Katz et al., 2021), correlation of magmatic metal tenors with the ore metal tenors (Halter et al., 2005), evidence of coeval mineralization and degassing is lacking and, therefore, a genetic link between the MIC and Au deposits is still unclear. More generally, research on synvolcanic intrusive complexes associated with VMS districts has focused on establishing the

emplacement sequence and level, as well as using bulk rock methods (e.g., geochemistry, stable and radiogenic isotopes) to infer conditions of source melting, magma source affinity, and tectonic setting.

In the Archean, the composition of the synvolcanic intrusions underlying VMS deposits are most commonly low-Al (< 15 wt% Al_2O_3) tonalite–trondhjemite–diorite/granodiorite (TTD or TTG) composite intrusions (Galley, 2003). The MIC is primarily composed of tonalite, trondhjemite, and quartz diorite lithologies with subordinate gabbroic and diorite, classifying it as a TTD/TTG suite (Galley & Lafrance, 2014). Additionally, similar to the MIC, some other Archean TTG suites within or not within VMS districts are host to porphyry-style Cu-Au-Mo mineralization (e.g., Flavrian-Powell intrusive complex, Goldie et al., 1979; Galley, 2003; Chester intrusive complex, Katz et al., 2017, 2021; Chibougamau Pluton, Pilote et al., 1995). The shallow to mid-crustal emplacement conditions suggested for synvolcanic intrusions in the VMS environment (~3-10 km) are considered to be essential to generate high heat flow in the shallow crust thereby driving the hydrothermal fluid convection cells and the intrusion may contribute metals to the hydrothermal system through magmatic volatile exsolution (Galley, 2003; Franklin et al., 2005; Piercey et al., 2011). While the emplacement may be at relatively shallow crustal levels, the source conditions of these TTG suites are estimated to be at P ~1.0 to >1.5 GPa and T ~700° to 1000°C (e.g., Rapp et al., 1991; Martin, 1999; Smithies, 2000; Hart et al., 2004; Condie, 2005; Martin et al., 2005; Clemens et al., 2006; Piercey et al., 2008; Getsinger et al., 2009; De Almeida et al., 2011; Moyen & Martin, 2012; Qian & Hermann, 2013; Galley & Lafrance, 2014; Hoffman et al., 2014; Vezinet et al., 2018). Conditions of source magma formation can be similar to the estimates for magmas generated in subduction zone settings that may lead to the formation of porphyry Cu ± Au deposits (e.g., Richards, 2003; Annen et al., 2006; Carter et al., 2022). However, these estimated conditions are obtained through experimental studies or inference from bulk rock geochemical patterns and

ratios, and do not provide measured or direct thermobarometric constraints on the source conditions, conditions of early-stage crystallization, and evolution within the magma chambers at depth for specific environments. Additionally, using bulk rock geochemistry to estimate these conditions can be challenging because intrusive rock compositions are typically modified by magmatic processes during ascent and at or near their emplacement level (e.g., contamination and assimilation, volatile exsolution), and/or by post-solidus processes (e.g., magmatic-hydrothermal alteration, metamorphic alteration). Therefore, data from bulk methods may be ambiguous. A question that is unclear in the TTG literature is understanding how these magmas, which were generated at depth, are transported to their final emplacement position at relatively shallow levels in the crust and what happens to these magmas along their ascent and crystallization path. In the porphyry Cu ± Au models, much of the literature has focused on the transport of magmas from mid-crustal magma chambers (~10-15 km depth) to their shallow emplacement, but less work has been done on how these magmas are transported from their deep source regions to these mid-crustal storage chambers (Richards, 2003; Annen et al., 2006; Seedorff et al., 2008; Large et al., 2021).

In order to better understand the magmatic history of a suspected TTG intrusion, and its possible role in the development of spatially- and temporally associated Au deposits in the DBL, integration of field-based studies with in-situ analytical techniques is necessary to provide first order constraints on the evolution of potentially causative magmas. In particular, emphasis in the DBL has been placed on field relationships to document the near surface emplacement sequence and attempting to link these sequences to the geochronological order of magma formation and evolution at depth. In other environments such as large mafic-ultramafic complexes (e.g., Bushveld, Stillwater), the inferred emplacement sequence based on field relationships is not consistent with new high-precision geochronology. These complexes were not formed/emplaced in a sequential geochronological order, but rather younger sills were injected into older units

(Mungall et al., 2016; Wall et al., 2018). These results demonstrate that the stratigraphic order of units at surface cannot solely be relied upon to construct the geochronological evolution of a system.

In porphyry Cu ± Au systems, coupling zircon trace element chemistry with geochronology from sequentially emplaced intrusive units within an intrusive complex or batholith provides evidence of systematic changes in the T and chemical evolution of magma chamber(s) during the lifetime of the magmatic system (e.g., Buret et al., 2017; Large et al., 2018, 2021; Carter et al., 2022). Therefore, the analysis of zircon has the potential to provide insight into the T-chemistry-time evolution of an intrusive complex and constrain the duration of intrusive activity and metallogenic evolution. In addition, zircon is also a reliable geothermometer for estimating the T of crystallization based on its Ti concentration (Ti-in-zircon; Ferry & Watson, 2007). Other relevant geothermometers and geothermometers include the Zr-in-rutile (Ferry & Watson, 2007; Tomkins et al., 2007), Zr-in-titanite (Hayden et al., 2008), and Ti-in-quartz (Thomas et al., 2010). In porphyry Cu ± Au ± Mo systems, a combination of these thermobarometers has been used to estimate the crystallization conditions of syn-mineralized felsic porphyries as well as in combination with fluid inclusion isochores to estimate the conditions of pre-, syn-, and post-mineralized quartz veining (e.g., Audétat, 2015; Maydagán et al., 2015). However, very few studies have combined these thermobarometers to determine the P and T conditions of crystallization for relevant intrusive complexes in ore forming environments. A combination of techniques that see through secondary processes (i.e., alteration and metamorphic events), and can quantitatively constrain source melting, magma chamber evolution and the age of the intrusives, can provide a better understanding of the role of synvolcanic intrusions associated with Au-rich VMS and affiliated deposits.

In addition to understanding the source conditions of magma formation and the potential link to Au mineralization, the magma composition and evolution needs to be understood. One main question unaddressed with respect to the MIC and the spatially associated Au deposit is: what is the metal tenor of magmas and are they metal-enriched? In relation to the metal tenor, it is crucial to understand the magmatic evolution and processes that may hinder or promote the metal tenor of the magma, such as the oxidation state of the magma. Magmatic fO_2 conditions have a strong influence of the formation of magmatic-hydrothermal ore deposits since fO_2 exhibits a strong control on the solubility of some metals in the melt and is a primary control on the stability, formation, and abundance of an immiscible sulfide phase (e.g., Botcharnikov et al., 2010; Richards, 2011; Audétat and Simon, 2012; Zajacz et al., 2012, 2013). Early saturation of an immiscible sulfide phase has been proposed to be detrimental to the development of a magmatic-hydrothermal Au ± Cu deposit since the sulfide phase will incorporate metals, leading to lower metals in the silicate melt and therefore less metals available to the exsolving ore fluid (Müller et al., 2001; Park et al., 2015, 2019). However, there has been accumulating evidence that early sulfide saturation can be a temporary storage location for metals and potentially be an important process in the development of magmatic-hydrothermal Au ± Cu deposits (Keith, et al., 1997; Halter et al., 2004, 2005; Audétat and Pettke, 2006, Zhang and Audétat, 2017; Du and Audétat, 2020). Early metal-rich sulfides can then be broken down during crystallization and volatile exsolution, allowing metals to be transferred from the sulfide phase and into the exsolving fluids that lead to deposit formation (Audétat and Simon, 2012). The microanalysis of silicate melt inclusions (SMI) is a powerful tool to understand the metal budgets of intrusive systems spatially and temporarily associated with magmatic-hydrothermal ore deposits (e.g., Audétat and Pettke, 2003; Student and Bodnar, 2004; Halter et al., 2004, 2005; Audétat and Pettke, 2006; Grondahl and Zajacz, 2017). Silicate melt inclusions can be relatively unaffected by post-solidus processes. Thus, they may

preserve melt compositions at various stages of magma evolution allowing the influence of processes such as fractionation, assimilation, sulfide saturation, and degassing to be tracked In particular, they can provide insight into which magma(s) within composite intrusions were the most metal-endowed and what magmatic processes (e.g., magma mixing, assimilation) may have triggered the transfer of metals from the melt to the hydrothermal system (Halter et al., 2004).

1.2 PRIMARY THESIS OBJECTIVE AND STRUCTURE OF THESIS

This primary objective of this thesis is to document and characterize the magmatic evolution of the Mooshla Intrusive Complex (MIC) and characterize gold deposits hosted in the MIC through multiple microanalytical techniques to understand the role(s) and influence the intrusion may have played in the formation of the gold deposits.

This PhD dissertation is organized into five chapters. Chapters two to four are written as standalone manuscripts planned for submission, or already submitted, to peer-reviewed academic journals. Therefore, repetition may be present between chapters with respect to geological background and select methodologies. The title and primary objective of each chapter are listed below.

Chapter two is a manuscript entitled "**Constraints on the origin and metal fertility of the Archean Mooshla Intrusive Complex (MIC), Doyon-Bousquet-LaRonde mining district, Abitibi greenstone belt, Québec, Canada: Part I: Accessory mineral chemistry, thermobarometry, and geochronology**". This manuscript has been submitted to the Journal of Petrology (Accepted with Revisions) and utilizes a combination of petrography, high-precision CA-ID-TIMS zircon U-Pb geochronology, accessory mineral thermobarometry, and zircon trace element chemistry to provide the first high resolution constraints on the pressure-temperature-time evolution of this magmatic system.

Chapter three is a manuscript entitled "**Constraints on the origin and metal fertility of the Mooshla Intrusive Complex (MIC), Doyon-Bousquet-LaRonde mining district, Abitibi greenstone belt, Quebec, Canada, II: Silicate melt inclusions in magmatic zircon and quartz**" and has been submitted to the Journal of Petrology (In Review). This manuscript provides the first characterization of silicate melt inclusion hosted in quartz and zircon from an Archean intrusive complex that provide constraints on the major, minor, trace, and ore metal chemistry of magmas responsible for the formation of the Mooshla Intrusive Complex.

Chapter four is a manuscript entitled "**Ore mineralogy, sulfide geochemistry and S isotopes of magmatic-hydrothermal Au mineralization associated with the Mooshla Intrusive Complex (MIC), Doyon-Bousquet-LaRonde mining camp, Abitibi greenstone belt, Québec**". This manuscript is intended for publication in Mineralium Deposita or Economic Geology (plan to submit in Fall 2024). In this manuscript multiple microanalytical techniques are utilized to characterize the ore mineralization of two deposits hosted within the Mooshla Intrusive Complex to provide constraints on Au and ore metal precipitation mechanisms.

1.3 REFERENCES

Annen, C., Blundy, J.D., and Sparks, R.S.J., 2006, The genesis of intermediate and silicic magmas in deep crustal hot zones: Journal of Petrology, v. 47, p. 505-536.

Audétat, A., 2015, Compositional evolution and formation conditions of magmas and fluids related to porphyry Mo mineralization at Climax, Colorado: Journal of Petrology, v. 56, p. 1519-1546.

Audétat, A., and Pettke, T., 2003, The magmatic-hydrothermal evolution of two barren granites: A melt and fluid inclusion study of the Rito del Medio and Cañada Pinabete plutons in northern New Mexico (USA): Geochimica et Cosmochimica Acta, v. 67, p. 97-121.

Audétat, A., and Pettke, T., 2006, Evolution of a porphyry-Cu mineralized magma system at Santa Rita, New Mexico (U.S.A.): Journal of Petrology, v. 47, p. 2021-2046.

Audétat, A., and Simon, A.C., 2012, Magmatic controls on porphyry copper genesis: Society of Economic Geologists Special Publication 16, p. 553–572.

Botcharnikov, R.E., Linnen, R.L., and Holtz, F., 2010, Solubility of Au in Cl- and S-bearing hydrous silicate melts: Geochimica et Cosmochimica Acta, v. 74, p. 2396-2411.

Buret, Y., Wotzlaw, J-F., Roozen, S., Guillong, M., von Quadt, A., Heinrich, C.A., 2017, Zircon petrochronological evidence for a plutonic-volcanic connection in porphyry copper deposits: Geology, v. 45, p. 623-626.

Carter, L.C., Tapster, S.R., Williamson, B.J., Buret, Y., Selby, D., Rollinson, G.K., Millar, I. and Parvaz, D.B., 2022, A rapid change in magma plumping taps porphyry copper deposit-forming magmas: Scientific Reports, v. 12, p. 1-20, https://doi.org/10.1038/s41598-022-20158-y

Clemens, J.D., Yearron, L.M., and Stevens, G., 2006, Barberton (South Africa) TTG magmas: geochemical and experimental constraints on source-rock petrology, pressure of formation and tectonic setting: Precambrian Research, v. 151, p. 53-78.

Condie, K.C., 2005, TTGs and adakites: are they both slab melts?: Lithos, v. 80, p. 33-44.

De Almeida, J. A. C., Dall'Agnol, ., Oliveira, M.A., Macambira, M.J.B., Pimentel, M.M., Rämö, O.T., Guimarães, F.V., Leite, A.A.S., 2011, Zircon geochronology, geochemistry and origin of the TTG suites of the Rio Maria granite-greenstone terrane: implications for the growth of the Archean crust of the Carajás province, Brazil: Precambrian Research, v. 187, p. 201-221.

Du, J., and Audétat, A., 2020, Early sulfide saturation is not detrimental to porphyry Cu-Au formation: Geology, https://doi.org/10.1130/G47169.1.

Ferry, J.M., and Watson, E.B., 2007, New thermodynamic models and revised calibrations for the Ti-in-zircon and Zr-in-rutile thermometers: Contributions to Mineralogy and Petrology, v. 154, p. 429-437.

Franklin, J.M., Gibson, H.L., Jonasson, I.R., and Galey, A.G., 2005, Volcanogenic Massive Sulfide Deposits: Economic Geology 100th Anniversary Volume, p.523-560.

Galley, A.G., 2003, Composite synvolcanic intrusions associated with Precambrian VMS-related hydrothermal systems: Mineralium Deposita, v. 387, p. 443-473.

Galley, A.G., and Lafrance, B., 2014, Setting and evolution of the Archean synvolcanic Mooshla Intrusive Complex, Doyon-Bousquet-LaRonde mining camp, Abitibi greenstone belt: emplacement history, petrogenesis, and implications for Au metallogenesis: Economic Geology, v. 109, p. 205-229.

Getsinger, A., Rushmer, T., Jackson, M.D., and Baker, D., 2009, Generating high Mg-numbers and chemical diversity in tonalite-trondhjemite-granodiorite (TTG_ magmas during melting and melt segregation in the continental crust: Journal of Petrology, v. 50, p. 1935-1954.

Goldie, R., Kotila, B., and Seward, D., 1979, The Don Rouyn mine: An Archean porphyry copper deposit near Noranda, Quebec: Economic Geology, v. 74, p. 1680–1684.

Gosselin, G., 1998, Veines de Quartz Aurifères Précoces à la Zone Ouest de la Mine Doyon, Canton de Bousquet, Preissac, Abitibi: M.Sc. thesis, Université du Québec à Chicoutimi, 125 p.

Grondahl, C., and Zajacz, Z., 2017, Magmatic controls on the genesis of porphyry Cu-Mo-Au deposits: The Bingham Canyon example: Earth and Planetary Science Letters, v. 480, p. 53-65.

Halter, W.E., Pettke, T., and Heinrich, C.A., 2004, Laser-ablation ICP-MS analysis of silicate and sulfide melt inclusions in an andesitic complex II: evidence for magma mixing and magma chamber evolution: Contributions to Mineralogy and Petrology, v. 147, p. 397-412.

Halter, W.E., Heinrich, C.A., and Pettke, T., 2005, Magma evolution and the formation of porphyry Cu-Au ore fluids: evidence from silicate and sulfide melt inclusions: Mineralium Deposita, v. 39, p. 845-863.

Hart, T.R., Gibson, H.L., and Lesher, C.M., 2004, Trace element geochemistry and petrogenesis of felsic volcanic rocks associated with volcanogenic massive Cu-Zn-Pb sulfide deposits: Economic Geology, v. 99, p. 1003-1013.

Hayden, L.A., Watson, B.E., and Wark, D.A., 2008, A thermobarometer for sphene (titanite): Contributions to Mineralogy and Petrology, v. 155, p. 529-540.

Hoffman, J.E., Nagel, T.J., Münker, C., Naeraa, T., and Rosing, M.T., 2014, Constraining the process of Eoarchean TTG formation in the Itsaq Gneiss Complex, southern Greenland: Earth and Planetary Science Letters, v. 388, p. 374-386.

Katz, L.R., Kontak, D.J., Dubé, B., and McNicoll, V., 2017, The geology, petrology, and geochronology of the Archean Côté Gold large-tonnage, low-grade intrusion-related Au(-Cu) deposit, Swayze greenstone belt, Ontario, Canada: Canadian Journal of Earth Science, v. 54, p. 173-202.

Katz, L.R., Kontak, D.J., Dubé, B., McNicoll, V., Creaser, R., and Petrus, J.A., 2021, An Archean porphyry-type gold deposit: The Côté Gold Au(-Cu) deposit, Swayze greenstone belt, Superior province, Ontario, Canada: Economic Geology, v. 116, p. 47-89.

Keith, J.D., Whitney, J.A., Hattori, K., Ballantyne, G.H., Christiansen, E.H., Barr, D.L., Cannan, T.M., and Hook, C.J., 1997, The role of magmatic sulfides and mafic alkaline magmas in the Bingham and Tintic mining districts, Utah: Journal of Petrology, v. 38, p. 1679-1690.

Lafrance, B., Davis, D.W., Goutier, J., Moorhead, J., Pilote, P., Mercier-Langevin, P., Dubé, B., and Galley, A., 2005, Nouvelles datations isotopiques dans la portion quebecoise du Groupe de Blake River et des unites adjacentes: Ministere des Ressources naturelles et de la Faune, Québec Report RP 2005-01, 26 p.

Large, S.J.E., von Quadt, A., Wotzlaw, J-F., Guillong, M., and Heinrich, C.A., 2018, Magma evolution leading to porphyry Au-Cu mineralization at the Ok Tedi deposit, Papua New Guinea: trace element geochemistry and high-precision geochronology of igneous zircon: Economic Geology, v. 113, p. 39-61.

Large, S.J.E., Buret, Y., Wotzlaw, J.F., Karakas, O., Guillong, M., von Quadt, A., Heinrich, C.A., 2021, Copper-mineralised porphyries sample the evolution of a large-volume silicic magma reservoir from rapid assembly to solidification: Earth and Planetary Science Letters, v. 563, https://doi.org/10.1016/j.epsl.2021.116877.

Martin, H., 1999, Adakitic magmas: modern analogues of Archean granitoids: Lithos, v. 46, p. 411-429.

Martin, H., Smithies, R.H., Rapp, R., Moyen, J.-F., and Champion, D., 2005, An overview of adakite, tonalite-trondhjemite-granodiorite (TTG), and sanukitoid: relationships and some implications for crustal evolution: Lithos, v. 79, p. 1-24.

Maydagán, L., Franchini, M., Rusk, B., Lentz, D.R., McFarlane, C., Impiccini, A., Ríos, F.J., and Rey, R., 2015, Porphyry to Epithermal Transition in the Altar Cu-(Au-Mo) Deposit, Argentina, Studied by Cathodoluminescence, LA-ICP-MS, and Fluid Inclusion Analysis: Economic Geology, v. 110, p. 889-923.

McNicoll, V., Goutier, J., Dubé, B., Mercier-Langevin, P., Ross, P-S., Dion, C., Monecke, T., Legault, M., Percival, J., and Gibson, H., 2014, U-Pb geochronology of the Blake River Group, Abitibi greenstone belt, Quebec, and implications for base metal exploration: Economic Geology, v. 109, p. 27–59.

Mercier-Langevin, P., Dubé, B., Hannington, M.D., Davis, D.W., Lafrance, B., and Gosselin, G., 2007a, The LaRonde Penna Au-rich volcanogenic massive sulfide deposit, Abitibi greenstone belt, Quebec: Part 1. Geology and geochronology: Economic Geology, v. 102, p. 585−609.

Mercier-Langevin, P., Dubé, B., Hannington, M.D., Richer-Lafleche, M., and Gosselin G., 2007b, The LaRonde Penna Au-rich volcanogenic massive sulfide deposit, Abitibi greenstone belt,

Quebec: Part 2. Lithogeochemistry and paleotectonic setting: Economic Geology, v. 102, p. 611−631.

Mercier-Langevin, P., Dubé, B., Lafrance, B., Hannington, M., Galley, A., Moorhead, J., and Gosselin, P., 2007c, Metallogeny of the Doyon-Bousquet-LaRonde mining camp, Abitibi greenstone belt, Quebec: Geological Association of Canada, Mineral Deposits Division, Special Publication 5, p. 673−701.

Mercier-Langevin, P., Dubé, B., Fortin, D., 2021, The Doyon-Bousquet-LaRonde Mining Camp: Resources Mines & Industry, Fall 2021, p. 44-61.

Moyen, J.-F., and Martin, H., 2012, Forty years of TTG research: Lithos, v. 148, p. 312-336.

Müller, D., Franz, L., Herzig, P.M., and Hunt, S., 2001, Potassic igneous rocks from the vicinity of epithermal gold mineralization, Lihir Island, Papua New Guinea, v. 57, p. 163-186.

Mungall, J.E., Kamo, S.L., and McQuade, S., 2016, U-Pb geochronology documents out-of-sequence emplacement of ultramafic layers in the Bushveld Igneous Complex of South Africa: Nature Communications 7, 13385.

Park, J-W., Campbell, I.H., Kim, J., and Moon, J-W., 2015, The role of late sulfide saturation in the formation of a Cu- and Au-rich magma: Insights from the platinum group element geochemistry of Niuatahi-Motutahi lavas, Tonga rear arc: Journal of Petrology, v. 56, p. 59-81.

Park, J-W., Campbell, I.H., Malaviarachchi, S.P.K., Cocker, H., Hao, H., and Kay, S.M., 2019, Chalcophile element fertility and the formation of porphyry Cu ± Au deposits: Mineralium Deposita, v. 54, p. 657-670.

Perelló, J., Sillitoe, R.H., and Creaser, R.A., 2020, Mesoproterozoic porphyry copper mineralization at Mamainse Point, Ontario, Canada in the context of Midcontinent rift metallogeny: Ore Geology Reviews, v. 127, https://doi.org/10.1016/j.oregeorev.2020.103831.

Piercey, S.J., 2011, The setting, style, and role of magmatism in the formation of volcanogenic massive sulfide deposits: Mineralium Deposita, v. 46, p. 449-471.

Piercey, S.J., Chaloux, E.C., Péloquin, A.S., Hamilton, M.A., and Creaser, R.A., 2008, Synvolcanic and younger plutonic rocks from the Blake River Group: Implications for regional metallogenesis: Economic Geology, v. 103, p. 1243-1268.

Pilote, P., Robert, F., Sinclair, W.D., Kirkham, R.V., and Daigneault, R., 1995, Porphyry-type mineralization in the Doré Lake Complex: Clark Lake and Merrill Island areas: Geological Survey of Canada, Open File 3143, p. 65–86.

Qian, Q., and Hermann, J., 2013, Partial melting of lower crust at 10-15 kbar: constraints on adakite and TTG formation: Contributions to Mineralogy and Petrology, v. 165, p. 1195-1224.

Rapp, R.P., Watson, E.B., Miller, C.F., 1991, Partial melting of amphibolite/eclogite and the origin of Archaean trondhjemites and tonalites: Precambrian Research, v. 51, p. 1- 25.

Richards, J.P., 2003, Tectono-magmatic precursors for porphyry Cu-(Mo-Au) deposit formation: Economic Geology, v. 98, p. 1515-1533.

Richards, J.P., 2011, Magmatic to hydrothermal metal fluxes in convergent and collided margins: Ore Geology Reviews, v. 40, p. 1-26.

Seedorff, E., Barton, M.D., Stavast, W.J.A., and Maher, D.J., 2008, Root zones of porphyry systems: Extending the porphyry model to depth: Economic Geology, v. 103, p. 939-956.

Selby, D. and Creaser, R.A., 2001, Re-Os geochronology and systematics in molybdenite from the Endako porphyry molybdenum deposit, British Columbia, Canada: Economic Geology, v. 96, p. 197-204.

Smithies, R.H., 2000, The Archean tonalite-trondhjemite-granodiorite (TTG) series is not an analogue of Cenozoic adakite: Earth and Planetary Science Letters, v. 182, p. 115-125.

Student, J.J., and Bodnar, R.J., 2004, Silicate melt inclusions in porphyry copper deposits: identification and homogenization behavior: The Canadian Mineralogist, v. 42, p. 1583-1599.

Thomas, J.B., Watson, E.B., Spear, F.S., Shemella, P.T., Nayak, S.K., and Lanzirotti, A., 2010, TitaniQ under pressure: the effect of pressure and temperature on the solubility of Ti in quartz: Contributions to Mineralogy and Petrology, v. 160, p. 743-759.

Tomkins, H.S., Powell, R., and Ellis, D.J., 2007, The pressure dependence of the zirconium-in-rutile thermometer: Journal of Metamorphic Petrology, v. 25, p. 703-713.

Valliant, R.I., and Hutchinson, R.W., 1982, Stratigraphic distribution and genesis of gold deposits, Bousquet region, northwestern Quebec: Canadian Institute of Mining and Metallurgy Special Volume 24, p. 27−40.

Vezinet, A., Pearson, D.G., Thomassot, E., Stern, R.A., Sarkar, C., Luo, Y., and Fisher, C.M., 2018, Hydrothermally-altered mafic crust as source for early Earth TTG: Pb/Hf/O isotope and trace element evidence in zircon from TTG of the Eoarchean Saglek Block, N. Labrador: Earth and Planetary Science Letters, v. 503, p. 95-107.

Wall, C.J., Scoates, J.M, Weis, D., Friedman, R.M., Amini, M., and Meurer, W.P., 2018, The Stillwater Complex: integrated zircon geochronological and geochemical constraints on the age, emplacement history and crystallization of a large, open-system layered intrusion: Journal of Petrology, v. 59, p. 153-190.

Yergeau, D., Mercier-Langevin, P.L., Dubé, B., Malo, M., and Savoie, A., 2022a, The Westwood Deposit, Southern Abitibi Greenstone Belt, Canada: An Archean Au-Rich Polymetallic Magmatic-Hydrothermal System—Part I. Volcanic Architecture, Deformation, and Metamorphism: Economic Geology, v. 117, p. 545-575.

Yergeau, D., Mercier-Langevin, P.L., Dubé, B., McNicoll, V., Jackson, S.E., Malo, M., and Savoie, A., 2022b, The Westwood Deposit, Southern Abitibi Greenstone Belt, Canada: An Archean Au-

Rich Polymetallic Magmatic-Hydrothermal System—Part II. Hydrothermal Alteration, Mineralization, and Geologic Model: Economic Geology, v. 117, p. 577-608.

Zajacz, Z., Candela, P.A., Piccoli, P.M., Wälle, M., and Sanchez-Valle, C., 2012, Gold and copper in volatile saturated mafic to intermediate magmas: solubilities, partitioning, and implications for ore deposit formation: Geochimica et Cosmochimica Acta, v. 91, p. 140-159.

Zajacz, Z., Candela, P.A., Piccoli, P.M., Sanchez-Valle, C., and Wälle, M., 2013, Solubility and partitioning behavior of Au, Cu, Ag, and reduced S in magmas: Geochimica et Cosmochimica Acta, v. 112, p. 288-304.

Zhang, D., and Audétat, A., 2017, What caused the formation of the giant Bingham Canyon porphyry Cu-Mo-Au deposit? Insights from melt inclusions and magmatic sulfides: Economic Geology, v. 112, p. 221-244.

Chapter 2: Constraints on the origin and metal fertility of the Archean Mooshla Intrusive Complex (MIC), Doyon-Bousquet-LaRonde mining district, Abitibi greenstone belt, Québec, Canada: Part I: Accessory mineral composition, thermobarometry, and geochronology

Kevin Neyedley[1], Jacob J. Hanley[1], Patrick Mercier-Langevin[2, 3] James L. Crowley[4], Alexandra Tsay[5], Zoltán Zajacz[5] Mostafa Fayek[6], Ryan Sharpe[6]

[1] Department of Geology, Saint Mary's University, Halifax, Nova Scotia, Canada

[2] Geological Survey of Canada, Québec, Québec, Canada

[3]Current address: Agnico Eagle Mines Limited, Toronto, Ontario, Canada

[4] Isotope Geology Lab, Department of Geosciences, Boise State University, Boise, ID, USA

[5] Department of Earth Sciences, University of Geneva, Geneva, Switzerland

6 Department of Earth Sciences, University of Manitoba, Winnipeg, Manitoba, Canada

2.1 ABSTRACT

The Mooshla Intrusive Complex (MIC) is an Archean low-Al polyphase tonalite-trondhjemite-quartz diorite-gabbroic magmatic body located in the Doyon-Bousquet-LaRonde mining camp of the Abitibi greenstone belt, Québec, Canada. The MIC is spatially and temporally associated with numerous gold-rich volcanogenic massive sulfide (VMS), epizonal intrusion-related Au ± Cu, and shear zone-hosted orogenic gold and/or remobilized VMS deposits. The igneous units are grouped into two distinct stages, the tholeiitic to transitional Mouska-stage and the transitional to calc-alkaline Doyon stage. Using a combination of petrography, high-precision zircon U-Pb geochronology, accessory mineral thermobarometry, and zircon trace element compositions from the different phases that comprise the MIC this study provides new constraints on the pressure-temperature-time and compositional evolution of this magmatic system. The results demonstrate that individual phases crystallized relatively synchronously and likely in distinct magma chambers at deep levels within the crust (~700° to 800°C; ~0.5 to 1.2 GPa, 16 to 40 km), slightly cooler and shallower than conditions for tonalite-trondhjemite-granodiorite (TTG) magma generation. The entire intrusive complex formed over a maximum of ~1.44 Ma, with the formation of the Mouska and Doyon stages occurring within a ~1 Ma window. This indicates a rapid change in tectonic setting from a rift- to arc-dominated environment, early in the magmatic evolution of the MIC magmas. Based on distinct zircon trace element ratios and ranges associated with each of the individual MIC lithologies multiple, broadly coeval magma chambers were required at depth. Processes documented at the level of near-seafloor emplacement in this geological setting (e.g., from field relationships) do not fully capture the duration and compositional complexity of deep crustal magmatic processes that can be directly involved in the magmatic contributions of metals to Au-rich VMS and intrusion-related deposit styles in the Doyon-Bousquet-LaRonde mining camp and other similar environments in Archean terranes.

2.2 INTRODUCTION

The Mooshla Intrusive Complex (MIC) is an Archean polyphase magmatic body located in the Doyon-Bousquet-LaRonde mining camp of the Abitibi greenstone belt, Québec. The Doyon-Bousquet-LaRonde mining camp is hosted in the 2704–2695 Ma Blake River Group, consisting primarily of tholeiitic to transitional mafic volcanic rocks and transitional to calc-alkaline intermediate to felsic volcanic rocks (Lafrance *et al.*, 2005; McNicoll *et al*., 2014). Together with the Blake River Group volcanics, the MIC is spatially and temporally associated with numerous gold-rich volcanogenic massive sulfide (VMS; e.g., LaRonde Penna and Bousquet 2-Dumagami), epizonal intrusion-related Au ± Cu (e.g., Doyon), and shear zone-hosted orogenic gold and/or remobilized VMS mineralization (e.g., Mouska and Mic Mac) deposits. Historic gold production by the end of 2019 for the entire Doyon-Bousquet-LaRonde mining camp totaled 107.48 Mt with an average grade of 4.85 g/t Au equating to a total of 521 t (16.8 Moz) of Au (Mercier-Langevin *et al.,* 2021). Combining past production, current reserves, and estimated resources, the total Au budget of the camp is roughly 894 t (28.7 Moz) of Au, making it one of the most important precious metal districts in the Abitibi greenstone belt.

Previous studies (e.g., Valliant & Hutchinson, 1982; Gosselin, 1998; Mercier-Langevin, 2007a, b; Galley & Lafrance, 2014; Yergeau, 2022a, b) have highlighted a possible genetic link between the MIC and Au deposits in the area based on geochronology, mapping/field relations, petrography, and lithogeochemistry. However, direct evidence such as the age of mineralization itself, correlation of magmatic metal tenors with the ore metal tenors, evidence of coeval mineralization and degassing is lacking and, therefore, a genetic link between the MIC and Au deposits is still unclear. More generally, research on synvolcanic intrusive complexes associated with VMS districts has focused on establishing the emplacement sequence and level, as well as

using bulk rock methods (e.g., geochemistry, stable and radiogenic isotopes) to infer conditions of source melting, magma source affinity, and tectonic setting.

In the Archean, the composition of the synvolcanic intrusions underlying VMS deposits are most commonly low-Al (< 15 wt% Al_2O_3) tonalite–trondhjemite–diorite/granodiorite (TTD or TTG) composite intrusions (Galley, 2003). The MIC is primarily composed of tonalite, trondhjemite, and quartz diorite lithologies with subordinate gabbroic and diorite, classifying it as a TTD/TTG suite (Galley & Lafrance, 2014). Additionally, similar to the MIC, some other Archean TTG suites within or not within VMS districts are host to porphyry-style Cu-Au-Mo mineralization (e.g., Flavrian-Powell intrusive complex, Goldie *et al.,* 1979; Galley, 2003; Chester intrusive complex, Katz *et al.,* 2017, 2021; Chibougamau Pluton, Pilote *et al.,* 1995). The shallow to mid-crustal emplacement conditions suggested for synvolcanic intrusions in the VMS environment (~3-10 km) are considered to be essential to generate high heat flow in the shallow crust thereby driving the hydrothermal fluid convection cells, and the intrusion may contribute metals to the hydrothermal system through magmatic volatile exsolution (Galley, 2003; Franklin *et al.,* 2005 Piercey *et al.,* 2011). While the emplacement may be at relatively shallow crustal levels, the source conditions of these TTG suites are estimated to be at ~1 to >1.5 GPa and ~700° to 1000°C (e.g., Rapp *et al.,* 1991; Martin, 1999; Smithies, 2000; Hart *et al.,* 2004; Condie, 2005; Martin *et al.,* 2005; Clemens *et al.,* 2006; Piercey *et al.,* 2008; Getsinger *et al.,* 2009; De Almeida *et al.,* 2011; Moyen & Martin, 2012; Qian & Hermann, 2013; Galley & Lafrance, 2014; Hoffman *et al.,* 2014; Vezinet *et al.,* 2018). Conditions of source magma formation can be similar to the estimates for magmas generated in subduction zone settings that may lead to the formation of porphyry Cu ± Au deposits (e.g., Richards, 2003; Annen *et al.,* 2006; Carter *et al.,* 2022). However, these estimated conditions are obtained through experimental studies or inference from bulk rock geochemical patterns and ratios, and do not provide measured or direct thermobarometric constraints on the

source conditions, conditions of early-stage crystallization, and evolution within the magma chambers at depth for specific environments. Additionally, using bulk rock geochemistry to estimate these conditions can be challenging because intrusive rock compositions are typically modified by magmatic processes during ascent and at or near their emplacement level (e.g., contamination and assimilation, volatile exsolution), and/or by post-solidus processes (e.g., magmatic-hydrothermal alteration, metamorphic alteration). Therefore, data from bulk methods may be ambiguous. A question that is unclear in the TTG literature is understanding how these magmas, which were generated at depth, are transported to their final emplacement position at relatively shallow levels in the crust and what happens to these magmas along their ascent and crystallization path. In the porphyry Cu ± Au models, much of the literature has focused on the transport of magmas from mid-crustal magma chambers (~10-15 km depth) to their shallow emplacement, but less work has been done on how these magmas are transported from their deep source regions to these mid-crustal storage chambers (Richards, 2003; Annen *et al.,* 2006; Large *et al.,* 2021).

In order to better understand the magmatic history of a suspected TTG intrusion, and its possible role in the development of spatially- and temporally associated Au deposits in the Doyon-Bousquet-LaRonde mining camp, integration of field-based studies with *in-situ* analytical techniques is necessary to provide first order constraints on the evolution of potentially causative magmas. In particular, emphasis in the Doyon-Bousquet-LaRonde mining camp has been placed on field relationships to document the near surface emplacement sequence and attempting to link these sequences to the geochronological order of magma formation and evolution at depth. Previous geochronological techniques applied in the Doyon-Bousquet-LaRonde mining camp had relatively larger weighted mean errors (± 0.4 to 2.6 Ma) compared to what is possible using new high-resolution geochronology methods which employ the EARTHTIME ^{202}Pb-^{205}Pb tracer

solution (ET2535; Condon *et al.*, 2015; McLean *et al.*, 2015), which decreases analytical uncertainties, with weighted mean errors between 0.15 and 0.38 Ma. In other environments such as large mafic-ultramafic complexes (e.g., Bushveld, Stillwater), the simple magmatic stratigraphic sequence of emplacement based on field relationships is not consistent with new high-precision geochronology. These complexes were not formed/emplaced in a sequential geochronological order, but rather younger sills were injected into older units (Mungall *et al.*, 2016; Wall *et al.*, 2018). These results demonstrate that the apparent stratigraphic order of units at surface cannot solely be relied upon to construct the geochronological evolution of a system.

In porphyry Cu ± Au systems, coupling zircon trace element composition with geochronology from sequentially emplaced intrusive units within an intrusive complex or batholith provides evidence of systematic changes in the temperature and chemical evolution of magma chamber(s) during the lifetime of the magmatic system (e.g., Buret *et al.*, 2017; Large *et al.*, 2018, 2021; Carter *et al.*, 2022). Therefore, the analysis of zircon has the potential to provide insight into the temperature-chemistry-time evolution of an intrusive complex and constrain the duration of intrusive activity and metallogenic evolution. In addition, zircon is also a reliable geothermometer for estimating the temperature of crystallization based on its Ti concentration (Ti-in-zircon; Ferry & Watson, 2007). Other relevant geothermometers and geothermometers include the Zr-in-titanite (Hayden *et al.*, 2008) and Ti-in-quartz (Thomas *et al.*, 2010). In porphyry Cu ± Au ± Mo systems, a combination of these thermobarometers has been used to estimate the crystallization conditions of syn-mineralized felsic porphyries as well as in combination with fluid inclusion isochores to estimate the conditions of pre-, syn-, and post-mineralized quartz veining (e.g., Audétat, 2015; Maydagán *et al.*, 2015). However, very few studies have combined these thermobarometers to determine the pressure and temperature conditions of crystallization for relevant intrusive complexes in ore forming environments. A combination of techniques that see through secondary

processes (i.e., alteration and metamorphic events), and can quantitatively constrain source melting, magma chamber evolution and the age of the intrusives, can provide a better understanding of the role of synvolcanic intrusions associated with Au-rich VMS and affiliated deposits.

In this study, we utilize a combination of petrography and *in situ* techniques (e.g., mineral composition of zircon) and applicable geothermobarometry calibrations (e.g., Ti-in-quartz ; Ti-in-zircon ; Zr-in-titanite) to provide pressure-temperature estimates and constraints on fractionation behavior on the early stages of crystallization within magma chamber(s) that sourced the MIC. Additionally, high-precision geochronology on multiple phases of the intrusion has been conducted to understand the timing between the different main stages of the MIC. Combining these methods allows us to evaluate the origin of suspected TTG magmas in a composite intrusion in the Doyon-Bousquet-LaRonde district and discuss the implications of these constraints on the evolution of Au-rich VMS and related deposits.

2.3 GEOLOGY OF THE DOYON-BOUSQUET-LARONDE MINING CAMP

The Doyon-Bousquet-LaRonde mining camp's geology and geologic setting of its contained mineral deposits have been described in detail by Gunning (1941), Fillion *et al.* (1977), Valiant & Hutchinson (1982), Marquis *et al.* (1990), Trudel *et al.* (1992), Lafrance *et al.* (2003, 2005), Mercier-Langevin *et al.* (2004, 2005, 2007b, 2011), Galley & Lafrance (2014), and Yergeau *et al.* (2022a, b). The mining camp contains > 28 Moz of Au, making it one of the world's largest Archean Au districts, and contains two world-class Au-rich VMS deposits (LaRonde Penna and Bousquet 2-Dumagami), two major Au-rich sulfide vein deposits (Bousquet 1 and Westwood), epizonal "intrusion-related" Au-Cu vein systems (Doyon and Westwood Zone 2 Extension), and shear-hosted Au deposits (Mouska and Mic Mac), along with a number of smaller Au occurrences

(Lafrance *et al.*, 2003; Mercier-Langevin *et al.*, 2007b, 2009, 2011, 2017; Yergeau *et al.*, 2022a, b).

The Doyon-Bousquet-LaRonde mining camp lies in the eastern portion of the Blake River Group (2704-2695 Ma; McNicoll *et al.*, 2014) of the Archean Abitibi greenstone belt in the Superior Province (Fig 2.1A; Mercier-Langevin, *et al.*, 2007b; Galley & Lafrance, 2014). In the mining camp, the Blake River Group strikes east-west and is a steeply dipping, south-facing homoclinal volcanic sequence (Lafrance *et al.*, 2003; Mercier-Langevin *et al.*, 2007b, Galley & Lafrance, 2014). The Blake River Group in the Doyon-Bousquet-LaRonde mining camp consists of the Hébécourt Formation in the north and the stratigraphically overlying and younger Bousquet Formation in the south (Fig. 2.1B; Lafrance *et al.*, 2003). Along the northern contact of the Blake River Group is the Lac Parfouru Fault, which separates the Hébécourt Formation from the sedimentary rocks of the Kewagama Group (<2686 Ma; Davis, 2002) and along the southern contact the Bousquet Formation is disconformably overlain by the sedimentary rocks of the Cadillac Group (<2687.4 ± 1.2 Ma; Lafrance *et al.*, 2005).

The Hébécourt Formation forms the base of the Blake River Group in the Doyon-Bousquet-LaRonde mining camp and is predominantly composed of massive to pillowed tholeiitic basaltic and basaltic andesite flows and sills (Lafrance *et al.*, 2003; Mercier-Langevin *et al.*, 2007b; Galley & Lafrance, 2014). The earliest evidence of VMS mineralization in the Doyon-Bousquet-LaRonde mining camp is present in minor rhyolite dome complexes near the upper contact of the Hébécourt Formation (Mouska and Mic Mac deposits; Belkabir & Hubert, 1995).

Overlying the Hébécourt Formation is the Bousquet Formation which is divided into two members: the tholeiitic to transitional (tholeiitic to calc-alkaline) lower member and the transitional to calc-alkaline upper member (Lafrance *et al.*, 2005; Mercier-Langevin, 2007c). In the western portion of the Doyon-Bousquet-LaRonde mining camp quartz porphyritic rhyolite sills (unit 2.1;

2698.6 ± 1.5, Lafrance *et al.*, 2005) intruded along the upper contact of the Hébécourt Formation and form the lowermost unit of the lower Bousquet Formation (Galley & Lafrance, 2014). Above unit 2.1, intermediate composition scoriaceous tuffs and tuff-breccias predominantly contain basaltic to andesitic fragments (unit 3.3; 2695.4 +2.6/-1.7 Ma; Mercier-Langevin, 2008; Ross *et al.*, 2011). These tuffs are overlain by tholeiitic to transitional schistose massive to pillowed, mafic to intermediate flows of unit 4.4 (Lafrance *et al.*, 2003). Intrusions of glomeroporphyritic dacite (unit 4.2; 2698.3 ± 0.9 Ma, Lafrance *et al.*, 2005) and rhyolitic to dacitic schists (unit 4.3a) were emplaced as sills near the contact between units 3 and 4.4 (Yergeau *et al.*, 2022a, b). These shallow intrusive units are host to the Zone 1 and a portion of the Zone 2 lenses of the Doyon Au (± Cu) deposit (Savoie *et al.*, 1991; Galley & Lafrance, 2014). The upper member of the Bousquet Formation is composed of dacitic to rhyodacitic flows, and flow breccias (Lafrance *et al.*, 2003; Mercier-Langevin, 2007a, c). It is the upper member of the Bousquet Formation that is host to a majority of the Au-rich VMS deposits in the Doyon-Bousquet-LaRonde mining camp (Fig. 2.1B; i.e., LaRonde Penna, Bousquet 2-Dumagami; Dubé *et al.*, 2007, 2014; Mercier-Langevin *et al.*, 2007a, 2009). Units 5.2b (rhyodacite-rhyolite), 5.3 (feldspar and quartz-phyric rhyolite), and 5.5 (upper felsic unit) of the upper Bousquet Formation have been dated at 2698.3 ± 0.8 Ma, 2697.8 ± 1 Ma, and 2697.5 ± 1.1 Ma, respectively (Mercier-Langevin, 2007a; McNicoll *et al.*, 2014).

At least three phases of deformation affected the lithologies of the Doyon-Bousquet-LaRonde mining camp (Langshur, 1990; Savoie *et al.*, 1991; Belkabir & Hubert, 1995). A weak, moderately inclined northeast-southwest foliation defines the first phase of deformation (D_1). A strong penetrative east-west fabric, with shear planes and faults that dip steeply to the south represents the second deformation phase (D_2). Dextral transpressive brittle-ductile faults related to the third phase of deformation (D_3) overprint D_2. Regional metamorphism in the camp ranges from greenschist- to amphibolite-facies and is approximately coeval with D_2. However, in the MIC,

unorientated porphyroblasts of actinolite and biotite suggest peak metamorphism slightly postdates D_2 (Tourigny *et al.*, 1989; Marquis *et al.*, 1990; Belkabir & Hubert, 1995; Dubé *et al.*, 2004; Mercier-Langevin, 2005).

2.4 GEOLOGY OF THE MOOSHLA INTRUSIVE COMPLEX

The emplacement of the MIC occurred along the contact between the Hébécourt and Bousquet Formations in the western portion of the Doyon-Bousquet-LaRonde mining camp and has an oval form of about 4x2 km (Fig. 2.2; Galley & Lafrance, 2014). The MIC is grouped into two distinct stages of formation: (i) Mouska stage consists of five intrusive phases (phases A-E) ranging from gabbro to tonalite; and (ii) Doyon stage comprises four intrusive phases (phases F-I) ranging from tonalite to trondhjemite (Fig. 2.2; Galley & Lafrance, 2014). Galley & Lafrance (2014) distinguished each intrusive phase by chemical composition, variable intrusion style, and by distinctive overprinting relationships. They provide visual representations of the magmatic emplacement and evolution of the MIC demonstrating that the Mouska-stage intrusive phases were emplaced along the contact of the Hébécourt Formation and the lower member of Bousquet Formation, whereas the Doyon-stage phases crosscut the Mouska stage and the lower member of the Bousquet Formation (see Fig. 12 and 13 in Galley & Lafrance, 2014). A comprehensive summary of the units from Galley & Lafrance (2014) can be found in the Supplementary Material Document. The MIC is crosscut by a large Proterozoic diabase dyke and D_2 shear zones crosscut and bound the intrusion to the north and south (Fig. 2.2; Galley & Lafrance, 2014). As well, a number of late north-south brittle-ductile faults dislocated the upper part of the MIC that is currently adjacent to the Lower Bousquet member (Galley & Lafrance, 2014).

The synvolcanic age of the MIC and coeval nature with the Bousquet Formation has been documented through field relationships and geochemistry (Galley & Lafrance, 2014), as well as U-

Pb geochronology. McNicoll *et al.* (2014) obtained a U-Pb zircon date of 2698.5 ± 0.4 Ma from a Mouska stage quartz diorite (Phase C) and Lafrance *et al.* (2005) dated a Doyon-stage trondhjemite (Phase H) at 2696.9 ± 1 Ma. Existing geochronology, suggest the MIC and Bousquet volcanics are coeval and is supported by similar geochemical compositions and evolutions. However, it should be noted that there is considerable overlap between the dates from all the Bousquet volcanics with the MIC and therefore it is not possible to reliably link the Mouska and Doyon stages of the MIC with the upper or lower Bousquet Formations.

2.5 METHODOLOGY

Initial sample collection involved sampling of outcrop and drill core. Outcrop samples were taken as far away from quartz veining and/or dykes/sills (when present) to obtain unaltered or minimally altered samples. Drill core samples were collected from two drill holes interpreted to represent a nearly complete stratigraphic column of the entire MIC (Galley & Lafrance, 2014; A. Galley, communication, 2016). Drill hole MSK-6-810 contains phase A (diorite), B (gabbro), and C (quartz diorite) of the Mouska stage and drill hole 1106-96 contains phase E (Doyon quartz diorite) of the Mouska stage and phases G (plagioclase-phyric tonalite), H (phyric trondhjemite), and I (aphyric trondhjemite) of the Doyon stage. Doyon-stage phase F (plagioclase-amphibole-phyric tonalite) and Mouska-stage phase D (tonalite) were not present in either of these drill holes. A drill hole that contains phase F (plagioclase-amphibole-phyric tonalite) could not be located, but phase D (tonalite; surface samples Stop 10 and 11) was collected from outcrop.

For detailed information on all analytical work performed in this study, refer to the Supplementary Material Document. Zircon and titanite mineral separation, scanning electron microscope cold cathodoluminescence (SEM-CL) imaging of zircon, and high-precision chemical abrasion isotope dilution thermal ionization mass spectrometry (CA-TIMS) was conducted at the

Boise State University Isotope Geology Laboratory. Scanning electron microscope back-scattered electron (SEM-BSE) imaging and hot CL, and electron probe microanalysis (EPMA) were conducted at Saint Mary's University and the University of Toronto, respectively. The major, minor, and trace element composition of accessory minerals (zircon, titanite, and quartz) was determined by laser ablation-inductively coupled mass spectrometry (LA-ICP-MS) at the Magmatic and Ore-Forming Processes Research Laboratory at the University of Toronto. Zircon trace element distribution maps (also by LA-ICP-MS) were obtained at the University of New Brunswick. Oxygen isotope ratios ($^{18}O/^{16}O$) of zircon were measured by secondary ion mass spectrometry (SIMS) at the Manitoba Isotope Research Facility, University of Manitoba.

2.6 RESULTS

2.6.1 Sample Petrography

Optical petrography and SEM-BSE imaging were used to characterize the mineralogy of representative phases of the MIC. In particular, the textural relationships between major and accessory igneous minerals (zircon, titanite, allanite, epidote, apatite) were established as these relationships are relevant to the crystallization sequence of the MIC phases prior to, during, and following emplacement.

2.6.1.1 Gabbro (Phase B; MSK-6-810-715.6)

Sample MSK-6-810-715.6 (referred to here as Mouska-stage gabbro or gabbro) is a medium- to coarse-grained gabbro with adcumulate plagioclase and amphibole (after pyroxene; cf Galley & Lafrance, 2014) with some plagioclase and amphibole showing subophitic texture. Quartz comprises 1-2 vol% of the sample, is subhedral, and occurs as a late, interstitial phase between plagioclase and amphibole (Fig. 2.3A). Trace amounts of apatite, zircon, and ilmenite are present

and occur along grain boundaries between major rock forming minerals (i.e., plagioclase-amphibole, plagioclase-plagioclase, and amphibole-amphibole grain boundaries). Overall, the sample is moderately altered with some pervasive epidote alteration of plagioclase and chloritization of amphibole. Zircon is euhedral to subhedral, ranges from 90 to 500 μm in diameter and has aspect ratios of 1:1 to 1:2 (width:length; Table 2.1). Cold SEM-CL imaging show zircon with both oscillatory and sector zoning (Fig. 2.4A).

2.6.1.2 Quartz diorite (Phase C; MSK-6-810-493.7)

Sample MSK-6-810-493.7 (low-Th/U quartz diorite; see zircon composition section below for description) is a medium- to coarse-grained quartz diorite with 5-15 vol% interstitial quartz that has planar boundaries with earlier plagioclase and amphibole (former primary pyroxene?; Fig. 2.3B; cf Galley & Lafrance, 2014). Hot CL colour response for quartz shows short-lived blue colours typical of magmatic quartz (whereas metamorphic quartz is generally purple to red-brown in amphibolite to greenschist facies rocks, respectively; Fig. 2.3C; Götze *et al.*, 2001 and references therein). Trace amounts of apatite, zircon, and ilmenite are present. These trace mineral phases occur along grain boundaries between quartz, plagioclase, and/or amphibole (e.g., Fig. 2.3B). Epidote alteration of plagioclase is present but is less intense than in sample 715.6. Zircon grains are euhedral to subhedral, range from 100 to 620 μm in diameter and have aspect ratios of 1:1 to 1:3 (Table 2.1). Cold SEM-CL imaging reveals zircon with both oscillatory and sector zoning (Fig. 2.4B).

2.6.1.3 Quartz diorite (Phase C; MSK-6-810-127.6)

Sample MSK-6-810-127.6 (high-Th/U quartz diorite) is another sample of quartz diorite but is slightly finer grained than 493.7, contains only minor amounts of amphibole, and has

plagioclase highly altered to sericite instead of epidote (Fig. 2.3D). Biotite occurs in grain clusters throughout the sample and is likely an alteration product after hornblende or pyroxene. Biotite can be completely or partially altered to chlorite as well as partially replaced by rutile. Trace amounts of apatite and zircon occur along plagioclase and quartz grain boundaries. Zircon is subhedral to anhedral, ranges from 100 to 400 μm in diameter and has aspect ratios of 1:1 to 1:4 (Table 2.1). Cold SEM-CL imaging reveals that zircon displays both oscillatory and sector zoning (Fig. 2.4C). Unlike zircon from other samples, zircon in this quartz diorite has resorption features occurring between internal (i.e., core) and external (i.e., rim) zones, indicating that partial dissolution of zircon occurred (Fig. 2.4C).

2.6.1.4 Tonalite (Phase D; Stop 10/ Stop 11)

Tonalite samples from Stop 10 and Stop 11 are very similar. Both are medium- to coarse-grained with plagioclase (moderately altered to sericite) and quartz (up to ~50 vol%) showing textures reminiscent of adcumulates in mafic-ultramafic rocks suggesting that they are coeval. Trace amounts of apatite, zircon, and ilmenite are hosted along grain boundaries between plagioclase and quartz (Fig. 2.3E, F). Rarely, apatite is partially overgrown by zircon (Fig. 2.3F). Titanite (1-2 vol%) in both samples displays similar characteristics, occurring as weakly to moderately fractured, subhedral grains (and grain aggregates). Titanite grains are 100-700 μm in diameter and occur as interstitial relative to plagioclase and quartz (Fig. 2.5A, B). However, in Stop 10 remnant (i.e., remaining after partial replacement) inclusions, or partial inclusions, of Fe-Ti-oxides (ilmenite, magnetite, rutile) are present in titanite (Fig. 2.5B) whereas in Stop 11, titanite is devoid of any Fe-Ti-oxide inclusions (Fig. 2.5A, D). SEM-BSE images show titanite with oscillatory zoning (Fig. 2.5E), whereas other grains of titanite show simple, or very weak zoning patterns that are likely an artifact of the orientation of the grain in the polished mount (Fig. 2.5F).

Epidote and allanite occur as subhedral grains occurring as late, interstitial phases with roughly planar grain boundaries with (i.e., appearing like an intercumulate phase) plagioclase and quartz (Fig. 2.5D, G-J). Epidote commonly shows mutual grain boundaries with titanite (Fig. 2.5D). In cross-polarized light, allanite is often moderately to strongly zoned (Fig. 2.5H, J). Zircon is euhedral to subhedral, ranges from 100 to 560 μm in diameter and has aspect ratios of 1:1 to 1:3 (Table 2.1). Cold SEM-CL imaging reveals that zircon displays both oscillatory and sector zoning (Fig. 2.4D, E).

2.6.1.5 Aphyric trondhjemite (Phase I; 1106-96-1323/1106-96-1444.5)

Trondhjemite samples 1106-96-1323 and -1444.5 are fine- to medium-grained and commonly displays graphitic texture between plagioclase and quartz. Plagioclase is weakly altered to sericite and trace amounts of zircon occur along grain boundaries between plagioclase and quartz (Fig. 2.3G). Epidote occurs in both samples as a late interstitial phase between plagioclase and quartz (Fig. 2.5K). Separated zircon grains are much finer grained compared to all other samples with grains ranging from 50 to 160 μm in diameter. Zircon grains are euhedral to subhedral, have aspect ratios of 1:1 to 1:2, and display oscillatory and sector zoning (Fig. 2.6A, B; Table 2.1).

2.6.2 Zircon Composition

Zircon from three phases of the Mouska stage (gabbro, quartz diorite, and tonalite) and one phase from the Doyon stage (aphyric trondhjemite) of the MIC were analyzed for trace elements by LA-ICP-MS to evaluate changes in magma composition throughout the evolution of the MIC. Core and rim zones of individual zircon grains were analyzed to evaluate relative changes in magma composition during crystallization of the parental magmatic phases. Full zircon LA-ICP-MS results are tabulated in Supplementary Materials Table 2.1. Spot locations for LA-ICP-MS

analyses were selected based on transmitted light petrography and CL images. Care was taken to avoid melt and mineral inclusions in zircon during analysis to avoid contamination from these phases.

Zircon trace element compositions show two distinct grain populations based on Th/U ratios. All phases of the MIC generally have low Th/U ratios ranging from 0.4 to 1.65, but one sample of phase C quartz diorite has distinctly higher Th/U ratios, ranging from 1.65-2.95. Therefore, the two different quartz diorite samples will be referred to as low-Th/U quartz diorite and high-Th/U quartz diorite. The Ti concentrations are slightly different for the low- and high-Th/U populations, with the low-Th/U group having Ti contents < 18 ppm, while the high-Th/U group has Ti contents ranging from 9 to 25 ppm.

The REE concentrations in zircon and titanite (presented later in results section) were normalized to chondritic values from McDonough & Sun (1995). Chondrite normalized REE patterns are very similar for all MIC phases and both low- and high-Th/U zircon populations, with all showing relative enrichment in heavy rare-earth elements (HREE) and depletion in light-rare earth elements (LREE), a negative Eu anomaly ($Eu/Eu^* = Eu_n/[Sm_n \times Gd_n]^{½}$; where "n" indicates chondrite-normalized zircon values), and a positive Ce anomaly ($Ce/Ce^* = Ce_n/[La_n \times Pr_n]^{1/2}$; Fig. 2.7). However, since concentrations of La and Pr in zircon are often below the limits of detection and contamination by LREE-rich mineral inclusions (e.g., apatite), the traditional equation to calculate the Ce anomaly may lead to false estimates. Loader *et al.* (2017) proposed using the equation $Ce/Ce^* = Ce_n/[Nd_n^2/Sm_n]$ to calculate the Ce anomaly (used in this study) based on the greater compatibility of Sm and Nd in zircon compared to La and Pr.

Titanium contents in zircon of the Mouska-stage gabbro range from 4.07 to 13.21 ppm (~8.06 ± 1.85 ppm; 1σ; n = 70) and zircon cores (8.59 ± 1.47 ppm; n = 18) are slightly elevated in Ti compared to zircon rims (7.87 ± 1.95 ppm; n = 52; Fig. 2.8A). Of the two quartz diorite samples,

the high-Th/U quartz diorite has higher zircon Ti contents (~15.1 ± 3.20 ppm; n = 45) compared to low-Th/U quartz diorite (493.7; ~9.74 ± 2.39 ppm; n = 66; Fig. 2.8B). Cores and rims of zircon from the high-Th/U quartz diorite have mean Ti contents of 15.98 ± 3.02 ppm (n = 27) and 13.79 ± 3.09 ppm (n = 18), respectively, whereas low-Th/U quartz diorite zircon has mean core and rim concentrations of 10.87 ± 2.21 (n = 23) and rim 9.13 ± 2.28 (n = 43), respectively (Fig. 2.8B). The Ti-in-zircon concentrations of phase D tonalite have means of ~7.69 ± 2.24 ppm (n = 46) and ~8.19 ± 2.12 ppm (n = 56) for samples Stop 10 and Stop 11, respectively (Fig. 2.8C). Zircon rims for Stop 10 (~7.25 ± 1.75 ppm; n = 36) and Stop 11 (~7.58 ± 1.53; n = 42) are slightly depleted in Ti compared to the zircon core for each sample, with Stop 10 and Stop 11 Ti core concentrations of ~9.30 ± 3.10 ppm (n = 10) and ~10.01 ± 2.61 (n = 14), respectively (Fig. 2.8C).

The Doyon-stage phase I aphyric trondhjemite has similar Ti-in-zircon contents between the two samples analyzed with means of ~8.10 ± 1.12 ppm (n = 19) and ~8.13 ± 1.37 ppm (n = 20) for samples 1323 and 1444.5, respectively, and there are no appreciable differences between core and rim analyses (Fig. 2.8D).

All Mouska-stage lithologies (gabbro, quartz diorite, tonalite) of the MIC have similar ranges in Hf content in zircon, ~7,500 and ~11,000 ppm (Fig. 2.8E-G). Zircon from the Doyon-stage aphyric trondhjemite has a smaller range in Hf contents, from ~7,500 to ~9,000 ppm (Fig. 2.8H). For all samples, Hf concentrations generally increase with decreasing Ti concentration.

Zircon from the Mouska-stage gabbro and high-Th/U quartz diorite have similar mean Eu/Eu* values of ~0.25 ± 0.03 (n = 70; Fig. 2.9A) and ~0.27 ± 0.03 (n = 45; Fig. 2.9B), respectively, whereas the low-Th/U quartz diorite zircon has a slightly higher Eu/Eu* value of ~0.32 ± 0.02 (n = 66; Fig. 2.9B). Both samples of Mouska-stage tonalite have the highest zircon Eu/Eu* values of all samples: 0.36 ± 0.01 (n = 46) and 0.37 ± 0.02 (n = 56) for Stop 10 and 11, respectively (Fig.

2.9C). Both samples of the Doyon-stage aphyric trondhjemite have similar zircon Eu/Eu* values of 0.25 ± 0.02 (n = 19) and 0.27 ± 0.03 (n = 19) for 1323 and 1444.5, respectively (Fig. 2.9D).

Values of zircon Ce/Ce* are quite variable in all lithologies, with ranges from 6 to 80, 9 to 150, 10 to 65, 10 to 40, for the gabbro, both quartz diorites, tonalite, and trondhjemite, respectively (Fig. 2.9A-D). Interestingly, zircon from the high- and low-Th/U quartz diorite have nearly identical variation in Ce/Ce* (Fig. 2.9B). Values of Ce/Ce* >40 are predominately in zircon rim analyses, with only a few core analyses >40 in the gabbro, quartz diorites, and tonalites. However, it is important to note that not all zircon rim analyses are >40, and that most rim analyses overlap with core Ce/Ce* values. Comparing zircon Ce/Ce* and Eu/Eu* values (Fig. 2.9A-D), no correlations are evident, except for in the gabbro, where some of the highest Ce/Ce* values correspond to the lowest Eu/Eu* values (Fig. 2.9A).

Overall, the general zircon trace element composition from each MIC phase are similar and consistent with a magmatic origin based on the follow parameters of Hoskin & Schaltegger (2003): I) consistent compositions within a given sample, II) Th/U ratios < 4, III) LREE < HREE normalized profile, IV) a moderate to large negative Eu anomaly, and V) a positive Ce anomaly. Additionally, *in situ* zircon $\delta^{18}O$ compositions (~5.0 ± 1.0; 1σ; n=160) are consistent with magmatic values (5.3 ± 0.3 ‰; Valley *et al.*, 1998) and are similar to zircon $\delta^{18}O$ values from the previous studies on the MIC and the Upper and Lower Bousquet Formations (Supplementary Material Table 2.2; cf Mole *et al.*, 2021).

2.6.3 Zircon Trace Element Distribution Maps

In addition to LA-ICP-MS spot analyses from individual zircon grains, representative LA-ICP-MS quantitative trace element distribution maps were also obtained from 6 grains. Grains

mapped were from the low-Th/U quartz diorite and tonalite. Cathodoluminescence and SEM-BSE images of some of the mapped zircon grains are shown in Figures 2.10A, 2.11A, 2.12A, and 2.13A.

Consistent with results of spot analyses, Ti distribution maps for all mapped zircon grains show a decrease in Ti and increase in Hf concentrations from core to rim (Figs. 2.10B, C, 2.11B, C, 2.12B, C, and 2.13B, C). Additionally, in a grain from the low-Th/U quartz diorite, the Hf concentration shows an oscillatory pattern, indicating oscillation in magma Zr/Hf ratio during growth of zircon (Fig. 2.10C). This oscillation in Hf is mimicked by Ce, Eu, Lu, and Th/U.

In a grain from the low-Th/U quartz diorite, REE concentrations and the Th/U ratio show similar oscillations (Fig. 2.10D-G). However, in the grain fragments from the low-Th/U quartz diorite (Fig. 2.11D-G), REE concentrations and the Th/U ratio show different patterns compared to the grain in Figure 2.10. In Figure 2.11, HREE and MREE are concentrated in the core and concentrations decrease towards the rim, however Ce concentrations do not follow this same pattern (Fig. 2.11D). In all grains mapped, Nb and Ta are enriched in the same zones as Ce. The Th/U ratio within all grains mapped varies as well. In the full zircon grain map from the low-Th/U quartz diorite, the Th/U ratio mimics the Hf oscillatory profile (Fig. 2.10G). Whereas, in Figure 2.11G, the Th/U ratio is the highest in the core and decreases sharply, coinciding with an increase in Ce and a decrease in Eu concentrations (Fig. 2.11D and E). Zircon trace element distribution maps in the tonalite and quartz diorite are similar, showing sector zoning, and both non-oscillatory or oscillatory zoning (compare Fig. 2.12D-F, 2.13D-F). Maps of Eu/Eu* in zircon for both the quartz diorite and tonalite do not show variations within individual grains (Fig. 2.10H, 2.11H, 2.12H, 2.13H).

2.6.4 High Precision CA-ID-TIMS U-Pb Geochronology

Fifty single zircon grains from the earlier emplaced Mouska-stage gabbro, quartz diorite, and tonalite, and from the later-emplaced phyric and aphyric trondhjemites from the Doyon stage of the MIC were dated by CA-ID-TIMS (Fig. 2.14; Supplementary Materials Table 2.3). Grains selected for dating (Figs. 2.4, 2.6) were selected based on trace element composition determined by LA-ICP-MS (e.g., composition consistent with a magmatic origin) and screened for CL characteristics (e.g., a lack of inherited cores and resorption surfaces, no metamorphic overgrowths).

2.6.4.1 Mouska stage

Six grains from the gabbro (phase B) yield a weighted mean date of 2698.47 ± 0.17 Ma (MSWD = 0.5, probability of fit [pof] = 0.77; Fig. 2.14; Fig 2.15A). Zircon from both the high- and low-Th/U quartz diorite (phase C) were analyzed. Five grains from the high-Th/U quartz diorite yield a weighted mean date of 2698.53 ± 0.21 Ma (MSWD = 1.1, pof = 0.33, n = 5; Fig. 2.14; Fig 2.15B), with a slightly older grain with a date of 2699.26 ± 0.37 Ma that is interpreted as containing an inherited component. Six grains from the low-Th/U quartz diorite yield a weighted mean date of 2698.34 ± 0.16 Ma (MSWD = 0.2, pof = 0.94, n = 6; Fig. 2.14; Fig. 2.15C) that overlaps with the date from the high-Th/U quartz diorite. Two samples from the Mouska-stage tonalite (phase D; Stop 10 and 11) were analyzed and seven grains from Stop 10 yield a weighted mean date of 2698.38 ± 0.15 (MSWD = 0.9, pof = 0.5, n = 7; Fig. 2.14; Fig. 2.15D), and one grain with a date of 2699.13 ± 0.30 is interpreted as containing an inherited component. Six grains from Stop 11 yield a weighted mean date of 2698.71 ± 0.17 Ma (MSWD = 1.1, pof = 0.35, n = 6; Fig. 2.14; Fig. 2.15E), the oldest of all samples analyzed.

2.6.4.2 Doyon stage

Four grains from a sample from the phyric trondhjemite (phase H; Bousquet 4; Fig. 2.6C), which previously yielded a weighted mean date of 2696.9 ± 1.0 Ma (Lafrance *et al.*, 2005), yield an older and more precise weighted mean date of 2698.80 ± 0.38 (MSWD = 0.4, pof = 0.78, n = 4; Fig. 2.14; Fig. 2.15F). Two samples from the aphyric trondhjemite (phase I; 1323 and 1444.5) were dated. Six grains from sample 1323 yield a weighted date of 2698.37 ± 0.24 (MSWD = 0.6, pof = 0.7, n = 6; Fig. 2.14; Fig. 2.15G). Six grains from sample 1444.5 yield a weighted mean date of 2697.96 ± 0.22 Ma (MSWD = 1.4, pof = 0.23; Fig. 2.14; Fig. 2.15H), and dates from two grains were discordant (0.7%) and were not included in the weighted mean calculation.

2.6.5 Titanite Composition

Major and minor element compositions of titanite were determined for two samples from the Mouska-stage tonalite of the MIC (phase D; Stop 10 and Stop 11) and results are presented in Supplementary Materials Table 2.4 and 2.5. Both samples have a relatively narrow range in Fe content of 0.02 - 0.05 and 0.02 - 0.06 atoms per formula unit (apfu) for Stop 10 and Stop 11, respectively (Fig. 2.16A). Aluminum contents for Stop 10 titanite range from 0.02 to 0.15 apfu, with 90% of the analyses ranging from 0.02 to 0.04 apfu (Fig. 2.16A). Titanite from Stop 11 has Al contents between 0.03 to 0.13 apfu, with 85% of the analyses ranging between 0.03 and 0.06 apfu (Fig. 2.16A). Aluminum and Fe contents display a negative correlation with Ti, which is consistent with the substitution (Al, Fe^{3+}) + (F, OH) ↔ Ti + O (Tiepolo *et al.*, 2002; Fig. 2.16B).

Trace element concentrations were also determined in titanite, including Zr, which was measured in order to apply the Zr-in-titanite thermometer of Hayden *et al.* (2008). Full titanite LA-ICP-MS results are in tabulated Supplementary Materials Table 2.5. Care was taken to avoid fractures and mineral inclusions in titanite during analysis to avoid any contamination.

The Zr content is highly variable in titanite from both samples, ranging from 26 to 82 ppm (~51 ± 17.6 ppm; n = 18) and 85 to 524 ppm (~241 ± 126 ppm; n = 14) at Stop 10 and 11, respectively. Using BSE greyscale contrast as a guide, light and dark zones in titanite have some differences in trace element concentrations. Both samples show that dark-BSE zones have ΣREE concentrations between 5,300 and 10,600 ppm whereas light-BSE zones have concentrations between 10,400 and 16,600 ppm. The trace elements Y, Nb, As, and Sn are relatively enriched in light-BSE zones and no systematic difference in Zr concentration exists between dark- and light-BSE zones.

Chondrite-normalized REE patterns (Fig. 2.16C, D) are consistent between titanite from the two samples of Phase D tonalite, with enrichment in middle rare-earth elements (MREE) over LREE and HREE, typical of magmatic titanite (Rasmussen *et al.,* 2013; Aleinikoff *et al.,* 2002; Fig. 2.16C, D). The magnitude of the negative Eu anomaly in titanite grains is similar within a given sample but is slightly different between the two samples with Stop 10 and Stop 11 (Eu/Eu* = 0.34 ± 0.09; [n = 18] vs. 0.25 ± 0.08; [n = 14]), respectively.

2.6.6 Quartz Ti Content

Magmatic quartz from the gabbroic, quartz diorite, and tonalite phases of the Mouska stage and the aphyric trondhjemite of the Doyon stage of the MIC were analysed by LA-ICP-MS to determine Ti concentration in order to apply the modified Ti-in-quartz thermometer of Thomas *et al.* (2010). Quartz from the gabbro and low-Th/U quartz diorite have mean Ti contents of 84 ± 27 ppm (n = 27) and 118 ± 30 ppm (n = 62), respectively. Quartz from the high-Th/U quartz diorite has higher mean Ti contents compared to the low-Th/U quartz diorite, with a mean of 174 ± 36 ppm Ti (n = 13). Quartz from the two tonalite samples have mean Ti contents of 140 ± 31 ppm (n = 20) and 110 ± 26 ppm (n = 9), for samples Stop 10 and Stop 11, respectively. Quartz from three

different samples of the aphyric trondhjemite (samples 534.8, 1323, and 1444.5) yielded mean Ti contents of 79 ± 29 (n = 16), 177 ± 33 ppm (n = 20), and 155 ± 41 ppm (n = 21), respectively. Titanium-in-quartz concentrations are tabulated in Supplementary Materials Table 2.6.

2.6.7 Mineral Thermometry

The Ti-in-zircon (Ferry & Watson, 2007), Zr-in-titanite (Hayden *et al.,* 2008), and Ti-in-quartz (Thomas *et al.,* 2010; Osborne *et al.,* 2022) thermometers were collectively applied to the MIC lithologies to estimate conditions in an evolving magmatic system. Mineral thermometers utilized in this study and summarized below, are justified based on petrographic relationships that show coeval crystallization (e.g., mineral inclusions, mutual grain boundary relationships) and by mineral compositions consistent with magmatic origins (see relevant sections above). Each thermometer is dependent on specific parameters being constrained in the system, including the activities of SiO_2 ($a$$SiO_2$) and TiO_2 ($a$$TiO_2$), and pressure (GPa). The $a$$SiO_2$ is required for all thermometers except the Ti-in-quartz thermometer for which it was set to 1, based on the presence of magmatic quartz in all samples (Ferry & Watson, 2007). All thermometers require a constraint on $a$$TiO_2$. Based on the occurrence of magmatic titanite and/or Fe-Ti-oxides in the tonalite (phase D) and aphyric trondhjemite (phase I; samples 1323 and 1444.5), $a$$TiO_2$ was set to 0.7 (e.g., Fig. 2.5A-D; Ferry & Watson, 2007; Hayden & Watson, 2007; Chelle-Michou *et al.,* 2014; Large *et al.,* 2018). For the gabbroic and quartz diorite lithologies, $a$$TiO_2$ was set to 1 because of the presence of accidentally trapped rutile in quartz- and zircon-hosted silicate melt inclusions, which would indicate rutile was a co-crystallization phase with quartz and zircon (Neyedley *et al.,* 2024, companion paper). An uncertainty in $a$$TiO_2$ of ± 0.1 results in an error of ± 15°C, ± 10°C, and ± 5°C over the calculated temperature range for the Ti-in-Zircon, Ti-in-quartz, and Zr-in-titanite thermometers, respectively. The Ti-in-zircon thermometer (Ferry & Watson, 2007) was calibrated

at 1 GPa and is sensitive to pressure but the equation does not require pressure to be known. The associated error for the Ti-in-zircon thermometer is 50°C/GPa. Pressure of crystallization is currently unconstrained for the MIC, so no pressure correction is applied to the temperature calculations. Since pressure is currently unconstrained, we cannot directly use the Zr-in-titanite or Ti-in-quartz because these equations are all dependant on the crystallization pressure.

Based on individual spot analyses mean zircon crystallization temperatures for the gabbro are 724° ± 22°C (1σ; n = 70), with similar temperatures between zircon cores (731° ± 16°C; n = 18) and rims (721° ± 23°C; n = 52). The high-Th/U quartz diorite records the highest temperatures from all samples with mean of 784° ± 22°C (n = 45). The low-Th/U quartz diorite has mean crystallization temperature of 741° ± 23°C (n = 66). For both quartz diorite samples, cores are ~15°C higher than rims, with cores for the high- and low-Th/U quartz diorite being 790° ± 19°C (n = 27) and 752° ± 19°C (n = 23), respectively. Zircon in the tonalite from Stop 10 and 11 record similar crystallization temperatures with values of 752° ± 26°C (n = 46) and 758° ± 23°C (n = 56), respectively. For both Stops 10 and 11, zircon cores record ~20°C higher temperatures than rims, with cores being 769° ± 30°C (n = 10) and 778° ± 22°C (n = 14) and rims 747° ± 23°C (n = 36) and 752° ± 19°C (n = 42) for Stops 10 and 11, respectively. Both samples from the aphyric trondhjemite record identical mean temperatures with values of 759° ± 13°C (n = 19) and 759° ± 16°C (n = 20) for samples 1323 and 1445.4, respectively. No differences were noted between core and rim temperature in the aphyric trondhjemite.

2.7 DISCUSSION

2.7.1 Geochronological Evidence for Multiple, Coeval Magma Chambers Sourcing the MIC

In polyphase intrusive systems, high precision zircon U-Pb dating can constrain the crystallization age of individual rock units, thereby delineating the relative timing of

compositionally different magma chambers and duration of crystallization. For the MIC, Figure 2.14 summarizes individual and weighed mean dates for various phases of the MIC, arranged in order of inferred emplacement based on field observations (e.g., crosscutting relationships and xenolith populations among the different phases; Galley & Lafrance, 2014). Also shown in Figure 2.14 are previously published zircon U-Pb dates from the MIC and coeval volcanics of the Bousquet Formation for comparison. The U-Pb dates obtained in this study were calculated using the $^{238}U/^{235}U$ of Hiess *et al.* (2012) while the previously published dates used the $^{238}U/^{235}U$ of Jaffey *et al.* (1971). All published dates described here, and in Figure 2.2 and 2.14, were recalculated using the U decay constant of Hiess *et al.* (2012), and therefore are 0.74 Ma younger than the dates presented in their respective publications.

The new geochronological data have petrological implications to understanding the evolution of the MIC. The closure temperature of Ti (~1000°C; Cherniak & Watson, 2007) and Pb diffusion (~900°C; Cherniak & Watson, 2000) in zircon are well above our calculated temperatures from thermobarometry. Since TTG magmas form at relatively low temperature (only ~50° to 100°C above the solidus; Moyen & Martin, 2012) and petrographic evidence shows that zircon is a relatively early accessory mineral in the MIC lithologies, the calculated temperatures record an early stage of MIC magma crystallization.

All phases of the Mouska stage of the MIC have weighted mean dates within error of each other, suggesting zircon saturation (i.e., crystallization) in these magma chambers was occurring contemporaneously among the compositionally distinct magma phases over a maximum duration of ~0.70 Ma. The maximum duration of early crystallization related to the Doyon stage (and for the entire MIC) is ~1.44 Ma. A minimum duration of crystallization cannot be estimated for the MIC because the maximum age of the Doyon-stage aphyric trondhjemite (2698.80 ± 0.38 Ma) and minimum age of the Mouska-stage low-Th/U quartz diorite (2698.34 ± 0.16 Ma) overlap by ~1

Ma. This indicates that the two parental MIC magmas may have begun crystallizing in separate (but relatively coeval) magma chambers within ~1 Ma of each other. Previous geochronology data for the MIC reported a minimum age difference of 0.4 Ma between the Mouska and Doyon stages (Lafrance *et al.,* 2005; McNicoll *et al.,* 2014) but this time gap between the two stages in no longer valid (Fig. 2.14). Notably, the date determined in this study for the phyric trondhjemite (phase H; 2698.80 ± 0.38 Ma) is a minimum of 1.22 Ma older than previously reported (2696.2 ± 1.0 Ma; Lafrance *et al.,* 2005). As the zircons reported previously did not undergo chemical abrasion prior to TIMS analyses, the younger date previously reported may reflect the presence of metamict domains (Fig. 2.14; Lafrance *et al.,* 2005) that suffered Pb loss at ancient times. The slightly older date obtained in this study for the quartz diorite (2698.34 ± 0.16 Ma) compared to the published date of 2697.8 ± 0.4 Ma (McNicoll *et al.,* 2014) may also reflect this difference in sample treatment, as only half of the grains from McNicoll *et al.* (2014) analyzed underwent chemical abrasion (with the other half being air abraded) to produce a single weighted mean date. This new time scale (< 1.44 Ma) of magmatic activity significantly reduces the window of time previously thought (~3 Ma; Lafrance *et al.,* 2005; McNicoll *et al.,* 2014) it took the MIC to evolve, and this new window of time is comparable to the magmatic evolution of major Cu-Au porphyry systems (Large *et al.,* 2021).

Magma chambers for both the Mouska and Doyon stages began crystallizing over a similar time window. These magmas were tapped and mixtures of crystals + melt were transported from depth to the level of emplacement. The coeval nature of the Mouska and Doyon stages (i.e., ~1 Ma overlap between all lithologies; Fig. 2.14) appears inconsistent with the sequence of localized emplacement based on field and stratigraphic relationships (Galley and Lafrance, 2014; Mungall *et al.,* 2016; Wall *et al.,* 2018). Importantly, these cross-cutting relationships do not constrain the absolute duration of magmatism, whereas geochronology requires all of the individual lithologies

of the MIC to have been emplaced over a much shorter time window than previously determined. Within this time window, these localized cross cutting relationships developed but have no significant bearing on the coeval nature of these magmas at depth.

2.7.2 Zircon Trace Element Chemical Evolution

Trace element concentrations in zircon can be used to track magma evolution and crystal fractionation in composite intrusions (Lee *et al.,* 2017; Olson *et al.,* 2017; Large *et al.,* 2018; Lee *et al.,* 2020). In this study the distinct trends in zircon trace element composition in the MIC lithologies likely reflect distinct crystallizing accessory mineral assemblages that require multiple magmatic reservoirs evolving simultaneously at depth, consistent with the geochronological results (cf Claiborne *et al.,* 2006). The fractionation of minerals such as amphibole, apatite, and titanite can control trace element abundances and ratios in magmas due to high mineral-melt partition coefficients for select elements (e.g., Sm, Ce, Yb, Gd, Th, and U) and these changes in trace element abundances and ratios are recorded as zircon crystallizes from the same magma(s) (Blundy & Wood, 2003; Prowatke & Klemme, 2005, 2006; Richards & Kerrich, 2007; Rubatto & Hermann, 2007; Claiborne *et al.,* 2010; Large *et al.,* 2018). Below, such variations in trace element systematics recorded in the MIC zircon are explored.

Both Hf and Zr are incompatible elements; their concentrations will increase in a magma until zircon saturation is reached, after which there is a decrease of both Hf and Zr in the residual magma. However, this will cause the Zr/Hf ratio of the magma to decrease because Zr has a higher compatibility (as a major element) in zircon than Hf. Therefore, as zircon continues to crystallize the Hf content of zircon will increase over time as the Zr/Hf ratio of the melt decreases, corresponding to an increasing degree of magma fractionation (Claiborne *et al.,* 2006). All zircon from the Mouska-stage phases (gabbro, quartz diorite, tonalite) of the MIC show an increase in Hf

concentrations with decreasing temperature (Fig. 2.8A-C, Ti-in-zircon thermometer) consistent with cooling and zircon crystallization in a magma chamber (Claiborne *et al.,* 2006; Lee *et al.,* 2020). The aphyric trondhjemite of the Doyon stage also displays a weak correlation of decreasing Ti with increasing Hf (Fig. 2.8H). However, in examining core and rim analyses for individual grains, several zircon grains from the Mouska stage show an inverse relationship (i.e., increase in Ti coinciding to a decrease in Hf: Fig. 2.17A; cf Lee *et al.,* 2017), suggesting a magma recharge event occurred causing a reverse from the general cooling and fractionation trend. Additionally, the zircon trace element distribution map from the low-Th/U zircon quartz diorite (Fig. 2.10C) has a zone of elevated Hf in the central portion of the grain followed by an outward decrease in Hf, and then a build up of Hf towards the rim, also consistent with a magma recharge event.

Trace element ratios in zircon such as $(Yb/Gd)_n$, $(Sm/Ce)_n$, and Th/U provide a means to track the crystallization of minerals such as amphibole, titanite, allanite, and apatite. Modelling involving zircon and coeval accessory mineral (i.e., titanite, apatite, allanite, amphibole) formation under batch crystallization conditions demonstrates the effects these accessory minerals influence the trace element concentrations and ratios in the melt and co-crystallizing zircon. In particular, modelling can aid in understanding what accessory mineral(s) have the dominant control on melt and zircon composition. The batch crystallization modelling equation was utilized:

$$C^e_{solid} = C^e_{int} * (D / ((1-F)+D))$$

where C^e_{solid} = concentration of an element (e) in the final crystallized solids; C^e_{int} = concentration of an element (e) in the initial melt; D = bulk partition coefficient for a given element; and F = melt fraction. Mineral-melt partition coefficients utilized were from Bachmann *et al.* (2005; zircon and titanite), Prowatke & Klemm (2005; apatite), Hermann (2002; allanite), and Tiepolo *et al.* (2007; amphibole). The melt fraction (F) was held constant at 0.5, since at the temperature of zircon crystallization (~800°C) for a fluid-saturated dioritic-granodioritic melt at low pressure the system

would have been composed of crystals (~50%) and a significant melt fraction (~50%; cf Chelle-Michou *et al.*, 2017). This is likely to be an underestimate of the relevant value of F since for arc-related felsic-intermediate magmas formed at 1.0 to 1.5 GPa through melting of hydrous-amphibolite the melt fraction will be even higher (Moyen & Stevens, 2006). However, increasing or decreasing F does not influence the general trends produced by the crystallization of accessory minerals, but as F increases the range in $(Yb/Gd)_n$ and Th/U values increases and the range in $(Sm/Ce)_n$ decreases. Different scenarios of zircon + accessory mineral (e.g., titanite) were modelled to determine the relative changes individual minerals have on the zircon composition as well as the effect multiple, co-crystallizing accessory minerals have. Other minerals were considered (i.e., amphibole and apatite) but these exert a very weak control on the trace element ratios in zircon, having a negligible influence on Th/U, $(Yb/Gd)_n$, and $(Sm/Ce)_n$ ratios in zircon (cf Olsen *et al.*, 2017; Loader *et al.*, 2017).

Trajectories for crystallizing accessory minerals impacting zircon trace element compositions are shown in Figure 2.17B and C. The trajectories are based on the crystallization of single accessory minerals (i.e., zircon, titanite, and allanite) as they impact both zircon and melt composition incrementally (i.e., starting melt composition modified after each crystallization increment). As well, a trajectory is also show that reflects the co-crystallization of titanite and zircon at a proportion of 3:1 titanite to zircon. If zircon is the only accessory mineral crystallizing, $(Yb/Gd)_n$ and $(Sm/Ce)_n$ ratios will decrease and Th/U will increase in subsequently forming zircon due to the higher partition coefficients of Yb, Sm, and U into zircon (Fig. 2.17B and C). Adding titanite to a crystallizing assemblage with zircon will cause Th/U and $(Sm/Ce)_n$ ratios in zircon to decrease substantially and cause $(Yb/Gd)_n$ to increase due to higher partition coefficients of Th, Sm, and Gd into titanite compared to zircon (Fig. 2.17B and C; Bachmann *et al.*, 2005). The addition of any amount of allanite to the crystallizing assemblage will cause $(Sm/Ce)_n$ in zircon to

increase as allanite has higher partition coefficient for Ce over Sm (K_d(Sm/Ce) ~0.57; Fig. 2.17C; Klimm *et al.,* 2008). Additionally, Th/U in zircon will decrease sharply, whereas $(Yb/Gd)_n$ will increase only slightly with allanite crystallization (Fig. 2.17B). Other modelling scenarios were considered. Fractional crystallization scenarios do not reproduce the trends observed in zircon data for the ratios of interest. Batch crystallization was also modelled but implementing changes in melt composition as crystallization preceded (i.e., less open-system behaviour, higher zircon: melt fraction). However, this also did not reproduce the trends present in the natural zircon data set. Therefore, equilibrium crystallization whereby the crystallizing assemblage is interacting with a large melt fraction in an open-system crystal mush is the most appropriate and likely scenario of crystallization mode for the MIC magmas at the conditions of zircon growth.

Zircon from both the Mouska and Doyon stages of the MIC display a trend of decreasing Th/U coinciding to an increase in $(Yb/Gd)_n$, as well as a decrease in $(Sm/Ce)_n$ with an increase in $(Yb/Gd)_n$, suggesting coeval crystallization of other accessory minerals (i.e., titanite; Fig. 2.18 and 19). Additionally, zircon rim analyses consistently show elevated $(Yb/Gd)_n$ and lower Th/U and $(Sm/Ce)_n$ indicating accessory minerals were crystallizing simultaneously with zircon growth (Fig. 2.18). However, within and between the different lithologies the proportions of zircon and titanite crystallizing were different leading to distinct compositional ranges and slopes in the trace element ratio trends. For example, $(Yb/Gd)_n$ extends to higher values in the gabbro compared to the trondhjemite suggesting zircon in the gabbro grew from a melt that crystallized a different proportion of titanite to zircon. In general, allanite is not likely an important mineral controlling the trace element signatures in zircon. However, a shift to slightly higher $(Sm/Ce)_n$ values at relatively constant $(Yb/Gd)_n$ is seen in zircon in the low-Th/U quartz diorite and tonalite (Fig. 2.18F, G). This could indicate that allanite was crystallizing sporadically throughout the history of zircon growth. Within individual zircon grains there can be distinct differences in the Th/U ratio

in the core and rim (Fig. 2.11G). The CL image of the zircon in Figure 2.11 shows uninterrupted oscillatory and sector zoning with no evidence of resorption occurring between the different Th/U zones; therefore, the drop in Th/U from core to rim is consistent with the onset of titanite crystallization.

In contrast to the general trends recorded for the entire zircon population in a given lithology, individual zircon grains from the Mouska stage can display a decrease in $(Yb/Gd)_n$ (Fig. 2.17B) with an increase in Th/U from core to rim, suggesting zircon fractionation was the dominant mineral crystallizing during these individual grain growth histories, or that there has been a recharge in the magmatic system to disturb the dominant cooling and fractionation trend (cf, Large *et al.,* 2021). As well, some grains show an increase in $(Sm/Ce)_n$ from core to rim with increasing $(Yb/Gd)_n$ suggesting allanite crystallization occurred during the growth of zircon or a magmatic recharge event occurred (Fig. 2.17C). Additionally, in the zircon trace element map shown in Figure 2.10, in which high Hf content is seen in the middle of the grain, this increase in Hf coincides with a drop in Th/U, followed by an increase in Th/U moving towards the rim. This is another indication that there has been a magmatic recharge event.

The absolute Th/U ratios vary between lithologies as well as between different samples from the same phase of the MIC. Within the Mouska-stage phases, there is a hierarchy of Th/U, with the most primitive (highest Th/U) zircon occurring in the high-Th/U quartz diorite, followed by the tonalites, low-Th/U quartz diorite, and finally the gabbro (Fig. 2.18A-D). However, there are no evolutionary trends suggesting zircon in all the Mouska stage phases grew from a single, homogeneous magma chamber. If this were the case, there should be continuous trends linking Mouska phase zircon populations together. For example, if the tonalite and quartz diorite were derived from the same batch of magma as the gabbro, there should be a decrease in Ti in zircon shifting from gabbro through to tonalite coinciding with an increase in Hf. However, the highest

Ti is recorded in zircon in the high-Th/U quartz diorite whereas the low-Th/U quartz diorite, tonalite, and gabbro all have similar Ti concentrations in zircon. The lowest Hf is present in zircon in the tonalite and the highest in the quartz diorite, all opposite of what would be expected in a normal fractionation trend. The zircon Th/U ratio increasing from the gabbro to the low-Th/U quartz diorite to the tonalite could occur if zircon was the only accessory mineral crystallizing (since zircon prefers U over Th). However, as discussed above, based on other trace element ratios in zircon (Fig. 2.17, 2.18) and petrographic evidence we know that accessory minerals were crystallizing coevally with zircon. Overall, based on zircon composition, magmas responsible for the formation of the different MIC lithologies must have evolved separately at depth prior to emplacement.

Zircon in the gabbro and aphyric trondhjemite are similar; trends involving certain ratios (i.e., Th/U, $(Yb/Gd)_n$, and $(Sm/Ce)_n$) suggest zircon in both lithologies are comparable and may have started growing from the same source magma or from two different but similar magmas. In the gabbro, $(Yb/Gd)_n$ extends to higher values compared to the aphyric trondhjemite, suggesting zircon in the gabbro had a longer growth period in the magma chamber as other accessory minerals (e.g., titanite) were co-crystallizing. However, the zircon Hf content of the two lithologies is very different; zircon in the gabbro records Hf contents primarily between 8750 and 10500 ppm whereas zircon in the trondhjemite records lower Hf between 7000 and 8750 ppm (Fig. 2.8E, H). This is inconsistent with these two lithologies being sourced from the same magma as the zircon from more primitive composition (i.e., gabbro) should record lower Hf than the more evolved (i.e., trondhjemite) composition (Claiborne *et al.,* 2006). When the zircon composition is plotted on tectonic discrimination diagrams suited for this mineral (Fig. 2.20), zircon from the gabbro lies in a transitional field between MORB-like and continental arc affinities, while the trondhjemite zircon

firmly plots in the continental arc-like field, indicating that the transition from the Mouska- to Doyon-stages involved a shift in tectonic affinity for the source magmas for these lithologies.

Zircon in the high- and low-Th/U quartz diorite suggests these different samples of the same lithology did not evolve from the same magma source. In addition to different Th/U ratios, zircon from the high-Th/U quartz diorite has significantly higher Ti concentrations but have similar Hf contents. If these two quartz diorite samples were sourced from the same magma (with the high-Th/U being the first to crystallize) there should be a continuum of decreasing Ti with increasing Hf from the high-Th/U to low-Th/U zircon, but that is not the case (Fig. 2.18B). Additionally, if they were sourced from the same magma batch then zircon $(Yb/Gd)_n$ should be higher in the low-Th/U quartz diorite compared to the high-Th/U quartz diorite, but $(Yb/Gd)_n$ is relatively the same between the two (Fig. 2.18B). The $(Sm/Ce)_n$ ratio should also be higher in the high-Th/U sample if it was the earlier zircon to crystallize, but it has a lower $(Sm/Ce)_n$ ratio compared to the low-Th/U zircon (Fig. 2.18F). The zircon morphology, based on CL imaging, is also very different in the two lithologies. Zircon in the low-Th/U quartz diorite is primarily euhedral to subhedral with well-preserved oscillatory and sector zoning, whereas zircon in the high-Th/U quartz diorite has more subhedral grain form and zoning patterns that appear to be interrupted, suggesting a period of resorption occurred in the magma chamber in which the high-Th/U zircon grew (Fig. 2.4B, C). Therefore, based on zircon composition and zoning pattern differences between the high- and low-Th/U quartz diorites, these samples of the same phase of the MIC grew from distinct magmas or chambers. The high-Th/U zircon grew from a more primitive, less evolved magma (higher Ti and Th/U) compared to the low-Th/U quartz diorite.

In addition to accessory minerals that exert control on the Th/U ratio in zircon, the amount of zircon present in the source region and the amount of unmelted zircon left in the source region, can influence the concentrations of U, Th, REE, Y and Hf in crystallizing zircon (Watson, 1979;

Watson & Harrison, 1983). The high- and low-Th/U zircon populations from the quartz diorite, could indicate that these two populations had different source magmas that may reflect how much zircon was present or left behind in the restite. Alternatively, magmas originated from the same source, but at different times, and therefore, would have different compositions. It is interesting to note that the zircon Pb concentrations in the high-Th/U quartz diorite are elevated and the U concentrations are lower compared to zircon in the low-Th/U quartz diorite. The U-Pb geochronology yields the same date within error for the two samples, indicating that the elevated Pb and lower U is not a consequence of decay. This is another line of geochemical evidence that the two quartz diorite samples are not related to the same magma or chamber evolution.

2.7.3 Relative Changes in Magma Oxidation

A critical parameter in the evolution of magmatic-hydrothermal (e.g., porphyry-epithermal, intrusion-related) Au ± Cu deposit formation is oxygen fugacity (fO_2). Oxygen fugacity influences the stability, formation, and abundance of immiscible sulfide phases, as well as Au and Cu solubility in the silicate melt itself (Botcharnikov *et al.,* 2010; Richards, 2011; Audétat & Simon, 2012; Zajacz *et al.,* 2012, 2013). At higher fO_2 (>FMQ + 1.0) S^{6+} becomes the dominant S species relative to S^{2-}, limiting the stability of sulfides. Such conditions favour metals such as Au, Ag, and (to a lesser extent) Cu concentrating in the silicate melt and thus their availability to partition into exsolving magmatic-hydrothermal fluids (William-Jones & Heinrich, 2005; Audétat & Simon, 2012; Du and Audétat, 2020).

With particular application to evaluating the relative metal fertility of magmatic-hydrothermal ore magmas (e.g., porphyry Cu-Au), the magnitude of, and relative changes in, Eu and Ce anomalies in zircon are proposed as an indicator of relative fO_2 during the evolution of a magmatic system. Europium and Ce have two common oxidation states (Eu^{2+} and Eu^{3+} and Ce^{3+} and Ce^{4+};' Ballard *et al.,* 2002; Trail *et al.,* 2012; Dilles *et al.,* 2015; Loader *et al.,* 2017; Smythe

& Brenan, 2016). At more oxidized conditions ratios of Ce^{4+}/Ce^{3+} and Eu^{3+}/Eu^{2+} increase in the melt and since Ce^{4+} and Eu^{3+} substitute for Zr^{4+} in zircon due to similar ionic radii, the total Ce and Eu content in zircon is higher (Ballard *et al.,* 2002; Trail *et al.,* 2012; Dilles *et al.,* 2015; Loader *et al.,* 2017; Smythe & Brenan, 2016). Thus, at more reducing conditions Ce/Ce* and Eu/Eu* values in zircon will be lower.

However, there are problematic petrological and methodological issues that arise with the use and calculation of Eu and Ce anomalies (Eu/Eu* and Ce/Ce*). The crystallization of REE-bearing minerals (e.g., titanite, apatite, allanite) and plagioclase prior or synchronous to zircon will modify Eu and other REE (e.g., Sm, Gd, Ce, Nd) concentrations in the melt, therefore changing the magnitude of the anomalies recorded in zircon (Ballard *et al.,* 2002; Trail *et al.,* 2012; Dilles *et al.,* 2015; Loader *et al.,* 2017). Since titanite has a greater affinity for Sm and Nd compared to Ce, as the amount of titanite crystallizing increases, this causes the melt to become depleted in Sm and Nd relative to Ce and therefore in zircon crystallizing coevally with or post-titanite crystallization. Apatite and allanite both have similar partition coefficients for Ce, Nd, and Sm and therefore will have little influence on the Ce/Ce* calculation. Overall, the Ce/Ce* values are variable in the Mouska stage ranging from 6 to 150 and in the Doyon stage the Ce anomaly ranges from 8 to 40 (Fig. 2.9).

Plagioclase incorporates Eu^{2+} into its crystal structure; thus, the crystallization of plagioclase depletes a magma in Eu creating a negative Eu/Eu* anomaly in the melt. This anomaly is later inherited by crystallizing zircon (Ballard *et al.,* 2002). Additionally, Eu^{2+} is more compatible in plagioclase with higher albite content; therefore, plagioclase crystallizing from more evolved magmas produce larger Eu/Eu* anomalies in the associated melt than more primitive magmas (Dilles *et al.,* 2015). In addition to the effect of plagioclase crystallization, the growth of titanite also falsely magnifies the magnitude of the Eu anomaly in zircon forming coevally or post-

titanite crystallization (Bachmann *et al.*, 2005; Colombini *et al.*, 2011; Olson *et al.*, 2017; Loader *et al.*, 2017). Since Sm and Gd have much higher mineral-melt partition coefficients associated with titanite compared to Eu, the growth of accessory titanite (as little as ~0.1 wt%; Loader *et al.*, 2017; Loader *et al.*, 2022) will create, or magnify, a positive Eu/Eu* anomaly in the melt. Zircon crystallizing with, or after, titanite will inherit higher Eu/Eu* values compared to a titanite-free fractionation (Loader *et al.*, 2017). Batch crystallization modelling in this study confirmed this effect of titanite on Eu/Eu* values in zircon. Additionally, the effect of apatite and allanite on the Eu/Eu* was also modelled. Apatite crystallization, like titanite, will increase the Eu/Eu* value of the melt and therefore in zircon crystallizing coeval with or after apatite crystallization, whereas allanite crystallization only leads to a minor increase in the Eu/Eu* value and is relatively unimportant compared to the control titanite and apatite exert on the Eu anomaly. Overall, the Eu/Eu* values are variable in the Mouska stage rocks (0.18 to 0.40) and in the Doyon-stage aphyric trondhjemite the Eu anomaly ranges from 0.21 to 0.30 (Fig. 2.9).

Zircon Ti content (as a proxy for temperature) and Eu/Eu* have a weak correlation and decrease together from core to rim in the gabbro, tonalite, and low-Th/U quartz diorite (Fig. 2.21A-C). Zircon Ti and Eu/Eu* are not correlated in high-Th/U quartz diorite and aphyric trondhjemite (Fig. 2.21B, D). The gabbro and high-Th/U quartz diorite are the only lithologies in which Hf increase is negatively correlated with Eu/Eu* (decrease) and Ti in zircon from core to rim, together with a decrease in Ti content (Fig. 2.21A, E). These correlations involving Eu/Eu* are likely explained by plagioclase crystallization during magma cooling and fractionation. Zircon trace element distribution maps for the low-Th/U quartz diorite and tonalite do not show any systematic correlations between Eu/Eu* and temperature or Eu/Eu* and Hf (Figs. 2.10-2.13), consistent with the spot analyses (Fig. 2.21B, C, F and G). Based on trace element patterns and trends recorded in zircon, combined with the problematic issues of titanite and plagioclase crystallization influencing

the Eu and Ce anomalies, the variations observed in both anomalies are a result of titanite and plagioclase crystallizing prior to, or synchronous with, zircon.

Differences in the Eu anomaly from lithology to lithology do exist. However, changes in fO_2 may also be involved. In order of observed emplacement, the zircon Eu anomaly increases from the gabbro (~0.25), through to the high-Th/U quartz diorite (~0.27), low-Th/U quartz diorite (~0.32) and tonalite (~0.37). The zircon from the Doyon-stage aphyric trondhjemite has a Eu anomaly of ~0.26. The highest Eu/Eu* values are recorded in the Mouska-stage tonalite (~0.37), consistent with the observed mineral assemblage of titanite + Fe-Ti-oxides + quartz (Fig. 2.5B), suggesting the magma crystallized under relatively oxidizing conditions (Dilles, 1987; Wones, 1989). Additionally, the presence of magmatic epidote coeval with titanite (Fig. 2.5D) adds another mineralogical indicator that the tonalite formed under relatively more oxidized conditions than the other Mouska-stage lithologies (Schmidt & Poli, 2004). Zircon in the tonalite shares the same textural settings as titanite and epidote indicating they are coeval, interstitial magmatic minerals. Titanite was only observed in the tonalite, but epidote is also present in the aphyric trondhjemite indicating the aphyric trondhjemite also formed under relatively more oxidized conditions (Fig. 2.5K). However, the Eu anomaly of zircon in the aphyric trondhjemite (~0.26) is lower than the tonalite and similar to the gabbro and high-Th/U quartz diorite. This could indicate plagioclase crystallization influenced the Eu anomaly in the aphyric trondhjemite and raises the question, is more useful to use mineral trace element ratios or mineralogically evidence to evaluate the relative fO_2 of a system.

The Ce^{4+}/Ce^{3+} ratio in zircon was not calculated to estimate fO_2 conditions because this calculation requires knowledge of the Ce concentration in the melt that zircon crystallized from (Ballard *et al.*, 2002; Smythe & Brennan, 2016) and owing to modification by synmagmatic processes (contamination and assimilation, crystal accumulation, degassing) and post-solidus

processes (metamorphism, alteration, and degassing) bulk rock compositions do not generally preserve the actual melt composition. As an alternative, zircon Ce/Ce* values may be used as a proxy for fO_2 and were calculated based on the equation of Loader *et al.* (2017). Calculated zircon Ce/Ce* values are quite variable between, and within, lithologies with values ranging from 5 to 150 based on individual spot analyses (Fig. 2.9). Correlations between Eu/Eu* and Ce/Ce* are lacking (Fig. 2.9A-D), but a weak negative correlation is noted between increasing Ce/Ce* and decreasing Th/U ratio (Fig. 2.22A-D). As well, a positive correlation exists between Ce/Ce* and $(Yb/Gd)_n$ (Fig. 2.22E-H). Examining the spot data extracted from LA-ICP-MS maps of zircon, in a plot of $(Yb/Gd)_n$ vs. Th/U, with data grouped by Ce/Ce* values, the highest Ce/Ce* values occur at low Th/U ($\sim\leq 1$), but these show variable $(Yb/Gd)_n$ (Fig. 2.19B and D). The highest Ce/Ce* values are present at the highest $(Yb/Gd)_n$ and lowest Th/U values in the zircon rim (Fig. 2.19B and D). These observations in the trace element data are consistent with the results of modelling showing that titanite crystallization strongly influenced Th/U and $(Yb/Gd)_n$ ratios. The elevated Ce/Ce* (like Eu/Eu*) values may be coincidental to titanite fractionation because the equation of Loader *et al.* (2017) relies on concentrations of Ce and the MREE, the latter partitioning preferentially into titanite (Prowatke & Klemme, 2005), artificially magnifying the Ce/Ce* anomaly in the MIC zircons making it impossible to constrain fO_2 using this method. The magnitude of Ce/Ce* is even higher in the mapped grains. Difficulty in filtering out micron-scale accessory REE mineral inclusions, particularly in mapped grains, exacerbates this issue further (cf. Zhong et al., 2018; Ni et al., 2020) Clearly, on the basis of data presented here, relative fO_2 changes during magma evolution for the MIC rocks estimated using zircon Ce/Ce* values cannot be easily separated from mineralogical controls.

Robust constraints on fO_2 may be made with knowledge of the true Ce^{4+}/Ce^{3+} ratio of zircon (Ballard *et al.*, 2002; Smythe & Brenan, 2016) and other methods involving zircon compositional

parameters and age (Loucks et al., 2020). These approaches avoid issues related to coeval accessory mineral crystallization that likely plague much of the literature employing zircon Ce/Ce* as an fO_2 proxy. A related study (Neyedley et al., 2024, in prep) will address this.

2.7.4 Pressure-Temperature Crystallization Conditions

The pressure-temperature conditions of crystallization were estimated using a combination of empirical thermobarometers applied to magmatic mineral phases that show coeval growth (i.e., zircon, titanite, quartz; Thomas *et al.,* 2010). The Ti-in-zircon thermometer of Ferry & Watson (2007) is relatively pressure insensitive with an error of ~50°C/GPa. Whereas the Ti-in-quartz (Thomas *et al.,* 2010) and Zr-in-titanite (Hayden *et al.,* 2008) thermobarometers require either pressure or temperature to be constrained independently. However, by using the crystallization temperature obtained from the Ti-in-zircon thermometer and the method of intersecting isopleths (Thomas *et al.,* 2010), the pressure-temperature conditions of magma crystallization (i.e., at the time of accessory mineral growth) can be estimated (Fig. 2.23). The Ti-in-zircon thermometer is calibrated at 1 GPa and pressure is not needed in the equation to calculate temperature. However, the Ti-in-quartz and Zr-in-titanite thermometers are pressure-dependant, the calculated isopleths were determined by fixing pressure at 0.1 to 2 GPa and using the mean mineral Ti or Zr concentration ± 1σ to determine an upper and lower isopleth in pressure-temperature space for each mineral.

The results of integrating isopleths from the different phases (i.e., zircon, quartz, titanite) show crystallization pressure-temperature conditions at significant depths, inconsistent with the near sea-floor emplacement characteristics of the MIC and considerably deeper than post-solidus regional metamorphic conditions. The intersection of Ti-in-quartz and Ti-in-zircon isopleths in the Mouska-stage gabbro yields the highest pressure conditions of all samples (0.77 to 1.18 GPa, 700º

and 750ºC (Fig. 2.23A). The pressure-temperature intersections for the low- and high-Th/U quartz diorite, based on Ti-in-quartz and Ti-in-zircon isopleths, record nearly identical pressure (0.71 to 1.07 GPa, and 0.72 to 1.04 GPa; respectively; Fig. 2.23A), but at slightly different temperature conditions (770º to 810ºC and 720º to 770ºC for high- and low-Th/U quartz diorite, respectively; Fig. 2.23A). A more recent calibration of the TitaniQ Ti-in-quartz thermobarometer (Osborne *et al.*, 2022) provides a possible improvement on the Ti-in-quartz solubility model of Thomas *et al.*, (2010). Use of this revision leads to an approximate 0.15-0.2 GPar decrease in the pressure intersection window for Ti-in-quartz and Ti-in-zircon constraints (Fig. 2.23A). This alternate calibration does not influence the results of this thermobarometric exercise significantly and does not impact the key conclusions in the study. Additionally, pressure-temperature estimates are still well above regional metamorphic conditions and lie in the ascent/storage pressure-temperature window between TTG magma generation and emplacement condition.

For the tonalite sample from Stop 11, pressure-temperature conditions are constrained by the intersection of the Ti-in-quartz, Ti-in-zircon, and Zr-in-titanite isopleths. These isopleths show good pressure-temperature consistency and provide conditions similar to the low-Th/U quartz diorite (0.66 and 1.03 GPa and 740º and 785ºC; Fig. 2.23B). Estimated conditions of titanite crystallization are at or below the maximum temperature of titanite stability (< ~780ºC; Claiborne *et al.*, 2006; Olsen *et al.*, 2017, and references therein). However, for a tonalite sample from Stop 10 the isopleths show no overlap between the Ti-in-quartz, Ti-in-zircon, and Zr-in-titanite isopleths (Fig. 2.23C). The Ti-in-quartz and Ti-in-zircon isopleths yield a pressure-temperature range (0.52 to 0.88 GPa, 740° to 795°C), slightly lower than conditions for Stop 11. The intersection of the Zr-in-titanite and Ti-in-quartz isopleths yields atypically low pressure (<0.23 GPa) and temperature (565º to 625ºC) conditions, while the intersection of the Zr-in-titanite and Ti-in-zircon isopleths gives a similar temperature range to other lithologies (705º to 755ºC) but record significantly

elevated pressure (1.1 and 1.69 GPa; Fig. 2.23C). Since isopleth intersections involving Ti-in-quartz and Ti-in-zircon provide similar pressure-temperature results for all other lithologies from the Mouska stage, it is likely that titanite at Stop 10 is not in equilibrium with quartz and zircon.

Based on the intersection of the Ti-in-quartz and Ti-in-zircon isopleths, both samples from the aphyric trondhjemite record similar pressure-temperature conditions, with nearly identical temperatures (760º to 790ºC and 755º to 790ºC, for samples 1323 and 1444.5, respectively; Fig. 2.23D) but subtle differences in pressure (0.52 to 0.76 GPa and 0.54 to 0.87 GPa for samples 1323 and 1444.5, respectively; Fig. 2.23D).

Overall, the consistency in pressure-temperature estimates (~0.5 to 1.2 GPa = 16 to 40 km) for the crystallization of quartz and accessory minerals in the MIC lithologies (i.e., deep crust, rather than near-sea floor) provide robust constraints on the crystallization conditions of certain minerals in early crystal mushes of the MIC magmatic system prior to their emplacement. The ascent of the MIC and implications are discussed in a later section. However, there are uncertainties associated with each thermometer that also need to be discussed. Ti-in-quartz concentrations due to down-temperature cooling resulting in exsolution of Ti through the quartz lattice to produce rutile needles, which are present in quartz in all studied samples in the MIC, can lower the Ti-in-quartz concentration locally in an induvial quartz grain in the vicinity of the rutile exsolution needles (Cherniak *et al.,* 2007). As well, possible diffusion of Ti through quartz during metamorphism can lower the Ti-in-quartz concentration (Cherniak *et al.,* 2007). The maximum estimated temperature during metamorphism in the Doyon-Bousquet-LaRonde mining camp was ~575°C (Yergeau, 2022a). At this temperature, Ti diffusion likely had minimal effect on the measured Ti-in-quartz concentrations because, the effective diffusion distance of Ti is relatively short (~2 µm) over the span of 1.0 Ma (Cherniak *et al.,* 2007). Additionally, due to the near-solidus temperature recorded by Ti-in-zircon thermometry and the inferred rapid ascent from depth to

emplacement level (discussed below), we consider the effects of Ti diffusion due to residence time in the magma chamber negligible over the maximum 1.44 Ma crystallization window for the MIC (cf Mercer & Reed, 2013). By using a beam size of 25 µm to ablate quartz and analyzing areas devoid of rutile exsolution needles, any diffusional alteration or depletion of Ti should be minimized (Mercer & Reed, 2013, Mercer *et al.,* 2015).

Using a different estimate of $a\mathrm{TiO_2}$ in the thermometric equations leads to a difference in calculated temperature (e.g., ±0.1 $a\mathrm{TiO_2}$ results in an uncertainty of ±15°C for Ti-in-zircon thermometer). However, while the use of a different $a\mathrm{TiO_2}$ will change the temperature calculated for each thermometer, it does not significantly change the range in pressure determined through intersecting isopleths for the Ti-in-zircon and Ti-in-quartz thermometers. For example, the pressure-temperature range estimated for the gabbro at $a\mathrm{TiO_2}$ = 1 is 0.77 to 1.18 GPa and 700° to 750°C, whereas at $a\mathrm{TiO_2}$ = 0.7, pressure-temperature range is between 0.74 and 1.17 GPa and 735° and 785°C. Furthermore, a change in $a\mathrm{TiO_2}$ for the determined intersection of the Ti-in-zircon, Ti-in-quartz, and Zr-in-titanite thermometers appears to only have an effect if the $a\mathrm{TiO_2}$ is lowered. At $a\mathrm{TiO_2}$ = 0.7, the pressure-temperature conditions were 0.66 to1.03 GPa and 740° and 785°C, whereas at $a\mathrm{TiO_2}$ = 0.8, the pressure range is similar (0.63 to 1.03 GPa), and the temperature range is slightly lower (730° to 780°C). If $a\mathrm{TiO_2}$ = 0.6, the range of intersection for all three isopleths shrinks and results in a pressure-temperature range from 0.77 to 0.94 GPa and 755° to 780°C. Overall, uncertainty in $a\mathrm{TiO_2}$ do not result in significant differences to the estimated pressure-temperature conditions of crystallization.

2.7.5 Titanite Disequilibrium

Whereas the intersection of three independent mineral thermobarometers yields a reliable pressure-temperature range for tonalite sample Stop 11 of Phase D, constraints using all three

thermobarometers for Stop 10, do not provide an intersection (Fig. 2.23C). Specifically, in Stop 10 the intersections for the titanite isopleths with quartz and zircon isopleths, yield anomalously low- and high-pressure intersections that are inconsistent with the constraints from all other Mouska-stage samples (Fig. 2.23C). Titanite from both tonalite samples are texturally distinct from one another: in Stop 10, titanite contains inclusions of and forms rims around Fe-Ti-oxide grains, consistent with the replacement of ilmenite/Fe-Ti-oxides by titanite indicating an increase in magma fO_2 (i.e., high-temperature hydrothermal replacement; Dilles, 1987; Wones, 1989; Fig. 2.5B, C), whereas Stop 11 titanite does not exhibit oxide replacement textures but titanite can share mutual grain boundaries with Fe-Ti-oxides, suggesting co-crystallization (Fig. 2.5A). Both Stop 10 and Stop 11 titanite have similar Fe:Al ratios (~ 1; Fig. 2.16A), typical of magmatic titanite (Rasmussen *et al.,* 2013; Aleinikoff *et al.,* 2002), and only a few grains have elevated Fe:Al ratios (Fig. 2.16A) consistent with a metamorphic or alteration origin (Aleinikoff *et al.,* 2002; Rasmussen *et al.,* 2013). However, the absolute Fe content of titanite at Stop 10 is lower than at Stop 11 (Fig. 2.16B), which could be related to the timing of titanite growth between the two samples. One possibility is that titanite at Stop 10 is poorer in Fe because significant amounts of Fe have been removed by earlier (and still partly preserved) Fe-Ti-oxides whereas at Stop 11, relatively coeval formation of titanite and Fe-Ti-oxides (represented by mutual grain boundaries textures) would have limited the amount of Fe removed from the melt until titanite and oxides formed. Additionally, the mean Eu anomaly is less negative in Stop 10 (Eu/Eu* = 0.34 ± 0.09) compared to Stop 11 (Eu/Eu* = 0.25 ± 0.08; Fig. 2.16C, D). Since the K_d of Eu^{3+} (K_d ~1000; Bachmann *et al.,* 2005) is much greater than Eu^{2+} into titanite (K_d~0.37), the less negative Eu anomaly in titanite indicates relatively more oxidizing conditions (Loader *et al.,* 2017). Alternatively, plagioclase may have crystallized prior to titanite growth, causing the melt to become depleted in Eu.

Given the textures and chemical evidence demonstrating the relative timing of titanite growth in Stop 10 being later than growth in Stop 11, it would suggest titanite in Stop 10 would not have been forming at/around the same time as zircon and quartz, causing the titanite isopleth for Stop 10 not to be coincident with zircon and quartz as it is for Stop 11 (Fig. 2.23B, C). It is interesting to note that if by the time titanite began to crystallize at the expense of ilmenite and the pressure remained constant, based on the titanite isopleths, the titanite would have grown at temperatures ~150°C cooler than zircon and quartz (Fig. 2.23C).

2.7.6 Implications for Evolution of the MIC

Estimates of the pressure-temperature window for quartz + zircon (± titanite) crystallization for the gabbro, quartz diorites, and tonalite of the Mouska stage of the MIC range from ~0.5 to ~1.2 GPa (16-40 km) and ~700° to ~810°C, whereas quartz ± zircon crystallization for the aphyric trondhjemite of the Doyon stage yielded a range between ~0.5 and ~0.9 GPa (16-30 km) and ~675° to 790°C. (Fig. 2.23). These estimates are similar to, or slightly lower than, experimental pressure-temperature constraints on TTG magma generation. The experimental studies implicate the partial melting of hydrous mafic (e.g., amphibolite or basalt) source rock to produce TTG magmas at ~0.8 to >1.5 GPa and ~700° to 1000°C, with most studies suggesting temperatures of < 900°C (e.g., Rapp *et al.,* 1991; Martin, 1999; Smithies, 2000; Condie, 2005; Martin *et al.,* 2005; Clemens *et al.,* 2006; Getsinger *et al.,* 2009; De Almeida *et al.,* 2011; Moyen & Martin, 2012; Qian & Hermann, 2013; Hoffman *et al.,* 2014). Notably, the temperatures recorded by the MIC zircon are below the closure temperature for Ti diffusion (~1000°C; Cherniak & Watson, 2007) and Pb diffusion (~900°C; Cherniak & Watson, 2000). Therefore, considering the pressure-temperature estimates of crystallization, the U-Pb ages record MIC zircon crystallization at depth (i.e., not crystallization on ascent, or emplacement and not near-solidus conditions).

If only pressure-temperature estimates for the gabbro and high- and low-Th/U quartz diorite are considered, zircon in these magmas crystallized at similar depth in the crust but at slightly different temperatures, suggesting growth in the same magma chamber (Fig. 2.23). However, based on the zircon composition, the magmas that produced the Mouska-stage lithologies (i.e., both quartz diorites, tonalite, and gabbro) could not have evolved from one another. In fact, the differences in trace element composition (i.e., evolutionary trends, ranges in Th/U, Yb/Gd, Sm/Ce; Fig. 2.18), imply each lithology crystallized distinct zircon populations in separate magma chambers to produce the range in trace element concentrations and trends recorded in zircon. Multiple magmas chambers were required (coevally) in the crust to produce the Mouska stage. The Doyon stage trondhjemite records zircon crystallization at higher levels in the crust compared to the Mouska stage. Based on zircon trace element composition, there is no compositional continuum between the Mouska and Doyon stages lithologies, suggesting the Doyon stage trondhjemite was also crystallizing zircon in compositionally distinct magma chambers. It is interesting to note that the mafic-intermediate phases (gabbro, quartz diorite) record zircon crystallization at deeper levels compared to the felsic phases (tonalite, trondhjemite) suggesting that certain depth levels in the crust were more conducive to magma storage and protracted fractionation in this setting.

Geochemical patterns and ratios (e.g., LREE>HREE, low La/Yb and Sr/Y; Galley & Lafrance, 2014) used previously to classify TTG suites show that lithologies of the MIC plot in the "normal"-arc field dominated by plagioclase fractionation (rather than controlled by garnet ± amphibole fractionation) and are more consistent with post-2.5 Ga than pre-2.5 Ga TTG suites (low-Al TTG; Getsinger *et al., 2009*; Moyen and Martin, 2012). Based solely on these geochemical patterns and with no thermobarometric constraints applied, a deep amphibolite source (~40 km) and temperatures between 800° and 850°C was inferred as a source region for the MIC magmas (Galley & Lafrance, 2014). The pressure-temperature conditions from thermobarometry presented

here provide the first direct indications that the magmas for the MIC started to crystallize at conditions overlapping with or slightly shallower and cooler than TTG magma source conditions from experimental studies.

Ascent and emplacement of the partially crystallized MIC magmas would require supersolidus transport during considerable ascent to various emplacement levels (e.g., sub-seafloor). This is perhaps difficult to envisage considering that the magmas were already near-solidus based on zircon thermobarometry, and would require rapid transport as crystal mush along major, heated structural pathways. Both of these requirements are supported for the MIC setting.

Field relationships (e.g., Galley & Lafrance, 2014; this study) suggest that the MIC lithologies were emplaced as sills and dikes, with magmas transported to emplacement depth through dike propagation rather than diapiric rise of entire magma bodies. By this process of dike propagation, experimental studies show that the ascent of felsic magmas from 0.8 GPa depth (Brandon *et al.,* 1996) and emplacement into the shallow crust can occur on time scales of < 100 years, even for magmas with relatively low water content (~1-2 wt% H_2O; Petford *et al.,* 1993; Brandon *et al.,* 1996; Petford *et al.,* 2000). This is up to 10^6 times faster than diapiric rise and aids in bringing relatively cool magmas from depth to the surface. At the zircon crystallization temperature (700° to 800°C) and at moderate water (~3.5 wt%), the MIC magmas could have remained predominately liquid until slightly above their solidus temperature (e.g., > 75 liquid % at ~ 40°C super-solidus; Nekvasil, 1988), preventing stalling in the crust and allowing rapid ascent to their emplacement level. Furthermore, because the emplacement of these magmas via dyke propagation is likely to occur at time scales far less than the uncertainty on individual zircon ages (or weighted mean ages), the reported zircon ages are therefore interpreted to be equivalent to the ages of emplacement.

As well, high volumes of magma transported along the same structure over a relatively short period of time will heat the surrounding crust and help promote further magma ascent (Singer *et al.*, 1989; Petford *et al.*, 2000; Richards, 2003; Annen *et al.*, 2006; Cao *et al.*, 2016). In a back arc rifting environment (such as the interpreted tectonic setting for the Doyon-Bousquet-LaRonde mining camp; Mercier-Langevin, 2007c), major structures produced due to the extensional setting can extend to lower crustal depths, providing pathways for the rapid ascent of magma from depth and allow for the accommodation of shallow level magma emplacement (Richards, 2003; Candela & Piccoli, 2005; Franklin *et al.*, 2005).

Rapid MIC magma ascent from depth is also supported by the presence of unaltered, interstitial magmatic epidote in the tonalite and aphyric trondhjemite of the MIC (Fig. 2.5D, G, and K). The minimum pressure of epidote stability at 750°C (similar to Ti-in-zircon temperature for tonalites and aphyric trondhjemite; Fig. 2.23B, D) is ~0.5 GPa at fO_2 = FMQ +5 (i.e., HM buffer) and ~0.9 GPa at fO_2 = FMQ +1 (NNO buffer). Given estimates of fO_2 for typical Archean TTG suites range between FMQ -1 to FMQ +2.7 (Meng *et al.*, 2021), epidote stability in TTG magmas is likely between ~0.5 and ~0.9 GPa (Fig. 2.23). The occurrence of magmatic epidote in the MIC is consistent with partial crystallization conditions at depth and supports the requirement for rapid dike propagation rather than diapiric rise to prevent epidote dissolution and resorption (Brandon *et al.*, 1996). However, it is unclear how compositionally distinct magma chambers were tapped relative to the order of emplacement at shallow levels. In contrast to the inferred shallow emplacement depth (< 50 MPa) based solely on field relationships (e.g., angular xenoliths, highly fractured roof rocks, large miarolitic cavities, and granophyric textures; Galley & Lafrance, 2014), the pressure-temperature conditions of early stages of crystallization from thermobarometry demonstrates the MIC magma mushes were transported from a deep source region rapidly through

the crust in order to be emplaced at shallow conditions. Thus, the sub-seafloor emplacement history does not capture the full igneous history of the intrusive complex.

Reconciling the pressure-temperature estimates from thermobarometry with the zircon geochronology, and evidence for rapid ascent/emplacement, the entire Mouska stage crystallization and sequence, from early mushes crystallizing at depth to near sea-floor emplacement documented through field relationships occurred over a maximum duration of 0.7 Ma. For the Doyon stage, the maximum duration of magmatism was ~1.44 Ma. Considering the oldest and youngest zircon grains are from the Doyon stage, this duration of magmatism applies to the MIC as a whole. Furthermore, the coincident dates for all lithologies suggests that the tholeiitic to transitional Mouska stage and transitional to calc-alkaline Doyon stage were coeval, reinforcing zircon trace element results requiring distinct magma chambers at different levels in the crust.

Tectonic discrimination diagrams based on zircon trace element compositions (cf Grimes *et al.*, 2015) show an evolutionary trend from the Mouska-stage lithologies, falling predominantly in the MORB-like affinity field and extending into the continental arc field, transitioning to the Doyon-stage aphyric trondhjemite that falls firmly in the continental arc field (Fig. 2.20). This confirms that as the MIC evolved, deeply crystallized zircon recorded the change in tectonic setting of melt generation from a rift- to arc-dominated environment, suggesting influx of a subducted slab component as the Mousa-stage evolved (cf Mercier-Langevin *et al.,* 2007c). These authors note that the tholeiitic to transitional nature of the Mouska stage of the MIC was likely the result of early stages of back-arc development when melts were generated during crustal extension and mantle diapirism under the back-arc rift environment causing partial melting of thickened arc crust. An influx of melt generated during partial melting of the subducted slab produced the transitional nature for some of the Mouska-stage magmas. Galley & Lafrance (2014) suggested that the

Mouska stage was produced by fractionation in a single magma chamber. However, based on zircon composition and pressure-temperature estimates, this is unlikely.

The early transitional nature of the Mouska stage based on tectonic discrimination (Fig. 2.20) diagrams and coeval geochronology with the calc-alkaline Doyon stage (Fig. 2.14) are supported by other data from recent studies. For example, silicate melt inclusion analyses from Unit 2.0 of the Lower Bousquet (2697.9 ± 1.5 Ma; Lafrance *et al.,* 2005) record a range in compositions extending from tholeiitic to calc-alkaline (Meagher, 2020), suggesting the shift to an arc-type setting began prior to or as the source magma for the Lower Bousquet Formation was being generated. While silicate melt inclusion analyses from Unit 5.3 of the Upper Bousquet (2697.1 ± 1 Ma; Mercier-Langevin *et al.*, 2007a) record compositions in the transitional and calc-alkaline field (Meagher, 2020), suggesting magma generation at this time was occurring in a predominantly arc-type setting.

The relatively short time span (maximum of 1.44 Ma) for the shift from rift-dominated to arc-dominated magmatism is line with timescales for major porphyry systems to evolve from a barren- to mineralized-system (Chiaradia, 2021; Large *et al.,* 2021). As well, the total gold endowment in the Doyon-Bousquet-LaRonde mining camp is similar to the gold endowment in Cu-Au porphyry deposits that have a similar duration of magmatism, in contrast to Au-rich alkaline porphyry systems which have a much shorter magmatic history (Chiaradia, 2021). In combination with the deep-seated magma chambers responsible for Cu-Au porphyry mineralization (cf Lowenstern, 1994; Shinohara *et al.,* 1995; Chelle-Michou *et al.,* 2017; Chiaradia & Caricchi, 2022; Carter *et al.,* 2022), this may have a connection between the Au-rich deposits in the Doyon-Bousquet-LaRonde mining camp and the deep-seated magma chambers responsible for the evolution of the MIC. Additionally, Cu-Au porphyry-style deposits are present in other TTG suites in the Abitibi greenstone belt (e.g., Pilote *et al.,* 1995; Galley, 2003; Katz *et al.,* 2017, 2021;

Mathieu & Racicot, 2019) and the influence of these processes on their formation must be reconsidered in light of the results of this study.

Extensive fractionation at depth, supported by zircon trace element composition, can promote processes such as sulfide saturation, crystal accumulation, and volatile saturation (e.g., Lowenstern, 1994; Lowenstern, 2001; Richards, 2011; Audétat & Simon, 2012; Chelle-Michou *et al.*, 2017; Du & Audétat, 2020; Large *et al.*, 2021; Carter *et al.*, 2022). For the MIC, this shifts the focus onto magmatic controls for metal endowment in related Au-rich deposits styles in the Doyon-Bousquet-LaRonde mining camp away from shallow degassing to deeper processes in deep-seated magma chambers. Magmatic recharge events, contamination and magma mixing, as well as magma ascent rates also influence the volatile evolution and metal tenors of magmas related to intrusion-related mineral deposits (Lowenstern, 1994; Shinohara *et al.*, 1995; Hattori & Keith, 2001; Lowenstern, 2001; William-Jones & Heinrich, 2005; Halter *et al.*, 2005; Audétat & Simon, 2012; Chelle-Michou *et al.*, 2017; Large *et al.*, 2021; Chiaradia & Caricchi, 2022). The timing of volatile saturation is a key factor in the development of mineralized magmatic-hydrothermal systems. While much of the focus on the role of volatiles has been in shallow crustal environments (< 4 km; e.g., Williams-Jones & Heinrich, 2005) extensive fractionation at depth can induce volatile saturation in magma chambers at depths up to 20 km (Lowenstern, 1994; Shinohara *et al.*, 1995; Lowenstern, 2001; Capriolo *et al.*, 2020; Chiaradia & Caricchi, 2022). The results of this study highlight the value of utilizing zircon to constrain magmatic processes occurring at deeper levels of the crust, prior to emplacement of syn-volcanic intrusions.

2.8 CONCLUSIONS

Using a combination of high-precision U-Pb geochronology, thermobarometric determinations, and zircon trace element trends from compositionally different igneous phases that

comprise the Archean Mooshla Intrusive Complex new constraints on the pressure-temperature-time evolution of this magmatic system are provided. Individual lithologies of both the Mouska and Doyon stages crystallized partially in distinct magma chambers at deep levels within the crust (~20 to 40 km) at conditions slightly lower in temperature and pressure compared to established TTG magma formation conditions. The entire intrusive complex formed over a maximum of 1.44 Ma, with the formation of the tholeiitic-dominant Mouska stage and the calc-alkaline-dominant Doyon stage occurring within a ~1 Ma window. This indicates a rapid change in tectonic setting from a rift- to arc-dominated sources, early in the magmatic evolution of the MIC magmas. Individual lithologies in the MIC were sourced from distinct magma chambers and were evolving coevally at depth, indicating that bulk rock chemistry and surface crosscutting relationships do not capture the full igneous history of the intrusive complex. A greater focus on the duration and compositional complexity of deep crustal magmatic processes is required to fully evaluate the timing and source of magmatic contributions to the metal budget of Au-rich VMS and intrusion-related deposit styles in the Abitibi subprovince of Canada and in similar geological environments globally.

2.9 ACKNOWLEDGEMENTS

Financial support for this project came from the Targeted Geoscience Initiative (TGI) program of the Geological Survey of Canada. The authors thank B. Boucher (University of New Brunswick) for their valuable contribution to LA-ICP-MS trace element analysis of accessory phases and sample preparation. Alan Galley and David Yergeau provided valuable assistance in the field during sample collection and discussions about the regional and local geology. The authors are grateful to the geology departments and staff at the Westwood (Iamgold Corporation) and LaRonde Penna (Agnico Eagle Mines Ltd) mines for access to drill core and tours of the properties.

K. Neyedley acknowledges scholarship support from the Natural Sciences and Engineering Research Council of Canada (NSERC) and the Nova Scotia Research & Innovation Graduate Scholarship program. We appreciate the detailed reviews by John Dilles and an anonymous reviewer that helped improve this manuscript. This is Natural Resources Canada contribution number 20230181.

2.10 REFERENCES

Aleinikoff, J.N., Winstch, R.P., Fanning, C.M. & Doarais, M.J. (2002) U-Pb geochronology of zircon and polygenetic titanite from the Glastonbury Complex, Connecticut, USA: an integrated SEM, EMPA, TIMS, and SHRIMP study. *Chemical Geology*, 188, 125-147.

Annen, C., Blundy, J.D. & Sparks, R.S.J. (2006) The genesis of intermediate and silicic magmas in deep crustal hot zones. *Journal of Petrology*, 47, 505-536.

Audétat, A. & Simon, A. C. (2012) Magmatic controls on porphyry Cu genesis. In: (Hedenquist J. W., Harris M. & Camus F. (eds)) *Economic Geology Monograph in honor of Richard Sillitoe Society of Economic Geologists Special Publication* 16, pp. 553–572.

Bachmann, O., Dungan, M.A. & Bussy, F. (2005) Insights into shallow magmatic processes in large silicic magma bodies: The trace element record in the Fish Canyon magma body, Colorado. *Contributions to Mineralogy and Petrology*, 149, 338–349.

Ballard, J.R., Palin, J.M. & Campbell, I.H. (2002) Relative oxidation states of magmas inferred from Ce(IV)/Ce(III) in zircon: Application to porphyry copper deposits of northern Chile. *Contributions to Mineralogy and Petrology*, 144, 347–364.

Belkabir, A. & Hubert, C. (1995) Geology and structure of a sulfide-rich gold deposit: an example from the Mouska gold mine, Bousquet district, Canada. *Economic Geology*, 90, 1064-1079.

Blundy, J. & Wood, B. (2003) Mineral–melt partitioning of uranium, thorium and their daughters. *Reviews in Mineralogy and Geochemistry*, 52, 59-123.

Botcharnikov, R.E., Linnen, R.L., Wilke, M., Holtz, F., Jugo, P.J. & Berndt, J. (2011) High gold concentrations in sulfide-bearing magma under oxidizing conditions. *Nature Geoscience*, 4, 112-115.

Brandon, A.D., Creaser, R.A. & Chacko, T. (1996) Constraints on rates of granitic magma transport from epidote dissolution kinetics. *Science*, 271, 1845-1847.

Buret, Y., Wotzlaw, J-F., Roozen, S., Guillong, M., von Quadt, A., Heinrich, C.A. (2017) Zircon petrochronological evidence for a plutonic-volcanic connection in porphyry copper deposits. *Geology*, 45, 623-626.

Candela, P.A. & Piccoli, P.M. (2005) Magmatic Processes in the Development of Porphyry-Type Ore Systems. *Economic Geology 100th Anniversary Volume*, 25-37.

Cao, W., Kaus, B.J.P. & Paterson, S. (2016) Intrusion of granitic magma into the continental crust facilitated by magma pulsing and dike-diapir interactions: numerical simulations. *Tectonics*, 35, 1575-1594.

Capriolo, M., Marzoli, A., Aradi, L., Callegaro, S., Dal Corso, J., Newton, R.J., Mills, B.J.W., Bartoli, O., Baker, D.R., Youbi, N., Remusat, L., Spiess, R. & Szabó, C. (2020) Deep CO_2 in the

end-Triassic Central Atlantic Magmatic Province. *Nature Communications*, https://doi.org/10.1038/s41467-020-15325-6.

Carter, L.C., Tapster, S.R., Williamson, B.J., Buret, Y., Selby, D., Rollinson, G.K., Millar, I. & Parvaz, D.B. (2022) A rapid change in magma plumping taps porphyry copper deposit-forming magmas. *Scientific Reports*, 12, 1-20, https://doi.org/10.1038/s41598-022-20158-y

Chelle-Michou, C., Chiaradia, M., Ovtcharova, M., Ulianov, A. & Wotzlaw, J-F. (2014) Zircon petrochronology reveals the temporal link between porphyry systems and the magmatic evolution of their hidden plutonic roots (the Eocene Coroccohuayco deposit, Peru). *Lithos*, 198-199, 129-140.

Chelle-Michou, C., Rottier, B., Caricchi, L. & Simpson, G. (2017) Tempo of magma degassing and the genesis of porphyry copper deposits. *Scientific Reports*, 7, 1-12.

Chiaradia, M. (2021) Magmatic controls on metal endowment of porphyry Cu-Au deposits. *Economic Geology Special Publication* 24, 1-16.

Chiaradia, M. & Caricchi, L. (2022) Supergiant porphyry copper deposits are failed large eruptions. *Communication Earth and Environment*, 3, https://doi.org/10.1038/s43247-022-00440-7

Cherniak, D.J., Watson, E.B. & Wark, D.A. (2007) Ti diffusion in quartz. *Chemical Geology*, 236, 65-74.

Claiborne, L.L., Miller, C.F., Walker, B.A., Wooden, J.L., Mazdab, F.K. & Bea, F. (2006) Tracking magmatic processes through Zr/Hf ratios in rocks and Hf and Ti zoning in zircons: an example from the Spirit Mountain batholith, Nevada. *Mineralogical Magazine*, 70, 517-543.

Claiborne, L.L., Miller, C.F. & Wooden, J.L. (2010) Trace element composition of igneous zircon: a thermal and compositional record of the accumulation and evolution of a large scale silicic batholith, Spirit Mountain, Nevada. *Contributions to Mineralogy and Petrology,* 160, 511-531.

Clemens, J.D., Yearron, L.M. & Stevens, G. (2006) Barberton (South Africa) TTG magmas: geochemical and experimental constraints on source-rock petrology, pressure of formation and tectonic setting. *Precambrian Research*, 151, 53-78.

Condie, K.C. (2005) TTGs and adakites: are they both slab melts?. *Lithos*, 80, 33-44.

Condon, D.J., Schoene, B., McLean, N.M., Bowring, S.A. & Parrish, R. (2015) Metrology and traceability of U-Pb isotope dilution geochronology (EARTHTIME Tracer Calibration Part I). *Geochimica et Cosmochimica Acta*, 164, 464-480.

Davis, D.W. (2002) U-Pb geochronology of Archean metasedimentary rocks in the Pontiac and Abitibi subprovinces, Quebec, constraints on timing, provenance, and regional tectonics. *Precambrian Research*, 115, 97−117.

De Almeida, J. A. C., Dall'Agnol., Oliveira, M.A., Macambira, M.J.B., Pimentel, M.M., Rämö, O.T., Guimarães, F.V., & Leite, A.A.S. (2011) Zircon geochronology, geochemistry and origin of

the TTG suites of the Rio Maria granite-greenstone terrane: implications for the growth of the Archean crust of the Carajás province, Brazil. *Precambrian Research*, 187, 201-221.

Dilles, J.H. (1987) Petrology of the Yerington Batholith, Nevada: evidence for evolution of porphyry copper ore fluids. *Economic Geology*, 82, 1750-1789.

Dilles, J.H., Kent, A.J.R., Wooden, J.L., Tosdal, R.M., Koleszar, A., Lee, R.G. & Farmer, L.P. (2015) Zircon compositional evidence for sulfur-degassing from ore-forming arc magmas. *Economic Geology*, 110, 241-251.

Du, J. & Audétat, A. (2020) Early sulfide saturation is not detrimental to porphyry Cu-Au formation. *Geology*, 48, 519–524.

Dubé, B., Mercier-Langevin, P., Hannington, M.D., Davis, D.W. & Lafrance, B. (2004) Le gisement de sulfures massifs volcanogenes auriferes LaRonde, Abitibi, Québec: Alteration, mineralisations, genese et implications pour l'exploration. *Ministere des Ressources naturelles, de la Faune et des Parcs, Québec* Report MB 2004-03, 112 p.

Dubé, B., Mercier-Langevin, P., Hannington, M.D., Lafrance, B., Gosselin, P. & Gosselin, G. (2007), The LaRonde Penna giant gold-rich volcanogenic massive sulfide deposit, Abitibi, Quebec: alteration footprint, genesis and implications for exploration. *Economic Geology*, 102, 633-666.

Dubé, B., Mercier-Langevin, P., Kjarsgaard, I., Hannington, M., Bécu, V., Côté, J., Moorhead, J., Legault, M. & Bédard, N. (2014) The Bousquet 2-Dumagami world-class Archean Au-rich

volcanogenic massive sulfide deposit, Abitibi, Quebec: metamorphosed submarine advanced argillic alteration footprint and genesis. *Economic Geology*, 109, 121-166.

Ferry, J.M. & Watson, E.B. (2007) New thermodynamic models and revised calibrations for the Ti-in-zircon and Zr-in-rutile thermometers. *Contributions to Mineralogy and Petrology*, 154, 429-437.

Fillion, M., Vallee, M. & Lavoie, C. (1977) Les gisements d'or de la SOQUEM Silverstack, Canton Bousquet, Québec. *CIM Bulletin*, 70, 159−172.

Franklin, J.M., Gibson, H.L., Jonasson, I.R. & Galley, A.G. (2005) Volcanogenic Massive Sulfide Deposits. *Economic Geology 100th Anniversary Volume*, 523-560.

Galley, A.G. (2003) Composite synvolcanic intrusions associated with Precambrian VMS-related hydrothermal systems. *Mineralium Deposita*, 387, 443-473.

Galley, A.G. & Lafrance, B. (2014) Setting and evolution of the Archean synvolcanic Mooshla Intrusive Complex, Doyon-Bousquet-LaRonde mining camp, Abitibi greenstone belt: emplacement history, petrogenesis, and implications for Au metallogenesis. *Economic Geology*, 109, 205-229.

Getsinger, A., Rushmer, T., Jackson, M.D. & Baker, D. (2009) Generating high Mg-numbers and chemical diversity in tonalite-trondhjemite-granodiorite (TTG) magmas during melting and melt segregation in the continental crust. *Journal of Petrology*, 50, 1935-1954.

Goldie, R., Kotila, B. & Seward, D. (1979) The Don Rouyn mine: An Archean porphyry copper deposit near Noranda, Quebec. *Economic Geology*, 74, 1680–1684.

Götze, J., Plötze, M. & Habermann, D. (2001) Origin, spectral characteristics and practical applications of the cathodoluminescence (CL) of quartz - a review. *Contributions to Mineralogy and Petrology*, 71, 225-250.

Grimes, C.B., Wooden, J.L., Cheadle, M.J. & John, B.E. (2015) "Fingerprinting" tectono-magmatic provenance using trace elements in igneous zircon. *Contributions to Mineralogy and Petrology*, 170, doi.org/10.1007/s00410-015-1199-3.

Gunning, H.C. (1941) Region de Bousquet-Joannes, Quebec. *Geological Survey of Canada Memoir* 206, 80 p.

Halter, W.E., Heinrich, C.A. & Pettke, T. (2005) Magma evolution and the formation of porphyry Cu-Au ore fluids: evidence from silicate and sulfide melt inclusions. *Mineralium Deposita*, 39, 845-863.

Hart, T.R., Gibson, H.L. & Lesher, C.M. (2004) Trace element geochemistry and petrogenesis of felsic volcanic rocks associated with volcanogenic massive Cu-Zn-Pb sulfide deposits. *Economic Geology*, 99, 1003-1013.

Hattori, K.H. & Keith, J.D. (2001) Contribution of mafic melt to porphyry copper mineralization: evidence from Mount Pinatubo, Philippines, and Bingham Canyon, Utah, USA. *Mineralium Deposita*, 36, 799-806.

Hayden, L.A. & Watson, B.E. (2007) Rutile saturation in hydrous siliceous melts and its bearing on Ti-thermometry of quartz and zircon. *Earth and Planetary Science Letters*, 258, 561-568.

Hayden, L.A., Watson, B.E. & Wark, D.A. (2008) A thermobarometer for sphene (titanite). *Contributions to Mineralogy and Petrology*, 155, 529-540.

Hermann, J. (2002) Allanite: thorium and light rare earth element carrier in subducted crust. *Chemical Geology*, 192, 289-306.

Hiess, J., Condon, D.J., McLean, N. & Noble, S.R. (2012) $^{238}U/^{235}U$ systematics in terrestrial uranium-bearing minerals. *Science*, 335, 1610-1614.

Hoffman, J.E., Nagel, T.J., Münker, C., Naeraa, T. & Rosing, M.T. (2014) Constraining the process of Eoarchean TTG formation in the Itsaq Gneiss Complex, southern Greenland. *Earth and Planetary Science Letters*, 388, 374-386.

Hoskin, P. W. O. & Schaltegger, U. (2003) The composition of zircon and igneous and metamorphic petrogenesis. In: Hanchar, J. M. & Hoskin, P.W. O. (eds) *Zircon. Mineralogical Society of America and Geochemical Society, Reviews in Mineralogy and Geochemistry*, 53, 27-62.

Jaffey, A.H., Flynn, K.F., Glendenin, L.E., Bentley, W.C. & Essling, A.M. (1971) Precision measurements of half-lives and specific activities of ^{235}U and ^{238}U. *Physical Review C*, 4, 1889-1906.

Katz, L.R., Kontak, D.J., Dubé, B. & McNicoll, V. (2017) The geology, petrology, and geochronology of the Archean Côté Gold large-tonnage, low-grade intrusion-related Au(-Cu) deposit, Swayze greenstone belt, Ontario, Canada. *Canadian Journal of Earth Science*, 54, 173-202.

Katz, L.R., Kontak, D.J., Dubé, B., McNicoll, V., Creaser, R. & Petrus, J.A. (2021) An Archean porphyry-type gold deposit: The Côté Gold Au(-Cu) deposit, Swayze greenstone belt, Superior province, Ontario, Canada. *Economic Geology*, 116, 47-89.

Klimm, K., Blundy, J.D. & Green, T.H. (2008) Trace Element Partitioning and Accessory Phase Saturation during H_2O-Saturated Melting of Basalt with Implications for Subduction Zone Chemical Fluxes. *Journal of Petrology*, 49, 523-553.

Lafrance, B., Moorhead, J. & Davis, D.W. (2003) Cadre geologique du camp minier de Doyon-Bousquet-LaRonde. *Ministere des Ressources naturelles, de la Faune et des Parcs, Québec Reports* ET 2002-07, 45 p., and ET 2002-07 C001 1:20,000 map sheet.

Lafrance, B., Davis, D.W., Goutier, J., Moorhead, J., Pilote, P., Mercier-Langevin, P., Dubé, B., & Galley, A. (2005) Nouvelles datations isotopiques dans la portion quebecoise du Groupe de Blake

River et des unites adjacentes. *Ministere des Ressources naturelles et de la Faune, Québec Report* RP 2005-01, 26 p.

Langshur, A. (1990) The geology, geochemistry and structure of the Mooshla intrusion, Bousquet mining centre, Quebec: Unpublished M.Sc. thesis, Ottawa, Canada, University of Ottawa, 172 p.

Large, S.J.E., von Quadt, A., Wotzlaw, J-F., Guillong, M. & Heinrich, C.A. (2018) Magma evolution leading to porphyry Au-Cu mineralization at the Ok Tedi deposit, Papua New Guinea: trace element geochemistry and high-precision geochronology of igneous zircon. *Economic Geology*, 113, 39-61.

Large, S.J.E., Buret, Y., Wotzlaw, J.F., Karakas, O., Guillong, M., von Quadt, A. & Heinrich, C.A. (2021) Copper-mineralised porphyries sample the evolution of a large-volume silicic magma reservoir from rapid assembly to solidification. *Earth and Planetary Science Letters*, 563, https://doi.org/10.1016/j.epsl.2021.116877.

Lee, R.G., Dilles, J.H., Tosdal, R.M., Wooden, J.L. & Mazdab. F.K. (2017) Magmatic evolution of granodiorite intrusions at the El Salvador porphyry copper deposit, Chile, based on trace element composition and U/Pb age of zircons. *Economic Geology*, 112, 245-273.

Lee, R.G., Byrne, K, D'Angelo, M., Hart, C.J.R., Hollings, P., Gleeson, S.A. & Alfaro, M. (2020) Using zircon trace element composition to assess porphyry copper potential of the Guichon Creek batholith and Highland Valley Copper deposit, south-central British Columbia. *Mineralium Deposita*, 56, 215-238.

Loader, M.A., Wilkinson, J.J. & Armstrong, R.N. (2017) The effect of titanite crystallisation on Eu and Ce anomalies in zircon and its implication for the assessment of porphyry Cu deposit fertility. *Earth and Planetary Science Letters*, 472, 107-119.

Loader, M.A., Nathwani, C.L., Wilkinson, J.J. & Armstrong, R.N. (2022) Controls on the magnetite of Ce anomalies in zircon. *Geochimica et Cosmochimica Acta*, 328, 242-257.

Lowenstern, J.B. (1994) Dissolved volatile concentrations in an ore-forming magma. *Geology*, 22, 893-896.

Lowenstern, J.B. (2001) Carbon dioxide in magmas and implications for hydrothermal systems. *Mineralium Deposita*, 36, 490-502.

Marquis, P., Hubert, Brown, A.C. & Rigg, D.M. (1990) An evaluation of genetic models for gold deposits of the Bousquet district, Quebec, based on their mineralogical, geochemical and structural characteristics. *Canadian Institute of Mining and Metallurgy Special Volume* 24, 383−399.

Martin, H. (1999) Adakitic magmas: modern analogues of Archean granitoids. *Lithos*, 46, 411-429.

Martin, H., Smithies, R.H., Rapp, R., Moyen, J.-F. & Champion, D. (2005) An overview of adakite, tonalite-trondhjemite-granodiorite (TTG), and sanukitoid: relationships and some implications for crustal evolution. *Lithos*, 79, 1-24.

Mathieu, L. & Racicot, D. (2019) Petrogenetic Study of the Multiphase Chibougamau Pluton: Archaean Magmas Associated with Cu–Au Magmato-Hydrothermal Systems. *Minerals*, 9, 174.

Maydagán, L., Franchini, M., Rusk, B., Lentz, D.R., McFarlane, C., Impiccini, A., Ríos, F.J., and Rey, R. (2015) Porphyry to Epithermal Transition in the Altar Cu-(Au-Mo) Deposit, Argentina, Studied by Cathodoluminescence, LA-ICP-MS, and Fluid Inclusion Analysis. *Economic Geology*, 110, 889-923.

McDonough, W.F. & Sun, S.-S. (1995) The composition of the Earth. *Chemical Geology*, 120, 223-253.

McLean, N.M., Condon, D.J., Schoene, B. & Bowring, S.A. (2015) Evaluating uncertainties in the calibration of isotopic reference materials and multi-element isotopic tracers (EARTHTIME tracer calibration part 2). *Geochimica et Cosmochimica Acta*, 164, 481-501.

McNicoll, V., Goutier, J., Dubé, B., Mercier-Langevin, P., Ross, P-S., Dion, C., Monecke, T., Legault, M., Percival, J. & Gibson, H. (2014) U-Pb geochronology of the Blake River Group, Abitibi greenstone belt, Quebec, and implications for base metal exploration. *Economic Geology*, 109, 27–59.

Meagher, D.J. (2020) A melt inclusion study of rhyolitic volcanics in the Bousquet Formation, Doyon-Bousquet-LaRonde district, Abitibi Subprovince, Québec: insight into Archean magmatic processes. Unpublished MSc thesis, Saint Mary's University, 270 p.

Meinhold, G. (2010) Rutile and its application in earth sciences. *Earth-Science Reviews*, 102, 1-28.

Meng, X., Richards, J.P., Kontak, D.J., Simon, A.C., Kleinsasser, J.M., Marsh, J.H., Stern, R.A. & Jugo, P.J. (2021) Variable mode of formation for tonalite-trondhjemite-granodiorite(TTG)-related porphyry-type Cu±Au deposits in the Neoarchean southern Abitibi subprovince (Canada): Evidence from petrochronology and oxybarometery. *Journal of Petrology*, 62, 1-29.

Mercer, C.N. & Reed, M.H. (2013) Porphyry Cu-Mo Stockwork Formation by Dynamic, Transient Hydrothermal Pulses: Mineralogic Insights from the Deposit at Butte, Montana. *Economic Geology*, 108, 1347-1377.

Mercer, C.N., Reed, M.H. & Mercer, C.M. (2015) Time Scales of Porphyry Cu Deposit Formation: Insights from Titanium Diffusion in Quartz. *Economic Geology*, 110, 587-602.

Mercier-Langevin, P. (2005) Geologie du gisement de sulfures massifs volcanogenes auriferes LaRonde, Abitibi, Quebec. Unpublished Ph.D. thesis, Quebec, Canada, Institut National de la Recherche Scientifique, Centre Eau, Terre et Environnement, 689 p.

Mercier-Langevin, P., Dubé, B., Hannington, M.D., Davis, D.W. & Lafrance, B. (2004) Contexte geologique et structural des sulfures massifs volcanogenes auriferes du Gisement LaRonde, Abitibi. *Ministere des Ressources naturelles, de la Faune et des Parcs, Québec, Report* ET 2003-03, 47 p.

Mercier-Langevin, P., Dubé, B., Hannington, M.D., Davis, D.W., Lafrance, B. & Gosselin, G. (2007a) The LaRonde Penna Au-rich volcanogenic massive sulfide deposit, Abitibi greenstone belt, Quebec: Part 1. Geology and geochronology. *Economic Geology*, 102, 585−609.

Mercier-Langevin, P., Dubé, B., Lafrance, B., Hannington, M., Galley, A., Moorhead, J. & Gosselin, P. (2007b) Metallogeny of the Doyon-Bousquet-LaRonde mining camp, Abitibi greenstone belt, Quebec. *Geological Association of Canada, Mineral Deposits Division, Special Publication* 5, 673−701.

Mercier-Langevin, P., Dubé, B., Hannington, M.D., Richer-Lafleche, M. & Gosselin G. (2007c) The LaRonde Penna Au-rich volcanogenic massive sulfide deposit, Abitibi greenstone belt, Quebec: Part 2. Lithogeochemistry and paleotectonic setting. *Economic Geology*, 102, 611−631.

Mercier-Langevin, P., Ross, P.-S., Lafrance, B. & Dubé, B. (2008) Volcaniclastic rocks of the Bousquet scoriaceous tuff units north of the LaRonde Penna mine, Doyon-Bousquet-LaRonde mining camp, Abitibi greenstone belt, Quebec. *Geological Survey of Canada Current Research Paper* 2008-11, 19 p.

Mercier-Langevin, P., Wright-Holfeld, A., Dubé, B., Bernier, C., Houle, N., Savoie, A. & Simard, P. (2009) Stratigraphic setting of the Westwood-Warrenmac ore zones, Westwood project, Doyon-Bousquet-LaRonde mining camp, Abitibi, Quebec. *Geological Survey of Canada Current Research Paper* 2009-03, 20 p.

Mercier-Langevin, P., Goutier, J., Ross, P.-S., McNicoll, V., Monecke, T., Dion, C., Dubé, B., Thurston, P., Becu, V., Gibson, H., Hannington, M. & Galley, A. (2011) The Blake River Group of the Abitibi greenstone belt and its unique VMS and gold-rich VMS endowment. *Geological Survey of Canada Open File Report* 6869, 61 p.

Mercier-Langevin, P., Dubé, B., Blanchet, F., Pitre, D. & Laberge, A. (2017) The LaRonde Penna Au-rich volcanic-hosted massive sulfide deposit. *Reviews in Economic Geology*, 19, 225–245.

Mercier-Langevin, P., Dubé, B. & Fortin, D. (2021) The Doyon-Bousquet-LaRonde Mining Camp. *Resources Mines & Industry*, Fall 2021, 44-61.

Mole, D.R., Thurston, P.C., Marsh, J.H., Stern, R.A., Ayer, J.A., Martin, L.A.J. & Lu, Y.J. (2021) The formation of Neoarchean continental crust in the south-east Superior Craton by two distinct geodynamic processes. *Precambrian Research*, 356, https://doi.org/10.1016/j.precamres.2021.106104.

Moyen, J.-F. & Stevens, G. (2006) Experimental constraints on TTG petrogenesis: implications for Archean geodynamics: In: Benn, K., Mareschal, J.-C., Condie, K.C. (Eds.), *Archean geodynamics and environments, Monographs, AGU*, 149–178.

Moyen, J.-F. & Martin, H. (2012) Forty years of TTG research. *Lithos*, 148, 312-336.

Mungall, J.E., Kamo, S.L. & McQuade, S. (2016) U-Pb geochronology documents out-of-sequence emplacement of ultramafic layers in the Bushveld Igneous Complex of South Africa. *Nature Communications* 7, 13385.

Nekvasil, H. (1988) Calculated effect of anorthite component on the crystallization paths of H_2O-undersaturated haplogranitic melts. *American Mineralogist*, 73, 966-981.

Ni, Z., Arevalo, R., Piccoli, P., & Reno, B. L. (2020). A novel approach to identifying mantle-equilibrated zircon by using trace element chemistry. *Geochemistry, Geophysics, Geosystems*, 21, e2020GC009230. https://doi.org/10.1029/2020GC009230

Olson, N.H., Dilles, J.H., Kent, A.J.R. & Lang, J.R. (2017) Geochemistry of the Cretaceous Kaskanak Batholith and genesis of the Pebble porphyry Cu-Au-Mo deposit, southwest Alaska. *American Mineralogist*, 102, 1597-1621.

Osborne, Z.R., Thomas, J.B., Nachlas, W.O., Angel, R.J., Hoff, C.M. & Watson, E.B. (2022) TitaniQ revisited: expanded and improved Ti-in-quartz solubility model for thermobarometry. Contributions to Mineralogy and Petrology, 177, https://doi.org/10.1007/s00410-022-01896-8.

Petford, N., Kerr, R.C. & Lister, J.R. (1993) Dike transport of granitoid magmas. *Geology*, 21, 845-848.

Petford, N., Cruden, A.R., McCaffrey, K.J.W. & Vigneresse, J.-L. (2000) Granite magma formation, transport and emplacement in the Earth's crust. *Nature*, 408, 669-673.

Piercey, S.J. (2011) The setting, style, and role of magmatism in the formation of volcanogenic massive sulfide deposits. *Mineralium Deposita*, 46, 449-471.

Piercey, S.J., Chaloux, E.C., Péloquin, A.S., Hamilton, M.A. & Creaser, R.A. (2008) Synvolcanic and younger plutonic rocks from the Blake River Group: Implications for regional metallogenesis. *Economic Geology*, 103, 1243-1268.

Pilote, P., Robert, F., Sinclair, W.D., Kirkham, R.V. & Daigneault, R. (1995) Porphyry-type mineralization in the Doré Lake Complex: Clark Lake and Merrill Island areas. *Geological Survey of Canada, Open File* 3143, 65–86.

Prowatke, S. & Klemme, S. (2005) Effect of melt composition on the partitioning of trace elements between titanite and silicate melt. *Geochimica et Cosmochimica Acta*, 69, 695-709.

Prowatke, S. & Klemme, S. (2006) Trace element partitioning between apatite and silicate melts. *Geochimica et Cosmochimica Acta*, 70, 4513-4527.

Qian, Q. & Hermann, J. (2013) Partial melting of lower crust at 10-15 kbar: constraints on adakite and TTG formation. *Contributions to Mineralogy and Petrology*, 165, 1195-1224.

Rapp, R.P., Watson, E.B. & Miller, C.F. (1991) Partial melting of amphibolite/eclogite and the origin of Archaean trondhjemites and tonalites. *Precambrian Research*, 51, 1- 25.

Rasmussen, B., Fletcher, I. R. & Muhling, J.R. (2013) Dating deposition and low-grade metamorphism by in situ U-Pb geochronology of titanite in the Paleoproterozoic Timeball Hill Formation, South Africa. *Chemical Geology*, 351, 29-39.

Richards, J.P. (2003) Tectono-magmatic precursors for porphyry Cu-(Mo-Au) deposit formation. *Economic Geology*, 98, 1515-1533.

Richards, J.P. (2011) Magmatic to hydrothermal metal fluxes in convergent and collided margins. *Ore Geology Reviews*, 40, 1-26.

Richards, J.P. & Kerrich, R. (2007) Special paper: Adakite-like rocks: Their diverse origins and questionable role in metallogenesis. *Economic Geology*, 102, 537-576.

Ross, P.-S., McNicoll, V., Goutier, J., Mercier-Langevin, P. & Dubé, B. (2011) Basaltic to andesitic volcaniclastic rocks in the Blake River Group, Abitibi Greenstone Belt: 2. Origin, geochemistry, and geochronology. *Canadian Journal of Earth Sciences*, 48, 757-777.

Rubatto, D. & Hermann, J. (2007) Experimental zircon/melt and zircon/garnet trace element partitioning and implications for the geochronology of crustal rocks. *Chemical Geology*, 241, 38–61.

Savoie, A., Trudel, P., Sauve, P., Hoy, L. & Lao, K. (1991) Geologie de la mine Doyon (region de Cadillac). *Ministere de l'Energie et des Ressources, Québec, Report* ET 90-05, 80 p.

Schmidt, M.X. & Poli, S. (2004) Magmatic epidote. *Reviews in Mineralogy and Geochemistry*, 56, 399-430.

Seedorff, E., Barton, M.D., Stavast, W.J.A. & Maher, D.J. (2008) Root zones of porphyry systems: Extending the porphyry model to depth. *Economic Geology*, 103, 939-956.

Shinohara, H., Kazahaya, K. & Lowenstern, J.B. (1995) Volatile transport in a convecting magma column: implications for porphyry Mo mineralization. *Geology*, 23, 1091-1094.

Singer, B.S., Myers, J.D., Linneman, S.R. & Angevine, C.L. (1989) The thermal history of ascending magma diapirs and the thermal and physical evolution of magmatic conduits. *Journal of Volcanology and Geothermal Research*, 37, 273-289.

Smithies, R.H. (2000) The Archean tonalite-trondhjemite-granodiorite (TTG) series is not an analogue of Cenozoic adakite. *Earth and Planetary Science Letters*, 182, 115-125.

Smythe, D.J. & Brenan, J.M. (2016) Magmatic oxygen fugacity estimated using zircon-melt partitioning of cerium. *Earth and Planetary Science Letters*, 453, 260-266.

Thomas, J.B., Watson, E.B., Spear, F.S., Shemella, P.T., Nayak, S.K. & Lanzirotti, A. (2010) TitaniQ under pressure: the effect of pressure and temperature on the solubility of Ti in quartz. *Contributions to Mineralogy and Petrology*, 160, 743-759.

Tiepolo, M., Oberti, R., & Vannucci, R. (2002) Trace-element incorporation in titanite: constraints from experimentally determined solid/liquid partition coefficients. *Chemical Geology*, 191, 105-119.

Tiepolo, M., Oberti, R., Zanetti, A., Vannucci, R. & Foley, S.F. (2007) Trace-element partitioning between amphibole and silicate melt. *Reviews in Mineralogy and Petrology*, 67, 417-452.

Tourigny, G., Hubert, C., Brown, A.C. & Crépeau, R. (1989) Structural control of gold mineralization at the Bousquet mine, Abitibi, Quebec. *Canadian Journal of Earth Sciences*, 26, 157-175.

Trail, D., Watson, E.B. & Tailby, N.D. (2012) Ce and Eu anomalies in zircon as proxies for the oxidation state of magmas. *Geochimica et Cosmochimica Acta*, 97, 70-87.

Trudel, P., Sauve, P., Tourigny, G., Hubert, C. & Hoy, L. (1992) Synthese des caracteristiques geologiques des gisements de la region de Cadillac (Abitibi). *Ministere des Ressources naturelles, Québec, Report* MM 91-01, 106 p.

Valliant, R.I. & Hutchinson, R.W. (1982) Stratigraphic distribution and genesis of gold deposits, Bousquet region, northwestern Quebec. *Canadian Institute of Mining and Metallurgy Special Volume* 24, 27−40.

Valley, J.W., Kinny, P.D., Schulze, D.J. & Spicuzza, M.J. (1998) Zircon megacrysts from kimberlite: oxygen isotope variability among mantle melts. *Contributions to mineralogy*

and petrology, 133, 1-11.

Vezinet, A., Pearson, D.G., Thomassot, E., Stern, R.A., Sarkar, C., Luo, Y., & Fisher, C.M. (2018) Hydrothermally-altered mafic crust as source for early Earth TTG: Pb/Hf/O isotope and trace element evidence in zircon from TTG of the Eoarchean Saglek Block, N. Labrador. *Earth and Planetary Science Letters*, 503, 95-107.

Wall, C.J., Scoates, J.M, Weis, D., Friedman, R.M., Amini, M. & Meurer, W.P. (2018) The Stillwater Complex: integrated zircon geochronological and geochemical constraints on the age, emplacement history and crystallization of a large, open-system layered intrusion. *Journal of Petrology*, 59, 153-190.

Watson, E.B. (1979) Zircon saturation in felsic liquids: experimental results and applications to trace element geochemistry. *Contributions to Mineralogy and Petrology*, 70, 407-419.

Watson, E.B. & Harrison, T.M. (1983) Zircon saturation revisited: temperature and composition effects in a variety of crustal magma types. *Earth and Planetary Sciences Letters*, 64, 295-304.

Wiemer, D., Schrank, C.E., Murphy, D.T., Wenham, L., & Allen, C.M. (2018) Earth's oldest stable crust in the Pilbara craton formed by cyclic gravitational overturns. *Nature Geoscience*, 11, 357-361.

Williams-Jones, A.E. & Heinrich, C.A. (2005) Vapor transport of metals and the formation of magmatic-hydrothermal ore deposits. *Economic Geology*, 100, 1287-1312.

Wones, D.R. (1989) Significance of the assemblage titanite + magnetite + quartz in granitic rocks. *American Mineralogist*, 74, 744-749.

Yergeau, D., Mercier-Langevin, P.L., Dubé, B., Malo, M. & Savoie, A. (2022a) The Westwood Deposit, Southern Abitibi Greenstone Belt, Canada: An Archean Au-Rich Polymetallic Magmatic-Hydrothermal System-Part I. Volcanic Architecture, Deformation, and Metamorphism. *Economic Geology*, 117, 545-575.

Yergeau, D., Mercier-Langevin, P.L., Dubé, B., McNicoll, V., Jackson, S.E., Malo, M. & Savoie, A. (2022b) The Westwood Deposit, Southern Abitibi Greenstone Belt, Canada: An Archean Au-Rich Polymetallic Magmatic-Hydrothermal System—Part II. Hydrothermal Alteration, Mineralization, and Geologic Model. *Economic Geology*, 117, 577-608.

Zajacz, Z., Candela, P.A., Piccoli, P.M., Wälle, M. & Sanchez-Valle, C. (2012) Gold and copper in volatile saturated mafic to intermediate magmas: solubilities, partitioning, and implications for ore deposit formation. *Geochimica et Cosmochimica Acta*, 91, 140-159.

Zajacz, Z., Candela, P.A., Piccoli, P.M., Sanchez-Valle, C. & Wälle, M. (2013) Solubility and partitioning behavior of Au, Cu, Ag, and reduced S in magmas. *Geochimica et Cosmochimica Acta*, 112, 288-304.

Zen E. & Hammarstrom, J.M. (1984) Magmatic epidote and its petrologic significance. *Geology*, 12, 515-518.

Zhang, C., Holtz, F., Koepke, J., Wolff, P., Ma, C., and Bédard, J. (2013). Constraints from experimental melting of amphibolite on the depth of formation of garnet-rich restites, and implications for models of Early Archean crustal growth. Precambrian Research, 231, 206-217.

Zhong, S., Feng, C., Seltman,, R., Li, D., & Qau, H. (2018) Can magmatic zircon be distinguished from hydrothermal zircon by trace element composition? The effect of mineral inclusions on zircon trace element composition. *Lithos*, 314-315, 646-657.

Table 2.1. Summary of zircon grain size and zoning types

Lithology	Mooshla Phase	Sample	UTM E*	UTM N*	DDH	Depth (m)	Size (μm)	Form	Aspect Ratio	Zoning	Comments
Gabbro	Mouska-stage B	MSK-6-810-715.6	680356	5348611	MSK-G-810	715.6	90 - 500	Eu-subhedral	1:1 - 1:2	Oscillatory, sector	Very rare resportion features along internal zones, rare mineral and melt inclusions
Low-Th/U quartz diorite	Mouska-stage C	MSK-6-810-493.7	680356	5348611	MSK-G-810	493.7	100 - 620	Eu-subhedral	1:1 - 1:3	Oscillatory, sector	Very rare resportion features along internal zones, rare mineral and melt inclusions
High-Th/U quartz diorite	Mouska-stage C	MSK-6-810-127.6	680356	5348611	MSK-G-810	127.6	100 - 400	Subhedral	1:1 - 1:4	Oscillatory, sector	Common resportion features along internal zones, rare mineral and melt inclusions
Tonalite	Mouska-stage D	Stop 10	682654	5348871	NA	NA	120 - 560	Eu-subhedral	1:1 - 1:3	Oscillatory, sector	Very rare resportion features along internal zones, rare mineral and melt inclusions
Tonalite	Mouska-stage D	Stop 11	682756	5348794	NA	NA	120 - 540	Eu-subhedral	1:1 - 1:3	Oscillatory, sector	Very rare resportion features along internal zones, rare mineral and melt inclusions
Phyric Trondhjemite	Doyon-stage H	Bousquet-4	681930	5348034	NA	NA					
Trondhjemite	Doyon-stage I	1106-96-1323	682222	5347354.5	1106-96	1323	70 - 100	Eu-subhedral	1:1 - 1:2	Oscillatory, sector	Very rare resportion features along internal zones, rare mineral and melt inclusions
Trondhjemite	Doyon-stage I	1106-96-1444.5	682222	5347354.5	1106-96	1444.5	50 - 160	Eu-subhedral	1:1 - 1:2	Oscillatory, sector	Very rare resportion features along internal zones, rare mineral and melt inclusions

*UTM Zone 17N

2.12 FIGURES

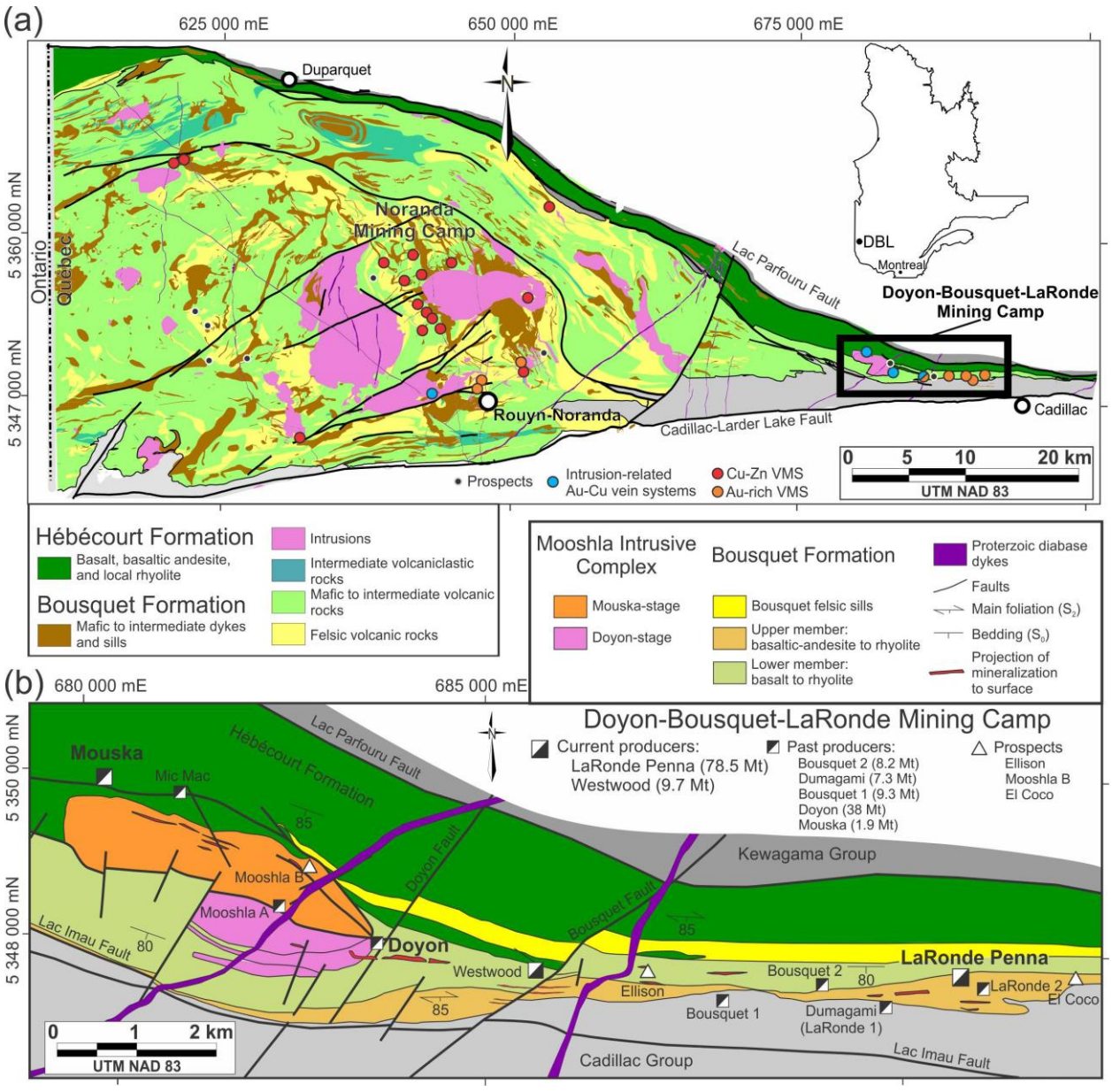

Fig. 2.1. (a) Simplified geological map of the eastern Blake River Group of the Abitibi greenstone belt showing the location of the Doyon-Bousquet-LaRonde mining camp. (b) Simplified geological map of the Doyon-Bousquet-LaRonde mining camp showing the location of the Mooshla intrusive complex and spatial relationship to mines in the area. Modified from Mercier-Langevin (2009).

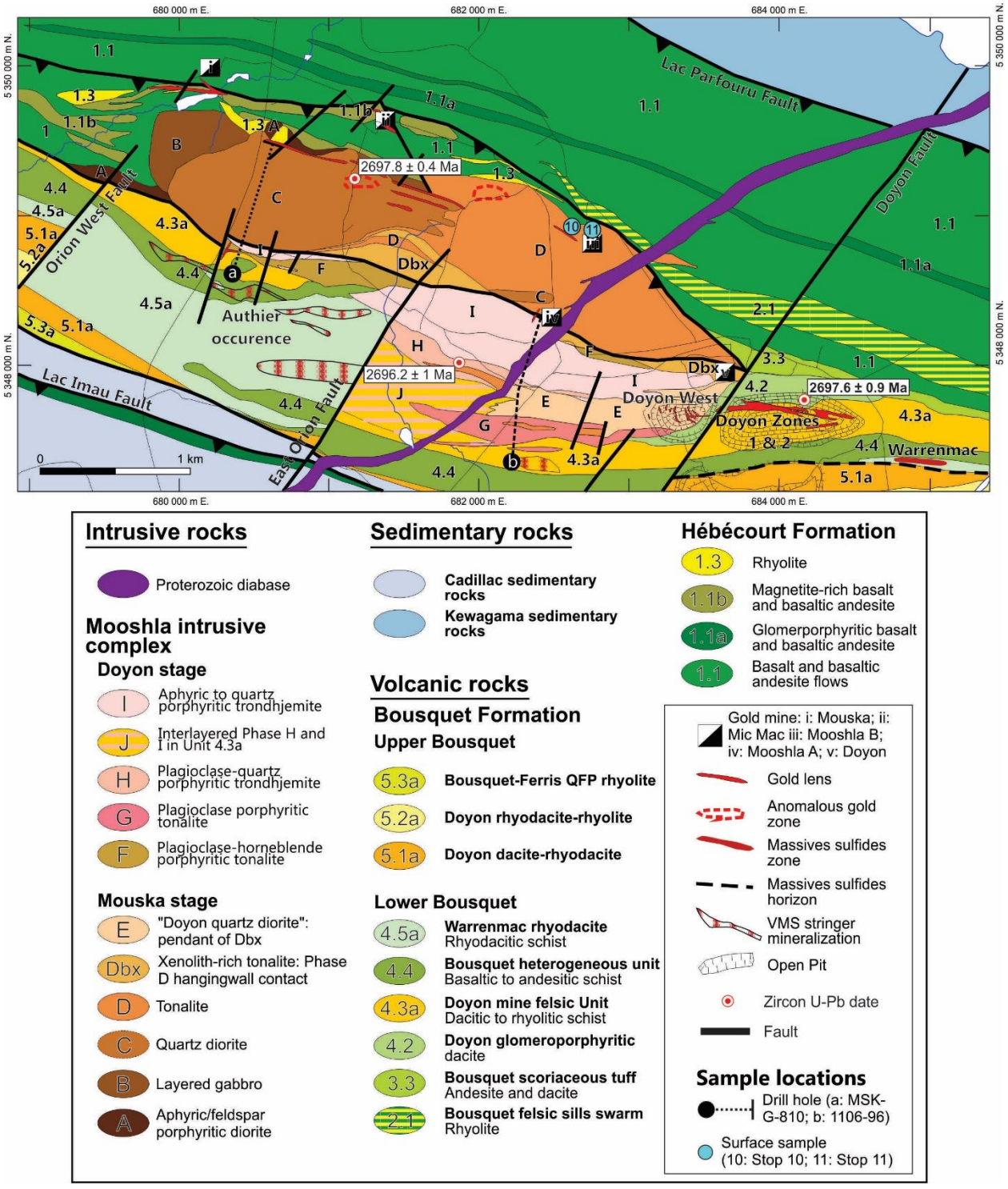
680 000 m E.
682 000 m E.
684 000 m E.
5 350 000 m N.
5 348 000 m N.
Lac Parfouru Fault
Doyon Fault
Orion West Fault
Lac Imau Fault
East Orion Fault
Authier occurence
Doyon West
Doyon Zones
Warrenmac
2697.8 ± 0.4 Ma
2696.2 ± 1 Ma
2697.6 ± 0.9 Ma
0
1 km
Intrusive rocks
Proterozoic diabase
Mooshla intrusive complex
Doyon stage
I Aphyric to quartz porphyritic trondhjemite
J Interlayered Phase H and I in Unit 4.3a
H Plagioclase-quartz porphyritic trondhjemite
G Plagioclase porphyritic tonalite
F Plagioclase-horneblende porphyritic tonalite
Mouska stage
E "Doyon quartz diorite": pendant of Dbx
Dbx Xenolith-rich tonalite: Phase D hangingwall contact
D Tonalite
C Quartz diorite
B Layered gabbro
A Aphyric/feldspar porphyritic diorite
Sedimentary rocks
Cadillac sedimentary rocks
Kewagama sedimentary rocks
Volcanic rocks
Bousquet Formation
Upper Bousquet
5.3a Bousquet-Ferris QFP rhyolite
5.2a Doyon rhyodacite-rhyolite
5.1a Doyon dacite-rhyodacite
Lower Bousquet
4.5a Warrenmac rhyodacite Rhyodacitic schist
4.4 Bousquet heterogeneous unit Basaltic to andesitic schist
4.3a Doyon mine felsic Unit Dacitic to rhyolitic schist
4.2 Doyon glomeroporphyritic dacite
3.3 Bousquet scoriaceous tuff Andesite and dacite
2.1 Bousquet felsic sills swarm Rhyolite
Hébécourt Formation
1.3 Rhyolite
1.1b Magnetite-rich basalt and basaltic andesite
1.1a Glomerporphyritic basalt and basaltic andesite
1.1 Basalt and basaltic andesite flows
Gold mine: i: Mouska; ii: Mic Mac iii: Mooshla B; iv: Mooshla A; v: Doyon
Gold lens
Anomalous gold zone
Massives sulfides zone
Massives sulfides horizon
VMS stringer mineralization
Open Pit
Zircon U-Pb date
Fault
Sample locations
Drill hole (a: MSK-G-810; b: 1106-96)
Surface sample (10: Stop 10; 11: Stop 11)

Fig. 2.2. Geological map of the Mooshla intrusive complex (modified from Galley & Lafrance, 2014). Location of drill holes and surface samples utilized in the study are indicated. Zircon U-Pb ages are from Lafrance *et al.* (2005) and McNicoll *et al.* (2014) and are recalculated using the U decay constant of Hiess et al. (2012).

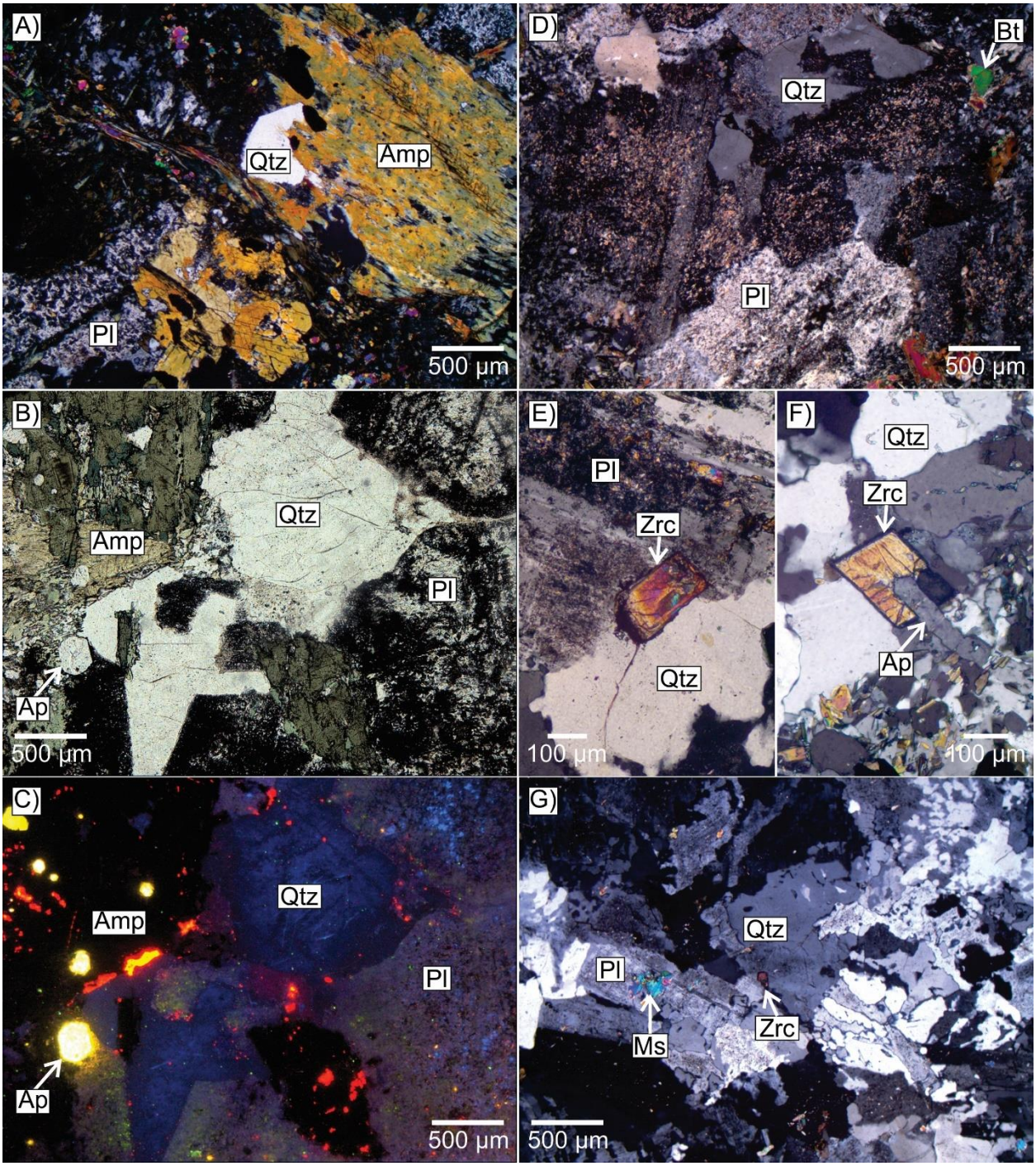
A)
Qtz
Amp
Pl
500 µm
D)
Bt
Qtz
Pl
500 µm
B)
Amp
Qtz
Pl
Ap
500 µm
E)
Pl
Zrc
Qtz
100 µm
F)
Qtz
Zrc
Ap
100 µm
C)
Amp
Qtz
Pl
Ap
500 µm
G)
Qtz
Pl
Ms
Zrc
500 µm

Fig. 2.3. Representative photomicrographs and hot-CL images of various phases from the Mooshla intrusive complex. (a) Coarse amphibole (former pyroxene?) with interstitial quartz and moderately to strongly altered plagioclase from phase B gabbro (sample 715.6; cross- polarized light [XPL]). (b) Coarse interstitial quartz occurring between amphibole and plagioclase from phase C low-Th/U quartz diorite. Interstitial apatite is also present (sample 493.7; plane-polarized light [PPL]). (c) Hot-CL image of the same location as frame B. The blue CL colour of quartz is consistent with a magmatic origin (cf Götze *et al.*, 2001 and references therein). (d) Interstitial quartz to moderately to strongly altered plagioclase from high-Th/U quartz diorite phase C (sample 127.6; XPL). (e) Interstitial, tabular zircon from phase D tonalite (sample Stop 10; XPL). (f) Interstitial zircon intergrown with apatite from phase D tonalite (sample Stop 11; XPL). (g) Quartz and plagioclase displaying a weak graphic texture (top right corner) and zircon occurring interstitial to quartz and plagioclase in phase I aphyric trondhjemite (sample 1444.5; XPL). Amp = amphibole; Ap = apatite; Bt = biotite; Ms = muscovite; Pl = plagioclase; Qtz = quartz; Zrc = zircon.

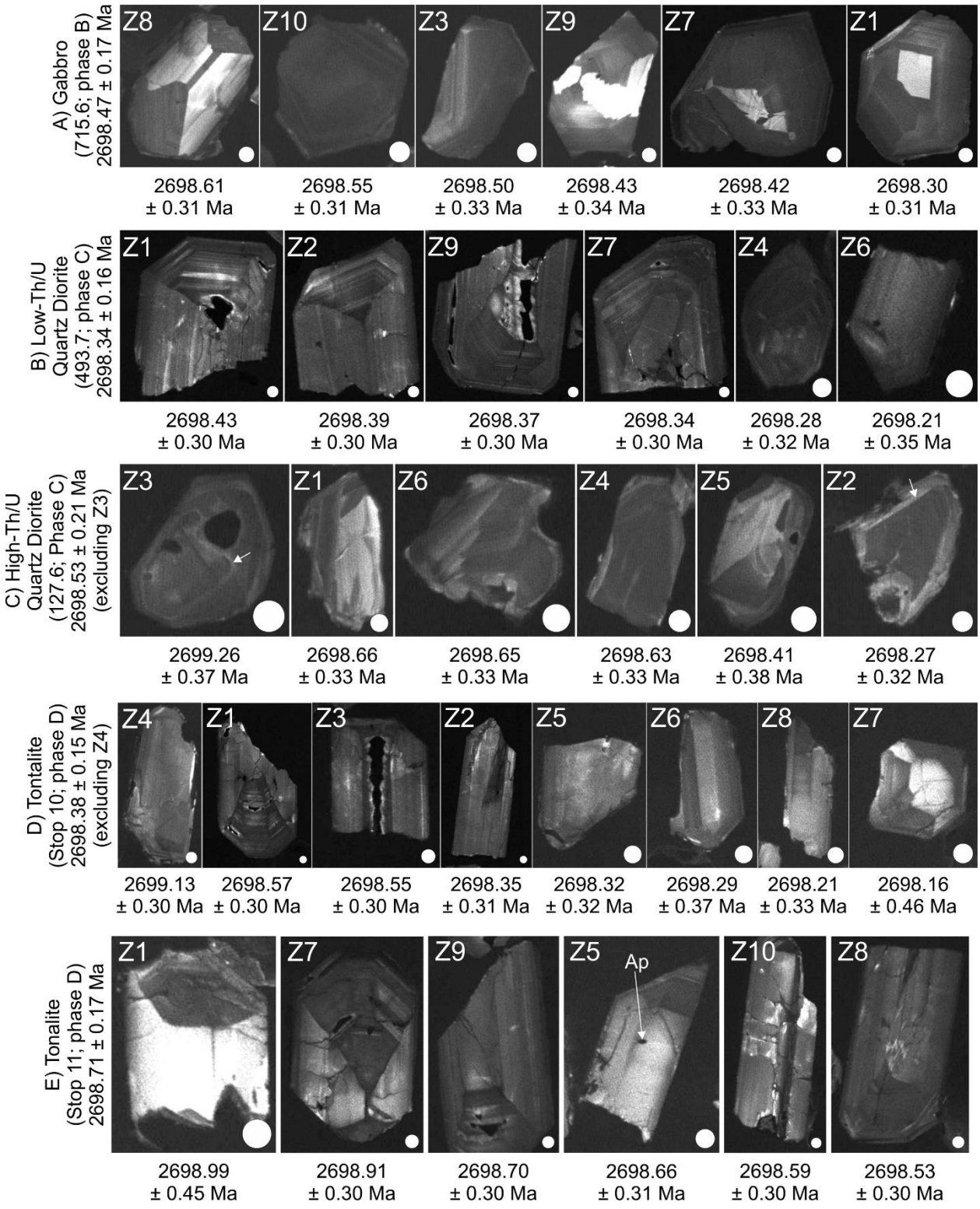
A) Gabbro
(715.6; phase B)
2698.47 ± 0.17 Ma
Z8
Z10
Z3
Z9
Z7
Z1
2698.61 ± 0.31 Ma
2698.55 ± 0.31 Ma
2698.50 ± 0.33 Ma
2698.43 ± 0.34 Ma
2698.42 ± 0.33 Ma
2698.30 ± 0.31 Ma
B) Low-Th/U
Quartz Diorite
(493.7; phase C)
2698.34 ± 0.16 Ma
Z1
Z2
Z9
Z7
Z4
Z6
2698.43 ± 0.30 Ma
2698.39 ± 0.30 Ma
2698.37 ± 0.30 Ma
2698.34 ± 0.30 Ma
2698.28 ± 0.32 Ma
2698.21 ± 0.35 Ma
C) High-Th/U
Quartz Diorite
(127.6; Phase C)
2698.53 ± 0.21 Ma
(excluding Z3)
Z3
Z1
Z6
Z4
Z5
Z2
2699.26 ± 0.37 Ma
2698.66 ± 0.33 Ma
2698.65 ± 0.33 Ma
2698.63 ± 0.33 Ma
2698.41 ± 0.38 Ma
2698.27 ± 0.32 Ma
D) Tontalite
(Stop 10; phase D)
2698.38 ± 0.15 Ma
(excluding Z4)
Z4
Z1
Z3
Z2
Z5
Z6
Z8
Z7
2699.13 ± 0.30 Ma
2698.57 ± 0.30 Ma
2698.55 ± 0.30 Ma
2698.35 ± 0.31 Ma
2698.32 ± 0.32 Ma
2698.29 ± 0.37 Ma
2698.21 ± 0.33 Ma
2698.16 ± 0.46 Ma
E) Tonalite
(Stop 11; phase D)
2698.71 ± 0.17 Ma
Z1
Z7
Z9
Z5
Ap
Z10
Z8
2698.99 ± 0.45 Ma
2698.91 ± 0.30 Ma
2698.70 ± 0.30 Ma
2698.66 ± 0.31 Ma
2698.59 ± 0.30 Ma
2698.53 ± 0.30 Ma

Fig. 2.4. Cold CL images of zircon grains from the Mouska stage of the Mooshla intrusive complex that were analyzed by CA-ID-TIMS. Weighted mean U-Pb age and uncertainty (95% confidence level) are listed for each sample on the left-hand side and U-Pb age and uncertainty (2σ) are listed below each individual grain and full results are presented in Supplementary Materials Table 2.3. Circles in each image are 25 μm. (a) Zircon from phase B gabbro (sample 715.6). (b) Low-Th/U quartz diorite from phase C (sample 493.7). (c) High-Th/U quartz diorite from phase C (sample 127.6). Arrows in Z3 and Z2 point toward resorption margins. (d) Zircon from phase D tonalite (sample Stop 10). (e) Zircon from phase D tonalite (sample Stop 11). Note apatite (Ap) inclusion in Z5.

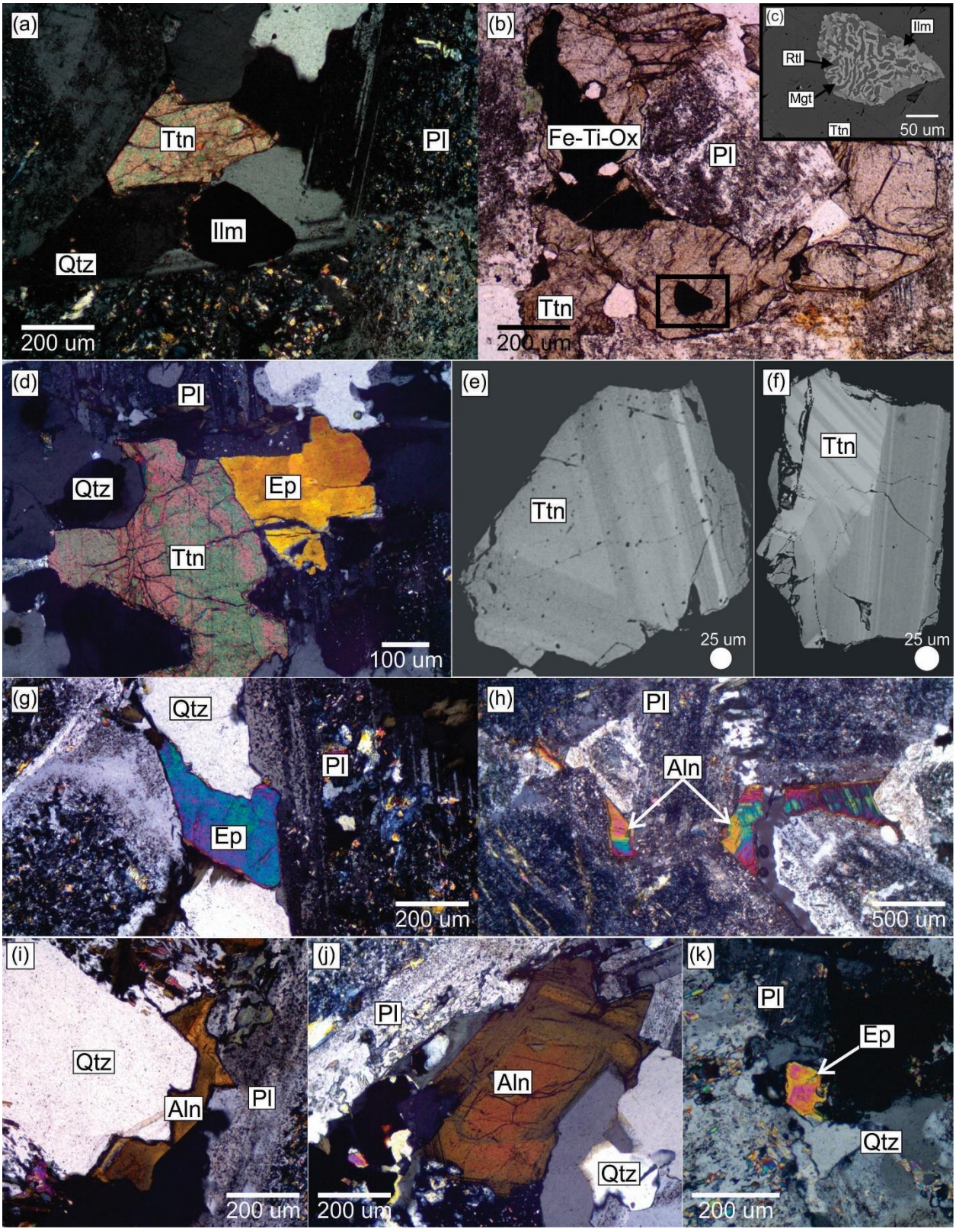
(a)
Ttn
Pl
Ilm
Qtz
200 um
(b)
Fe-Ti-Ox
Pl
Ttn
200 um
(c)
Ilm
Rtl
Mgt
Ttn
50 um
(d)
Pl
Qtz
Ep
Ttn
100 um
(e)
Ttn
25 um
(f)
Ttn
25 um
(g)
Qtz
Pl
Ep
200 um
(h)
Pl
Aln
500 um
(i)
Qtz
Aln
Pl
200 um
(j)
Pl
Aln
Qtz
200 um
(k)
Pl
Ep
Qtz
200 um

Fig. 2.5. Representative photomicrographs of accessory minerals in various phases from the Mooshla intrusive complex. (a) Interstitial titanite and ilmenite from phase D tonalite (sample from Stop 11; XPL). (b) Interstitial titanite with inclusions and partial inclusions of Fe-Ti-oxides (see frame c) from phase D tonalite (sample Stop 10; PPL). (c) subsolidus Fe-Ti-oxide assemblage composed of rutile, ilmenite, and magnetite in titanite (sample from Stop 10; SEM-BSE image). (d) Interstitial titanite and epidote sharing a mutual grain boundary in phase D tonalite (sample from Stop 11; XPL). (e) Titanite displaying oscillatory zoning (sample from Stop 11; SEM-BSE image). (f) Titanite displaying oscillatory and sector zoning (sample from Stop 10; SEM-BSE image). (g) Interstitial, wedge-shaped epidote in phase D tonalite (sample from Stop 11). (h) Interstitial allanite from phase D tonalite (sample from Stop 10; XPL). (i-j) Interstitial allanite from phase D tonalite (sample from Stop 11; XPL). (k) Epidote occurring interstitial to plagioclase and quartz (sample 1323; XPL). Aln = allanite; Ep = epidote; Fe-Ti-Ox = Fe-Ti-Oxide; Ilm = ilmenite; Mgt = magnetite; Pl = plagioclase; Qtz = quartz; Rtl = rutile; Ttn = titanite; Zrc = zircon.

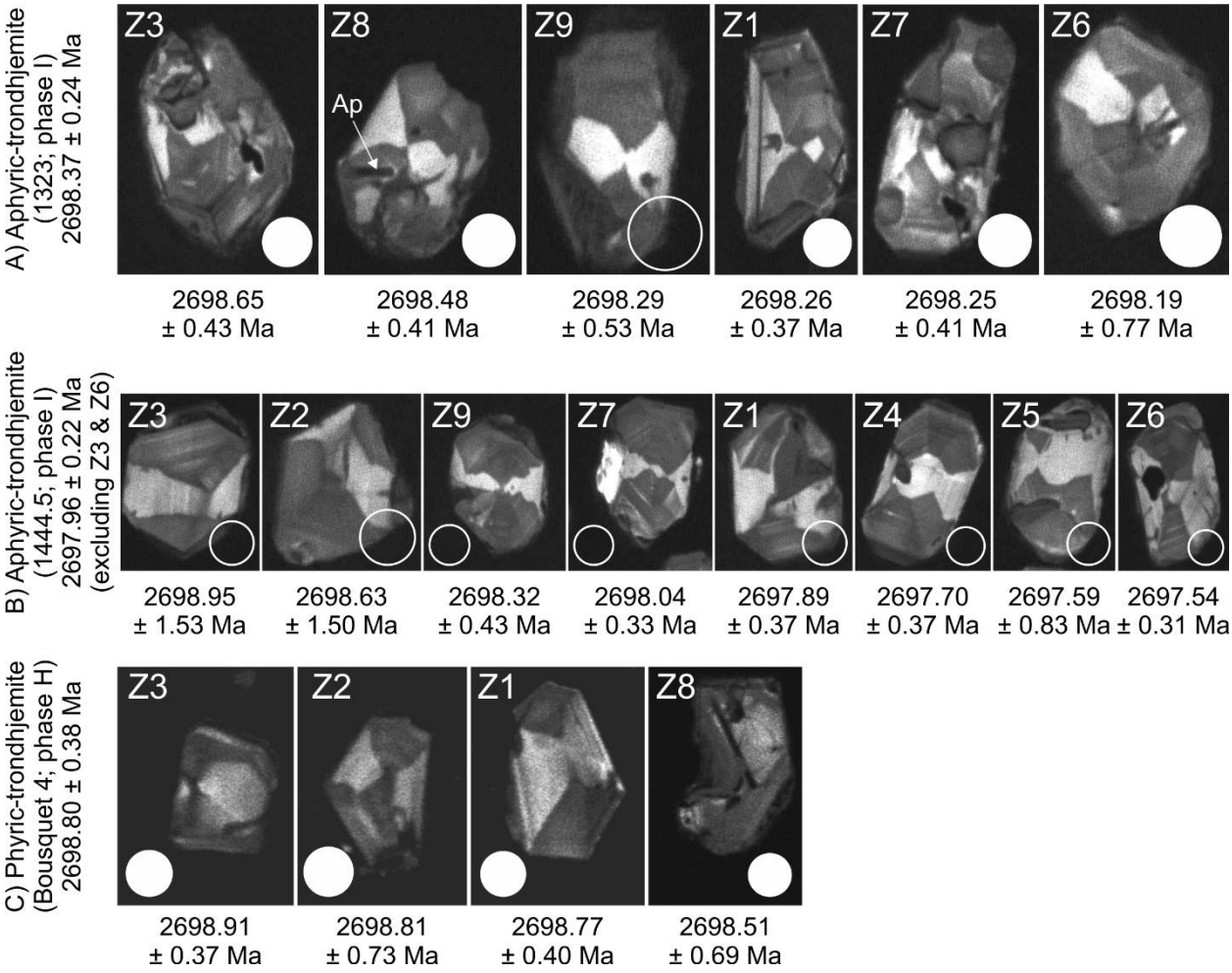

Fig. 2.6. Cold CL images of zircon grains from the Doyon stage of the Mooshla intrusive complex that were analyzed by CA-ID-TIMS. Weighted mean U-Pb age and uncertainty (95% confidence level) are listed for each sample on the left-hand side and U-Pb age and uncertainty (2σ) are listed below each individual grain and full results are presented in Supplementary Materials Table 2.2. Circles in each image are 25 µm. (a) Zircon from aphyric trondhjemite phase I (sample 1323). Note apatite (Ap) inclusion in Z8. (b) Zircon from aphyric trondhjemite phase I (sample 1444.5). (c) Zircon from phyric trondhjemite phase H (sample from Bousquet 4; sample collected from historical UofT collection; Lafrance *et al.*, 2005).

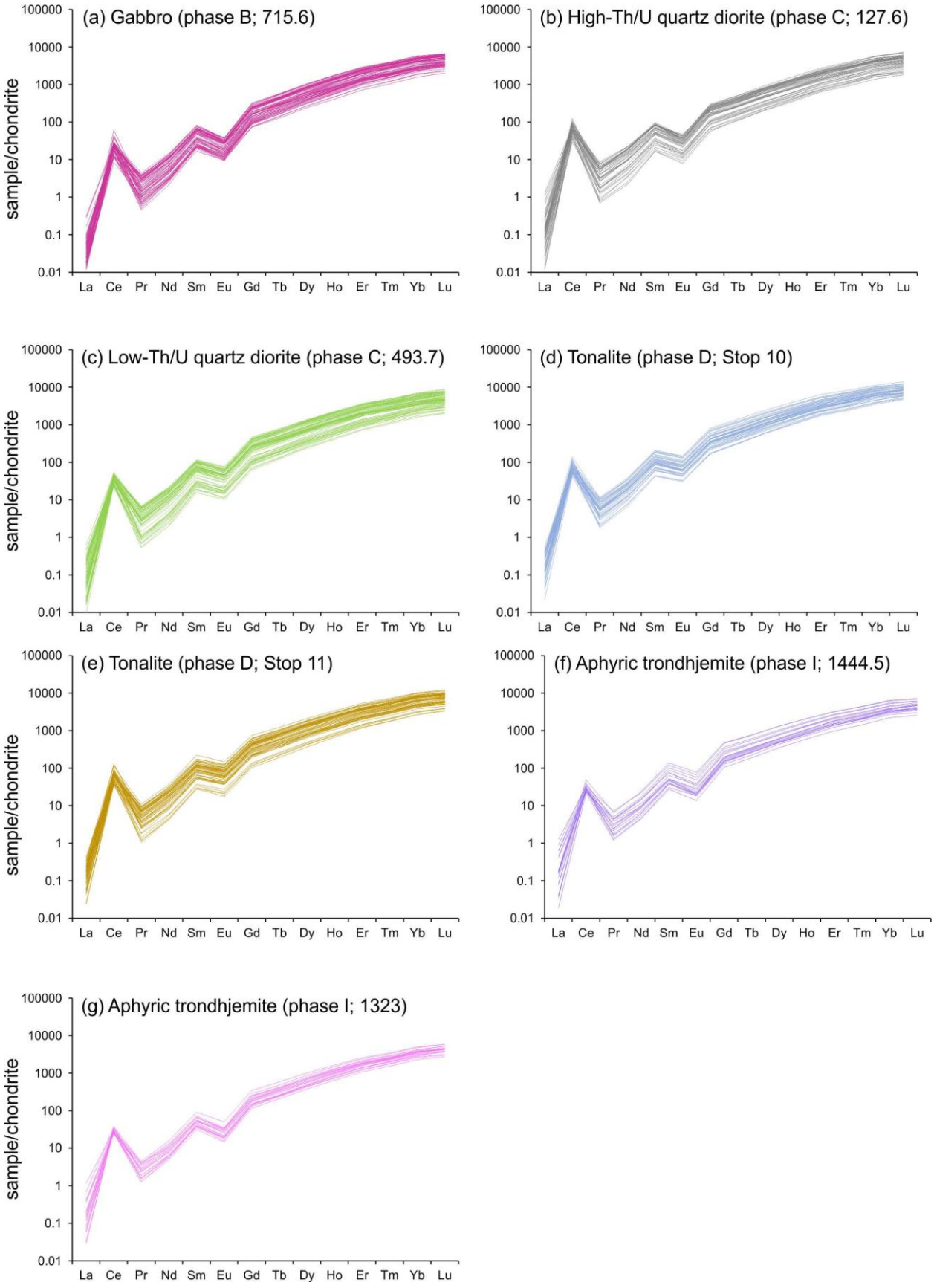
(a) Gabbro (phase B; 715.6)
(b) High-Th/U quartz diorite (phase C; 127.6)
(c) Low-Th/U quartz diorite (phase C; 493.7)
(d) Tonalite (phase D; Stop 10)
(e) Tonalite (phase D; Stop 11)
(f) Aphyric trondhjemite (phase I; 1444.5)
(g) Aphyric trondhjemite (phase I; 1323)
sample/chondrite
100000
10000
1000
100
10
1
0.1
0.01
La Ce Pr Nd Sm Eu Gd Tb Dy Ho Er Tm Yb Lu

Fig. 2.7. Chondrite-normalized zircon trace element patterns for (a) phase B gabbro (sample 715.6), (b) High-Th/U quartz diorite of phase C (sample 127.6), (c) Low-Th/U quartz diorite phase C (sample 493.7), (d) Phase D tonalite (sample Stop 10), (e) Phase D tonalite (sample Stop 11), (f) Phase I aphyric trondhjemite (sample 1444.5), and (g) Phase I aphyric trondhjemite (sample 1323). All analyses were normalized using chondritic values from McDonough & Sun, 1995.

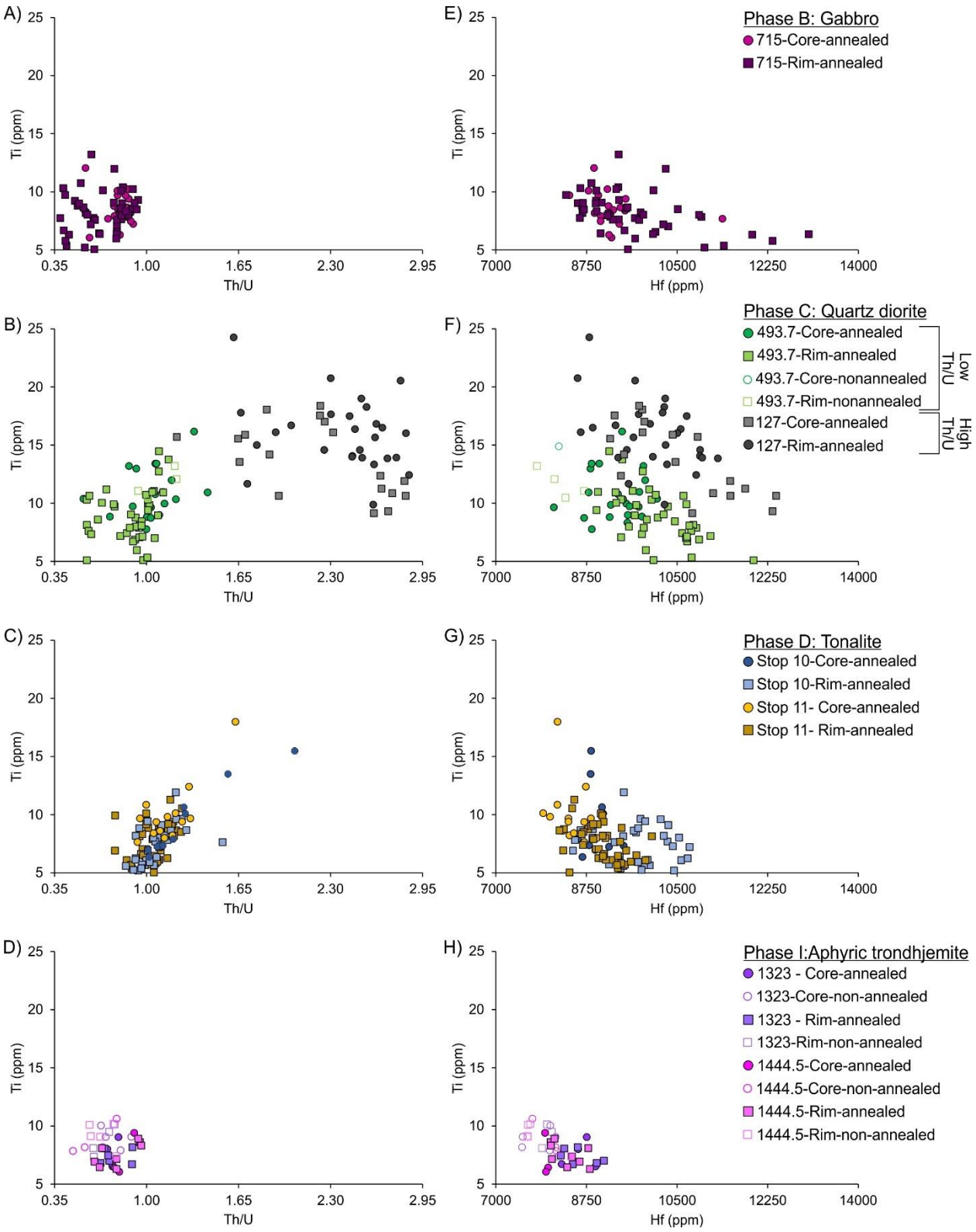
A)
B)
C)
D)
E)
F)
G)
H)
Ti (ppm)
Th/U
Hf (ppm)
Phase B: Gabbro
715-Core-annealed
715-Rim-annealed
Phase C: Quartz diorite
493.7-Core-annealed
493.7-Rim-annealed
493.7-Core-nonannealed
493.7-Rim-nonannealed
127-Core-annealed
127-Rim-annealed
Low Th/U
High Th/U
Phase D: Tonalite
Stop 10-Core-annealed
Stop 10-Rim-annealed
Stop 11- Core-annealed
Stop 11- Rim-annealed
Phase I:Aphyric trondhjemite
1323 - Core-annealed
1323-Core-non-annealed
1323 - Rim-annealed
1323-Rim-non-annealed
1444.5-Core-annealed
1444.5-Core-non-annealed
1444.5-Rim-annealed
1444.5-Rim-non-annealed

Fig. 2.8. Trace element plots from individual zircon grains. (a-d) Ti (ppm) plotted against Th/U ratio for each phase and the significant difference in Th/U ratio in (b) distinguishing the high-Th/U (sample 127.6) from the low-Th/U (sample 493.7) quartz diorite. (e-h) Ti (ppm) plotted against Hf (ppm). For each phase, there is a decrease in Ti content with increasing Hf content.

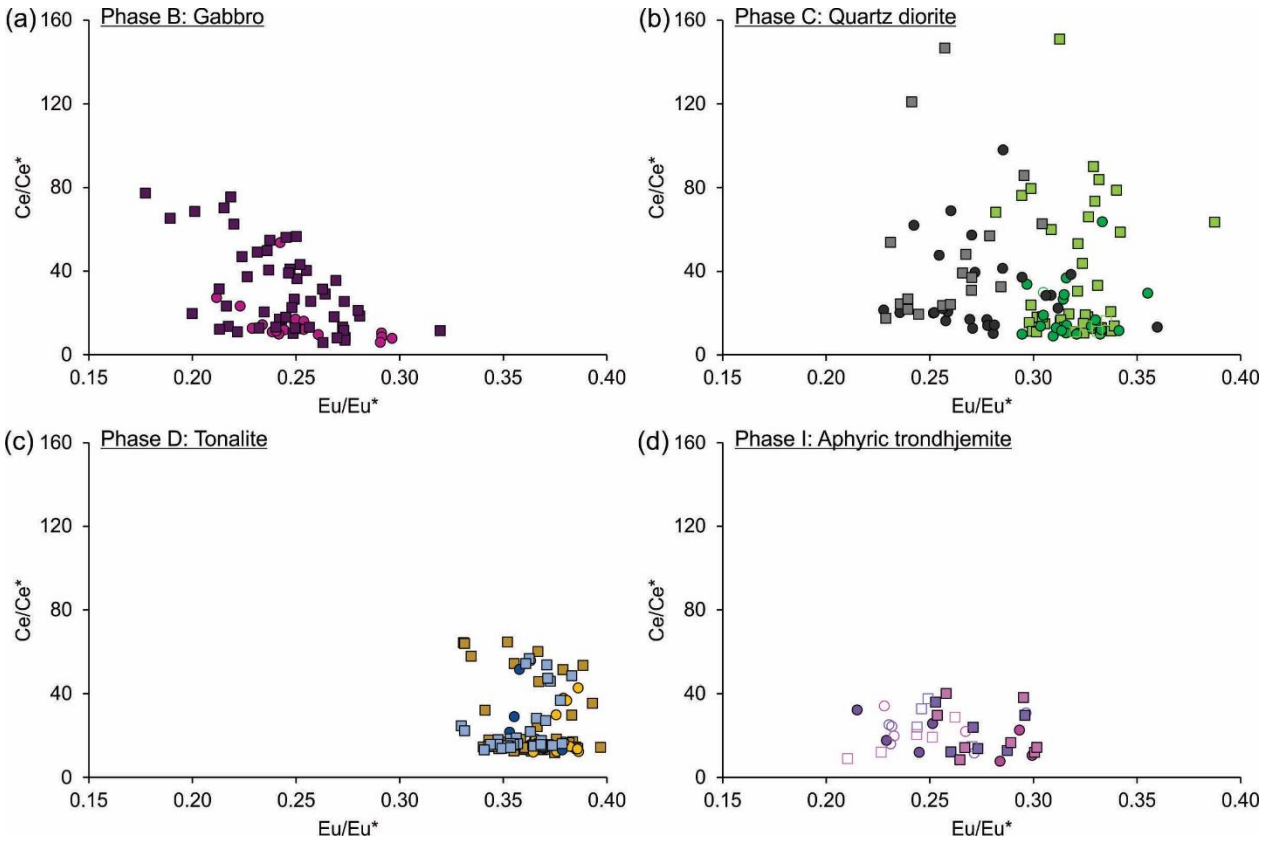

Fig. 2.9. Eu anomaly (Eu/Eu*) plotted against Ce anomaly (Ce/Ce*) in zircon for (a) Phase B gabbro, (b) phase C high- and low-Th/U quartz diorite, (c) Phase D tonalite, and (d) phase I aphyric trondhjemite. Legend is the same as shown in Figure 8.

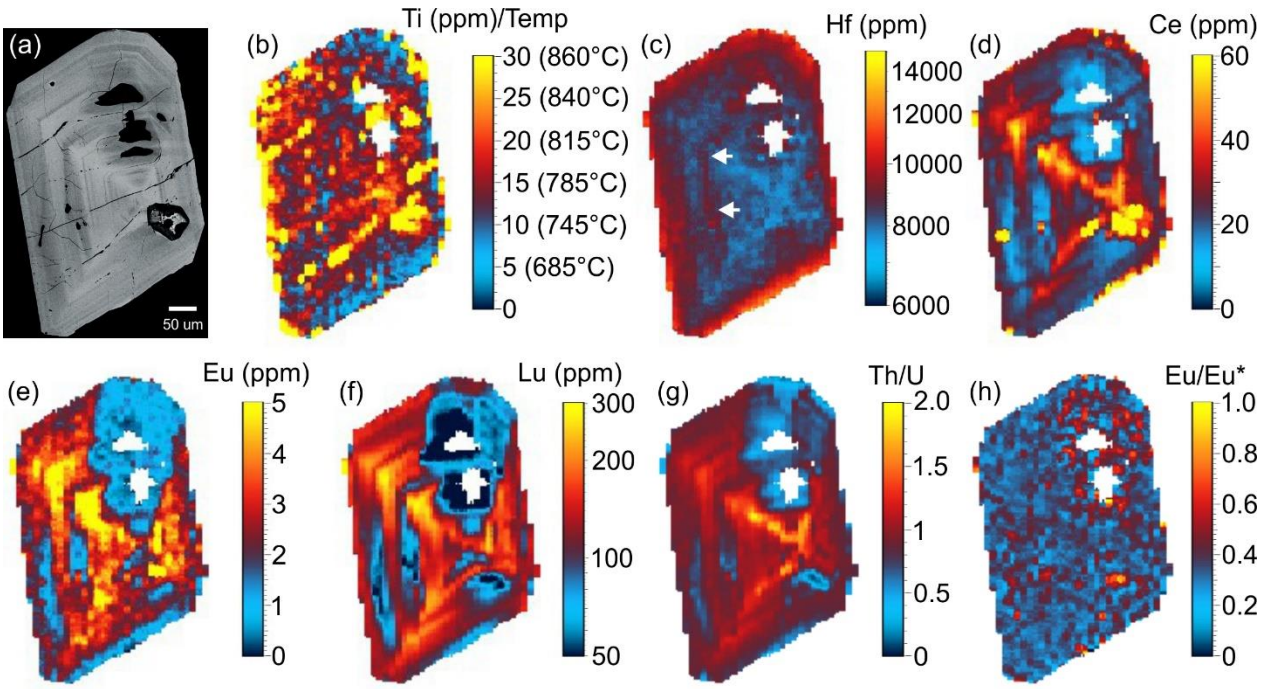

Fig. 2.10. Select trace element distribution maps for a full zircon grain from low-Th/U quartz diorite (phase C; sample 493.7). (a) SEM-BSE image for mapped grain. (b) Ti (ppm) distribution map and calculated temperatures based on the equation of Ferry & Watson (2007). Note temperatures decrease along the bottom and upper right rim. (c). Hf (ppm) distribution map. Notice the occurrence of some higher Hf in the middle of the grain (indicated by the white arrows) and in the entire rim. (d) Ce (ppm) distribution map showing weak oscillatory/sector zoning pattern. (e) Eu (ppm) distribution map displaying a similar pattern as the Ce distribution. (f) Lu (ppm) distribution map, following a similar pattern as Eu and Ce. (g) Th/U ratio map displaying oscillatory zoning and following the oscillatory pattern as the REE. Low Th/U ratios in the middle-left part of the grain, coincide with elevated Hf contents. (h) Eu anomaly distribution showing the anomaly is relatively the same throughout the entire grain. Note, the disturbed region in the upper right corner of the maps corresponds to a reaction zone between a mineral inclusion and the host zircon (e.g., diffusion halo).

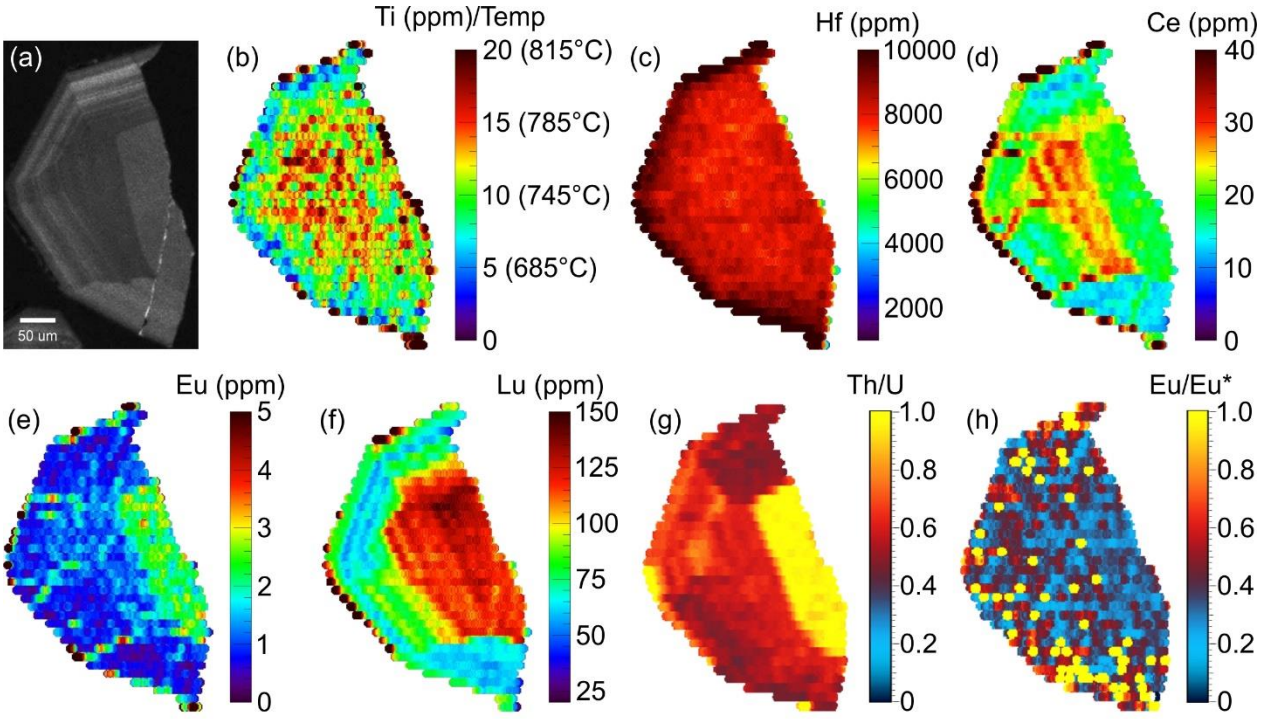

Fig. 2.11. Select trace element distribution maps for a zircon grain fragment from low-Th/U quartz diorite (phase C; sample 493.7). (a) Cold CL image of the mapped grain. (b) Ti (ppm) distribution map and calculated temperatures based on the equation of Ferry & Watson (2007) and temperatures decrease toward the rim. (c) Hf (ppm) distribution map. The Hf content is highest along the rim. (d) Ce (ppm) distribution map, which displays sectoral zoning. The highest contents occur in the central portion of the grain, which are flanked by moderate values, and the lowest Ce values occur in the bottom of the grain. (e) Eu (ppm) distribution map, elevated concentrations of Eu occur in the right portion of the grain and concentrations drop significantly moving towards the rim. (f) Lu (ppm) distribution map, elevated Lu concentrations overlap with both the high Eu and Ce zones. Concentrations of Lu are lower in the outer rim zone. (g) Th/U ratio distribution map shows elevated Th/U ratio in the central portion of the grain, coinciding with elevated Eu and Lu, and the Th/U ratio significantly drops off, mimicking the Eu pattern. (h) Eu anomaly map indicating no significant variations occur throughout the grain.

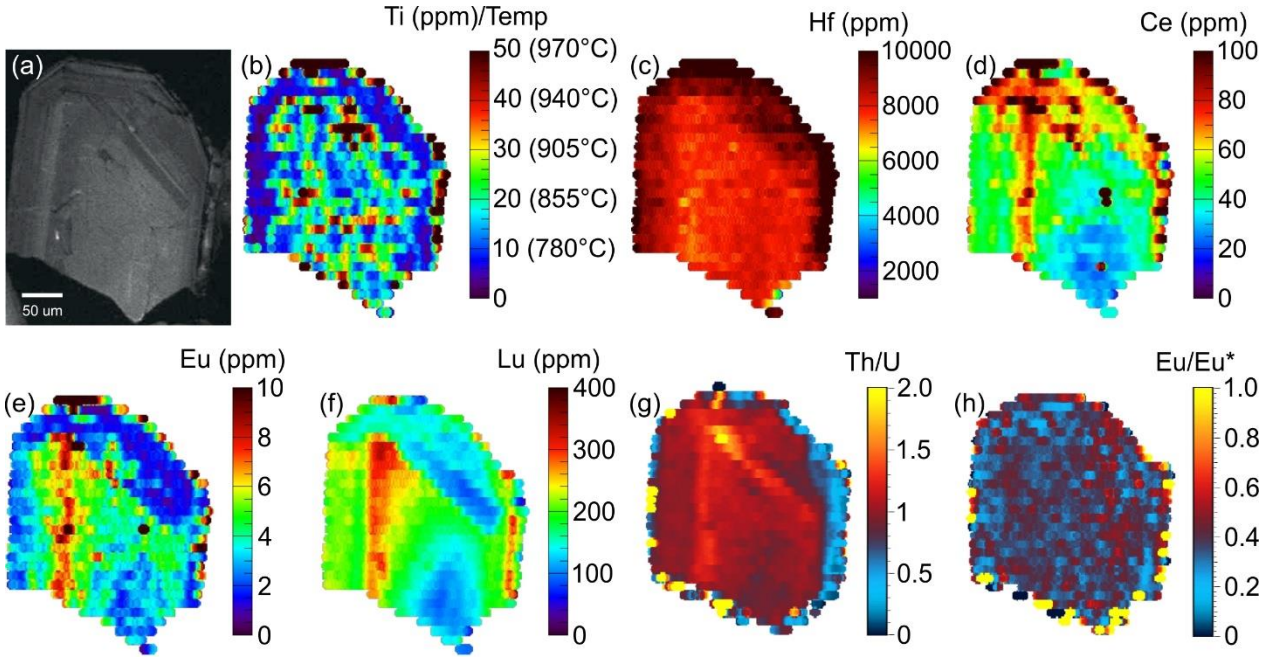

Fig. 2.12. Select trace element distribution maps for a zircon grain fragment from a tonalite (phase D; sample Stop 10). (a) Cold CL image of the mapped grain. (b) Ti (ppm) distribution map and calculated temperatures based on the equation of Ferry & Watson (2007). Temperature decreases towards the rim. (c) Hf (ppm) distribution map, the highest Hf occurs along the rim. (d) Ce (ppm) distribution map displays sectoral zoning patterns with the highest Ce occurring in the upper left zone and along a band going north-south through the grain. (e) Eu (ppm) distribution map shows sectoral zoning similar to Ce, with the highest Eu occurring along the north-south band and relatively lower Eu occurs along the rim. (f) Lu (ppm) distribution map shows similar sector zoning to the Eu map. (g) Th/U ratio distribution map and slightly elevated ratios occur along the north-south band and lower Th/U along the rim. (h) Eu anomaly map indicating no significant variations occur throughout the grain.

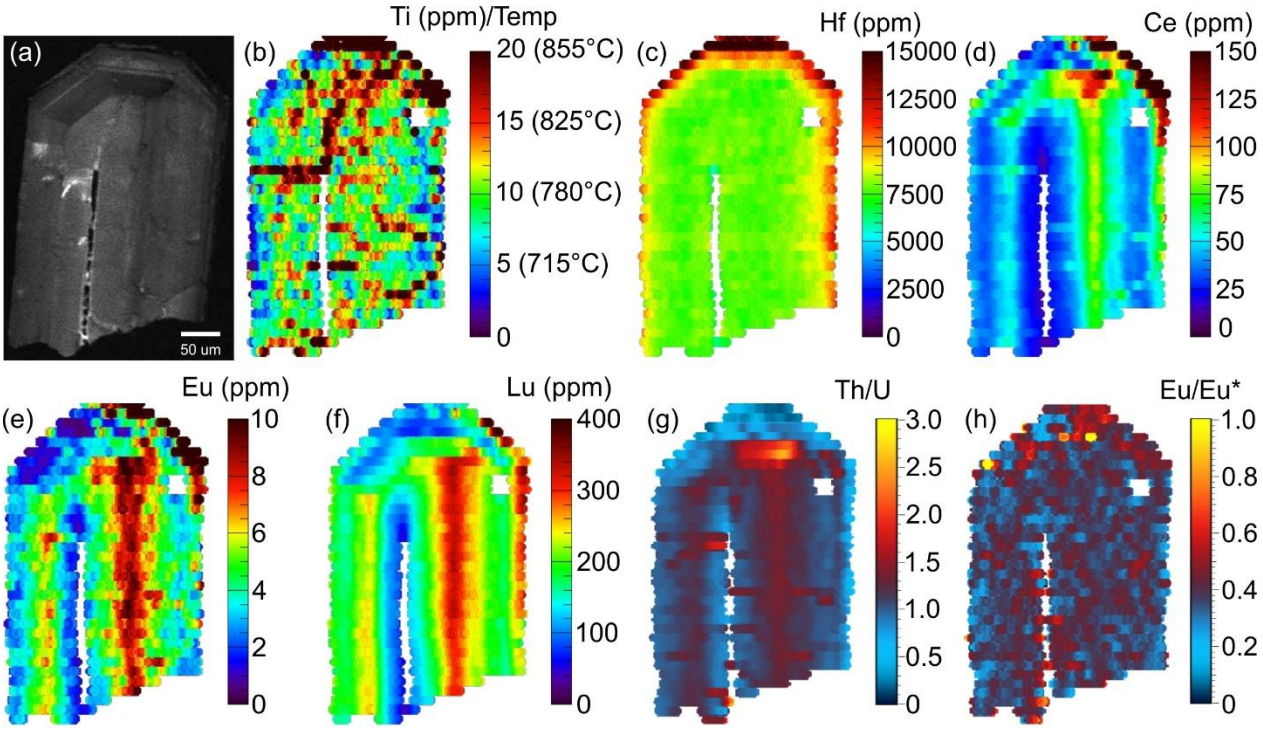

Fig. 2.13. Select trace element distribution maps for a zircon grain fragment from a tonalite (phase D; sample Stop 10). (a) Cold CL image of the mapped grain. (b) Ti (ppm) distribution map and calculated temperatures based on the equation of Ferry & Watson (2007). Temperature decreases along most of the rim. (c) Hf (ppm) distribution map showing the highest Hf content is along the rim. (d) Ce (ppm) distribution map displays a sectoral zoning pattern. (e) Eu (ppm) distribution map and Eu follows the same sectoral zoning pattern as Ce. (f) Lu (ppm) distribution map follows the same sectoral zoning patterns as the other REE. (g) Th/U ratio distribution map. Elevated Th/U ratios tend to align with elevated REE domains and the lowest Th/U ratios occur along the rim. (h) Eu anomaly map indicating no significant variations occur throughout the grain.

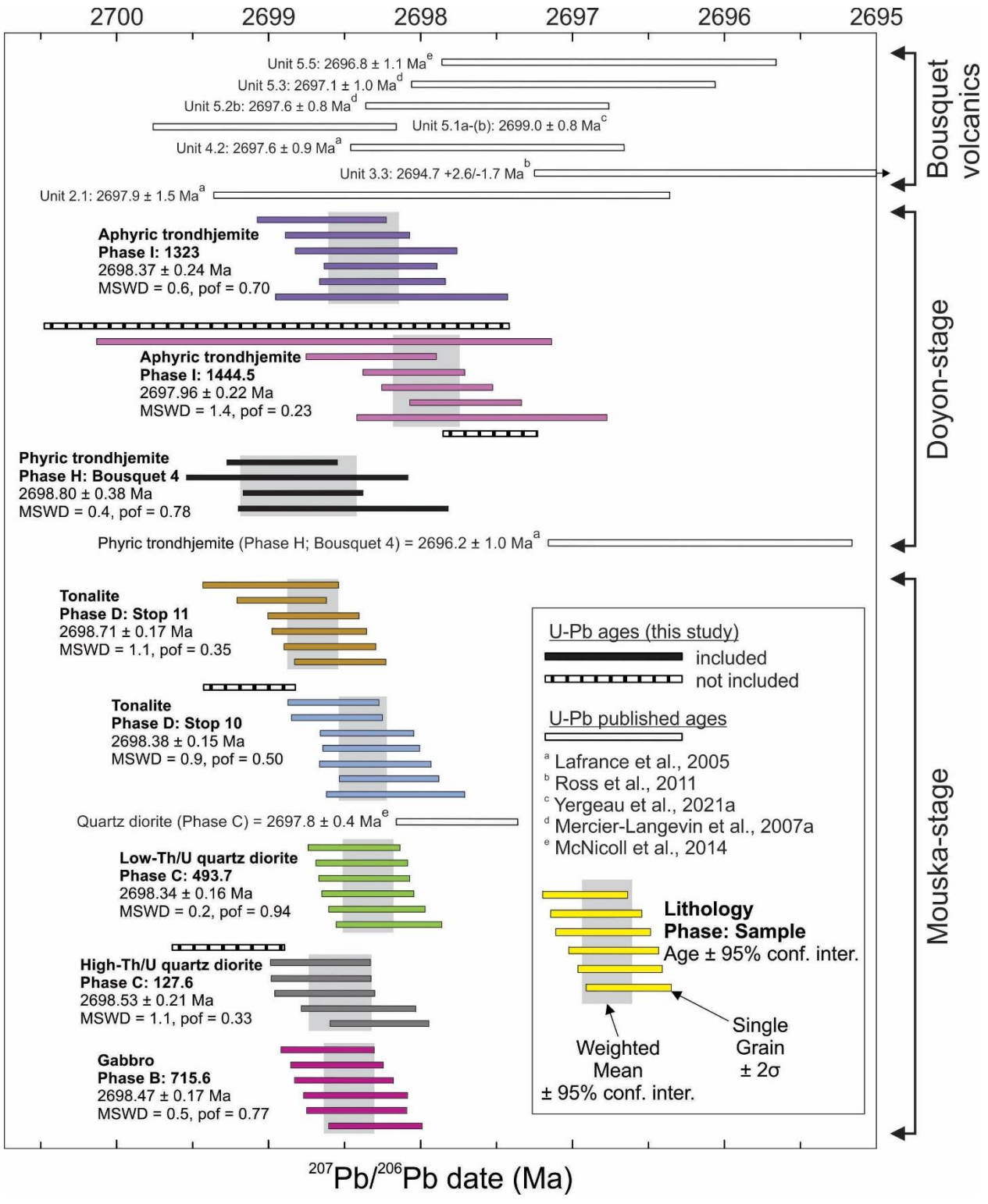
2700
2699
2698
2697
2696
2695
Unit 5.5: 2696.8 ± 1.1 Ma[e]
Unit 5.3: 2697.1 ± 1.0 Ma[d]
Unit 5.2b: 2697.6 ± 0.8 Ma[d]
Unit 5.1a-(b): 2699.0 ± 0.8 Ma[c]
Unit 4.2: 2697.6 ± 0.9 Ma[a]
Unit 3.3: 2694.7 +2.6/-1.7 Ma[b]
Unit 2.1: 2697.9 ± 1.5 Ma[a]
Bousquet volcanics
Aphyric trondhjemite
Phase I: 1323
2698.37 ± 0.24 Ma
MSWD = 0.6, pof = 0.70
Aphyric trondhjemite
Phase I: 1444.5
2697.96 ± 0.22 Ma
MSWD = 1.4, pof = 0.23
Phyric trondhjemite
Phase H: Bousquet 4
2698.80 ± 0.38 Ma
MSWD = 0.4, pof = 0.78
Phyric trondhjemite (Phase H; Bousquet 4) = 2696.2 ± 1.0 Ma[a]
Doyon-stage
Tonalite
Phase D: Stop 11
2698.71 ± 0.17 Ma
MSWD = 1.1, pof = 0.35
Tonalite
Phase D: Stop 10
2698.38 ± 0.15 Ma
MSWD = 0.9, pof = 0.50
Quartz diorite (Phase C) = 2697.8 ± 0.4 Ma[e]
Low-Th/U quartz diorite
Phase C: 493.7
2698.34 ± 0.16 Ma
MSWD = 0.2, pof = 0.94
High-Th/U quartz diorite
Phase C: 127.6
2698.53 ± 0.21 Ma
MSWD = 1.1, pof = 0.33
Gabbro
Phase B: 715.6
2698.47 ± 0.17 Ma
MSWD = 0.5, pof = 0.77
U-Pb ages (this study)
included
not included
U-Pb published ages
[a] Lafrance et al., 2005
[b] Ross et al., 2011
[c] Yergeau et al., 2021a
[d] Mercier-Langevin et al., 2007a
[e] McNicoll et al., 2014
Lithology
Phase: Sample
Age ± 95% conf. inter.
Weighted Mean ± 95% conf. inter.
Single Grain ± 2σ
Mouska-stage
207Pb/206Pb date (Ma)

Fig. 2.14. Age ranked plot showing $^{207}Pb/^{206}Pb$ dates of individual zircons for all analyses. Plotted with Isoplot 3.0 (Ludwig, 2003). Error bars for the weighted mean age dates are at the 95% confidence level for ages obtained in this study and are at 2σ for previously published ages. Weighted mean date is shown and represented by gray box behind the error bars. Error bars for individual grains are 2σ. MSWD = Mean Square of Weighted Deviation. pof = probability of fit.

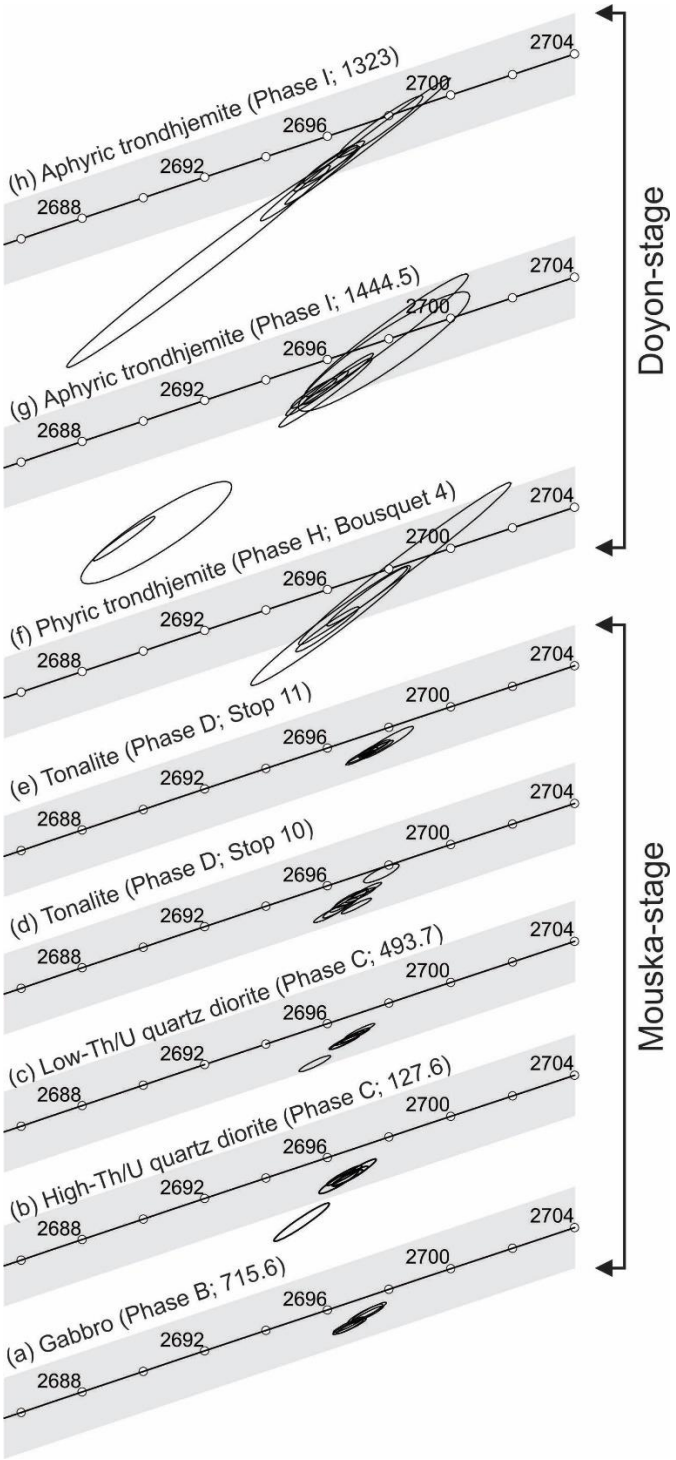

Fig. 2.15. Concordia plots of CA-TIMS U-Pb dates from zircon (ages in Ma). Error ellipses are 2σ. Gray area behind concordia shows the decay constant uncertainties on concordia.

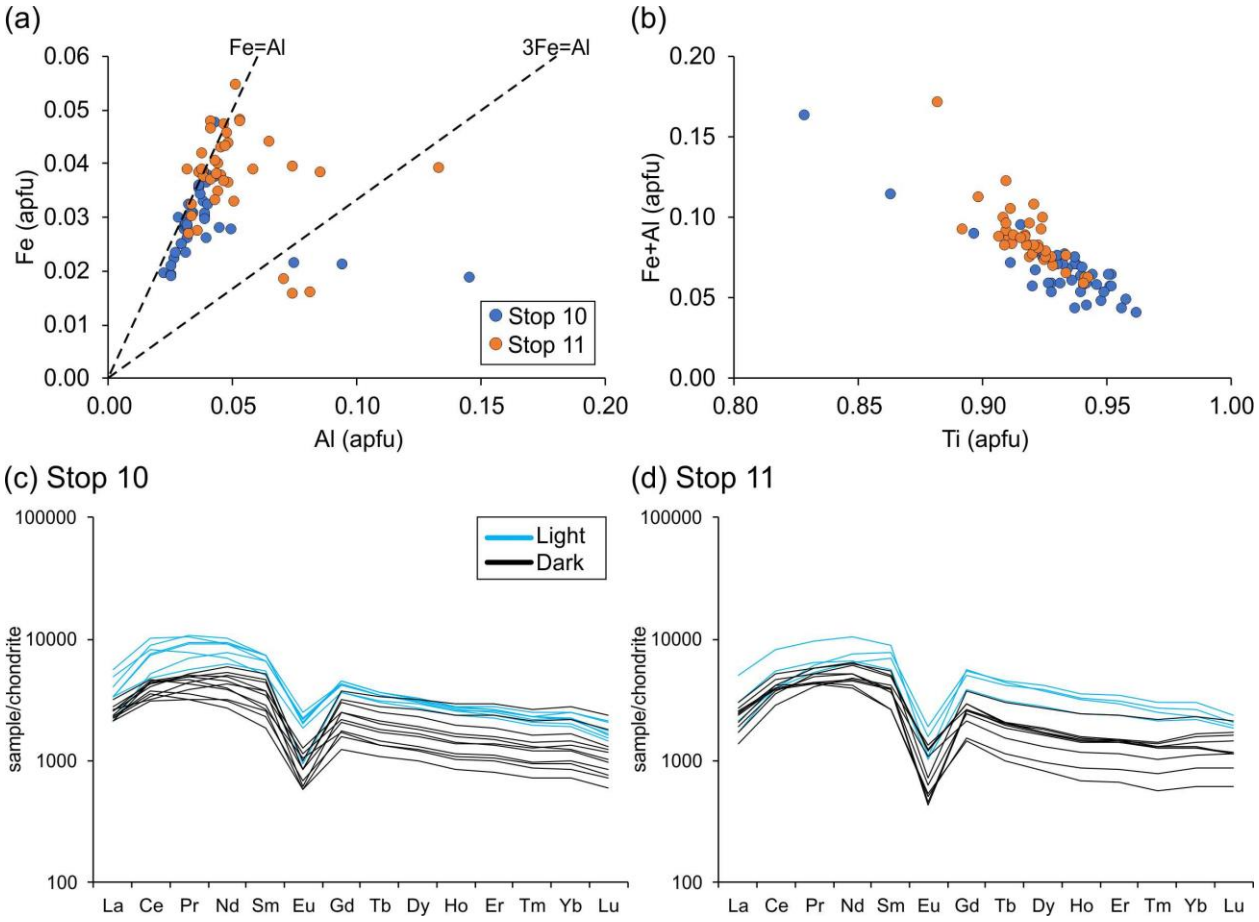

Fig. 2.16. Titanite compositional characteristics from phase D tonalite (samples from Stops 10 and 11). (a) Fe (atoms per formula unit [apfu]) plotted against Al (apfu), showing that Stop 11 titanite contains slightly more Fe and Al than at Stop 10. Generally, titanite with Fe=Al is considered to be of magmatic origin whereas titanite with >3Fe=Al is typical of metamorphic origin (Rasmussen *et al.*, 2013; Aleinikoff *et al.*, 2002). (b) Ti (apfu) plotted against Fe+Al (apfu) plot indicating that titanite from Stop 10 contains slightly more Ti than at Stop 11. (c) Chondrite-normalized REE diagram for titanite from Stop 10, organized into light and dark domains as observed in SEM-BSE images. Overall, light domains are elevated in REE compared to dark domains. (d) Chondrite-normalized REE diagram for titanite from Stop 11. Similar to Stop 10, light domains are elevated in REE compared to dark domains. Values used for chondrite normalization are from McDonough & Sun, 1995.

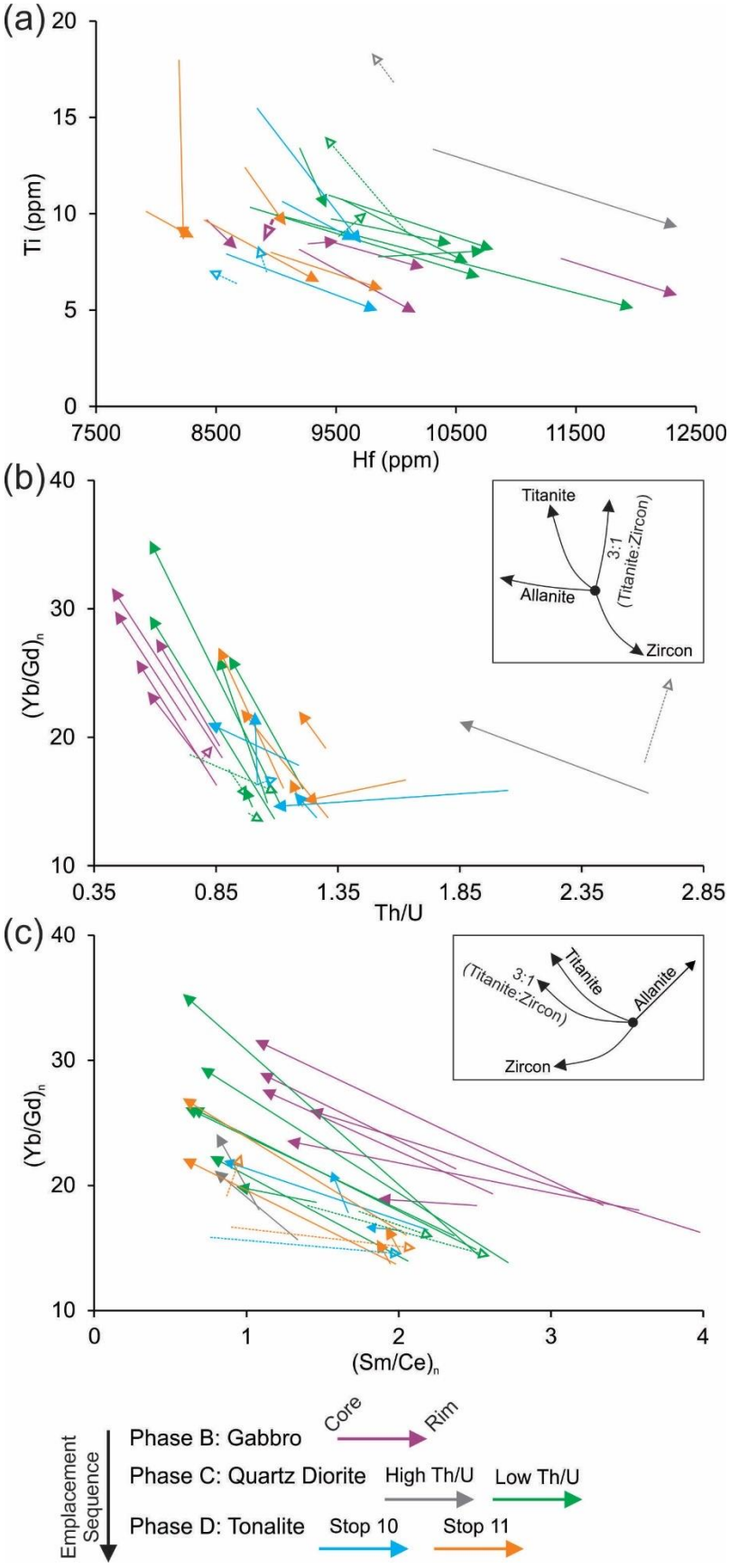
(a)
Ti (ppm)
Hf (ppm)
(b)
(Yb/Gd)n
Th/U
Titanite
3:1
(Titanite:Zircon)
Allanite
Zircon
(c)
(Yb/Gd)n
(Sm/Ce)n
Titanite
3:1
(Titanite:Zircon)
Allanite
Zircon
Emplacement Sequence
Phase B: Gabbro
Core
Rim
Phase C: Quartz Diorite
High Th/U
Low Th/U
Phase D: Tonalite
Stop 10
Stop 11

Fig. 2.17. Zircon trace element abundance and ratio relationships for core-rim analyses of individual grains. Arrows indicate core to rim compositional change. (a) Ti (ppm) plotted against Hf (ppm). (b) $(Yb/Gd)_n$ plotted against Th/U. (c) $(Yb/Gd)_n$ plotted against $(Sm/Ce)_n$. Dotted lines indicate core to rim relationships opposite to the typical evolutionary trend. For the trajectories shown in the upper right corners, these are based on the crystallization of single accessory minerals (i.e., zircon, titanite, and allanite) as they impact both zircon and melt composition incrementally. As well, a trajectory is shown reflecting the co-crystallization of titanite and zircon incrementally at a proportion of 3:1 titanite to zircon.

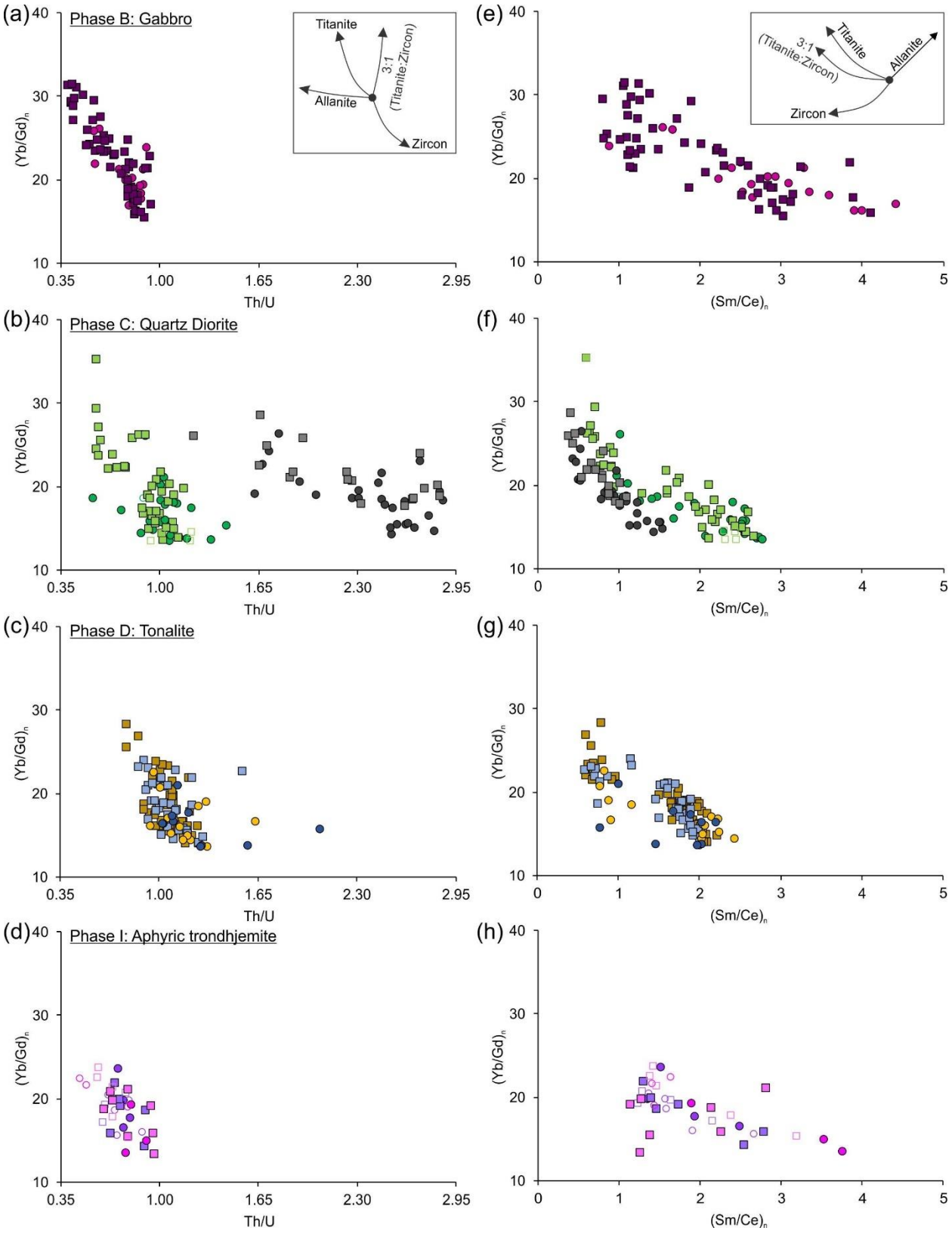
(a)
Phase B: Gabbro
Titanite
3:1
(Titanite:Zircon)
Allanite
Zircon
(e)
Titanite
3:1
(Titanite:Zircon)
Allanite
Zircon
(b)
Phase C: Quartz Diorite
(f)
(c)
Phase D: Tonalite
(g)
(d)
Phase I: Aphyric trondhjemite
(h)
(Yb/Gd)n
Th/U
(Sm/Ce)n
10
20
30
40
0.35
1.00
1.65
2.30
2.95
0
1
2
3
4
5

Fig. 2.18. Trace element abundance and ratio relationships from individual zircon grains. Refer to Figure 8 for legend. (a-d) $(Yb/Gd)_n$ plotted against Th/U for each MIC phase. For each MIC phase, there is a decrease in Th/U ratio with an increase in $(Yb/Gd)_n$. (e-h) $(Yb/Gd)_n$ vs $(Sm/Ce)_n$. For each phase, there is a decrease in $(Sm/Ce)_n$ with an increase in $(Yb/Gd)_n$. The trajectories shown in the upper right-hand corners are the same as described in the text and in Figure 17.

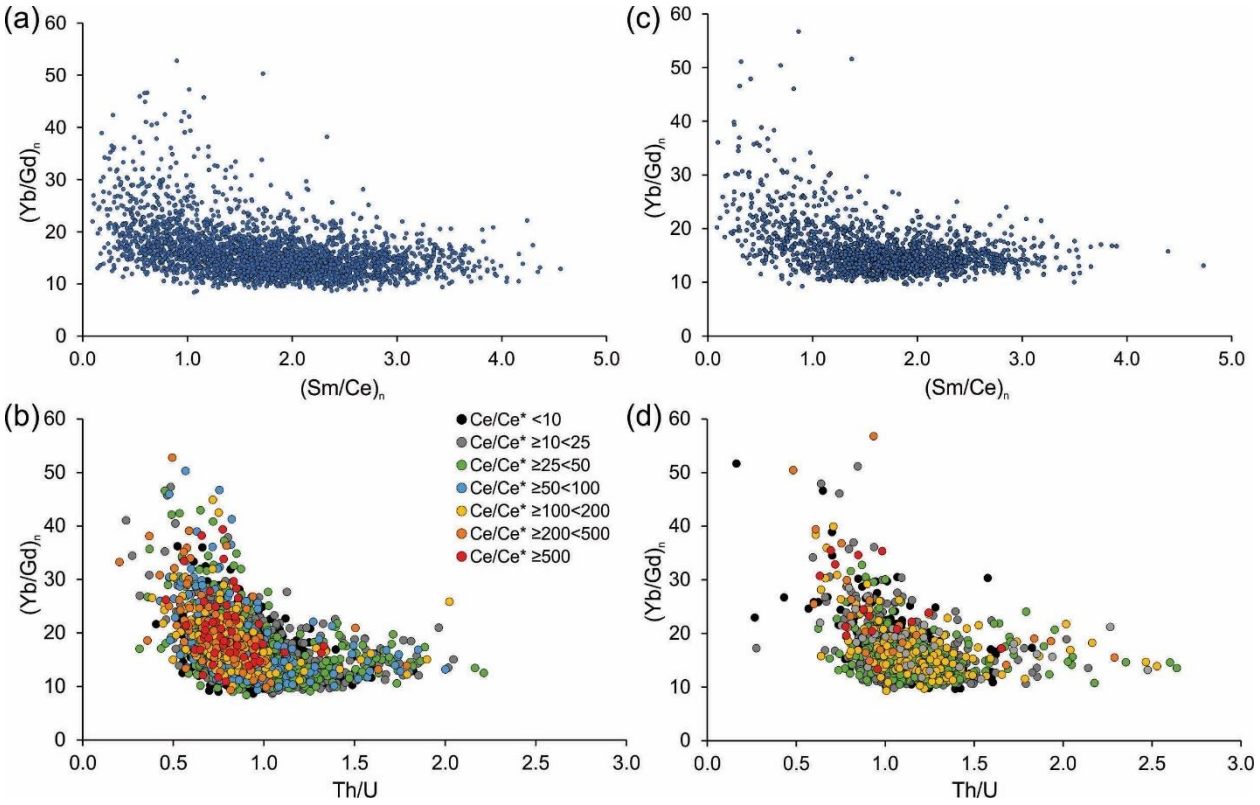

Fig. 2.19. Scatter plots for various trace elements and ratios in zircon generated using spot data extracted from trace element distribution maps. (a-b) Trace element concentrations and ratios for the zircon grain shown in Figure 10 from the low-Th/U quartz diorite (phase C; sample 493.7; n = 3019). (a) $(Yb/Gd)_n$ plotted against $(Sm/Ce)_n$. (b)$(Yb/Gd)_n$ plotted against Th/U grouped by Ce/Ce* values (calculated using equation of Loader et al. (2017). (c-d) Trace element concentrations and ratios for the zircon grain shown in Figure 13 from a tonalite (phase D; sample Stop 10; n = 1694). (c) $(Yb/Gd)_n$ plotted against $(Sm/Ce)_n$. (d) $(Yb/Gd)_n$ plotted against Th/U grouped by Ce/Ce* values (calculated using equation of Loader et al. (2017).

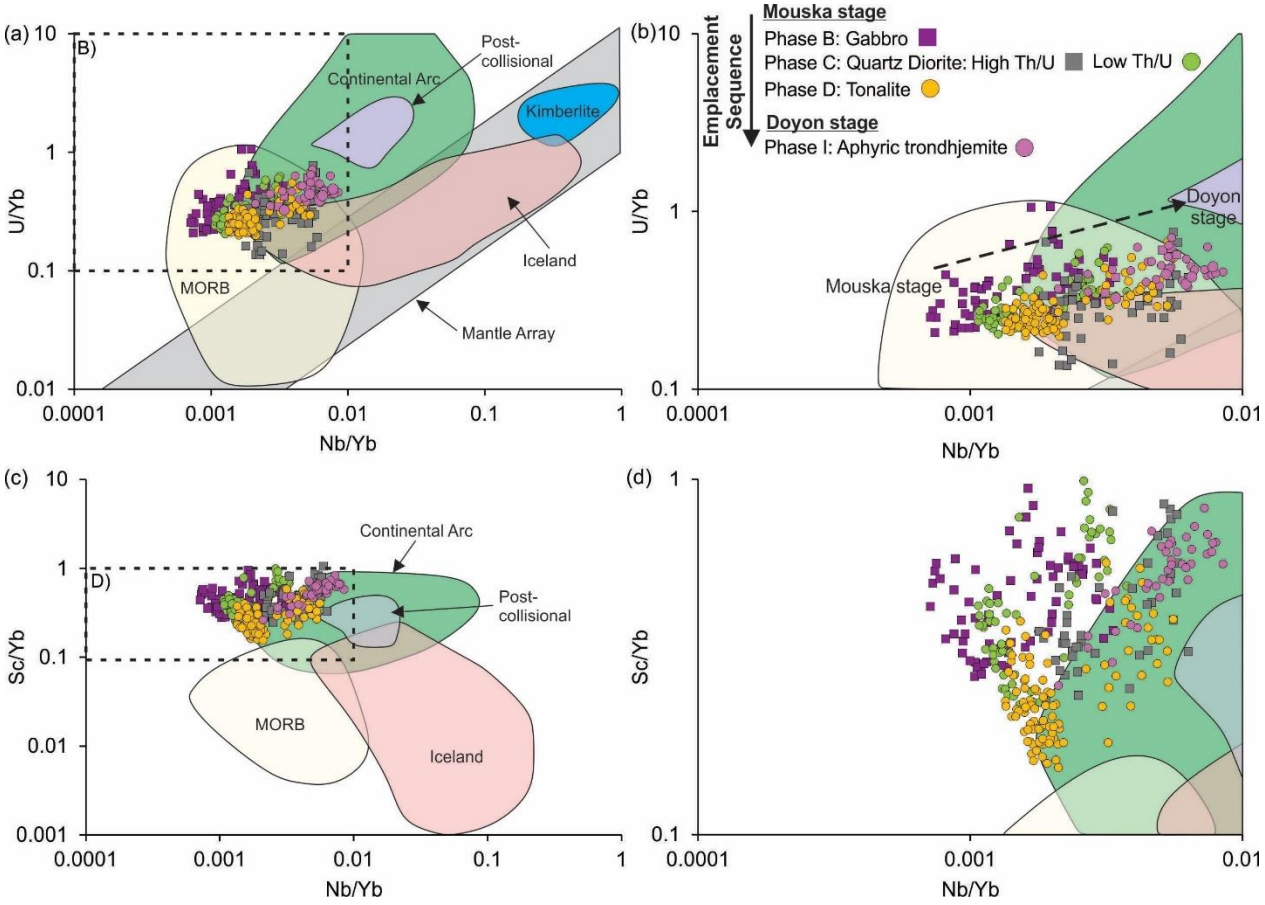

Fig. 2.20. Tectonic discrimination diagrams utilizing zircon trace element composition (modified after Grimes *et al.*, 2015). (a-b) U/Yb plotted against Nb/Yb. (c-d) Sc/Yb plotted against Nb/Yb. Zircon from the Mouska-stage phases plots predominantly in the MORB-like field and extend into the continental arc field, whereas zircon from the Doyon-stage aphyric trondhjemite plots firmly in the continental arc field.

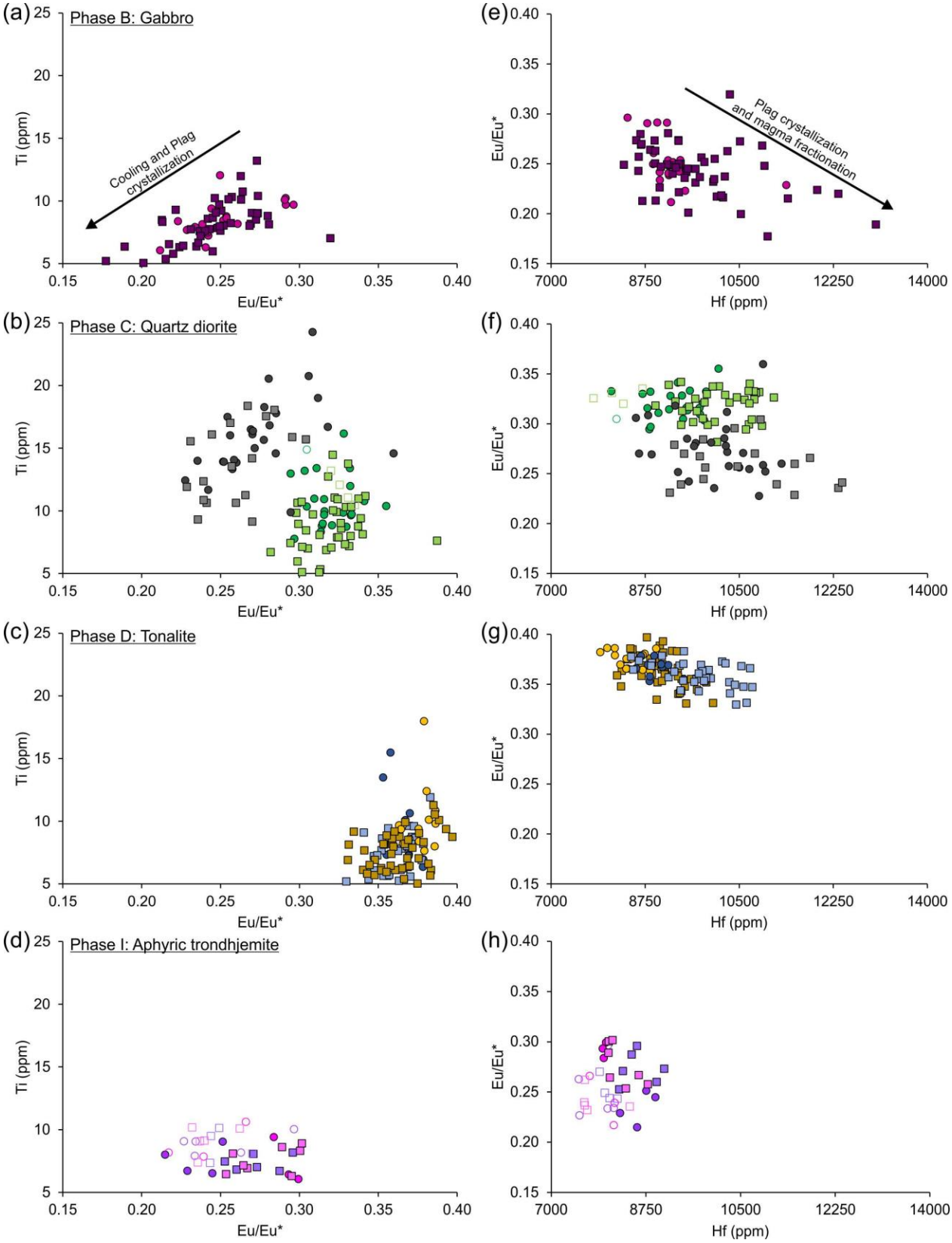
(a)
Phase B: Gabbro
Cooling and Plag crystallization
Ti (ppm)
Eu/Eu*
(b)
Phase C: Quartz diorite
Ti (ppm)
Eu/Eu*
(c)
Phase D: Tonalite
Ti (ppm)
Eu/Eu*
(d)
Phase I: Aphyric trondhjemite
Ti (ppm)
Eu/Eu*
(e)
Plag crystallization and magma fractionation
Eu/Eu*
Hf (ppm)
(f)
Eu/Eu*
Hf (ppm)
(g)
Eu/Eu*
Hf (ppm)
(h)
Eu/Eu*
Hf (ppm)

Fig. 2.21. Trace element abundance and ratio plots from individual zircon grains. Refer to Figure 8 for legend. (a-d) Ti (ppm) plotted against Eu/Eu* for each MIC phase. (e-h) Eu/Eu* plotted against Hf (ppm) for each MIC phase.

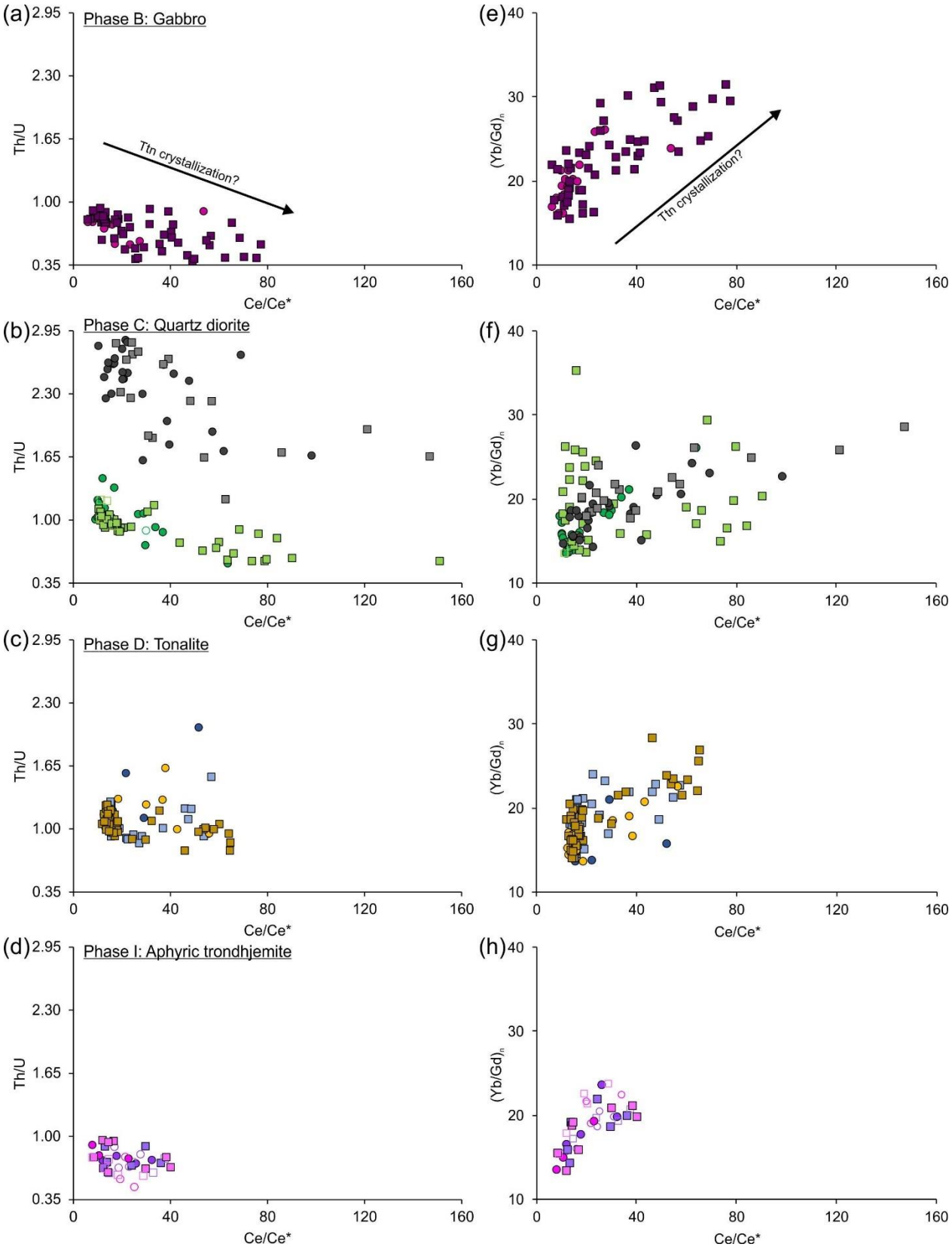
(a)
Phase B: Gabbro
Th/U
Ttn crystallization?
Ce/Ce*
(e)
(Yb/Gd)n
Ttn crystallization?
Ce/Ce*
(b)
Phase C: Quartz diorite
Th/U
Ce/Ce*
(f)
(Yb/Gd)n
Ce/Ce*
(c)
Phase D: Tonalite
Th/U
Ce/Ce*
(g)
(Yb/Gd)n
Ce/Ce*
(d)
Phase I: Aphyric trondhjemite
Th/U
Ce/Ce*
(h)
(Yb/Gd)n
Ce/Ce*

Fig. 2.22. Trace element abundance and ratio plots from individual zircon grains. Refer to Figure 8 for legend. (a-d) Th/U plotted against Ce/Ce* for each MIC phase. (e-h) $(Yb/Gd)_n$ plotted against Ce/Ce* for each MIC phase.

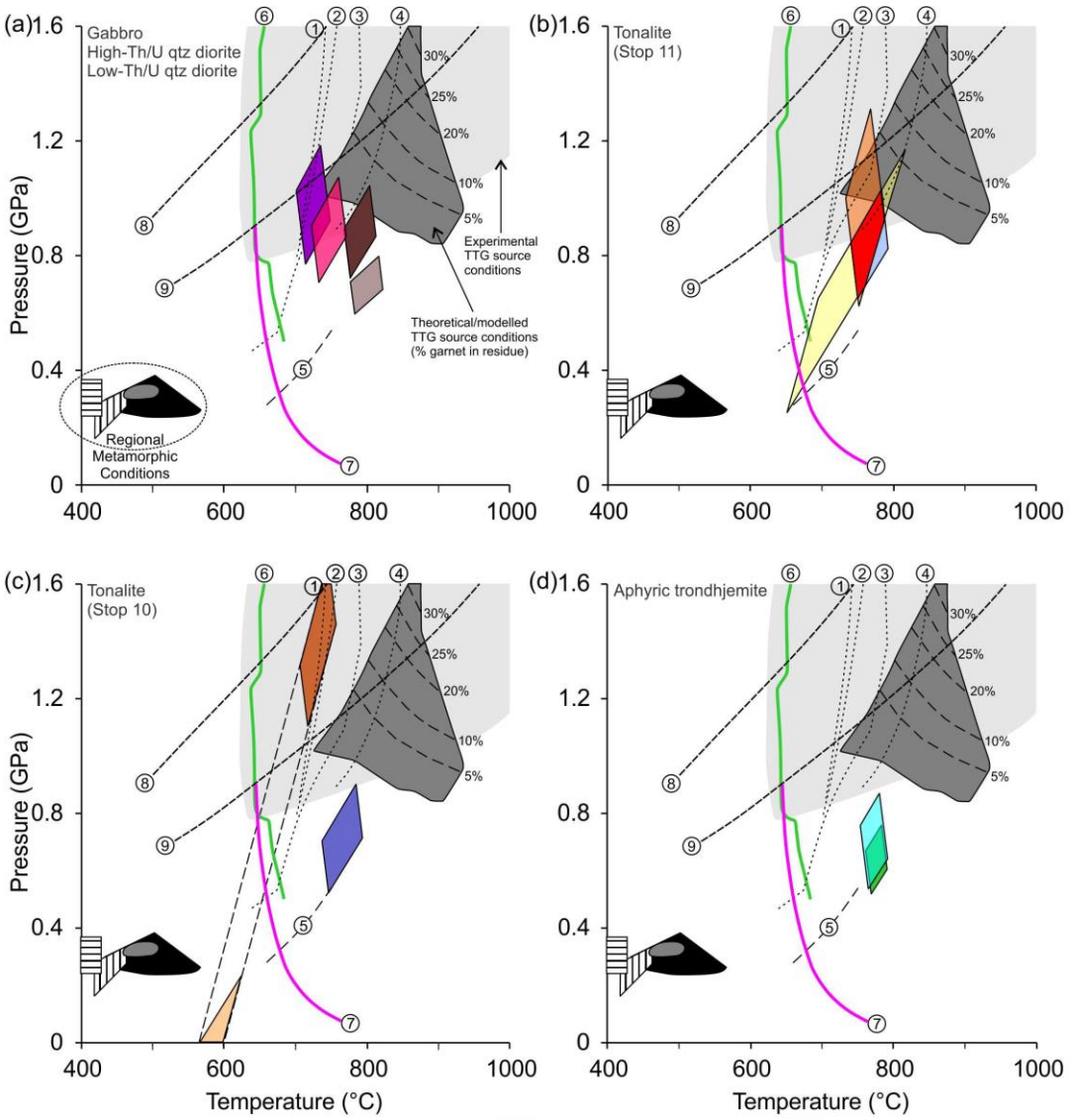
(a)
Gabbro
High-Th/U qtz diorite
Low-Th/U qtz diorite
(b)
Tonalite
(Stop 11)
(c)
Tonalite
(Stop 10)
(d)
Aphyric trondhjemite
Pressure (GPa)
Temperature (°C)
30%
25%
20%
10%
5%
Experimental
TTG source
conditions
Theoretical/modelled
TTG source conditions
(% garnet in residue)
Regional
Metamorphic
Conditions
Gabbro (phase B; 715.5)
Ti-in-zrc + Ti-in-qtz
Low-Th/U quartz diorite
(phase C; 493.7)
Ti-in-zrc + Ti-in-qtz
High-Th/U quartz diorite
(phase C; 493.7)
Ti-in-zrc + Ti-in-qtz
Tonalite (phase D; Stop 10)
Ti-in-zrc + Zr-in-ttn
Tonalite (phase D; Stop 10)
Ti-in-zrc + Ti-in-qtz
Tonalite (phase D; Stop 10)
Ti-in-qtz + Zr-in-ttn
Tonalite (phase D; Stop 11)
Ti-in-zrc + Zr-in-ttn
Tonalite (phase D; Stop 11)
Ti-in-zrc + Ti-in-qtz
Tonalite (phase D; Stop 11)
Ti-in-qtz + Zr-in-ttn
Tonalite (phase D; Stop 11)
Ti-in-zrc + Ti-in-qtz + Zr-in-ttn
Aphyric trondhjemite (phase I; 1323)
Ti-in-zrc + Ti-in-qtz
Aphyric trondhjemite (phase I; 1444.5)
Ti-in-zrc + Ti-in-qtz
1 Max. epidote stability (trondhjmeitic rock); fO2 = NNO (Johnston & Wyllie, 1988; Van der Laan & Wyllie, 1992)
2 Max. epidote stability (granodioritic rock); fO2 = NNO (Naney, 1983; Schmidt & Thompson, 1996)
3 Max. epidote stability (tonalitic rock); fO2 = NNO (Schimdt & Thompson, 1996)
4 Max. epidote stability (CMASH system); fO2 = NNO (Thompson & Ellis 1994; Quirion & Jenkins 1998)
5 Max. epidote stability (tonalitic rock); fO2 = HM (Schimdt & Thompson, 1996)
6 Wet solidus basalt (Wiemer et al., 2018)
7 Wet solidus tonalite (Wiemer et al., 2018)
8 Modern day geotherm (Wiemer et al., 2018)
9 Minimum Archean geotherm (Wiemer et al., 2018)
Max metamorphic P-T conditions at Westwood mine (Yergeau, 2021a)
Max metamorphic P-T conditions at LaRonde-Penna mine (Mercier-Langevin, 2005)
Max metamorphic P-T conditions at Dumagami mine (Marquis et al., 1990)
Max metamorphic P-T conditions at Bousquet 1 mine (Tourigny et al., 1989)

Fig. 2.23. Pressure-temperature constraints for the crystallization of accessory phases (zircon, titanite) and quartz for various phases of the MIC. Pressure-temperature fields (coloured rhombs) for various MIC lithologies are based on the overlap of calculated Zr-in-titanite, Ti-in-quartz, and/or Ti-in-zircon temperatures (see text for explanation and references). Constraints for the maximum metamorphic pressure-temperature are shown in grey, black and hatched fields, and range from ~0.2 to 0.4 GPa and ~400-550°C (mid-greenschist to lower amphibolite; references listed in legend). The pressure-temperature field for experimental TTG suite magma generation is from Moyen & Martin (2012) and references therein. The theoretical/modelled TTG source conditions are from Zhang et al. (2013). Also shown are epidote stability boundaries in magmatic systems of various compositions and at various fO_2 (references in legend). (a) Pressure-temperature estimates determined by the intersection of the Ti-in-quartz and Ti-in-zircon thermometers for the gabbro (phase B) and high- and low-Th/U quartz diorite (phase C). (b) Pressure-temperature estimates determined by the intersection of the Ti-in-quartz, Ti-in-zircon, and Zr-in-titanite thermometers for tonalite (phase D; sample Stop 11). (c) Pressure-temperature estimates determined by the intersection of the Ti-in-quartz and Ti-in-zircon thermometers for tonalite (phase D; sample Stop 10). Intersections of the Zr-in-titanite thermometer yield inconsistent results (see text for explanation). (d) Pressure-temperature estimates determined by the intersection of the Ti-in-quartz and Ti-in-zircon thermometers.

2.13: Chapter 2 - Supplementary Materials File

MOOSHLA INTRUSIVE COMPLEX PHASE DESCRIPTIONS

Below is a summary of the nine distinct intrusive phases that comprise the MIC and are described in their interpreted order of emplacement. For a complete and detailed description of each phase see Galley & Lafrance (2014). Note that dimensions described below for individual phases reflect surface dimensions.

Mouska stage

Phase A: Aphyric to plagioclase porphyritic diorite

Phase A comprises aphyric to plagioclase-phyric diorite sills that are concentrated along the northwest edge of the MIC in contact with and commonly crosscutting the top of the Hébécourt Formation (Galley & Lafrance, 2014). These diorite sills are commonly crosscut and brecciated by later MIC intrusive phases. Two diorite varieties comprise Phase A: (i) aphyric to plagioclase-phyric diorite and (ii) aphyric diorite with interstitial blue quartz (Galley & Lafrance, 2014). Phase A diorite sills are zoned, consisting of a massive, fine-grained aphyric top grading to 10-20 mm, white plagioclase phenocrysts comprising 20-30 vol% at the base. Phase A was intruded above and below the contact between the Hébécourt and Bousquet Formations.

Phase B: Layered gabbro

Phase B is composed of an up to 300 m thick and 1,500 m long gabbroic sill that occurs primarily in the northwest corner of the MIC (Langshur, 1990). The base of Phase B is composed of 5-10 m plagioclase-actinolitic hornblende gabbro cumulate that is finely rhythmically layered (5-20 mm thick layers). This layered gabbro is overlain by a more coarsely layered adcumulate

gabbro (Langshur, 1990). The upper 100 m of Phase B is composed of a variably textured melanogabbro with minor pegmatitic patches (Galley & Lafrance, 2014). Compositional and textural variations in Phase B, indicate it was likely formed through the injection of numerous gabbroic sills and in situ crystal fractionation.

Phase C: Quartz diorite

Phase C quartz diorite accounts for approximately 30% of the Mouska stage and is ~1200 by 600 m in size (Galley & Lafrance, 2014). Sharp contacts are present between Phase C and the older intrusive phases (Galley & Lafrance, 2014). The contact with the younger Phase D is sharp to transitional, likely due to brecciation and crude mixing of the partially solidified Phase C by the Phase D magma (Galley & Lafrance, 2014). Xenoliths of Phase A and the Hébécourt Formation are present along the basal (northern) contact of Phase C and along the top contact xenoliths of Phase A and lower Bousquet Formation basaltic andesite are present (Unit 4.4; Galley & Lafrance, 2014). Numerous mafic and felsic dykes crosscut Phase C. The felsic dykes are up to 15 m wide, are texturally and compositionally similar to Doyon-stage trondhjemite and tonalite phases and possibly similar to felsic volcanic units of the upper Bousquet Formation (Galley & Lafrance, 2014). Numerous alteration "pods" up to 40 cm in size, consisting of epidote-albite-chlorite-calcite occur in Phase C and these pods become more abundant towards the upper contact of Phase C (Galley & Lafrance, 2014). Phase C intruded into the upper portions of Phase B and these sills combined to form a poorly layered laccolithic body. Compositional and textural variability within the laccolithic Phase C suggests, similar to Phase B, that Phase C formed through multiple magma injections and in situ crystal fractionation.

Phase D: Tonalite

Phase D tonalite is the largest (volumetrically) phase of the Mouska stage, accounting for over 50 vol% and is approximately 2000 by 700 m (Galley & Lafrance, 2014). Both the lower and upper contacts of Phase D contain abundant xenoliths. The lower contact contains xenoliths of the Hébécourt Formation, Phase A, and unit 2.1 (quartz-phyric rhyolite sills) of the lower Bousquet Formation (Galley & Lafrance, 2014). The upper contact zone of Phase D can be over 100 m in thickness and contains more xenoliths than the lower contact zone. Xenoliths in the upper contact zone consist of Phases A, B, and C, as well as aphyric basalt (Galley & Lafrance, 2014). Along the margins of xenoliths in the upper contact zone various extents of partial assimilation are observed and the margins are variably altered to actinolite, magnetite, and epidote. As well, in the upper contact zone, actinolite, epidote, clinozoisite, magnetite, and bluish quartz increase in abundance, possibly reflecting the interaction of the magma, and partial assimilation of, mafic to intermediate wall rock xenoliths (Galley & Lafrance, 2014). Numerous aplitic veins occur in the upper contact zone that are 10 to 20 cm wide and are crosscut by tonalite and trondhjemite dykes of the younger Doyon stage of the MIC. Phase C was likely not completely crystallized prior to the emplacement of Phase D and magma mixing may have occurred between the two phases.

Phase E: Doyon quartz diorite

Phase E is approximately 1500 by 300 m, highly xenolithic, and has similar texture and composition to the upper contact zone of Phase D (Galley & Lafrance, 2014). Phase E forms the top of the Mouska stage and likely represents an outlier of Phase D or a “roof-pendant” of Phase D that became separated from the main Phase D body during the injection of sills and dykes related to the Doyon-stage tonalites and trondhjemites as numerous sharp-walled dykes of Phases F, G, and H crosscut Phase E (Galley & Lafrance, 2014). Miarolitic cavities in Phase E may have formed in response to partial assimilation of Phase D (Galley & Lafrance, 2014).

The Doyon-stage trondhjemite and tonalite phases were emplaced after all Mouska stage phases were all crystallized as indicated by: i) Doyon-stage dykes and sills that cross-cut Mouska-stage phases are sharp-sided, and ii) along the upper contact of Phase D, intrusion of Doyon-stage sills hydraulically separated a large pendant of Phase D, referred to as Phase E ("Doyon quartz diorite).

Doyon stage

Phase F: Plagioclase-amphibole porphyry tonalite

Phase F occurs at the southwest contact of the MIC and intrudes the Mouska-stage phases and the overlying units of the lower Bousquet Formation in the form of numerous sills and dykes (Galley & Lafrance, 2014). Abundant angular, rhyolitic to basaltic xenoliths are present in Phase F. Emplacement of Phase F occurred along the top contact of Phase C as well as into the overlying lower Bousquet Formation.

Phase G: Plagioclase porphyry tonalite

Phase G occurs as <1 m dykes that crosscut Phases C, D, and F, as well as portions of the lower Bousquet Formation southwest of the MIC (Galley & Lafrance, 2014). Phase G represents the immediate hanging wall to Phase E, where it occurs as a < 300 m thick series of overlapping sills (Galley & Lafrance, 2014). The plagioclase phenocrysts are ~4 mm in length and comprise up to 15 vol % of the unit. Phase G lies within the alteration halo of the Doyon Au deposit (Galley & Lafrance, 2014). Near the top of the lower Bousquet Formation, Phase G dykes were emplaced after Phase F.

Phase H: Plagioclase-quartz porphyry trondhjemite

Phase H mainly comprises a series of sills in the upper portions of the MIC but also occurs as dykes crosscutting Phases A, C, and D of the Mouska stage (Galley & Lafrance, 2014). A maximum thickness of ~300 m is suggested for Phase H, but due to the strong quartz-sericite-aluminosilicate-pyrite alteration that affects the MIC upper contact and the felsic volcanics the MIC are in contact with, an accurate maximum thickness of Phase H is problematic (Galley & Lafrance, 2014). Following Phase F, Phase H was emplaced between Phases F and G as a series of sills. Abundant miarolitic cavities formed in both trondhjemite phases through *in situ* volatile exsolution.

Phase I: Aphyric to quartz porphyritic trondhjemite

Phase I forms dykes and sills that crosscut Mouska-stage phases as well as the Bousquet Formation and Phase I is not crosscut by any phase of the MIC (Galley & Lafrance, 2014). The base of each sill is massive and equigranular that becomes gradually finer and granophyric towards the top and commonly contains blue quartz phenocrysts (Galley & Lafrance, 2014). Contacts between individual Phase I sills vary from gradual to sharp. The thickest portion of Phase I is approximately 700 m and is composed of at least seven distinct sills. Miarolitic cavities are a characteristic feature of this phase and can be up to several centimeters in diameter (Galley & Lafrance, 2014). The emplacement history of Phase I is similar to Phase H.

METHODOLOGY

Sample Collection

Initial sample collection took place during July and August, 2016, and involved sampling of outcrop and drill core. Outcrop samples were taken as far away from quartz veining and/or dykes/sills (when present) to obtain unaltered or minimally altered samples. Drill core samples

were collected from two drill holes that are interpreted to represent a near complete stratigraphic column of the entire MIC (Galley & Lafrance, 2014; A. Galley, communication, 2016). Drill hole MSK-6-810 contains phase A (diorite), B (gabbro), and C (quartz diorite) of the Mouska-stage and drill hole 1106-96 contains phase E (Doyon quartz diorite) of the Mouska-stage and phases G (plagioclase-phyric tonalite), H (phyric-trondhjemite), and I (aphyric-trondhjemite) of the Doyon-stage. Doyon-stage phase F (plagioclase-amphibole-phyric tonalite) and Mouska-stage phase D (tonalite) were not present in either of these drill holes, and a drill hole that contains phase F (plagioclase-amphibole-phyric tonalite) could not be located, however phase D (tonalite) was collected from outcrop.

Zircon and Titanite Mineral Separation and Imaging

Six samples from four phases of the MIC were selected for zircon and/or titanite mineral separation based on transmitted light petrography. Samples were sent to Boise State University for separation, picking, mounting, and CL imaging of zircon. Titanite was only recovered from two samples (Stop 10; Stop 11) both from the phase D tonalite of the MIC. After zircon separation, half of the zircon grains picked underwent high temperature annealing in a muffle furnace (~900°C for 60 hours in quartz crucibles) to enhance the SEM-CL response, whereas the other half were not annealed to preserve any silicate and/or sulfide melt inclusions that may be trapped in the zircon for future study. Both annealed and non-annealed zircon and titanite were mounted in epoxy and polished until the center level of the grains were exposed. Cold cathodoluminescence (SEM-CL) images of annealed zircon were obtained with a JEOL JSM-1300 scanning electron microscope and Gatan MiniCL. Titanite was not annealed and SEM-BSE images were collected using a TESCAN MIRA 3 LMU Variable Pressure Schottky Field Emission SEM equipped with a BSE detector at Saint Mary's University, Halifax, Nova Scotia, Canada.

CA-ID-TIMS U-Pb Geochronology Methods

U-Pb dates were obtained by the chemical abrasion isotope dilution thermal ionization mass spectrometry (CA-TIMS) method from analyses composed of single zircon grains, modified after Mattinson (2005). Zircon was removed from the epoxy mounts for dating based on CL images (e.g., lack of inherited cores, resorption surfaces, metamorphic overgrowths) and LA-ICPMS chemistry (e.g., magmatic REE patterns). Analysis was done at three times; 30 analyses were done in July 2020 and 20 analyses were done in December 2021.

Zircon was put into 3 ml Teflon PFA beakers and loaded into 300 µl Teflon PFA microcapsules. Fifteen microcapsules were placed in a large-capacity Parr vessel and the zircon partially dissolved in 120 µl of 29 M HF for 12 hours at 190°C. Zircon was returned to 3 ml Teflon PFA beakers, HF was removed, and zircon was immersed in 3.5 M HNO_3, ultrasonically cleaned for an hour, and fluxed on a hotplate at 80°C for an hour. The HNO_3 was removed and zircon was rinsed twice in ultrapure H_2O before being reloaded into the 300 µl Teflon PFA microcapsules (rinsed and fluxed in 6 M HCl during sonication and washing of the zircon) and spiked with the EARTHTIME mixed ^{233}U-^{235}U-^{202}Pb-^{205}Pb tracer solution (ET2535). Zircon was dissolved in Parr vessels in 120 µl of 29 M HF with a trace of 3.5 M HNO_3 at 220°C for 48 hours, dried to fluorides, and re-dissolved in 6 M HCl at 180°C overnight. U and Pb were separated from the zircon matrix using an HCl-based anion-exchange chromatographic procedure (Krogh, 1973), eluted together and dried with 2 µl of 0.05 N H_3PO_4.

Pb and U were loaded on a single outgassed Re filament in 5 µl of a silica-gel/phosphoric acid mixture (Gerstenberger & Haase, 1997), and U and Pb isotopic measurements made on a GV Isoprobe-T or IsotopX Phoenix multicollector thermal ionization mass spectrometer equipped with an ion-counting Daly detector. The mass spectrometer and Pb detector routine used are indicated

for each analysis in Supplementary Data Table 2.7. Pb isotopes from 18 analyses with larger amounts of radiogenic Pb were measured on the Isoprobe-T mass spectrometer by a Faraday-Daly routine that cycles 200-300 times between placing mass 204 in the axial Daly collector and masses 205-208 on the H1-H4 Faraday detectors to placing mass 205 in the axial Daly and masses 206-208 in the H1-H3 Faradays, providing real-time Daly gain correction. Pb isotopes from one analysis with larger amounts of radiogenic Pb were measured on the Phoenix mass spectrometer by a Faraday-Daly routine. Pb isotopes from 31 analyses with smaller amounts of radiogenic Pb were measured on the Phoenix mass spectrometer by peak-jumping all isotopes on the Daly detector for 160-250 cycles. Pb mass fractionation was corrected using the known $^{202}Pb/^{205}Pb$ of the ET2535 tracer solution. Transitory isobaric interferences due to high-molecular weight organics, particularly on ^{204}Pb and ^{207}Pb, disappeared within approximately 30 cycles, while ionization efficiency averaged 104 cps/pg of each Pb isotope. Linearity (to ≥1.4 x 106 cps) and the associated deadtime correction of the Daly detector were determined by analysis of NBS982. Uranium was analyzed as UO_2^+ ions in static Faraday mode on 1012 ohm resistors for 200-300 cycles, and corrected for isobaric interference of $^{233}U^{18}O^{16}O$ on $^{235}U^{16}O^{16}O$ with an $^{18}O/^{16}O$ of 0.00206. Ionization efficiency averaged 20 mV/ng of each U isotope. U mass fractionation was corrected using the known $^{233}U/^{235}U$ of the ET2535 tracer solution.

U-Pb dates and uncertainties were calculated using the algorithms of Schmitz & Schoene (2007), calibration of ET2535 tracer solution (Condon *et al.*, 2015) of $^{235}U/^{205}Pb$ = 100.233, $^{233}U/^{235}U$ = 0.99506, $^{205}Pb/^{204}Pb$ = 8474, and $^{202}Pb/^{205}Pb$ = 0.99924, U decay constants recommended by Jaffey *et al.* (1971), and $^{238}U/^{235}U$ of 137.818 (Hiess *et al.*, 2012). The $^{206}Pb/^{238}U$ ratios and dates were corrected for initial ^{230}Th disequilibrium using $D_{Th/U} = 0.2 \pm 0.1$ (2σ) and the algorithms of Crowley *et al.* (2007), resulting in an increase in the $^{206}Pb/^{238}U$ dates of ~0.09 Ma. All common Pb in analyses was attributed to laboratory blank and subtracted based on the

measured laboratory Pb isotopic composition and associated uncertainty. U blanks are estimated at 0.013 pg.

The $^{207}Pb/^{206}Pb$ dates are used in age interpretations because they are not affected by recent Pb loss, unlike the $^{206}Pb/^{238}U$ dates. The effects of recent Pb loss are considered to minimal because most dates are concordant within the decay constant uncertainties on concordia. The average discordance is 0.14% for 47 of the 50 analyses (discordance is 0.6-7% in the other 3 analyses). The effects of ancient Pb loss are considered to be minimal because the vast majority of dates are equivalent within each sample (probability of fit >0.05).

Weighted mean $^{207}Pb/^{206}Pb$ dates are calculated from equivalent dates (probability of fit >0.05) using Isoplot 3.0 (Ludwig, 2003). Errors are at the 95% confidence interval. It is computed as the internal standard deviation multiplied by the Student's t-distribution multiplier for a two-tailed 95% critical interval and n-1 degrees of freedom when the reduced chi-squared statistic, mean squared weighted deviation (MSWD; Wendt & Carl, 1991), takes a value less than its expectation value plus its standard deviation at the same confidence interval, which is when MSWD is <1+2*sqrt[2/(n-1)]. This error is expanded via multiplication by the sqrt(MSWD) when the MSWD is ≥1+2*sqrt[2/(n-1)] to accommodate unknown sources of over dispersion. Errors on weighted mean $^{207}Pb/^{206}Pb$ dates are given as ± x / z, where x is the internal error based on analytical uncertainties only, including counting statistics, subtraction of tracer solution, and blank and initial common Pb subtraction, and z includes the ^{238}U and ^{235}U decay constant uncertainties propagated in quadrature. Internal errors should be considered when comparing our dates with $^{206}Pb/^{238}U$ dates from other laboratories that used the same tracer solution or a tracer solution that was cross-calibrated using EARTHTIME gravimetric standards. Errors including the ^{238}U decay constant (Jaffey *et al.*, 1971) should be considered when comparing our dates with those derived from other decay schemes (e.g., $^{40}Ar/^{39}Ar$, ^{187}Re-^{187}Os). Errors on individual dates are at 2σ.

To assess the accuracy and precision of our dates, the 2000 Ma solution from EARTHTIME was analyzed during the same time periods as the zircon analyses, using the same detectors for Pb isotopes with similar amounts of radiogenic Pb (Supplementary Materials Table 2.7; Supplementary Materials Figure 2.1). In July 2020, the Isoprobe-T yielded a weighted mean based on four Faraday-Daly analyses of 1999.89 ± 0.27 Ma (MSWD = 0.3, probability of fit = 0.80). In December 2021, the Phoenix yielded a weighted mean based on four Faraday-Daly analyses of 1999.92 ± 0.27 Ma (MSWD = 0.1, probability of fit = 0.96). In July 2020, the Phoenix yielded a weighted mean based on seven Daly analyses of 1999.71 ± 0.18 Ma (MSWD = 0.5, probability of fit = 0.80). In December 2021, the Phoenix yielded a weighted mean based on eight Daly analyses of 1999.79 ± 0.16 Ma (MSWD = 1.3, probability of fit = 0.27). The weighted mean from all 23 dates is 1999.81 ± 0.08 Ma (MSWD = 0.8, pof = 0.71). Our dates from zircon are considered to be accurate within their given precision based on agreement between the dates from the 2 Ga solution analyzed at different times and on different detectors. Moreover, the dates agree with the weighted mean of 1999.94 ± 0.06 Ma (Supplementary Materials Figure 2.1) based on 59 analyses from Schaltegger *et al.* (2021).

Electron Probe Microanalyses of Titanite

Electron probe microanalyses of titanite were performed using a JEOL JXA8230 electron microprobe equipped with five wavelength-dispersive spectrometers and an energy-dispersive spectrometer at the University of Toronto. The instrument operated at a 15 kV accelerating voltage with a 50 nA beam current for all analyses and the beam diameter was 20 μm. Raw microprobe data count rates were converted to concentrations using the ZAF matrix correction scheme using JEOL software.

Laser ablation ICP-MS (LA-ICP-MS) Analyses of Accessory Minerals and Quartz

The major, minor, and trace element composition of accessory minerals (zircon, titanite, rutile, and quartz) was determined by LA-ICP-MS at the Magmatic and Ore-Forming Processes Research Laboratory at the University of Toronto. A New Wave Research® 193 nm ArF Excimer laser ablation system attached to an Agilent 7900 quadrupole mass spectrometer was used. The instrument was tuned to maximum sensitivity while maintaining robust plasma conditions (U≈Th on National Institute of Standards and Technology Standard Reference Material 610 silicate glass (NIST610) and low oxide and doubly charge ion production rates (ThO/Th < 0.3%; Mass 21/42 < 0.3%). Helium was used as a carrier gas at a flow rate of 1.0 L/min. The reference standard NIST610 (e.g., Gagnon *et al.*, 2008) was used for the quantification of element concentration ratios and calibration of analyte sensitivities. Analyses of ~16 unknowns were bracketed by 2 standard analyses at the beginning and the end of each analysis block. During analytical sessions where zircon trace elements were collected, 91500 and Plesovice zircon reference materials (Wiedenbeck *et al.*, 2004; Sláma *et al.*, 2008) were used as quality control monitors during trace element quantification. Trace element quantification of minerals was performed using the software SILLS (Guillong *et al.*, 2008). For quartz, an internal standard of 99.99 wt% SiO_2 was used, 32.7 wt% SiO_2 for zircon, 30.6 wt% SiO_2 for titanite, and 99 wt% TiO_2 for rutile based on ideal stoichiometry. Dwell times for all elements were 10 ms. Exceptions for zircon analyses were Ti^{49} (50 ms) and La^{139} and Pr^{141} (30 ms). Exceptions for titanite were Zr^{90} (40 ms) and Cr^{53}, Cu^{63}, Cu^{65}, Zn^{66}, As^{75}, Mo^{95}, and Sn^{118} (20 ms). Spot locations for LA-ICP-MS analyses were selected based on a combination of transmitted light, SEM-BSE, and/or SEM-CL petrography.

Quantifying 91500 zircon using NIST610 showed most elements within 10% of published values (Supplementary Materials Table 2.8). Elements that have relatively low concentrations in zircon (e.g., Nb, Ta, Nd, Sm) were within 20% of published values. Titanium, used for temperature

calculations, was lower (~30%) than the published 91500 value, resulting in temperatures being lower by ~40°C. A plot comparing the recommended versus quantified data for 91500 is presented in Supplementary Materials Figure 2.2.

Trace element distribution maps (ppm) for zircon were obtained using a Resonetics COMPexPro® 102 ArF 193 nm Excimer laser ablation system, with a set output energy of 170 mJ at 50% attenuation, coupled to an Agilent 7700 quadrupole ICP-MS at the University of New Brunswick, Fredericton, New Brunswick. Maps were generated using a beam spot size of 17 μm, scan speed 10 μm/s and repetition rate of 10 Hz. Each ablation line scan was bracketed by 20 s of background (laser off, gas blank). The raw data (count rates vs. time) from traverses were imported into the *Iolite3*™ software package (Hellstrom *et al.,* 2008; Paton *et al.,* 2011), an add-in for Wavemetrics *Igor Pro v.6.32*™. Trace element maps were quantified using the CellSpace Image function in *Iolite* with ideal SiO_2 = 32.7 wt% as an internal standard and using NIST610 for the calibration of analyte sensitivities. Relative instrument uncertainties (2σ) based on counting statistics for quantified spots within the maps ranged from ±8-10 % for ^{49}Ti to ±6-9% for ^{238}U, and they are similar for other isotopes measured. Routine detection limits were <15% of the quantified values for ^{49}Ti and <0.001% for ^{238}U, with detection limits for other quantified analytes within this range of relative percentage of quantified totals. The impact of the internal standard value for zircon deviating from the ideal value of 32.7 wt% SiO_2 would be a scaled proportionality. However, as element substitution for Si in zircon is negligible deviations from this ideal value were not considered further.

Secondary Ion Mass Spectrometry (SIMS) of Zircon

Oxygen isotope ratios ($^{18}O/^{16}O$) of zircon grains from the MIC were collected using a CAMECA 7f SIMS at the University of Manitoba, Winnipeg, Manitoba. A cesium (Cs+) primary

beam with a 6.5 nA current was accelerated (+10 kV) onto the sample surface with a sputtering diameter of ~15 μm. The instrument operated with a 300 V offset, –9 kV secondary accelerating voltage, and a mass resolving power of 350. For a detailed description of operating conditions and strategy for correction of instrumental mass fractionation and matrix effects, see Sheahan *et al.* (2016). Grains of Temora 2 zircon with a $\delta^{18}O$ value of 8.2 ‰ (Black *et al.*, 2004) were used as the zircon reference material for oxygen isotope analysis and had a spot-to-spot reproducibility of 0.6‰ (1σ). All isotopic data are presented using standard δ-notation relative to the appropriate standards, Vienna Standard Mean Ocean Water (V-SMOW) for $^{18}O/^{16}O$.

Hot Cathodoluminescence of Quartz

Qualitative CL imaging completed at Saint Mary's University provided textural information for, and constraints on the origin of quartz. This was obtained using a Lumic HC4-LM® hot-cathode CL microscope coupled to an Olympus BXFM® focusing mount with images captured by a Kappa DX40C® Peltier cooled camera operated using the DX40C-285FW® software package. The hot CL was operated at an acceleration voltage between 12.4 and 13.1 kV, a beam current of 0.35 mA, a filament current of 2.3 A, a deflection of 10 V and a focus of 5.5 V.

REFERENCES

Black, L.P., Kamo, S.L., Allen, C.M., Davis, D.W., Aleinikoff, J.N., Valley, J.W., Mundil, R., Campbell, I.H. Korsch, R.J., Williams, I.S. & Foudoulis, C. (2004) Improved 206Pb/238U microprobe geochronology by the monitoring of a trace-element-related matrix effect: SHRIMP, ID-TIMS, ELA-ICP-MS and oxygen isotope documentation for a series of zircon standards. *Chemical Geology,* 205, 115-140.

Condon, D.J., Schoene, B., McLean, N.M., Bowring, S.A. & Parrish, R. (2015) Metrology and traceability of U-Pb isotope dilution geochronology (EARTHTIME Tracer Calibration Part I). *Geochimica et Cosmochimica Acta*, 164, 464-480.

Crowley, J.L., Schoene, B. & Bowring, S.A. (2007) U-Pb dating of in the Bishop Tuff at the millennial scale. *Geology*, 35, 1123-1126.

Gagnon, J., Fryer, B., Samson, I.M. & Williams-Jones, A.E. (2008) Quantitative analysis of silicate certified reference materials by LA-ICPMS with and without an internal reference standard. *Journal of Analytical Atomic Spectroscopy*, 23, 1529-1537.

Galley, A.G. & Lafrance, B. (2014) Setting and evolution of the Archean synvolcanic Mooshla Intrusive Complex, Doyon-Bousquet-LaRonde mining camp, Abitibi greenstone belt: emplacement history, petrogenesis, and implications for Au metallogenesis. *Economic Geology*, 109, 205-229.

Gerstenberger, H. & Haase, G. (1997) A highly effective emitter substance for mass spectrometric Pb isotope ratio determinations. *Chemical Geology*, 136, 309-312.

Guillong, M.M., Maier, D.L., Allan, M.M., Heinrich, C.A. & Yardley, B.W.D. (2008) Appendix A6: SILLS: a MATLAB based program for the reduction of laser ablation ICP-MS data of homogeneous materials and inclusions. *In* Laser Ablation ICP-MS in the Earth Sciences: Current Practices and Outstanding Issues. Edited by P. Sylvester. *Mineralogical Association of Canada Short Course Series* volume 40.

Hiess, J., Condon, D.J., McLean, N. & Noble, S.R. (2012) $^{238}U/^{235}U$ systematics in terrestrial uranium-bearing minerals. *Science*, 335, 1610-1614.

Hellstrom, J., Paton, C., Woodhead, J. & Hergt, J. (2008) Iolite: software for spatially resolved LA-(quad and MC) ICPMS analysis. *Mineralogical Association of Canada Short Course*, 40, 343-348.

Jaffey, A.H., Flynn, K.F., Glendenin, L.E., Bentley, W.C. & Essling, A.M. (1971) Precision measurements of half-lives and specific activities of ^{235}U and ^{238}U. *Physical Review C*, 4, 1889-1906.

Krogh, T.E. (1973) A low contamination method for hydrothermal decomposition of and extraction of U and Pb for isotopic age determination. *Geochimica et Cosmochimica Acta*, 37, 485-494.

Ludwig, K.R. (2003) User's Manual for Isoplot 3.00. Berkeley Geochronology Center: Berkeley, CA, 70 p.

Mattinson, J.M. (2005) U-Pb chemical abrasion ("CA-TIMS") method: combined annealing and multi-step partial dissolution analysis for improved precision and accuracy of ages. *Chemical Geology*, 220, 47-66.

Paton, C., Hellstrom, J., Paul, B., Woodhead, J. & Hergt, J. (2011) Iolite: freeware for the visualisation and processing of mass spectrometric data. *Journal of Analytical Atomic Spectrometry*, 26, 2508-2518.

Schaltegger, U., Ovtcharova, M., Gaynor, S.P., Schoene, B., Wotzlaw, J-F., Davies, J.F.H.L., Farina, F., Breber, N.D., Szymanowski, D. & Chelle-Michou, C. (2021) Long-term repeatability and interlaboratory reproducibility of high-precision ID-TIMS U-Pb geochronology. *Journal of Analytical Atomic Spectrometry*, 36, 1466-1477.

Schmitz, M.D. & Schoene, B. (2007) Derivation of isotope ratios, errors and error correlations for U-Pb geochronology using ^{205}Pb-^{235}U-(^{233}U)-spiked isotope dilution thermal ionization mass spectrometric data. *Geochemistry, Geophysics, Geosystems (G^3)*, 8, Q08006, doi:10.1029/2006GC001492.

Sheahan, C., Fayek, M., Quirt, D. & Jefferson, C.W. (2016) A combined ingress-egress model for the Kianna unconformity-related uranium deposit, Shea Creek project, Athabasca Basin, Canada. *Economic Geology*, 111, 225-257.

Sláma, J., Košler, J., Condon, D.J., Crowley, J.L., Gerdes, A., Hanchar, J.M., Horstwood, M.S.A., Morris, G.A., Nasdala, L., Norberg, N., Schaltegger, U., Schoene, B., Tubrett, M.N. & Whitehorse, M.J. (2008) Plešovice zircon-a new natural reference material for U-Pb and Hf isotopic microanalysis. *Chemical Geology*, 249, 1-35.

Wendt, I. & Carl, C. (1991) The statistical distribution of the mean square weighted deviation. *Chemical Geology*, 86, 275–285.

Wiedenbeck, M., Hanchar, J.M., Peck, W.H., Sylvester, P., Valley, J., Whitehouse, M., Kronz, A., Morishita, Y. & Nasdala, L. (2004) Further characterisation of the 91500 zircon crystal. *Geostandards and Geoanalytical Research*, 28, 9-39.

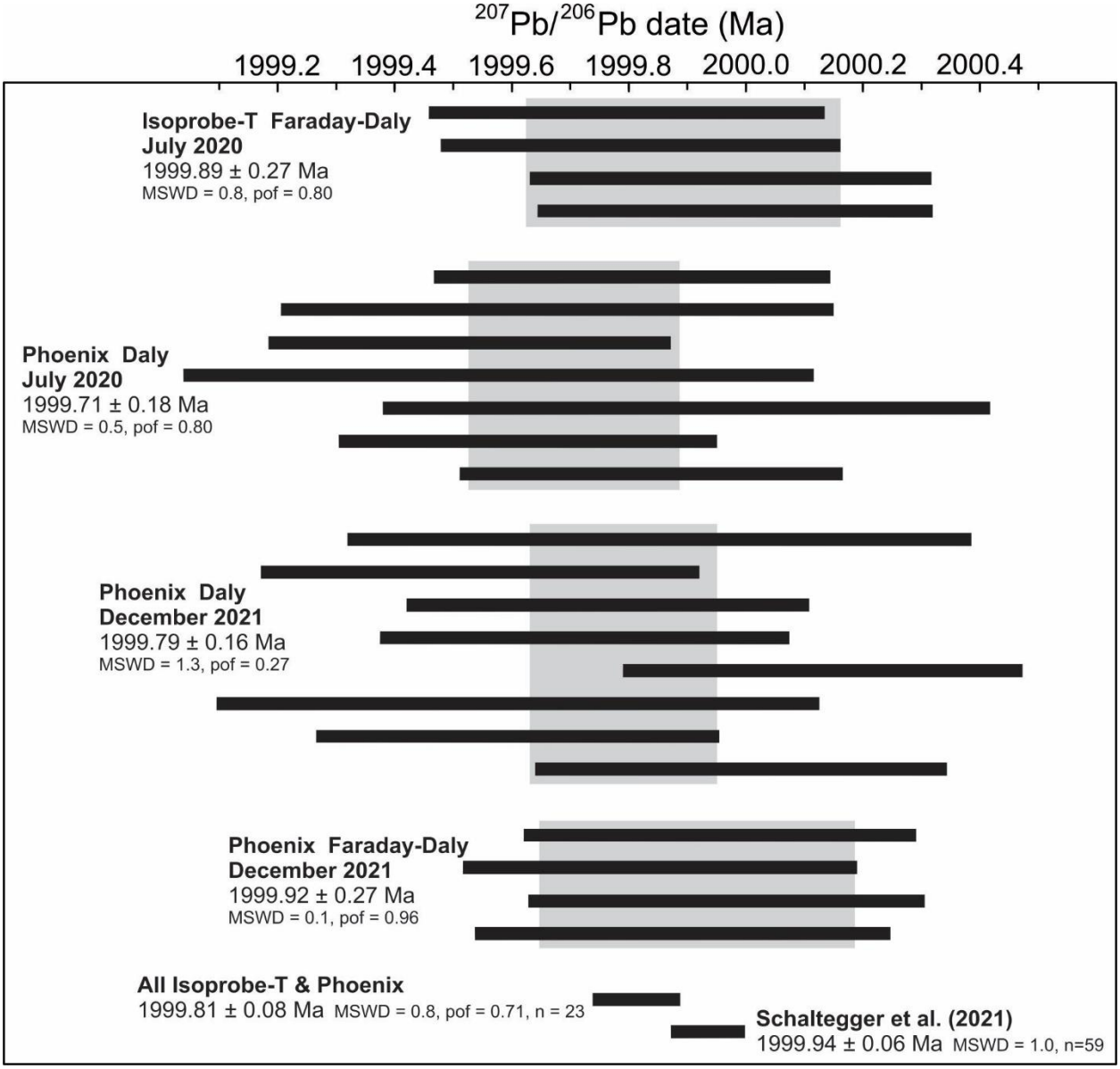

Supplementary Materials Fig. 2.1. Age ranked plot showing $^{207}Pb/^{206}Pb$ dates of the 2000 Ma solution from EARTHTIME from the different analytical sessions and compared to the analysis of the same solution from Schaltegger *et al.*, 2021.

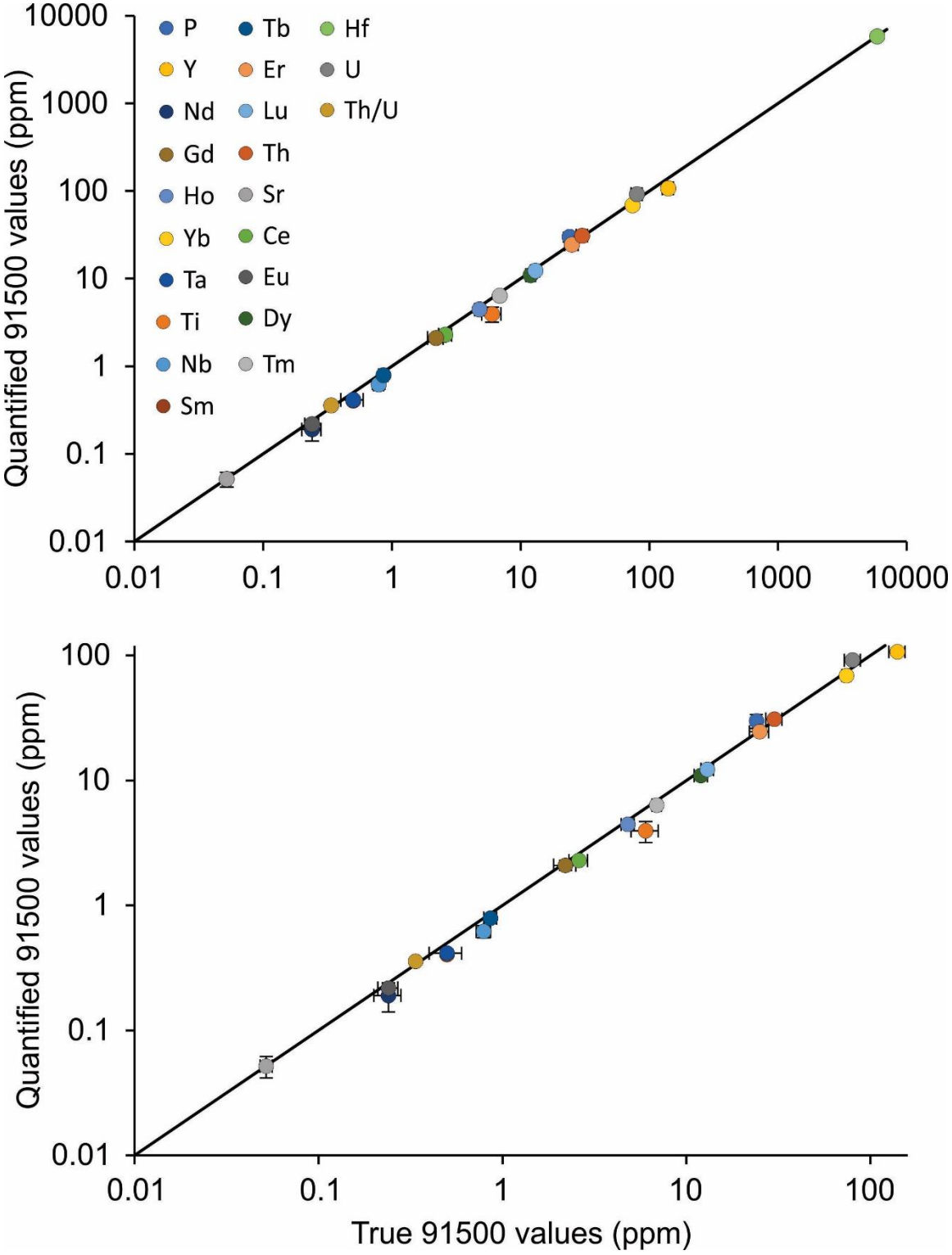

Supplementary Materials Fig. 2.2. Comparison of quantified 91500 zircon values using NIST610 as an internal calibration plotted against the published values of 91500 zircon.

Chapter 3: Constraints on the origin and metal fertility of the Mooshla Intrusive Complex (MIC), Doyon-Bousquet-LaRonde mining district, Abitibi greenstone belt, Quebec, Canada, II: Silicate melt inclusions in magmatic zircon and quartz

Kevin Neyedley[1], Patrick Mercier-Langevin*[2], Alexandra Tsay[3] Zoltan Zajacz[3], Mostafa Fayek[4], James L. Crowley[5], Jacob J. Hanley[1]

[1]Department of Geology, Saint Mary's University, Halifax, Nova Scotia, Canada

[2]Geological Survey of Canada, Quebec, Quebec

*Present address: Agnico Eagle Mines ltd., Toronto, Ontario, Canada

[3]Earth and Environmental Sciences, University of Geneva, Geneva

[4]Department of Geological Sciences, University of Manitoba, Winnipeg, Manitoba, Canada

[5]Isotope Geology Lab, Department of Geosciences, Boise State University, Boise, ID, USA

3.1 ABSTRACT

The synvolcanic Mooshla Intrusive Complex (MIC) in the Doyon-Bousquet-LaRonde mining camp, Abitibi greenstone belt, Canada, may be genetically associated with numerous Au-rich VMS, epizonal intrusion-related Au ± Cu, and shear zone-hosted orogenic Au and/or remobilized VMS deposits. To understand the magmatic evolution of the MIC and its relationship to these Au-rich deposits, analysis of silicate melt inclusions (SMI) preserved in zircon and quartz provide a means to determine the original major and trace element composition and metal tenor of the magmatic system. The use of SMI is preferred for quantification of the pre-emplacement melt chemistry (in particular, ore metals) compared to bulk rock compositions that are commonly modified by magmatic (e.g., degassing) and post-solidus processes. Characterization of SMI chemistry from different lithologies of the MIC (gabbro, quartz diorite, tonalite, and trondhjemite) was done by integrating petrography with SEM-EDS, EMPA, LA-ICP-MS analyses.

Silicate melt inclusions preserved in quartz and zircon recorded rhyolitic compositions in a wide range of lithologies from the MIC and SMI provide various lines of evidence that help understand processes that operated during the evolution of the MIC. The low Cs concentrations and normative Rb-Sr-Ba contents imply that the trapped melt was not highly fractionated. Additionally, specific ratios (e.g., Al_2O_3 vs SiO_2, Sr/Y, La/Yb) suggest the melt is consistent with low-Al TTG suites and that plagioclase fractionation and accumulation was a dominant magmatic process and assimilation of SiO_2-rich material occurred. Accidentally trapped sulfide present in SMI implies sulfide saturation occurred early on and at depth (0.5-1.2 GPa) in the magmatic system. Additionally, these sulfides have similar ore metal ratios to Au-rich deposits in the Doyon-Bousquet-LaRonde mining camp suggesting early magmatic sulfides influenced the ore metal tenors of these syn-volcanic and intrusion-hosted deposits. Early sulfide saturation means sulfides acted as a temporary storage medium for metals and were destroyed upon magma ascent,

crystallization, and volatile exsolution, allowing for metals to be transferred to exsolving volatiles, contributing metals to ore forming system. Therefore, the enrichment of SMI in Au and other metals (e.g., Ag, Cu, Bi) that are typical of porphyry-epithermal environments in arc settings reinforces that consideration must be made for the direct involvement of magmatically-sourced metals transferred into shallow ore-forming hydrothermal systems through deep magmatic devolatilization.

3.2 INTRODUCTION

The Archean Mooshla Intrusive Complex (MIC) is predominately a tonalite, trondhjemite, and quartz diorite polyphase magmatic body located in the Doyon-Bousquet-LaRonde mining camp of the Abitibi greenstone belt, Québec (Galley & Lafrance, 2014). The MIC is classified as a low-Al (< 15 wt.% Al_2O_3) tonalite-trondhjemite-diorite/granodiorite (TTD/TTG) suite and in the Archean, these type of synvolcanic intrusions are commonly present underlying VMS deposits (Galley, 2003; Galley & Lafrance, 2014). Additionally, similar to the MIC, Archean TTG suites can be host to porphyry-style Cu-Au-Mo mineralization (e.g., Flavrian-Powell intrusive complex, Goldie *et al.*, 1979; Galley, 2003; Chester intrusive complex, Katz *et al.*, 2017, 2021; Chibougamau Pluton, Pilote *et al.*, 1995). The Doyon-Bousquet-LaRonde mining camp has a historic Au production of 107.48 Mt with an average grade of 4.85 g/t Au totalling 521 t (16.8 Moz) of Au and combining past production, current reserves, and estimated resources, the total Au budget is 28.7 Moz (Mercier-Langevin *et al.*, 2021). Numerous Au deposits are spatially and temporally associated with the MIC and include Au-rich volcanogenic massive sulfide (VMS; e.g., LaRonde Penna), epizonal intrusion-related Au ± Cu (e.g., Doyon), and shear zone-hosted orogenic gold and/or remobilized VMS mineralization (e.g., Mouska) deposits (Mercier-Langevin *et al.*, 2007c). In the past, studies have suggested the MIC has played a significant role in the development of the

Au endowment in the Doyon-Bousquet-LaRonde mining camp (Valliant & Hutchinson, 1982; Gosselin, 1998; Mercier-Langevin, 2007a, b; Galley & Lafrance, 2014; Yergeau et al.,, 2022a, b; Galley & Mercier-Langevin, 2024), but no direct evidence such as similar ages of mineralization and intrusive units (cf Endako porphyry, Selby & Creaser, 2001; Jogran porphyry, Perelló *et al.*, 2020; Côté Gold porphyry-type, Katz *et al.*, 2021) or magmatic metal tenors corresponding to deposit metal tenors (e.g., Halter *et al.*, 2005) has been established to directly make this genetic association. Therefore, confirming the hypothesis that Au-enriched magmatic volatiles were supplied to the hydrothermal system through devolatilization and fluid-melt partitioning during crystallization of the MIC remains to be done.

Using bulk rock geochemistry to understand the source and magmatic processes (e.g., contamination and assimilation, volatile exsolution) during magma ascent through the crust is problematic because intrusive rock compositions are commonly affected by post-solidus processes (e.g., magmatic-hydrothermal alteration, metamorphic alteration) that can modify their chemical signature and origin. The microanalysis of silicate melt inclusions (SMI) is a powerful tool to understand the metal budgets of intrusive systems spatially and temporarily associated with magmatic-hydrothermal ore deposits (e.g., Audétat & Pettke, 2003; Student & Bodnar, 2004; Halter *et al.*, 2004b, 2005; Audétat & Pettke, 2006; Grondahl & Zajacz, 2017). Silicate melt inclusions can be relatively unaffected by post-solidus processes because of the chemical and physical robustness of the host mineral(s). Thus, they may preserve melt compositions at various stages of magma evolution allowing the influence of processes such as fractionation, assimilation, and degassing to be tracked. In particular, they can provide insight into which magma(s) within composite intrusions were the most metal-endowed and what magmatic processes (e.g., magma mixing, assimilation) may have triggered the transfer of metals from the melt to the hydrothermal system (Halter *et al.*, 2004b).

In this study, quartz- and zircon-hosted SMI were studied using a variety of microanalytical techniques (scanning electron microscopy-backscattered electron [SEM-BSE] imaging, SEM-energy dispersive spectroscopy [EDS], electron probe microanalyzer [EPMA], laser Raman microspectroscopy, laser ablation-inductively coupled plasma-mass spectrometry [LA-ICPMS]) to provide a detailed mineralogical and geochemical characterization of SMI and constrain the magmatic metal tenor of various phases of the MIC. Combining these methods allows for evaluation of the origin and magmatic processes of the suspected TTG magmas in the Doyon-Bousquet-LaRonde mining camp, the potential timing and influence of volatile exsolution and sulfide saturation on metal endowment, and discuss the implications and potential role the MIC played in the development of Au-rich VMS and related deposits.

3.3 GEOLOGICAL SETTING

3.3.1 Geology of the Doyon-Bousquet-LaRonde Mining Camp

The regional geology and geologic setting of the Doyon-Bousquet-LaRonde mining camp and its mineral deposits have been described in detail by Gunning (1941), Fillion *et al.* (1977), Valiant & Hutchinson (1982), Marquis *et al.* (1990), Trudel *et al.* (1992), Lafrance *et al.* (2003), Mercier-Langevin *et al.* (2007a, b, c, 2011, 2017), Galley & Lafrance (2014), and Yergeau *et al.* (2022a, b). The mining camp contains > 28 Moz of Au, making it one of the world's largest Archean Au districts (Mercier-Langevin *et al.,* 2021). Gold deposits in the camp consists of Au-rich VMS (e.g., LaRonde Penna), epizonal intrusion-related Au ± Cu (e.g., Doyon), and shear zone-hosted orogenic gold and/or remobilized VMS mineralization (e.g., Mouska, Mic Mac) deposits as well as a number of smaller Au occurrences (Lafrance *et al.,* 2003; Mercier-Langevin, 2007c, 2009, 2011, 2017; Yergeau *et al.,* 2022a, b).

The eastern portion of the Blake River Group (2704-2695 Ma; McNicoll *et al.*, 2014) of the Archean Abitibi greenstone belt in the Superior Province is host to the Doyon-Bousquet-LaRonde mining camp (Fig 3.1A; Mercier-Langevin, *et al.*, 2007c; Galley & Lafrance, 2014). The Blake River Group in the Doyon-Bousquet-LaRonde mining camp consists of the Hébécourt Formation in the north and the Bousquet Formation in the south (Fig. 3.1B; Lafrance *et al.*, 2003). Along the northern contact of the Blake River Group is the Lac Parfouru Fault, separating the Hébécourt Formation from the Kewagama Group (<2686 Ma; Davis, 2002). The southern contact of the Bousquet Formation is disconformably overlain by the Cadillac Group (<2687.4 ± 1.2 Ma; Lafrance *et al.*, 2005). In the mining camp, the Blake River Group strikes east-west and is a steeply dipping, south-facing homoclinal volcanic sequence (Lafrance *et al.*, 2003; Mercier-Langevin *et al.*, 2007c, Galley & Lafrance, 2014).

The base of the Blake River Group in the Doyon-Bousquet-LaRonde mining camp (Hébécourt Formation) is predominantly composed of massive to pillowed tholeiitic basaltic and basaltic andesite flows and sills (Lafrance *et al.*, 2003; Mercier-Langevin *et al.*, 2007c; Galley & Lafrance, 2014). The Bousquet Formation overlies the Hébécourt Formation and is divided into the lower and upper Bousquet Formation. The lower Bousquet Formation is composed of mafic to intermediate volcanic and volcaniclastic rocks that range in composition from mafic to felsic and tholeiitic to transitional. A portion of the intrusion-related Doyon Au (±Cu) deposit is hosted in the lower Bousquet Formation (Guha *et al.*, 1982; Savoie *et al.*, 1991; Gosselin, 1998; Mercier-Langevin *et al.*, 2007c; Galley & Lafrance, 2014). In the lower member, a quartz porphyritic rhyolite sill, intermediate scoriaceous tuff, and a glomeroporphyritic dacite yield ages of 2698.6 ± 1.5 Ma, 2695.4 +2.6/-1.7 Ma, and 2698.3 ± 0.9 Ma, respectively (Lafrance *et al.*, 2005; Ross *et al.*, 2011). The upper Bousquet Formation ranges in composition from transitional to calc-alkaline and is composed of intermediate to felsic, volcanic and volcaniclastic rocks (Lafrance *et al.*, 2003;

Mercier-Langevin *et al.,* 2007a, b). Minor tholeiitic basaltic dikes and sills intrude the upper Bousquet Formation. The Au-rich VMS deposits in the Doyon-Bousquet-LaRonde mining camp are hosted in the felsic units of the upper Bousquet Formation (Fig. 3.1B; Dubé *et al.,* 2007; Mercier-Langevin *et al.,* 2007a, 2009; Boily-Auclair, *et al.,* 2020). A rhyodacite-rhyolite, feldspar and quartz-phyric rhyolite, and a rhyolite flow breccia have been dated at 2698.3 ± 0.8 Ma, 2697.8 ± 1 Ma, and 2697.5 ± 1.1 Ma, respectively (Mercier-Langevin, 2007a; McNicoll *et al.,* 2014).

Deformation and metamorphic events have affected the Doyon-Bousquet-LaRonde mining camp and are partly responsible for the current geometry of the volcanic rocks and ore deposits (Langshur, 1990; Savoie *et al.,* 1991; Belkabir & Hubert, 1995). At least three phases of deformation have affected the camp, with the first phase of deformation (D1) defined by a weak, moderately inclined northeast-southwest foliation. A strong penetrative east-west fabric, with shear planes and faults that dip steeply to the south represents the second deformation phase (D2). Overprinting D2 is dextral transpressive brittle-ductile faults related to the third phase of deformation (D3). Regional metamorphism in the Doyon-Bousquet-LaRonde mining camp ranges from greenschist- to lower-amphibolite-facies and is approximately coeval with D2. However, in the MIC, unorientated porphyroblasts of actinolite and biotite suggest peak metamorphism may slightly postdate D2 (Marquis *et al.,* 1990; Belkabir & Hubert, 1995; Dubé *et al.,* 2004; Mercier-Langevin *et al.,* 2007a).

3.3.2 Geology of the Mooshla Intrusive Complex

The MIC was emplaced along the contact of the Hébécourt and Bousquet Formations in the western portion of the Doyon-Bousquet-LaRonde mining camp (Fig. 3.2; Galley & Lafrance, 2014). The MIC is divided into two stages based on chemical composition, variable intrusion style, and by distinctive overprinting relationships (Galley & Lafrance, 2014). The lower portion of the

MIC (Mouska stage) is composed of five intrusive phases (phases A-E) ranging from gabbro to tonalite and varies in composition from tholeiitic to transitional. The upper portion (Doyon stage) consists of four intrusive phases (phases F-I) ranging from tonalite to trondhjemite of transitional to calc-alkaline magmatic affinity (Galley & Lafrance, 2014). The Mouska stage is interpreted to have been emplaced along the contact of the Hébécourt Formation and the lower member of Bousquet Formation, whereas the Doyon-stage phases crosscut the Mouska stage and the lower member of the Bousquet Formation (Galley & Lafrance, 2014). For a complete and detailed description of each phase comprising the Mouska and Doyon stages see Galley & Lafrance (2014). Crosscutting the MIC is a large Proterozoic diabase dike and bounding the intrusion to the north and south are D2 shear zones (Fig. 3.2; Galley & Lafrance, 2014). Late north-south brittle-ductile faults dislocated the upper part of the MIC that is currently adjacent to the Lower Bousquet member (Galley & Lafrance, 2014). Recent zircon U-Pb CA-TIMS (Neyedley *et al.*, 2024, companion paper) on multiple phases of the MIC demonstrate that the MIC evolved over a maximum of ~1.44 Ma (2699.18 to 2697.74 Ma) and that the Mouska and Doyon stages were crystallizing synchronously.

3.4 METHODOLOGY

Drill core samples were collected from two drill holes interpreted to represent a near complete stratigraphic column of the entire MIC (Galley & Lafrance, 2014; A. Galley, communication, 2016). Drill hole MSK-G-810 contains phases A (diorite), B (gabbro), and C (quartz diorite) of the Mouska stage and drill hole 1106-96 contains phase E (Doyon quartz diorite) of the Mouska stage and phases G (plagioclase-phyric tonalite), H (phyric trondhjemite), and I (aphyric trondhjemite) of the Doyon stage. Doyon-stage phase F (plagioclase-amphibole-phyric tonalite) and Mouska-stage phase D (tonalite) were not present in either of these drill holes and a

drill hole that contains phase F (plagioclase-amphibole-phyric tonalite) could not be located, but phase D (tonalite) was collected from outcrop. Outcrop samples were taken as far away from quartz veining and/or dikes/sills (when present) to obtain unaltered or minimally altered samples. Sample locations are listed in Supplementary Table 3.1 and representative images of lithologies in hand sample are shown in Supplementary Material Document.

For detailed information on all analytical work performed in this study, as well as details on melt inclusion composition quantification, refer to the Supplementary Material Document. Polished thick sections, and quartz and zircon mineral separates were examined by petrographic microscope to identify mineral inclusions and SMI. Zircon separation was done at the Boise State University Isotope Geology Laboratory; half of the zircon grains separated from each lithology underwent high temperature annealing (~900°C for 60 hours in quartz crucibles at 1 atm) while the other half were not annealed. This temperature was somewhat higher than the actual entrapment conditions (Neyedley *et al.,* 2024; companion paper). Modification of annealing conditions to higher temperature and longer annealing times negligibly impact zircon-hosted SMI compositions (as zircon is a sparingly soluble phase) and was done to promote complete melting of larger inclusions (A. Terekhova, communication, 2023). Annealed zircon grains were then imaged by SEM- cathodoluminescence (SEM-CL)

Select quartz grain separates containing SMI underwent high pressure-temperature piston cylinder experiments (950 ± 10°C and 1500 ± 50 bar) and muffle furnace (1 atm) experiments (1050°C) to homogenize SMI. The high pressure-temperature experiments generated homogenized melt inclusions that were analyzed by Raman spectroscopy for qualitative H_2O determination, and both 1-atm and high pressure-temperature runs were used to assess melt composition and accidental (saturated) phases present at the time of melt entrapment. The experimental temperature in excess of entrapment conditions do impact quartz-hosted inclusions by causing too much quartz-host to

melt back into the inclusions. This dilutes all other elements while raising the SiO_2 content. Raman spectroscopy was conducted successfully on a small number of homogenized, exposed and buried, glassy zircon-hosted SMI and quartz-hosted SMI (from high pressure-temperature runs only, as 1-atm runs suffered from H_2O loss) to semi-quantitatively estimate H_2O concentrations.

Exposed, homogenized (in annealing zircon) and unhomogenized, glassy to crystalline SMI were analyzed by SEM-EDS and EPMA to determine major and minor element and volatile (Cl, F, H_2O) concentrations. Scanning electron microscope back-scattered electron (SEM-BSE) imaging, and Raman spectroscopy, and hot CL were conducted at Saint Mary's University. Electron probe microanalysis (EPMA) data on annealed SMI were conducted at the University of Toronto. Due to the small size of SMI (~10 μm), contamination by host zircon in the SEM and EPMA excitation volume was common; this required data renormalization after removing ZrO_2 and a proportional amount of SiO_2 from the contaminated analysis (using ideal zircon composition). For EPMA analyses (Cl, F, and H_2O), exposed, glassy, zircon-hosted SMI H_2O concentrations were obtained for only a small number of inclusions, and results were assumed to be the difference from 100 wt.% totals. For SEM-EDS analyses (Cl), a spot rather than a raster analysis was utilized because the analytical excitation volume is large relative to the small SMI size. Exposed, homogenized quartz-hosted SMI were also analyzed by SEM-EDS to constrain major element and Cl concentrations. Due to the small size of SMI and host-quartz over-melting described earlier, SMI have slightly elevated SiO_2 concentrations relative to their true compositions.

The major, minor, and trace element composition of quartz- and zircon-hosted SMI and anhydrite were determined by laser ablation-inductively coupled mass spectrometry (LA-ICP-MS) at the Magmatic and Ore-Forming Processes Research Laboratory at the University of Toronto, Canada. The general approach to ablating, quality control, and data quantification methodologies

for SMI are described in Halter *et al.* (2002, 2004a), Zajacz & Halter (2007), and Chang & Audétat (2021). The software SILLS was utilized in this study to quantify SMI and sulfide inclusion compositions (Guillong *et al.*, 2008). An internal standard Al_2O_3 value for each inclusion is needed for quantification. This was determined by analyzing exposed, glassy SMI by SEM-EDS (Saint Mary's University, Halifax, Canada) that provided a differentiation trend for major elements and major element concentration ratios (cf Halter *et al.*, 2002, 2004a). Each inclusion has a unique major element concentration ratio (e.g., Al_2O_3/SiO_2 in zircon-SMI and Al_2O_3/CaO in quartz-SMI) and by comparing those to the differentiation trend, an Al_2O_3 concentration for each SMI can be determined for quantification.

For quantification of sulfide-bearing inclusions, an estimate of the sulfide phase composition can be obtained by using a set Fe concentration and assuming all metals are predominantly present in the sulfide phase since metals (i.e., Cu, Bi, Ag, Au) strongly partition into sulfide over silicate melt (Zajacz *et al.*, 2013; Li & Audétat, 2015). It is likely that some inclusions contain both Cu-rich and Fe-rich sulfide minerals. However, as it is not possible to predict the proportion of these in single inclusions, two sulfide end-member quantifications were done, one with a pyrrhotite compositional constraint (internal standard Fe = 62.34 wt.%) and a second with a chalcopyrite compositional constraint (internal standard Fe = 30.43 wt.%). This provides maximum (pyrrhotite) and minimum (chalcopyrite) estimates on the metal concentrations in the sulfide phase which scale linearly with the value of the Fe concentration. Petrographic observations and LA-ICP-MS raw data justify the use of these two end-member Fe contents. For simplicity, only the maximum metal concentrations are presented unless otherwise stated.

Oxygen ($^{18}O/^{16}O$) and sulfur ($^{34}S/^{32}S$) isotope ratios in anhydrite were measured at the University of Manitoba, Winnipeg, Canada using secondary ion mass spectrometry (SIMS).

3.5 RESULTS

3.5.1 Petrography and Mineral Chemistry

3.5.1.1 Melt Inclusion Host Minerals and Accessory Minerals

Petrographic descriptions of host lithologies and zircon characteristics are described in detail in Neyedley *et al.*, (2024; companion paper) and below is a summary of important petrographic features as well as descriptions of anhydrite introduced in this study.

Zircon-hosted SMI were examined in the gabbro (phase B), quartz diorite (phase C), and tonalites (phase D) of the Mouska-stage. As well zircon-hosted SMI were examined in the phyric- (phase H) and aphyric-trondhjemite (phase I) of the Doyon-stage. As described in Neyedley *et al.* (2024; companion paper), the two quartz diorite samples of phase C are divided into the high- and low-Th/U quartz diorite based on their contrasting zircon Th/U ratios and this terminology is used throughout this melt inclusion study. Lithologies of the MIC that contained quartz-hosted SMI include the gabbro (phase B) and low-Th/U quartz diorite (phase C) of the Mouska-stage, and the aphyric trondhjemite (phase I) of the Doyon-stage.

Zircon occurs as inclusions in primary igneous minerals (e.g., quartz) and as an interstitial magmatic mineral occurring along plagioclase, quartz, and/or amphibole (former pyroxene?) grain boundaries (Fig. 3.3A, B). The estimated pressure-temperature conditions at which zircon grew are ~0.5 to 1.2 GPa and ~700° to 800°C, implying zircon was an early magmatic mineral crystallizing relatively deep (deep crust rather than near sea-floor conditions; Neyedley *et al.*, 2024, companion paper). Cold SEM-CL revealed zircon preserved oscillatory and sector zoning with no or limited resorption features in all lithologies expect for the high-Th/U quartz diorite which displays resorption features between internal (i.e., core) and external (i.e., rim) zones, indicating that partial dissolution of zircon occurred. In the tonalite, titanite, epidote, and allanite are all primary magmatic minerals with planar grain boundaries with plagioclase and quartz and inclusions of Fe-

Ti-oxides occurring in titanite (Fig. 3.3C-F). Epidote is also present in the aphyric trondhjemite as a late, interstitial magmatic phase occurring between plagioclase and quartz.

Quartz-hosted SMI were identified in the gabbro (phase B), low-Th/U quartz diorite (phase C), and aphyric trondhjemite (phase I). Quartz from these lithologies has a strong blue luminescence color under hot CL, characteristic of magmatic quartz compared to metamorphic quartz that is generally purple to red-brown in amphibolite to greenschist facies rocks, respectively (Fig. 3.3G; Götze *et al.*, 2001 and references therein). In the gabbro and low-Th/U quartz diorite, quartz is medium- to coarse-grained and occurs interstitial to plagioclase and amphibole (former pyroxene?) with roughly planar grain boundaries.

3.5.1.2 Anhydrite Petrography and Chemistry

Samples of the aphyric trondhjemite (phase I) can contain up to 8 vol% anhydrite, occurring as (i) primary inclusions within quartz and plagioclase (Fig. 3.4A-D), (ii) interstitial phase with other magmatic minerals (e.g., quartz, plagioclase) showing planar crystal boundaries (Fig. 3.4C-H), and (iii) graphically intergrown with quartz and feldspar (Fig. 3.4I). Textural observations are consistent with a magmatic origin for anhydrite. As well, plagioclase in this unit is not intensely altered, with a sodic (An_{0-13}) composition that does not increase in An-content moving away from mutual grain boundaries with anhydrite. Interstitial anhydrite domains vary from ~50 µm to ~600 µm in diameter, whereas inclusions within quartz and plagioclase range from ~10 µm to ~100 µm in diameter. Subspherical, ~10 µm to ~120 µm diameter inclusions of rutile and rare zircon inclusions occur in anhydrite (Fig. 3.4G).

The trace element composition of interstitial anhydrite is presented in Supplementary Table 3.2. Primitive mantle-normalized REE patterns of anhydrite show light rare earth element (LREE) enrichment over heavy rare earth elements (HREE) and a negative Eu anomaly (0.20 to 0.87; ~0.54

± 0.15), suggesting anhydrite crystallization coeval with, or after, plagioclase (Fig. 3.5A-B). Stable oxygen and sulfur isotope compositions for interstitial anhydrite and anhydrite inclusions (in quartz phenocrysts) are presented in Supplementary Table 3.3. The mean $\delta^{18}O$ values of interstitial (~7.4 ± 1.2 ‰; n=9) and inclusion anhydrite (~6.8 ± 0.9 ‰; n=4) are similar. However, interstitial anhydrite $\delta^{34}S$ values range from 11.0 to 19.7 ‰ (15.0 ± 4.2 ‰; n=8) whereas inclusion anhydrite has lower $\delta^{34}S$ values with a range of 6.1 to 8.2 ‰ (7.3 ± 1.0 ‰; n=4; Fig. 3.5C).

3.5.2 Petrography of Zircon-hosted Silicate Melt Inclusions and Other Included Phases

Silicate melt inclusions and other included phases in zircon separates were characterized in samples used for high-precision CA-ID-TIMS geochronology (Neyedley *et al.,* 2024; companion paper). Select major and trace element concentrations of zircon host surrounding SMI were determined through SILLS during signal deconvolution (unmixing of inclusion from inclusion + host) and are reported in Supplementary Table 3.4 (Halter *et al.*, 2002; Guillong *et al.*, 2008). The elements collected during analyses were limited to maximize the counting times for elements of interest in SMI, therefore only a limited number of zircon-compatible elements are reported. Full trace element chemistry of zircon is described and interpreted in detail in Neyedley *et al.* (2024; companion paper) and the zircon trace element composition from each MIC phase are similar and consistent with a magmatic origin based on the parameters of Hoskin and Schaltegger (2003). The criteria for magmatic zircon are 1) consistent zircon compositions within a given sample, 2) Th/U ratios < 4, 3) LREE < HREE normalized profile, 4) a moderate to large negative Eu anomaly, and 5) a positive Ce anomaly. The same zircon grains that meet these criteria are the same grains that have been utilized for melt inclusion characterization and analysis in this study. Importantly, the conditions of zircon crystallization are consistent with it being an early magmatic phase (~0.5 to 1.2 GPa and ~700° to 800°C; Neyedley *et al.*, 2024, companion paper) and the Ti-in-zircon

thermometry of the pre-SMI (or a spot immediately adjacent to the inclusion) signal from LA-ICPMS analyses are consistent with these temperatures. Therefore, zircon was trapping SMI at these conditions.

Identification of SMI and other mineral phases was done using a combination of transmitted light microscopy, SEM-EDS and -BSE, Raman, and EPMA. During LA-ICPMS analyses, accidentally trapped minerals in SMI were also identified based on the time vs count signal and subsequent quantification. A summary of zircon-hosted inclusion varieties in each sample is presented in Table 3.1. In all lithologies, and in homogenized and unhomogenized, zircon-hosted SMI have a glassy appearance at room temperature (~24°C), are subspherical to elliptical in shape, and range in size from ~ 1 μm to ~15 μm, with rare SMI up to ~30 um.

3.5.2.1 Gabbro (Phase B; MSK-G-810-715.6)

In phase B gabbro, SMI occur as single inclusions and rare melt inclusion assemblages (MIA) occurring along growth zones (indicated by zoning in CL imaging) in zircon, indicating MIA are primary in origin (i.e., trapped at the time of crystal growth; Roedder, 1984; Fig. 3.6A-C). Single inclusions have an indeterminant origin (i.e., cannot be classified as primary or secondary) as they occur in various locations within a zircon (e.g., in the core or along the rim), but cannot be directly tied to growth zones. However, single SMI do not occur along or near fractures and the host zircon chemistry is consistent with a magmatic origin, suggesting they could be primary in origin. Primary mineral inclusions hosted in zircon are quartz, albite, K-feldspar, and biotite and all occur in inclusions together. Quartz is the only monomineralic inclusion type present. Inclusions that have been compromised (e.g., cross-cut by fractures in the host zircon) have been altered and are comprised of quartz and/or chlorite.

3.5.2.2 Quartz diorite (Phase C; MSK-G-810-127.6)

In the phase C high-Th/U quartz diorite, SMI occur as isolated, single SMI or as MIA comprised of two to four SMI. Single SMI and MIA are present either in the center of their host grain or along growth zones at inflection points in zircon (Fig. 3.6D and E), the latter indicating they are primary in origin (Fig. 3.6D). Single SMI are indeterminant in origin but suspected primary similar to single SMI in the gabbro. Inclusions contain only melt (Fig. 3.7A) or can contain accidentally trapped minerals such as magnetite and ilmenite (Fig. 3.7B-C). Quartz, albite, K-feldspar, biotite, apatite, titanite, and/or epidote occur in a variety of composite, primary magmatic inclusions in zircon (Fig. 3.8A-B), while quartz (Fig. 3.7C) and albite (Fig. 3.8C) are the only monomineralic inclusions. Importantly, the composite inclusions are consistent with the host rock mineralogy (cf Neyedley *et al.,* 2024; companion paper) providing evidence that these are likely crystallized silicate melt inclusions (Bodnar and Student, 2006; Webster and Thomas, 2006). Compromised inclusions can contain primary minerals but also contain chlorite and/or calcite. A full summary of trapped mineral inclusions in zircon is presented in Table 3.1.

3.5.2.3 Quartz diorite (Phase C; MSK-G-810-493.7)

Silicate melt inclusions in the low-Th/U quartz diorite of phase C are primarily hosted along zircon growth zones in MIA of up to ~15 inclusions along a single growth zone (Fig. 3.6F-H; Fig. 3.7D). Single inclusions of indeterminant origin (suspected primary as discussed above) are present but rare. Accidentally trapped minerals in SMI include quartz, albite, and magnetite (Fig. 3.7D). Apatite (Fig. 3.8D), quartz, albite (Fig. 3.8E), and epidote are commonly found as isolated, monomineralic inclusions in zircon. Additionally, composite inclusions composed of quartz, albite, K-feldspar, biotite, amphibole(?), apatite, titanite, epidote, ilmenite, and/or rutile are present in

zircon (Fig. 3.8E-I; Table 3.1). Compromised inclusions can contain residual primary minerals but also contain chlorite and/or calcite (Table 3.1).

3.5.2.4 Tonalite (Phase D; Stop 10/ Stop 11)

Silicate melt inclusions in the phase D tonalite are more common in sample Stop 11 than in Stop 10. In both tonalite samples, SMI display primary origin as MIA occur along growth zones of their host zircon (Fig. 3.7E-F). Single inclusions of indeterminant origin (suspected primary as discussed above) are present but rare. Accidentally trapped minerals in SMI are more common in Stop 11 and include quartz, albite, biotite, magnetite, and Cu-Fe-sulfides (chalcopyrite?; Fig. 3.7F). Monomineralic inclusions present in both samples include quartz, apatite, and albite, whereas biotite and magnetite are only present in Stop 10 and only epidote (Fig. 3.8J) in Stop 11 (Table 3.1). Primary mineral phases present as inclusions in zircon in both tonalite samples is similar and include composite inclusions composed of quartz, albite, K-feldspar, biotite, amphibole(?), apatite, epidote, titanite, ilmenite, magnetite, and/or monazite (Fig. 3.8K-P; Table 3.1).

3.5.2.5 Aphyric trondhjemite (Phase I; 1106-96-1323/1106-96-1444.5)

Silicate melt inclusions are rare in zircon from the aphyric trondhjemite. Inclusions occur as single, SMI present near the center of their host grain or along growth zones (Fig. 3.6K-L; Fig. 3.9A-C). Inclusions present along growth zones are primary in origin whereas inclusions in the core are indeterminant but suspected to be primary as discussed above. The only accidentally trapped mineral phase with melt is apatite (Fig. 3.9A). Apatite is the most common mineral inclusion and rare monazite is present trapped with apatite (Fig. 3.9F). Other primary mineral inclusions observed include albite with epidote (Fig. 3.9G; Table 3.1).

3.5.3 Petrography of Quartz-hosted Silicate Melt Inclusions and Other Included Phases

Quartz-hosted SMI are rare and difficult to locate and identify in all lithologies of the MIC. Quartz-hosted SMI have similar characteristics in all lithologies and are classified as having an indeterminant origin, however it is important to note that there is no evidence of secondary overprinting where SMI occur as CL confirms a magmatic origin, SMI do not occur along healed fractures, and the crystallization pressure-temperature conditions of quartz are well above the local metamorphic conditions (Neyedley *et al.*, 2024, companion paper). Inclusions occur primarily isolated near the center of their host grain and rarely occur in clusters of two of three SMI to form a MIA (Fig. 3.10A-D). Inclusions range from ~10 to ~60 um (typically ~15 to 30 um) and have irregular to oval shape. Inclusions are composed of a variable proportion of glass or finely recrystallized melt and crystals (i.e., minerals) and at room temperature, inclusions do not contain a vapor bubble (Fig. 3.10B, D). Furnace experiments conducted on quartz separates to homogenize quartz-hosted SMI from the low-Th/U quartz diorite occurred at 1050°C and 1 atm and held at this temperature for ~5 days (~116 hours). This resulted in homogenized, glassy, inclusions that now contain a contraction bubble, and confirms these inclusions are SMI (Fig. 3.10E-G). High pressure-temperature piston cylinder experiments (950 ± 10°C and 1500 ± 50 bar) conducted on quartz separates from the gabbro, also resulted in homogenizing SMI to a glassy state containing a contraction vapor bubble (Fig. 3.10H). In one inclusion from the gabbro, a grain of albite trapped in quartz is surrounded by melt (Fig. 3.10H). Through SEM-EDS, LA-ICPMS, and Raman spectroscopy analyses, accidentally trapped mineral phases in the inclusions include rutile, titanite, zircon, apatite, epidote, and sulfides (Fig. 3.10I, J; Table 3.2), many of which are also present as inclusions in zircon (e.g., Fig. 3.8; Table 3.1). Muscovite and calcite are also present in compromised inclusions.

3.5.4 Composition of Zircon-hosted Silicate Melt Inclusions

Zircon utilized in this study has been extensively screened for geochronology (i.e., devoid of inherited cores, metamict zones, and extensive fracturing) and the chemistry is consistent with a magmatic origin (Neyedley *et al.,* 2024, companion paper). Additionally, trace element diffusion rates in zircon are slow preventing chemical modification between trapped melt inclusions and the zircon host and/or melt (Cherniak et al. 1997; Cherniak & Watson, 2003; Thomas *et al.,* 2003). Boundary layer effects were evaluated for zircon-hosted SMI by comparing inclusions size to moderately to strongly incompatible elements (e.g., Rb, Sr, Nb, La; cf Thomas *et al.,* 2003). No correlations exist between size (5 – 20um), concentrations in SMI, and calculated mineral-melt partition coefficients (i.e., host zircon/SMI composition). If there was a boundary layer effecting the SMI compositions, a correlation between these components would be expected (Thomas *et al.,* 2003). Therefore, analyses of zircon-hosted SMI provide reliable major, trace, and metal concentrations of the melt from which they grew.

3.5.4.1 Major, minor and trace elements

The major, minor, trace, and metal concentrations in buried, annealed and non-annealed, zircon-hosted SMI determined by LA-ICPMS are presented in Supplementary Table 3.5. Representative SEM-EDS analyses for zircon-hosted SMI are presented in Table 3.3 and full results are available in Supplementary Table 3.6. Representative transient LA-ICPMS signals (count rate vs. time) from SMI ablations are presented in Figure 3.11A-H that show typical signals for inclusions containing only trapped melt, and inclusions containing accidentally trapped phases (e.g., sulfide, apatite, and/or Fe-oxide saturated at time of silicate melt entrapment). In a typical SMI, free of accidentally trapped phases (Fig. 3.11A-D), count rates for silicate melt-linked analytes are synchronous, whereas analytes concentrated in accidentally trapped phases will be

time-offset from the silicate-melt linked analytes (Fig. 3.11E-H). For inclusions containing accidentally trapped phases, these inclusion types were filtered out of the data set by examining each individual transient signal for irregularities from normal melt signal patterns, such as flat intensity profiles for major elements and elevated count rates for select elements based on the type of mineral inclusion (e.g., ^{44}Ca = apatite or calcite; ^{56}Fe = magnetite or sulfide; ^{31}P + LREE = apatite). Additionally, once inclusions were quantified, analyses that demonstrated the presence of accidentally trapped minerals (e.g., elevated CaO + P_2O_5 + LREE = apatite; FeO + TiO_2 = Fe-oxide; FeO + MgO + Al_2O_3 = chlorite; ^{56}Fe + ^{65}Cu = sulfide) were removed from the final data set.

On a total alkalis (Na_2O + K_2O) - SiO_2 diagram (TAS; La Bas *et al.*, 1986), zircon-hosted SMI compositions (all SMI data collected by SEM, EPMA, and LA-ICPMS are grouped together for each lithology) are rhyolitic in composition for all lithologies analyzed, except two SMI that fall in the trachyte field (Fig. 3.12A, B). Except for the Doyon-stage phase I aphyric trondhjemite, SMI have significantly higher SiO_2, and total alkalis contents compared to bulk rock compositions (Fig. 3.12A). Melt inclusion compositions from all lithologies form an array that spans across the alkaline – subalkaline boundary. The exception is SMI from the gabbro which plots in the subalkaline field. For the phase D tonalite and the high Th/U-quartz diorite there is a clear trend of increasing SiO_2 content with a decrease in total alkalis, primarily related to variations in Na_2O or K_2O content (Fig. 3.13A, B). There is no correlation between the Na_2O and K_2O contents. Concentrations of Al_2O_3 decrease with increasing SiO_2 (Fig. 3.13C), and in some lithologies K_2O and Al_2O_3 show a positive correlation.

For exposed SMI analyzed by SEM-EDS and EPMA, Al_2O_3 concentrations are relatively consistent for each lithology (12.6 to 14.1 wt%). Compared to bulk rock concentrations, SMI have ~4 to 5 wt% less Al_2O_3, consistent with the host rocks representing plagioclase-rich cumulates. This observation is characteristic with the liquid line of descent for calc-alkaline series magmas.

The highest Na_2O concentrations in SMI occur in the phase D tonalite (mean Na_2O = 6.8 ± 1.5 wt%; 1σ; n = 13; Fig. 3.13A). Melt inclusions from the tonalite also have the lowest K_2O concentrations (mean K_2O = ~2.9 ± 0.4 wt%; n = 13; Fig. 3.13B). All other lithologies have mean SMI Na_2O concentrations between 4.6 and 5.9 wt%, except for the gabbro (2.5 to 2.9 wt%). Mean K_2O concentrations for all other lithologies range from 3.2 to 4.3 wt% (Fig. 3.13B). Notably, for individual MIA, Na_2O varies by ~1 wt% and K_2O by ~0.5 wt%. The Al_2O_3 concentrations within MIA vary by < 1 wt%, except a few MIA vary up to ~2.5 wt%. Compared to host rock composition, K_2O is higher in SMI whereas Na_2O is relatively similar.

For all lithologies and all data types (i.e., SEM, EPMA, and LA-ICPMS), SMI FeO and MgO concentrations are ≤ 2 and ≤ 0.5 wt%, respectively (Fig. 3.13D), except for SMI containing accidentally trapped magnetite, or impacted by post-entrapment chloritization. Concentrations of CaO in SMI are between 0.5 and 2.0 wt% for all lithologies, except for the phase B gabbro (2.1 to 2.4 wt%). The TiO_2 concentrations of SMI are consistently <0.75 wt%. Compared to host rock compositions, CaO, MgO, FeO, and TiO_2 are generally lower in SMI, except for the aphyric trondhjemite where concentrations are similar.

Chondrite-normalized LREE patterns (limited to those REE strongly incompatible in zircon host) for all lithologies display similar slightly negative slopes with $(Pr/La)_n$ and $(Nd/La)_n$ ratios generally < 1 and negative Ce-anomalies (Fig. 3.14A-D). For those lithologies where they could be calculated, mean values of Ce/Ce* ($Ce/Ce^* = Ce_n/[La_n \times Pr_n]^{1/2}$) for SMI are between 0.5 and 0.6 for quartz diorites and the phyric trondhjemite. However, the aphyric trondhjemite has a significantly lower Ce anomaly (0.06). The concentration of Ce was below detection in all SMI in the tonalites and using the lowest detection limit of Ce (~0.8 ppm), results in Ce/Ce* values of 0.003.

Due to the high partition coefficients of middle rare earth elements (MREE), HREE, and certain incompatible elements (e.g., Zr, Y, Hf, Th, U, Ta, Nb) in zircon, limited trace elements and REE were measure by LA-ICPMS in zircon-hosted SMI. Nevertheless, some REE (La, Ce, Pr, Nd, and Sm), incompatible elements (Rb, Sr, Ba, Cs, B), and metals (Cu, Co, V) can be accurately and precisely quantified. An initial review of SMI chemistry at different textural sites within the host zircon (i.e., rim vs core), differing occurrence style (i.e., single SMI vs MIA) showed that all SMI displayed no discernable differences in chemistry (e.g., Fig. 3.15A). This is in contrast to the host zircon chemistry that shows clear core to rim differences (cf Neyedley *et al.*, 2024; companion paper).

Generally, concentrations of Sr and Ba in SMI are relatively similar among all lithologies, whereas Rb contents vary between lithologies. Silicate melt inclusions from the low-Th/U quartz diorite and trondhjemites have the highest mean Rb contents, whereas mean SMI Rb from the tonalite and high-Th/U quartz diorite are lower (Fig. 3.15B). Within individual MIA from the low-Th/U quartz diorite incompatible elements (i.e., Rb, Sr, and Ba) show relatively consistent compositions expect one MIA which has variable Rb and Ba. On the Rb-Sr-Ba ternary (El Bouseily & El Sokkary, 1975) for differentiation of granites, SMI analyses all plot in the “normal” to “anomalous” granite fields (Fig. 3.16A). Host rock analyses show enrichment in Sr consistent with accumulation of plagioclase (Fig. 3.16A). Increasing SMI K_2O contents correlates with increasing Rb indicating magma evolution from the high-Th/U quartz diorite to the low-Th/U quartz diorite and trondhjemites (Fig. 3.15B). Consistent with this is a decrease in host zircon Ti concentration (proxy for T; Ferry & Watson, 2007) correlating with an increase in Rb-in-SMI concentrations from the high-Th/U quartz diorite to the low-Th/U quartz diorite and trondhjemites (Fig.3.15C). Opposite to the behavior of Rb and K_2O, the La-in-SMI concentrations decrease with increasing Rb-in-SMI contents and a decrease in Ti-in-zircon contents (Fig. 3.15D and E). This behavior of

La would be consistent with the crystallization of apatite and/or monazite (seen as inclusions in zircon; Fig. 3.6K and 3.8L) pre- and/or synchronous to melt inclusion entrapment implying SMI are being trapped as the magma is evolving.

Because B and Cs are strongly incompatible, they are sensitive indicators of crystal fractionation (cf. Audétat & Pettke, 2003). Only four SMI have Cs and B above detection and display a positive correlation. In all lithologies, SMI Cs and B concentrations are low (< 7 ppm, and 30 – 170 ppm). The low Cs and B concentrations in SMI indicate that the melt trapped was not very evolved.

The concentrations of ore metals in SMI are similar among all lithologies but owing to inclusion size, are rarely detected (Supplementary Table 3.5). Unfortunately, due to the oxide interferences of $^{91}Zr^{16}O$ on ^{107}Ag (Grondahl & Zajacz, 2017) and a similar interference of $^{90}Zr^{91}Zr^{16}O$ on ^{197}Au, Ag and Au concentrations in zircon-hosted inclusions cannot be quantified. However, other ore metals associated with arc and VMS environments that are detected (e.g., Cu, Bi, As, Mo) in SMI are utilized as proxies for Au owing to mutual chalcophile behavior.

Copper in the high-Th/U quartz diorite ranges between ~6 and ~50 ppm (n=8) whereas in the low-Th/U quartz diorite Cu is only above detection limits in one SMI with a concentration of ~9 ppm. In the high-Th/U quartz diorite, two inclusions contain accidentally trapped sulfide and have elevated Cu concentrations of 270 and 2940 ppm (Fig. 3.15F).SMI in the phyric trondhjemite has a similar range in Cu to the high-Th/U quartz diorite with values between ~7 and ~55 ppm (n=3) and two inclusions also contain accidentally trapped sulfide (Cu = ~150 and ~500 ppm; Fig. 3.15F). Copper in the tonalite and aphyric trondhjemite is always below detection limits, with the lowest detection limits being <11 and <13 ppm, respectively. However, one inclusion in the tonalite contains an accidentally trapped sulfide (Cu = 340 ppm). Overall, in all lithologies Cu ranges from

~6 to ~55 ppm, except where accidentally trapped sulfides are present (> 150 ppm) consistent with petrographic observations (e.g., Fig. 3.7F).

Molybdenum is above detection limits in one SMI from each of the high- and low-Th/U quartz diorites, both with concentrations of ~5 ppm. In the phyric trondhjemite Mo concentrations are between ~2 and ~6 ppm (n=2). Molybdenum in the tonalite (< 9 ppm) and aphyric trondhjemite (< 4 ppm) are always below detection limits. Bismuth was detected in one SMI from each of the high- and low-Th/U quartz diorite and phyric trondhjemite (Bi = 0.1, 1, and 2 ppm, respectively). In the tonalite (< 3 ppm) and aphyric trondhjemite (< 2 ppm) Bi is always below detection. Lead is only above detection limits in the high- and low-Th/U quartz diorites. In the high-Th/U quartz diorite Pb ranges from ~13 to ~210 ppm, with an outlier of 8250 ppm, which based on the transient LA-ICPMS signal, appears to contain an accidentally trapped Pb-bearing mineral (e.g., galena?). In the low-Th/U quartz diorite, Pb ranges from ~17 to ~620 ppm (n=7). Arsenic was only detected in three SMI from the high-Th/U quartz diorite (As= ~2, ~515, and ~1420 ppm). The later two As concentrations likely have an accidentally trapped As-bearing phase as the LA-ICPMS transient signals have a short As-spike either at the beginning or in the middle of the SMI ablation. No correlations between metals and other incompatible elements were noted in SMI for any lithologies (Fig. 3.15F), and no correlation exists between Ti-in-zircon and SMI Cu concentrations.

3.5.4.2 Volatiles

Concentrations of H_2O in zircon-hosted SMI determined by EPMA are variable (Table 3.3). One SMI from the phase B gabbro has a H_2O concentration of 3.7 wt.%. Three SMI from the phase C high-Th/U quartz diorite have H_2O concentrations of 0.7, 0.7, and 4.5 wt.% and two SMI from the phase C low Th/U quartz diorite have H_2O concentrations of 1.5 and 6.3 wt.% % (Table 3.3). In contrast to the EPMA data, Raman analysis of zircon-hosted SMI from all lithologies indicate

consistently low H_2O (<<2 wt.% H_2O; Table 3.3) content, based on comparisons of relative water band peak sizes with data obtained using the same instrumentation and settings (this study) from silicate glass reference materials of similar composition (c.f., Webster *et al.,* 2011; Fig. 3.17A). Chlorine concentrations are similar in zircon-hosted SMI from the high- and low-Th/U quartz diorites with mean concentrations of 0.4 ± 0.4 wt.% (n=16) and 0.4 ± 0.2 wt.% (n=6). The tonalite has a slightly lower mean Cl concentration (~0.3 ± 0.2 wt.%; n=11), whereas phyric trondhjemite has a significantly lower Cl concentration (~0.1 ± 0.1 wt.%; n=5). Only two SMI in the aphyric trondhjemite have Cl above detection with concentrations of 0.04 and 0.2 wt% and only one SMI in the gabbro has Cl above detection (0.01 wt.%).

3.5.5 Composition of Quartz-hosted Silicate Melt Inclusions

3.5.5.1 Major, minor and trace elements

SEM-EDS and LA-ICPMS-based compositional data for quartz-hosted SMI are presented in Table 3.5 and Supplementary Table 3.7 and representative transient LA-ICPMS signals for SMI without and with accidentally trapped phases (e.g., zircon and sulfide) are shown in Figure 3.18A-H. SMI are predominantly rhyolitic and subalkaline (Fig. 3.12C). Inclusions that fall in the dacitic field or have lower SiO_2 concentrations (Fig. 3.12C) are inclusions that contain melt and a variable amount of accidentally trapped epidote, causing the SiO_2 and alkali content to be lower than melt-only inclusions. No systematic trends exist within individual lithologies between total alkali content and SiO_2 (Fig. 3.12C). Compared to host rock compositions, SMI have higher alkali and SiO_2 contents (Fig. 3.12C), except for the aphyric trondhjemite in which SMI and host rock have similar alkali and SiO_2 concentrations (Fig. 3.12C). It should be noted that due to SiO_2 contamination from the host-quartz in SEM-EDS analyses, LA-ICPMS analyses have slightly higher concentrations for most major elements (e.g., Al_2O_3, Na_2O; Fig. 3.19A and B).

Melt inclusions containing accidentally trapped epidote have elevated FeO, CaO, Al_2O_3, and lower SiO_2 (Fig. 3.19C, D). Those SMI without accidentally trapped epidote have CaO <~4 wt.% and FeO <~2.5 wt.% (Fig. 3.19C). Although a few SMI in the low-Th/U quartz diorite have elevated FeO (~4 wt.%; Fig. 3.19C) they do not have elevated CaO, indicating they likely contain an accidentally trapped Fe-oxide phase. Overall, quartz-hosted SMI from all lithologies (gabbro, quartz diorite, and trondhjemite) range in SiO_2 and Al_2O_3 concentrations from 72 to 85 wt.% and 8.5 to 13.4 wt%, respectively (Fig. 3.19A) for all analyses. Generally, the highest SiO_2 (>79 wt.%) and lowest Al_2O_3 (<12 wt.%) are SEM-EDS analyses and therefore have overestimated SiO_2 (and lower Al_2O_3) due to contamination from the host quartz.

The MgO concentration in SMI is relatively the same in all lithologies (~<0.5 wt%) and MgO is similar in inclusions with accidentally trapped epidote (Fig. 3.19D). The K_2O concentrations are also similar between SMI and inclusions with accidentally trapped epidote with concentrations between 2 and 5 wt.% (Fig. 3.19E). The Na_2O concentrations determined by SEM-EDS for SMI in the gabbro and low-Th/U quartz diorite are also similar, ranging from ~2 to 5 wt.% (Fig. 3.19B). Inclusions with and without accidentally trapped epidote have similar TiO_2 concentrations, all are generally <0.5 wt.% (Fig. 3.19F).

The range of analytes measured by LA-ICPMS was reduced for some sessions to improve detection limits for metals (e.g., Ag, Au), comprehensive REE and trace elements are only available for a limited number of SMI. Only two inclusions from the low-Th/U quartz diorite have full chondrite-normalized REE patterns (Fig. 3.20A). One inclusion displays a negative slope (LREE>HREE) with a negative Eu anomaly (Eu/Eu* = 0.36), similar to the bulk rock REE pattern (Fig. 3.20A). However, the other SMI has a positive slope (LREE<HREE) and a positive Eu anomaly (Eu/Eu* = 1.36; Fig. 3.20A). Inclusions in the aphyric trondhjemite also display a positive slope and a positive Eu anomaly (Eu/Eu* = 1.82; Fig. 3.20B). Interestingly, melt inclusions

containing accidentally trapped epidote in the low-Th/U quartz diorite and gabbro have negative slopes (LREE>HREE) and generally have negative Eu anomalies (Eu/Eu* = 0.27 to 0.90; Fig. 3.20A, C). One inclusion containing melt + epidote in the low-Th/U quartz diorite has a slightly negative for LREE but HREE create a positive slope and this inclusion has a positive Eu anomaly (Eu/Eu* = 2.6; Fig. 3.20A).

Notably, SMI without and with accidentally trapped epidote have differing Sr contents, with epidote-bearing inclusions having elevated Sr (145 to 460 ppm) compared to epidote-free SMI (60 to 130 ppm; Fig. 3.21A). In the low-Th/U quartz diorite, epidote-bearing inclusions are lower in Rb (40 to 120 ppm) compared to epidote-free SMI (180 to 260 ppm), whereas epidote-free SMI in the aphyric trondhjemite has similar Rb (50 to 90 ppm) to epidote-bearing inclusions (Fig. 3.21B). Concentrations of Ba are slightly lower in epidote-free SMI (960 to 2190 ppm) compared to epidote-bearing inclusions (1860 to 4270 ppm; Fig. 3.21C). On the Rb-Sr-Ba ternary for differentiation of granites, epidote-free SMI plot in the "normal" granite field (similar to zircon-hosted SMI analyses), whereas epidote-bearing inclusions extend into the "anomalous" granite field due to their enrichment in Sr (Fig. 3.16B). Overall, there is a subtle positive correlation between Rb and K_2O, indicating an increase in magma evolution (Fig. 3.21D). Although limited data is available for Rb, the aphyric trondhjemite has the lowest K_2O and Rb contents whereas the low-Th/U quartz diorite has higher K_2O and Rb (Fig. 3.21D). No correlations exist between K_2O and Sr and Ba. A positive relationship exists between Sr and FeO, Al_2O_3, and CaO concentrations, again due to epidote contamination (e.g., Fig. 3.21A).

Similar to zircon-hosted SMI, Cs concentrations in all SMI are low (< 5 ppm; Fig. 3.21F). Inclusions contaminated by epidote generally have lower Cs concentrations (< 2 ppm) than epidote-free SMI (1 to 5 ppm). Boron concentrations are similar between epidote-free SMI and epidote-bearing melt inclusions, ranging from 30 to 400 ppm. Two inclusions in the low-Th/U quartz diorite

have significantly elevated B concentrations (~930 and ~8750 ppm), and could contain an accidentally trapped fluid inclusion causing the elevated B. In the aphyric trondhjemite, B is lower and ranges from 7 to 54 ppm. No correlation between Cs and B exists. As with the zircon-host SMI, the low Cs concentrations in SMI indicate that the melt trapped was not very evolved (cf Audétat & Pettke, 2003).

Gold concentrations were above detection limits in epidote-free SMI and in melt inclusions with accidentally trapped epidote from the gabbro and low-Th/U quartz diorite. Concentrations are similar between the two inclusion types and lithologies. Overall, Au concentrations range from 10 to 120 ppb (n=8) with one outlier of 1680 ppb in an epidote-bearing melt inclusion in the gabbro. Unlike other signals, there is no evidence of this high Au concentration being associated with a sulfide particle and could possibly represent an accidentally trapped Au particle. Inclusions in the aphyric trondhjemite always had Au below detection limits, with the lowest detection limits in each lithology being 13 ppb. Silver is above detection limits more often than Au and is slightly different among the lithologies and SMI compositional types. In the gabbro, the single epidote-free SMI has Ag below detection limits with a detection limit of 0.3 ppm. Whereas in epidote-bearing melt inclusions, Ag ranges from 0.1 to 0.3 ppm (n=6). In the low-Th/U quartz diorite, three epidote-free SMI have Ag concentrations of 0.5, 0.7, and 1.8 ppm and four epidote-bearing melt inclusions have Ag concentrations between 0.1 and 1.2 ppm. In the aphyric trondhjemite, six of seven inclusions contain accidentally trapped sulfide since their LA-ICPMS signals, Ag ± Cu ± As ± Bi peak together in the middle of the SMI signal. Silver contents in these sulfide-bearing inclusions range from ~5 to 125 ppm, whereas the one sulfide-free inclusion has a Ag content below detection (< 0.14 ppm). No correlations exist between Au and Ag with incompatible elements in the melt (i.e., Cs and B).

Copper concentrations in epidote-free SMI and epidote-bearing melt inclusions are relatively similar in the gabbro and low-Th/U quartz diorite. In the gabbro, Cu concentrations range from ~8 to ~70 ppm (n=3), with one outlier of 120 ppm which has an accidentally trapped sulfide. In the low-Th/U quartz diorite Cu are < 40 ppm (n=11) with one inclusion containing an accidentally trapped sulfide (Cu = ~130 ppm). In the aphyric trondhjemite, Cu in the sulfide free inclusion has a concentration of 2.3 ppm, whereas sulfide-bearing inclusions have up to 234 ppm Cu.

Across all lithologies and between epidote-free SMI and epidote-bearing melt inclusions, Mo concentrations are similar and range from 0.50 to ~5 ppm. One inclusion in the low-Th/U quartz diorite has a Mo concentration of ~20 ppm and could represent an accidentally trapped grain of molybdenite as the transient LA-ICPMS signal contains a Mo spike in the middle of the SMI ablation. Inclusions containing accidentally trapped sulfide have Mo concentrations ranging from 0.5 to 6 ppm. No correlations exist between Cu (and Mo) with incompatible elements in the melt (i.e., Cs and B; Fig. 3.21F). Other metals that are consistently above detection in all lithologies include Pb (~25 to 100 ppm), Sn (~1 to 8 ppm), W (0.5 to 6 ppm), As (~1 to 8 ppm), Bi (~0.1 to 0.8 ppm), and Sb (~0.2 to 2 ppm).

3.5.5.2 Volatiles

In quartz-hosted SMI (Table 3.4), Cl concentrations in the low-Th/U quartz diorite is slightly lower (~0.17 ± 0.08 wt%; n= 8; outlier 0.93 wt%). Chlorine in the gabbro from quartz-hosted SMI ranges from 0.32 to 0.5 wt% (n=3). Raman analyses yielded data for only 3 SMI in quartz that were homogenized at high pressure and temperature. Spectra for these inclusions are shown in Figure 3.17B. Comparison with spectra for glasses with known concentrations of H_2O again show very low water (<< 2 wt%), consistent with observations from zircon-hosted SMI.

3.5.6 Quartz-hosted sulfide compositions

Accidentally trapped sulfide is present in quartz-hosted melt inclusions from the low-Th/U quartz diorite, gabbro, and aphyric trondhjemite. As mentioned previously, only maximum metals concentrations will be presented in the results (unless otherwise stated) and that minimum values are roughly half of the maximum values. Results are presented in Supplementary Table 3.8. Maximum Cu concentrations in the gabbro range from 0.6 to 2.3 wt% (~1.7 ± 0.7 wt%; n=5). Silver is present in all sulfides from the gabbro and ranges between 4 and 30 ppm whereas Au is only above detection in two inclusions and has concentrations of 0.4 and 2 ppm. Other metals that are routinely above detection include Co, Pb, Mo, and Bi.

Sulfides in quartz-hosted melt inclusions from the low-Th/U quartz diorite have Cu concentrations that range from 0.04 to 9 wt%, however, five sulfides have Cu between 0.04 and 0.5 wt% whereas two inclusions have Cu concentrations of ~9 wt%, implying there are Cu-poor and Cu-rich sulfides present. Silver concentrations in the high-Cu sulfides are 23 and 36 ppm, whereas only one low-Cu inclusion has Ag above detection (126 ppm). Gold concentrations in the Cu-rich inclusions are 20 and 70 ppm, whereas Au is slightly lower (5 to 12 ppm) in the Cu-poor inclusions. Molybdenum is significantly enriched in the Cu-rich sulfides (up to ~8000 ppm) compared to the Cu-poor inclusions (< 115 ppm). Arsenic and Bi generally have similar concentrations between the Cu-rich and -poor inclusions.

Sulfides in the aphyric trondhjemite have different compositions than sulfide inclusions in the gabbro and low-Th/U quartz diorite, except for one inclusion. The one inclusion similar to the sulfides in the gabbro and low-Th/U quartz diorite has a Cu concentration of 0.02 wt% with Ag and Au concentrations of 30 and 0.4 ppm, respectively. The other sulfide inclusions contain Cu concentrations (2.4 to 3.7 wt%) intermediary to the Cu-rich and -poor varieties in the quartz diorite,

whereas Pb is highly elevated (0.3 to 7 wt%). The Ag concentrations in these intermediary Cu sulfides is elevated (~0.03 to 2.5 wt%) relative to the Cu-rich and -poor sulfides. Compared to the gabbro and low-Th/U quartz diorite, Ni (2 to 5.2 wt%) and As (0.7 to 2.2 wt%) are enriched in the trondhjemite. The lowest detection limit for Au in the moderate Cu inclusions is 42 ppm.

3.5.7 Zircon-hosted sulfide compositions

Accidentally trapped sulfides (co-saturated mineral grains, or sulfide melt) are present in zircon-hosted melt inclusions from the high-Th/U quartz diorite, tonalites, and phyric trondhjemite based on petrographic observations and LA-ICP-MS analyses. Maximum concentrations of metals in these sulfides are presented in Supplementary Table 3.8 (minimum concentrations are roughly half). Concentrations of Ag and Au in the sulfide could not be determined due to the interferences of $^{91}Zr^{16}O$ on ^{107}Ag (Grondahl & Zajacz, 2017) and a similar interference of $^{90}Zr^{91}Zr^{16}O$ on ^{197}Au. Due to this issue, Ag and Au were not measured as even in sulfides where the concentrations should be elevated compared to SMI, the interferences will swamp true metal values.

Similar to the quartz-hosted sulfides, two varieties of sulfides are present and are distinguished based on their Cu concentrations i) Cu-rich (suspected chalcopyrite) and ii) Cu-poor (pyrite, pyrrhotite, or Fe-S melt). Copper rich inclusions have Cu concentrations between ~19 and 28 wt% and occur in the high-Th/U quartz diorite and tonalite. They can contain up to 1.7 wt% Pb and contain minor Co, W, and Bi (Supplementary Table 3.8). Copper-poor inclusions occur in the high-Th/U quartz diorite, tonalite, and phyric trondhjemite and have Cu concentrations between 0.1 and 1.6 wt%. Lead concentrations are typically elevated (up to ~1 wt%) and Co concentrations are in the 100s of ppm range. Minor amounts of W and Bi are also present in the Cu-poor inclusions.

3.6 DISCUSSION

3.6.1 Comparison of Zircon- and Quartz-hosted SMI

It is important to compare and contrast the composition of zircon- and quartz-hosted SMI to understand if each mineral was trapping a similar melt at the same time. Primary mineral phases in zircon- and quartz-hosted SMI share some common and important characteristics that provide evidence zircon and quartz were trapping melt at relatively similar times. Such mineral phases include daughter phases that represent saturated mineral phases that grow from melt-only entrapment and accidental phases that represent saturated minerals trapped with melt. First, in quartz-hosted SMI, zircon is commonly present in LA-ICPMS analyses (Fig. 3.18A, C) and quartz is present as isolated inclusions and in trails with SMI in zircon (Fig. 3.7C), indicating both minerals are coeval. Accidentally trapped minerals of magmatic origin that are common in zircon- and quartz-hosted SMI include epidote (Fig. 3.8F, J and Fig. 3.10B), apatite, Fe-(±Ti)-oxides (Fig. 3.7C, D and Fig. 3.18B), titanite, and sulfides (Fig. 3.7F and Fig. 3.18H).

3.6.1.1 Major Elements

Where data are available for both zircon- and quartz-hosted SMI in the same lithology, SMI in both host minerals show similar major, minor, and trace element chemistry, a strong indication that zircon and quartz were broadly coeval and trapped a common melt. For example, the quartz-hosted SMI data overlap with the sub-alkaline range of the zircon SMI compositions in the TAS diagram (Fig 3.12B and C). This is further supported by the presence of accidentally trapped zircon in quartz-hosted SMI (Fig. 3.18C and E) and quartz in zircon (Figs. 3.7C and 8O); both minerals crystallized coevally over the same pressure-temperature conditions (Neyedley *et al.*, 2024; companion paper). Silicate melt inclusions from both host minerals are predominately rhyolitic and subalkaline in composition; some zircon-hosted SMI are more alkaline than quartz-hosted SMI (Fig. 3.12B, C). Some quartz-hosted SMI plot in the dacitic field, but those SMI contain

accidentally trapped epidote causing the lower SiO_2 (Fig. 3.12C). All other major elements in SMI are very similar in both host minerals, except for lower Na_2O in quartz-hosted SMI which can be related to diffusion (Audétat & Pettke, 2003; Zajacz *et al.*, 2008, 2009). Elevated FeO and CaO in quartz-hosted SMI can also be attributed to accidentally trapped epidote.

3.6.1.2 Trace Elements

Incompatible trace elements that are quantifiable in SMI in both hosts are also very similar and include Cs-Rb-Sr-Ba-Nb-V, and LREE (e.g., Fig. 3.16A, B). If zircon- and quartz-hosted SMI had substantially different incompatible element signatures, this would indicate they were not trapping a common melt and were not crystallizing coevally. But given their similarities, it implies zircon and quartz were crystallizing coevally and therefore trace elements (e.g., Zr, Hf, Y, and HREE) and metals not detected or quantified in zircon-hosted SMI (i.e., Au and Ag) can be inferred from quartz-hosted SMI. However, only a limited comparison can be made because of the high detection limits in zircon-hosted SMI.

Silicate melt inclusion from both host minerals predominately fall in the "normal" granite field on the Rb-Sr-Ba ternary (Fig. 3.16A, B). This would suggest prior and/or synchronous to trapping of SMI plagioclase fractionation was occurring at depth and is supported by the presence of accidentally trapped albite in SMI (e.g., Fig. 3.10H) and as a mineral phase in zircon (e.g., Fig. 3.8F). Additionally, since Rb and K_2O concentrations display a positive relationship, this indicates K-feldspar fractionation was not occurring at depth.

The Cs concentrations are low (< 10 ppm) in both zircon- and quartz-hosted SMI for all lithologies (Fig. 3.15F and 3.21F). Only a direct comparison in the low-Th/U quartz diorite can be made between quartz- and zircon-hosted SMI for Cs contents and they range from 0.85 to 4.8 ppm (n = 11) and 3.7 to 5.0 ppm (n = 3), respectively. The similarly low Cs contents between quartz-

and zircon-hosted SMI would imply they are broadly coeval. Importantly, the low Cs contents indicate the melt at the time of quartz and zircon crystallization was not highly fractionated. Cesium is highly incompatible and sensitive to increasing degrees of magma crystallization) and if zircon was a very late crystallizing phase (i.e., crystallizing from a small volume of melt), it would have trapped a melt with a more evolved Cs content (Audétat & Pettke, 2003). For comparison, quartz-hosted SMI in miarolitic cavities in the Cañada Pinabete pluton (New Mexico, USA) have a few thousand ppm Cs, whereas the least evolved SMI in the host granite only contain ~1 to 5 ppm Cs (Audétat & Pettke, 2003). Boron is also highly incompatible, unfortunately no direct comparison between quartz- and zircon-hosted SMI within a single lithology can be made due to high detection limits for B (e.g., < 56 to < 450 ppm in the low-Th/U quartz diorite), which are in the range of B concentrations of quartz-hosted SMI in the same unit (90 to 350 ppm). However, the low B concentrations in quartz-hosted SMI provide additional evidence that the trapped melt was not very evolved and consistent with the Cs concentrations.

Chondrite-normalized LREE patterns for zircon-hosted SMI, generally have a negative slope (Fig. 3.14A-D; $[Nd/La]_n < 1$), similar to the quartz-hosted SMI LREE pattern for some SMI in the low-Th/U quartz diorite (Fig. 3.20A) and gabbro (Fig. 3.20C). Many zircon-hosted SMI have a negative Ce-anomaly (Fig. 3.14A-D), indicating zircon was crystallizing slightly before SMI were trapped. However, quartz-hosted SMI (Fig. 3.20A-C) and some zircon-hosted SMI (Fig. 3.14A) do not display such a negative anomaly. This would suggest that quartz-hosted SMI are relatively early before zircon saturation, however the presence of accidentally trapped zircon in some quartz-hosted SMI would indicate these two minerals were crystallizing relatively coeval. The lack of a negative Ce-anomaly in some zircon-hosted SMI would suggest they are relatively early compared to SMI that display the negative Ce-anomaly.

3.6.1.3 Metals

Metal concentrations are relatively similar between zircon- and quartz-hosted SMI. Although Cu is more commonly above detection in quartz-hosted (~80%) compared to zircon-hosted SMI (~40%), Cu concentrations span a similar range (~5 to 70 ppm). It is important to note that the lower number of zircon-hosted SMI in which Cu was detected, and the higher Cu detection limits, is the result of the smaller size of zircon-hosted SMI analyzed (~5 to 15 um) compared to quartz-hosted SMI (~15 to 30 um). Copper is known to be problematic due to diffusion in quartz-hosted SMI (Zajacz *et al.,* 2009) and in other SMI-host minerals such as plagioclase and orthopyroxene (Audétat *et al.,* 2018), but given the slow diffusion rates of trace elements in zircon, Cu diffusion is likely not an issue (Cherniak *et al.,* 1997, Cherniak & Watson, 2003; Thomas *et al.,* 2003). Since the concentrations of Cu in zircon- and quartz-hosted SMI are similar, it would suggest they have trapped a common melt and that Cu is not being modified in quartz-hosted SMI. Overall, detection limits for metals (e.g., As, Mo, Sn, Sb, W, and Bi) in zircon-hosted SMI are higher than metal concentrations determined in quartz-hosted SMI. However, when these metals are above detection in zircon-hosted SMI, they are similar in concentration to quartz-hosted SMI. For example, in the low-Th/U quartz diorite the maximum concentrations of Mo (~5 ppm), W (~2 ppm), and Bi (~1 ppm) are similar in SMI between both host minerals (Supplementary Tables 3.5 and 6). Additionally, for metals that are below detection limits in zircon-hosted SMI, their detection limits are either above or similar to the maximum concentration in quartz-hosted SMI. This is the case for As where the detection limit in zircon-hosted SMI (< 15 ppm) exceeds the maximum concentration in quartz-hosted SMI (~7 ppm). For Sn, the maximum detection limit (< 5 ppm) is lower than the highest concentration in quartz-hosted SMI (~8 ppm).

Overall, given the similarity of accidentally trapped magmatic minerals in SMI from both host minerals, and relatively similar SMI chemistry between and within individual lithologies this

provides evidence that zircon and quartz were trapping a similar melt at relatively the same time. Going forward in the discussion, unless specifically stated, zircon- and quartz-hosted SMI compositions for each lithology will be discussed as one data set.

3.6.2 Tectonic Discrimination and Magma Parentage

The MIC has been suggested to be a potential source of Au and fluids to the numerous Au deposits that have a spatial and temporal association with the intrusion (Valliant & Hutchinson, 1982; Gosselin, 1998; Dubé *et al.*, 2007, 2014; Mercier-Langevin, 2007a, b; Galley & Lafrance, 2014; Yergeau *et al.*, 2022a, b). Therefore, constraining the origin of the MIC and magmatic processes that can affect its metal tenor are crucial to understand the magmatic evolution and the role these processes may have played in the development of the nearby Au deposits.

Bulk rock chemistry deviates from magmatic liquid compositions due to magmatic processes such as crystal accumulation, degassing, and/or contamination or by secondary metamorphic and alteration events. Since SMI have been trapped in robust host minerals that began crystallizing at significant depth (0.5 to 1.2 GPa; Neyedley *et al.*, 2024, companion paper), SMI chemistry is more representative of the instantaneous melt chemistry at depth compared to their non-liquidus, emplacement, and post-emplacement bulk rock compositions. Therefore, SMI chemistry is plotted (and compared to bulk rock) on tectonic discrimination diagrams to classify the parental magma(s) of the MIC. Since many commonly used discrimination diagrams are constructed using zircon-compatible elements (e.g., Zr, Y, and Yb), data from only quartz-hosted SMI are utilized for classification purposes. Additionally, quartz-hosted SMI that contain accidentally trapped epidote or zircon are omitted from the discrimination diagrams due to elevated Y and Zr, respectively.

The setting of the MIC and coeval Bousquet Formation volcanics is interpreted to have been a back-arc-style basin with initial magmatism related to crustal extension and mantle diapirism producing the tholeiitic to transitional Mouska stage (and lower Bousquet Formation), followed by magmatic differentiation in mid-crustal magma chambers to produce the subduction-style, transitional to calc-alkaline Doyon stage (and upper Bousquet Formation; Mercier-Langevin *et al.,* 2007b; Galley & Lafrance, 2014). Whole-rock chemistry for the SMI-bearing lithologies is inconsistent with this distinction between the Mouska and Doyon stages (Fig. 3.22A). However, SMI from the low-Th/U quartz diorite of the Mouska-stage have Zr/Y ratios consistent with a calc-alkaline composition rather than their tholeiitic bulk-rock composition (Fig. 3.22A). Inclusions form the aphyric trondhjemite are calc-alkaline, consistent with the Doyon-stage (Fig. 3.22A). Most commonly SMI from all lithologies fall in the volcanic arc granite (VAG) to syn-collisional granite fields (Syn-COLG; Fig. 3.22B and C). This is consistent with a subduction-style origin for the aphyric trondhjemite (i.e., calc-alkaline Doyon-stage), but inconsistent with the early rifting associated with back-arc basin development and evolution of the tholeiitic Mouska-stage. With SMI from the low-Th/U quartz diorite of the Mouska-stage consistently falling in the VAG fields, it would suggest that the transition from rift- to subduction-dominated-style melt evolution was initiated before the Mouska-stage magmas were sourced. These results are consistent with zircon U/Yb, Sc/Yb, and Nb/Yb ratios (Grimes *et al.,* 2015) from Mouska-stage lithologies that record a range in composition from rift- to arc-style-related magmas (Neyedley *et al.,* 2024; companion paper).

Geochemically two types of Archean TTG suites are distinguished based on whole rock SiO_2 (generally $\geq$ 70 wt% SiO_2) and Al_2O_3 concentration, the more common high-Al type (>15 wt%) and rarer, low-Al type (<15 wt%; Martin *et al.,* 2005). Low-Al TTG suites are characterized by low Sr concentrations (< 300 ppm) and low Sr/Y (< 50) and $(La/Yb)_n$ (<30) ratios (Condie,

2005; Martin *et al.,* 2005; Moyen, 2009). Additionally, low-Al TTG suites typically have a negative Eu anomaly and a relatively unfractionated chondrite-normalized REE pattern compared to high-Al TTG suites. Genetically, the high-Al TTG suites are related to high-pressure melting of hydrated basalt in the garnet stability field whereas the low-Al type are related to low-pressure melting in the plagioclase stability field, causing the negative Eu anomaly and lower Sr/Y ratios (Condie, 2005; Martin *et al.,* 2005; Moyen, 2009). However, there is increasing evidence that high Sr/Y ratios can be generated by plagioclase accumulation combined with amphibole fractionation (Liou & Guo, 2019; Laurent *et al.,* 2020; Rollinson, 2021). This suggests that crystal accumulation and fractionation can be important processes in the development of TTG magmas and that partial melting alone may not explain the different trace element signatures between high-pressure (high-Al) and low-pressure (low-Al) type TTG magmatic suites.

The Al_2O_3 concentration of both zircon- and quartz-hosted SMI from the MIC are consistent with low-Al TTG suites as SMI are generally < 15 wt% Al_2O_3 with few SMI being > 15 wt% (Fig. 3.23A, B). All bulk-rock analyses from the Mouska-stage (gabbro, quartz diorites, tonalites) show Al_2O_3 > 15wt% and < 70 wt% SiO_2, preventing classification as TTG rocks (but with Al_2O_3 values consistent with high-Al TTG). In contrast, the Doyon-stage aphyric trondhjemite has bulk rock SiO_2 and Al_2O_3 concentrations that lie within the array of SMI analyses, consistent with the low-Al TTG suite (Fig. 3.23A, B). The Sr concentrations in quartz- and zircon-hosted SMI (~40 to 150 ppm) are well below 300 ppm, adding an additional line of evidence that these SMI can be classified as low-Al TTG melts (Fig. 3.23C). Quartz-hosted inclusions that contain accidentally trapped epidote record higher Sr due to the high compatibility of Sr in epidote (Frei *et al.,* 2004). The Sr/Y ratios for quartz-hosted SMI are generally low (<50) in line with plagioclase fractionation or partial melting of a plagioclase-rich source and post-2.5 Ga TTG suites and typical arc-related rocks. The few high Sr/Y ratios are akin to Archean TTG and adakitic rocks and are the

result of either amphibole accumulation or partial melting of a garnet and/or amphibolitic source region (Fig. 3.23D). However, the SMI with elevated Sr/Y ratios have low Sr (~100 ppm) and very low Y (~1 ppm) concentrations, leading to these high ratios and based on the low Sr content, these SMI are likely classified as low-Al TTG melts (Fig. 3.23C). Quartz-hosted SMI have low $(La/Yb)_n$ ratios (< 20) in line with the post-2.5 Ga TTG suites and typical arc-related rocks and plagioclase fractionation (Fig. 3.23E). Bulk rock compositions for all lithologies also plot in the low-Al TTG field based on their Sr/Y and $(La/Yb)_n$ ratios (Fig. 3.23D, E).

The low water contents (<< 2 wt%) of SMI, combined with the temperature of zircon crystallization (and SMI entrapment; 700-800°C) are at odds with each other because the suspected source for TTG suites is tholeiitic basalt and will have a solidus temperature of ~850°C (Moyen & Martin, 2012) over the estimated range in pressure for inclusion entrapment. In contrast, the solidus of an arc basaltic source can extend down to ~650°C at the pressure of inclusion entrapment due to a higher H_2O content in the resultant partial melt. While it is reasonable to implicate an amphibole-rich source for the MIC magmas, it is important to note that ≥ 4 wt% H_2O in the melt is needed for amphibole to form (Ridolfi *et al.*, 2010) and this is at odds with the low water contents of SMI. Rather, these low water contents would favor plagioclase fractionation, consistent with the low Sr contents, low Sr/Y and La/Yb ratios, and negative Eu anomalies in melt inclusions. Importantly, all SMI analyzed by Raman, have low H_2O (<<2 wt%) contents indicating the melt has lost some of it's volatiles prior to melt entrapment, whereas only a few SMI analyzed by EPMA have H_2O > 1 wt%. The origin of these rare, more H_2O-rich inclusions is not understood as they are not petrographically-distinct (i.e., paragenetically earlier or later).

Based on the various tectonic and TTG discrimination diagrams, as well as relatively low H_2O content in SMI, it is clear that zircon- and quartz-hosted SMI from all lithologies are predominately consistent with an arc-related, low-Al TTG magma, which the bulk rock

compositions do not provide and therefore bulk rock compositions are not representative of the original melt composition (with the exception of the aphyric trondhjemite). This would suggest the bulk rock compositions were formed through cumulate processes (e.g., plagioclase accumulation) in mid- to upper-crustal magma chambers. This has been noted in previous studies in TTG suites globally (Eastern Hebei region, North China Craton, Liou & Guo, 2019; Barberton greenstone belt, South Africa, Laurent *et al.,* 2020; Lewisian Complex, Scotland, Rollinson, 2021; Limpopo belt, Zimbabwe, Rollinson, 2021) but not previously discussed in the Abitibi greenstone belt. Additionally, these previous studies have shown the influence amphibole fractionation (i.e., removal) from the melt and plagioclase crystallization and accumulation can have on the bulk rock composition and that partial melting alone may not explain the difference between high- (high Sr/Y ratios) and low-pressure (low Sr/Y ratios) TTG suites. Starting with a dioritic melt composition, the crystallization and removal of amphibole from the melt will cause Sr/Y ratios to increase and thereby it can give a false impression that these high Sr/Y ratios are related to deep partial melting with garnet ± amphibole in the source region (Liou & Guo, 2019; Laurent *et al.,* 2020). It is important to note that it is still reasonable for deep partial melting of an eclogitic source to give rise to high Sr/Y magmas, but it is not the only process that can lead to these high ratios.

3.6.3 Magmatic processes impacting the development of the MIC

Except for the trondhjemite that has bulk composition very similar to the SMI composition, the rocks of the MIC do not represent bulk liquid compositions but rather crystallized mushes containing non-liquidus crystal proportions (i.e., cumulates). The rhyolitic SMI compositions in all lithologies are not overly fractionated as would be expected if they were very late interstitial liquids. Rather, they have normal granitic compositions based on their normative Rb-Sr-Ba contents (Fig. 3.16A and B) and relatively low Cs – a sensitive proxy for the degree of melt

fractionation (cf Audétat & Pettke, 2003). To yield the range in bulk rock composition in the MIC, a more intermediate to mafic composition must have been present early during melt evolution. No trapped samples of earlier, more mafic melt compositions were observed.

Crosscutting relationships and bulk rock geochemistry suggest that the Mouska and Doyon stages were sourced from a single magma chamber without recharge (Galley & Lafrance, 2014). Generally, magma fractionation and crystal accumulation involving an intermediate starting liquid composition could produce the lithologies of the MIC from a single magma chamber, in the order of inferred emplacement (gabbro-quartz diorite-tonalite-trondhjemite; Galley & Lafrance, 2014). Fractionation of mafic minerals and plagioclase of labradorite-andesine composition would produce the gabbroic and dioritic lithologies. This would be followed by continuing plagioclase accumulation, evolution from andesine to albitic compositions, to produce tonalitic and trondhjemitic lithologies, respectively. If a single magma chamber model is invoked, SMI from the various lithologies that crystallized from that magma should display a trend of increasing degree of melt fractionation. The least evolved rhyolitic melt would be expected to be trapped in zircon from the gabbro and the most evolved rhyolitic melt preserved in the trondhjemite. Silicate melt inclusions from individual lithologies display fractionation trends (i.e., increasing SiO_2 with decreasing Al_2O_3) but the range in these trends overlap between lithologies which would not be expected if all were sourced from a single fractionating magma chamber. As well, the behavior of incompatible elements in SMI (e.g., K_2O, Rb, La; Fig. 3.15B and D) is inconsistent with expected fractionation trends. For example, SMI in the tonalite should have higher K_2O and Rb concentrations than the earlier-emplaced quartz diorites and the trondhjemites have similar K_2O and Rb to the low-Th/U quartz diorite. Rather, the SMI in the tonalite have intermediate compositions between the quartz diorites, thus disrupting the expected fractionation trend for a single magma chamber. The observations from SMI are consistent with zircon trace element ratios

and trends (Neyedley *et al.,* 2024; companion paper). The trace elements show no evolutionary pattern connecting the least (gabbro) to most evolved (trondhjemite) lithologies together, which would be expected if zircon was forming from a single fractionating magma chamber (e.g., Large *et al.,* 2021). Instead, each lithology shows a distinct pattern and even within single lithologies substantial differences are present (i.e., high- and low-Th/U quartz diorite; Fig. 3.25A and C; Neyedley *et al.,* 2024, companion paper). Based on new evidence presented here it implies that the MIC was sourced from multiple magma chambers. It is important to reiterate the estimated pressure-temperature range (0.5 to 1.2 GPa, ~700-800°C; Neyedley *et al.*, 2024, companion paper) of zircon-titanite-quartz co-crystallization, consistent with the presence of epidote as an igneous accessory mineral in the rocks, and accidentally trapped in SMI (e.g., Fig. 3.10B; Schmidt & Thompson, 1996). As well, textural observations indicate that zircon and associated accessory phases providing thermobarometric constraints are not late, interstitial minerals associated with the final stages of crystallization of these rocks. Together, these findings indicate that SMI entrapment conditions are not representative of near-sea floor depth emplacement conditions (cf Galley & Lafrance, 2014). Conditions of source melting to produce TTG magmas generally range from 1 to 3 GPa and 700 to 1000°C (Arndt, 2013) and the SMI entrapment conditions overlap with the lower end of this range, and extend ~0.5 GPa shallower. Thus, melts trapped in zircon would have cooled by a maximum of ~200-300°C from source to inclusion entrapment.

Previous bulk rock data was used to argue that assimilation modified the composition of the Doyon stage magmas of the MIC (Galley & Lafrance, 2014). The mineralogy of SMI provides constraints on this process. Using the abundances of normative constituents of quartz, albite, and orthoclase, the pressure of SMI entrapment can be estimated using a haplogranite ternary projection (Fig. 3.24A; Holtz *et al.,* 1992, Johannes & Holtz, 1996, Holland & Powell, 2001, Wilke *et al.,* 2017). Additionally, the influence of assimilating a quartz-rich country rock (i.e., dry-country rock)

can be evaluated. It should be noted that the cotectic curves are drawn for an anorthite-free system and as the anorthite content increases, the cotectic curves shifts away from the albite corner towards the quartz and orthoclase side of the ternary (Wilke *et al.,* 2017; Fig. 3.24B, C). Additionally, the cotectic curves are drawn for a system with ~1.4 wt% H_2O and for systems with higher H_2O concentrations, the cotectic curves will shift slightly towards the albite corner of the ternary (Wilke *et al.,* 2017; Fig. 3.24C).

Organizing SMI by their anorthite content aids in understanding the pressure estimates and patterns they record. For inclusions with anorthite < 3.5 wt% (Fig. 3.24A), inclusions record a wide range in pressure from >3 GPa to <0.01 GPa. There are two clusters of pressure estimates that are at odds with the previous geothermobarometric constraints, one is the pressures that are >2 GPa and the other is the large cluster of data < 0.1 GPa. As the anorthite content of SMI increases to >3.5, more SMI have pressure estimates similar to the previous estimates (Fig. 3.24B, C). Additionally, this diagram is only suitable for melt compositions with SiO_2 concentrations between 70 and 78 wt%. Zircon-hosted SMI with SiO_2 concentrations outside of this range are indicated in Figure 3.24.

The low-pressures estimated for quartz-hosted inclusions (diamond symbols), can be attributed to SiO_2 contamination by the host quartz (cf Fig. 3.19A, B) resulting in the dilution of the other major element concentrations and therefore provide a falsely high normative quartz composition. However, this does not explain the low-pressure estimates for zircon-hosted inclusions (< 0.5 GPa). For zircon inclusions that are elevated in normative quartz (low-pressure group), the full or partial assimilation of quartz or a quartz-dominant lithology, can cause the normative quartz value to be elevated (Sigmarsson *et al.,* 2013; Dallai *et al.,* 2022). To estimate the amount of quartz that would need to be added to the melt to elevate the normative quartz to give pressures < 0.1 GPa, melt compositions for the low-Th/U quartz diorite equating to pressures

between ~0.8 and ~1.2 GPa were used as starting compositions and an increasing amount of quartz was added to the melt resulting in a new melt composition. The same modelling was applied to an inclusion in the high-Th/U quartz diorite equating to a pressure of ~0.9 GPa. A maximum of 10 to 25 wt% quartz would need to be assimilated into the melt to give these artificially low pressures. These are maximum values because the melt could have been trapped in zircon as low as 0.5 GPa and therefore a smaller amount of quartz-rich material would need to be assimilated into the melt to give the artificially lower pressure. A similar amount of assimilation is needed to account for the lower pressures in the tonalite and trondhjemites. Some inclusions with lower anorthite content fall on the orthoclase-side of the cotectic curve, but these inclusions have ~1.5 to 2 wt% anorthite content and given the shift in cotectic from 0 to 3.5 wt% anorthite, it would suggest these inclusions would be on the albite side of the line. As the anorthite content of a melt increases the cotectic curves shift away from the albite corner (Fig. 3.24C, D). Inclusions with anorthite contents >3.5 wt% that would have been < 0.5 GPa when plotted in an anorthite-free system (Fig. 3.24A) are now around the 0.5 GPa range (Fig. 3.24C, D). This indicates that as the anorthite content of the melt increases, a lower amount of quartz assimilation is needed to record pressures < 0.5 GPa. Additionally, it is not unreasonable to suggest that the increase in melt anorthite content is tied to assimilation as well. There are no basement rocks exposed in the Doyon-Bousquet-LaRonde mining camp to know what rock type(s) the MIC assimilated, but inherited zircon in the Upper Bousquet Formation with an age of 2721 Ma suggests the Blake River Group is underlain by an older volcano-plutonic assemblage (Mercier-Langevin *et al.*, 2007a). There is ample evidence for assimilation in the Mouska stage tonalites and Doyon stage trondhjemites which can contain up to 10% absorbed xenoliths throughout (Galley and Lafrance, 2017).

It is important to note that the cotectic curve compositions in the haplogranite ternary represent melt minimum (i.e., eutectic) compositions and that partial melting near solidus

temperatures results in non-eutectic melt compositions (Acosta-Vigil *et al.*, 2006). This suggests SMI do not represent minimum melt compositions and therefore would give rise to false pressure estimates. For the melt compositions that plot at high pressures (>2 GPa; Fig. 3.24A) these could represent inclusions that were trapped along the albite liquidous curve, resulting in higher Na contents. As the melt moved down the albite liquidus, it would have continuously fractionated albite causing the melt composition to shift towards higher quartz contents, this can also be accompanied by a drop in pressure (cf Dallia *et al.*, 2022). Additionally, albite is a common mineral present trapped in zircon in the tonalite (Fig. 3.8N, P), suggesting it was a fractionating phase prior to and/or coeval with zircon. Albite is also present trapped with melt in quartz (Fig. 3.10K). Therefore, it is likely that these more albitic melts do not represent eutectic compositions and result in artificially high-pressure estimates.

Overall, normative melt inclusion compositions record a variety of processes (Fig. 3.24A-D). The SMI with high normative albite contents record non-eutectic melt compositions that were trapped on the albite-saturated liquidus curve. Melt trapped in zircon over the 0.5-1.2 GPa window (cf. Neyedley *et al.*, 2024, companion paper) likely experienced decompression and albite fractionation, shifting melt compositions to higher normative quartz contents. Additionally, an increase in normative quartz would result from assimilation of quartz-rich lithologies, resulting in the anomalous low pressures estimates shown graphically in Figure 3.24 and shifting magmas to more felsic bulk compositions. As well, assimilation of a dry-country rock would dilute the H_2O content of the melt and may contribute to explaining the low H_2O contents of melt inclusions.

3.6.4 Constraints on magmatic oxygen fugacity

The oxidation state of a magma plays an important role in the formation of magmatic-hydrothermal ore deposits since fO_2 has a strong influence on the solubility of some metals in the

melt and is a primary control on the stability, formation, and abundance of an immiscible sulfide phase (e.g., Botcharnikov *et al.*, 2010; Richards, 2011; Audétat & Simon, 2012; Zajacz *et al.*, 2012, 2013). Previous studies have utilized Eu and Ce anomalies in zircon to estimate magmatic fO_2 conditions (e.g., Ballard *et al.*, 2002; Shen *et al.*, 2015; Lu *et al.*, 2016; Lee *et al.*, 2017). However, many recent studies have shown those anomalies tend to be strongly influenced by growth of common major and accessory minerals (e.g., plagioclase, titanite; Loader *et al.*, 2017, 2022) and by simple cooling of the system (Loader *et al.*, 2022) leading to incorrect fO_2 estimates.

Using the zircon composition from Neyedley *et al.* (2024; companion paper) an estimate on fO_2 conditions can be made using the equation of Loucks *et al.* (2020) that utilizes the Ce, Ti, and initial U (U_i) content of zircon. In magmatic zircon, the concentrations of U, Ce, and Ti are all at concentration levels that can be precisely measured by LA-ICPMS and the U_i concentration can be calculated using the radioactive decay constants for ^{238}U and ^{235}U and the age of crystallization. The age of zircon crystallization is known from CA-ID-TIMS zircon geochronology that provide high precision ages for the same population of zircon from which melt inclusion data were obtained (Neyedley *et al.*, 2024; companion paper). Additionally, the Loucks *et al.* (2020) equation does not rely on the pressure and/or temperature of zircon crystallization or the parental melt composition and H_2O concentration to be known, reducing the number of variables in the calculation.

Using the zircon composition, fO_2 values are relatively similar within individual samples, except for the gabbro, which displays a broad range in values. In the gabbro fO_2 conditions range from FMQ-1.66 to FMQ+1.24 (~FMQ-0.10 ± 0.53; n=70; Fig. 3.25A). Rim analyses span the entire range of FMQ values and core analyses have a slightly narrower range between FMQ-1.62 and FMQ+0.4. The fO_2 conditions of the low-Th/U quartz diorite range from FMQ+0.39 to FMQ+1.17 (~FMQ+0.7 ± 0.18; 1σ, n=66; Fig. 3.25A) whereas the high-Th/U quartz diorite records slightly higher fO_2, ranging from FMQ+1.0 to FMQ+1.9 (~FMQ+1.5 ± 0.18; n=45; Fig. 3.25A).

Overall, both quartz diorite samples display an increase in FMQ with a decrease in temperature. In the low-Th/U quartz diorite, only zircon rim analyses have FMQ>+0.8, but rim and core analyses extend to similar lower FMQ values (~FMQ+0.4). Core and rim analyses in the high-Th/U quartz diorite span a similar range in FMQ values. The two tonalite samples have similar average FMQ values to the high-Th/U quartz diorite with values of FMQ+1.66 ± 0.19 (n=46) and FMQ+1.52 ± 0.24 (n=56) for samples Stop 10 and Stop 11, respectively (Fig. 3.25A). The aphyric trondhjemite samples record the lowest fO_2 conditions of all lithologies with FMQ+0.20 ± 0.18 (n=19) and FMQ+0.17 ± 0.17 (n=20) for samples 1323 and 1444.5, respectively (Fig. 3.25A). No differences are present between core and rim FMQ values and there is no correlation between temperature and FMQ values in the tonalite and aphyric trondhjemite.

Individual zircon core – rim analyses in the gabbro show variable relationships with a drop in temperature coinciding with either increasing, decreasing, or relatively constant FMQ values (Fig. 3.25B). In the high-Th/U quartz diorite relatively similar FMQ values occur between core and rim analyses for individual zircon grains (Fig. 3.25B). For the tonalite, most zircon grains display relatively constant FMQ values as temperature decreases from core to rim, with only a few grains showing an increase in FMQ toward the rim (Fig. 3.25B). A majority of grains in the low-Th/U quartz diorite have an increase in FMQ from core to rim with a decrease in temperature (Fig. 3.25B).

The FMQ values calculated using the equation of Loucks *et al.* (2020) are consistent with the petrographic observations. Values of FMQ > +1 for the tonalite are consistent with the presence of magmatic, interstitial titanite and epidote and inclusions of those minerals in zircon and quartz (Wones 1989, Schmidt & Thompson, 1996). The values of FMQ > +1 for the high-Th/U quartz diorite are also consistent with the presence of titanite inclusions in zircon. Inclusions of titanite and epidote in zircon and quartz are present in the low-Th/U quartz diorite, but only some rim

analyses of zircon record >FMQ+1 suggesting the magma was initially at fO_2 conditions of < FMQ +1 and as crystallization progressed, the system became more oxidized. Additionally, the presence of titanite forming along the rim of an ilmenite inclusion in zircon (Fig. 3.8I), is further support to an increase in fO_2 conditions (Wones, 1989). The < FMQ+1 values for the gabbro are generally consistent with petrographic observations as no titanite or epidote inclusions occur in zircon, however, epidote is present in quartz accidentally trapped with silicate melt (Fig. 3.10B). This would suggest at the time of melt entrapment in quartz that the system was epidote saturated and at > FMQ+1 (Schmidt & Thompson, 1996). Few FMQ values are >+1 and this could indicate silicate melts became entrapped in quartz late in the crystallization sequence when the system was more oxidized. The aphyric trondhjemite records the lowest fO_2 conditions with FMQ values typically between FMQ-0.2 and FMQ+0.6. However, rare interstitial, magmatic epidote is present and rare epidote inclusions occur in zircon trapped with albite, suggesting fO_2 conditions were >FMQ+1.

The low-pressure source region documented by SMI compositions is consistent with the pressure conditions determined by geothermobarometry with pressures ranging from ~0.5 to ~1.2 GPa (18.5-44 km) for the Mouska stage and ~0.5 and ~0.9 GPa (18.5-33 km) for the Doyon stage of the MIC (Neyedley *et al.*, 2024; companion paper). These pressure conditions are similar to or slightly lower than the experimentally determined TTG formation conditions (~0.8 to >1.5 GPa; Rapp et al, 1991; Smithies, 2000; Condie, 2005; Martin *et al.,* 2005; Getsinger *et al.,* 2009; Moyen & Martin, 2012; Qian & Hermann, 2013). The presence of epidote inclusions in zircon (Fig. 3.8F, J, and O) and accidentally trapped epidote with silicate melt in quartz (Fig. 3.10B) provide additional evidence that these melts and the source region for the MIC was at least 0.5 GPa (at 750°C and FMQ+5; Schmidt & Thompson, 1996) but given FMQ values for the MIC range from FMQ+0.2

to FMQ+2, formation conditions were likely deeper as epidote is stable at 0.9 GPa at FMQ +1 and 750°C (Schmidt & Thompson, 1996).

In the Mouska stage the emplacement order is interpreted to begin with an aphyric diorite (Phase A) followed by the gabbro (Phase B), quartz diorite (Phase C) and tonalite (Phase D). For the Mouska-stage lithologies studied here, fO_2 increases from the gabbro to quartz diorite (low-Th/U variety) to tonalite with an increase in zircon Th/U ratio and temperature (Fig. 3.25C). The high-Th/U quartz diorite has the highest temperatures and similar FMQ values to the tonalites (Fig. 3.25A). Importantly, if these lithologies all crystallized in the same magma chamber and began to crystallize in their order of emplacement, zircon from the gabbro should record the highest temperature and highest Th/U and subsequent cooling and accessory mineral crystallization (i.e., titanite and apatite) causing a decrease in Th/U over time (Neyedley *et al.,* 2024; companion paper), however, this is not the case. Based on the evidence provided by zircon trace element chemistry in Neyedley *et al.* (2024; companion paper), each lithology of the MIC had to crystallize in separate magma chambers to produce the evolutionary trends and ranges in zircon trace element concentrations and ratios (e.g., Th/U, Yb/Gd, Sm/Ce) and therefore to produce the different FMQ values recorded by zircon. Additionally, zircon core to rim relationships between FMQ and temperature (drop in temperature coinciding with increase, drop, and/or constant FMQ) are different between individual lithologies and demonstrates each lithologies magma chamber were operating independent of each other. Zircon from the Doyon-stage aphyric trondhjemite has a similar range in FMQ and Th/U ratios to the gabbro (Fig. 3.25C) but the trondhjemite records higher temperatures and has distinct $(Yb/Gd)_n$ and $(Sm/Ce)_n$ ratios and began to crystallize at lower pressures than the gabbro (Neyedley *et al.,* 2024; companion paper), implying the trondhjemite must have also crystallized in it's own magma chamber.

Other calculations to estimate fO_2 conditions were also considered, such as the equation of Smythe & Brennan (2016). To use this calculation, the full REE, Y, Th, and U concentrations of the melt need to be known. Since some MREE, all HREE, Y, Th, and U are highly compatible in the host zircon, concentrations of these elements in zircon-hosted SMI cannot be determined and therefore zircon-hosted SMI do not provide enough information on the melt chemistry to use for fO_2 calculations. Additionally, the major element composition and H_2O content of the melt is needed. However, since zircon and quartz are interpreted to be relatively coeval (based on inclusions of quartz in zircon and zircon inclusions in quartz-hosted SMI), the melt composition of quartz-hosted SMI can be used. Quartz-hosted SMI come with their own set of challenges though as many inclusions contain accidentally trapped minerals, resulting in a melt composition that is contaminated. Additionally, Na_2O concentrations determined by LA-ICPMS in quartz-hosted SMI are commonly compromised due to diffusion-related issues and therefore do not provide a robust constraint on the major element chemistry of the parental melt composition. Since the MIC lithologies do not have suitable SMI parameters required to calculate fO_2 conditions, a parental melt composition would have to be calculated based on experimental zircon/melt partition coefficients. The absolute H_2O content of the parental melt is unconstrained and is a highly sensitive parameter in the Smythe & Brennan (2016) formulation, for example increasing the H_2O content from 2 to 4 wt% results in an increase in of FMQ by 0.9. Preliminary calculations of fO_2 conditions were estimated and results in values between FMQ-0.2 and FMQ for the various lithologies with large errors up to ± 2.31. These preliminary FMQ estimates are inconsistent with petrographic observations. In zircon, epidote and/or titanite are common inclusions either as isolated or multi-mineral composite inclusions and in quartz, epidote is a common accidentally trapped mineral in melt inclusions. Both epidote and titanite are only stable under relatively oxidizing condition (>FMQ+1; Wones, 1989; Schmidt & Thompson, 1996) suggesting the

calculated magma fO_2 conditions using the method of Smythe & Brenan (2016), provide FMQ values too low for this system.

3.6.5 Anhydrite Origin and Magmatic Processes

The presence of magmatic anhydrite in relation to ore-forming processes and potential has implications for the oxidation state of the magma and the availability of sulfur in the system. For anhydrite to form the system must be relatively oxidizing (>FMQ+1.5; Jugo *et al.*, 2010) when S^{2-} predominantly transitions to S^{6+}. The textural relationships present in the aphyric trondhjemite between anhydrite and major and trace mineral phases provide evidence for the magmatic origin of anhydrite. The open space filling texture (i.e., straight planar mutual grain boundaries; cf Stern *et al.*, 2007) between anhydrite and plagioclase and quartz (Fig. 3.4H) as well as anhydrite intergrown with graphic quartz and plagioclase (Fig. 3.4I) show that anhydrite was crystallizing coevally with and after these primary magmatic minerals. Additionally, the presence of zircon and rutile inclusions in anhydrite (Fig. 3.4G) suggest anhydrite was crystallizing slightly later in the paragenetic sequence than these trace minerals. The sodic composition of plagioclase (An_{0-13}) suggests anhydrite was sequestering Ca from the melt as plagioclase crystallized (Stern *et al.*, 2007). As well, anhydrite has a negative Eu anomaly (Fig. 3.5A), indicating plagioclase crystallized prior to and/or coevally with anhydrite. The same textural relationships and geochemical evidence has been documented in barren and mineralized plutonic systems and have all used this evidence to support a magmatic anhydrite origin (Barth & Dorais, 2000; Stern *et al.*, 2007, Chambefort *et al.*, 2008).

The presence of magmatic anhydrite would indicate that the fO_2 conditions of the magma were at least FMQ +1.5 (Jugo *et al.*, 2010), this it at odds with the calculated fO_2 conditions based on zircon chemistry for the aphyric trondhjemite, which record relatively reduced conditions

between FMQ-0.23 and FMQ+0.60 (Fig. 3.25A). However, since zircon is present as inclusions within anhydrite (cf Fig. 3.4G), the fO_2 conditions it records may be earlier in the magmatic history of the magma chamber the aphyric trondhjemite was evolving in. Epidote is also an interstitial mineral in the aphyric trondhjemite (Neyedley *et al.*, 2024; companion paper) suggesting relatively oxidized conditions as well (Schmidt & Thompson, 1996). In other lithologies, such as the low-Th/U quartz diorite, ilmenite inclusions in zircon are rimmed by titanite (Fig. 3.8I) implying near the end of zircon crystallization the magma became more oxidized (Wones, 1989). This increase in oxidation state can be related to timing of volatile exsolution which can be induced by decompression, cooling, and/or crystallization. The role of oxidation and volatile exsolution has an important role in ore forming processes as the volatile phase can destabilize pre-existing sulfides and the importance of volatile loss relative to sulfide stability is discussed in following sections.

The $\delta^{34}S$ composition of anhydrite supports the textural evidence for a magmatic origin as well as the inference of volatile loss. Values of $\delta^{34}S$ are notably different in anhydrite inclusions in igneous silicate minerals (6.1 to 8.2 ‰; Fig. 3.5C) compared to interstitial anhydrite (11.0 to 19.7 ‰; Fig. 3.5C). Early Archean magmatic sulfides have $\delta^{34}S$ compositions of ~0 ‰ (Hattori & Cameron, 1986). Isotopic fractionation between sulfate and sulfide ranges from 5 to 8‰ at 900° to 700°C, respectively (Miyoshi *et al.*, 1984); therefore, the $\delta^{34}S$ values for the anhydrite inclusions (6.1 to 8.2‰) is consistent with its formation at magmatic temperatures from an initial melt with a near-zero bulk $\delta^{34}S$ composition. However, the range in $\delta^{34}S$ values for interstitial anhydrite (11 to 19.7‰) requires an alternative explanation. Degassing models for magmatic systems at fO_2 conditions similar to those for the aphyric trondhjemite and when magmatic anhydrite is stable (FMQ to FMQ+2.0) generate wide ranges in the bulk $\delta^{34}S$ melt composition (Luhr *et al.*, 2002). At fO_2 conditions below the anhydrite stability window (< FMQ +1.5), the bulk $\delta^{34}S$ melt composition would decrease due to the loss of ^{34}S to the volatile phase, whereas at fO_2 conditions above

≥FMQ+1.5, the bulk $\delta^{34}S$ composition of the melt can increase up to 14‰ as degassing progresses due to preference of ^{34}S in SO_3 dissolved in the melt (cf Luhr *et al.,* 2002). Additionally, as temperature decreases, the bulk $\delta^{34}S$ melt compositions increase at fixed fO_2 conditions as degassing progresses and water loss raises the solidus temperature promoting magmas to crystallize and stall at depth (Luhr *et al.,* 2002). In the MIC, H_2O contents of SMI are low (<< 2 wt % H_2O) in the aphyric trondhjemite. As well, textural observations indicate that anhydrite growth was synchronous to (Fig. 3.4A and B) and postdated both quartz-SMI entrapment (Fig. 3.4D-H), and zircon-SMI entrapment (Fig. 3.4G). Therefore, we interpret the magma to have already degassed thereby explaining the range in $\delta^{34}S$ for interstitial anhydrite.

3.6.6 Magma fO_2 Conditions in Relation to Au SMI Concentrations

The solubility of Au in silicate melt is largely controlled by the amount of reduced S (S^{2-}) in and fO_2 conditions of the melt (Jégo *et al.,* 2010; Botcharnikov *et al.,* 2010, 2011; Bell *et al.,* 2011; Zajacz *et al.,* 2012). Maximum Au solubility in andesitic melts occur below the S^{2-}/S^{6+} transition (FMQ +1.2) and in between FMQ+0.5 to FMQ+1.0 (Jugo *et al.,* 2010; Botcharnikov *et al.,* 2011; Zajacz *et al.,* 2012). At these FMQ conditions dissolved S^{2-} concentration is maximized, indicating Au is likely dissolved as the complex $Au^{1+}S^{2-}H^{1+}$ and sulfate (S^{6+}) plays no role (Zajacz *et al.,* 2012).

Gold concentrations in SMI in the low-Th/U quartz diorite range from 14 to 120 ppb (66 ± 44 ppb; n=5), and between 10 and 20 ppb (14 ± 6 ppb; n=3) in the gabbro, with one SMI containing anomalously high Au (1680 ppb) likely related to the entrapment of a saturated gold-rich phase. For SMI in the low-Th/U quartz diorite and gabbro containing accidentally trapped sulfide, Au concentrations of the bulk SMI range between 20 and 30 ppb, whereas sulfide-free SMI have Au concentrations between 10 and 120 ppb. Estimate of fO_2 (based on zircon chemistry) for the gabbro

ranges widely from FMQ-1.66 to FMQ+1.24 but > 75% of values fall between FMQ-0.5 and FMQ+0.5. Estimate of fO_2 for the low-Th/U quartz diorite is from FMQ+0.39 to FMQ+1.17 (~0.71 ± 0.18), indicating more oxidizing conditions and within the optimal window for maximum Au solubility in silicate melt.

It is notable that SMI in the gabbro and low-Th/U quartz diorite contain accidentally trapped Au-bearing sulfides in SMI (Fig. 3.10J and 3.18H) and no accidentally trapped anhydrite, indicating the dominant S species was S^{2-} at the time of zircon and quartz crystallization and SMI entrapment in these minerals, at depth (0.5-1.2 GPa; Neyedley *et al.*, 2024; companion paper). This is consistent with fO_2 estimates for both lithologies being below the S^{2-}/S^{6+} transition (<FMQ+1.2). Therefore, if sulfide saturation occurred prior to SMI entrapment, Au (and other metal) concentrations in SMI would be minimums due to the high sulfide-silicate partition coefficient ($D^{SUL/SM}$) for Au (180 to 440, Zajacz *et al.*, 2013; 90 to 510, Li & Audétat, 2015; 150 ± 100, Li & Audétat, 2015). However, if sulfide is an accidentally trapped phase in SMI, then Au (and other metal) concentrations would be over-reported and their concentrations would not be representative of the true silicate melt composition. Given the range of Au concentrations in sulfide-free and -bearing SMI overlap, it could suggest that SMI were entrapped at different stages of melt evolution prior to, synchronous with, or post-sulfide saturation and that range of Au concentrations (10 to 120 ppb) in sulfide-free SMI are likely representative of the true melt composition.

3.6.7 Importance of Early Sulfide Saturation

At the temperature of melt entrapment (~700° to ~800°C, Neyedley *et al.*, 2024, companion paper), the trapped sulfide is more likely to represent monosulfide solid solution (MSS) than sulfide liquid as MSS generally begins to crystallize from sulfide liquid at temperatures >1000°C (Ebel & Naldrett, 1997). Formation of MSS enriches residual sulfide liquid in Cu which crystallizes

intermediate sulfide solid-solution (ISS) and subsequently recrystallizes to chalcopyrite (±cubanite). The occurrence of accidentally trapped Cu-Fe sulfide in some SMI, (i.e., Fig. 3.7F), without coentrapped MSS (i.e., pyrrhotite ± pentlandite), indicates that the Cu-Fe sulfide phase was already a saturated phase at the time of SMI entrapment, whereas other SMI contain only accidentally trapped Fe-sulfide.

Partition coefficients for metals between sulfide and silicate melt of a rhyolitic composition ($D^{SUL/SM}$) can be calculated using concentrations determined by LA-ICP-MS. However, the true composition of the sulfide phase is unknown (i.e., MSS, MSS + Cu-Fe sulfide, and/or Cu-Fe sulfide), therefore these values are only estimates. The $D^{SUL/SM}$ for Au and Ag range from 70 to 360 and 30 to 90, respectively. Whereas Cu has a much wider range in $D^{SUL/SM}$ between 130 and 4300. Given the compositions of sulfide determined by LA-ICP-MS show variable Cu:Fe ratios from inclusion to inclusion suggest trapping of variable sulfide compositions that could represent MSS, MSS + Cu-Fe sulfide, and/or Cu-Fe sulfide, this could be an explanation for the wide range in $D^{SUL/SMI}$ for Cu between different lithologies. Limited $D^{SUL/SM}$ are available for porphyry and porphyry-type felsic magmatic systems and even though the composition of the sulfide from the MIC is not constrained, the range in $D^{SUL/SMI}$ are similar to values from experimental studies and natural samples (Zajacz *et al.*, 2013; Li & Audétat, 2015).

The use of metal ratios in sulfide inclusions in comparison to associated ore deposits has been used as evidence of early sulfide crystallization acting as a temporary storage medium for metals during magma evolution (e.g., Cu/Au ratios; Halter *et al.*, 2005). The Cu/Au ratios of quartz-hosted sulfide inclusions are similar to the Cu/Au ratio of bulk ore in the LaRonde and Westwood Au-rich VMS deposits as well as the intrusion-related Au-Cu Doyon deposit and the shear-hosted Mouska Au-Cu deposit (Fig. 3.26A, B). Additionally, metals that are classically related to a magmatic affinity (e.g., Bi, Sn, W) generally have ratios in sulfide inclusions comparable to the

ore deposits (Fig. 3.26B-D). Overall, comparing the metal ratios in sulfide-bearing inclusions to ore metal concentrations and ratios in various deposits across the Doyon-Bousquet-LaRonde mining camp (LaRonde, Doyon, Westwood, and Mouska) demonstrates significant overlap suggesting early magmatic sulfides influenced ore metal tenors in these syn-volcanic and intrusion-hosted deposits.

Coentrapped sulfides occur in zircon- and quartz-hosted melt inclusions indicating sulfide saturation occurred at depth (0.5-1.2 GPa; Neyedley *et al.*, 2024, companion paper) relatively early in crystal mushes of the various lithologies of the MIC. Early sulfide saturation is suggested to be detrimental to the development of a magmatic-hydrothermal Au ± Cu deposit since the sulfide phase will incorporate metals, leading to lower metals in the silicate melt and therefore less metals available to the exsolving ore fluid (Müller *et al.*, 2001; Park *et al.*, 2015, 2019). However, there has been accumulating evidence that early sulfide saturation may act only as a temporary storage location for metals and these sulfides can then be broken down during crystallization and volatile exsolution, allowing metals to be transferred from the sulfide phase and into the exsolving fluids that led to deposit formation (Keith, *et al.*, 1997; Halter *et al.*, 2004b, 2005; Audétat & Pettke, 2006, Zhang & Audétat, 2017; Du & Audétat, 2020).

The timing of volatile saturation relative to sulfide saturation at depth in the MIC forming magmas is a crucial factor determining when, and at what depth, sulfides destabilize and therefore the relative importance of volatile versus sulfides in supplying metals to the magmatic-hydrothermal ore system. Silicate melt inclusions have low H_2O contents (<< 2 wt %; e.g., Fig. 3.17). For comparison, in the coeval Bousquet volcanics, SMI trapped in early quartz phenocrysts at comparable depths to zircon in this study are also very low in H_2O (< 0.5 wt%; Meagher, 2020). In the MIC lithologies the presence of accidentally trapped sulfides in SMI indicates that at the time of sulfide entrapment the coeval silicate melt had already lost volatiles due to crystallization

and magma ascent, prior to zircon crystallization at depth (0.5-1.2 GPa; Neyedley *et al.*, 2024; companion paper; *cf* Lowenstern, 1994; Shinohara *et al.*, 1995; Lowenstern, 2001; Capriolo *et al.*, 2020; Chiaradia & Caricchi, 2022). Therefore, sulfides not only acted as a temporary storage medium but also prevented metal loss during deep volatile exsolution. Further ascent and crystallization of magmas would lead to volatile exsolution and destruction of these sulfides, allowing for metals to be transferred to exsolving volatiles, contributing metals to ore forming system. If the sulfide-volatile relationship has exerted an influence on the metal endowments in the camp, would a lack of sulfide saturation at depth have been detrimental to the Au endowment of the Doyon-Bousquet-LaRonde mining camp?

3.7 CONCLUSIONS

Silicate melt inclusions preserved in quartz and zircon in a wide range of lithologies from the MIC record the relatively early (i.e., not late intercumulus) trapping of a rhyolitic liquid derived from variably crystallized parental liquids. The inclusions provide new constraints on processes operating during the evolution of the magmas that produced the MIC, linked to Au-rich VMS and other Au-rich magmatic-hydrothermal ore systems in this world class mining district. The presence of accidentally trapped sulfide in SMI implies sulfide saturation occurred prior to or synchronously at the melt entrapment at a significant depth (0.5-1.2 GPa). As well, the concentrations of metals in SMI constrain the metal tenor of the magmatic system at various times and for various magma chambers for different lithologies. Related to magma evolution, the low Cs concentrations and normative Rb-Sr-Ba contents imply the trapped melt was not a very late phase nor highly fractionated. Finally, specific ratios (e.g., Al_2O_3 vs SiO_2, Sr/Y, La/Yb) suggest the melt is consistent with low-Al TTG suites, that plagioclase fractionation and accumulation was a dominant magmatic process and that significant assimilation of SiO_2-rich crust occurred. Recent

thermobarometric calculations indicate that these processes were operating at depth (0.5-1.2 GPa; Neyedley *et al.,* 2024, companion paper) where SMI were trapped in zircon and quartz, not at the depth of MIC crystal mush emplacement and final crystallization.

The composition of accidentally trapped sulfide in SMI have significant overlap with ore metal ratios in various deposits across the Doyon-Bousquet-LaRonde mining camp suggesting early magmatic sulfides strongly influenced ore metal tenors in these syn-volcanic and intrusion-hosted deposits. Additionally, this would mean sulfides acted as a temporary storage medium and upon magma ascent and crystallization volatile exsolution would have destroyed these sulfides, allowing for metals to be transferred to exsolving volatiles, contributing metals to ore forming system. If the sulfide-volatile relationship influenced the metal endowments in the Doyon-Bousquet-LaRonde mining camp, would a lack of sulfide saturation at depth have been detrimental to the Au endowment of the Doyon-Bousquet-LaRonde mining camp and therefore early sulfide-saturation be crucial to the formation of these Au-rich deposits?

3.8 ACKNOWLEDGEMENTS

Financial support for this project came from the Targeted Geoscience Initiative Phase 5 program of the Geological Survey of Canada. The authors thank Ryan Sharpe for his valuable contribution to SIMS analysis of anhydrite. Alan Galley and David Yergeau provided valuable assistance in the field during sample collection and discussions about the regional and local geology. The authors are grateful to the geology departments and staff at the Westwood (Iamgold Corporation) and LaRonde Penna (Agnico Eagle Mines Ltd) mines for access to drill core and tours of the properties. K. Neyedley acknowledges scholarship support from the Natural Sciences and Engineering Research Council of Canada and the Nova Scotia Research & Innovation Graduate Scholarship program.

3.9 REFERENCES

Acosta-Vigil, A., London, D. & Morgan, G.B. (2006). Experiments on the kinetics of partial melting of a leucogranite at 200 MPa H2O and 690-800°C: compositional variability of melts during the onset of H_2O-saturated crustal anatexis. *Contributions to Mineralogy and Petrology,* 151, 539-557.

Arndt, N. T. (2013). The formation and evolution of the continental crust. *Geochemical Perspectives*, 2, 405-533.

Audétat, A. (2015). Compositional evolution and formation conditions of magmas and fluids related to porphyry Mo mineralization at Climax, Colorado. *Journal of Petrology*, 56, 1519-1546.

Audétat, A. & Pettke, T. (2003). The magmatic-hydrothermal evolution of two barren granites: A melt and fluid inclusion study of the Rito del Medio and Cañada Pinabete plutons in northern New Mexico (USA). *Geochimica et Cosmochimica Acta,* 67, 97-121.

Audétat, A. & Pettke, T. (2006) Evolution of a porphyry-Cu mineralized magma system at Santa Rita, New Mexico (U.S.A.). *Journal of Petrology,* 47, 2021-2046.

Audétat, A. & Simon, A.C. (2012). Magmatic controls on porphyry copper genesis: *Society of Economic Geologists Special Publication* 16, 553–572.

Audétat, A., Zhang, L. & Ni, H. (2018). Copper and Li diffusion in plagioclase, pyroxenes, olivine and apatite, and consequences for the composition of melt inclusions. *Geochimica et Cosmochimica Acta,* 243, 99-115.

Bachmann, O., Dungan, M.A. & Bussy, F. (2005). Insights into shallow magmatic processes in large silicic magma bodies: The trace element record in the Fish Canyon magma body, Colorado. *Contributions to Mineralogy and Petrology,* 149, 338–349.

Ballard, J.R., Palin, J.M. & Campbell, I.H. (2002). Relative oxidation states of magmas inferred from Ce(IV)/Ce(III) in zircon: Application to porphyry copper deposits of northern Chile. *Contributions to Mineralogy and Petrology,* 144, 347–364.

Barker, F. (1979). Trondhjemites, dacites and related rocks. Elsevier, New York, 659 p.

Barth, A. P. & Dorais, M.J. (2000). Magmatic anhydrite in granitic rocks: first occurrence and potential petrologic consequences. *American Mineralogist,* 85, 430-435.

Bell, A.S., Simon, A. & Guillong, M. (2011). Gold solubility in oxidized and reduced, water-saturated mafic melt. *Geochimica et Cosmochimica Acta,* 75, 1718-1732.

Belkabir, A. & Hubert, C. (1995). Geology and structure of a sulfide-rich gold deposit: an example from the Mouska gold mine, Bousquet district, Canada. *Economic Geology,* 90, 1064-1079.

Beaudoin, Y., Scott, S.D., Gorton, M.P., Zajacz, Z. & Halter, W. (2007). Pb and other ore metals in modern seafloor tectonic environments: evidence from melt inclusions. *Marine Geology*, 242, 271-289.

Bodnar, R.J. & Student, J.J. (2006). Melt inclusions in plutonic rocks: petrography and microthermometry. In: Webster, J.D. (Ed.), Melt Inclusions in Plutonic Rocks. Mineralogical Association of Canada, Montreal, Quebec, Canada, 1-25.

Boily-Auclair, E., Mercier-Langevin, P., Ross, P.-S. & Pitre, D. (2020). Stratigraphic setting of the LZ5 and Ellison mineralized zones, LaRonde Zone 5 Project, Doyon-Bousquet-LaRonde mining camp, Abitibi, Quebec: Geological Survey of Canada, Open File 8712, 57-73.

Botcharnikov, R.E., Linnen, R.L. & Holtz, F. (2010). Solubility of Au in Cl- and S-bearing hydrous silicate melts. *Geochimica et Cosmochimica Acta*, 74, 2396-2411.

Botcharnikov, R.E., Linnen, R.L., Wilke, M., Holtz, F., Jugo, P.J. & Berndt, J. (2011). High gold concentrations in sulphide-bearing magma under oxidizing conditions. *Nature Geoscience*, 4, 112-115.

Burnham, C.W. (1985). Energy release in subvolcanic environments: implications for breccia formation. *Economic Geology*, 80, 1515-1522.

Capriolo, M., Marzoli, A., Aradi, L., Callegaro, S., Dal Corso, J., Newton, R.J., Mills, B.J.W., Bartoli, O., Baker, D.R., Youbi, N., Remusat, L., Spiess, R. & Szabó, C. (2020). Deep CO2 in the

end-Triassic Central Atlantic Magmatic Province. *Nature Communications,* https://doi.org/10.1038/s41467-020-15325-6.

Chambefort, I., Dilles, J.H. & Kent, A.J.R. (2008). Anhydrite-bearing andesite and dacite as a source for sulfur in magmatic-hydrothermal mineral deposits. *Geology,* 36, 719-722.

Chang, J. & Audétat, A. (2021). LA-ICP-MS analysis of crystallized melt inclusions in olivine, plagioclase, apatite and pyroxene: quantification strategies and effects of post-emplacement modifications. *Journal of Petrology,* 62, https://doi.org/10.1093/petrology/egaa085.

Cherniak, D.J. & Watson, E.B. (2003). Diffusion in zircon. *Reviews in Mineralogy and Geochemistry,* 53, 113-143.

Cherniak, D.J., Hanchar, J.M. & Watson, E.B. (1997). Rare-earth diffusion in zircon. *Chemical Geology,* 134, 289-301.

Chiaradia, M. & Caricchi, L. (2022). Supergiant porphyry copper deposits are failed large eruptions. *Communication Earth and Environment,* 3, https://doi.org/10.1038/s43247-022-00440-7.

Colombini, L.L., Miller, C.F., Gualda, G.A.R., Wooden, J.L. & Miller, J.S. (2011). Sphene and zircon in the Highland Range volcanic sequence (Miocene, southern Nevada, USA): elemental partition, phase relations, and influence on evolution of silicic magma. *Contributions to Mineralogy and Petrology,* 102, 29-50.

Condie, K.C. (2005). TTGs and adakites: are they both slab melts?. *Lithos,* 80, 33-44.

Craddock, P.R. & Bach, W. (2010). Insights to magmatic-hydrothermal processes in the Manus back-arc basin as recorded by anhydrite. *Geochimica et Cosmochimica Acta,* 74, 5514-5536.

Dallai, L., Bianchini, G., Avanzinelli, R., Deloule, E., Natali, C., Gaeta, M., Cavallo, A. & Conticelli, S. (2022). Quartz-bearing rhyolitic melts in the Earth's mantle. *Nature,* https://doi.org/10.1038/s41467-022-35382-3.

Davis, D.W. (2002). U-Pb geochronology of Archean metasedimentary rocks in the Pontiac and Abitibi subprovinces, Quebec, constraints on timing, provenance, and regional tectonics. *Precambrian Research,* 115, 97−117.

Defant, M.J. & Drummond, M.S. (1990). Derivation of some modern arc magmas by melting of young subducted lithosphere. *Nature,* 347, 662–665.

Du, J. & Audétat, A. (2020). Early sulfide saturation is not detrimental to porphyry Cu-Au formation. *Geology,* https://doi.org/10.1130/G47169.1.

Dubé, B., Mercier-Langevin, P., Hannington, M.D., Davis, D.W. & Lafrance, B. (2004). Le gisement de sulfures massifs volcanogenes auriferes LaRonde, Abitibi, Quebec: Alteration, mineralisations, genese et implications pour l'exploration. Ministere des Ressources naturelles, de la Faune et des Parcs, Quebec Report MB 2004-03, 112 p.

Dubé, B., Mercier-Langevin, P., Hannington, M., Lafrance, B., Gosselin, G. & Gosselin, P. (2007). The LaRonde Penna world-class Au-rich volcanogenic massive sulfide deposit, Abitibi, Quebec: Mineralogy and geochemistry of alteration and implications for genesis and implications. *Economic Geology,* 102, 633-666.

Ebel, D.S. & Naldrett, A.J. (1997). Crystallization of sulfide liquids and the interpretation of ore composition. *Canadian Journal of Earth Sciences,* 34, 352-365.

El-Bouseily, A.M. & El-Sokkary, A.A. (1975). The relation between Rb, Ba, and Sr in granitic rocks. *Chemical Geology,* 16, 207-219.

Ferry, J.M. & Watson, E.B. (2007). New thermodynamic models and revised calibrations for the Ti-in-zircon and Zr-in-rutile thermometers. *Contributions to Mineralogy and Petrology,* 154, 429-437.

Fillion, M., Vallee, M. & Lavoie, C. (1977). Les gisements d'or de la SOQUEM Silverstack, Canton Bousquet, Quebec. *CIM Bulletin,* 70, 159−172.

Frei, D., Liebscher, A., Franz, G. & Dulski, P. (2004). Trace element chemistry of epidote minerals. *Reviews in Mineralogy and Geochemistry*, 56, 553-605.

Galley, A.G. (2003). Composite synvolcanic intrusions associated with Precambrian VMS-related hydrothermal systems. *Mineralium Deposita,* 387, 443-473.

Galley, A.G. & Lafrance, B. (2014). Setting and evolution of the Archean synvolcanic Mooshla Intrusive Complex, Doyon-Bousquet-LaRonde mining camp, Abitibi greenstone belt: emplacement history, petrogenesis, and implications for Au metallogenesis. *Economic Geology*, 109, 205-229.

Galley, A.G. & Mercier-Langevin, P. (in press). Mineralization and alteration at the Doyon deposit, Doyon-Bousquet-LaRonde mining camp, Québec, Canada: Example of an Archean subsea-floor Au(-Cu) porphyry-epithermal-style system. Geological Survey of Canada, Open File.

Getsinger, A., Rushmer, T., Jackson, M.D. & Baker, D. (2009). Generating high Mg-numbers and chemical diversity in tonalite-trondhjemite-granodiorite (TTG) magmas during melting and melt segregation in the continental crust. *Journal of Petrology*, 50, 1935-1954.

Goldie, R., Kotila, B. & Seward, D. (1979). The Don Rouyn mine: An Archean porphyry copper deposit near Noranda, Quebec. *Economic Geology*, 74, 1680–1684.

Gosselin, G. (1998). Veines de Quartz Aurifères Précoces à la Zone Ouest de la Mine Doyon, Canton de Bousquet, Preissac, Abitibi. M.Sc. thesis, Université du Québec à Chicoutimi, 125 p.

Götze, J. (2012). Application of cathodoluminescence microscopy and spectroscopy in geosciences. *Microscopy and Microanalysis*, 18, 1270-1284.

Grimes, C.B., Wooden, J.L., Cheadle, M.J. & John, B.E. (2015). “Fingerprinting” tectono-magmatic provenance using trace elements in igneous zircon. *Contributions to Mineralogy and Petrology,* 170, doi.org/10.1007/s00410-015-1199-3.

Grondahl, C. & Zajacz, Z. (2017). Magmatic controls on the genesis of porphyry Cu-Mo-Au deposits: The Bingham Canyon example. *Earth and Planetary Science Letters,* 480, 53-65.

Guha, J., Gauthier, A., Vallée, M., Descarreaux, J. & Lange-Brard, F. (1982). Gold mineralization at the Doyon mine (Silverstack), Bousquet, Quebec, in Hodder, R.W., and Petruk, W., eds., Geology of Canadian Gold Deposits. Canadian Institute of Mining and Metallurgy, Special Volume 24, 50-57.

Gunning, H.C. (1941). Region de Bousquet-Joannes, Quebec. Geological Survey of Canada Memoir 206, 80 p.

Halter, W.E., Pettke, T., Heinrich, C.A. & Rothern-Rutishauser, B. (2002). Major to trace element analysis of melt inclusions by laser-ablation ICP-MS: methods of quantification. *Chemical Geology,* 183, 63-86.

Halter, W.E., Pettke, T. & Heinrich, C.A. (2004a). Laser-ablation ICP-MS analysis of silicate and sulfide melt inclusions in an andesitic complex I: analytical approach and data evaluation. *Contributions to Mineralogy and Petrology,* 147, 385-396.

Halter, W.E., Pettke, T. & Heinrich, C.A. (2004b). Laser-ablation ICP-MS analysis of silicate and sulfide melt inclusions in an andesitic complex II: evidence for magma mixing and magma chamber evolution. *Contributions to Mineralogy and Petrology,* 147, 397-412.

Halter, W.E., Heinrich, C.A., & Pettke, T. (2005). Magma evolution and the formation of porphyry Cu-Au ore fluids: evidence from silicate and sulfide melt inclusions. *Mineralium Deposita*, 39, 845-863.

Hattori, K. & Cameron, E.M. (1986). Archean magmatic sulphate. *Nature,* 319, 45-47.

Holland, T. & Powell, R. (2001). Calculation of phase relations involving haplogranitic melts using an internally consistent thermodynamic dataset. *Journal of Petrology,* 42, 673-683.

Holtz, F., Pichavant, M., Barbey, P. & Johannes, W. (1992). Effects of H_2O on liquidus phase relations in the haplogranite system at 2 and 5 kbar. *American Mineralogist,* 77, 1223-1241.

Hoskin, P. W. O. & Schaltegger, U. (2003). The composition of zircon and igneous and metamorphic petrogenesis. In: Hanchar, J. M. & Hoskin, P.W. O. (eds) Zircon. Mineralogical Society of America and Geochemical Society, Reviews in Mineralogy and Geochemistry, 53, 27-62.

Jégo, S., Pichavant, M. & Mavrogenes, J.A. (2010). Controls on gold solubility in arc magmas: An experimental study at 1000C and 4 kbar. *Geochimica et Cosmochimica Acta,* 74, 2165-2189.

Johannes, W. & Holtz, F. (1996). Petrogenesis and experimental petrology of granitic rocks. Berlin: Springer, 335 p.

Jugo, P.J., Wilke, M. & Botcharnikov, R.E. (2010). Sulfur K-edge XANES analysis of natural and synthetic basaltic glasses: Implications for S speciation and S content as function of oxygen fugacity. *Geochimica et Cosmochimica Acta,* 74, 5926-5938.

Katz, L.R., Kontak, D.J., Dubé, B. & McNicoll, V. (2017). The geology, petrology, and geochronology of the Archean Côté Gold large-tonnage, low-grade intrusion-related Au(-Cu) deposit, Swayze greenstone belt, Ontario, Canada. *Canadian Journal of Earth Science,* 54, 173-202.

Katz, L.R., Kontak, D.J., Dubé, B., McNicoll, V., Creaser, R. & Petrus, J.A. (2021). An Archean porphyry-type gold deposit: The Côté gold Au(-Cu) deposit, Swayze Greenstone Belt, Superior Province, Ontario, Canada. *Economic Geology,* 116,47-89.

Keith, J.D., Whitney, J.A., Hattori, K., Ballantyne, G.H., Christiansen, E.H., Barr, D.L., Cannan, T.M. & Hook, C.J. (1997). The role of magmatic sulfides and mafic alkaline magmas in the Bingham and Tintic mining districts, Utah. *Journal of Petrology,* 38, 1679-1690.

Kullerud G., Yund R. A. & Moh G. H. (1969). Phase relations in the Cu–Fe–S, Cu–Ni–S and Fe–Ni–S system: In Magmatic Ore Deposits (eds. H.D.B Wilson), Economic Geology Monograph 4, 232-243.

Lafrance, B., Moorhead, J. & Davis, D.W. (2003). Cadre geologique du camp minier de Doyon-Bousquet-LaRonde. Ministere des Ressources naturelles, de la Faune et des Parcs, Quebec Reports ET 2002-07, 45 p., and ET 2002-07 C001 1:20,000 map sheet.

Lafrance, B., Davis, D.W., Goutier, J., Moorhead, J., Pilote, P., Mercier-Langevin, P., Dubé, B. & Galley, A. (2005). Nouvelles datations isotopiques dans la portion quebecoise du Groupe de Blake River et des unites adjacentes. Ministere des Ressources naturelles et de la Faune, Quebec Report RP 2005-01, 26 p.

Langshur, A. (1990). The geology, geochemistry and structure of the Mooshla intrusion, Bousquet mining centre, Quebec. Unpublished M.Sc. thesis, Ottawa, Canada, University of Ottawa, 172 p.

Large, S.J.E., Buret, Y., Wotzlaw, J.F., Karakas, O., Guillong, M., von Quadt, A. & Heinrich, C.A. (2021). Copper-mineralised porphyries sample the evolution of a large-volume silicic magma reservoir from rapid assembly to solidification. *Earth and Planetary Science Letters,* 563, https://doi.org/10.1016/j.epsl.2021.116877.

Laurent, O., Björnsen, J., Wotzlaw, J-F., Bretscher, S., Silva, M.P., Moyen, J-F., Ulmer, P. & Bachmann, O. (2020). Earth's earliest granitoids are crystal-rich magma reservoirs tapped by silicic eruptions. *Nature Geoscience,* https://doi.org/10.1038/s41561-019-0520-6.

Le Bas, M.J., Le Maitre, R.W., Streckeisen, A. & Zanettin, B. (1986). A chemical classification of volcanic rocks based on the total alkali-silica diagram. *Journal of Petrology,* 27, 745-750.

Lee, R.G., Dilles, J.H., Tosdal, R.M., Wooden, J.L. & Mazdab. F.K. (2017). Magmatic evolution of granodiorite intrusions at the El Salvador porphyry copper deposit, Chile, based on trace element composition and U/Pb age of zircons. *Economic Geology,* 112, 245-273.

Li, Y. & Audétat, A. (2015). Effects of temperature, silicate melt composition, and oxygen fugacity on the partitioning of V, Mn, Co, Ni, Cu, Zn, As, Mo, Ag, Sn, Sb, W, Au, Pb, and Bi between sulfide phases and silicate melt. *Geochimica et Cosmochimica Acta,* 162, 25-45.

Liou, P. & Guo, J. (2019). Generation of Archean TTG gneisses through amphibole-dominated fractionation. *Journal of Geophysical Research: Solid Earth,* 124, 3605–3619.

Loader, M.A., Wilkinson, J.J. & Armstrong, R.N. (2017). The effect of titanite crystallisation on Eu and Ce anomalies in zircon and its implication for the assessment of porphyry Cu deposit fertility. *Earth and Planetary Science Letters,* 472, 107-119.

Loucks, R.R., Fiorentini, M.L. & Henriquez, G.J. (2020). New magmatic oxybarometer using trace elements in zircon. *Journal of Petrology,* 61, 1-30.

Lowenstern, J.B. (1994). Dissolved volatile concentrations in an ore-forming magma. *Geology*, 22, 893-896.

Lowenstern, J.B. (2001). Carbon dioxide in magmas and implications for hydrothermal systems. *Mineralium Deposita,* 36, 490-502.

Lu, Y.J., Loucks, R.R., Fiorentini, M.L., McCuaig, T.C., Evans, N.J., Yang, Z.M., Hou, Z.Q., Kirkland, C.L., Parra-Avila, L.A. & Kobussen, A. (2016). Zircon compositions as a pathfinder for porphyry Cu ± Mo ± Au mineral deposits. *Society of Economic Geologists, Special Publication* 19, 329–347

Luhr, J.F. (2002). Sulfur isotope systematics of the 1982 El Chichón trachyandesite: an ion microprobe study. *Geochimica et Cosmochimica Acta,* 66, 3303-3316.

Luhr, J.F. (2008). Primary igneous anhydrite: Progress since its recognition in the 1982 El Chichón trachyandesite. *Journal of Volcanology and Geothermal Research,* 175, 394-407.

Marquis, P., Hubert, Brown, A.C. & Rigg, D.M. (1990). An evaluation of genetic models for gold deposits of the Bousquet district, Quebec, based on their mineralogical, geochemical and structural characteristics. *Canadian Institute of Mining and Metallurgy Special volume* 24, 383-399.

Martin, H. (1999). Adakitic magmas: modern analogues of Archean granitoids. *Lithos,* 46, 411-429.

Martin, H., Smithies, R.H., Rapp, R., Moyen, J.-F. & Champion, D. (2005). An overview of adakite, tonalite-trondhjemite-granodiorite (TTG), and sanukitoid: relationships and some implications for crustal evolution. *Lithos*, 79, 1-24.

McNicoll, V., Goutier, J., Dubé, B., Mercier-Langevin, P., Ross, P-S., Dion, C., Monecke, T., Legault, M., Percival, J. & Gibson, H. (2014). U-Pb geochronology of the Blake River Group, 241

Abitibi greenstone belt, Quebec, and implications for base metal exploration. *Economic Geology,* 109, 27-59.

Meagher, D.J. (2020). A melt inclusion study of rhyolitic volcanics in the Bousquet Formation, Doyon-Bousquet-LaRonde district, Abitibi Subprovince, Québec: insight into Archean magmatic processes. Unpublished MSc thesis, Saint Mary's University, 270 p.

Meng, X., Richards, J.P., Kontak, D.J., Simon, A.C., Kleinsasser, J.M., Marsh, J.H., Stern, R.A. & Jugo, P.J. (2021). Variable modes of formation for tonalite-trondhjemite-granodiorite-diorite(TTG-related porphyry-type Cu+-Au deposits in the Neoarchean southern Abitibi subprovince (Canada): evidence from petrochronology and oxybarometery. *Journal of Petrology,* 62, 1-29.

Mercier-Langevin, P., Dubé, B., Hannington, M.D., Davis, D.W., Lafrance, B. & Gosselin, G. (2007a). The LaRonde Penna Au-rich volcanogenic massive sulfide deposit, Abitibi greenstone belt, Quebec: Part 1. Geology and geochronology. *Economic Geology,* 102, 585−609.

Mercier-Langevin, P., Dubé, B., Hannington, M.D., Richer-Lafleche, M. & Gosselin G. (2007b) The LaRonde Penna Au-rich volcanogenic massive sulfide deposit, Abitibi greenstone belt, Quebec: Part 2. Lithogeochemistry and paleotectonic setting. *Economic Geology,* 102, 611−631.

Mercier-Langevin, P., Dubé, B., Lafrance, B., Hannington, M., Galley, A., Moorhead, J. & Gosselin, P. (2007c). Metallogeny of the Doyon-Bousquet-LaRonde mining camp, Abitibi

greenstone belt, Quebec. Geological Association of Canada, Mineral Deposits Division, Special Publication 5, 673−701.

Mercier-Langevin, P., Wright-Holfeld, A., Dubé, B., Bernier, C., Houle, N., Savoie, A. & Simard, P. (2009). Stratigraphic setting of the Westwood-Warrenmac ore zones, Westwood project, Doyon-Bousquet-LaRonde mining camp, Abitibi, Quebec. Geological Survey of Canada Current Research Paper 2009-03, 20 p.

Mercier-Langevin, P., Goutier, J., Ross, P.-S., McNicoll, V., Monecke, T., Dion, C., Dubé, B., Thurston, P., Becu, V., Gibson, H., Hannington, M. & Galley, A. (2011). The Blake River Group of the Abitibi greenstone belt and its unique VMS and gold-rich VMS endowment. Geological Survey of Canada Open File Report 6869, 61 p.

Mercier-Langevin, P., Dube, B., Blanchet, F., Pitre, D. & LaBerge, A. (2017). The LaRonde Penna Au-rich volcanogenic massive sulfide deposit. *Reviews in Economic Geology,* 19, 225-245.

Mercier-Langevin, P., Dubé, B. & Fortin, D. (2021). The Doyon-Bousquet-LaRonde Mining Camp. *Resources Mines & Industry,* Fall 2021, 44-61.

Miyoshi, T., Sakai, H. & Chiba, H. (1984). Experimental study of sulfur isotope fractionation factors between sulfate and sulfide in high temperature melts. *Geochemical Journal,* 18, 75-84.

Moyen, J.-F. (2009). High Sr/Y and La/Yb ratios: The meaning of the “adakitic signature”. *Lithos,* 112, 556-574.

Moyen, J.-F. & Martin, H. (2012). Forty years of TTG research. *Lithos*, 148, 312-336.

Müller, D., Franz, L., Herzig, P.M. & Hunt, S. (2001). Potassic igneous rocks from the vicinity of epithermal gold mineralization, Lihir Island, Papua New Guinea. *Lithos*, 57, 163-186.

Park, J-W., Campbell, I.H., Kim, J. & Moon, J-W. (2015). The role of late sulfide saturation in the formation of a Cu- and Au-rich magma: Insights from the platinum group element geochemistry of Niuatahi-Motutahi lavas, Tonga rear arc. *Journal of Petrology*, 56, 59-81.

Park, J-W., Campbell, I.H., Malaviarachchi, S.P.K., Cocker, H., Hao, H. & Kay, S.M. (2019). Chalcophile element fertility and the formation of porphyry Cu ± Au deposits. *Mineralium Deposita*, 54, 657-670.

Pearce, J.A., Harris, N.B.W. & Tindle, A.G. (1984). Trace element discrimination diagrams for the tectonic interpretation of granitic rocks. *Journal of Petrology*, 25, 956-983.

Perelló, J., Sillitoe, R.H. & Creaser, R.A. (2020). Mesoproterozoic porphyry copper mineralization at Mamainse Point, Ontario, Canada in the context of Midcontinent rift metallogeny. *Ore Geology Reviews*, 127, https://doi.org/10.1016/j.oregeorev.2020.103831.

Pilote, P., Robert, F., Sinclair, W.D., Kirkham, R.V. & Daigneault, R. (1995). Porphyry-type mineralization in the Doré Lake Complex: Clark Lake and Merrill Island areas. Geological Survey of Canada, Open File 3143, 65–86.

Qian, Q. & Hermann, J. (2013). Partial melting of lower crust at 10-15 kbar: constraints on adakite and TTG formation. *Contributions to Mineralogy and Petrology,* 165, 1195-1224.

Rapp, R.P., Watson, E.B. & Miller, C.F. (1991). Partial melting of amphibolite/eclogite and the origin of Archaean trondhjemites and tonalites. *Precambrian Research,* 51, 1- 25.

Richards, J.P. (2011). Magmatic to hydrothermal metal fluxes in convergent and collided margins. *Ore Geology Reviews,* 40, 1-26.

Richards, J.R. & Kerrich, R. (2007). Special paper: adakite-like rocks: their diverse origins and questionable role in metallogenesis. *Economic Geology,* 102, 537–576.

Roedder, E. (1984). Fluid inclusions. Mineralogical Society of America. In ed. Ribbe, P.H., Reviews in Mineralogy, 12, 1-646.

Rollinson, H. (2021). Do all Archaean TTG rock compositions represent former melts?. *Precambrian Research,* 367, https://doi.org/10.1016/j.precamres.2021.106448.

Ross, P.-S. & Bédard, J.H. (2009). Magmatic affinity of modern and ancient subalkaline volcanic rocks determined from trace-element discriminant diagrams. *Canadian Journal of Earth Sciences,* 46, 823-839.

Ross, P.-S., McNicoll, V., Goutier, J., Mercier-Langevin, P. & Dubé, B. (2011). Basaltic to andesitic volcaniclastic rocks in the Blake River Group, Abitibi Greenstone Belt: 2. Origin, geochemistry, and geochronology. *Canadian Journal of Earth Sciences,* 48, 757-777.

Savoie, A., Trudel, P., Sauve, P., Hoy, L. & Lao, K. (1991). Geologie de la mine Doyon (region de Cadillac). Ministere de l'Energie et des Ressources, Quebec, Report ET 90-05, 80 p.

Schmidt, M.W. & Thompson, A.B. (1996). Epidote in calc-alkaline magmas: An experimental study of stability, phase relationships, and the role of epidote in magmatic evolution. *American Mineralogist,* 81, 462-474.

Selby, D. & Creaser, R.A. (2001). Re-Os geochronology and systematics in molybdenite from the Endako porphyry molybdenum deposit, British Columbia, Canada. *Economic Geology*, 96, 197-204.

Shen, P., Hattori, K., Pan, H.D., Jackson, S. & Seitmuratova, E. (2015). Oxidation condition and metal fertility of granitic magmas: Zircon trace element data from porphyry Cu deposits in the Central Asian orogenic belt. *Economic Geology,* 110, 1861–1878.

Shinohara, H., Kazahaya, K. & Lowenstern, J.B. (1995). Volatile transport in a convecting magma column: implications for porphyry Mo mineralization. *Geology,* 23, 1091-1094.

Sigmarsson, O., Laporte, D., Carpentier, M., Devouard, B., Devidal, J-L. & Marti, J. (2013). Formation of U-depleted rhyolite from a basanite at El Hierro, Canary Islands. *Contributions to Mineralogy and Petrology*, 165, 601-622.

Smithies, R.H. (2000). The Archean tonalite-trondhjemite-granodiorite (TTG) series is not an analogue of Cenozoic adakite. *Earth and Planetary Science Letters*, 182, 115-125.

Smythe, D.J. & Brenan, J.M. (2016). Magmatic oxygen fugacity estimated using zircon-melt partitioning of cerium. *Earth and Planetary Science Letters*, 453, 260-266.

Stern, C.R., Funk, J.A., Skewes, M.A. & Arévalo, A. (2007). Magmatic anhydrite in plutonic rocks at the El Teniente Cu-Mo deposit, Chile, and the role of sulfur- and copper-rich magmas in its formation. *Economic Geology*, 102, 1335-1344.

Strauss, H. (2003). Sulphur isotopes and the early Archean sulphur cycle. *Precambrian Research*, 126, 349-361.

Student, J.J. & Bodnar, R.J. (2004). Silicate melt inclusions in porphyry copper deposits: identification and homogenization behavior. *The Canadian Mineralogist*, 42, 1583-1599.

Thomas, J.B., Bodnar, R.J., Shimizu, N. & Chesner, C.A. (2003). Melt Inclusions in Zircon. *Reviews in Mineralogy and Geochemistry*, 53, 63–87.

Trudel, P., Sauve, P., Tourigny, G., Hubert, C. & Hoy, L. (1992). Synthese des caracteristiques geologiques des gisements de la region de Cadillac (Abitibi). Ministere des Ressources naturelles, Quebec, Report MM 91-01, 106 p.

Tuttle, O. F. & Bowen, N. L. (1958). Origin of granite in the light of experimental studies in the system $NaAlSi_3O_8$–$KAlSi_3O_8$–SiO_2–H_2O. *Geological Society of America, Memoirs* 74, 146 p.

Valiant, R.I. & Hutchinson, R.W. (1982). Stratigraphic distribution and genesis of gold deposits, Bousquet region, northwestern Quebec. *Canadian Institute of Mining and Metallurgy Special Volume* 24, 27−40.

Watson, E.B. & Harrison, T.M. (1983). Zircon saturation revisited: temperature and composition effects in a variety of crystal magma types. *Earth and Planetary Science Letters,* 64, 295-304.

Webster, J.D. & Thomas, R. (2006). Silicate melt inclusions in felsic plutons: a synthesis and review. In: Webster JD (ed) Melt inclusions in plutonic rocks, vol 36. Mineralogical Association of Canada Short Course, Canada, 165–188.

Webster, J.D., Goldoff, B. & Shimizu, N. (2011). C-O-H-S fluids and granitic magma: how S partitions and modifies CO_2 concentrations of fluid-saturated felsic melt at 200 MPa. *Contributions to Mineralogy and Petrology,* 162, 849-865.

Wilke, S., Holtz, F., Neave, D.A. & Almeev, R. (2017). The effect of anorthite content and water on quartz-feldspar cotectic compositions in the rhyolitic system and implication for geobarometry. *Journal of Petrology,* 58, 789-818.

Wones, D.R. (1989). Significance of the assemblage titanite + magnetite + quartz in granitic rocks. *American Mineralogist,* 74, 744-749.

Yergeau, D., Mercier-Langevin, P.L., Dubé, B., Malo, M. & Savoie, A. (2022a). The Westwood Deposit, Southern Abitibi Greenstone Belt, Canada: An Archean Au-Rich Polymetallic Magmatic-Hydrothermal System-Part I. Volcanic Architecture, Deformation, and Metamorphism. *Economic Geology,* 117, 545-575.

Yergeau, D., Mercier-Langevin, P.L., Dubé, B., McNicoll, V., Jackson, S.E., Malo, M. & Savoie, A. (2022b). The Westwood Deposit, Southern Abitibi Greenstone Belt, Canada: An Archean Au-Rich Polymetallic Magmatic-Hydrothermal System—Part II. Hydrothermal Alteration, Mineralization, and Geologic Model. *Economic Geology,* 117, 577-608.

Zajacz, Z. & Halter, W.E. (2007). LA-ICPMS analyses of silicate melt inclusions in co-precipitated minerals: quantification, data analysis and mineral/melt partitioning. *Geochimica et Cosmochimica Acta,* 71, 1021-1040.

Zajacz, Z., Halter, W.E., Pettke, T. & Guillong, M. (2008). Determination of fluid/melt partition coefficients by LA-ICPMS analysis of co-existing fluid and silicate melt inclusions: controls on element partitioning. *Geochimica et Cosmochimica Acta,* 72, 2169-2197.

Zajacz, Z., Hanley, J.J., Heinrich, C.A., Halter, W.E. & Guillong, M. (2009). Diffusive reequilibration of quartz-hosted silicate melt and fluid inclusions: are all metal concentrations unmodified? *Geochimica et Cosmochimica Acta*, 73, 3013-3027.

Zajacz, Z., Candela, P.A., Piccoli, P.M., Wälle, M. & Sanchez-Valle, C. (2012). Gold and copper in volatile saturated mafic to intermediate magmas: solubilities, partitioning, and implications for ore deposit formation. *Geochimica et Cosmochimica Acta*, 91, 140-159.

Zajacz, Z., Candela, P.A., Piccoli, P.M., Sanchez-Valle, C. & Wälle, M. (2013). Solubility and partitioning behavior of Au, Cu, Ag, and reduced S in magmas. *Geochimica et Cosmochimica Acta*, 112, 288-304.

Zhang, D. & Audétat, A. (2017). What caused the formation of the giant Bingham Canyon porphyry Cu-Mo-Au deposit? Insights from melt inclusions and magmatic sulfides. *Economic Geology*, 112, 221-244.

3.10 TABLES

Table 3.1: Mineralogy of Zircon-hosted silicate melt and mineral inclusions

Lithology	Gabbro	High Th/U Quartz Diorite	Low Th/U Quartz Diorite	Tonalite	Tonalite	Aphyric Trondhjemite	Aphyric Trondhjemite
Sample	715.6	127.6	493.7	Stop 10	Stop 11	1323	1444.5
Inclusion Varieties							
SMI[1]	A	A	A	A	A	A	A
SMI + Quartz			A		A		
SMI + Albite			A, B		A		
SMI + Biotite					A		
SMI + Magnetite			A		A		
SMI + Ilmenite		A					
SMI + Chalcopyrite					A, C		
Titanite + SMI?		A					
Apatite			A, B, C	A, B	A, B, C	A	A
Quartz		A, B	A, B	A, B	A, B		
Epidote			A		A		
Albite		A, B	A	A	A, B		
Biotite				A			
Magnetite				A	C		
Chlorite[2]	A	A	A, B	A	A		A
Quartz + Biotite		A					
Quartz + Titanite		A					
Quartz + Epidote			A		A		
Quartz + Magnetite		C		A	A		
Albite + K-feldspar			A	A			
Albite + Epidote				A			A
Apatite + Magnetite				A			
Apatite + Monazite					A	A	
Quartz + Chlorite[2]		A	A	A			
Quartz + Calcite[2]		A					
Albite + Calcite[2]		A					
Apatite + Chlorite[2]			A			A	
Magnetite + Chlorite[2]					A		
Titanite + Chlorite[2]				A			
Epidote + Calcite[2]			A				
Quartz + Albite + K-feldspar		A			A		
Quartz + Albite + Biotite			A	A			
Quartz + K-feldspar + Biotite			A				
Albite + K-feldspar+ Biotite				A	A		
Albite + K-feldspar + Ilmenite					A		
Albite + Titanite + Epidote					A		
Ilmenite + Rutile + Titanite			A				
Quartz + Biotite + Chlorite[2]					A		
Albite + Magnetite + Chlorite[2]				A			
Quartz + Albite + K-feldspar + Biotite	A			A	A		
Albite + K-feldspar + Biotite + Apatite		A					
Quartz + Epidote + Amphibole? + Chlorite[2]				A			
Quartz + Albite + K-feldspar + Biotite + Apatite		A					
Albite + K-feldspar + Biotite + Apatite + Titanite		A					
Quartz + Albite + K-feldspar + Biotite + Titanite			A				

[1] SMI = silicate melt inclusion

[2] Indicates alteration mineral

Method of identification: A = SEM-EDS, B = EPMA, C = LA-ICPMS, D = Raman

Table 3.2: Mineralogy of quartz-hosted silicate melt and mineral inclusions

Lithology	Gabbro	Low-Th/U Quartz Diorite	Roof Quartz Diorite	Aphyric Trondhjemite
Phase	B	C	E	I
Sample	715.6	493.7	459	534
SMI	A, C	A, C	C	C
Melt + Albite	A			
Melt + Rutile	C	C	C	
Melt + Zircon	C	C	C	C
Melt + Epidote	C	C		
Melt + Sulphide	C	C	C	C
Albite			C	
K-feldspar				C
Titanite + Muscovite		D		
Epidote + Muscovite		D		
Albite + Epidote + Calcite		D		
Epidote + Rutile + Calcite		D		

Method of identification: A = SEM-EDS, B = EPMA, C = LA-ICPMS, D = Raman

Table 3.3: Representative Zircon-hosted Silicate Melt Inclusion Compositions determined by SEM-EDS and EPMA on Exposed Inclusions

Lithology	MIC Phase	Sample	Method	Inclusion ID	SiO_2 (wt%)	TiO_2	Al_2O_3	FeO	MnO	MgO	CaO	Na_2O	K_2O	P_2O_5	Cl	F	H_2O	SO_3
Gabbro	B	715.6-NA-M	SEM-EDS	2	76.31	0.03	13.98	0.25		0.00	2.41	2.89	4.13					
Gabbro	B	715.6-An-L	EMPA	A1-d	78.02	0.02	11.19	0.05	0.01	0.00	2.14	2.50	2.33	0.00	0.01	0.05	3.7	0.00
High Th/U QD	C	127.6-NA-Sm	SEM-EDS	9	77.37	0.19	13.21	0.56		0.04	1.93	2.88	3.82		0.01			
High Th/U QD	C	127.6-An-L	SEM-EDS	2	75.83	0.54	12.47	0.64		0.00	0.64	5.39	4.51		0.48			
High Th/U QD	C	127.6-An-M	SEM-EDS	8	70.65	0.43	16.02	0.60		0.16	1.89	5.51	4.75		0.82			
High Th/U QD	C	127.6-An-Sm	EMPA	A2-2	71.06	0.04	20.48	0.05	0.00	0.01	0.69	4.81	2.13	0.00	0.02	0.00	0.7	0.00
High Th/U QD	C	127.6-An-M	EMPA	A2-b	73.07	0.47	13.63	1.04	0.06	0.06	1.50	2.34	3.23	0.00	0.08	0.00	4.5	0.04
Low Th/U QD	C	493.7-NA-L	SEM-EDS	5	77.15	0.26	12.54	0.52		0.13	0.97	5.12	3.31					
Low Th/U QD	C	493.7-NA-L	SEM-EDS	26	74.09	0.21	13.82	0.40		0.16	0.84	6.10	4.38					
Low Th/U QD	C	493.7-An-L	EMPA	A6-b	75.04	0.68	12.51	1.35	0.00	0.06	1.44	3.03	3.56	0.00	0.38	0.4	1.5	0.00
Low Th/U QD	C	493.7-An-L	EMPA	A7	72.41	0.35	12.51	0.39	0.07	0.02	1.37	2.62	3.28	0.00	0.41	0.3	6.3	0.00
Tonalite	D	Stop 11-NA-L	SEM-EDS	40	75.02	0.20	14.45	0.56		0.16	1.03	5.83	2.75					
Tonalite	D	Stop 11-An-L	SEM-EDS	12	76.57	0.22	13.40	0.00		0.20	1.07	7.06	1.49		0.11			
Tonalite	D	Stop 11-An-L	SEM-EDS	14	67.81	0.58	15.20	2.02		1.17	1.75	8.59	2.88		0.36			
Tonalite	D	Stop 10-NA-L	SEM-EDS	34	74.94	0.00	13.46	1.67		0.19	0.00	6.12	3.62					
Tonalite	D	Stop 10-An-L	SEM-EDS	3	76.69	0.06	11.68	0.83		0.12	1.24	5.67	3.72		2.13			
Phyric Trondhjemite	H	Bousquet-4	SEM-EDS	117	75.77	0.00	14.17	0.37		0.30	1.68	4.25	3.45		0.19			
Phyric Trondhjemite	H	Bousquet-4	SEM-EDS	120	71.84	0.34	15.86	0.45		1.29	1.01	5.53	3.68		0.22			
Aphyric Trondhjemite	I	1323-NA-XS	SEM-EDS	8	76.46	0.00	13.97	0.15		0.08	0.99	4.60	3.76					
Aphyric Trondhjemite	I	1323-NA-XS	SEM-EDS	10	73.41	0.00	14.55	0.00		0.33	1.68	5.29	4.74		0.04			
Aphyric Trondhjemite	I	1444.5-NA-XS	SEM-EDS	6	72.31	0.00	14.72	0.11		0.55	1.13	6.54	4.64					
Aphyric Trondhjemite	I	1444.5-NA-XS	SEM-EDS	6	77.43	0.36	12.31	1.03		0.30	0.45	4.65	3.47		0.15			

Table 3.4: Quartz-hosted Silicate Melt Inclusion Compositions determined by SEM-EDS and EPMA on Exposed Inclusions

Lithology	MIC Phase	Sample	Method	Inclusion ID	SiO_2 (wt%)	TiO_2	Al_2O_3	FeO	MnO	MgO	CaO	Na_2O	K_2O	P_2O_5	Cl	F	H_2O	SO_3
Gabbro	B	715.6	SEM-EDS	1-2	77	0.12	12.82	0.49		0.03	0.32	5.18	3.67		0.32			
Gabbro	B	715.6	SEM-EDS	3-1	79.53	0.09	10	1.45		0.41	0.18	3.88	3.96		0.5			
Gabbro	B	715.6	SEM-EDS	4-1	77.82	0.04	11.5	1.52		0.37	0.2	3.63	4.37		0.36			
Low Th/U QD	C	493.7	SEM-EDS	4-1	82.2	0.19	8.53	1.84		0.11	1.68	3.21	2.06		0.18			
Low Th/U QD	C	493.7	SEM-EDS	1-2	81.74	0.1	10.11	0.85		0.12	0.24	3.36	3.25		0.22			
Low Th/U QD	C	493.7	SEM-EDS	1-3	77.16	0.2	13.16	0.88		0.24	0.33	4.25	3.66		0.13			
Low Th/U QD	C	493.7	SEM-EDS	2-4	77.69	0.14	11.57	1.77		0.11	3.14	2.67	2.89		0.02			
Low Th/U QD	C	493.7	SEM-EDS	1-5	81.27	0.12	9.6	1.18		0.11	1.53	4.31	1.7		0.18			
Low Th/U QD	C	493.7	SEM-EDS	1-6	80.66	0.04	11.2	2.12		0.2	0.35	2.28	2.97		0.19			
Low Th/U QD	C	493.7	SEM-EDS	1-7	77.51	0.28	8.7	4.32	0.02	0.05	1.93	3.7	2.57		0.93			
Low Th/U QD	C	493.7	SEM-EDS	1-8	85.25	0.18	9.24	0.12	0	0.04	0.72	3.96	0.21		0.28			
Low Th/U QD	C	493.7	SEM-EDS	1-10	76.85	0.29	11.88	4.16	0.03	0.33	0.56	2.47	3.26		0.17			

3.11 FIGURES

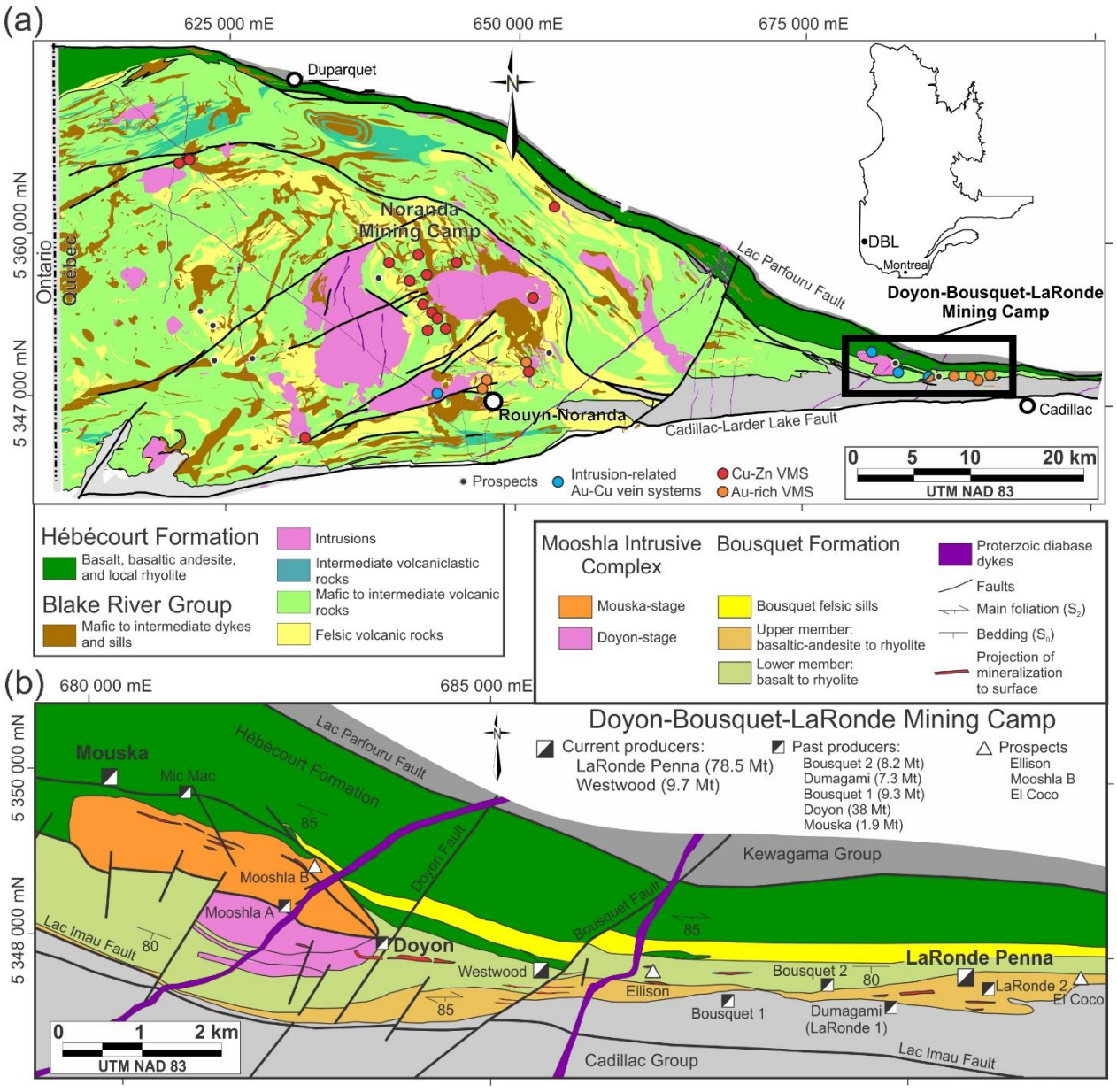

Fig. 3.1: (a) Simplified geological map of the eastern Blake River Group of the Abitibi greenstone belt showing the location of the Doyon-Bousquet-LaRonde mining camp. (b) Simplified geological map of the Doyon-Bousquet-LaRonde mining camp showing the location of the Mooshla intrusive complex and spatial relationship to mines in the area. Modified from Mercier-Langevin, 2009.

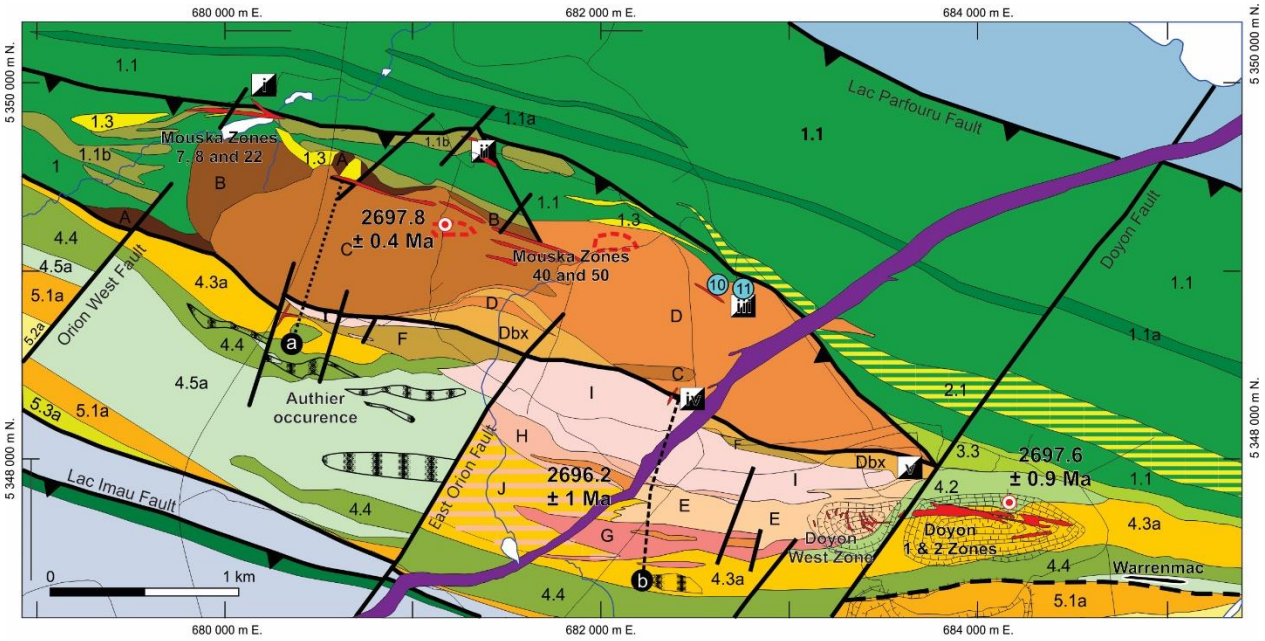

Intrusive rocks

- Proterozoic diabase

Mooshla intrusive complex

Doyon stage

- I — Aphyric to quartz porphyritic trondhjemite
- J — Interlayered Phase H and I in Unit 4.3a
- H — Plagioclase-quartz porphyritic trondhjemite
- G — Plagioclase porphyritic tonalite
- F — Plagioclase-horneblende porphyritic tonalite

Mouska stage

- E — "Doyon quartz diorite": pendant of Dbx
- Dbx — Xenolith-rich tonalite: Phase D hangingwall contact
- D — Tonalite
- C — Quartz diorite
- B — Layered gabbro
- A — Aphyric/feldspar porphyritic diorite

Sedimentary rocks

- **Cadillac sedimentary rocks**
- **Kewagama sedimentary rocks**

Volcanic rocks

Bousquet Formation

Upper Bousquet

- 5.3a — **Bousquet-Ferris QFP rhyolite**
- 5.2a — **Doyon rhyodacite-rhyolite**
- 5.1a — **Doyon dacite-rhyodacite**

Lower Bousquet

- 4.5a — **Warrenmac rhyodacite** Rhyodacitic schist
- 4.4 — **Bousquet heterogeneous unit** Basaltic to andesitic schist
- 4.3a — **Doyon mine felsic Unit** Dacitic to rhyolitic schist
- 4.2 — **Doyon glomeroporphyritic** dacite
- 3.3 — **Bousquet scoriaceous tuff** Andesite and dacite
- 2.1 — **Bousquet felsic sills swarm** Rhyolite

Hébécourt Formation

- 1.3 — Rhyolite
- 1.1b — Magnetite-rich basalt and basaltic andesite
- 1.1a — Glomerporphyritic basalt and basaltic andesite
- 1.1 — Basalt and basaltic andesite flows

Mineralization

- Gold mine: i: Mouska; ii: Mic Mac iii: Mooshla B; iv: Mooshla A; v: Doyon
- Gold lens
- Anomalous gold zone
- Massives sulfides zone
- Massives sulfides horizon
- VMS stringer mineralization
- Open Pit

Sample locations

- Drill hole (a: MSK-G-810; b: 1106-96)
- Surface sample (10: Stop 10; 11: Stop 11)

Fig. 3.2: Geological map of the Mooshla intrusive complex (modified from Galley & Lafrance, 2014). Location of drill holes and surface samples utilized in the study are indicated. Zircon U-Pb ages are from Lafrance *et al.*, 2005 and McNicoll *et al.*, 2014.

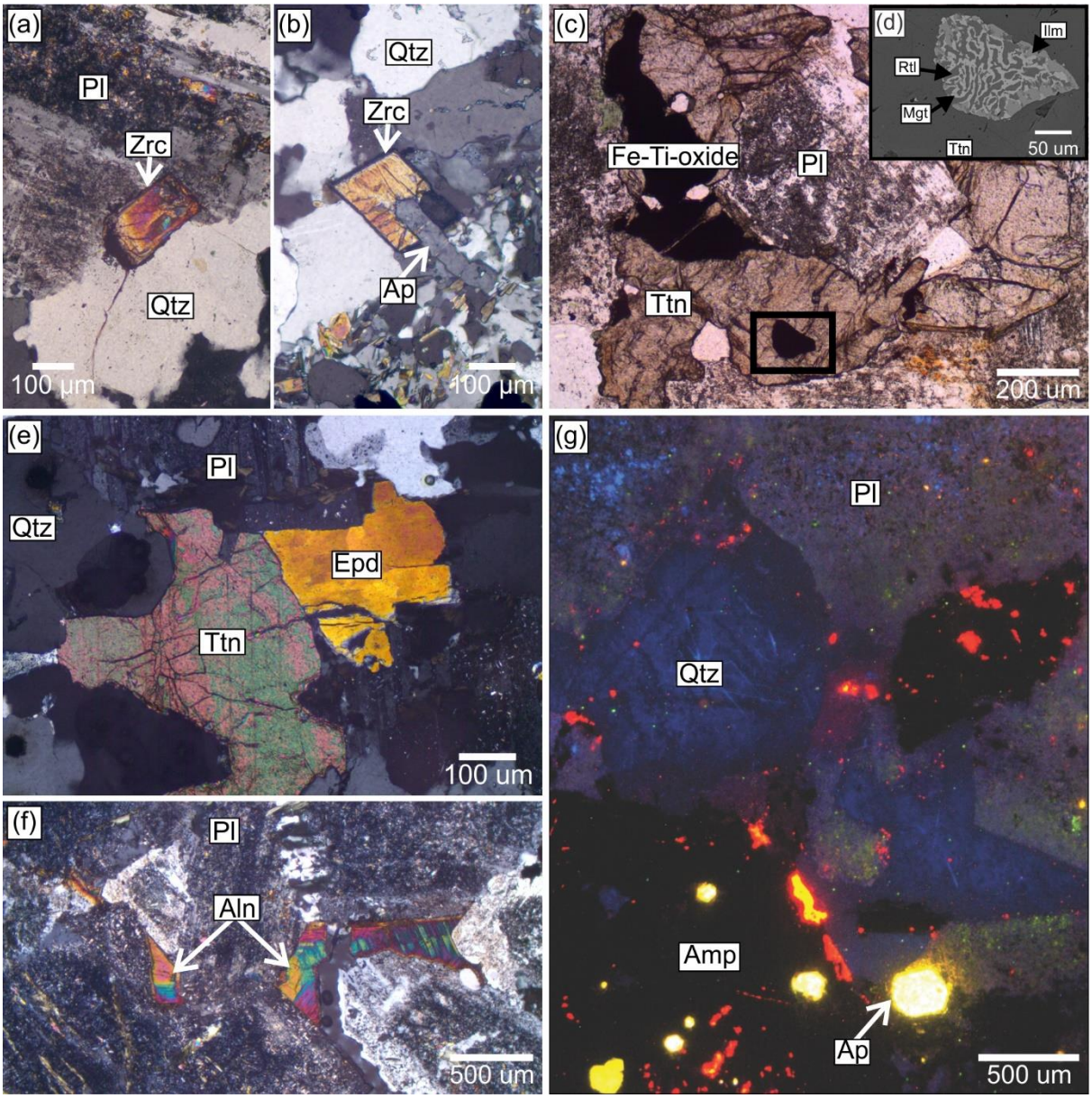
(a)
Pl
Zrc
Qtz
100 µm
(b)
Qtz
Zrc
Ap
100 µm
(c)
Fe-Ti-oxide
Pl
Ttn
200 um
(d)
Ilm
Rtl
Mgt
Ttn
50 um
(e)
Pl
Qtz
Epd
Ttn
100 um
(f)
Pl
Aln
500 um
(g)
Pl
Qtz
Amp
Ap
500 um

Fig. 3.3: Accessory mineral petrography. (a) Interstitial, tabular zircon from phase D tonalite (sample Stop 10; XPL). (b) Interstitial zircon intergrown with apatite from phase D tonalite (sample Stop 11; XPL). (c) Interstitial titanite with inclusions and partial inclusions of Fe-Ti-oxides (see frame d) from phase D tonalite (sample from Stop 10; plane-polarized light [PPL]). (d) Fe-Ti-oxide inclusion composed of rutile, ilmenite, and magnetite in titanite (sample form Stop 10; SEM-BSE image). (e) Interstitial titanite and epidote sharing a mutual grain boundary in phase D tonalite (sample from Stop 11; XPL). (f) Interstitial allanite from phase D tonalite (sample from Stop 10; XPL). (g) A hot-CL image of coarse interstitial quartz occurring between amphibole and plagioclase from phase C low-Th/U quartz diorite. Interstitial apatite is also present. Note the blue CL color of quartz consistent with a magmatic origin, whereas metamorphic quartz related to regional metamorphic conditions (greenschist to lower amphibolite facies) would be red-brown (Götze *et al.*, 2001 and references therein). Aln = allanite; Amp = amphibole; Ap = apatite; Epd = epidote; Ilm = ilmenite; Mgt = magnetite; Pl = plagioclase; Qtz = quartz; Rtl = rutile; Ttn = titanite; Zrc = zircon.

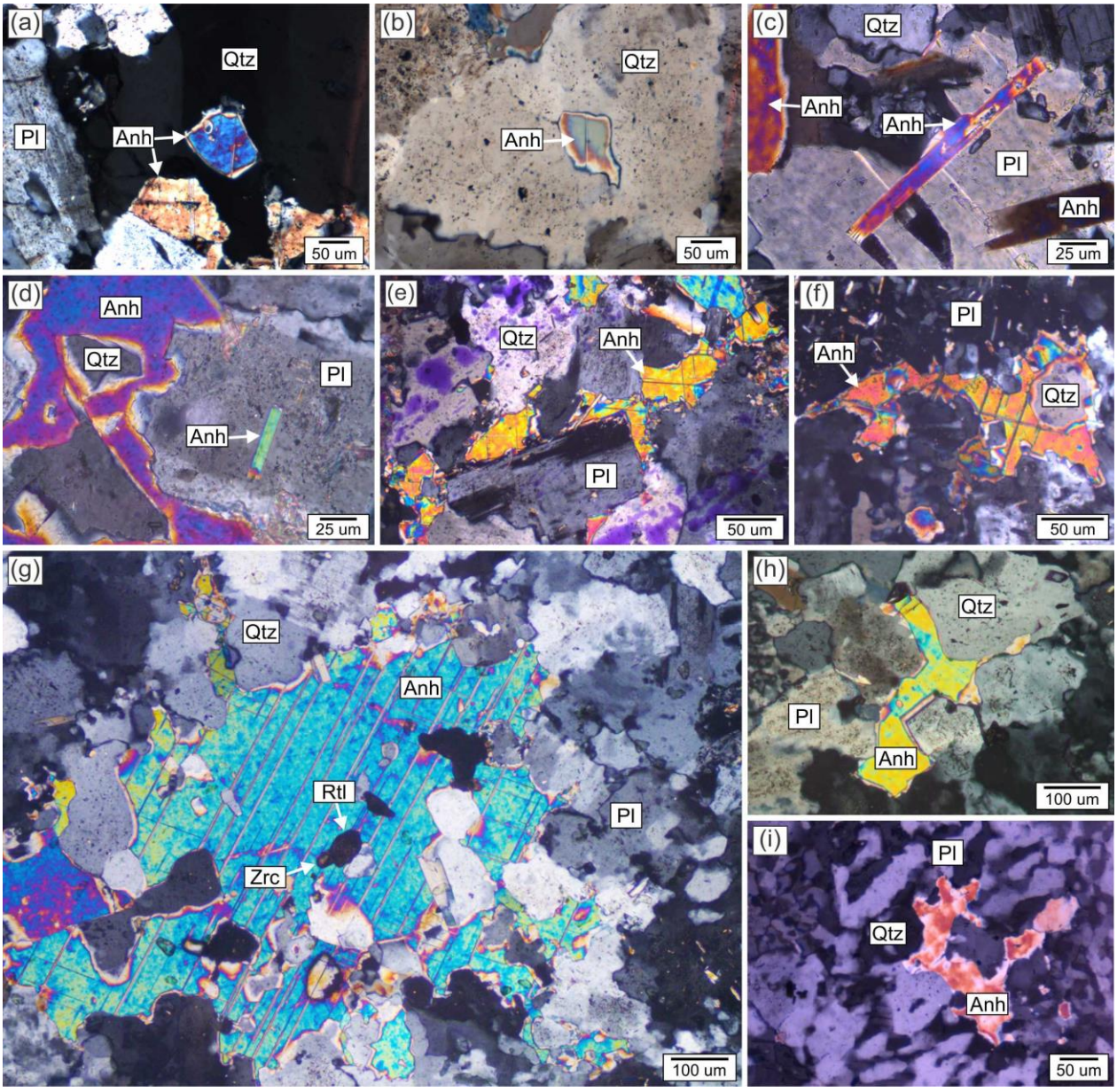
(a)
Qtz
Pl
Anh
50 um
(b)
Qtz
Anh
50 um
(c)
Qtz
Anh
Anh
Pl
Anh
25 um
(d)
Anh
Qtz
Pl
Anh
25 um
(e)
Qtz
Anh
Pl
50 um
(f)
Pl
Anh
Qtz
50 um
(g)
Qtz
Anh
Rtl
Pl
Zrc
100 um
(h)
Qtz
Pl
Anh
100 um
(i)
Pl
Qtz
Anh
50 um

Fig. 3.4: Representative photomicrographs of anhydrite in the aphyric trondhjemite. All images were taken in cross polarized light. (a) Inclusion of anhydrite in quartz and interstitial anhydrite located on the edge of quartz grains. (b) Anhydrite inclusion in quartz. (c-d) Inclusions of anhydrite in plagioclase and anhydrite occurring interstitial to plagioclase and quartz. (e-f) Anhydrite occurring interstitial to plagioclase and quartz. (g) Coarse-grained interstitial anhydrite with inclusions of rutile and zircon. (h) Interstitial anhydrite with straight, planar grain boundaries with plagioclase and quartz. (i) Anhydrite occurring interstitial with graphic texture of quartz and plagioclase. Anh = anhydrite; Pl = plagioclase; Qtz = quartz; Rtl = rutile; Zrc = zircon.

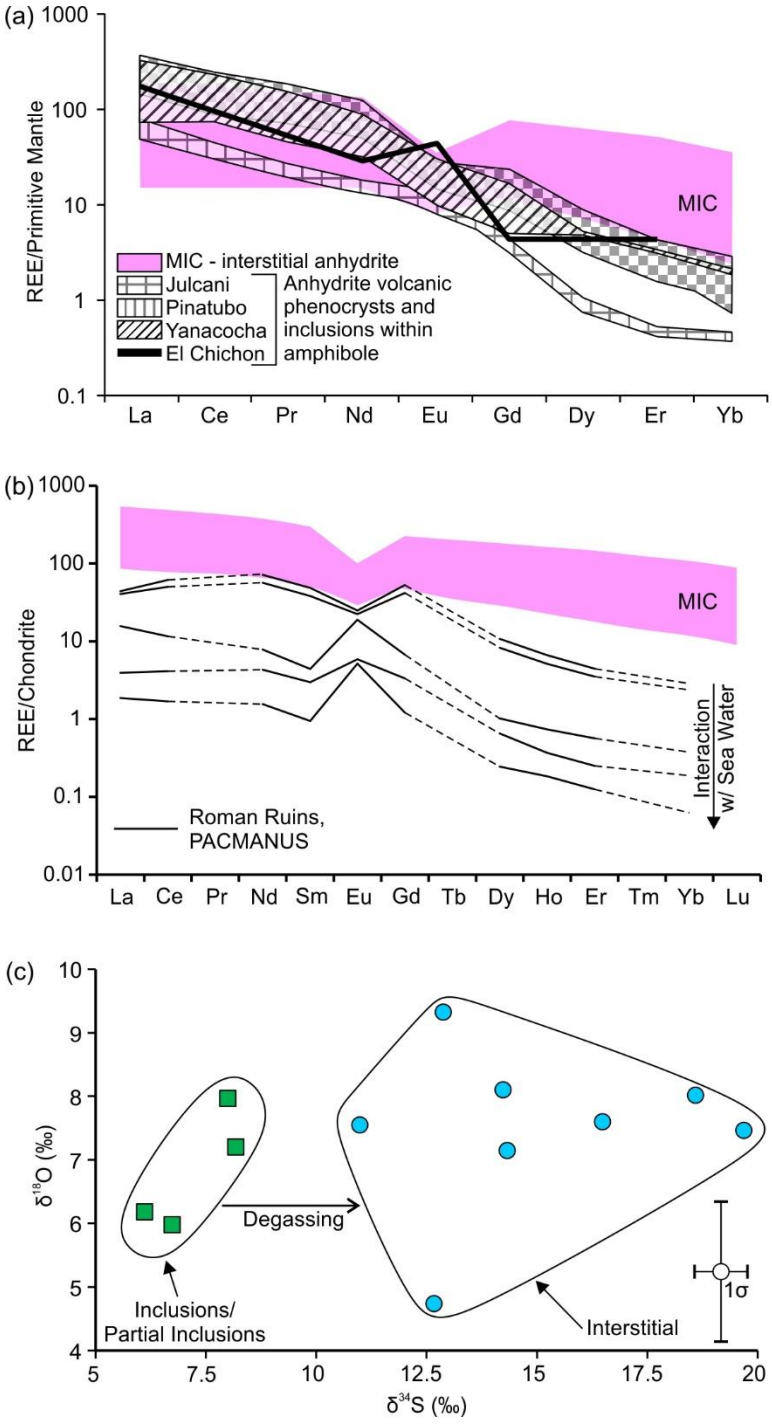
(a)
1000
100
10
1
0.1
REE/Primitive Mantle
MIC
MIC - interstitial anhydrite
Julcani
Pinatubo
Yanacocha
El Chichon
Anhydrite volcanic phenocrysts and inclusions within amphibole
La Ce Pr Nd Eu Gd Dy Er Yb
(b)
1000
100
10
1
0.1
0.01
REE/Chondrite
MIC
Interaction w/ Sea Water
Roman Ruins, PACMANUS
La Ce Pr Nd Sm Eu Gd Tb Dy Ho Er Tm Yb Lu
(c)
10
9
8
7
6
5
4
δ18O (‰)
Degassing
Inclusions/ Partial Inclusions
Interstitial
1σ
5 7.5 10 12.5 15 17.5 20
δ34S (‰)

Fig. 3.5: Anhydrite trace element and isotopic compositions in the MIC compared to different magmatic-hydrothermal settings. (a) Primitive-mantle normalized REE diagram comparing anhydrite composition from the MIC to volcanic anhydrite phenocrysts and anhydrite inclusions in amphibole and clinopyroxene from volcanic rocks (Julcani, Yanacocha, and Pinatubo data from Chambefort *et al.*, 2008; El Chichon data from Luhr, 1990). (b) Chondrite normalized REE plots of anhydrite from the MIC and anhydrite from the Roman Ruins vent field, PACMANUS Basin (Craddock and Bach, 2010). It is important note in the Roman Ruins analyses that the shift from high REE and positive Eu anomalies to lower REE contents and positive Eu anomalies records the shift from hydrothermal-dominant to seawater-dominant process. (c) Oxygen ($\delta^{18}O$) plotted against sulfur ($\delta^{34}S$) isotopic compositions for MIC anhydrite. Inclusion and partial inclusion anhydrite have significantly lower $\delta^{34}S$ values compared to interstitial anhydrite and is the result of degassing (see text for discussion).

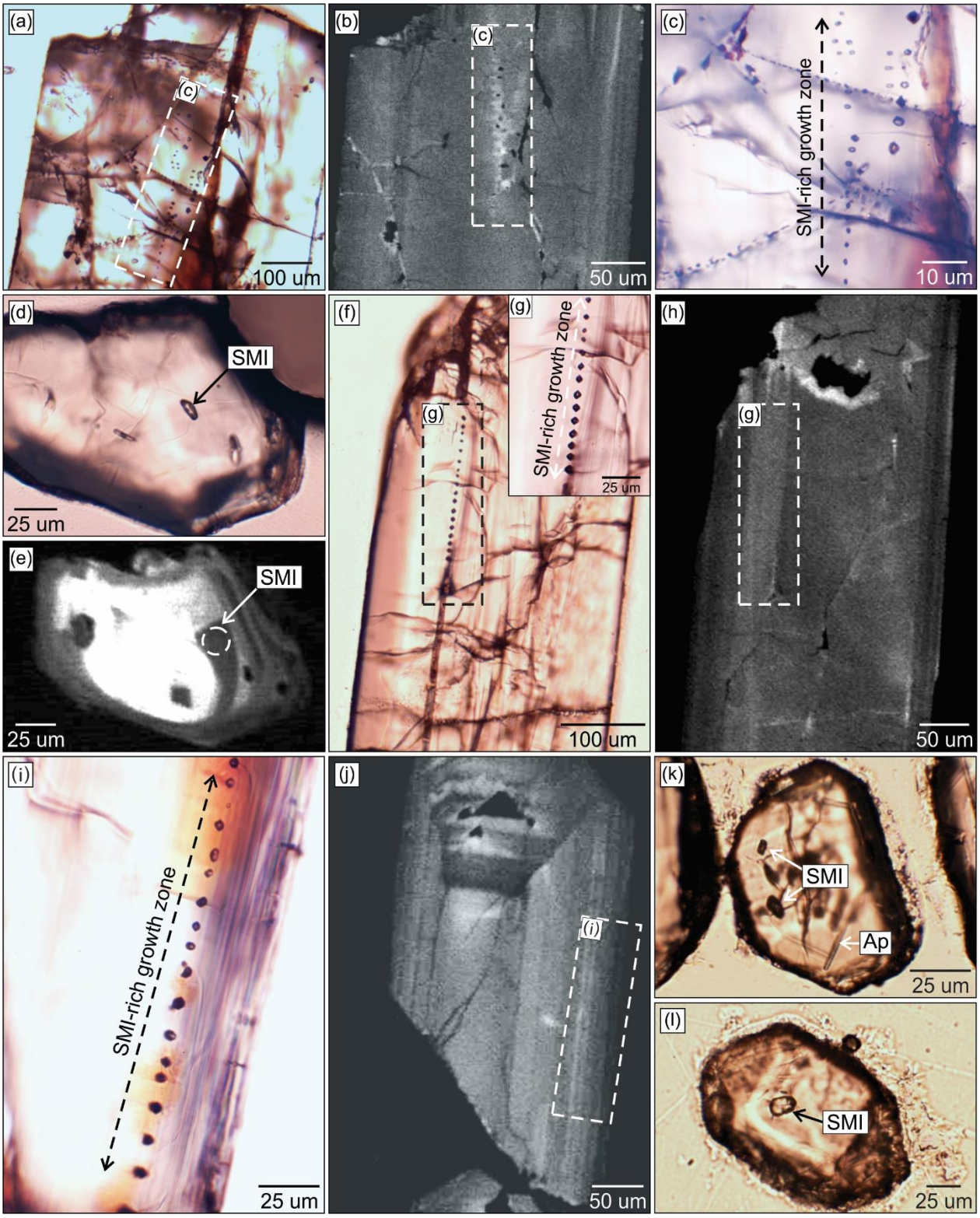
(a)
(c)
100 um
(b)
(c)
50 um
(c)
SMI-rich growth zone
10 um
(d)
SMI
25 um
(e)
SMI
25 um
(f)
(g)
(g)
SMI-rich growth zone
25 um
100 um
(h)
(g)
50 um
(i)
SMI-rich growth zone
25 um
(j)
(i)
50 um
(k)
SMI
Ap
25 um
(l)
SMI
25 um

Fig. 3.6: Representative photomicrographs and SEM-CL images of zircon-hosted silicate melt inclusions (SMI) from various phases in the Mooshla intrusive complex. (a) Zircon from the phase B gabbro with a silicate melt inclusion assemblage occurring in the center of the grain (outlined by hashed rectangle; sample 715.6; plane-polarized light [PPL]. (b) Same zircon as in (a), except it is a SEM-CL image. Note there is no inherited cores or disrupted zoning patterns where the SMI assemblage is occurring. (c) Magnified view of the zircon-hosted SMI assemblage outlined in (a) and (b). (d) Zircon from the high-Th/U quartz diorite of phase C hosting a SMI that occurs in a growth zone that parallels the grain boundary (sample 127.6; PPL). (e) SEM-CL image of the same grain displayed in (d). The dashed circle in the center right of the grain is the growth zone hosting the SMI shown in (d). (f) Zircon from the low-Th/U quartz diorite of phase C with an SMI assemblage occurring along a growth zone (sample 493.7; PPL). (g) Magnified view of the SMI assemblage outlined in (f). (h) SEM-CL image of the same grain displayed in (f). Note the lack of inherited core and consistent growth zoning pattern where the SMI assemblage is occurring, indicating the SMI are of primary origin. (i) Zircon from the phase D tonalite hosting an assemblage of SMI along a growth zone that parallels the outer edge of the grain (sample Stop 11; PPL). (j) SEM-CL image of the same grain displayed in (i). Note the lack of inherited core and consistent growth zoning pattern where the SMI assemblage is occurring, indicating the SMI are of primary origin. (k) Zircon from the phase I aphyric trondhjemite containing SMI that occur in growth zones that parallel the outer edges of the grain. Apatite inclusions are present in random orientations compared to the SMI (sample 1444.5; PPL). (l) Zircon from the phase I aphyric trondhjemite containing SMI that occurs in the center of the grain (sample 1323; PPL). SMI = silicate melt inclusion; Ap = apatite.

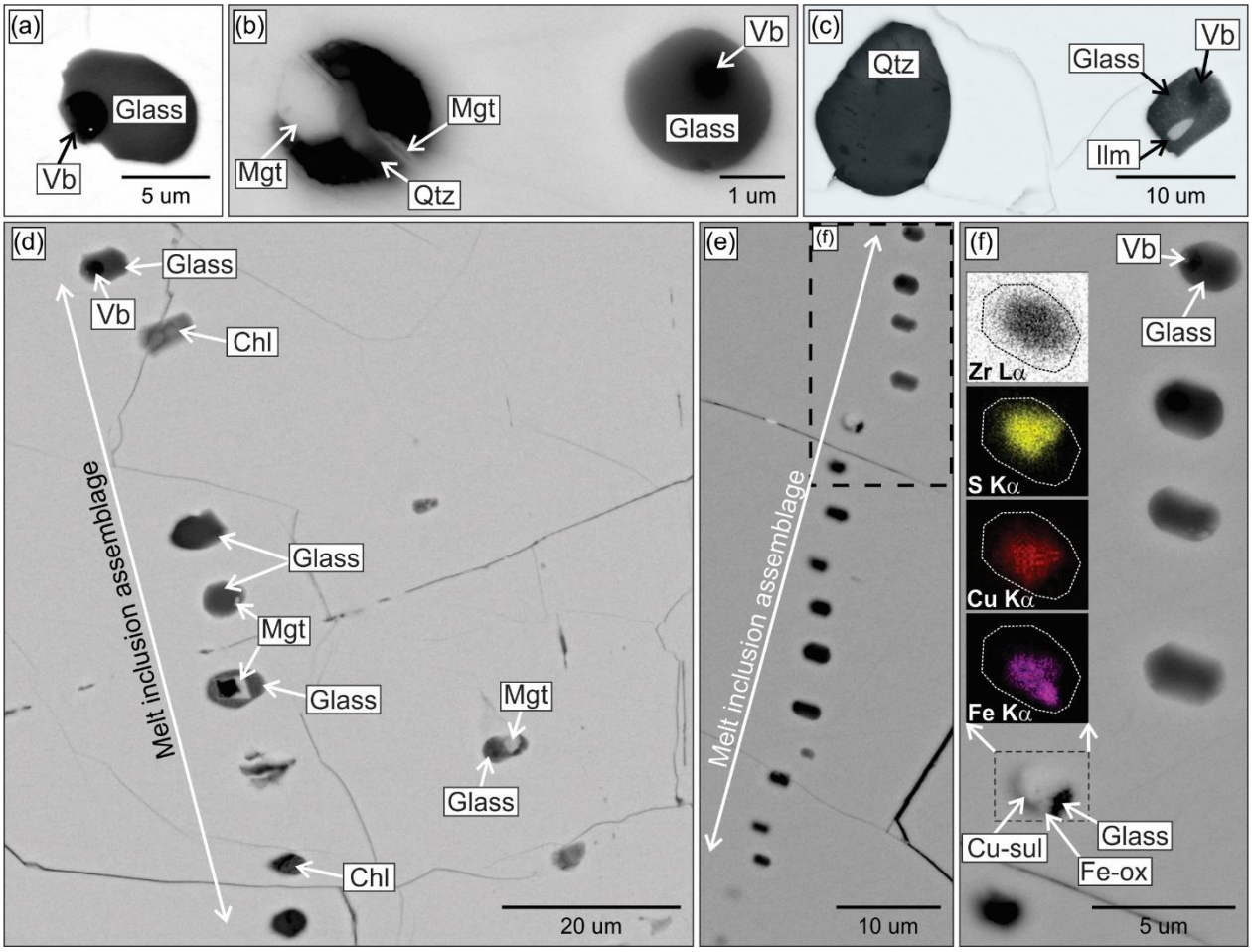
(a)
Glass
Vb
5 um
(b)
Vb
Mgt
Glass
Mgt
Qtz
1 um
(c)
Qtz
Glass
Vb
Ilm
10 um
(d)
Glass
Vb
Chl
Melt inclusion assemblage
Glass
Mgt
Glass
Mgt
Glass
Chl
20 um
(e)
(f)
Melt inclusion assemblage
10 um
(f)
Vb
Glass
Zr Lα
S Kα
Cu Kα
Fe Kα
Cu-sul
Glass
Fe-ox
5 um

Fig. 3.7: Representative individual and assemblages of silicate melt inclusions and other inclusions in zircon from the quartz diorites and tonalites. All images were captured by SEM-BSE. (a) A single isolated glassy silicate melt inclusion in the phase C high-Th/U quartz diorite with a contraction vapor bubble (sample 127.6). (b) Two inclusions in the zircon from the phase C high-Th/U quartz diorite, one composed entirely of crystallized silicate melt (i.e., glass) with a contraction vapor bubble, whereas the other inclusion is composed of quartz and magnetite (sample 127.6). (c) Another pair of inclusions in the phase C high-Th/U quartz diorite. One inclusion is composed entirely of quartz whereas the other predominantly contains glassy silicate melt, a contraction vapor bubble, and an accidentally trapped grain of ilmenite (sample 127.6). (d) Silicate melt inclusion assemblage in zircon from the phase C low-Th/U quartz diorite. The assemblage contains a mixture of pristine, glassy silicate melt inclusions, glass silicate melt inclusions with accidentally trapped magnetite, and inclusions that have been altered to chlorite (sample 493.7). (e) Silicate melt inclusion assemblage in zircon from the phase D tonalite. All inclusions contain glassy silicate melt (sample Stop 11). (f) Zoomed in view of a portion of the melt inclusion assemblage in (e). Note, the one inclusion contains an accidentally trapped grain of chalcopyrite, indicating the magma was sulfide saturated at the time of melt inclusion entrapment. Inset shows a SEM-EDS element map with relative intensities for Zr (proxy for zircon host), S, Cu, and Fe. Note the elevated Fe count rates in the lower right corner indicating the presence of a Fe-oxide grain with chalcopyrite. Cu-sul = Cu-sulfide; Chl = Chlorite; Fe-ox = Fe-oxide; Glass = crystallized silicate melt; Ilm = Ilmenite; Mgt = magnetite; Qtz = quartz; SMI = silicate melt inclusion; Vb = contraction vapor bubble.

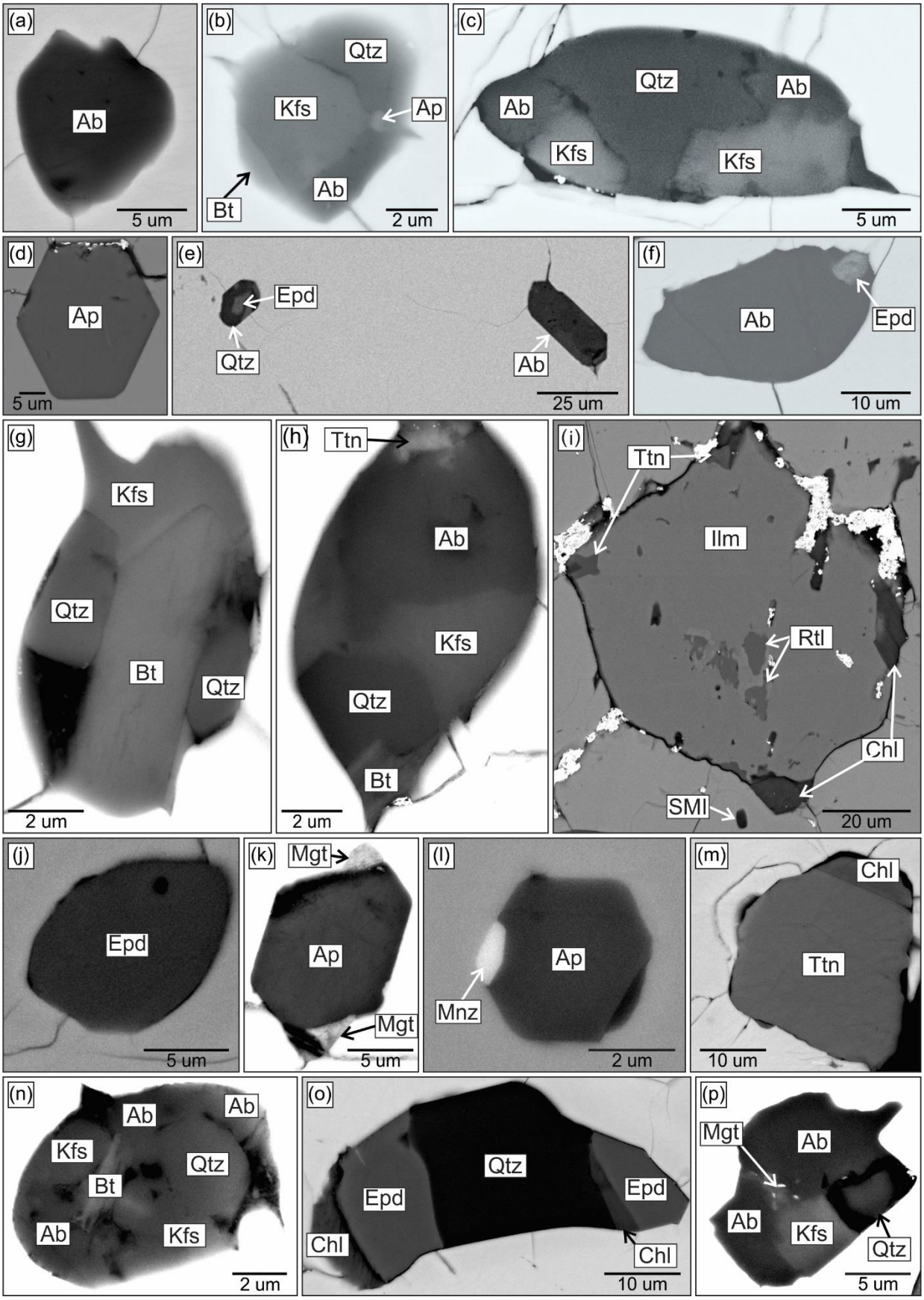
(a)
Ab
5 um
(b)
Qtz
Kfs
Ap
Bt
Ab
2 um
(c)
Qtz
Ab
Ab
Kfs
Kfs
5 um
(d)
Ap
5 um
(e)
Epd
Qtz
Ab
25 um
(f)
Ab
Epd
10 um
(g)
Kfs
Qtz
Bt
Qtz
2 um
(h)
Ttn
Ab
Kfs
Qtz
Bt
2 um
(i)
Ttn
Ilm
Rtl
Chl
SMl
20 um
(j)
Epd
5 um
(k)
Mgt
Ap
Mgt
5 um
(l)
Ap
Mnz
2 um
(m)
Chl
Ttn
10 um
(n)
Ab
Ab
Kfs
Qtz
Bt
Ab
Kfs
2 um
(o)
Qtz
Epd
Epd
Chl
Chl
10 um
(p)
Mgt
Ab
Ab
Kfs
Qtz
5 um

Fig. 3.8: Representative monomineralic and composite inclusion varieties in zircon. All images were captured by SEM-BSE. (a) Inclusion entirely composed of albite in the phase C high-Th/U quartz diorite (sample 127.6). (b) Composite inclusion composed of quartz, albite, K-feldspar, biotite, and apatite hosted in zircon from the phase C high-Th/U quartz diorite (sample 127.6). (c) Composite inclusion composed of multiple K-feldspar and albite grains and one large quartz grain (phase C high-Th/U quartz diorite; sample 127.6). (d) Euhedral apatite inclusion in zircon. Bright spots along edges are gold coating (phase C low-Th/U quartz diorite; sample 493.7). (e) Two inclusions in zircon, one entirely composed of albite and the second composed of quartz and epidote in zircon from the phase C low Th/U quartz diorite (sample 493.7). (f) Inclusion consisting predominately of albite with a minor grain of epidote in the upper right corner (phase C low Th/U quartz diorite; sample 493.7). (g) Composite inclusion composed of multiple quartz grains and K-feldspar and biotite from the phase C low Th/U quartz diorite (sample 493.7). (h) Inclusion composed of albite, quartz, K-feldspar, biotite, and titanite (phase C low Th/U quartz diorite; sample 493.7). (i) Large inclusion of ilmenite hosted in zircon with inclusions of rutile. Titanite and minor chlorite occur along the outer margins of ilmenite. Note the small silicate melt inclusion below the ilmenite inclusion (phase C low Th/U quartz diorite; sample 493.7). (j) Inclusion entirely composed of epidote in zircon from the phase D tonalite (sample Stop 11). (k) Inclusion of apatite with minor magnetite occurring along the margins of apatite (phase D tonalite; sample Stop 10). (l) An apatite inclusion with a small grain of monazite along the edge (phase D tonalite; sample Stop 11). (m) Inclusion of titanite with minor chlorite along the edge (phase D tonalite; sample Stop 10). (n) Composite inclusion composed of quartz, albite, K-feldspar, and biotite in the phase D tonalite (sample Stop 10). (o) Inclusion composed of quartz and multiple grains of epidote and chlorite (phase D tonalite; sample Stop 10). (p) Composite inclusion composed of quartz, albite, K-feldspar, and magnetite (phase D tonalite; sample Stop 11). Ab = albite; Ap = apatite; Bt =

biotite; Chl = chlorite; Epd = epidote; Ilm = ilmenite; Kfs = K-feldspar; Mgt = magnetite; Mnz = monazite; Qtz = quartz; Rtl = rutile; Ttn = titanite; SMI = silicate melt inclusion.

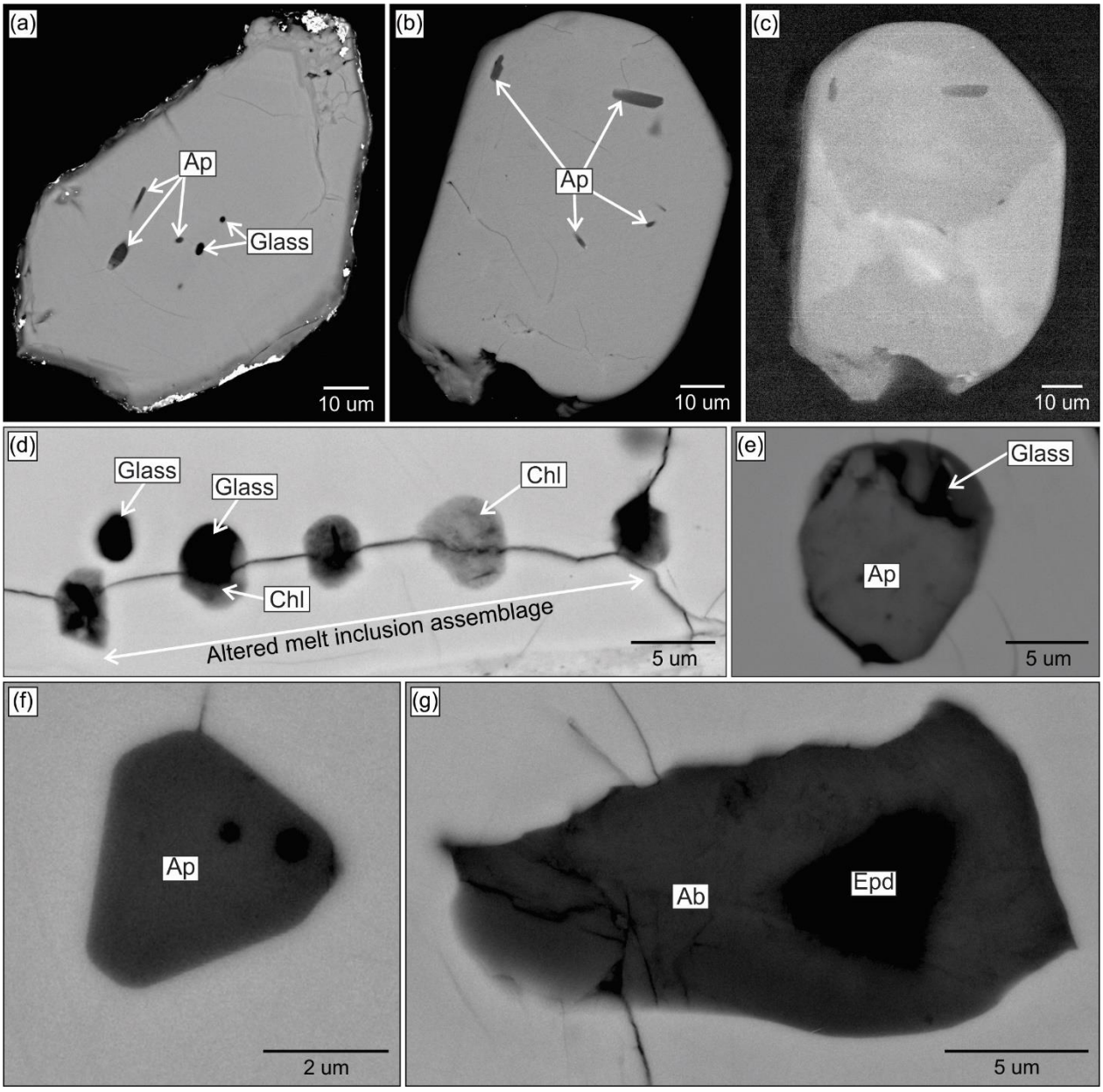
(a)
Ap
Glass
10 um
(b)
Ap
10 um
(c)
10 um
(d)
Glass
Glass
Chl
Chl
Altered melt inclusion assemblage
5 um
(e)
Glass
Ap
5 um
(f)
Ap
2 um
(g)
Ab
Epd
5 um

Fig. 3.9: Representative individual and assemblages of silicate melt inclusions and other mineral inclusions in zircon from the Doyon-stage trondhjemite lithologies. All images were captured by SEM-BSE, except for (e) which is a SEM-CL image. (a) An entire zircon grain from the phase I aphyric trondhjemite contain numerous apatite inclusions as well as two glassy, silicate melt inclusions in the center of the grain (sample 1323). (b) Numerous apatite inclusions occurring in zircon from the phase I aphyric trondhjemite (sample 1323). (c) Same zircon featured in (d) but is a SEM-CL image. (f) An isolated, euhedral apatite inclusion in zircon from the phase I aphyric trondhjemite (sample 1323). (d) A predominantly altered silicate melt inclusion assemblage in the phase H phyric trondhjemite where inclusions are now mostly chlorite with a few inclusions contain a portion of glassy silicate melt, whereas only one inclusion is free of alteration and is completely composed of glassy, silicate melt (sample Bousquet 4). (e) Single, isolated inclusion in the phase H phyric trondhjemite that is composed of a mixture of apatite and a minor amount of a glassy silicate melt (sample Bousquet 4). (g) An inclusion composed of albite and epidote from the phase I aphyric trondhjemite (sample 1444.5). Ab = albite; Ap = apatite; Chl = chlorite; Epd = epidote; Glass = crystallized silicate melt.

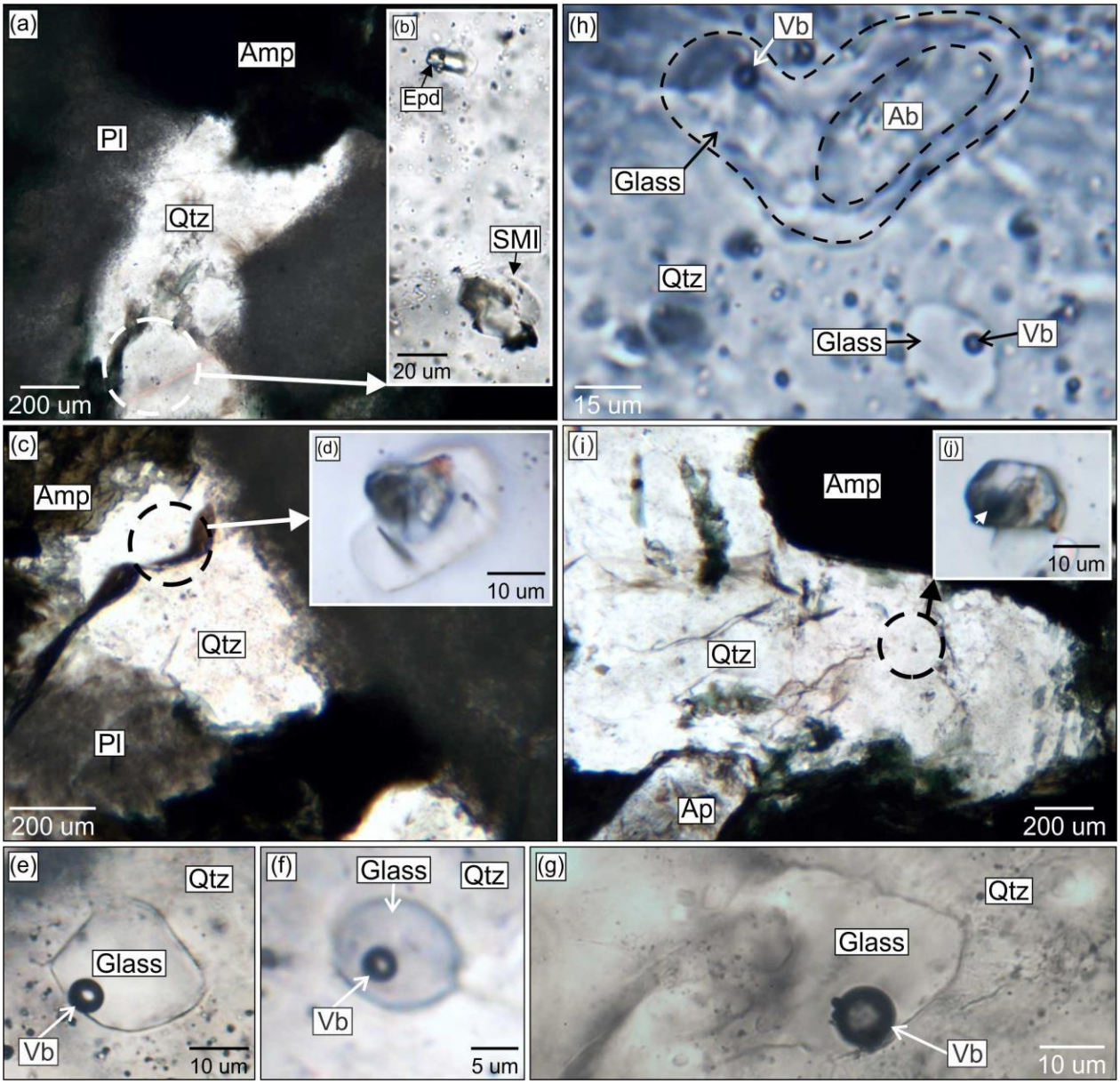
(a)
Amp
Pl
Qtz
200 um
(b)
Epd
SMI
20 um
(h)
Vb
Ab
Glass
Qtz
Glass
Vb
15 um
(c)
Amp
Qtz
Pl
200 um
(d)
10 um
(i)
Amp
Qtz
Ap
200 um
(j)
10 um
(e)
Qtz
Glass
Vb
10 um
(f)
Glass
Qtz
Vb
5 um
(g)
Qtz
Glass
Vb
10 um

Fig. 3.10: Representative photomicrographs and SEM-BSE images of quartz-hosted SMI from various phases in the Mooshla intrusive complex. (a) Interstitial quartz grain in contact with plagioclase and amphibole from the gabbro. Quartz is host to a melt inclusion assemblage featured in (b). (b) Melt inclusion assemblage consisting of two SMI that are both recrystallized. For LA-ICPMS analysis of these inclusions refer to Supplementary Table 3.7 (715.6B-A2-a;2018_19_a09, 715.6B-A2-2; 2018_19_a08, for the inclusion on the top and bottom, respectively). Note, that the top inclusion contains accidentally trapped epidote. (c) Quartz occurring interstitial to amphibole and plagioclase in the low-Th/U quartz diorite, hosting a recrystallized SMI featured in (d). (d) Small, recrystallized SMI hosted in quartz. For LA-ICPMS analysis of this inclusion refer to Supplementary Table 3.7 (MSK-493.7e-A3; 2017_11_03a08). (e-g) Homogenized, quartz-hosted SMI that now contain a contraction vapor bubble from the low-Th/U quartz diorite. Inclusions were homogenized at 1050°C and 1 atm. (h) Quartz-hosted SMI that have been homogenized at 950 ± 10°C and 1500 ± 50 bar in the gabbro. One SMI (lower right) is circular and completely glassy with a contraction vapor bubble, whereas as the second inclusion contains a large grain of albite that is surrounded by silicate melt that contains a contraction vapor bubble. (i) Quartz and apatite occurring interstitial to amphibole in the low-Th/U quartz diorite. A small, recrystallized SMI is present in quartz and is featured in (j). (j) Small, recrystallized, Quartz-hosted SMI. A minor accidentally trapped sulfide grain is present in this inclusion (indicated by white arrow in lower left corner). Ab = albite; Amp = amphibole; Ap = apatite; Epd = epidote; Glass = crystallized silicate melt; Pl = plagioclase; Qtz = quartz; SMI = silicate melt inclusion; Vb = contraction vapor bubble.

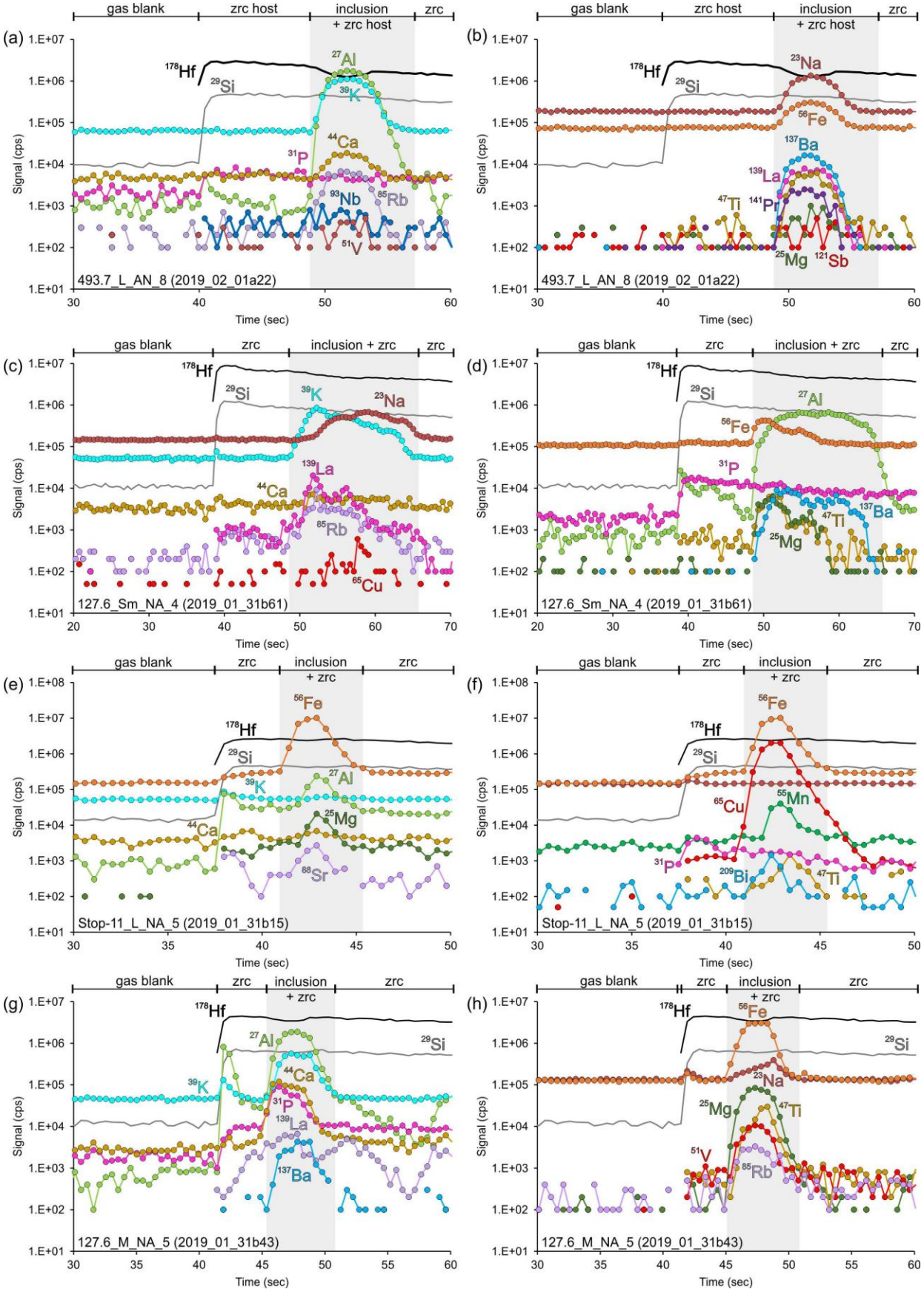
(a)
gas blank
zrc host
inclusion + zrc host
zrc
493.7_L_AN_8 (2019_02_01a22)
(b)
gas blank
zrc host
inclusion + zrc host
zrc
493.7_L_AN_8 (2019_02_01a22)
(c)
gas blank
zrc
inclusion + zrc
zrc
127.6_Sm_NA_4 (2019_01_31b61)
(d)
gas blank
zrc
inclusion + zrc
zrc
127.6_Sm_NA_4 (2019_01_31b61)
(e)
gas blank
zrc
inclusion + zrc
zrc
Stop-11_L_NA_5 (2019_01_31b15)
(f)
gas blank
zrc
inclusion + zrc
zrc
Stop-11_L_NA_5 (2019_01_31b15)
(g)
gas blank
zrc
inclusion + zrc
zrc
127.6_M_NA_5 (2019_01_31b43)
(h)
gas blank
zrc
inclusion + zrc
zrc
127.6_M_NA_5 (2019_01_31b43)
Signal (cps)
Time (sec)

Fig. 3.11: Representative LA-ICP-MS signals of SMI and inclusions with melt with accidentally trapped minerals hosted in zircon. All element signals are in counts per second (cps). For each signal, a gas background was collected for 35-40 seconds, the laser was then turned on and the host zircon was ablated for 5 to 10 seconds until the inclusion was encountered, and ablation of the inclusion lasted 5 to 10 seconds depending on it's size. (a-b) LA-ICPMS signal for a SMI from the low-Th/U quartz diorite. The SMI is represented by the increase in count rates for Al, K, Ca, Na, and Fe, as well as other trace elements and REE. There is a corresponding decrease in Hf counts when the SMI ablation begins. Note the increase in V and Sb counts in the SMI signal. (c-d) LA-ICPMS signal for a SMI from the high-Th/U quartz diorite. The SMI is indicated by increased counts in K, Na, Fe, and Al and other trace elements and REE. Note the increase in Cu count rates throughout the signal compared to the count rates in the background and zircon. (e-f) LA-ICPMS signal for an inclusion containing melt and an accidentally trapped sulfide grain in a zircon from the tonalite. The melt portion is represented by Al, Mg, Sr, Mn, and Ti, whereas the sulfide is indicated by high count rates for Fe, Cu, and Bi. (g-h) LA-ICPMS signal for an inclusion containing melt and an accidentally trapped apatite grain in a zircon from the high-Th/U quartz diorite. The apatite is represented by increase count rates in Ca, P, and La, whereas the melt is indicated by Al, K, Fe, Ba, Rb, Mg, and Ti.

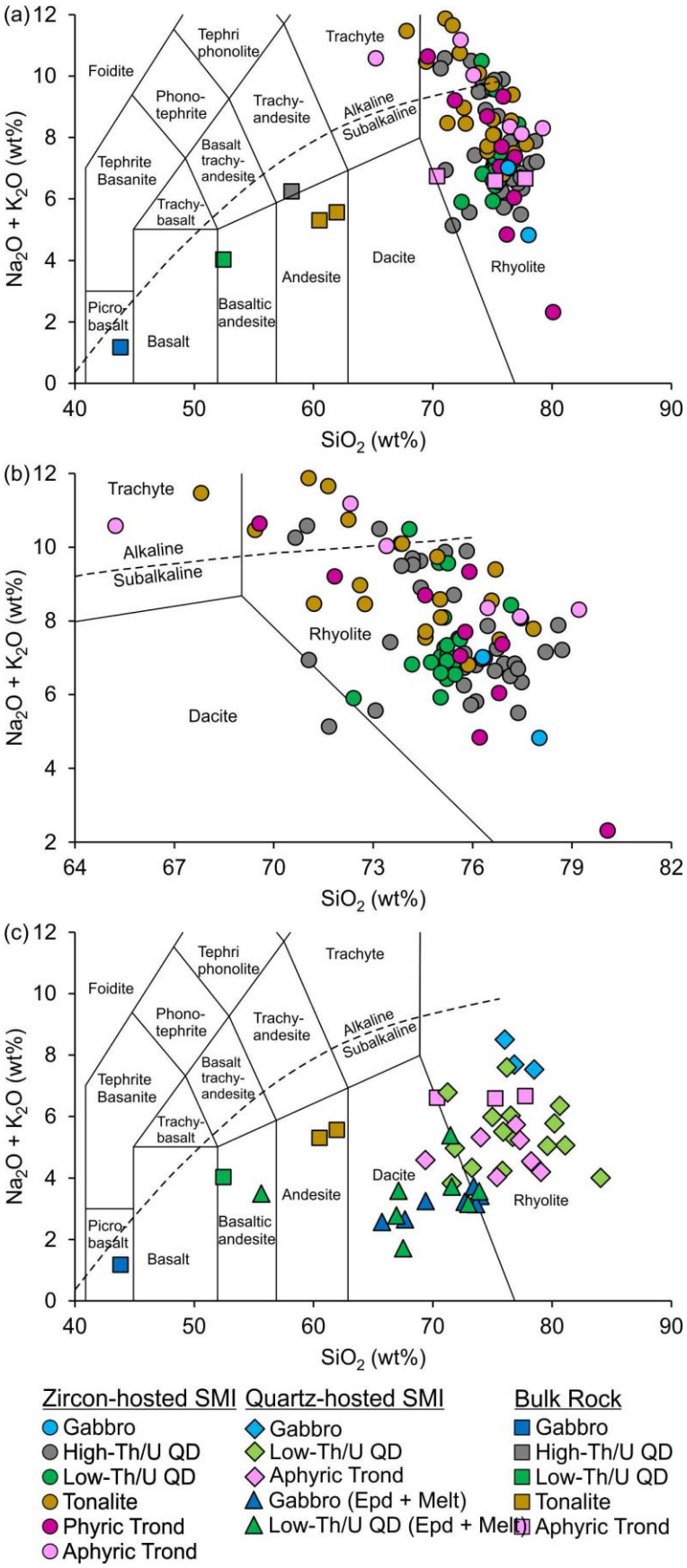
(a)
(b)
(c)
Foidite
Tephri phonolite
Trachyte
Phono-tephrite
Trachy-andesite
Alkaline
Subalkaline
Tephrite Basanite
Basalt trachy-andesite
Trachy-basalt
Dacite
Rhyolite
Andesite
Picro-basalt
Basaltic andesite
Basalt
Na2O + K2O (wt%)
SiO2 (wt%)
Zircon-hosted SMI
Gabbro
High-Th/U QD
Low-Th/U QD
Tonalite
Phyric Trond
Aphyric Trond
Quartz-hosted SMI
Gabbro
Low-Th/U QD
Aphyric Trond
Gabbro (Epd + Melt)
Low-Th/U QD (Epd + Melt)
Bulk Rock
Gabbro
High-Th/U QD
Low-Th/U QD
Tonalite
Aphyric Trond

Fig. 3.12: Total alkali ($Na_2O + K_2O$) vs silica (SiO_2) (TAS diagram) rock type classification diagram from La Bas et al. (1986) with zircon- (a, b) and quartz-hosted (c) SMI and bulk rock data shown. All SMI data collected by SEM, EPMA, and LA-ICPMS are grouped together for each lithology. (a) Zircon-hosted SMI are predominantly rhyolitic and vary between alkaline and sub-alkaline in composition. Whereas bulk rock data are all sub-alkaline and are SiO_2-deplted compared to SMI, with the exception of the aphyric trondhjemite. (b) Same data as shown in A, except the SiO_2 range is limited to display spread in the zircon-hosted SMI data. (c) Quartz-hosted SMI plotted on the TAS diagram. Inclusions are predominately rhyolitic and sub-alkaline in composition. Inclusions that contain melt + epidote plot in the dacite due to epidote contamination lowering SiO_2 and alkalis.

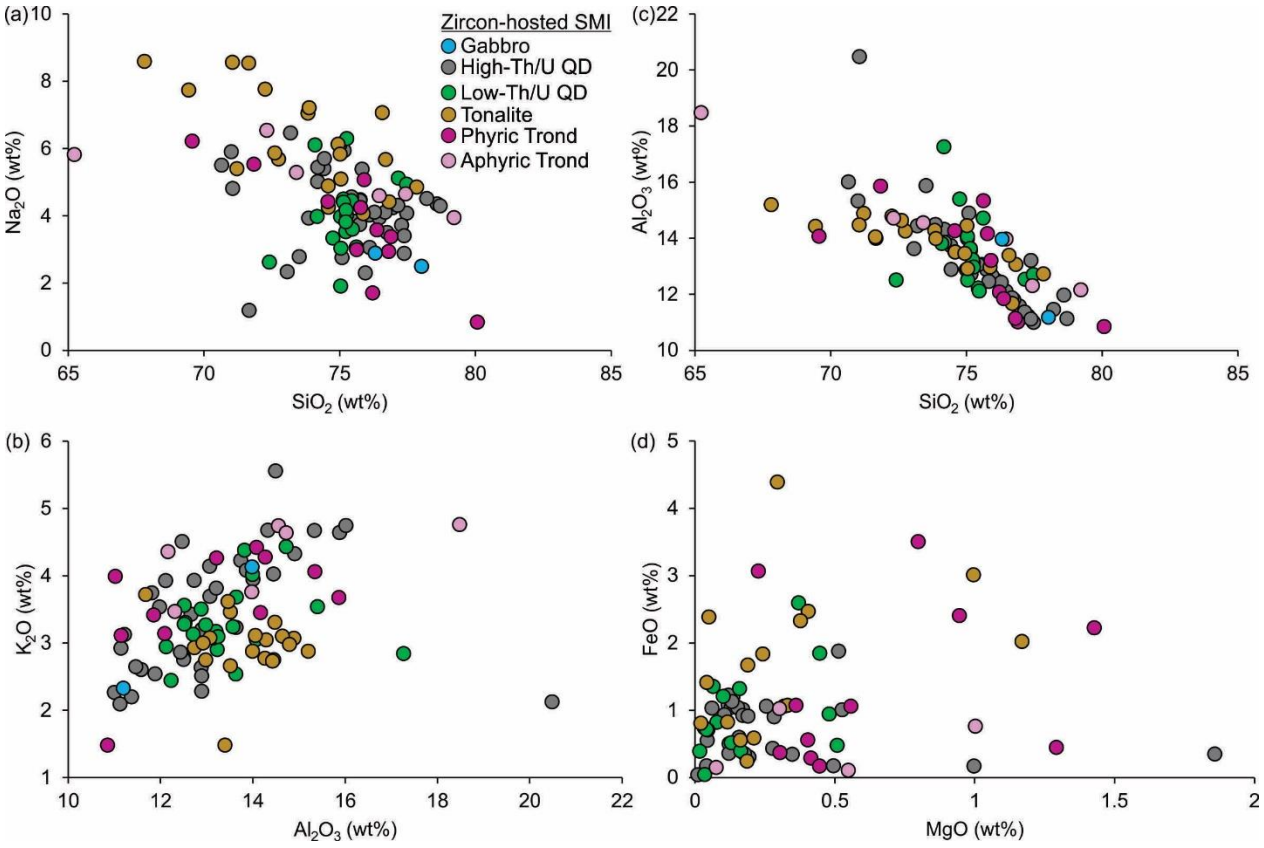

Fig. 3.13: Harker diagrams for various major elements of zircon-hosted SMI. All data types (SEM, EPMA, and LA-ICPMS) are grouped together for each lithology. (a) SiO_2 plotted against Na_2O. Overall, there is a decrease in Na_2O with an increase in SiO_2. Individual lithology do (e.g., tonalite) and do not (low-Th/U quartz diorite) follow this negative correlation. (b) Al_2O_3 plotted against K_2O. Overall, there is a weak positive correlation between the two elements. Individual lithology do (e.g., high-Th/U quartz diorite) and do not (tonalite) follow this positive correlation. (c) SiO_2 plotted against Al_2O_3. Note the negative correlation as Al_2O_3 decreases, SiO_2 increases. (d) MgO plotted against FeO and concentrations are relatively the same between all lithologies.

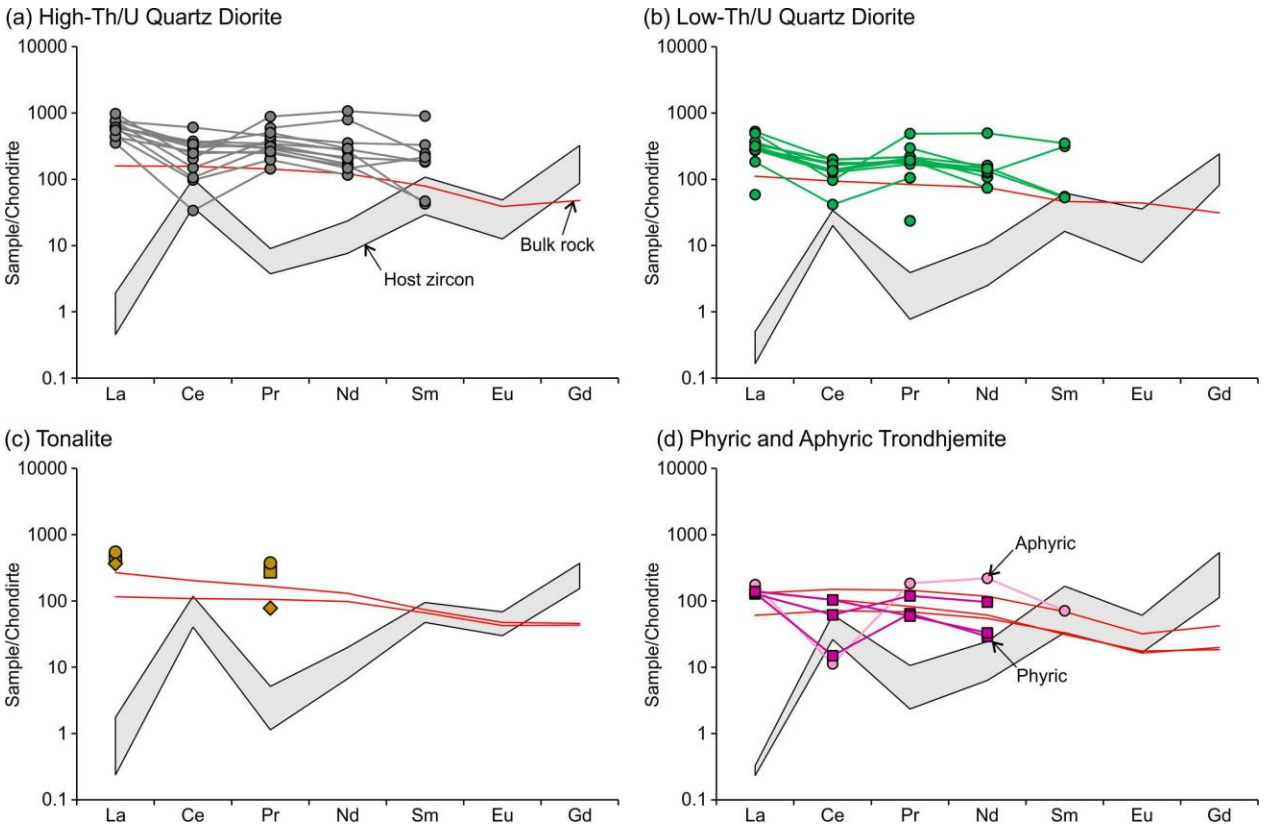

Fig. 3.14: Chondrite normalized REE diagrams showing zircon-hosted SMI, host-zircon, and bulk rock patterns. (a) High-Th/U quartz diorite, (b) low-Th/U quartz diorite, (c) tonalite, and (d) phyric and aphyric trondhjemite. Note, for all lithologies (except the tonalite due to below detection Ce) that the SMI displays a negative Ce-anomaly whereas the host-zircon has a positive Ce-anomaly.

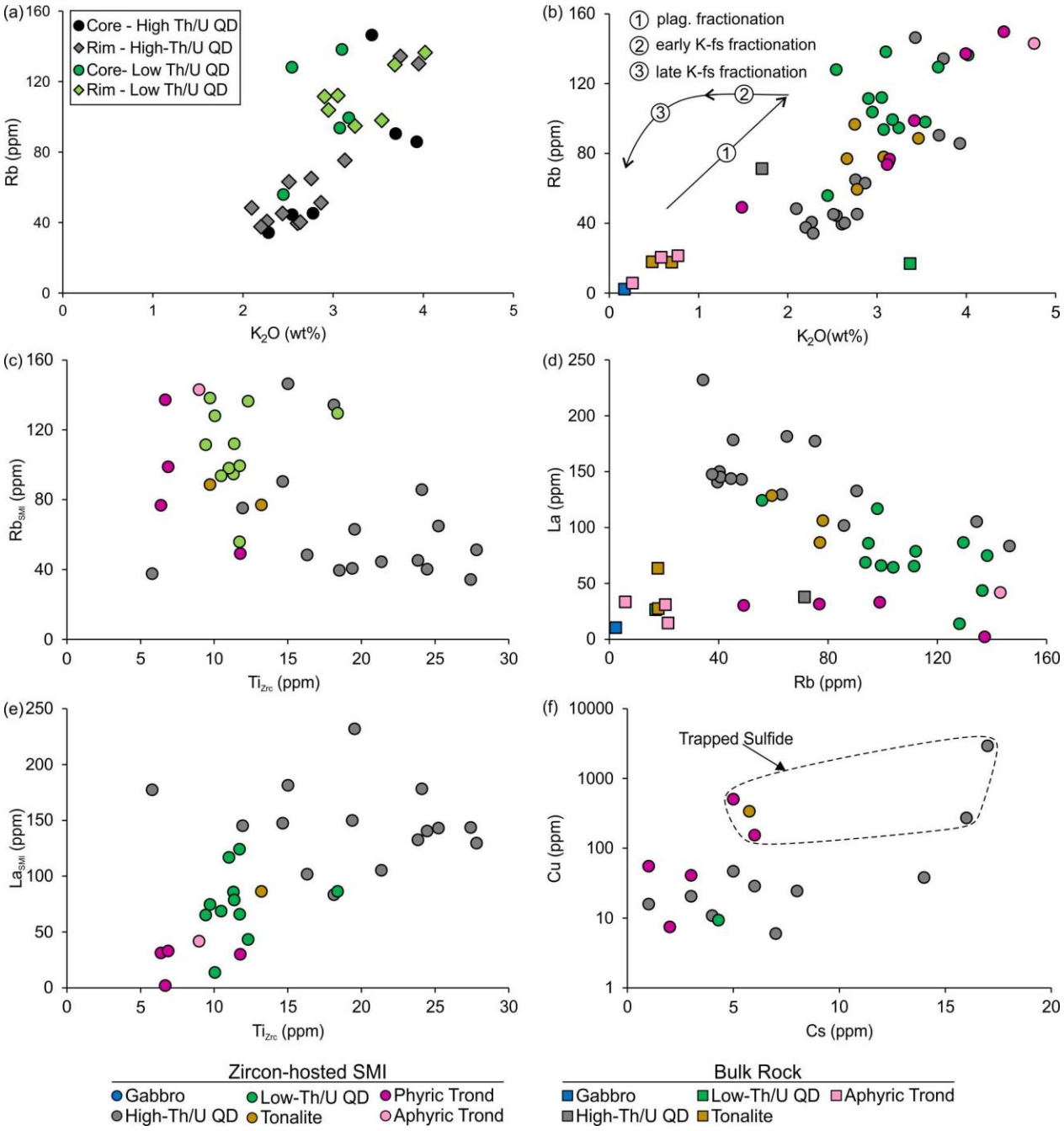
(a)
Core - High Th/U QD
Rim - High-Th/U QD
Core- Low Th/U QD
Rim - Low Th/U QD
Rb (ppm)
K2O (wt%)
(b)
① plag. fractionation
② early K-fs fractionation
③ late K-fs fractionation
Rb (ppm)
K2O(wt%)
(c)
RbSMI (ppm)
TiZrc (ppm)
(d)
La (ppm)
Rb (ppm)
(e)
LaSMI (ppm)
TiZrc (ppm)
(f)
Trapped Sulfide
Cu (ppm)
Cs (ppm)
Zircon-hosted SMI
Gabbro
Low-Th/U QD
Phyric Trond
High-Th/U QD
Tonalite
Aphyric Trond
Bulk Rock
Gabbro
Low-Th/U QD
Aphyric Trond
High-Th/U QD
Tonalite

Fig. 3.15: Scatter plots of zircon-hosted SMI composition plotted against each other, and SMI compositions plotted against host-zircon compositions. All data plotted is from LA-ICPMS analysis. (a) K_2O plotted against Rb concentration in SMI from the high- and low-Th/U quartz diorites. Data is organized by location in the host-zircon (i.e., in the core or in the rim of zircon). This shows that the composition of SMI is not influenced by the location in the host zircon. (b) K_2O plotted against Rb concentration in SMI for all zircon-hosted SMI and bulk rock compositions. Overall, there is a positive relationship between Rb and K_2O SMI concentrations, as well, SMI are significantly more enriched in Rb and K_2O compared to their respective bulk rock compositions. Arrows in upper left corner of the plot represent the relative evolution a melt would undergo during plagioclase and early and late K-feldspar fractionation. The trend recorded in the SMI display strong evidence that plagioclase fractionation occurred prior to and/or synchronous with trapping of SMI. (c) The Rb concentration of SMI (Rb_{SMI}) plotted against each SMIs respective zircon-host Ti concentration (Ti_{Zrc}), which is a proxy for temperature (Ferry and Watson, 2007). In the high-Th/U quartz diorite, a decrease in Ti_{Zrc} (increase in temperature) occurs with an increase in Rb_{SMI}. In the other lithologies, no correlation exists. (d) Rb plotted against La concentrations in SMI. Overall, there is a negative relationship with an increase in Rb corresponding to a decrease in La, except for the phyric trondhjemite which shows similar La are variable Rb. (e) The concentration of Ti_{Zrc} plotted against La_{SMI}. Note the positive relationship, as Ti_{Zrc} increases (increase in temperature) so does the La_{SMI}. (f) Cs plotted against Cu concentrations in SMI. Note the elevated Cu concentrations in some SMI are the result of accidentally trapped sulfide.

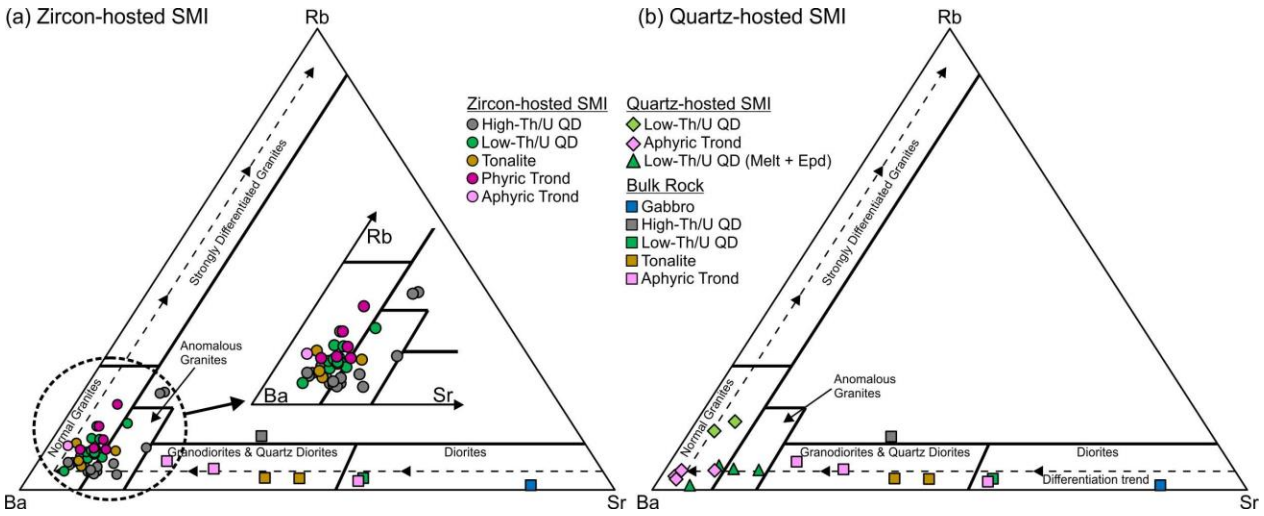

Fig. 3.16: Rubidium-strontium-barium ternary granitoid classification diagram showing zircon- and quartz-hosted SMI and bulk rock compositions. Diagram modified from El-Bouseily and El-Sokkary, 1975. (a) Zircon-hosed SMI plot primarily in the "normal" granite field with some falling into the "anomalous" granite field. Bulk rock compositions are more Sr-rich, caused by the accumulation of plagioclase. The slight spread in the high-Th/U QD along the Ba-Sr line is related to plagioclase fractionation prior to and/or synchronous with trapping of SMI. (b) Quartz-hosed SMI all plot in the "normal" granite field.

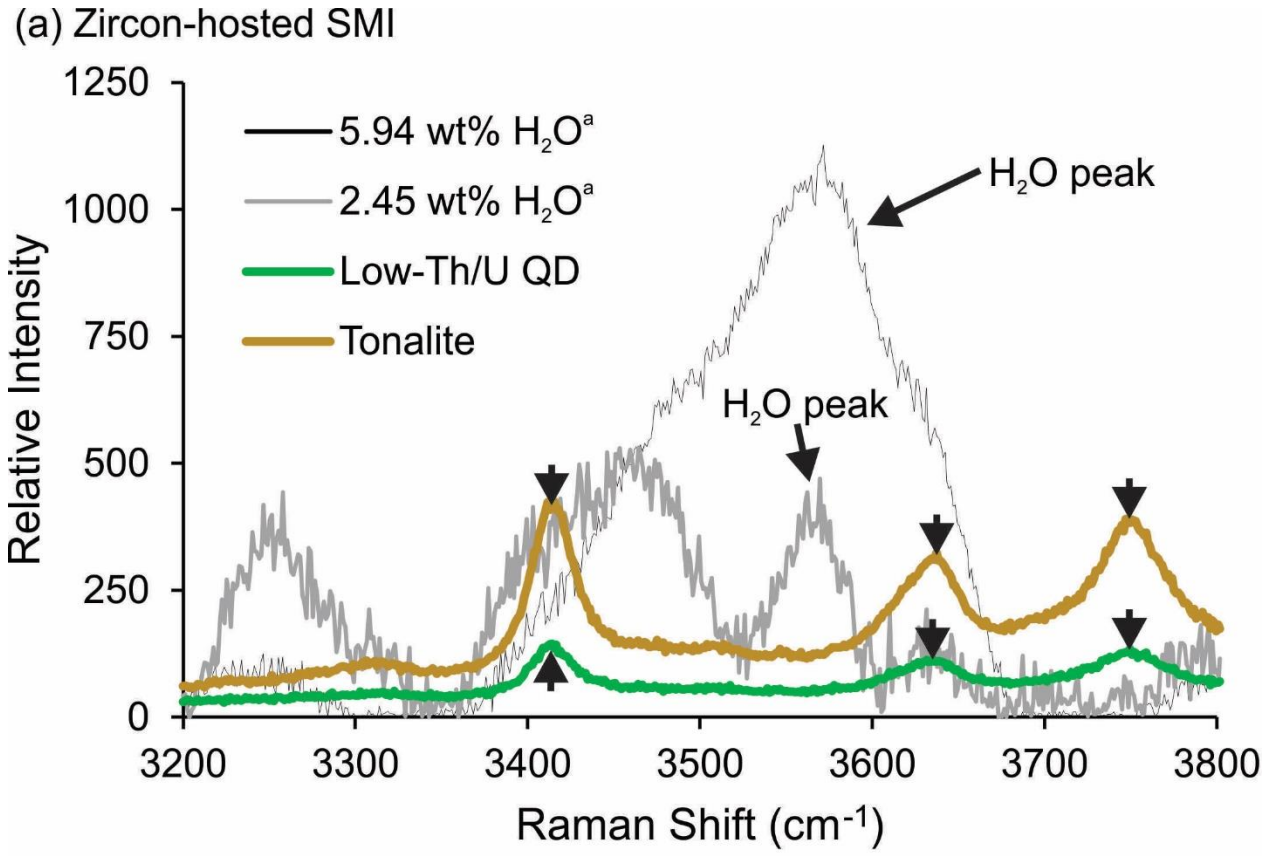
(a) Zircon-hosted SMI
1250
1000
750
500
250
0
Relative Intensity
5.94 wt% H2Oa
2.45 wt% H2Oa
Low-Th/U QD
Tonalite
H2O peak
H2O peak
3200
3300
3400
3500
3600
3700
3800
Raman Shift (cm-1)

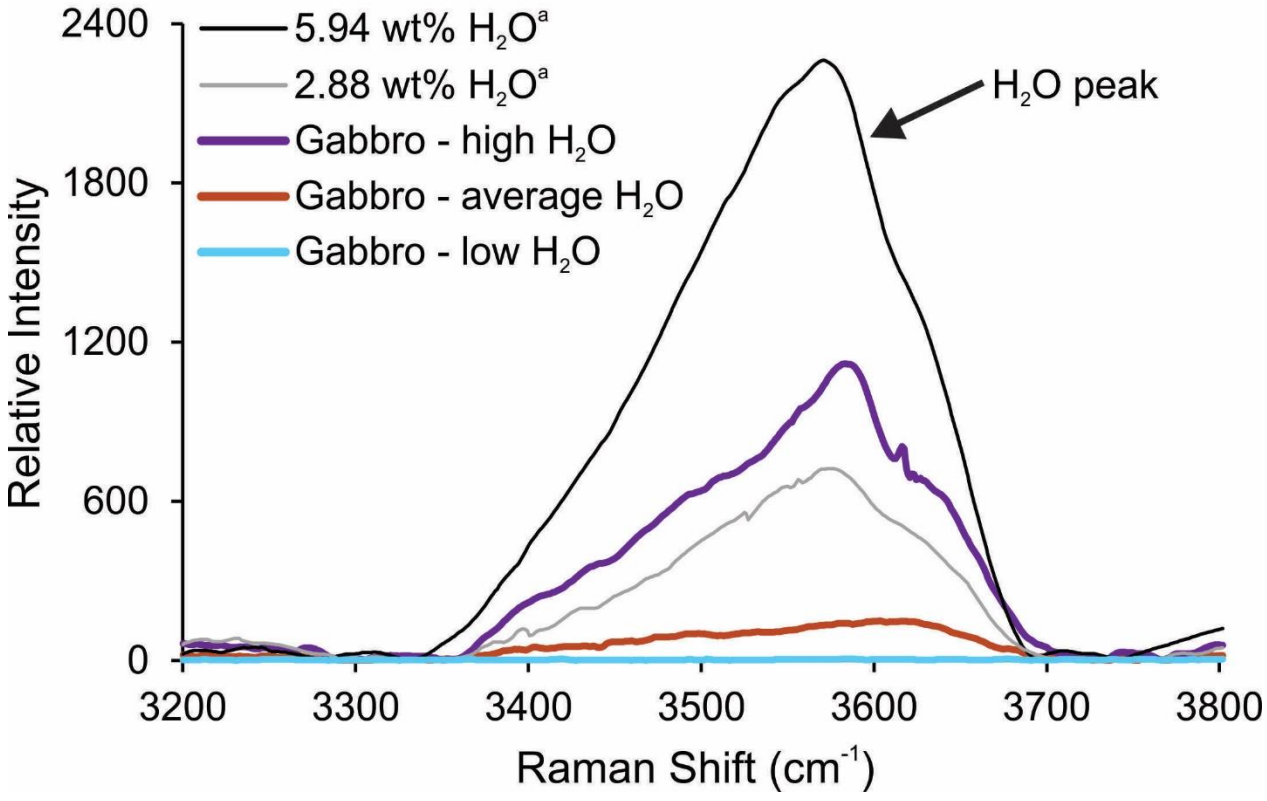
(b) Quartz-hosted SMI
2400
1800
1200
600
0
Relative Intensity
5.94 wt% H2Oa
2.88 wt% H2Oa
Gabbro - high H2O
Gabbro - average H2O
Gabbro - low H2O
H2O peak
3200
3300
3400
3500
3600
3700
3800
Raman Shift (cm-1)

Fig. 3.17: Raman spectra of SMI and reference glasses. (a) Zircon-hosted SMI from the tonalite and low-Th/U quartz diorite. The peak intensity of H_2O occurs between 3500 and 3650 cm^{-1} as can be seen for the reference glasses. The arrows pointing at the signals for the low-Th/U quartz diorite and tonalite are peaks from the host zircon. (b) Quartz-hosted SMI from the gabbro. Note that these quartz-hosted SMI were homogenized at 950°C and 0.15 GPa to limit volatile diffusion during homogenization experiments. [a] Reference glasses described in Webster et al. (2011) were analyzed for comparison and are all rhyolitic in composition.

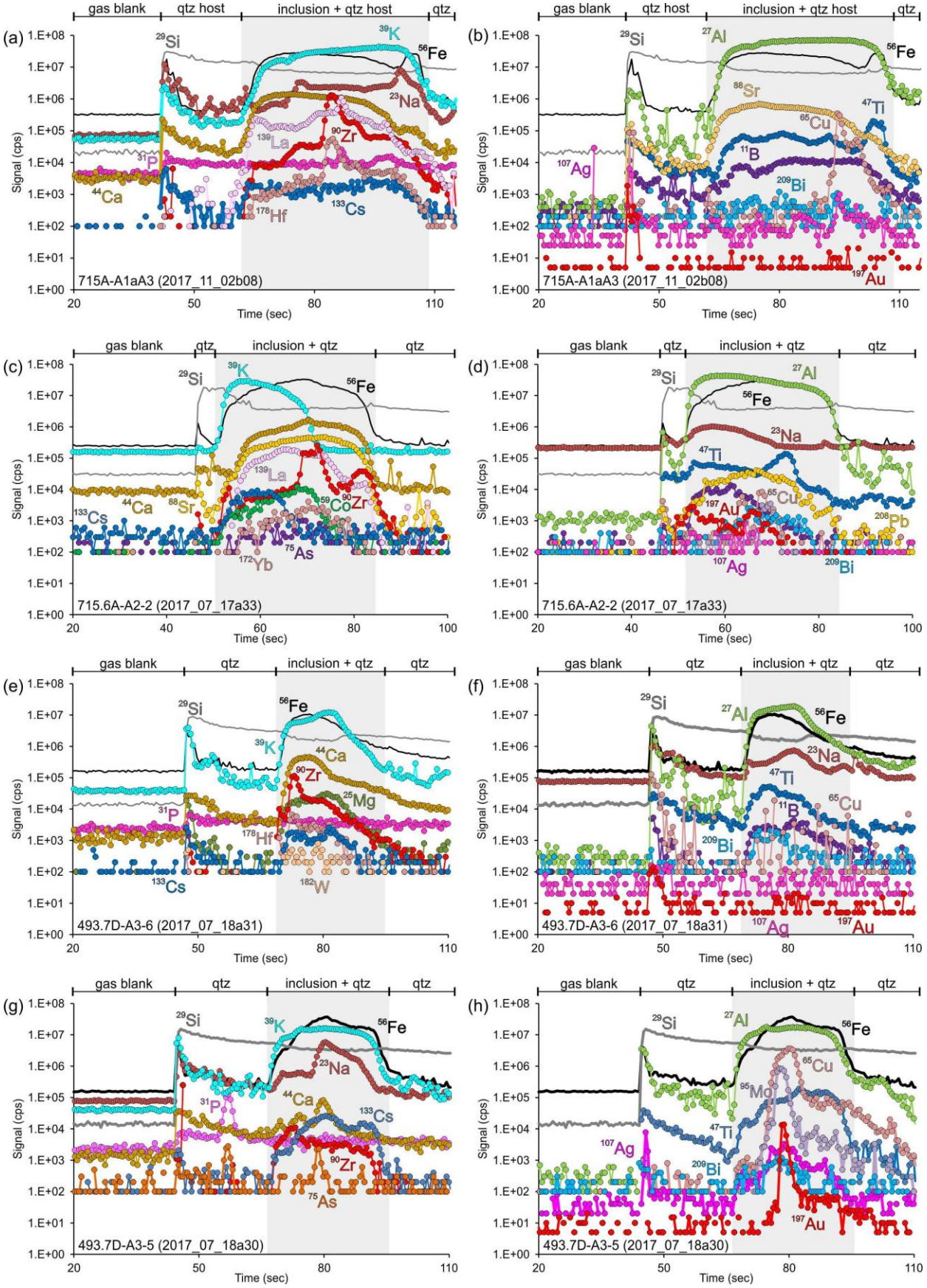
(a)
gas blank
qtz host
inclusion + qtz host
qtz
715A-A1aA3 (2017_11_02b08)
(b)
715A-A1aA3 (2017_11_02b08)
(c)
gas blank
qtz
inclusion + qtz
qtz
715.6A-A2-2 (2017_07_17a33)
(d)
715.6A-A2-2 (2017_07_17a33)
(e)
493.7D-A3-6 (2017_07_18a31)
(f)
493.7D-A3-6 (2017_07_18a31)
(g)
493.7D-A3-5 (2017_07_18a30)
(h)
493.7D-A3-5 (2017_07_18a30)
Signal (cps)
Time (sec)

Fig. 3.18: Representative LA-ICP-MS signals of SMI and inclusions with melt with accidentally trapped minerals hosted in quartz. All element signals are in counts per second (cps). For each signal, a gas background was collected for 40-50 seconds, the laser was then turned on and the host quartz was ablated for 5-20 seconds until the inclusion was encountered, and ablation of the inclusion lasted 25-40 seconds depending on it's size. (a-b) LA-ICPMS signal for a SMI from the gabbro. The SMI is represented by a decrease in Si counts and a corresponding increase in K, Fe, Na, Al, Sr, Cs, and B. Note, the spike of Zr and Hf mid-ablation indicating a small grain of zircon is accidentally trapped in the SMI, as well as the large spike in Fe, Ti (and Ta not shown) indicating a small grain of Fe-Ti-oxide was also accidentally trapped. Importantly, near the end of the SMI ablation, counts for Cu, Ag, and Au all increase indicating a small grain of sulfide was likely accidentally trapped. (c-d) LA-ICPMS signal for a SMI from the gabbro. This signal shows a signal typically of a SMI that has crystallized into multiple minerals after initial entrapment during cooling. Note the offset between K, Al, Na with Ca and Sr, indicating at least two major minerals are comprising the inclusion. A small grain of zircon is present in the inclusion indicating by the spike in Zr counts. Note, the increase in Au, Ag, Co, Cu, Bi, As in the inclusion. (e-f) LA-ICPMS signal for a SMI from the low-Th/U quartz diorite. The SMI is represented by increases in K, Fe, Al, Na, Mg, Ti, B, and Cs. The counts for Au are slightly elevated in the SMI compared to the background and host-quartz. (g-h) LA-ICPMS signal for an inclusion containing melt and an accidentally trapped sulfide grain in a zircon from the low-Th/U quartz diorite. The melt portion is represented by increase counts of K, Al, Na, Cs, and Zr, whereas the sulfide is indicated by large spikes in Cu, Mo, Au, Ag, Bi, and As.

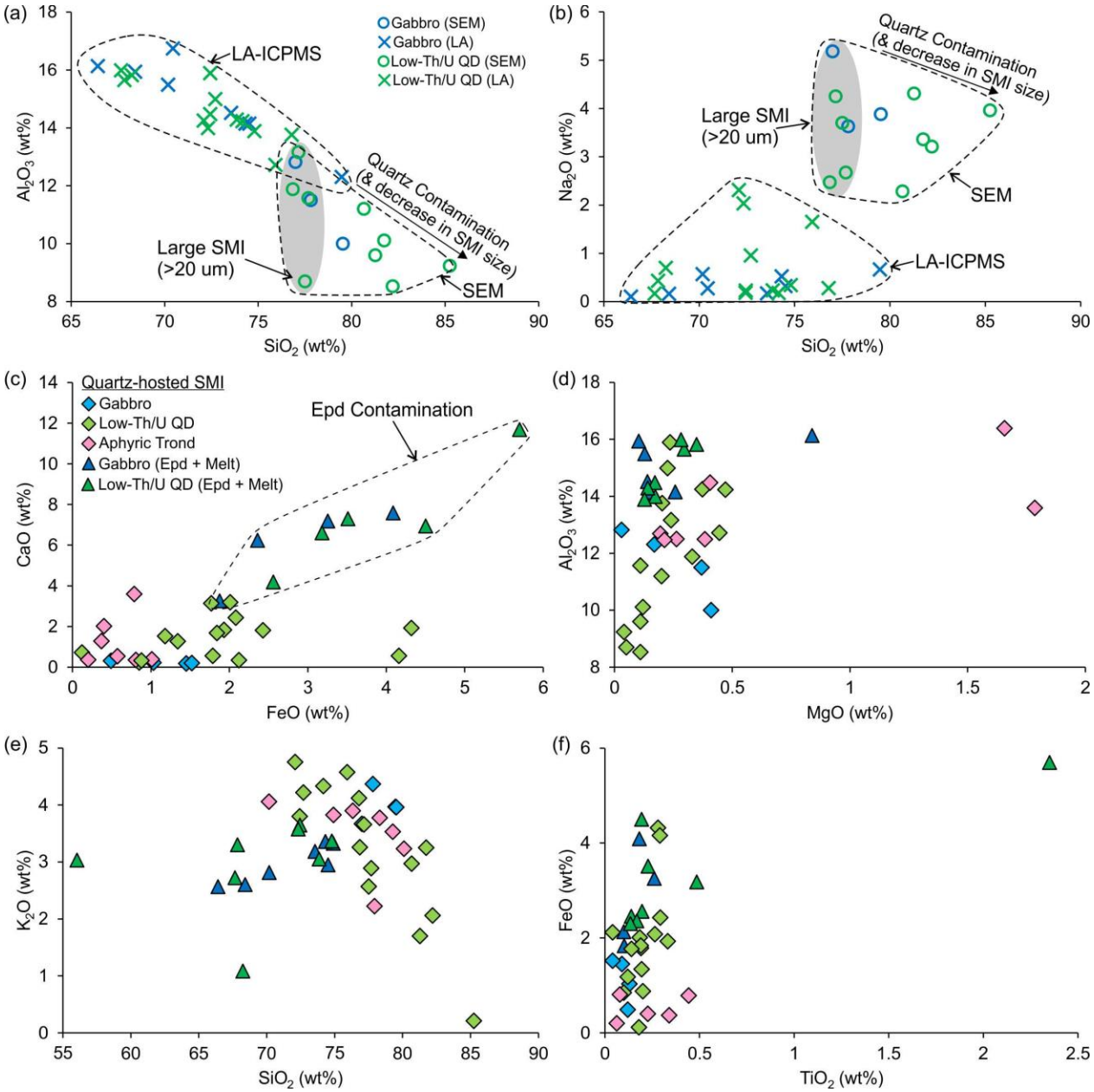
(a)
Gabbro (SEM)
Gabbro (LA)
Low-Th/U QD (SEM)
Low-Th/U QD (LA)
LA-ICPMS
Quartz Contamination (& decrease in SMI size)
Large SMI (>20 um)
SEM
Al2O3 (wt%)
SiO2 (wt%)
(b)
Quartz Contamination (& decrease in SMI size)
Large SMI (>20 um)
SEM
LA-ICPMS
Na2O (wt%)
SiO2 (wt%)
(c)
Quartz-hosted SMI
Gabbro
Low-Th/U QD
Aphyric Trond
Gabbro (Epd + Melt)
Low-Th/U QD (Epd + Melt)
Epd Contamination
CaO (wt%)
FeO (wt%)
(d)
Al2O3 (wt%)
MgO (wt%)
(e)
K2O (wt%)
SiO2 (wt%)
(f)
FeO (wt%)
TiO2 (wt%)

Fig. 3.19: Harker diagrams for quartz-hosted SMI. Frames (a) and (b) have SEM and LA-ICPMS analyses plotted separately whereas (c-f) the analyses are grouped together for each lithology. (a) SiO_2 plotted against Al_2O_3 concentrations and grouped by analytical method (SEM vs. LA-ICPMS). SMI analyzed by SEM consistently have higher SiO_2 and lower Al_2O_3 contents due to contamination of the host quartz during analysis. SMI that are relatively large (>~20 um) and analyzed by SEM, have SiO_2 and Al_2O_3 contents most similar to LA-ICPMS analyses. (b) SiO_2 plotted against Na_2O concentrations and grouped by analytical method (SEM vs. LA-ICPMS). Note the lower Na_2O concentrations in LA-ICPMS analyses due to Na diffusion out of the SMI and into the surrounding quartz upon colling after melt entrapment (Zajacz *et al.,* 2008). SMI analyzed by SEM had been homogenized (i.e., heated) and Na will diffuse back into the SMI (Zajacz *et al.,* 2009). (c) FeO plotted against CaO concentrations showing the distinction between SMI and melt inclusions contaminated by epidote. (d) MgO plotted against Al_2O_3. Overall, there is no difference in MgO concentrations between inclusions contaminated by epidote and those that are not. Note the higher Al_2O_3 concentrations in epidote-contaminated inclusions. (e) SiO_2 concentrations plotted against K_2O showing K_2O concentrations are slightly lower in epidote-contaminated inclusions. (f) TiO_2 plotted against FeO showing TiO_2 concentrations are similar between epidote contaminated inclusions and non-contaminated inclusions.

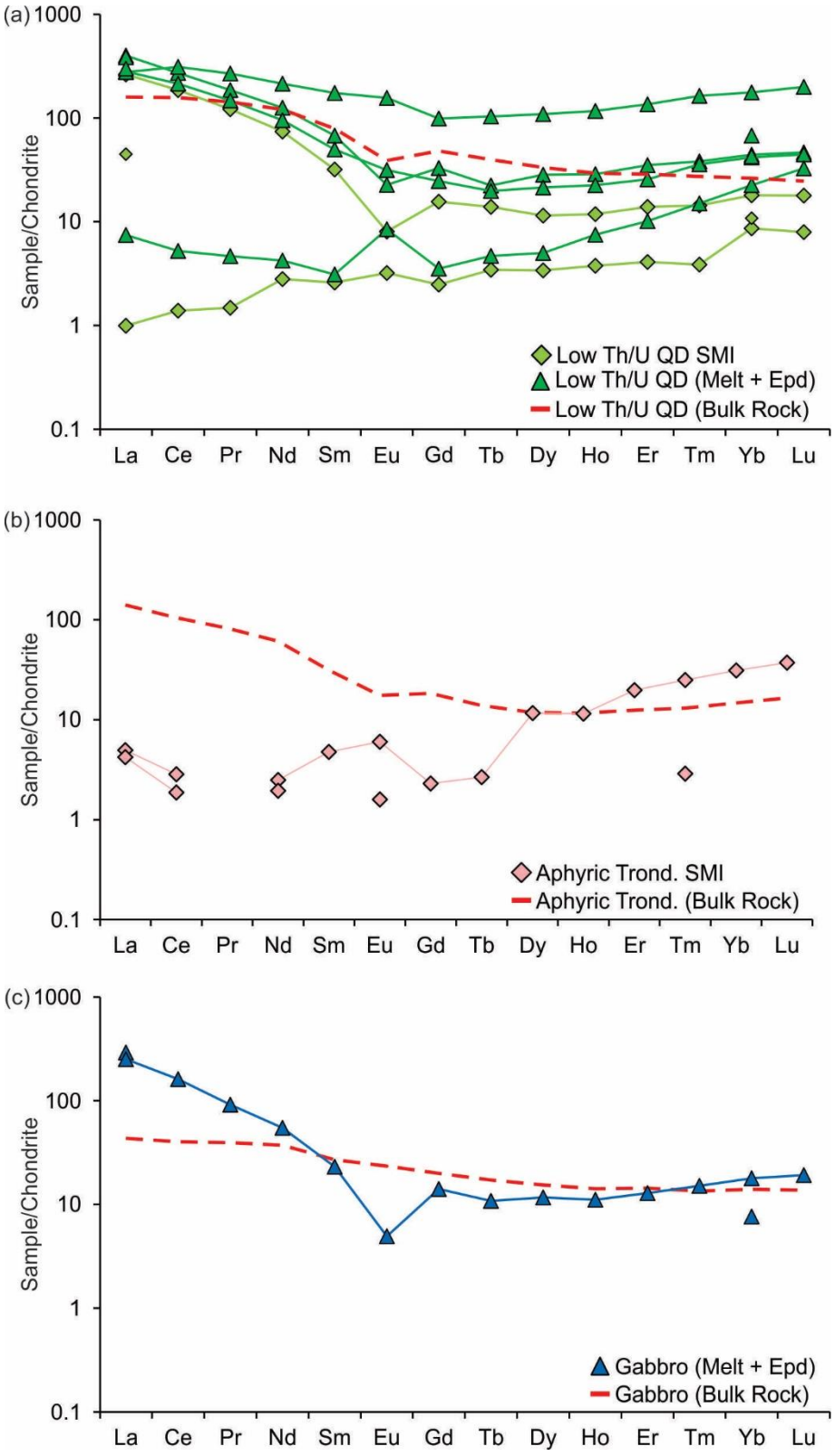
(a)
1000
100
10
1
0.1
Sample/Chondrite
La Ce Pr Nd Sm Eu Gd Tb Dy Ho Er Tm Yb Lu
Low Th/U QD SMI
Low Th/U QD (Melt + Epd)
Low Th/U QD (Bulk Rock)
(b)
1000
100
10
1
0.1
Sample/Chondrite
La Ce Pr Nd Sm Eu Gd Tb Dy Ho Er Tm Yb Lu
Aphyric Trond. SMI
Aphyric Trond. (Bulk Rock)
(c)
1000
100
10
1
0.1
Sample/Chondrite
La Ce Pr Nd Sm Eu Gd Tb Dy Ho Er Tm Yb Lu
Gabbro (Melt + Epd)
Gabbro (Bulk Rock)

Fig. 3.20: Chondrite normalized REE patterns for quartz-hosted SMI and bulk rock compositions. Limited data is present due to the limited number of elements acquired during LA-ICPMS analyses to improve detection limits for metals. (a) Low-Th/U quart diorite SMI and melt inclusions contaminated by epidote. (b) SMI in the aphyric trondhjemite. Importantly, these inclusions contain accidentally trapped sulfide. (c) Melt inclusion hosted in the gabbro that is contaminated by epidote.

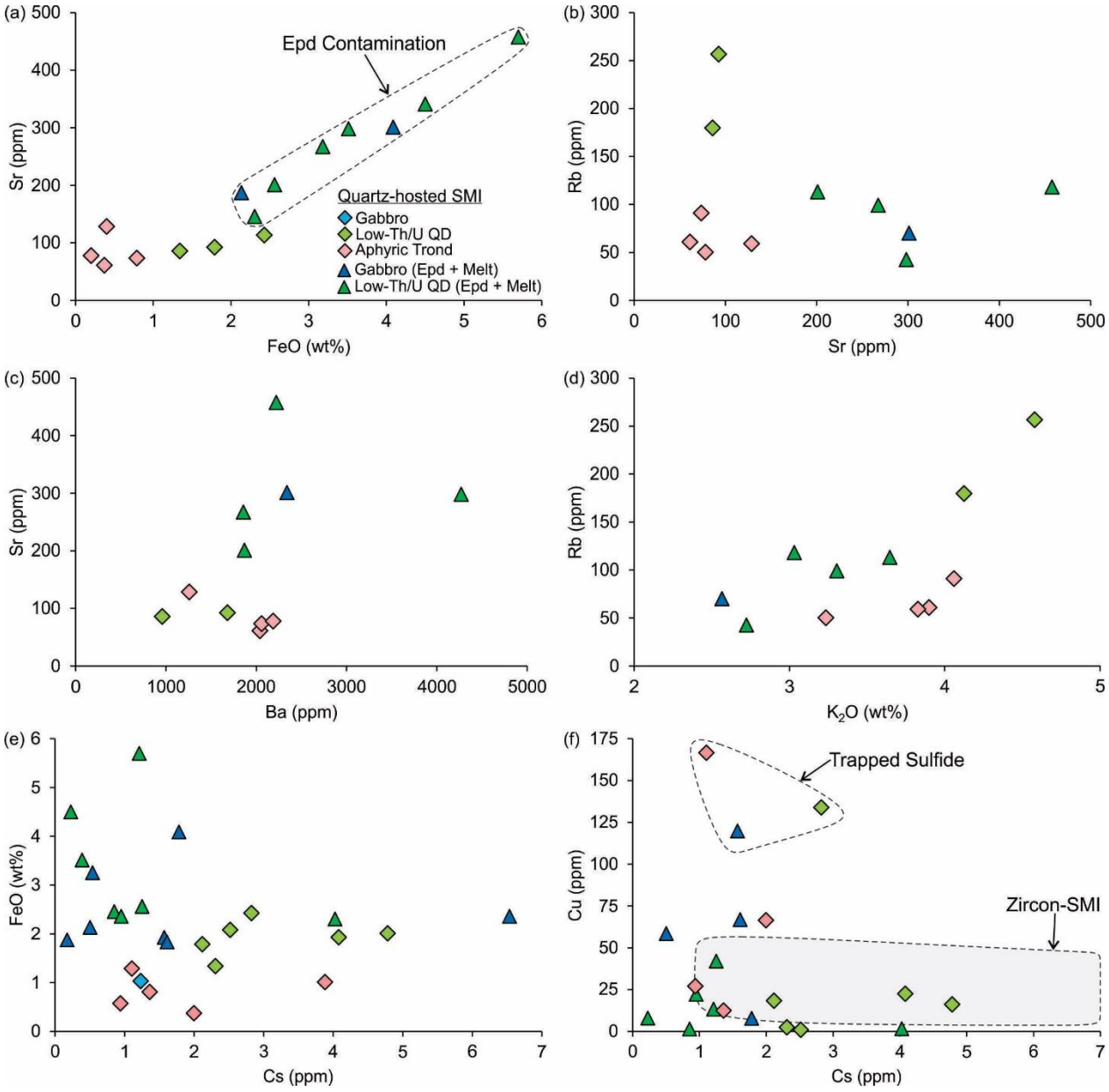
(a)
Epd Contamination
Quartz-hosted SMI
Gabbro
Low-Th/U QD
Aphyric Trond
Gabbro (Epd + Melt)
Low-Th/U QD (Epd + Melt)
Sr (ppm)
FeO (wt%)
(b)
Rb (ppm)
Sr (ppm)
(c)
Sr (ppm)
Ba (ppm)
(d)
Rb (ppm)
K2O (wt%)
(e)
FeO (wt%)
Cs (ppm)
(f)
Trapped Sulfide
Zircon-SMI
Cu (ppm)
Cs (ppm)

Fig. 3.21: Scatter plots of various major and trace elements in quartz-hosted SMI. (a) FeO plotted against Sr showing a positive relationship and that the epidote-contaminated melt inclusions are enriched in Sr compared to the non-contaminated inclusions. (b) Sr plotted against Rb showing the epidote contaminated inclusions have lower Sr than non-contaminated SMI in the low-Th/U quartz diorite. The aphyric trondhjemite SMI have similar Rb contents to the epidote-contaminated inclusions. (c) Ba plotted against Sr concentrations. (d) K_2O plotted against Rb concentrations showing a weak positive relationship. (e) Cs plotted against FeO concentrations showing that Cs is slightly lower in the epidote contaminated melt inclusions. (f) Cs plotted against Cu concentrations. Epidote-contaminated and non-contaminated inclusions show similar ranges in Cu. Note some inclusions have Cu > 100 ppm, and by examining the transient LA-ICPMS signal, these inclusions contain accidentally trapped sulfide. The range in Cu and Cs concentrations for zircon-hosted SMI are shown in the gray field (Cs concentrations do extend up to ~10 ppm).

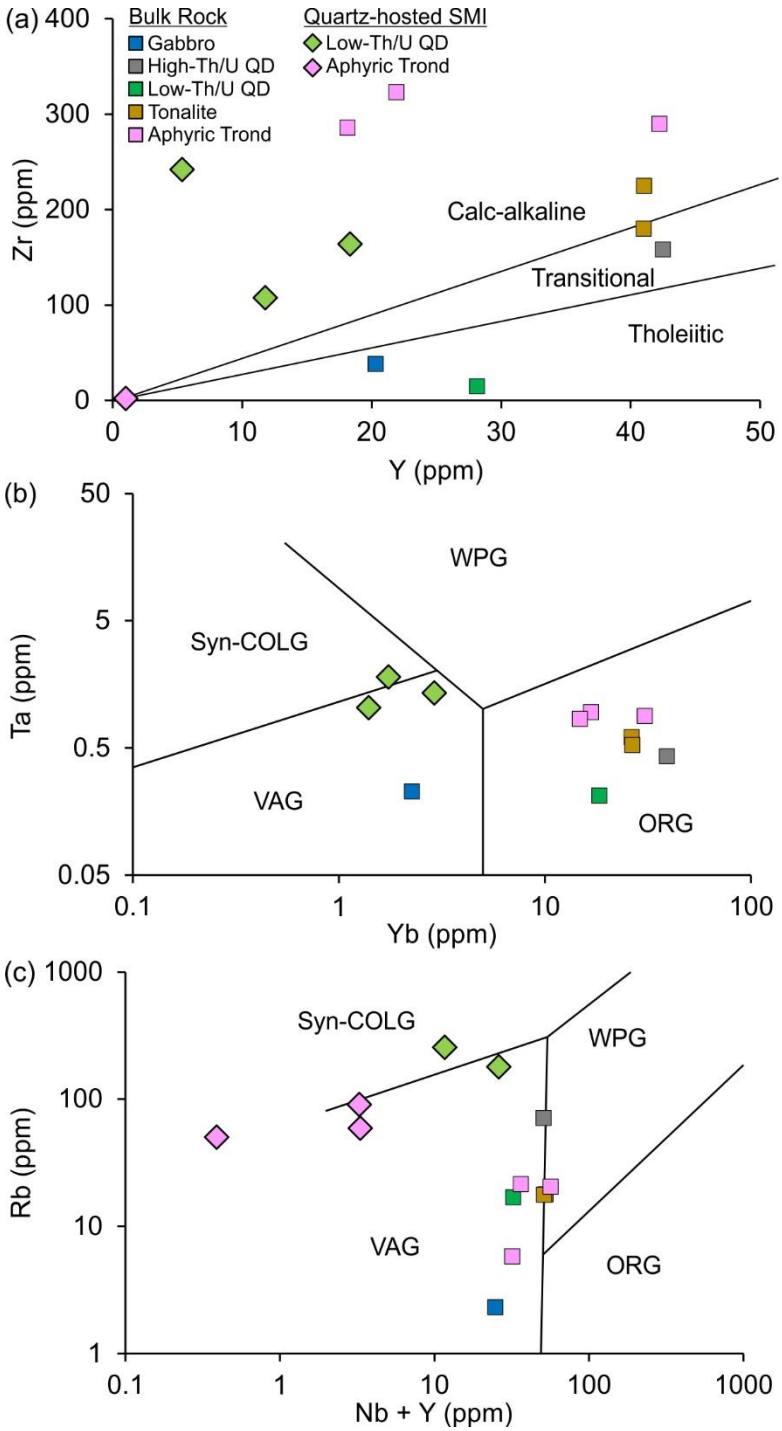
(a)
Bulk Rock
Gabbro
High-Th/U QD
Low-Th/U QD
Tonalite
Aphyric Trond
Quartz-hosted SMI
Low-Th/U QD
Aphyric Trond
Zr (ppm)
Y (ppm)
Calc-alkaline
Transitional
Tholeiitic
(b)
Ta (ppm)
Yb (ppm)
WPG
Syn-COLG
VAG
ORG
(c)
Rb (ppm)
Nb + Y (ppm)
Syn-COLG
WPG
VAG
ORG

Fig. 3.22: Tectonic discrimination diagrams showing compositional classifications of SMI and bulk rock analyses. (a) Zr (ppm) plotted against Y (ppm) shows the SMI from the Mouska-stage low-Th/U quart diorite plots in the calc-alkaline field whereas it's respective bulk rock composition plots in the tholeiitic field. The aphyric trondhjemite of the Doyon-stage and it's bulk rock composition plot in the calc-alkaline field. Compositional fields after Ross and Bédard, 2009. (b) Ta (ppm) plotted against Yb (ppm) shows that from the low-Th/U quartz diorite fall in the volcanic arc field and syn-collision granite field whereas the lone SMI from the aphyric trondhjemite plots in the within plate granite field. A majority of the bulk rock analyses plot in the ocean ridge granite field. Diagram after Pearce et al. (1984). (c) Rb (ppm) plotted against Nb + Y (ppm) shows a majority of SMI and bulk rock analyses plot in the volcanic arc granite field, however the bulk rock compositions extend to lower Rb concentrations. Diagram after Pearce et al. (1984). ORG = ocean ridge granite; Syn-COLG = syn-collisional granites; VAG = volcanic arc granites; WPG = within plate granites.

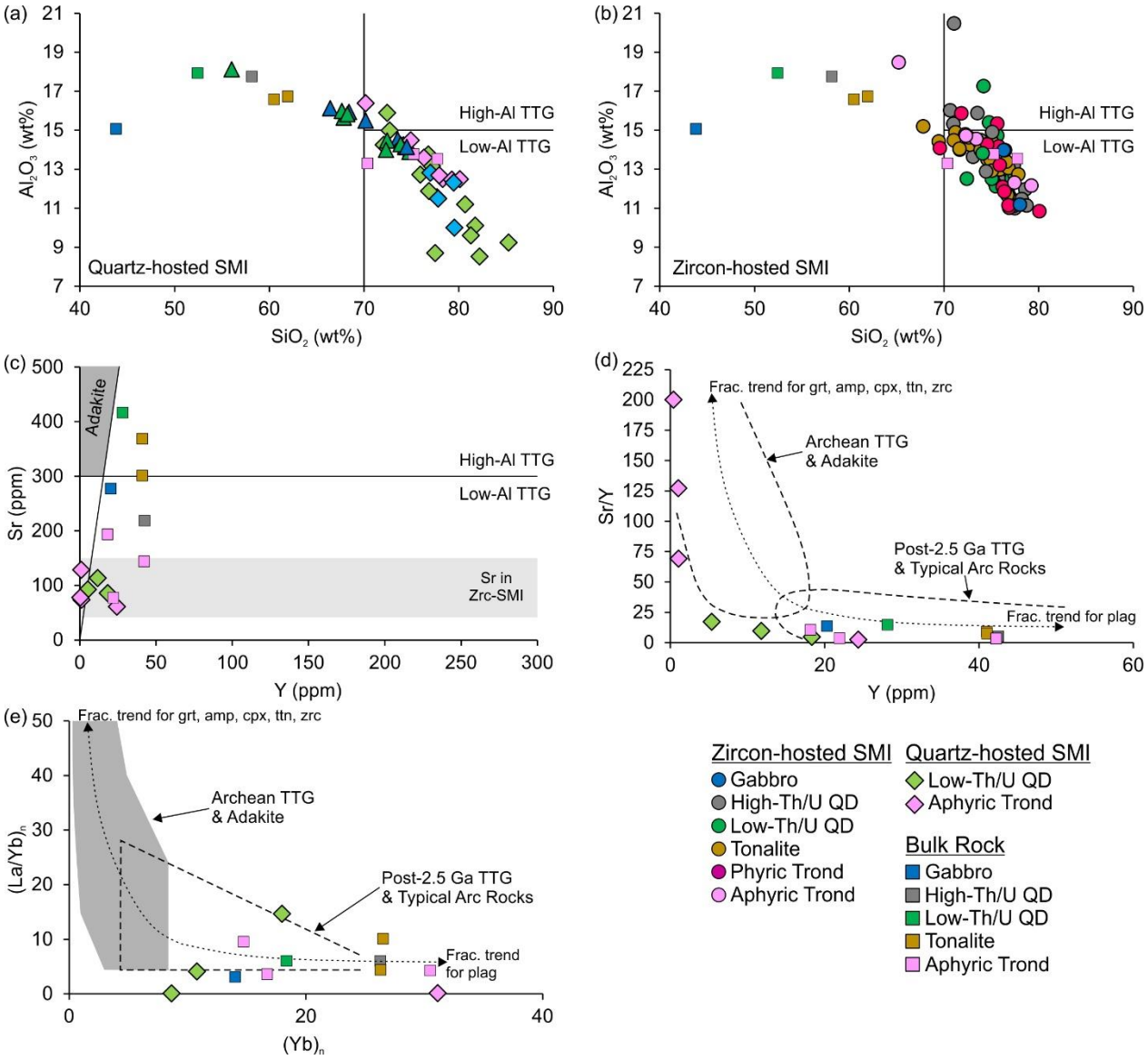
(a)
Al2O3 (wt%)
SiO2 (wt%)
High-Al TTG
Low-Al TTG
Quartz-hosted SMI
(b)
Zircon-hosted SMI
(c)
Sr (ppm)
Y (ppm)
Adakite
Sr in Zrc-SMI
(d)
Sr/Y
Frac. trend for grt, amp, cpx, ttn, zrc
Archean TTG & Adakite
Post-2.5 Ga TTG & Typical Arc Rocks
Frac. trend for plag
(e)
(La/Yb)n
(Yb)n
Zircon-hosted SMI
Gabbro
High-Th/U QD
Low-Th/U QD
Tonalite
Phyric Trond
Aphyric Trond
Quartz-hosted SMI
Low-Th/U QD
Aphyric Trond
Bulk Rock
Gabbro
High-Th/U QD
Low-Th/U QD
Tonalite
Aphyric Trond

Fig. 3.23: Zircon- and quartz-hosted SMI compositions plotted on various TTG classification diagrams. Bulk rock compositions are also shown. (a) Concentrations of SiO_2 (wt%) plotted against Al_2O_3 (wt%) for quartz-hosted SMI showing their compositions are typical of low-Al TTG suites (Barker, 1979). Inclusions > ~80 wt% SiO_2 have suffered from quartz-contamination during SEM-EDS analyses. (b) Concentrations of SiO_2 (wt%) plotted against Al_2O_3 (wt%) for zircon-hosted SMI showing their compositions are typical of low-Al TTG suites (Barker, 1979). (c) Sr (ppm) plotted against Y (ppm) for quartz-hosted SMI and bulk rock. The range in Sr (ppm) concentrations in zircon-hosted SMI is shown in a gray field. Important to note, that SMI plot in the low-Al TTG field and only SMI with accidentally trapped epidote plot near or in the high-Al TTG field. (d) Sr/Y plotted against Y (ppm) differentiating between adakite (Archean TTG) and typical arc rock (post 2.5 Ga TTG) compositions (Defant and Drummond, 1990; Richards and Kerrich, 2007) for quartz-hosted SMI and bulk rock compositions. Note how SMI compositions plot primarily in the typical arc rock (post-2.5 Ga rocks TTGs) field. (e) Chondrite normalized $(La/Yb)_n$ plotted against $(Yb)_n$ values showing quartz-hosted SMI are consistent with typical arc rocks (post-2.5 Ga rocks TTGs; Martin, 1999).

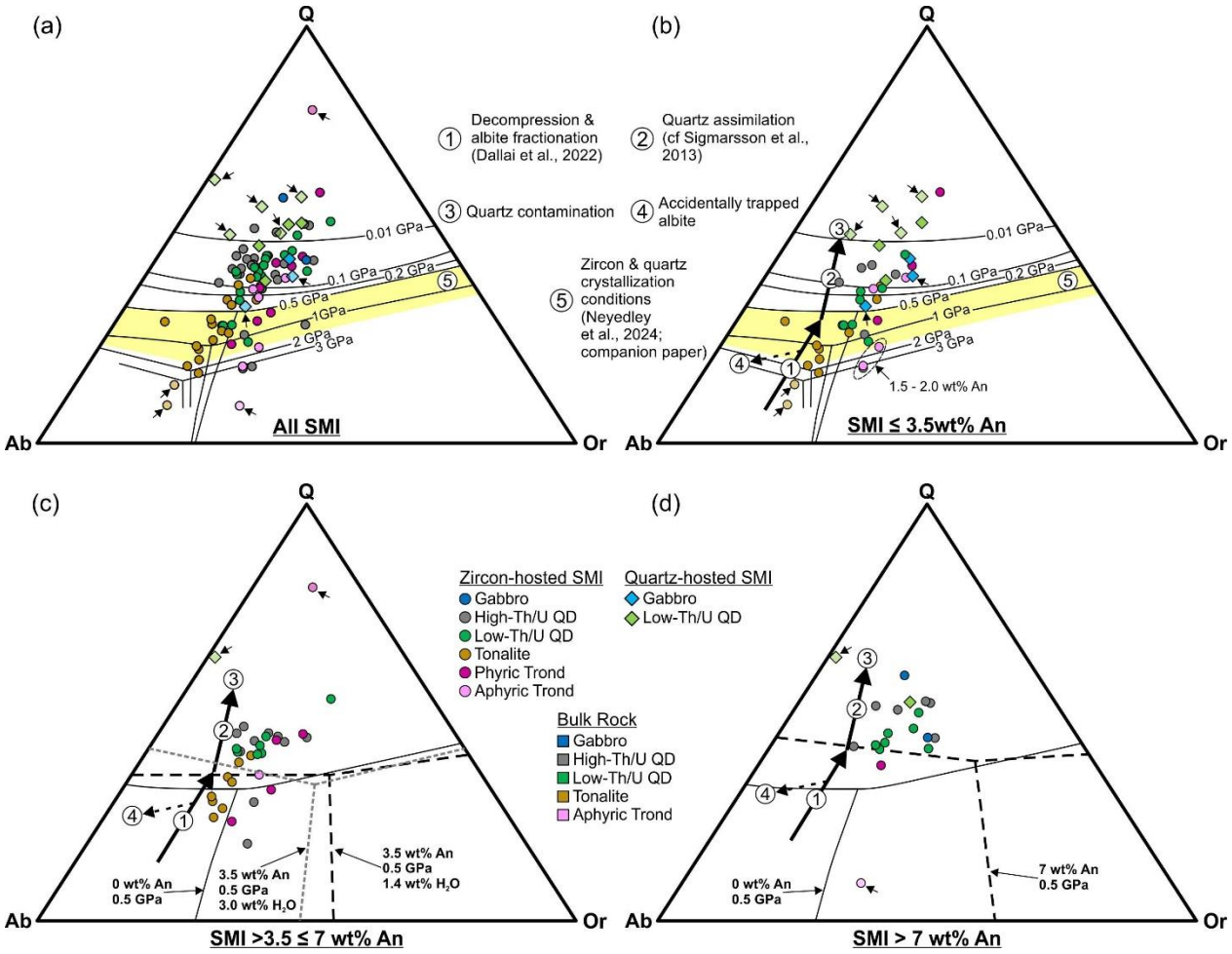
(a)
Q
Ab
Or
All SMI
0.01 GPa
0.1 GPa
0.2 GPa
0.5 GPa
1GPa
2 GPa
3 GPa
(b)
SMI ≤ 3.5wt% An
1.5 - 2.0 wt% An
① Decompression & albite fractionation (Dallai et al., 2022)
② Quartz assimilation (cf Sigmarsson et al., 2013)
③ Quartz contamination
④ Accidentally trapped albite
⑤ Zircon & quartz crystallization conditions (Neyedley et al., 2024; companion paper)
(c)
SMI >3.5 ≤ 7 wt% An
0 wt% An 0.5 GPa
3.5 wt% An 0.5 GPa 3.0 wt% H2O
3.5 wt% An 0.5 GPa 1.4 wt% H2O
(d)
SMI > 7 wt% An
0 wt% An 0.5 GPa
7 wt% An 0.5 GPa
Zircon-hosted SMI
Gabbro
High-Th/U QD
Low-Th/U QD
Tonalite
Phyric Trond
Aphyric Trond
Quartz-hosted SMI
Gabbro
Low-Th/U QD
Bulk Rock
Gabbro
High-Th/U QD
Low-Th/U QD
Tonalite
Aphyric Trond

Fig. 3.24: Pressure estimates based in normative quartz (Q) – albite (Ab) – orthoclase (Or) compositions of SMI with cotectic curves based on the haplogranite system. The cotectic lines drawn in (a) and (b) are for an anorthite-free and H_2O-saturated system (Tuttle and Brown, 1958). As the anorthite content increases and the system becomes undersaturated in H_2O, the cotectic lines are shifted away from the albite corner (Wilke *et al.,* 2017). This diagram is suitable for SiO_2 concentrations between 70 and 78 wt% and SMI with SiO_2 outside of this range are indicated by arrows. (a) All SMI compositions are plotted regardless of each inclusions anorthite content. (b) Inclusions with ≤ 3.5 wt% normative anorthite are plotted. These inclusions show that a majority have estimated pressures comparable to other geobarometric constraints on the MIC. The trend of decreasing pressure indicated by the arrow labeled (1), signifies decompression and albite fractionation in order for inclusions to move to higher quartz contents. Inclusions that lie above the 0.5 GPa line reflect compositions affected by assimilation of quartz-rich material (line 2). Inclusions that above the 0.01 GPa line are inclusions suffering from accidentally trapped quartz or are quartz-hosted SMI and suffer from host contamination. (c) SMI with anorthite contents between 3.5 and 7 wt% are plotted. Two cotectic lines are plotted for a system at 0.5 GPa and 3.5 wt% anorthite, one cotectic is for a system with 3.0 wt% H_2O and the other is for 1.4 wt% H_2O. The cotectic for an anorthite-free and H_2O-saturated system at 0.5 GPa is also shown. It is important display how anorthite content changes the position of the cotectic as some inclusions fall on the orthoclase-side of the cotectic at 0 wt% anorthite, but when using a cotectic for an anorthite-bearing system, these inclusions fall on the albite-side, consistent with the lower anorthite inclusions in (a). (d) SMI that have >7 wt% anorthite content. The 0.5 GPa is shifted to higher quartz contents and now inclusions in (a) that plotted < 0.1 GPa are now around 0.5 GPa, suggesting only minor amounts of quartz assimilation is needed to produce these compositions.

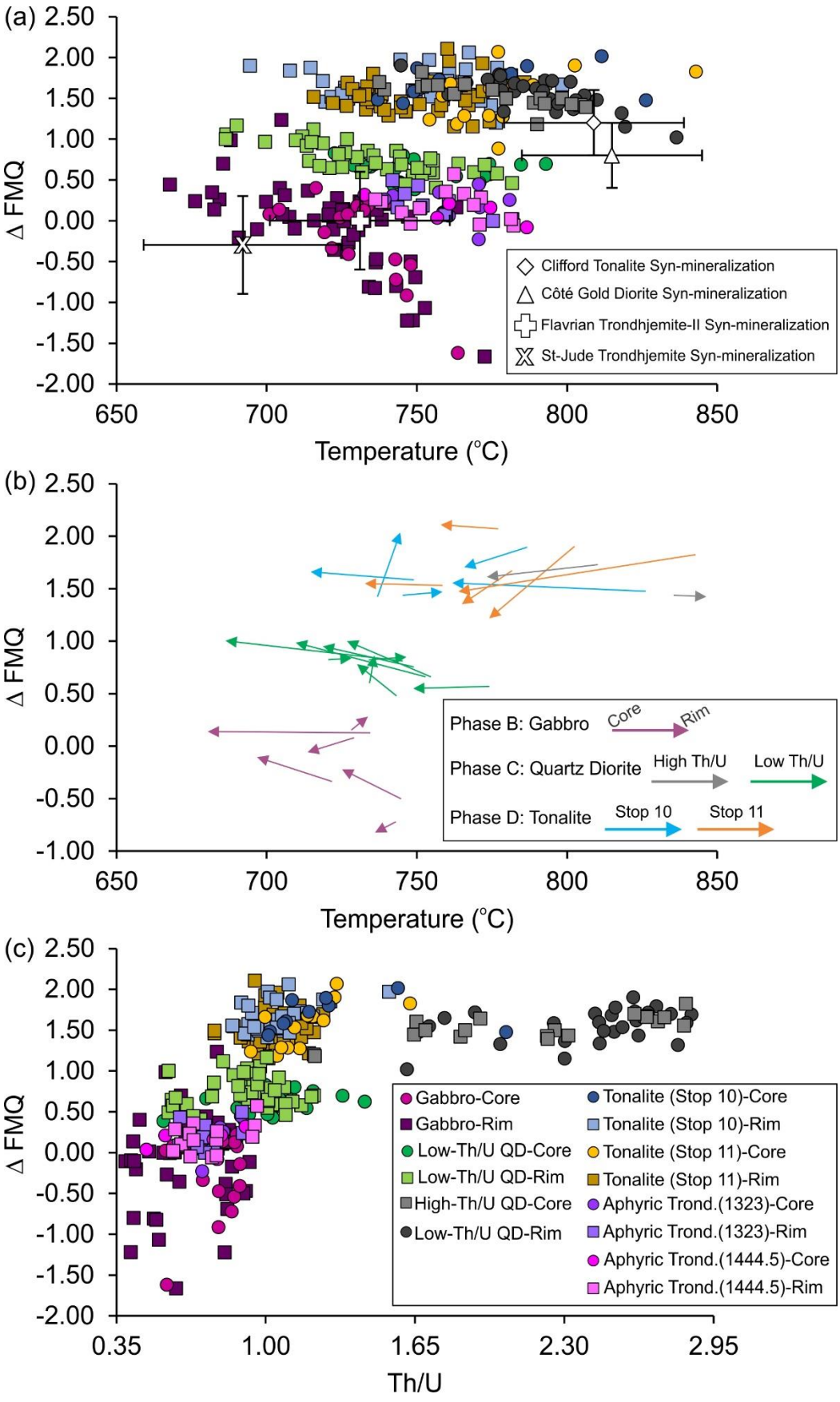
(a)
Δ FMQ
Temperature (°C)
Clifford Tonalite Syn-mineralization
Côté Gold Diorite Syn-mineralization
Flavrian Trondhjemite-II Syn-mineralization
St-Jude Trondhjemite Syn-mineralization
(b)
Δ FMQ
Temperature (°C)
Phase B: Gabbro
Core
Rim
Phase C: Quartz Diorite
High Th/U
Low Th/U
Phase D: Tonalite
Stop 10
Stop 11
(c)
Δ FMQ
Th/U
Gabbro-Core
Gabbro-Rim
Low-Th/U QD-Core
Low-Th/U QD-Rim
High-Th/U QD-Core
Low-Th/U QD-Rim
Tonalite (Stop 10)-Core
Tonalite (Stop 10)-Rim
Tonalite (Stop 11)-Core
Tonalite (Stop 11)-Rim
Aphyric Trond.(1323)-Core
Aphyric Trond.(1323)-Rim
Aphyric Trond.(1444.5)-Core
Aphyric Trond.(1444.5)-Rim

Fig. 3.25: (a) Plot of temperature (Ti-in-zircon thermometer; Ferry and Watson, 2007) against ΔFMQ conditions (Loucks *et al.*, 2020) for individual lithologies of the MIC and compared to other Archean TTG systems (Meng *et al.*, 2021). (b) Graph displaying core to rim changes in individual zircon grains temperature (Ti-in-zircon thermometer; Ferry and Watson, 2007) and ΔFMQ conditions (Loucks *et al.*, 2020). Arrows indicate core to rim compositional change. (c) Th/U ratio of zircon against ΔFMQ.

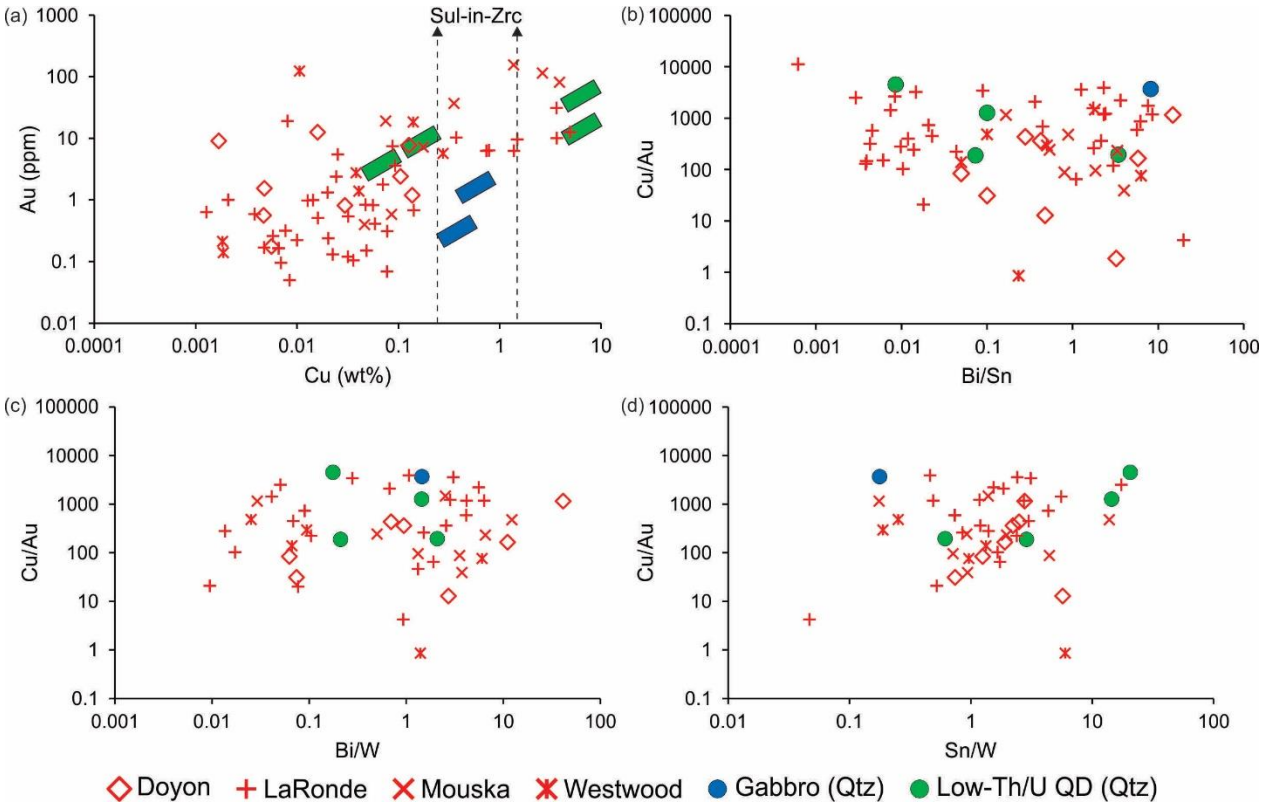

Fig. 3.26: Concentrations and ratios of accidentally trapped sulfides in melt inclusions compared to ore compositions from deposits in the Doyon-Bousquet-LaRonde mining camp. (a) Au (ppm) plotted against Cu (wt%). The boxes for sulfide inclusions represent the range in possible concentrations (see text for details). Since Au cannot be quantified in zircon-hosted sulfide inclusions, the range in Cu is shown by dashed vertical lines. The concentrations of Au and Cu are similar to grades in the deposits. (b) Cu/Au plotted against Bi/Sn. (c) Cu/Au plotted against Bi/W. (d) Cu/Au plotted against Sn/W. Data for Doyon deposit, Westwood deposit, and Mouska deposit ores from the Geological Survey of Canada, unpublished. Data for LaRonde is from Dubé *et al.*, 2004.

3.11: Chapter 3 - Supplementary Materials File

METHODOLOGY

Sample collection

Initial sample collection took place during July and August, 2016, and involved sampling of outcrop and drill core. Representative images of lithologies in hand sample are shown in Supplementary Figure 3.1. Outcrop samples were taken as far away from quartz veining and/or dykes/sills (when present) to obtain unaltered or minimally altered samples. Drill core samples were collected from two drill holes that are interpreted to represent a near complete stratigraphic column of the entire MIC (Galley and Lafrance, 2014; A. Galley, communication, 2016). Drill hole MSK-6-810 contains phase A (diorite), B (gabbro), and C (quartz diorite) of the Mouska stage and drill hole 1106-96 contains phase E (Doyon quartz diorite) of the Mouska stage and phases G (plagioclase-phyric tonalite), H (phyric-trondhjemite), and I (aphyric-trondhjemite) of the Doyon stage. Doyon-stage phase F (plagioclase-amphibole-phyric tonalite) and Mouska-stage phase D (tonalite) were not present in either of these drill holes, phase D (tonalite) was collected from outcrop, whereas a drill hole that contains phase F (plagioclase-amphibole-phyric tonalite) could not be located. The sampling strategy for drill core was to target textures that are known to host SMI (e.g., quartz phenocrysts) and areas that are representative of volatile saturation and/or separation (e.g., pegmatitic textures, miarolitic cavities; cf Audétat and Pettke, 2003).

Mineral separation and imaging

Six samples from four phases of the MIC were selected for zircon mineral separation based on transmitted light petrography. Samples were sent to Boise State University, Boise, USA for separation, picking, mounting, and scanning electron microscope cathodoluminescence (SEM-CL) imaging of zircon. After zircon separation, half of the zircon grains picked underwent high

temperature annealing in a muffle furnace (~900°C for 60 hours in quartz crucibles) to enhance the SEM-CL response, and to homogenize inclusions to yield a glass upon quench that were later analyzed by various methods. The other half aliquot of grains were not annealed. Both annealed and non-annealed zircon and titanite were mounted in epoxy and polished until the center level of the grains were exposed. SEM-CL images of annealed zircon were obtained with a JEOL JSM-1300 SEM and Gatan MiniCL. Images of non-annealed zircon were collected by SEM- back-scattered electron (BSE) using a TESCAN MIRA 3 LMU Variable Pressure Schottky Field Emission SEM equipped with a BSE detector at Saint Mary's University, Halifax, Canada.

SMI petrography

Petrography characterization, mapping, and selection of SMI for further detailed analyses were conducted initially on polished thick sections and in quartz and zircon mineral separates. Petrographic analysis of SMI provided the base for all analytical techniques conducted and described below. This involved characterizing and classifying SMI using the melt inclusion assemblage (MIA) method (cf. Goldstein, 2003; Bodnar and Student, 2006). The appearance and distribution of the SMI, and the relative timing of their entrapment in each intrusive phase sampled of the MIC was established, where possible. Inclusion distribution maps were created to guide the selection of individual SMI for analyses and provide constraints on the origin of the inclusions (i.e., primary, or secondary). Subsets of quartz- and zircon-hosted SMI were selected based on the following criteria: i) The abundance and size of SMI in their respective host; ii) the degree of SMI preservation (e.g., away from fractures in and/or near edges of host grains, absence of decrepitation halos); and iii) differentiating SMI containing accidentally trapped mineral inclusions from uncontaminated SMI. The abundance, size, and degree of preservation of SMI in quartz and zircon was the main limitation of this study.

304

Identification and major/minor element analyses were performed on exposed inclusions (mineral and SMI) in quartz and zircon using a TESCAN MIRA 3 LMU Variable Pressure Schottky Field Emission SEM (Saint Mary's University, Halifax, Canada). The SEM is equipped with BSE detector, energy dispersive spectroscopy (EDS), and cathodoluminescence (CL) functionality. For EDS, a solid-state, 80 mm^2 X-max Oxford Instruments EDS detector was used. The A beam voltage of 20 kV and an approximate working distance of 17-20 mm was used for all analyses.

Hot CL imaging of quartz

Hot CL emission imaging was performed on polished thin sections of select intrusive lithologies (quartz diorite, aphyric trondhjemite) to determine any growth zoning present in quartz and determine the luminescence color of quartz, which can be related to formation conditions (Götze, 2012) . Hot CL analysis was performed using a Lumic HC4-LM hot-cathode cathodoluminescence microscope at Saint Mary's University, Halifax, Canada. The cathodoluminescence microscope is coupled to an Olympus BXFM focusing mount with images captured by a Kappa DX40C peltier cooled camera operated using the DX40C-285FW software package. Conditions used for analyses were an acceleration voltage between 9.5 - 11.5 kV, a beam current of 0.25 mA, a filament current of 2.3 A, a deflection of 10 V, and a focus of 5.5 V.

Homogenization of quartz-hosted melt inclusions

Experiments were conducted at 1 atm and at high P-T to homogenize quartz-hosted inclusions to a silicate melt and quench to a silicate glass for the purpose of obtaining additional compositional constraints, including volatiles that could not be determined by LA-ICPMS. Ambient pressure runs were conducted in a one atmosphere muffle furnace at Saint Mary's

University. Quartz grains were separated from the rock using a standard jaw crusher and picking under a binocular microscope. Grains were loaded into quartz crucibles and placed into the furnace. The furnace was brought to a temperature of 1050°C over the course of eight hours and the temperature was held at 1050°C for ~5 days to ensure complete homogenization of SMI.

High pressure-temperature piston cylinder experiments were conducted using a Molybdenum hafnium carbide (MHC) cold-seal pressure vessel to homogenize quartz-hosted SMI. Inclusion homogenization was done by holding an aliquot of quartz at 950 ± 10°C and 1500 ± 50 bar in an externally-heated rapid quench MHC cold-seal pressure vessel assembly at the Magmatic and Ore-Forming Processes Research Laboratory at the University of Toronto, Toronto, Canada. Argon was used as a pressure medium and the pressure was monitored throughout the experiment using a factory calibrated digital pressure transducer. Each experiment had a 5 mm ⌀, 0.127 mm wall thickness, Pt capsule containing aluminum oxide powder, and 6 - 8 quartz grains that were roughly 0.25 mm in diameter. The sample capsule were welded using the 'ash-can' design and a Lampert PUK 3 welder in micro mode with output power at 20% (Sneeringer and Watson, 1985; Zhang et al., 2015).

Raman of homogenized and non-homogenized SMI

Confocal laser Raman microspectroscopy was performed at Saint Mary's University, Halifax, Canada, to determine the mineral phases composing quartz-hosted SMI and other mineral inclusions in quartz and to qualitatively estimate the H_2O content of glassy SMI. Analyses were performed using a Horiba Jobin-Yvon LabRam HR instrument (Saint Mary's University) equipped with a 100 mW (at source), 532 nm Nd-YAG diode laser (Laser Quantum) and a Synapse CCD detector (Horiba Jobin-Yvon). Pure silicon was used as a frequency calibration standard and analyses were performed using a 15 to 25 µm confocal hole diameter, depending on inclusion size

and inclusion depth. A 600 grooves/mm grating (spectral resolution of approximately ± 2 cm^{-1}) was used during spectrum collection. Spectra were collected by accumulating three, 15 to 30 s acquisitions at 100% laser power (~2.15 mW at sample surface through a 100x long working length objective) for mineral phase identification. For qualitative H_2O estimates of SMI, spectra were collected accumulating 10, 10 s acquisitions at 100% laser power. Two glass reference materials, one with ~2.27 to ~2.45 wt% H_2O (1-10-01A, B; Webster et al., 2011) and another with ~4.32 to ~5.94 wt% H_2O (1-09-10A, B; Webster et al., 2011) were analyzed to compare unknown SMI H_2O-peak spectral regions to glasses with known H_2O content.

Electron probe microanalyses of zircon-hosted silicate melt inclusions

Major and minor elements in silicate melt inclusions from each sample were analyzed using a JEOL JXA8230 electron microprobe equipped with five wavelength-dispersive spectrometers and an energy-dispersive spectrometer at the University of Toronto, Toronto, Canada. Calibration was performed using a variety of natural mineral standards (fluorapatite, pyrope garnet, sanidine, tugtupite, kaersutite, Durango apatite) and silicate glass standards (UA5831 obsidian). AthoG obsidian was employed as a secondary standard to monitor the consistency between different analytical sessions on analyte sensitivities and accuracy. An accelerating voltage of 15kV was used for all the analyses. In order to determine the optimal setting for beam current and beam diameter to avoid alkali and halogen mobility, several large inclusions (~15-25μm) were analyzed multiple times (never in the same location). A beam current of 2.0×10^{-8} A, coupled with a large beam diameter (3 μm) was found to be optimal for all elements. Reduction of beam current was shown to improve Na_2O accuracy but compromises the accuracy of F concentrations. Since F cannot be determined accurately by LA-ICP-MS but Na_2O can, we chose to optimize for F determination (2.0×10^{-8} A, 3 μm). Fluorine was analyzed using a TAPH crystal, since it is the most sensitive crystal

available that does not have peak overlap problems between F Kα and Fe Lα lines. A 20s on-peak counting time was applied for the analysis of all elements, except F, which required a 40s on peak counting time. Raw microprobe data count rates were converted to concentrations using the ZAF matrix correction scheme using JEOL software.

LA-ICPMS of quartz- and zircon-hosted SMI

The major, minor, and trace element composition of quartz- and zircon-hosted silicate melt inclusions were determined by LA-ICP-MS at the Magmatic and Ore-Forming Processes Research Laboratory at the University of Toronto, Toronto, Canada. An NWR 193UC ArF Excimer laser ablation system attached to an Agilent 7900 quadrupole mass spectrometer was used. The instrument was tuned to maximum sensitivity while maintaining robust plasma conditions (U≈Th on NBS SRM610) and low oxide and doubly charge ion production rates (ThO/Th < 0.3%; Mass 21/42 < 0.3%). Helium was used as a carrier gas at a flow rate of 1.0 L/min. The reference standard NIST SRM610 silicate glass was used for the quantification of element concentration ratios and calibration of analyte sensitivities. Analyses of ~20 unknowns were bracketed by two standard analyses at the beginning and the end of each analysis block. For each melt inclusion the size and shape of the beam varied to include the entire inclusion while minimizing the amount of host mineral ablated alongside.

Analyses of SMI were conducted on non-homogenized quartz-hosted SMI and on a combination of homogenized and non-homogenized zircon-hosted SMI. All quartz- and zircon-hosted SMI were unexposed and during analysis the entire SMI was ablated along with a small amount of their surrounding host mineral.

Trace element quantification of SMI was performed using the software SILLS (Guillong et al., 2008). This involved deconvoluting the mixed SMI-plus-host signal after calculation of

background-corrected count rates for each isotope, followed by quantification of inclusion and host compositions. The standard reference material (SRM) NIST610 silicate glass was used for the calibration of analyte sensitivities for SMI. For quartz-hosted SMI dwell times for all elements were 10 ms. A shortened element menu for quartz-hosted SMI was utilized to improve detection capabilities of metals, specifically ^{197}Au and ^{107}Ag. All elements on the shortened element menu were 10 ms, except for ^{197}Au (200 ms) and ^{107}Ag (50 ms). Interference corrections for $^{91}Zr^{16}O$ on ^{107}Ag, and $^{181}Ta^{16}O$ on ^{197}Au were performed manually, based on determination of oxide production rates using in-house zircon and rutile standards, respectively, and subtracting corresponding contributions (count rate basis) from Zr and Ta occurring in the SMI. For zircon-hosted SMI, dwell times for all elements were 10 ms. Exceptions were ^{59}Co, ^{65}Cu, ^{75}As, ^{125}Te, and ^{209}Bi which were all 20 ms and ^{107}Ag and ^{197}Au were not collected due to the interferences of $^{91}Zr^{16}O$ and $^{90}Zr^{91}Zr^{16}O$, respectively.

LA-ICPMS of anhydrite

The major, minor, and trace element composition of anhydrite was determined by LA-ICP-MS at the Magmatic and Ore-Forming Processes Research Laboratory at the University of Toronto, Toronto, Canada. A New Wave Research® 193 nm ArF Excimer laser ablation system attached to an Agilent 7900 quadrupole mass spectrometer was used. The instrument was tuned to maximum sensitivity while maintaining robust plasma conditions (U≈Th on National Institute of Standards and Technology Standard Reference Material 610 silicate glass (NIST610) and low oxide and doubly charge ion production rates (ThO/Th < 0.3%; Mass 21/42 < 0.3%). Helium was used as a carrier gas at a flow rate of 1.0 L/min. The reference standard NIST610 was used for the quantification of element concentration ratios and calibration of analyte sensitivities. Analyses of ~16 unknowns were bracketed by 2 standard analyses at the beginning and the end of each analysis

block. Trace element quantification of minerals was performed using the software SILLS (Guillong et al., 2008). An internal standard of 41.2 wt% CaO was used based on ideal stoichiometry. Dwell times for all elements were 10 ms.

Secondary Ion Mass Spectrometry of anhydrite

Oxygen ($^{18}O/^{16}O$) and sulfur ($^{34}S/^{32}S$) isotope ratios of anhydrite from the MIC were collected using a CAMECA 7f® SIMS at the University of Manitoba, Winnipeg, Manitoba. The conditions for sulfur and oxygen isotope analysis by SIMS are similar to each other. A cesium (Cs+) primary beam with a 6.5 nA current for oxygen and 3 nA current for sulfur was accelerated (+10 kV) onto the sample surface with a sputtering diameter of ~25 μm. The instrument operated with a 200 V offset for sulfur and for oxygen, –9 kV secondary accelerating voltage, and a mass resolving power of 350. For a detailed description of operating conditions and strategy for correction of instrumental mass fractionation and matrix effects, see Riciputi et al. (1998) for sulfur isotope analysis and Sheahan et al. (2016). for oxygen isotope analysis.

Grains of the University of Manitoba in-house anhydrite reference material (Pyrenees anhydrite] with $\delta^{18}O$ and $\delta^{34}S$ values of 14.1‰ and 14.9‰, respectively, were used as the reference material for anhydrite analyses. Spot-to-spot reproducibility for oxygen and sulfur analyses were 0.6‰ and 0.7‰, respectively. All isotopic data are presented using standard δ-notation relative to the appropriate standards, Vienna Standard Mean Ocean Water (V-SMOW) for $^{18}O/^{16}O$ and Vienna Canyon Diablo Troilite (V-CDT) for $^{34}S/^{32}S$.

COMPARISON OF ZIRCON-HOSTED SMI ANALYTICAL METHODS, QUANTIFICATION, AND UNCERTAINTIES

The major element chemistry of zircon-hosted SMI was determined by three different analytical methods (SEM-EDS, EPMA, and LA-ICPMS) for both unhomogenized and homogenized (i.e., annealed) inclusions.

Quantification of LA-ICPMS SMI analyses require an internal standard (e.g., Halter et al., 2002). This can be determined several ways (Halter et al., 2002; Halter et al., 2004a; Zajacz and Halter, 2007; Chang and Audétat, 2021), such as 1) analysis of exposed, glassy SMI by SEM-EDS and/or EPMA to determine inclusion major element concentrations and using an average concentration of a select major element from multiple SMI for a given lithology, 2) defined geochemical trends based on whole-rock analyses, 3) a known and constant partition coefficient between the host mineral and melt, and 4) determining the volume ratio between the inclusion and total ablation volume (host + melt). Minerals such as olivine, plagioclase, pyroxene, and quartz can all suffer from potential post-entrapment diffusion of some elements (e.g., Li, Na, Cu Ag; Zajacz et al., 2009; Audétat et al, 2018; Chang and Audétat, 2021), however given the slow diffusion rates of trace elements in zircon, diffusion is likely not an issue (Cherniak et al. 1997, Cherniak and Watson, 2003; Thomas et al., 2003).

All of these methods may introduce significant uncertainties. For example, assuming a constant internal standard value (based on EMPA or SEM analyses) to data sets where actual inclusion compositions vary systematically due to magma fractionation or other real igneous processes relative to the timing of melt entrapment. The SMI host minerals in this study (zircon and quartz) exclude Al_2O_3 and as it is the second most abundant major element in the SMI, its concentration was used as the internal standard for LA-ICPMS melt inclusion quantification (i.e., Halter et al., 2004a) by using the software SILLS (Guillong et al., 2008) allowing for a Al_2O_3 concentration to be entered for individual inclusions. First, the mean Al_2O_3 concentration from SEM-EDS (anhydrous basis) and EPMA (H_2O by difference) analyses was used as the internal

standard for SMI quantification. Using the high-Th/U quartz diorite as an example (mean SMI Al_2O_3 = 14.00 ± 2.09 wt%;1σ; n = 18), the mean Al_2O_3 ± 1σ results in a relative uncertainty on SiO_2, other major, and trace elements is ±5%, 12%, and 15%, respectively (Fig. 3.10). Such uncertainty in major elements can lead to SMI compositions plotting in different compositional fields (e.g., subalkaline or alkaline; Supplementary Figure 3.2) and, as stated, not capturing temporal changes in melt chemistry, thereby impacting petrogenetic interpretation; therefore, this approach was not considered further.

A more accurate approach is to determine the Al_2O_3 content of each inclusion analyzed by LA-ICPMS by utilizing defined geochemical trends from whole-rock analyses or SEM-EDS/EPMA data of exposed SMI (e.g., Halter et al., 2002; Halter et al., 2004; Chang and Audétat, 2020). From the analysis of exposed zircon SMI, clear trends of decreasing SiO_2 with increasing Al_2O_3 are observed for each lithology (Supplementary Figure 3.3A). Determination of a specific Al_2O_3 value for each inclusion involved fixing Al_2O_3 concentrations between 10 and 18 wt% (bracketing SEM-EDS data) for each inclusion in the SILLS quantification to calculate the corresponding SiO_2 concentrations at different hypothetical Al_2O_3 values (i.e., an initial 'model' trendline for each inclusion; Trend line 'A' in Supplementary Figure 3.3A). The ideal internal standard Al_2O_3 concentration to be used for the final SILLS quantification of each SMI corresponds to the intersection of the trendline determined from the fixed Al_2O_3 concentrations (Trend line 'A') and the trendline defined by the SEM-EDS/EPMA data for exposed SMI (Trend line 'B'; Supplementary Figure 3.3A), defining a unique Al_2O_3/SiO_2 ratio for each inclusion. It is important to note that LA-ICPMS major element concentrations were quantified assuming 2 wt% H_2O, therefore the major elements total 98 wt% whereas SEM-EDS analyses are 100 wt% totals. Renormalizing SEM-EDS analyses to 98 wt% total results in an increase of ~15 % relative on the Al_2O_3 concentrations (e.g., 11.60 vs. 13.60 wt% Al_2O_3). Given we do not have a tight constraint

on the total volatile content of the SMI and based on Raman analyses SMI have a maximum of 2 wt% H_2O, therefore there any major element total used in SILLS quantification will have some error associated with it.

With the quantification procedure for LA-ICPMS analyses discussed, the LA-ICPMS, SEM-EDS, and EPMA results can be compared. For FeO, MgO, TiO_2, and CaO no differences exist between the three different methods and have similar concentration ranges within each sample (Supplementary Figure 3.4A-B). Comparing unhomogenized and homogenized inclusions, no difference is apparent for TiO_2 and CaO in any lithology. For FeO, homogenized SMI in the high-Th/U quartz diorite extended to higher values but in the low-Th/U quartz diorite and tonalite, no difference is present between unhomogenized and homogenized SMI. For LA-ICPMS analyses in the high-Th/U quartz diorite, MgO is slightly higher (~0.1 wt%) in the unhomogenized SMI than in the homogenized SMI, but in the low-Th/U quartz diorite and tonalite no differences are noted. These variations in FeO and MgO are reflected to be real variations in melt chemistry and/or contamination from some accidentally trapped accessory phases (e.g., magnetite, chlorite).

No differences in SiO_2 and Al_2O_3 concentrations are noted between EPMA and SEM-EDS analyses and no differences are noted between unhomogenized and homogenized SMI (Supplementary Figure 3.4C). The concentration of Na_2O is consistently higher in SEM-EDS analyses compared to EPMA and LA-ICPMS analyses in all lithologies except for the phyric trondhjemite where SEM-EDS and LA-ICPMS have similar Na_2O concentrations (Supplementary Figure 3.4D-H). The higher Na_2O concentration in SEM-EDS analyses could be due to Na diffusion towards the beam during analyses, however since Na_2O concentrations within a MIA are consistent and MIA span a range in Na_2O within a given sample (e.g., ~5 to 9 wt % Na_2O; Supplementary Figure 3.4G), this suggests Na_2O concentrations within MIA are trapping slightly different melt compositions and are not related to the uncertainty related to Na diffusion.

In some lithologies (e.g., tonalite; Supplementary Figure 3.4G) homogenized SMI generally have higher Na_2O concentrations than unhomogenized SMI determined by SEM-EDS, whereas other lithologies show similar Na_2O concentrations between homogenized and unhomogenized SMI (e.g., low-Th/U quartz diorite; Supplementary Figure 3.4I). Since higher Na_2O is not observed in all homogenized SMI from all lithologies, the within-sample Na_2O variations are interpreted as real melt compositional variations and not an artifact of Na diffusion as is an issue in quartz-hosted SMI (Zajacz et al., 2008, 2009).

Overall, major elements show good consistency between all methods, validating the use of these methods to evaluate SMI chemistry in zircon. In cases where the LA-ICPMS results over or underreport concentrations, these can be accounted for by minor, accidentally trapped minerals in the inclusion. Unless stated otherwise, major element data from zircon-hosted SMI analyses by all methods will be utilized for the purpose of petrogenetic interpretation as a single data set.

COMPARISON OF QUARTZ-HOSTED SMI ANALYTICAL METHODS, QUANTIFICATION, AND UNCERTAINTIES

The major element chemistry of quartz-hosted SMI was determined on separate inclusions by SEM-EDS and LA-ICPMS. Homogenized SMI were analyzed by SEM-EDS whereas unhomogenized SMI were analyzed by LA-ICPMS. Since SMI are scarce in quartz, only very few analyses on exposed inclusions could be obtained.

Quantification methodologies require some discussion as well as comparison of data from homogenized vs unhomogenized SMI. For LA-ICPMS data, the use of a mean Al_2O_3 concentration (from SEM-EDS on exposed inclusions) was considered. The limitations of this approach are already discussed above for zircon-hosted SMI. As well, due to the small size of SMI in quartz, analyses were contaminated by host quartz in the electron beam analytical volume resulting in

overreported SiO_2 and underreported Al_2O_3 (Fig. 3.18A, B). For the zircon-hosted SMI, correction for host contamination, when relevant, can be achieved by removing Zr and the proportional amount of SiO_2 tied to Zr in zircon to obtain an uncontaminated SMI composition, this cannot be done for quartz-hosted inclusions as there are no other elements in quartz to facilitate the correction. The trend line intersection method (e.g., Halter et al., 2002; Halter et al., 2004) used for zircon-hosted SMI to estimate unique Al_2O_3 concentrations for individual inclusions analyzed by LA-ICPMS and quantified by SILLS was also applied to quartz-hosted SMI. However, due to SiO_2 contamination in the SEM-EDS analyses, using Al_2O_3-SiO_2 relationships is not possible. Rather, quartz-hosted SMI display a trend of increasing CaO with increasing Al_2O_3 and extends the same trend observed in the zircon-hosted SMI data to lower CaO and Al_2O_3 concentrations. (Supplementary Figure 3.3B), suggesting they are related through differentiation. Therefore, quartz- and zircon-hosted SMI analyses (by SEM-EDS/EPMA) were used to construct a single CaO-Al_2O_3 trendline (Trend line 'C'; Fig. 3.11B) for the purpose of quartz-hosted SMI quantification. Similar to the zircon-hosted SMI calculations, the Al_2O_3 concentration for each inclusion was fixed between 10 and 18 wt% in SILLS to determine an initial model Al_2O_3-CaO trendline (Trend line 'D'; Fig. 3.11B) for each inclusion, and the point of intersection between the two trendlines is the Al_2O_3 concentration used for LA-ICPMS internal standard quantification (Supplementary Figure 3.3B).

By this method, some quartz-hosted inclusions yield intersections at values of Al_2O_3 of >20 wt%. Using these Al_2O_3 values for SILLS quantification resulted in elevated CaO (>8 wt%) and FeO (>8 wt%) at low SiO_2 (45 to 60 wt%). These inclusions are interpreted to contain variable proportions of accidentally trapped epidote with melt (Fig. 3.10C). To provide a better Al_2O_3 estimate for these mixed melt + epidote inclusions, a mixing line was modelled by using the most felsic melt (i.e., low CaO and FeO) and adding increasing percentages of epidote to create a bulk

inclusion composition (Trend line 'E'; Supplementary Figure 3.3C). Following this, by using the Al_2O_3-CaO trendline determined for each inclusion by varying Al_2O_3 from 10 to 18 wt% and the melt + epidote trendline, the point of intersection would be the bulk Al_2O_3 concentration for the mixed melt + epidote inclusion (Supplementary Figure 3.3C). These results demonstrate that inclusions can contain 10 to 30 vol% accidentally trapped epidote. Inclusions that contain accidentally trapped epidote are not used for compositional and petrogenetic classification, but the bulk inclusion metal contents are presented and discussed.

It is important to note that LA-ICPMS major element concentrations were quantified assuming 2 wt% H_2O, therefore the major elements total 98 wt% whereas SEM-EDS analyses are 100 wt% totals. Therefore, major elements determined by SEM-EDS are slightly overreported by 2% relative. Overall, due to SiO_2 contamination from the host-quartz in SEM-EDS analyses, LA-ICPMS analyses have slightly higher concentrations for most major elements (i.e., Al_2O_3, FeO, CaO, and K_2O; Fig. 3.18A). Concentrations of TiO_2 and MgO are similar between the two methods, whereas Na_2O is consistently lower in LA-ICPMS analyses compared to SEM-EDS analyses (Fig.3.18B).

It is important to reiterate that LA-ICPMS analyses were conducted on unhomogenized (i.e., non-heated) SMI, whereas SEM-EDS analyses were conducted on homogenized (i.e., heated) SMI. Anomalously low Na_2O concentrations in unhomogenized quartz-hosted SMI has been observed in many studies before (e.g., Audétat and Pettke, 2003; Zajacz et al., 2008). These anomalously low Na_2O concentrations have been suggested to be a result of post-entrapment Na diffusion out of the SMI and into the surrounding quartz host during slow cooling of the intrusions (Zajacz et al., 2008). Additionally, it has been demonstrated that during heating experiments Na can diffusive back into quartz-hosted SMI (Zajacz et al., 2009). However, it is not clear if the post-heating Na_2O concentration is representative of the melt composition at the time of entrapment.

Comparing the Na_2O concentrations of homogenized, quartz-hosted SMI to zircon-hosted SMI, the concentrations are similar and therefore the homogenized, quartz-hosted SMI Na_2O are likely near the Na_2O concentration at the time of entrapment.

METHODOLOGY FOR CALCULATING TRAPPED SULFIDE COMPOSITIONS IN QUARTZ AND ZIRCON

During analysis and quantification of zircon- and quartz-hosted melt inclusions, certain inclusions had transient signals that had elevated Fe, Cu, and/or Mo, Bi, Ag, Au (e.g., Fig. 3.11F and 3.18H) resulting in elevated concentrations when quantified using the methodology described previously for SMI. The concentration of metals in inclusions determined using this methodology are inaccurate due to a wrong internal standard used in quantification. Since these inclusions contain a variable proportion of accidentally trapped sulfide with silicate melt and the composition of the sulfide phase is unknown, an accurate internal standard cannot be determined in order to calculate a bulk (i.e., sulfide + melt) inclusion composition. However, an estimate of the sulfide phase composition can be estimated by using a set Fe concentration and assuming all metals are predominantly present in the sulfide phase since metals (i.e., Cu, Bi, Ag, Au) strongly partition into sulfide over silicate melt (Zajacz et al., 2013, Li and Audétat, 2015).

Based on the transient LA-ICPMS signals and preliminary inclusion quantification, inclusions with distinct peaks for Fe + Cu ± Mo, Bi, Ag, Au offset from the main silicate melt signal were re-quantified to estimate the sulfide phase composition. Some inclusions had Cu > Fe in their transient signal suggesting a Cu-rich sulfide phase (e.g., chalcopyrite as seen trapped in zircon) whereas a majority of signals had Fe > Cu, suggesting a Fe-rich sulfide with variable Cu contents. Therefore, for all sulfide-bearing inclusions, two quantifications were conducted, one with Fe = 62.34 wt% implying a pyrrhotite composition and a second with Fe = 30.43 wt%

implying a chalcopyrite composition. This provides maximum (pyrrhotite) and minimum (chalcopyrite) estimates on the metal concentrations in the sulfide phase. It should be noted that since the Fe content of chalcopyrite is about half of pyrrhotites Fe content, the minimum metal concentrations are roughly half of the maximum values. For simplicity, only the maximum metal concentrations will be presented below, unless otherwise stated.

REFERENCES

Audétat, A., and Pettke, T., 2003, The magmatic-hydrothermal evolution of two barren granites: A melt and fluid inclusion study of the Rito del Medio and Cañada Pinabete plutons in northern New Mexico (USA): Geochimica et Cosmochimica Acta, v. 67, p. 97-121.

Audétat, A., Zhang, L., Ni, H., 2018, Copper and Li diffusion in plagioclase, pyroxenes, olivine and apatite, and consequences for the composition of melt inclusions: Geochimica et Cosmochimica Acta, v. 243, p. 99-115.

Bodnar, R.J., and Student, J.J., 2006, Melt inclusions in plutonic rocks: Petrography and microthermometry: *In* Melt inclusions in plutonic rocks. Edited by J.D. Webster. Mineralogical Association of Canada Short Course Series, v. 36, p. 1-25.

Chang, J. and Audétat, A., 2021, LA-ICP-MS analysis of crystallized melt inclusions in olivine, plagioclase, apatite and pyroxene: quantification strategies and effects of post-emplacement modifications: Journal of Petrology, v. 62, https://doi.org/10.1093/petrology/egaa085.

Cherniak, D.J. and Watson, E.B., 2003, Diffusion in zircon: Reviews in Mineralogy and Geochemistry, v. 53, p. 113-143.

Cherniak, D.J., Hanchar, J.M., and Watson, E.B., 1997, Rare-earth diffusion in zircon: Chemical Geology, v. 134, p. 289-301.

Galley, A.G., and Lafrance, B., 2014, Setting and evolution of the Archean synvolcanic Mooshla Intrusive Complex, Doyon-Bousquet-LaRonde mining camp, Abitibi greenstone belt: emplacement history, petrogenesis, and implications for Au metallogenesis: Economic Geology, v. 109, p. 205-229.

Goldstein, R.H., 2003, Petrographic analysis of fluid inclusions. *In* I. Samson, A. Anderson, and D. Marshall, eds. Fluid Inclusions: Analysis and Interpretation. Mineralogical Association of Canada, Short Course v. 32, 9-54.

Götze, J., 2012, Application of cathodoluminescence microscopy and spectroscopy in geosciences: Microscopy and Microanalysis, v. 18, p. 1270-1284.

Guillong, M.M., Maier, D.L., Allan, M.M., Heinrich, C.A., and Yardley, B.W.D., 2008, Appendix A6: SILLS: a MATLAB based program for the reduction of laser ablation ICP-MS data of homogeneous materials and inclusions. In Laser Ablation ICP-MS in the Earth Sciences: Current Practices and Outstanding Issues. Edited by P. Sylvester. Mineralogical Association of Canada Short Course Series v. 40.

Halter, W.E., Pettke, T., Heinrich, C.A., and Rothern-Rutishauser, 2002, Major to trace element analysis of melt inclusions by laser-ablation ICP-MS: methods of quantification: Chemical Geology, v. 183, p. 63-86.

Halter, W.E., Pettke, T., and Heinrich, C.A., 2004, Laser-ablation ICP-MS analysis of silicate and sulfide melt inclusions in an andesitic complex I: analytical approach and data evaluation: Contributions to Mineralogy and Petrology, v. 147, p. 385-396.

Riciputi, L.R., Paterson, B.A., and Ripperdan, R.L., 1998, Measurement of light stable isotope ratios by SIMS: Matrix effects for oxygen, carbon, and sulfur isotopes in minerals: International Journal of Mass Spectrometry, v. 178, p. 81–112.

Sheahan, C., Fayek, M., Quirt, D., and Jefferson, C.W., 2016, A combined ingress-egress model for the Kianna unconformity-related uranium deposit, Shea Creek project, Athabasca Basin, Canada: Economic Geology, v. 111, p. 225-257.

Sneeringer, M.A., and Watson, E.B., 1985, Milk cartons and ash cans: two unconventional welding techniques: American Mineralogist, v. 70, p. 200-201.

Thomas, J.B., Bodnar, R.J., Shimizu, N., and Chesner, C.A., 2003, Melt Inclusions in Zircon: Reviews in Mineralogy and Geochemistry v. 53, p. 63–87.

Webster, J. D., Goldoff, B., and Shimizu, N., 2011, C-O-H-S fluids and granitic magma: how S partitions and modifies CO2 concentrations of fluid-saturated felsic melt at 200 MPa: Contributions of Mineralogy and Petrology, v. 162, p. 849-865.

Zajacz, Z. and Halter, W.E., 2007, LA-ICPMS analyses of silicate melt inclusions in co-precipitated minerals: quantification, data analysis and mineral/melt partitioning: Geochimica et Cosmochimica Acta, v. 71, p. 1021-1040.

Zajacz, Z., Hanley, J.J., Heinrich, C.A., Halter, W.E., and Guillong, M., 2009, Diffusive reequilibration of quartz-hosted silicate melt and fluid inclusions: are all metal concentrations unmodified?: Geochimica et Cosmochimica Acta, v. 73, p. 3013-3027.

Zhang, Z., Fedortchouk, Y., and Hanley, J. J., 2015, Evolution of diamond resorption in a silicic aqueous fluid at 1-3 GPa: Application to kimberlite emplacement and mantle metasomatism: Lithos, v. 227, p. 179-193.

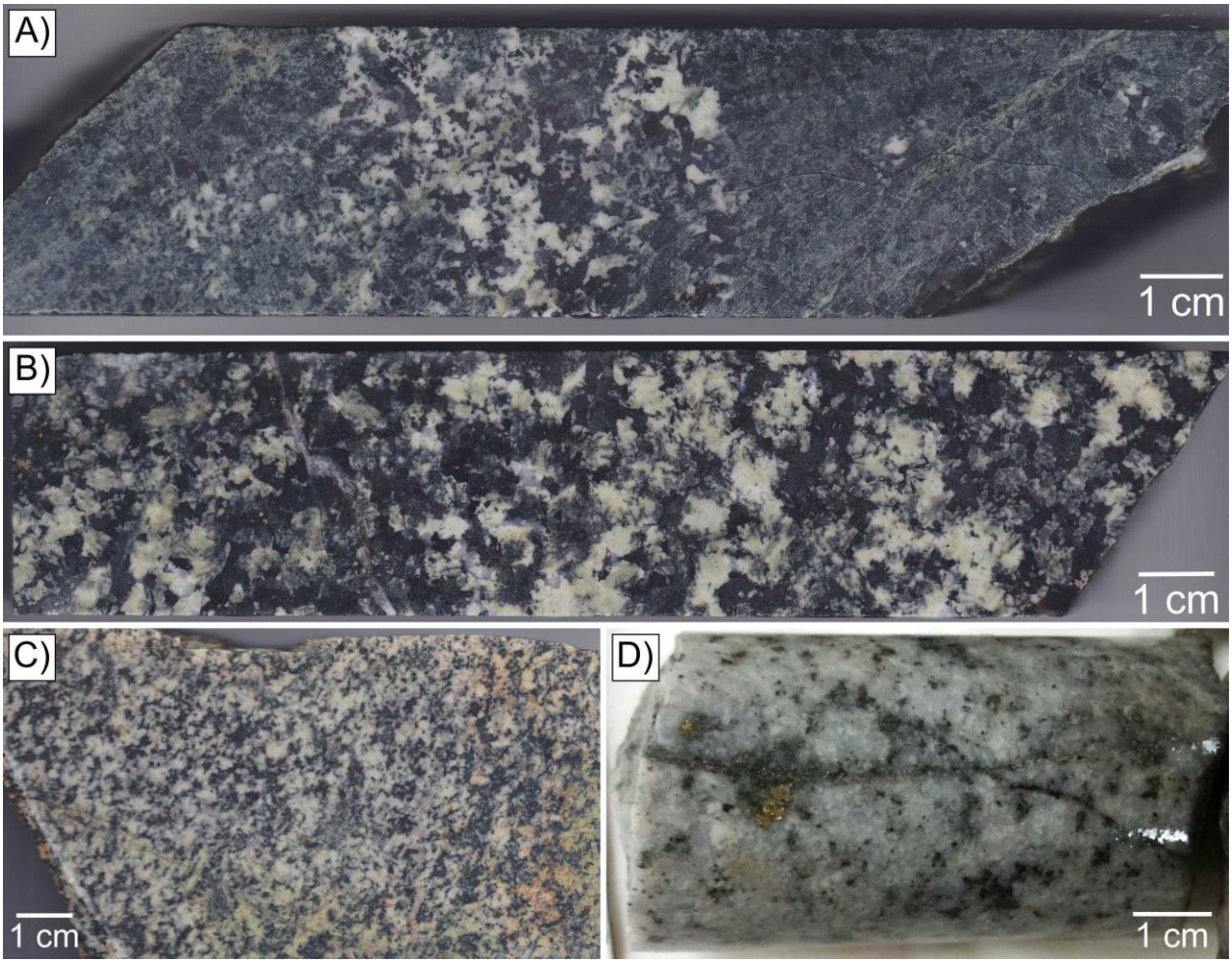

Supplementary Figure 3.1: Representative slabs of various lithologies from the MIC. A) Coarse-grained section within Phase B. Possible that this coarser grained section is associated with Phase C as it is more felsic than the surrounding gabbro, but margins are diffuse so could also be an isolated coarser-grained patch of Phase B (Sample MSK-715.6). B) Coarse-grained section of Phase C quartz diorite (Sample MSK-493.7). D) Slab of Phase D tonalite. Margins of the sample are slightly altered because this sample was taken from surface (Sample Stop 11). D) Representative core of Phase I trondhjemite (Sample 1106-96-1444.5).

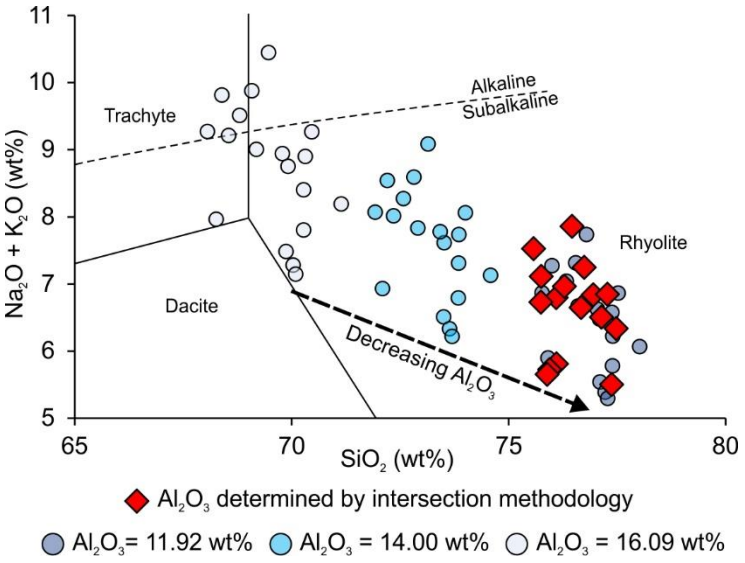

Supplementary Figure 3.2: Graph of SiO_2 against $Na_2O + K_2O$ displaying the variation in quantified LA-ICPMS data for zircon-hosted SMI from the high-Th/U quartz diorite by using different values of Al_2O_3 as the internal standard. The Al_2O_3 value of 14.00 wt% (blue circles) represents the mean Al_2O_3 concentration from SEM-EDS analyses of exposed SMI and the values of 16.09 (light blue circles) and 11.92 wt% (dark blue circles) represent 14.00 ± 1σ wt%. The Al_2O_3 values determined by the intersection method (see text for details) are shown in red diamonds.

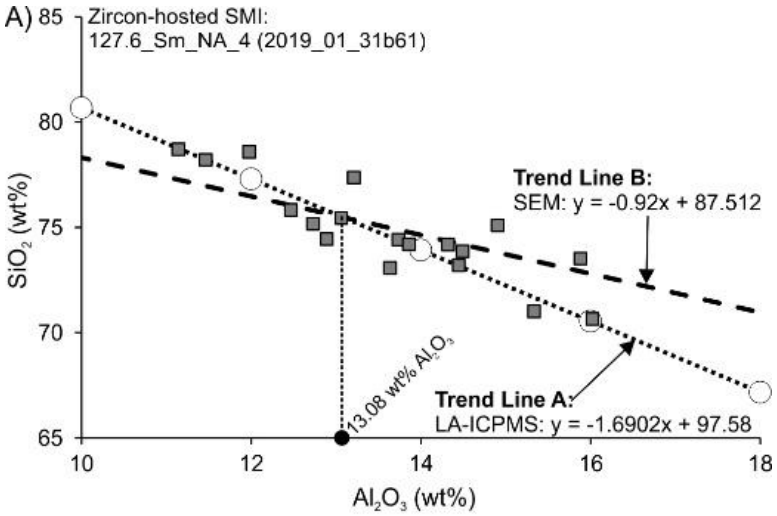
A)
Zircon-hosted SMI:
127.6_Sm_NA_4 (2019_01_31b61)
SiO2 (wt%)
Al2O3 (wt%)
Trend Line B:
SEM: y = -0.92x + 87.512
13.08 wt% Al2O3
Trend Line A:
LA-ICPMS: y = -1.6902x + 97.58

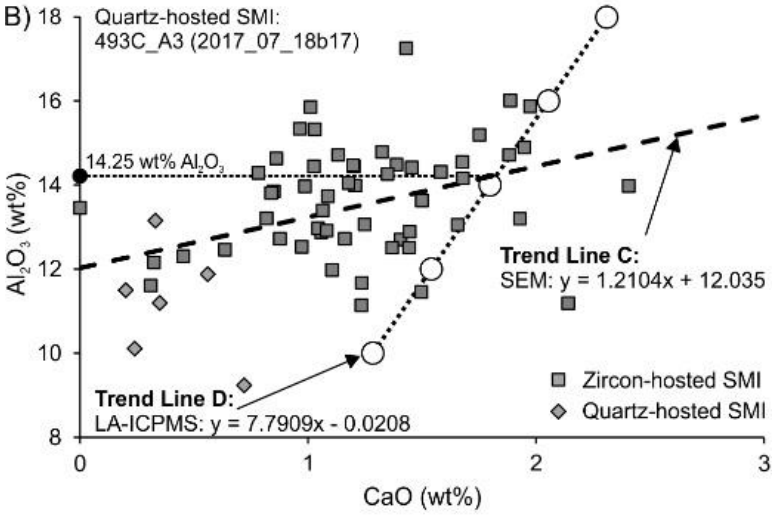
B)
Quartz-hosted SMI:
493C_A3 (2017_07_18b17)
14.25 wt% Al2O3
Trend Line C:
SEM: y = 1.2104x + 12.035
Trend Line D:
LA-ICPMS: y = 7.7909x - 0.0208
Zircon-hosted SMI
Quartz-hosted SMI
Al2O3 (wt%)
CaO (wt%)

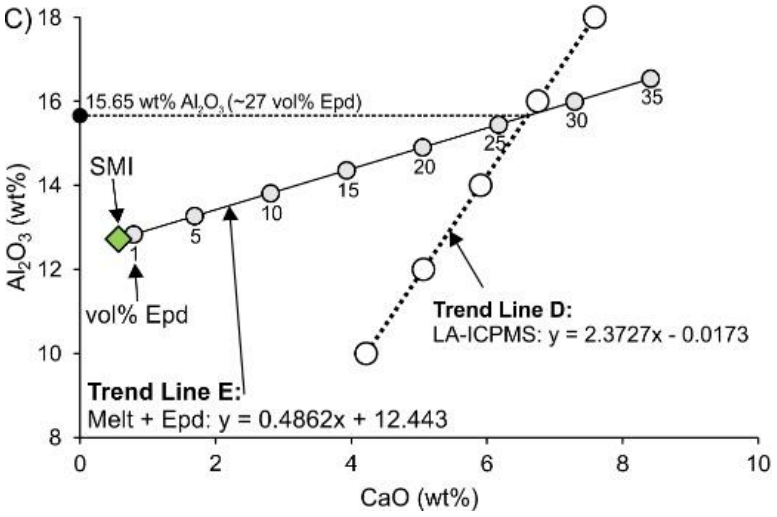
C)
15.65 wt% Al2O3 (~27 vol% Epd)
SMI
vol% Epd
Trend Line D:
LA-ICPMS: y = 2.3727x - 0.0173
Trend Line E:
Melt + Epd: y = 0.4862x + 12.443
Al2O3 (wt%)
CaO (wt%)

Supplementary Figure 3.3: Graphical representation of the intersection method used to determine the Al_2O_3 internal standard value for LA-ICPMS SMI quantification. A) The SiO_2 and Al_2O_3 concentrations from SEM-EDS analyses (grey squares) of exposed zircon-hosted SMI define a specific trend line for the SMI overall (Trend line 'B'). Fixing the Al_2O_3 concentrations of an individual SMI (open circles) during quantification defines a specific trend line for a SMI (Trend line 'A'). The point at which the two lines intersect, is the point where the SMI would fall along the SEM-EDS line and therefore be the correct Al_2O_3 concentration for that inclusion. In the example shown, the Al_2O_3 concentration used for LA-ICPMS quantification of the specified SMI is 13.08 wt%. B) To determine the Al_2O_3 internal standard for quartz-hosted SMI, the SiO_2-Al_2O_3 relationship cannot be used due to SiO_2 contamination during SEM-EDS analyses of exposed SMI. Therefore, the trendline (trend line 'C') determined between Al_2O_3 and CaO concentrations of zircon- (grey squares) and quartz-hosted (grey diamonds) is used. In the example shown, the Al_2O_3 concentration used for LA-ICPMS quantification of the specified SMI is 14.25 wt%. C) Graphical representation of calculating the bulk inclusion Al_2O_3 concentration for mixed melt + epidote inclusions. Using the most felsic SMI (green diamond) and adding increasing percentages of epidote creates a trendline (trend line 'E') and the point of intersection with the inclusions CaO-Al_2O_3 trendline is the bulk (melt + epidote) Al_2O_3 value used for quantification. In the example shown, the Al_2O_3 concentration used for LA-ICPMS quantification of the specified SMI is 15.65 wt%, representing approximately 27 vol% epidote is accidentally trapped in this melt inclusion.

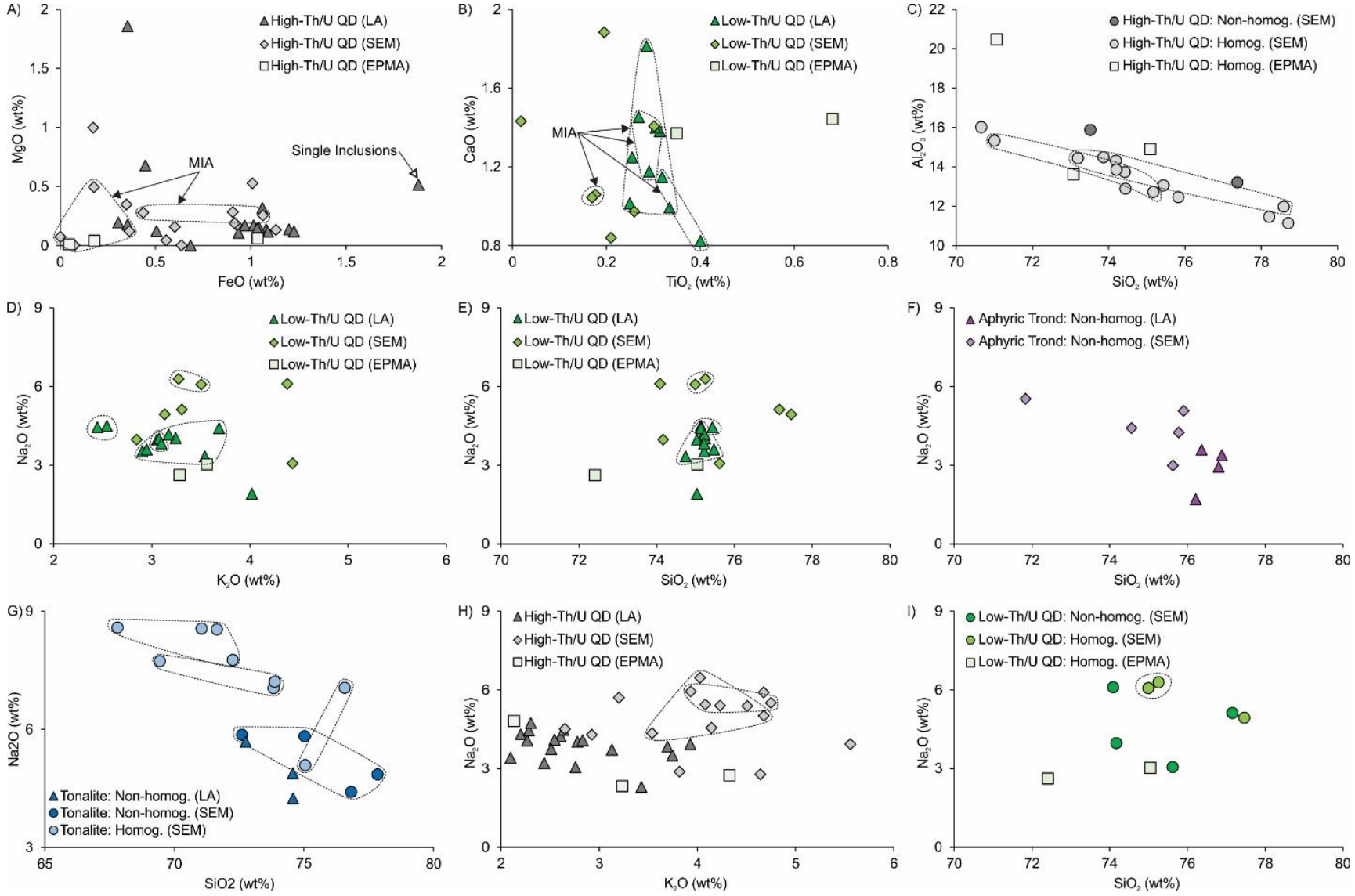
A)
High-Th/U QD (LA)
High-Th/U QD (SEM)
High-Th/U QD (EPMA)
MIA
Single Inclusions
MgO (wt%)
FeO (wt%)
B)
Low-Th/U QD (LA)
Low-Th/U QD (SEM)
Low-Th/U QD (EPMA)
MIA
CaO (wt%)
TiO2 (wt%)
C)
High-Th/U QD: Non-homog. (SEM)
High-Th/U QD: Homog. (SEM)
High-Th/U QD: Homog. (EPMA)
Al2O3 (wt%)
SiO2 (wt%)
D)
Low-Th/U QD (LA)
Low-Th/U QD (SEM)
Low-Th/U QD (EPMA)
Na2O (wt%)
K2O (wt%)
E)
Low-Th/U QD (LA)
Low-Th/U QD (SEM)
Low-Th/U QD (EPMA)
Na2O (wt%)
SiO2 (wt%)
F)
Aphyric Trond: Non-homog. (LA)
Aphyric Trond: Non-homog. (SEM)
Na2O (wt%)
SiO2 (wt%)
G)
Tonalite: Non-homog. (LA)
Tonalite: Non-homog. (SEM)
Tonalite: Homog. (SEM)
Na2O (wt%)
SiO2 (wt%)
H)
High-Th/U QD (LA)
High-Th/U QD (SEM)
High-Th/U QD (EPMA)
Na2O (wt%)
K2O (wt%)
I)
Low-Th/U QD: Non-homog. (SEM)
Low-Th/U QD: Homog. (SEM)
Low-Th/U QD: Homog. (EPMA)
Na2O (wt%)
SiO2 (wt%)

Supplementary Figure 3.4: Scatter plots comparing the three different analytical methods (SEM-EDS, EPMA, LA-ICPMS) used to determine the major element chemistry of zircon-hosted SMI. and comparing SMI that have been homogenized (i.e., heating) and SMI that have not been homogenized (i.e., not heated) Note, data points outlined by dashed lines indicated SMI belonging to a melt inclusion assemblage (MIA). As indicated in frame A, SMI that are not in an MIA (not within a dashed area) represent single SMI. All major elements are plotted in wt%. A) FeO plotted against MgO in the high-Th/U quartz diorite. Between the three analytical methods, these major elements have similar ranges in concentrations. Note, within individual MIA, there can be a range in concentrations. B) TiO_2 plotted against CaO and the three methods show similar ranges in concentrations for SMI in the low-Th/U quartz diorite. C) SiO_2 plotted against Al_2O_3 comparing SMI that have been homogenized and those that have not been in the high-Th/U quartz diorite. Both homogenized and non-homogenized SMI show a similar range in concentrations. D) K_2O plotted against Na_2O for SMI in the low-Th/U quartz diorite. Both elements show similar ranges in concentrations between the different analytical methods. E) SiO_2 plotted against Na_2O showing similar ranges in concentrations between the different methods for SMI in the low-Th/U quartz diorite. F) SiO_2 plotted against Na_2O for SMI in the aphyric trondhjemite. G) SiO_2 plotted against Na_2O for homogenized and non-homogenized SMI in the tonalite. Note, the variation in concentrations within MIA. H) K_2O plotted against Na_2O for SMI in the high-Th/U quartz diorite. Overall, SMI have similar ranges in concentrations between the different methods. I) SiO_2 plotted against Na_2O for homogenized and non-homogenized SMI in the low-Th/U quartz diorite, and both inclusion types have similar ranges in concentrations.

Chapter 4: Ore mineralogy, sulfide geochemistry and S isotopes of magmatic-hydrothermal Au mineralization associated with the Mooshla Intrusive Complex (MIC), Doyon-Bousquet-LaRonde mining camp, Abitibi greenstone belt, Québec

Kevin Neyedley[1], Patrick Mercier-Langevin[2,3], Richard Stern[4], Mostafa Fayek[5], Jacob J. Hanley[1]

[1]Department of Geology, Saint Mary's University, Halifax, Nova Scotia, Canada

[2]Geological Survey of Canada, Quebec, Quebec

[3]Current address: Agnico Eagle Mines Limited, Toronto, Ontario, Canada

[4]Department of Earth and Atmospheric Sciences, University of Alberta, Edmonton, Alberta, Canada

[5]Department of Geological Sciences, University of Manitoba, Winnipeg, Manitoba, Canada

4.1 ABSTRACT

The Mooshla Intrusive Complex (MIC) is an Archean polyphase magmatic body located in the Doyon-Bousquet-LaRonde (DBL) mining camp of the Abitibi greenstone belt, Québec, that is spatially associated with numerous world-class Au-rich VMS deposits, two major Au-rich sulfide vein deposits, epizonal "intrusion-related" (or porphyry-epithermal-style) Au-(Cu) vein systems, and shear-hosted Au deposits, along with a number of smaller Au occurrences. To elucidate any genetic links between deposits and the MIC, mineralized samples from two epizonal 'intrusion-related' Au-Cu vein deposits (Doyon and Grand Duc deposits) have been characterized using a combination of detailed petrography and trace element and sulfur isotope analyses of sulfide phases.

Mineralization styles at Doyon and Grand Duc (high- and moderate- to low-grade veins) have some similarities but distinct differences in the base metal sulfide and accessory ore mineral assemblages, pyrite trace element patterns, and subtle variations in $\delta^{34}S$ distribution patterns in pyrite occur. At Doyon and the lower-grade veins from Grand Duc, only trace amounts of pyrrhotite and chalcopyrite are present whereas the high-grade Grand Duc vein has significantly more pyrrhotite and chalcopyrite as well as sphalerite. In addition to gold, the accessory ore mineral assemblage at Doyon and in the lower-grade Grand Duc samples are similar and consist of a variety of Au-Ag-Te, whereas the high-grade Grand Duc vein only contains Bi-tellurides along with gold.

The pyrite trace element and S isotope signatures and patterns show similarities between Doyon and the lower-grade veins from Grand Duc. Both show relatively metal depleted cores followed by enrichment in As. At both deposits pyrite records an increase in $\delta^{34}S$ by ~1 to 2 ‰ from the metal-poor cores to zones enriched in As. The combination of an increase in As concentrations coincident with the increase in $\delta^{34}S$ suggests a reduction in the hydrothermal fluid and is likely induced by wall-rock sulfidation, which is considered to be the primary Au

precipitation mechanism. The ore metal-depleted signature of pyrite from Doyon and the lower-grade veins from Grand Duc, combined with the occurrence of gold and Au-Ag-Te minerals occurring along fractures and grain boundaries of sulfides and gangues minerals and the maximum temperature stability of these Au-Ag-Te minerals of ~300°C, would suggest that during regional metamorphism Au and other ore metals were remobilized from the pyrite structure and resulted in the precipitation of gold and Au-Ag-Te grains.

Pyrite from the high-grade vein at Grand Duc can display significantly different trace element and $\delta^{34}S$ patterns compared to lower-grade veins and those at Doyon. The pyrite core is generally metal-depleted whereas the rims have elevated concentrations of epithermal-related elements (i.e., Au-Ag-As-Te-Bi-Sb-Se) that are not related to accessory ore mineral inclusions. In contrast to Doyon and the lower-grade veins, pyrite in the higher-grade vein records a drop in $\delta^{34}S$ progressing from the core to the metal-rich rim. The combination of the decrease in $\delta^{34}S$ and increasing concentrations of epithermal-related elements along the pyrite rim suggests pyrite preserves a primary magmatic-hydrothermal fluid boiling event related to gold deposition. Although pyrite records a fluid boiling event, gold and tellurobismuthite occur synchronous with chlorite alteration, indicating gold and tellurides were likely a result of Au remobilization during regional metamorphism.

Although the trace element and ore mineral characteristics have been influenced by regional metamorphism, the $\delta^{34}S$ compositions and patterns have retained their magmatic signature as the $\Delta^{33}S$ values are near-zero within and between individual pyrite grains, representing a singular source of sulfur and rules out non-magmatic sulfur sources. Even though these deposits have been variably modified during regional metamorphism, the combination of methods applied here can identify primary magmatic-hydrothermal processes responsible for the development of these Au-rich deposits, potentially linking them to causative magmatism.

4.2 INTRODUCTION

The role of the Mooshla Intrusive Complex (MIC) in the formation of intrusion-associated and Au-rich VMS deposits in the Doyon-Bousquet-LaRonde mining camp has been a long-standing question. Many lines of indirect evidence such as geochronology, mapping/field relations, alteration patterns, petrography, and lithogeochemistry have been used to suggest a connection between the MIC and Au deposits as being part of a large magmatic-hydrothermal system, but limited evidence has been presented (Valliant and Hutchinson, 1982; Gosselin, 1998; Mercier-Langevin, 2007a, b; Sharman, 2011; Galley and Lafrance, 2014; Yergeau et al., 2022a, b). Recent detailed studies by Neyedley et al. (2024a, accepted) on the MIC have been able to provide tighter geochronological constraints and demonstrates the evolution of the MIC is consistent with time scales of major Phanerozoic Cu-Au porphyry camps (cf. Chiaradia, 2021; Large et al., 2021). Evidence of extensive fractional crystallization and assimilation occurred at significant depths (>16 km), some phases of the MIC were relatively oxidizing based on mineralogical evidence (e.g., epidote, titanite: Neyedley et al., 2024a, accepted). Additionally, the metal concentrations of silicate melt inclusions in the gabbro and quartz diorite of the MIC have Au and Cu concentrations comparable to inclusions from large porphyry Cu-Au deposits (e.g., Bingham: Grondahl and Zajacz, 2017). As well, the presence of trapped Au-bearing sulfide grains in silicate melt inclusions and sulfide grains in zircon, demonstrates the magmas of the MIC were sulfur and metal-rich (Neyedley et al., 2024b, in prep). Overall, there is multiple lines of evidence from previous and recent studies to demonstrate the MIC has the potential to contribute metals to the hydrothermal system(s) and detailed micro-analytical studies of intrusion-associated Au-deposits hosted in the MIC can help establish the connection. Moreover, this work provides further information and robust data to better understanding the evolution of magmatic-hydrothermal systems in the Archean, some of which having been compared to Phanerozoic porphyry-epithermal systems based

on their geological characteristics, contributing to what is identified as a knowledge gap in Archean metallogeny globally.

In this study, mineralization from the Doyon West deposit hosted in the Doyon quartz diorite (Phase E) and the Grand Duc deposit hosted in the aphyric trondhjemite (Phase I) of the MIC have been characterized. Detailed petrography of the ore veins was conducted to document the major sulfide and gangue minerals comprising each system as well as scanning electron microscopy- energy dispersive X-ray (SEM-EDS) analyses to document the various accessory ore minerals present and their textural relationships to sulfides. The trace element chemistry of pyrite and pyrrhotite was collected by laser ablation-inductively coupled mass spectroscopy (LA-ICP-MS) to characterize their trace element signatures and LA-ICP-MS mapping of pyrite was conducted to track the trace element distribution. Secondary ion mass spectrometry (SIMS) was conducted on different trace element zones in pyrite to track the evolution of $\delta^{34}S$ and $\Delta^{33}S$, which aid in understand the sulfur source through the growth history of pyrite. Combining all the different analytical techniques provides a comprehensive ore characterization of two intrusion-hosted Au systems in the Doyon-Bousquet-LaRonde mining camp and leads to understanding the fluid source and Au precipitation mechanisms associated with each deposit, contributing to an improved understanding of Archean magmatic-hydrothermal systems.

4.3 GEOLOGIC SETTING

4.3.1 Regional and Local Geology

The geology of the Doyon-Bousquet-LaRonde mining camp and geological setting of its contained mineral deposits (Fig. 4.1) have been described in detail by Gunning (1941), Fillion et al. (1977), Valliant and Hutchinson (1982), Marquis et al. (1990a), Stone (1990), Trudel et al. (1992), Lafrance et al. (2003, 2005), Mercier-Langevin (2005), Mercier-Langevin et al. (2004,

2007a, b, c, 2011), Galley and Lafrance (2014), and Yergeau (2022a, b). The mining camp contains >28 Moz of Au (>890 metric t Au), making it one of the world's largest Archean Au districts, including two world-class Au-rich VMS deposits (LaRonde Penna and Bousquet 2-Dumagami), two major Au-rich sulfide vein deposits (Bousquet 1 and Westwood), epizonal "intrusion-related" Au-(Cu) vein systems (Doyon and Westwood Zone 2 Extension), and shear-hosted Au deposits (Mouska and Mic Mac), along with a number of smaller Au occurrences (Mercier-Langevin et al., 2017).

The Doyon-Bousquet-LaRonde mining camp occurs in the eastern portion of the Blake River Group (2704-2695 Ma; McNicoll et al., 2014) of the Archean Abitibi greenstone belt in the Superior Province (Mercier-Langevin, et al., 2007c; Galley and Lafrance, 2014). In the mining camp, the Blake River Group strikes east-west and is a steeply dipping, south-facing homoclinal volcanic sequence (Lafrance et al., 2003; Mercier-Langevin et al., 2007a, b, Galley and Lafrance, 2014). The Blake River Group in the Doyon-Bousquet-LaRonde mining camp consists of the Hébécourt Formation in the north and the Bousquet Formation in the south (Fig. 4.1; Lafrance et al., 2003). Along the northern contact of the Blake River Group is the Lac Parfouru Fault, which separates the Hébécourt Formation from the sedimentary rocks of the Kewagama Group (<2686 Ma; Davis, 2002). Along the southern contact of the Blake River Group, the Bousquet Formation is disconformably overlain by the sedimentary rocks of the Cadillac Group (<2687.4 ± 1.2 Ma; Lafrance et al., 2005). The Hébécourt Formation represents the base of the Blake River Group in the Doyon-Bousquet-LaRonde mining camp, and it is overlain by the Bousquet Formation. The Bousquet Formation is divided into two members: the 2699-2698 Ma tholeiitic to transitional lower member and the 2698-2697 Ma transitional to calc-alkaline upper member (Lafrance et al., 2005; Mercier-Langevin et al., 2007a), each containing numerous units that vary greatly in composition

and nature (see Mercier-Langevin et al.,2007a, b, and Yergeau et al., 2022a, b for detailed descriptions of the Bousquet Formation units).

Emplacement of the MIC occurred along the contact between the Hébécourt and Bousquet formations in the western portion of the Doyon-Bousquet-LaRonde mining camp (Fig. 4.1A; Galley and Lafrance, 2014). The MIC has been divided into two distinct stages of formation: (i) the Mouska stage, which consists of five intrusive phases (A to E) that range from gabbroic to tonalitic compositions; and (ii) the Doyon stage, which comprises four intrusive phases (F to I) that range from tonalitic to trondhjemitic compositions (Galley and Lafrance, 2014). Galley and Lafrance (2014) distinguished the various phases by studying their chemical compositions, intrusion styles, and overprinting relationships.

The synvolcanic age of the MIC and coeval nature with the Bousquet Formation has been documented through field relationships and geochemistry (Galley and Lafrance, 2014), as well as U-Pb geochronology. Zircon U-Pb geochronology on the Doyon-stage trondhjemite (phase H) yielded an age of 2696.9 ± 1 Ma (Lafrance et al., 2005), which demonstrates that Phase H, and by association the Doyon-stage of the MIC, are synchronous with the upper member of the Bousquet Formation (2698−2696 Ma; Lafrance et al., 2005; Mercier-Langevin et al., 2007a, 2011; McNicoll et al., 2014). Zircon U-Pb geochronology of Phase C quartz diorite yielded an age of 2698.5 ± 0.4 Ma (McNicoll et al., 2014), which is synchronous with a glomeroporphyritic dacite in the lower Bousquet member that hosts part of the Doyon Au-(Cu) deposit, which has an age of 2698.3 ± 0.9 Ma (Lafrance et al., 2005).

At least three phases of deformation affected the lithologies of the Doyon-Bousquet-LaRonde mining camp (Langshur, 1990; Savoie et al., 1991; Belkabir and Hubert, 1995). A weak, moderately inclined northeast-southwest foliation defines the first phase of deformation (D_1; local nomenclature). A strong penetrative east-west fabric, with shear planes and faults that dip steeply

to the south, represents the second phase of deformation (D_2) (or D_3 in the regional context: cf. Dubé and Mercier-Langevin, 2020). Dextral transpressive brittle-ductile faults related to the third phase of deformation (D_3) overprint D_2. This deformation is responsible for major modifications to the primary volcanic and intrusive architecture and to the geometry of the ore zones as major flattening, stretching, folding and transposition affect the entire succession. Regional metamorphism in the camp ranges from greenschist- to amphibolite-facies and is approximately coeval with local D_2. However, in the MIC, unorientated actinolite and biotite porphyroblasts suggest that peak metamorphism postdates D_2 (Marquis et al., 1990a; Belkabir and Hubert, 1995; Dubé et al., 2004; Mercier-Langevin, 2005).

4.3.2 Epizonal "intrusion-related" Au and Au-rich VMS deposits

Epizonal "intrusion-related" Au-(Cu) vein deposits in the Doyon-Bousquet-LaRonde mining camp are present at the former Doyon mine, the Grand Duc deposit, and the Westwood mine Zone 2 Extension, which occur in the western portion of the camp in close proximity to or within the MIC (Fig. 4.1B; Guha et al., 1982; Gosselin, 1998; Yergeau, 2022a, b).

Mineralization in the Doyon mine consists of three different deposits, two (Zones 1 and 2) of which occur in highly altered sericite-chlorite schists in felsic and mafic volcanic rocks, in the upper portions of the lower member of the Bousquet Formation (Fig. 4.1B; Guha et al., 1982; Gosselin, 1998). The third mineralized zone at Doyon (i.e., Doyon West deposit) crosscuts Phase E of the MIC (Fig. 4.1B; Gosselin, 1998; Galley and Lafrance, 2007, 2014). Mineralization in the Doyon deposit Zone 1 is characterized by mm- to cm-wide pyrite-quartz veinlets that contain ~20 vol% sulfides (Guha et al., 1982; Savoie et al., 1991). Chalcopyrite, sphalerite, galena, arsenopyrite, and chalcocite are also present in these thin veinlets, although in very minor amounts (Guha et al., 1982). Gold is present as native gold and Au-tellurides and is disseminated and

interstitial to pyrite (Guha et al., 1982). Mineralization in the Doyon deposit Zone 2 and West consists of massive to brecciated pyrite-quartz veins that contain 10-75 vol% sulfides and vary between a few cm to 10s of cm in width (Savoie et al., 1991). Chalcopyrite can be locally as abundant as pyrite in these veins but other sulfides are relatively rare (e.g. sphalerite, pyrrhotite, galena, arsenopyrite, bornite, and chalcocite; Savoie et al., 1991). Similar to Zone 1, Au in Zone 2 and the West deposit occurs as native Au and Au-tellurides (Guha et al., 1982; Savoie et al., 1991). Importantly, the quartz veins are affected by the main deformation event (D_2), quartz and sulfide within mineralized veins and sericite and chlorite in the alteration halo surrounding veins are elongated parallel to D_2, and late-chlorite dike that crosscut mineralized veins are also affected by D_2 (Gosselin, 1998; Dubé et al., 2007; Mercier-Langevin et al., 2007c; Galley and Mercier-Langevin, 2024), providing numerous lines of evidence that mineralized quartz veins and their alteration halo at Doyon pre-date all deformation events and therefore suggested veins could be of a synvolcanic (i.e., syn-intrusion) origin.

The Grand Duc deposit, which is currently mined as low-grade high-tonnage open pit operation, occurs approximately 1 km to the west of the Doyon West deposit and mineralized veins largely occur within the MIC Phase I aphyric to quartz porphyritic trondhjemite (Fig. 4.1B). Mineralization at Grand Duc is characterized by disseminated pyrite and by mm- to cm-wide pyrite-chalcopyrite-quartz-chlorite±carbonate veins that contain ~10-30 vol% sulfides (granoblastic pyrite and interstitial chalcopyrite) and cm- to dm-thick sulfide masses (boudinaged veins: Galley and Mercier-Langevin, 2024).

Less than 2,000 m east of Doyon is the Westwood deposit, which consists of three corridors with the Zone 2 Extension present at the lowermost stratigraphic position in the deposits host succession, followed by the VMS-style North Corridor and Westwood Corridor deposits higher in the stratigraphy (Fig. 4.1B; Yergeau et al., 2022b). The Zone 2 Extension is interpreted to be the

eastward extension of the Doyon deposit and mineralization consists of quartz- and sulfide-rich veins and veinlets with disseminated to semi-massive Au-bearing pyrite ±chalcopyrite in m-wide alteration halos. The Zone 2 Extension veins occur near calk-alkaline felsic sills and along or near the contact between tholeiitic to transitional mafic rocks of the Lower Bousquet Formation (Yergeau et al., 2022b). Alteration halos surrounding mineralized veins are up to a few tens of meters thick and consist of metamorphosed muscovite-quartz-pyrite ± gypsum-andalusite kyanite-pyrophyllite argillic to advanced argillic assemblages (Yergeau et al., 2022b). The mineralized veins and alteration at the Zone 2 Extension have been affected by D_2 in a similar manner to Doyon (Gosselin, 1988; Yergeau et al., 2022b). An andesite dike that crosscuts mineralization and alteration and has been deformed by D_2, has an age of 2999.7 ± 0.8 Ma implying it is synchronous to the MIC and Bousquet volcanics, and by inference that the mineralization must be synvolcanic (Yergeau et al., 2022b). The characteristics of the Zone 2 Extension (and Doyon) are all consistent with an epizonal intrusion-related magmatic-hydrothermal ore system (Yergeau et al., 2022b) that is seen as a potential Archean porphyry-epithermal-style system analogue (Galley and Mercier-Langevin, 2024).

The Au-rich VMS North and Westwood Corridors occur higher in the stratigraphy along or near the contact of intermediate volcaniclastic rocks at the base of the Upper Bousquet Formation and calc-alkaline dacite domes and calc-alkaline rhyodacite of the Upper Bousquet Formation, respectively (Fig. 4.1B; Yergeau et al., 2022b). Mineralization in both corridors consists of Au-bearing disseminated, vein, semi-massive, and massive sulfide zones that have anomalously high Ag, Hg, As, and Te. A widespread, metamorphosed distal alteration assemblage consisting of biotite-Mn garnet-chlorite-carbonate ± muscovite-albite occurs across both corridors whereas a muscovite-quartz-chlorite-pyrite argillic alteration assemblage occurs more closely associated with mineralization (Fig. 4.1B; Yergeau et al, 2022b). The timing of ore deposition at

the North and Westwood Corridors is consistent with a synvolcanic origin based on field observations (e.g., stratabound sulfide lenses between lithological units; sulfide replacement textures in volcaniclastic rocks, large footwall semi-conformable alteration; Yergeau et al., 2022b). Based on the presence of (metamorphosed) advanced argillic-style alteration that occurs near mineralization, the enrichment in metals characteristic of an epithermal environment, and the proximity to intrusion-related Au deposits lower in the stratigraphy, it is inferred that the mixing between seawater-dominated VMS-related fluid and an epithermal magmatic-hydrothermal fluid is responsible for the Au-rich nature of these VMS systems (Yergeau et al., 2022b).

4.4 METHODOLOGY

4.4.1 Petrography

All samples were characterized petrographically using transmitted and reflected light on a Nikon Eclipse H550L microscope. All samples were carbon-coated and analyzed with a TESCAN MIRA 3 LMU Variable Pressure Schottky Field Emission SEM at Saint Mary's University, Halifax, Canada. The SEM is equipped with a back-scattered electron (BSE) detector coupled with EDS functionality. For the latter, a solid-state, 80 mm^2 X-max Oxford Instruments EDS detector was used. A beam voltage of 20 kV and an approximate working distance of 17 mm was used for all analyses. The SEM-EDS was used to characterize different types of zoning in pyrite, to identify other sulfide minerals present, and to document the textural settings of gold and identify accessory minerals. Petrography and SEM-EDS were used as the basis to select specific pyrite grains for LA-ICP-MS and SIMS analyses.

4.4.2 Geochemistry

Mineralized vein samples from Grand Duc and Doyon were analyzed at the Ontario Geoscience Laboratories, Sudbury, Canada, for bulk metal concentrations. All samples were pulverized using either an Al oxide ball mill or high chrome steel mills. Following mill preparation, samples were subjected to an aqua regia digestion followed by ICP-MS analysis (OGS package IML-101). Select samples that were over range for Cu by ICP-MS were analyzed again by AAS (OGS package AAF-101). Samples contain highly anomalous Au underwent lead fire assay with gravimetric finish (OGS package GFA-PBG).

4.4.3 EPM of Sphalerite, Pyrrhotite, and Chlorite

Electron microprobe analyses of sphalerite, pyrrhotite, and chlorite were performed using a JEOL JXA8230 electron microprobe (EMP) at University of Toronto, Canada. The instrument was operating at 15 kV accelerating voltage with a 30 nA beam current for all analyse and nominal beam diameter of 1 µm for sulfide analyses. For chlorite, the accelerating voltage was 15 kV, a beam current of 20 nA, and a beam size of ~10 µm. Raw microprobe data count rates were converted to concentrations using the ZAF matrix correction scheme using the JEOL software.

4.4.4 LA-ICP-MS spot analyses and maps of sulfides

Pyrite, pyrrhotite, and chalcopyrite spot analyses and pyrite trace element distribution maps were determined by LA-ICP-MS at the University of New Brunswick, Canada, using a Resonetics M-50 193 nm excimer laser system connected, via Nylon tubing, to an Agilent 7700x quadrupole ICP-MS equipped with dual external rotary pumps (McFarlane and Luo, 2012). Samples and standards were loaded together into a two-volume, low-volume Laurin Technic Pty sample cell that was repeatedly evacuated and backfilled with ultra-pure He to remove traces of air from the cell after each sample exchange.

Pyrite trace element mapping used a 17 μm beam diameter, a stage scan speed of 6 μm/s, and a 10 Hz repetition with the laser fluence regulated at ~3 J/cm^2. A He carrier gas was used at a flow rate of 300 mL/min that transported the ablated material out of the ablation cell and mixed downstream with 2 mL/min N_2 (to enhance sensitivity) and 930 mL/min Ar (from the ICP-MS) prior to reaching the ICP-MS torch. Oxide production rates were maintained below 0.3 % by monitoring ThO/Th. Dwell times for all measured isotopes (^{33}S, ^{55}Mn, ^{56}Fe, ^{57}Fe, ^{63}Cu, ^{66}Zn, ^{72}Ge, ^{75}As, ^{82}Se, ^{95}Mo, ^{111}Cd, ^{115}In, ^{118}Sn, ^{121}Sb, ^{125}Te, ^{202}Hg, ^{208}Pb, ^{209}Bi) was 10 ms except for ^{59}Co, ^{60}Ni, ^{107}Ag, ^{195}Pt, and ^{182}W were 15 ms, and ^{197}Au was 30 ms. Trace element concentrations in unknowns were calibrated against sulfide reference material MASS-1 (Wilson et al., 2002) to calibrate analyte sensitivities and an internal standard of 46.5 wt % Fe for ideal pyrite. At the end of the ablation sequence, the laser log file and ICP-MS intensity data file were synchronized using Iolite™ (Paton et al., 2011) running as a plug in for Wave metrics Igor Pro 6.22™. For trace element maps, non-pyrite material was removed using the Fe CPS elemental map as a guide; concentration scales for each map portray internally standardized absolute ppm levels.

For spot analyses of pyrite and pyrrhotite a ‘squid’ smoothing device was used to ensure low %RSD signals. Trace element concentrations in unknowns were calibrated against sulfide reference material MASS-1 (to calibrate analyte sensitivities) and an internal standard of 46.5 and 62.3 wt. % Fe for ideal pyrite and pyrrhotite, respectively. Dwell times for all measured isotopes (^{24}Mg, ^{27}Al, ^{33}S, ^{47}Ti, ^{55}Mn, ^{56}Fe, ^{57}Fe, ^{63}Cu, ^{66}Zn, ^{72}Ge, ^{75}As, ^{82}Se, ^{95}Mo, ^{111}Cd, ^{115}In, ^{118}Sn, ^{121}Sb, ^{125}Te, ^{202}Hg, ^{208}Pb, ^{209}Bi) was 10 ms except for ^{59}Co, ^{60}Ni, ^{105}Pd, ^{107}Ag, ^{108}Pd, ^{195}Pt, and ^{182}W were 15 ms, and ^{197}Au was 30 ms. At the end of the ablation sequence, the laser log file and ICP-MS intensity data file were synchronized using Iolite™ (Paton et al., 2011) running as a plug in for Wave metrics Igor Pro 6.22™. Individual ablation signals were inspected offline and adjusted when necessary to avoid artifacts related to ablating through thin grains or from the beam ablating

another mineral (e.g., silicates). Spikes in the data were automatically filtered using the default 2σ outlier rejection in the Iolite internally standardized trace-element data reduction scheme.

4.4.5 SIMS of pyrite and pyrrhotite

Preliminary sulfur isotope ratios ($^{34}S/^{32}S$) of pyrite and pyrrhotite from mineralized veins were collected using a CAMECA 7f SIMS at the University of Manitoba, Winnipeg, Canada. Samples and spot locations were chosen based on their representative textures of the different generations of pyrite. A cesium (Cs+) primary beam with a 3 nA current was accelerated (+10 kV) onto the sample surface with a sputtering diameter of ~15 μm. The instrument operated with a 200 V offset for sulfur, –9 kV secondary accelerating voltage, and a mass resolving power of 350. For a detailed description of operating conditions and strategy for correction of instrumental mass fractionation and matrix effects, see Riciputi et al. (1998) for sulfur isotope analysis. Balmat pyrite ($\delta^{34}S = 15.1 \pm 0.3‰$; Riciputi et al., 1998), and Anderson pyrrhotite ($\delta^{34}S = 1.4 \pm 0.2‰$; Crowe and Vaughan, 1996) were used as the pyrite and pyrrhotite reference materials, respectively. Spot-to-spot reproducibility for Balmat pyrite was 0.4‰ and 0.3‰ for Anderson pyrrhotite. Precision for individual analysis was 0.4 for pyrite and 0.3 for pyrrhotite, therefore, 1σ errors for pyrite and pyrrhotite are 0.4 and 0.3, respectively. SIMS results from the reference materials were compared to the accepted isotopic compositions in order to calculate correction factors that were applied to the unknowns measured during the same analytical session (e.g., Holliger and Cathelineau, 1988).

After preliminary $\delta^{34}S$ analyses of pyrite and pyrrhotite were obtained, more detailed sulfur isotope analyses ($^{34}S/^{33}S/^{32}S$) were collected at the Canadian Centre for Isotopic Microanalysis (CCIM), University of Alberta, Edmonton, Canada. Regions of interest (ROI) in thin- and thick-sections were cored or sawed out, and subsequently arrayed with pyrite and pyrrhotite reference materials (RMs) in a 25 mm diameter epoxy mount. The mount was diamond polished lightly to 1

micron finish, then cleaned, and finally coated with 15 nm of Au for SEM-BSE imaging. The SEM utilized a Zeiss EVO MA15 operating at 20 kV and ~3 nA. A further 85 nm Au coating was added prior to isotopic analysis by SIMS.

Sulfur isotope ratios ($^{34}S/^{33}S/^{32}S$) were determined using the IMS-1280 multi-collector ion microprobe at the CCIM. Primary beam conditions included the use of 20 keV $^{133}Cs+$ ions focused to form a probe with diameter ~15 µm and beam current ~ 1.0 nA. The primary beam was rastered across a 20 x 20 µm area for 30 s prior to analysis, to clean the surface of Au and contaminants, and implant Cs. Negative secondary ions were extracted through 10 kV potential to the grounded secondary column (Transfer section). Conditions for the Transfer section included an entrance slit width of 80 µm, field aperture of 5 x 5 mm, and a field aperture-to-sample magnification of 100 x. Automated tuning of the secondary ions in the Transfer section preceded each analysis. The energy slit was fully open. All secondary ions (^{32}S, ^{33}S, ^{34}S) were analyzed simultaneously in Faraday cups (L'2 using $10^{10}\Omega$ amplifier, L1 and H1 with $10^{11}\ \Omega$, respectively) at a mass resolution of ~4000, sufficient to resolve potential isobaric interferences (e.g., ^{32}SH and ^{33}S). Mean count rates for ^{32}S, ^{33}S, and ^{34}S were 1 x 10^9, 1 x 10^7, and 5 x 10^7 counts/s, respectively, determined over a 75 s counting interval. Faraday cup baselines were measured at the start of the session. The analytical sequence involved interspersing analyses of unknowns with the RMs (pyrite S0302A, $\delta^{34}S_{VCDT}$ = 0.0 ±0.2‰, $\Delta^{33}S = 0$; pyrrhotite S0322, $\delta^{34}S_{VCDT}$ = +1.15 ‰, $\Delta^{33}S = 0$) in a 4:1 sequence.

Instrumental mass fractionation for $^{33}S/^{32}S$ and $^{34}S/^{32}S$ was determined for the analytical session (IP20043) from utilizing the replicate analyses of the RM. The standard deviations for $^{33}S/^{32}S$ and $^{34}S/^{32}S$ ratios for S0302A pyrite were both 0.06 ‰ and for S0322 pyrrhotite were 0.08 ‰. Final uncertainties are reported at 95% confidence level (2σ) and propagate within-spot counting errors, between-spot errors to account for geometric effects, and between-session error that accounts for uncertainty in the mean IMF for the session. The total uncertainties in $\delta^{33}S_{VCDT}$,

$\delta^{34}S_{VCDT}$, and $\Delta^{33}S$ have typical values of ± 0.15 ‰ (2σ), ± 0.12 ‰, and ± 0.14 ‰ per spot, respectively. Isotopic anomalies were calculated as follows:

$$\Delta^{33}S = [(\delta^{33}S/1000 +1) – (\delta^{34}S/1000 + 1)^{0.515}] \bullet 1000 ‰$$

with δ values expressed in ‰, the exponential mass fractionation constant is from Farquhar et al. (2010), and the VCDT values for $^{33}S/^{32}S = 0.00787725$ and $^{34}S/^{32}S = 0.0441626$ (Ding et al., 2001). Mean values for secondary reference materials, pyrite S0329 are $\delta^{34}S_{VCDT}$ = +3.3 ± 0.19 ‰ (1σ, reference value +3.3 ‰) and $\Delta^{33}S$ = +0.07 ± 0.06 ‰ (1σ, reference value undetermined), and for S0325 pyrrhotite are $\delta^{34}S_{VCDT}$ = -0.49 ± 0.12 ‰ (1σ, reference value -0.59 ‰) and $\Delta^{33}S$ = -0.39 ± 0.08 ‰ (reference value -0.37 ‰).

4.5 RESULTS

4.5.1 Bulk rock geochemistry

Mineralized veins from Grand Duc and Doyon show an enrichment in a variety of metals (Table 4.1). Grand Duc samples are divided into high-grade (Au >10 g/t; sample = 18KN03) and low-grade (Au <10 g/t; samples 18KN07, 08, 09, 11). Both samples from Doyon are high-grade. The high-grade sample from Grand Duc returned 297.88 g/t Au and high-grade samples from Doyon returned 30.45 and 23.80 g/t Au. Silver concentration in the high-grade Grand Duc vein is 46.67 g/t, and 23.80 and 2.92 g/t in Doyon high-grade samples. Low-grade samples from Grand Duc range between 0.89 and 5.93 g/t Au and 0.54 to 2.21 g/t Ag. Bismuth is highly enriched in the Grand Duc high-grade sample with almost 600 ppm and Te is >40 ppm (over range). Bismuth content is relatively the same between low-grade samples from Grand Duc and high-grade Doyon samples, ranging from 0.36 to 2.55 ppm. Tellurium is highly enriched in Doyon (25-29 ppm) compared to low-grade Grand Duc samples (0.98-4.74 ppm). Within the high-grade Grand Duc sample, Co, Cu, Zn, Pb, Sb, In, Sn, and Cd are highly enriched relative to all samples from Grand

Duc and Doyon. Comparing low-grade Grand Duc and high-grade Doyon samples, As, Cu, Se, Cd, In, Sn, and Te are enriched in Doyon while Co and Pb are enriched in low-grade Grand Duc samples.

4.5.2 Doyon quartz vein and ore mineralogy

Two mineralized quartz-pyrite veins from the Doyon West deposit crosscut the Phase E (tonalite) of the MIC were sampled for this study. Both veins have sharp contacts with the host xenolith-rich tonalite and vary between 5 and 20 cm in width (Fig. 4.2A-B). The modal proportions of minerals vary between and within individual veins. Quartz and pyrite are the most abundant minerals in the mineralized veins, with quartz comprising 20−80 vol% and pyrite 20−80 vol%. Minor amounts of what is likely highly altered wallrock have been incorporated in the veins, comprising 0−5 vol% (Fig. 4.2C-D). These wallrock fragments have been strongly chloritized and sericitized.

Two different textural variations (possibly representing different generations) of quartz are identified and are termed Q1 and Q2. Individual grains of Q1 vary in size from 100−2000 μm and display some evidence of intracrystalline plastic strain (e.g., undulose extinction). Generation Q2 is finer-grained quartz (<100 μm) and occurs as isolated grain aggregates, or along the margins of Q1 grains as polycrystalline "ribbons". Minor amounts of muscovite and chlorite are present within the mineralized veins as well. Muscovite grains range in size from 50 to 600 μm and occur along the grain boundaries of all minerals in the veins, and rarely as inclusions within pyrite. Chlorite grains are 50−500 μm in size and are commonly found along the margins of pyrite grains, with rare occurrences along the interstices of quartz grains. Chlorite also appears to be replacing muscovite.

Mineralized veins in the Doyon West deposit contain the sulfide assemblage pyrite + chalcopyrite ± pyrrhotite. Pyrite ranges in size from 100−4000 μm and is not or only weakly sieved

and/or fractured (Fig. 4.3A). No clear zonation was present in pyrite prior to and after etching the samples with nitric acid, but individual grains were variably affected by the acid etching (Fig. 4.3B). Locally, pyrite cores are sieved and contain abundant inclusions of chalcopyrite ± pyrrhotite ± pyrite ± magnetite ± tellurides ± gold (Figs. 4.3B, C, and 4.4A). These sieved cores generally transition to clean (i.e., sieve-free), inclusion-free pyrite towards the edge of an individual grain (Fig. 4.3A-B). Acid etching affected the sieved core and sieve-free rim the same amount for individual grains (Fig. 4.3B). In the sieve-textured portions of pyrite grains, inclusions typically fill voids and display planar grain margins, indicative of open space filling (Fig. 4.3B). Acid etching exposed the presence of a later generation of pyrite (inclusions) that filled the voids of early, sieved pyrite (Fig. 4.3B).

The textural features and semi-quantitative composition of ore minerals were determined by SEM-BSE and SEM-EDS. Ore minerals identified include gold (with Ag concentration varying between 11 and 19 at.%), petzite (Ag_3AuTe_2), calaverite ($AuTe_2$), and hessite (Ag_2Te) and representative SEM-EDS analyses of ore minerals are presented in Table 4.2. Gold occurs in six textural settings: 1) composite inclusions in pyrite composed of gold + petzite ± calaverite is the most common textural occurrence (Fig. 4.4A-E); 2) along fractures of pyrite (Fig. 4.4F); 3) along grain boundaries between pyrite and quartz (Fig. 4.4G-H); 4) inclusions within pyrite (Fig. 4.4I); 5) within quartz fractures; and 6) inclusions in chalcopyrite (Fig. 4.4J). Additionally, some gold-bearing grains present within quartz and pyrite fractures are composed of a mixture of petzite and gold, but with no well-defined grain boundaries (Fig. 4.4K). The Au:Ag ratio (at. %) of gold ranges from 72:28 to 95:5 and is variable across all textural settings (Table 4.2).

The composite inclusions of gold + petzite ± calaverite are generally 5-10 μm in size but can be up to 85 μm (Fig. 4.4A-E). Inclusions typically have a bleb-like morphology, with some inclusions displaying open-space filling textures with sharp crystal faces in contact with the host

pyrite (Fig. 4.4B). The percentage each mineral phase occupies within the composite inclusions is highly variable, with gold occupying 2-38 vol%, petzite 58-92 vol%, and calaverite 24-66 vol% (n=12). Apart from co-existing with gold, petzite occurs as separate inclusions in pyrite, along fractures and grain boundaries of pyrite, along fractures in quartz, and rarely in contact with chalcopyrite or pyrrhotite as inclusions in pyrite (Fig. 4.4E, I). Calaverite is present as inclusions within pyrite and along fractures of quartz, and hessite is present as composite grains with petzite occurring as inclusions in pyrite. Other minerals identified as inclusions in pyrite include magnetite and cassiterite. Both of these minerals are present in contact with pyrrhotite and chalcopyrite in voids within sieved pyrite (Fig. 4.4L).

4.5.3 Grand Duc quartz vein and ore mineralogy

All veins studied from the Grand Duc deposit range from a few mm to a few cm in width and have relatively sharp but undulating contacts with the host rocks (Fig. 4.2E-G). The modal proportions of minerals vary between and within individual veins. Quartz, carbonate, and pyrite are the most abundant minerals in the mineralized veins, with quartz + carbonate comprising 70-90 vol% and pyrite 10-30 vol%. Alteration of the wallrock adjacent to mineralized veins consists of sericite, chlorite, and carbonate (Fig. 4.4F-G).

Gangue mineralogy in mineralized veins from the Grand Duc deposit consist predominately of quartz and carbonate minerals (mainly Fe-Mn-bearing calcite with minor Mg-bearing ankerite) with minor amounts of chlorite and sericite (Fig. 4.4E-G). Proportions of quartz and carbonate vary from vein to vein, comprising 20-40 vol% and 60-80 vol% of the gangue, respectively. Carbonate post-dates quartz as it is observed to have planar crystal boundaries with quartz, suggesting open space filling, and carbonate is present interstitial to quartz. Minor amounts of chlorite occur in mineralized veins and generally is only present in contact with sulfides along vein margins with

the wallrock or in wallrock fragments within the vein. Muscovite is closely associated with chlorite and can be partially to completely replaced by chlorite. Mineralized veins at Grand Duc contain the sulfide assemblage pyrite + chalcopyrite + pyrrhotite ± sphalerite and sulfide proportions vary from vein to vein, depending on the grade of the vein.

4.5.3.1 High-grade vein:

Pyrite occurs as large aggregate masses composed of multiple grains or as individual, isolated grains. Individual pyrite grains range in size from 40 to 2000 μm, but grains predominately range from 100 to 500 μm. In some pyrite grains, cores are moderately sieved while the rims are clean and sieve-free but other grains show sieve-free cores and sieved rims, suggesting multiple stages of pyrite growth (Figs. 4.3C, 4.5A). After etching samples with nitric acid, some pyrite grains displayed zoning with non-etched cores and weakly etched rims. However, the majority of grains were variably etched, and no qualitative correlation could be made between grains that were etched versus grains that were not etched. Interestingly, inclusions of tellurobismuthite (Bi2Te3) in pyrite (see SEM results below) that were exposed at surface prior to acid etching were no longer present after etching, suggesting that they were plucked out/dissolved during the etching process. Pyrrhotite occurs along grain boundaries/margins and fractures of pyrite and filling in voids in sieved pyrite (Fig. 4.3E). Pyrrhotite can display sieve texture but are less sieved compared to pyrite. Chalcopyrite shares the same textural settings as pyrrhotite in the high-grade vein (Fig. 4.3D-G). Both pyrrhotite and chalcopyrite locally display textures that are indicative of replacing pyrite in the high-grade vein (Fig. 4.3F). Rare sphalerite is present, occurring in fractures of pyrite and along grain margins of pyrite, pyrrhotite, and chalcopyrite (Fig. 4.3G).

Gold occurs in five different textural settings within the vein: 1) filling in voids in sieved pyrite (Fig. 4.5A); 2) along fractures in pyrite with or without pyrrhotite, chalcopyrite, and/or

sphalerite (Fig. 4.5B); 3) along grain boundaries of pyrrhotite, chalcopyrite, and/or sphalerite or quartz and/or carbonate (Fig. 4.5C); 4) filling in voids in sieved pyrrhotite (Fig. 4.5D); and 5) along grain boundaries and/or fractures of quartz and carbonate (Fig. 4.5E).

In addition to gold present within quartz-carbonate veins, gold is associated with strong chlorite and sericite alteration in the wallrock with minor pyrite, pyrrhotite, and chalcopyrite (Fig. 4.5F-H). Tellurobismuthite (see SEM results below) is also present in the strong chlorite alteration halo, sharing similar grain morphology to gold and can occur as composite grains with gold (Fig. 4.5F-H). Both gold and tellurobismuthite appear to be present along grain boundaries of chlorite and sericite (Fig. 4.5G-H).

The textural features and semi-quantitative composition of ore minerals were determined by SEM-BSE and -EDS. Ore minerals identified include gold, tellurobismuthite, altaite (PbTe), and tsumoite (BiTe) or tetradymite (Bi_2Te_2S). Due to the small grain size and close association with base metal sulfides, it is difficult to determine if the mineral is tsumoite or tetradymite. Representative SEM-EDS analyses of ore minerals are presented in Table 4.3. The Au:Ag ratio (at. %) of gold ranges from 81:19 to 91:9 and is variably across all textural settings (Table 4.3). Composite grains of gold + tellurobismuthite are present in the strong chlorite alteration as well as in voids in sieved pyrite (Fig. 4.5F-G). Composite grains of gold + altaite are also present but were only observed in the chlorite alteration. Tellurobismuthite and altaite share the same textural settings as gold, while tsumoite (or tetradymite) is predominately observed in the chlorite alteration with one instance of it observed filling in a void in sieved pyrite.

4.5.3.2 Moderate-low grade veins:

Pyrite in moderate to low-grade veins is relatively coarser-grained (100-2000 um) and shows more distinct sieved cores and clean rims compared to pyrite from the high-grade vein. A

second generation of pyrite is present occurring as clean, sieve-free grains along the margins of sieved-pyrite. Similar to the high-grade veins, individual pyrite grains were variably affected by nitric acid etching and no qualitative correlations could be made. Pyrrhotite and chalcopyrite are present in trace amounts filling in voids in sieved pyrite and rarely, chalcopyrite occurs on the margins of pyrite.

In one of the low-grade veins (sample 18KN09) two generations of pyrite-quartz-carbonate veins crosscut each other. The gangue and sulfide mineralogy of both veins is comparable to all other veins described above, but textural differences exist between the two veins. Pyrite size and morphology are similar between the two veins but one vein contains strongly sieved and fractured pyrite, while the other vein contains relatively "clean", weakly sieved, and fractured pyrite. Pyrite in both veins contains inclusions of pyrrhotite and chalcopyrite that are filling in voids in the sieved areas. Crosscutting relationships suggest the "clean" pyrite vein is younger than the strongly sieved pyrite vein.

Representative analyses of gold and accessory minerals are presented in Table 4.3. Gold occurs in three textural settings: 1) filling in voids in sieved pyrite (Fig. 4.5I-K); 2) along grain boundaries of pyrite and gangue; and 3) along fractures in pyrite, quartz, and carbonate. The Au:Ag (at. %) ratio of gold ranges from 60:40 to 78:22 for grains that occur along grain boundaries and fractures but gold occurring in voids within sieved pyrite is more Au-rich with Au:Ag ratio between 85:15 to 93:7 (Table 4.3). In sample 18KN09, gold occurs in both pyrite-quartz-carbonate vein generations along grain boundaries and fractures, but gold only occurs in voids in the strongly sieved pyrite vein. Gold can be present by itself in sieved pyrite voids or associated with base metals sulfides (chalcopyrite ± pyrrhotite ± sphalerite; Fig. 4.5J) and/or accessory minerals (e.g. calaverite). Accessory minerals present in the moderate-low grade veins include: tellurobismuthite, petzite, calaverite, altaite, volynskite ($AgBiTe_2$), hessite, and native Te. All accessory minerals

occur in voids in pyrite, except for hessite, which also occurs along pyrite grain boundaries (Fig. 4.5I-K). Numerous types of composite inclusions occur in pyrite voids such as, calaverite + gold, petzite + calaverite, tellurobismuthite + petzite, volynskite + hessite, and gold + petzite + tellurobismuthite + native Te + chalcopyrite (Fig. 4.5I-K). No accessory minerals were observed in the "clean" pyrite vein in sample 18KN09. Other minerals present in sieved pyrite include magnetite, which occurs in voids with pyrrhotite, chlorite, and/or carbonate (Fig. 4.5L).

4.5.4 Major element chemistry of sulfides and chlorite

4.5.4.1 Chlorite:

Chlorite intergrown with tellurides (Fig. 4.3G; 4.5G, H) and chlorite associated with base metal sulfides were analyzed by EMPA for their major element composition and to estimate formation temperatures (Cathelineau, 1988). Full major element chemistry of chlorite is available in Supplementary Table 4.1. Both textural settings of chlorite have the same composition, corresponding to chamosite with Fe/(Fe+Mg) values ranging from 0.61 to 0.76 (Fig. 4.6). Recalculation of chlorite chemistry to atoms per formula unit (apfu) results in Si ranging from 2.50 to 2.60 and $Al^{(IV)}$ between 1.40 and 1.50.

Chlorite from the Doyon West deposit does not have the same textural association with tellurides and base metal sulfides as at Grand Duc, but occurs along the edges of pyrite, similar to the textural setting of gold and tellurides. The Fe/(Fe+Mg) values are lower in chlorite from Doyon compared to Grand Duc, ranging from 0.17 to 0.24 (Fig. 4.6), corresponding to a clinochlore composition. The Si and $Al^{(IV)}$ apfu range between 2.64 to 2.90 and 1.10 to 1.36, respectively.

4.5.4.2 Sphalerite and Pyrrhotite:

The major element chemistry of sphalerite and pyrrhotite that occurs along the margins of pyrite and coeval with each other, chalcopyrite, and gold and telluride mineralization was determined by EMPA. Zinc concentration in sphalerite is extremely similar across all analyses ranging from 58.55 to 60.07 wt% (~59.13 ± 0.49 wt%; n=35). The Fe concentrations in sphalerite range from 5.36 to 7.77 wt% (~6.81 ± 0.58 wt%; n=35) and show a negative relationship with Zn concentration (R^2 = 0.4126). Sphalerite Cu and In concentrations are minor with average concentrations of 0.23 ± 0.22 wt% (n=18) and 0.04 ± 0.02 wt% (n=13), respectively. Manganese was only above detection limits in three analyses with concentrations of ~0.03 wt% whereas Pb was only above detection in one analysis with a concentration of 0.05 wt% in sphalerite. The Fe and S concentrations in pyrrhotite are extremely similar across all analyses with average concentrations of 61.37 ± 0.34 and 39.18 ± 0.26 wt% (n=28), respectively. Full major element chemistry of sphalerite and pyrrhotite are available in Supplementary Table 4.2.

4.5.5 Trace Element Distribution Patterns in Pyrite

Two pyrite grains from the Doyon West deposit and four from the Grand Duc deposit (two from the high-grade vein [sample 18KN03] and two from a lower grade vein [sample 18KN07]) were mapped by LA-ICP-MS to characterize their trace element distribution. Representative pyrite trace element maps from Doyon and Grand Duc are shown in Figures 4.7 and 4.8, and in Figures 4.9 and 4.10, respectively. Element maps show variable patterns between the two deposits but are relatively consistent within each system.

4.5.5.1 Doyon:

Both pyrite grains from the Doyon West deposit contain relatively clean (un-sieved) cores and sieved zones containing inclusions of base metal sulfides, gold, and tellurides (Fig. 4.7A, B

and 4.8A, B). The trace element patterns for both pyrite grains are characterized by four distinct stages of metal associations. Initially (Stage I) pyrite is metal-poor and there are no notable metal enrichments in the core. Arsenic enrichment occurs around the metal-poor cores to define Stage II (Fig. 4.7C, 4.8C). The third stage (Stage III) of metal associations is characterized by Co-Ni-Se and a significant drop in As content (Fig. 4.7C-F, 4.8C-F). Additionally, Se is slightly above detection limits throughout the entire pyrite grain but displays a subtle increase in concentration with Co and Ni. Stage IV metal associations are represented by Au-Ag-Te-Cu-Bi-Pb occurring along fractures and inclusions within pyrite, mostly concentrated as gold and telluride inclusions (Fig. 4.7B, G, H, 4.8B, G, H). Zinc, Sb, In, Cd, and Sn are all depleted in pyrite from Doyon.

4.5.5.2 Grand Duc, High-grade vein:

Pyrite from the high-grade vein in Grand Duc can display well-formed core to rim zoning patterns but complex patterns as well. The grain displaying core to rim zoning was selected based on the textures observed after acid etching revealed clear distinction between the core and rim (Fig. 4.9A, B). The core-rim boundary does not have a smooth transition and is very irregular, possibly indicating a period of pyrite dissolution prior to the growth of the pyrite rim. Additionally, pyrrhotite crosscuts pyrite, minor chalcopyrite occurs along the edge of the pyrite grain, and multiple inclusions of chalcopyrite occur in the porous rim of pyrite (Fig. 4.9A, B). Inclusions of gold are also present in the porous rim. As the acid etching revealed a well-formed core to rim break, this translates to the trace element domains present. Initially pyrite has moderate As, Co, and Ni concentrations (Stage I; Fig. 4.9C-E) followed by increasing As and Co and a drop in Ni content (Stage II; Fig. 4.9C-E). Selenium has relatively the same concentration throughout Stage I and II (Fig. 4.9F). Stage III is characterized by a sharp increase in As and Ni and a decrease in Co. This sharp transition corresponds to the core-rim boundary revealed by acid etching. The final trace

element stage (Stage IV) corresponds to the rim zone after the sharp As-Ni increase and marks the appearance of Au-Ag-Te-Bi-Sb-Se-Cu-Zn-Pb-Sn-In-Cd (Fig. 4.9G-K) with a drop in As and Ni contents.

The second grain mapped by LA-ICP-MS (not shown) was chosen based on its non-acid etched textures, that are representative of a majority of pyrite grains in this sample. This grain has a clean (non-sieved) core surrounded by a weak to moderately sieved zone that contains minor inclusions of pyrrhotite and chalcopyrite. Pyrrhotite and chalcopyrite also occur along the grain boundaries of pyrite. Minor tellurides and gold occur along pyrite grain boundaries as well. Trace element patterns in this pyrite grain are different than the core-rim zoning described for the previous grain. This grain displays an enrichment of Co-Ni-Se in the core followed by As-Te and an increase in Se content. The final stage of trace element enriched is characterized by Bi-Pb-Sb-Cu-Zn-Au-Ag. Elevated zones of Te-Bi-Pb are related to telluride minerals along pyrite grain boundaries.

4.5.5.3 Grand Duc, Moderate-low grade veins:

Pyrite from the moderate-low grade veins at Grand Duc also display variable patterns. The first grain was selected for LA-ICP-MS mapping because it is composed of multiple pyrite grains, some of which are weakly sieved whereas others are inclusion-free surrounding sieved-pyrite (Fig. 4.10A, B). This area is representative of most of the pyrite in this sample. The trace element patterns show that this grain is initially metal-depleted (Stage I) followed by an increase in As-Se-Co-Ni (Stage II; Fig. 4.10C-F). Stage III is marked by a drop in As contents with moderate to high Co-Ni and Se. Finally, (Stage IV) along the rim is marked by the highest Co contents in the grain. Fractures, grain boundaries, and inclusions are host to As-Au-Ag-Te-Bi-Pb-Cu, representing tellurides and/or gold (Stage V).

A second pyrite grain (not shown) was mapped because it is a single grain that has a moderately-sieved core and inclusion-free rim. This grain has an initially enriched core in Co-Se (Stage I) followed by a drop in Co with an increase in Ni and relatively constant Se (Stage II). Stage III is a metal-depleted domain. The inclusion-free rim (Stage IV) is characterized Co-Ni-Se-As. Finally, Au-Ag-Bi-Te-Pb-Sb are related to inclusions or grains of gold and/or tellurides in pyrite or along fractures.

4.5.6 Trace Element Scatter Plots based on LA-ICP-MS maps

4.5.6.1 Doyon:

Bivariate plots of various metals in pyrite allow for additional patterns to be discriminated that may not be readily apparent from the trace element maps. In the case of pyrite from Doyon, the trace element distribution in pyrite is relatively simple compared to pyrite from Grand Duc. The trace element bivariate plots display the same patterns for the grains shown in Figures 4.7 and 4.8, but data in Figure 4.11 is only shown for pyrite in Figure 4.8. Three As zones are present based on the trace element maps (Figs. 4.8C), plotting the concentration of As against Au (Fig. 4.11A) and Te (Fig. 4.11B), only distinguished two domains because the As-poor core and rim have considerable overlap in concentrations (although the rim does have slightly higher concentrations), making it distinguish between them. The solubility limit line for Au and Te occurring in solid solution as a function of As in pyrite (from Reich et al., 2005, and Keith et al., 2018) is plotted on Figure 4.11A, B. It is evident from reflected light and SEM petrography (Fig. 4.8B) that gold and Au-Ag-tellurides are common inclusions in pyrite as well as along grain margins and fractures of pyrite, therefore the large amount of Au and Te concentrations that represent nano-inclusions (or micro-inclusions) is not surprising. However, a large amount of these analyses may be due to

residual effects during the mapping process and are an artifact of ablating a Au-Ag-Te-bearing inclusion (cf. Boucher et al., 2023).

Cobalt concentrations are consistently below detection limits in the core (<0.05 ppm), therefore any bivariate plot with Co predominantly only records trends in the rim. As expected from the map, Co and Ni display a positive correlation (Fig. 4.11C). Cobalt and As predominately cluster between 0.1 and 1 ppm over a range of As concentrations (Fig. 4.11D), but Co > ~1 ppm displays a positive correlation with As, which can be correlated to minor zones in the rim with elevated As contents.

The temperature of pyrite formation has been estimated through the *semiquantitative* Se-in-pyrite geothermometer (Keith et al., 2018). The Se content of pyrite from Doyon is predominately <40 ppm, with Se concentrations >40 ppm generally occurring with elevated Au and low Te concentrations (Fig. 4.11E). Given the large difference in Co contents between the core (<0.05 ppm) and rim (>0.05 ppm) of pyrite (Fig. 4.8D), temperatures can be estimate for each. Pyrite core temperatures are similar between the two mapped grains and are estimated to be 489 ± 81°C (n=9303; Fig. 4.11F) and 458 ± 82°C (n=13188). The rim records temperatures of 430 ± 91°C (n=6716; Fig. 4.11F) and 440 ± 77°C (n=8069), slightly cooler than, but within error, of the core. It should be noted that the anomalously high (>40 ppm) Se concentrations will result in lower temperatures (<325°C) and are responsible for the low temperature side of the distribution curve in Figure 4.11F. Plotting Au concentrations against temperature, there is no clear correlation, except at < ~350°C Au contents are predominately >10 ppm (Fig. 4.11G). The two As domains show a similar range in temperate, but similar to Au, at < 350°C, As contents are elevated and generally are > 10 ppm (Fig. 4.11H).

4.5.6.2 Grand Duc, High-grade vein:

Bivariate plots of pyrite (Fig. 4.9) from the high-grade vein at Grand Duc can differentiate the various trace element stages primarily based on the Co and As contents (Fig. 4.12A). Plotting Au against As can distinguish Stages II and III from each other, but due to the similar As contents between Stages I and IV, it is hard to differentiate between them (Fig. 4.12B). As expected from the Au solubility line of Reich et al. (2005), the highest As domains contain the highest dissolved Au concentrations (Fig. 4.12B). This solubility line may differentiate some analyses of Stage IV from Stage I, because gold occurs as inclusions in the rim of pyrite (i.e., Stage IV), and therefore analyses that lie above the Au solubility line, are predominantly associated with Stage IV. The Te solubility line of Keith et al. (2018) is plotted on the Te vs As plot (Fig. 4.12C). The position of a majority of analyses above this line, especially those of the high-As Stage IV, begs the question if this line is appropriate given no tellurides are observed as inclusions in this pyrite grain. Metals that are primarily associated with Stage IV (e.g., Sb-Pb-Bi-Se-Cd-Cu) tend to display a positive correlation with each other (Fig. 4.12D).

Semiquantitative temperature estimates based on the Se content of pyrite (Keith et al., 2018), the average temperature is 370 ± 60°C (n=9219). Given that the majority of the pyrite core is > 2000 ppm Co and the rim is < 2000 ppm, an average temperature for the core and rim can be estimated. The average temperature of the core is 398 ± 54°C (n=5149; Fig. 4.12E) whereas the rim records an almost 50°C drop in temperature with an average of 344 ± 54°C (n=4497; Fig. 4.12E). Numerous analyses have anomalously high Se concentrations (>150 ppm) resulting in temperatures < 245°C as indicated by the very low end on the temperature distribution curve (Fig. 4.12E). Plotting As against temperature (Fig. 4.12F) clearly separates the Stages III and IV (i.e., rim) from I and II (i.e., core), showing that a greater proportion of core analyses extend to higher temperatures than the rim. When plotting all of the analyses it is difficult to distinguish any correlation between Au and temperature (Fig. 4.12G). However, when only plotting Au <20 ppm,

maximum Au dissolved in pyrite based on the As content (Fig. 4.12H), it is clear that at lower temperatures, Au content increases.

4.5.6.3 Grand Duc, Moderate-low grade veins:

Compared to trace element maps from the high-grade vein at Grand Duc and from Doyon, the moderate- to low-grade vein pyrite from Grand Duc does not display clear distinctions based on the time series data. Cobalt and As which separated out different stages in the other samples, have large overlaps between the different trace element zones (Fig. 4.13A) and therefore it is difficult to distinguish trace element stages from each other on a bivariate plot. Gold and Te concentrations have nearly identical patterns when plotted against As (Fig. 4.13A, B). Inclusions of gold and Au-Ag-tellurides occur along the grain margins and fractures of pyrite, which are responsible for elevated Au and Te concentrations and as in pyrite from Doyon, this has residual effects creating artificially elevated concentrations (Fig. 4.10B). The highest Au concentrations predominately occur at high Co contents (Fig. 4.13D), and this is likely due to the occurrence of gold and Au-Ag-tellurides along grain boundaries and the highest Co tend to occur along the outer margins of pyrite (Fig. 4.10E).

Since there are no correlations between Se and other metals in pyrite, no distinction between different trace element zones can be made and only an average temperature for the entire pyrite grain can be estimated, yielding a temperature of 426 ± 75°C (n=9730; Fig. 4.13E). Similar to Doyon, anomalously high (>40 ppm) Se concentrations result in lower temperatures (<325°C) and are responsible for the low temperature side of the distribution curve in Figure 4.13E. Plotting As against temperature also shows a large range in temperatures at various As contents (Fig. 4.13F). The same lack of correlation is observed between temperature and Co (not shown). However, based on the Se distribution map two different Se domains are present, one with temperatures between

430° and 500°C and a lower temperature domain between 350° and 400°C (Fig. 4.10D). Pyrite trace element Stages III and IV are aligned with the lower temperature domain, but Stages I and II show an overlap between the high and low temperature zones.

4.5.7 Trace Element Spot Analyses of Sulfides from Grand Duc

Trace element concentrations of pyrite in the high- and moderate- to low-grade veins were analyzed and paired with S isotope analyses by SIMS (see below) to track changes in chemistry throughout the growth history of pyrite. Trace element concentrations of pyrrhotite in the high-grade vein associated with both the quartz-carbonate vein and the strong chlorite alteration were analyzed and paired with S isotope as well. Full trace element results for pyrite and pyrrhotite are available in Supplementary Data Tables 4.3, 4.4, and 4.5.

4.5.7.1 Pyrite, Grand Duc, High-grade vein:

Individual pyrite grains associated with the quartz-carbonate vein do not show systematic core to rim relationships between different grains. For example, some grains display an increase in Ni from core to rim, whereas Ni concentrations decrease in others, but in all cases, Co decreases from core to rim (Fig. 4.14A). However, the elevated Ni regions of pyrite are in sieved portions of the grain, suggesting prolonged pyrite growth and subtle differences when each grain began to crystallize. Arsenic does consistently decrease in concentration from core to rim but no clear correlation between As and Au content exists in spot analyses (Fig. 4.14B). Gold concentrations are low (<0.3 ppm) regardless of location in the grain and concentrations above this are due to contamination by gold or Au-Ag-Te inclusions. A positive correlation exists between Au-Ag-Te and Te-Bi-Pb suggesting that submicron inclusions of tellurides are common in pyrite (e.g., Fig. 4.5A, C; Fig. 4.14C). Applying the semiquantitative Se-in-pyrite thermometer of Keith et al.

(2018), temperatures range from 295 to 385°C (335 ± 34°C; n=15), with one outlier at 479°C. Generally, most grains display similar temperatures between core and rim, however some grains display up to a ~70°C decrease in temperature along the rim relative to the core (Fig. 4.14D).

Pyrite in the strong chlorite alteration shows consistent increases from core to rim for Co, Ni, Se, Te, and Bi (Fig. 4.14A, C). Gold (<0.02 ppm) and As concentrations (~2-14 ppm) are comparable between core and rim (Fig. 4.14B). One analysis in the core has a Au concentration of 1.27 ppm and coincides with elevated Te (249 ppm) and Bi (250 ppm), suggesting this analysis was contaminated by a telluride. The Se-in-pyrite temperatures are relative lower (320°-330°C) along the rim compared to the core (350°-377°C; Fig. 4.14D).

4.5.7.2 Pyrrhotite, Grand Duc, High-grade vein:

Most trace elements have similar concentrations between the two textural varieties of pyrrhotite (e.g., vein vs. chlorite alteration associations), with the exception of Co and Se. Pyrrhotite associated with the chlorite alteration has Co concentrations ranging from ~280 to ~430 ppm, where as pyrrhotite in the quartz-carbonate vein has lower Co concentrations between ~170 and ~230 ppm (Fig. 4.15A). In both textural varieties, Ni contents are low, ranging from ~7 to ~30 ppm. Concentrations of Au are low in both textural settings (< 0.05 ppm) and are only above detection in 4 of 19 analyses.

4.5.7.3 Pyrite, Grand Duc, Moderate-low grade veins:

Individual spot analyses of the pyrite from the highly sieved pyrite vein (clean core, sieved outer core, and clean rim zones) from sample 18KN09 were analyzed to track variations in trace element chemistry between them. Overall, Co and Ni contents are the best discriminants between the three zones, generally with Co increasing and Ni decreasing moving from core to rim (Fig.

4.16A). Arsenic contents show a general increase in concentration from core to rim, similar to Co (Fig. 4.16B). Gold concentrations are generally low in the core (0.01 to 0.15 ppm), except one analysis that encountered a Au-Ag-Te inclusion that has a concentration of 275 ppm Au (Fig. 4.16C). Concentrations of Au in the outer core and rim consistently higher than the clean core with concentrations ranging from ~0.01 to ~ 1 ppm. Analyses with Au concentrations >1 ppm have elevated Ag and Te concentrations indicating the presence of Au-Ag-Te inclusions (Fig. 4.16D). Calculated temperatures (*semiquantitative* Se-in-pyrite thermometry; Keith et al., 2018) show systematic changes throughout the three different zones (Fig. 4.16E). The clean core has an average temperature of 327 ± 47°C (n=11) and progressing to the outer core zone temperature generally decreases, with an average of 305 ± 56°C (n=17). Finally, the rim records the highest temperatures with an average of 381 ± 36°C (n=16).

Similar to pyrite in the highly sieved vein, the clean pyrite vein crosscutting the highly sieved and fractured pyrite vein, Co is enriched in the rims (~106-850 ppm) relative to the core (~6 to 65 ppm). Selenium is also typically higher along the rim. Arsenic is generally higher in the core relative to the rim, but concentrations do overlap. Many analyses have elevated concentrations of Te, Bi, Ag, Au, and/or Pb indicating tellurides and/or gold inclusions were encountered during ablation and these elevated values occur in the core and rim of pyrite.

4.5.8 Multiple Sulfur Isotope Compositions

The $\delta^{34}S$ and $\Delta^{33}S$ composition of pyrite was obtained to determine if changes in $\delta^{34}S$ occur synchronously with variations in the trace element distribution. Additionally, pyrrhotite coeval with gold and tellurides from Grand Duc and inclusions of pyrrhotite in pyrite from Doyon were analyzed. Sulfur isotope results are available in Supplementary Data Tables 4.3 to 4.7 and presented in Figure 4.17A.

4.5.8.1 Doyon:

Both grains of pyrite that were mapped by LA-ICP-MS were analyzed for detailed SIMS (Figs. 4.7A and 4.8A). The $\delta^{34}S$ composition of the metal-depleted core (Stage I) in pyrite ranges between 1.44 and 1.71 ‰ (~1.54 ± 0.08 ‰; 1σ; n = 10; Fig. 4.17B). In the As-rich zone (Stage II), the $\delta^{34}S$ composition shifts higher with values between 2.33 and 3.03 (2.76 ± 0.21‰; n = 18; Fig. 4.17B). The Co-rich rim (Stage III) has similar $\delta^{34}S$ composition to the As-rich Stage II, ranging between 2.67 and 2.92 ‰ (~2.78 ± 0.07; n =17; Fig. 4.17B). One grain of pyrrhotite present as an inclusion in pyrite that occurs at the boundary between Stage I and II, has $\delta^{34}S$ composition ranging between 1.03 to 1.18 ‰ (n=3). Given the 2σ error on $\Delta^{33}S$ values is ± 0.11, no difference in $\Delta^{33}S$ values occurs between the different trace element domains in pyrite with values ranging between -0.14 and 0.13 ‰ (Fig. 4.17B). The pyrrhotite inclusion has $\Delta^{33}S$ values between -0.04 and -0.16 ‰. All $\Delta^{33}S$ values fall within the mass-dependent fractionation field (Fig. 4.17A).

4.5.8.2 Grand Duc, High-grade vein:

Multiple pyrite grains were analyzed by SIMS to pair with LA-ICP-MS spot analyses to track compositional changes within individual grains. For all analyses the range in $\delta^{34}S$ compositions is between 1.36 to 2.52 ‰ (n=16) and overall, there is an overlap in $\delta^{34}S$ compositions between core and rim. Some grains have similar $\delta^{34}S$ composition between the core and rim, whereas others have lower $\delta^{34}S$ composition along the rim relative to the core (Fig. 4.14D). No systematic variation in $\Delta^{33}S$ occur between core and rim in individual grains and overall, $\Delta^{33}S$ values range from -0.05 to 0.11 ‰ (Fig. 4.17A).

Pyrite in the chlorite alteration that displays enrichment in ore metals along the rim (as shown in Fig. 4.14D), records lower $\delta^{34}S$ compositions along the rim relative to the core. In these

grains, the core has $\delta^{34}S$ compositions between 2.14 and 2.20 ‰ (n=2) whereas the metal-rich rims are between 1.54 and 1.79 ‰ (n=3). No systematic variation in $\Delta^{33}S$ occurs with values ranging from 0.01to 0.08 in both the core and rim.

Pyrrhotite from the high-grade vein at Grand Duc was also analyzed for its sulfur isotope composition. Even though there are subtle differences in the trace element chemistry between pyrrhotite in the chlorite alteration and pyrrhotite in the quartz-carbonate vein, the $\delta^{34}S$ composition is similar (Fig. 4.15B). Pyrrhotite in the chlorite alteration has a range in $\delta^{34}S$ composition between 0.86 and 1.45 (~1.19 ± 0.19 ‰; n=11) and pyrrhotite in the quartz-carbonate vein ranges from 1.22 to 1.50 ‰ (~1.38 ± 0.12 ‰; n=7). The $\Delta^{33}S$ values are similar between the two types of pyrrhotite as well ranging from -0.05 to 0.13 and -0.16 to 0.11 for chlorite- and quartz-carbonate associated-pyrrhotite, respectively (Fig. 4.15C).

4.5.8.3 Grand Duc, Moderate-low grade veins:

One pyrite grain that was mapped by LA-ICP-MS (Fig. 4.10A) was selected for detailed SIMS analysis to track changes in sulfur isotope systematics based on trace element zoning. The metal-depleted core (Stage I) in pyrite has $\delta^{34}S$ composition ranging between 1.60 to 1.88 ‰ (n=3; Fig. 4.17C). Once the As content increases (Stage II), $\delta^{34}S$ composition also increases to values between 3.07 to 3.72 ‰ (~3.37 ± 0.2‰; n=10; Fig. 4.17C). Stage III which is marked by a significant drop in As with moderate to high Co-Ni-Se has a $\delta^{34}S$ composition intermediate to Stage I and II with a range in values from 2.46 to 2.87 (~2.66 ± 0.15‰; n=9; Fig. 4.17C). Finally, the Co-rich rim (Stage IV) has a range in $\delta^{34}S$ composition from 2.70 to 2.86‰ (~2.75 ± 0.05‰; n=8; Fig. 4.17C), similar to Stage III. Given the 2σ error on $\Delta^{33}S$ values is ± 0.11, no difference in $\Delta^{33}S$ values occurs between the different trace element domains in pyrite with values ranging between -0.14 and 0.08 ‰ (Fig. 4.17C).

Additional SIMS analysis were paired with LA-ICP-MS spot analysis to record compositional changes within individual pyrite grains from the lower grade vein sample 18KN09 (Fig. 4.16F). In the highly sieved and fractured pyrite, the $\delta^{34}S$ composition of the clean (un-sieved) core ranges from 1.77 to 1.97 ‰ (~1.86 ± 0.07; n=10). Analysis of the outer (sieved) core containing elevated Au-Ag-Te-Bi-Pb concentrations has a slightly higher $\delta^{34}S$ composition, ranging from 1.71 to 2.86 ‰ (~2.33 ± 0.36; n=12). The outer, clean rim of pyrite has a similar $\delta^{34}S$ composition to the sieved regions, ranging from 2.33 to 3.14 ‰ (~2.70 ± 0.34; n=4). No difference in $\Delta^{33}S$ values occurs between the different domains in pyrite with values ranging between -0.10 and 0.13 ‰.

No correlations exist between the different trace element domains and $\delta^{34}S$ composition in clean pyrite that crosscuts highly sieved and fractured pyrite (sample 18KN09). The $\delta^{34}S$ composition of the pyrite core ranges from 2.24 to 2.69 ‰ (~2.45 ± 0.17 ‰; n=6). The rim of pyrite differs in $\delta^{34}S$ composition depending on the side of the grain, with one rim having values between 2.12 and 2.53 ‰, whereas the other rim has a value of 3.49 ‰. One analysis in an outer core region has a $\delta^{34}S$ composition of 3.89 ‰. No difference in $\Delta^{33}S$ values occurs between the different domains in pyrite with values ranging between -0.06 and 0.10 ‰.

4.6 DISCUSSION

4.6.1 Comparison Between Doyon and Grand Duc Mineralization Styles

Mineralization styles at Doyon and Grand Duc (high- and moderate- to low-grade) have some similarities but distinct differences in the base metal sulfide and accessory ore mineral assemblages, pyrite trace element patterns, and subtle variations in $\delta^{34}S$ distribution patterns in pyrite occur (Table 4.4).

In terms of the major minerals that comprise mineralized veins all are predominantly composed of quartz and pyrite, however, at Grand Duc, mineralized veins also contain Mg-bearing ankerite with minor amounts of Fe-Mn-bearing calcite. Pyrrhotite is present in trace amounts filling in voids in sieved pyrite and rarely, chalcopyrite occurs on the margins of pyrite at Doyon and in the lower-grade veins at Grand Duc, whereas the high-grade Grand Duc vein has significantly more pyrrhotite and chalcopyrite in addition to sphalerite. However, it should be noted that chalcopyrite is a common ore mineral in the Doyon (cf Galley and Mercier-Langevin, 2024). Pyrrhotite in the high-grade vein is also present as inclusions in pyrite but is also replacing and crosscutting pyrite. In the high-grade vein, there is the strong-chlorite alteration halo that has a strong association with gold and tellurobismuthite (Fig. 4.3 G, H) and this strong-chlorite alteration halo is not observed at Doyon or in the lower-grade veins from Grand Duc.

Some accessory ore minerals are similar between Doyon and the lower-grade veins at Grand Duc, such as petzite, hessite, and calaverite, but the lower-grade Grand Duc veins also contain Bi- and Pb-tellurides (tellurobismuthite, native Te, volynskite, and altaite; Tables 4.2 and 4.3). The high-grade Grand Duc vein contains the same Bi- and Pb-tellurides as the lower-grade veins, in addition to tsumoite or tetradymite, but petzite, hessite, and calaverite are not present. Although subtle differences in the accessory ore mineralogy occur, the textural setting of these minerals and of gold, are similar and indicate ore deposition occurred post-pyrite or as a result of dissolution-reprecipitation mechanisms during regional metamorphism (e.g., Hastie et al., 2020).

The pyrite trace element and S isotope signatures and patterns show some similarities between Doyon and the lower-grade veins from Grand Duc (Figs. 4.7, 4.8, and 4.10) Both show relatively metal depleted cores followed by enrichment in As, however, Co and Ni become enriched with As in the lower-grade Grand Duc pyrite compared to pyrite in the lower-grade veins from Grand Duc. The rim of pyrite in Doyon and lower-grade Grand Duc veins both show relative

enrichment in Co and Ni, but the concentrations are significantly different between the two systems. At Doyon, Co and Ni concentrations along the rim are low (~0.2 - 1 ppm) whereas in the low-grade Grand Duc pyrite, Co (100's ppm) and Ni (~1-30 ppm) are significantly higher. Although differences exist in some metal concentrations and distribution in pyrite, the main ore (i.e., Au-Ag) and accessory ore metals (i.e., Te-Bi) share the same patterns, where they occur predominantly associated with gold or tellurides as either inclusions and along fractures or grain boundaries of pyrite. Sulfur isotopes at Doyon and the lower-grade veins at Grand Duc record similar compositions in similar trace element zones in pyrite. At both locations the metal-poor cores record $\delta^{34}S$ values ~1.4 to 1.9 ‰. Once As concentrations increase, $\delta^{34}S$ values increase by ~1 to 2 ‰ (Figs. 4.7A, 4.8A, and 4.10A).

Pyrite from the high-grade vein at Grand Duc can display significantly different trace element patterns compared to lower-grade veins and those at Doyon. Arsenic-Co-Ni follow a similar pattern to pyrite in the lower-grade vein, however the most significant difference is present near the rim, where there is a drastic increase in As and Ni contents (Stage III) followed by a significant decrease in Co that coincides with elevated concentrations of Au-Ag-Te-Bi-Sb-Se-Cu-Zn-Pb-Sn-In-Cd (Stage IV). The boundary between Stages III and IV is not smooth and is marked by an irregular interface, possibly indicating a period of pyrite dissolution prior to the growth of the metal-rich pyrite rim (Fig. 4.9A). In contrast to Doyon and the lower-grade veins, pyrite in the higher-grade vein records a drop in $\delta^{34}S$ progressing from core to the metal-rich rim (Fig. 4.14D).

4.6.2 Singular, Magmatic Sulfur Source

The contribution of magmatic volatiles to the ore forming system in the Doyon-Bousquet-LaRonde mining camp has been a long-standing question. The use of multiple sulfur isotopes can help elucidate and provide evidence concerning the origin of the fluids associated with magmatic-

hydrothermal ore deposits. In rocks older than 2.45 Ga, photochemically produced sulfate and sulfur by disassociation of SO_2 produced anomalous amounts of ^{33}S by mass independent fractionation (MIF) and accumulation of sulfur in the oceans can preserve this signature (Farquhar et al., 2000; Farquhar and Wing, 2003). Therefore, the influence of seawater sulfate and reduced seawater sulfur in the Archean can be monitored by changes in $\Delta^{33}S$ values (Farquhar and Wing, 2003), where negative values would suggest the influence of seawater sulfate (e.g., Noranda, Sharman et al., 2015) whereas positive $\Delta^{33}S$ values would reflect the incorporation of reduced sulfur (e.g., sedimentary rocks, LaFlamme et al., 2018a). If $\Delta^{33}S$ values record near-zero values (Farquhar and Wing, 2003; LaFlamme et al., 2018a; Fig. 4.17A), this can be taken as evidence that sulfur was derived directly from a magmatic source or was leached from surrounding volcanic (or intrusive) rocks, since MIF signatures are not strongly associated with purely magmatic processes (LaFlamme et al., 2018a).

Sulfur isotope analysis on pyrite and pyrrhotite from the Doyon and Grand Duc systems yield similar $\Delta^{33}S$ values. At Doyon, the overall range in $\Delta^{33}S$ is between -0.14 to 0.13‰ (~-0.01 ± 0.07‰; n=45). The $\Delta^{33}S$ composition in Stages I, II, and III are nearly identical with average $\Delta^{33}S$ values of -0.01 ± 0.09‰ (n=10) for Stage I and -0.01 ± 0.06‰ for Stages II (n=18) and III (n=17; Fig. 4.17A, B). These $\Delta^{33}S$ values are similar to bulk sulfur isotope analyses on pyrite from Doyon, which have $\Delta^{33}S$ values between -0.1 and 0.0‰ (Sharman, 2011). In the lower-grade veins from Grand Duc, no difference in $\Delta^{33}S$ values occur between the different trace element stages and the overall range in $\Delta^{33}S$ is between -0.14 and 0.13‰ (Fig. 4.17A, C). In the high-grade vein at Grand Duc $\Delta^{33}S$ also does not vary based on the different trace element zones and the overall range in $\Delta^{33}S$ is between -0.05 and 0.11‰ (Figs. 4.14D, 4.17A). By the $\Delta^{33}S$ composition not varying between different trace element zones in pyrite indicates only a single sulfur reservoir was involved during the evolution of both Doyon and Grand Duc (cf. LaFlamme et al., 2018b). Additionally,

based on the near-zero values of $\Delta^{33}S$ and they are all within the range of mass-dependent fractionation (Fig. 4.17A), suggests sulfur in the Doyon and Grand Duc systems was all magmatically derived and therefore it rules out fluid mixing as a gold precipitation mechanisms and processes such as fluid boiling, wallrock interactions, temperature changes, and fluid decompression need to be evaluated, which are discussed below for each deposit.

4.6.3 Temperature Constraints on Mineralization

Pre-, syn, and post-ore temperatures can be estimated based on pyrite (Keith et al., 2018) and chlorite geothermometers (Cathelineau, 1988) as well as the stability of telluride phases related to mineralization (Cabri, 1965). With respect to the Se-in-pyrite thermometer, it is important to note that the effect of having no Se-buffer is unclear. The concentration of dissolved Se-in-pyrite for pyrite from Doyon and the moderate to low-grade Grand Duc veins is up to ~40 ppm (Fig. 4.11E), however point data extracted from the LA-ICP-MS trace element maps can that Se can reach concentrations of ~5 wt%. In the high-grade Grand Duc vein, dissolved Se-in-pyrite is up to ~130 ppm, but point data from the LA-ICP-MS maps can be up to ~6 wt% Se. These anomalous Se concentrations provide evidence that there are Se-bearing accessory phases present as inclusions in pyrite. Evidence for Se saturation in this context justifies the use of the Se-in-pyrite thermometer in this setting as it has implications for fixing Se activity.

At Doyon, ore minerals occur post-pyrite since they are present as inclusions within, along grain boundaries of, and along fractures in pyrite, likely because of pyrite dissolution-reprecipitation during regional metamorphism (Fig. 4.4A, E, G). With the presence of gold-petzite-calaverite inclusions in pyrite (Fig. 4.4B), this ore mineral association provides a maximum temperature of ore precipitation at 304° ± 10°C (Cabri, 1965). Estimated peak metamorphic conditions in the Doyon-Bousquet-LaRonde mining camp are estimated to be between 450° and

500°C (Mercier-Langevin, 2005; Yergeau et al., 2022a), similar to temperatures recorded by pyrite rims (430° ± 91°C). The maximum telluride stability is cooler than the temperature obtained from pyrite rims suggesting the hydrothermal fluid cooled significantly prior to Au-Ag-Te precipitation, suggesting ore mineral deposition at the lower temperature-end of metamorphism. Chlorite texturally post-dates pyrite and has an average crystallization temperature of 342° ± 24°C (n=42), only slightly higher than telluride stability. However, while the genetic relationship between chlorite and ore minerals is unclear, chlorite shares similar textural settings to the ore minerals in that it occurs along grain boundaries and fractures of pyrite.

In the lower-grade veins at Grand Duc, trace element mapping shows a complex pattern (Fig. 4.10C-H), and it is difficult to discern if any core to rim temperature changes occur, but the average temperature for the entire grain is 426° ± 75°C (Fig. 4.13E). In other grains from lower grade veins (Fig. 4.16E), a drop of ~30°C occurs from the metal-poor core (327° ± 47°C; n=11) to metal-rich sieved portions (295° ± 42°C; n=16) of the grains, but an increase in temperature occurs along the outermost rim (381° ± 36°C; n=16). Telluride inclusions in the lower grade veins only provide maximum temperatures of ore mineral precipitation. Inclusions of gold and calaverite are only stable below 447°C (Barton and Skinner, 1979) and tellurobismuthite is stable over a wide range of conditions from below 588°C to <150°C (Shunk, 1969). The presence of gold-petzite-calaverite inclusions in pyrite (Fig. 4.5K), provides a maximum temperature of ore precipitation at 304° ± 10°C (Cabri, 1965). Given the average temperature of the highly sieved regions in pyrite is 295 ± 42°C, this is inline with the telluride stabilities and could represent the temperature of ore precipitation. Similar to Doyon, temperatures recorded by pyrite are near and/or similar to peak metamorphic conditions and could be the result of dissolution-reprecipitation of pyrite during regional metamorphism, whereas the temperature of telluride stability could be related to the lower end of metamorphism.

Individual pyrite grains in the high-grade vein at Grand Duc record slightly different temperatures, but the majority of pyrite cores yield temperatures between 400° and 350°C, whereas rims generally record lower temperatures between ~340° and 295°C. The mapped pyrite grain (Fig. 4.9) yields an average temperature in the core of 398° ± 54°C while the rim records a slightly lower temperature (344° ± 54°C). Pyrite in the strong chlorite alteration zone also yields slightly lower temperatures in the rim compared to the core. The limited variety of telluride minerals in the high-grade vein (tellurobismuthite, altaite, and tsumoite or tetradymite) provides only a relatively a wide range of temperature conditions as tellurobismuthite is stable below 588°C and down to <150°C (Shunk, 1969). However, chlorite that is intergrown with gold and tellurobismuthite, and associated with base metal sulfides, yields an average crystallization temperature of 405° ± 7°C (n=55).

4.6.4 Ore Forming Processes at Doyon Recorded by S Isotopes and Metal Domains in Pyrite

Coupling *in situ* S isotope and trace element analyses of pyrite allows for the assessment of geochemical variations throughout the growth history of pyrite and aids in the understanding of what processes (e.g., changes in temperature, pressure, pH, fO_2) may have played a role in the evolution of magmatic-hydrothermal ore deposit (e.g., Peterson and Mavrogenes, 2014; Tanner et al., 2016; Voute et al., 2019; Schaarschmidt et al., 2021; Börner et al., 2022; Boucher et al., 2023).

As a summary, at Doyon, pyrite records four dominant trace element domains, metal-poor (Stage I), As-rich (Stage II), and Co-Ni-Se-bearing (Stage III) and fracture and inclusion-controlled Au-Ag-Te-Cu-Bi-Pb (Stage IV). Stage I has an average $\delta^{34}S$ composition of 1.54 ± 0.08 ‰, whereas Stage II and III record slightly heavier $\delta^{34}S$ compositions of 2.76 ± 0.21‰ and 2.78 ± 0.07‰, respectively (Fig. 4.17B). Fluid phase separation induced by a significant drop in pressure or fluid boiling cannot account for the change in $\delta^{34}S$ composition either, as this process will cause $\delta^{34}S$ composition to decrease rather than increase (McKibben and Eldridge, 1990). This decrease

in $\delta^{34}S$ compositions is due to the loss of H_2 during fluid boiling and oxidizes aqueous H_2S to SO_4^{2-} with ^{34}S preferentially partitioning into SO_4^{2-}, leaving aqueous H_2S depleted in ^{34}S, and any subsequent pyrite precipitating from the aqueous fluid will have lower $\delta^{34}S$ compositions compared to pyrite formed from the non-boiled fluid (McKibben and Eldridge, 1990).

$$H_2S_{(aq)} + 4H_2O = SO_4^{2-} + 2H^+ + 4H_{2(g)}$$

A decrease in temperature can lead to an increase in $\delta^{34}S$, however, based on Se-in-pyrite thermometry, there is no difference in temperature between Stages I and II and only a ~60°C difference between Stages II (~490°C) and III (~430°C), which would only cause a ~0.1‰ increase in $\delta^{34}S$ (Ohmoto and Rye, 1979). A drop in temperature of at least 250°C would have had to occur for $\delta^{34}S$ to increase by ~1.0‰. Therefore, a drop in temperature is not a primary mechanism to produce the increase in $\delta^{34}S$ recorded between Stages I and II/III.

A mechanism that can produce an increase in $\delta^{34}S$ composition is through H_2S loss and wall-rock sulfidation and a subsequent reduction of the hydrothermal fluid (Neall and Phillips, 1987; Ward et al., 2017). Pyrite precipitation in the wall rock will consume ^{32}S leading to an increase of ^{34}S in the fluid and therefore any subsequent pyrite forming will have elevated $\delta^{34}S$ compositions. Additionally, As will substitute for S^{2-} in pyrite under more reducing conditions (Reich et al., 2005) and combined with the increase in As coincident with the increase in $\delta^{34}S$ in II, a reduction in the hydrothermal fluid is a likely mechanism to cause the increase in $\delta^{34}S$ recorded in pyrite. Previous studies at Doyon have documented sericite-pyrite-carbonate alteration halos around mineralized veins (~5 to 15 vol% pyrite; Gosselin, 1998) and a large-scale S anomaly of 150 to 350 m wide and at 3400 m long was identified around mineralized zones (Guha et al, 1982),

indicating wall-rock sulfidation was an important and widespread process in the evolution of the Doyon ore-forming system (Galley and Mercier-Langevin, 2024).

4.6.5 Ore Forming Processes at Grand Duc Recorded by S Isotopes and Metal Domains in Pyrite

For the lower-grade veins at Grand Duc, similar to Doyon, the core of pyrite records the lower $\delta^{34}S$ composition (~1.71 ± 0.15‰) and is also relatively metal-depleted (Stage I; Fig. 4.10A and 4.17C) compared to other zones in pyrite. This is followed by an increase of ~1.5‰ in $\delta^{34}S$ composition (3.37 ± 0.20‰) along with an increase in As content. The temperature difference is not significant between Stages I and II (< 50°C) and therefore cannot be responsible for the increase in $\delta^{34}S$ composition (Ohmoto and Rye, 1979). A reduction in the fO_2 conditions of the hydrothermal fluid would cause the $\delta^{34}S$ composition to become heavier and can be induced by wall-rock sulfidation, as is likely for Doyon (cf. Neall and Phillips, 1987). A reduction in fluid fO_2 would also lead to increasing As content in pyrite (Reich et al., 2005). However, after the As-rich Stage II, $\delta^{34}S$ composition drops by ~0.6‰ in Stages III (~2.66 ± 0.15‰) and IV (~2.75 ± 0.05‰; Figs. 4.10 and 4.17C). According to the distribution of Se-in-pyrite (Fig. 4.10D) and corresponding temperatures, Stages III and IV are similar to or only slightly cooler (~50°C) than Stage II, indicating a change in temperature is not responsible for the drop in $\delta^{34}S$ as decrease in temperature alone will raise the $\delta^{34}S$ composition; therefore, other process(es) must have occurred to produce this drop in $\delta^{34}S$, such as fluid boiling, fluid mixing, fluid leaching, or during regional metamorphism.

Other low-grade veins at Grand Duc record similar profiles in $\delta^{34}S$ compositions with As-poor pyrite cores having an average of ~1.86 ± 0.07‰ with temperatures of ~327° ± 47°C (Fig. 4.16F). These pyrite cores are clean (un-sieved) and have variable Co concentrations, ranging from

5 to 25 ppm in one grain whereas another has 340 to 800 ppm, but all other metals have similar concentrations and As is depleted in the core similar to pyrite in the other lower grade vein and from Doyon. Progressing outwards in pyrite to the highly sieved domains, metals concentrations (Au-Ag-Te-Se-Bi-Pb) are consistently higher than the clean core, however some analyses have been contaminated by Au-Ag-tellurides (Fig. 4.16D). Along with the increase in metal concentrations is an increase of ~0.5‰ in $\delta^{34}S$ (~2.33 ± 0.36‰) and a decrease of ~30°C (~295° ± 42°C) in temperature relative to the core (Fig. 4.16F). A decrease of ~30°C only results in an increase in $\delta^{34}S$ of ~0.1‰ (Ohmoto and Rye, 1979) and therefore cannot be the sole process operating to cause the shift in $\delta^{34}S$ between the clean core and highly sieved rim. As previously described, an increase in $\delta^{34}S$ can be achieved through a reduction in the fO_2 of the hydrothermal fluid, which could be induced by wall-rock sulfidation (Neall and Phillips, 1987).

For the high-grade vein at Grand Duc, individual pyrite grains show similar $\delta^{34}S$ composition between core and rim, but importantly, other grains record a drop in $\delta^{34}S$ from core to the rim (Fig. 4.14D). For example, in the quartz-carbonate vein a pyrite grain records $\delta^{34}S$ values of 2.43‰ in the core and between 1.36 and 1.98‰ along the rim. Pyrite in the chlorite alteration halo also records a decrease in $\delta^{34}S$ from core (2.14 to 2.20‰) to rim (1.54 to 1.79‰). In grains that record the ~0.5‰ decrease along the rim, they also record 20° to 75°C lower temperatures (increasing Se contents) along with increasing concentrations of As-Te-Pb-Bi-Ag±Cu (Fig. 4.14C, D). The concentration of Au is variable between individual grains and shows either an increase or decrease from core to rim, the same is true for Co concentrations (Fig. 4.14A, B). In the mapped pyrite grain (Fig. 4.9C-K), the outer rim records an increase in a wide variety of elements Au-Ag-Te-Bi-Sb-Se-Cu-Zn-Pb-Sn-In-Cd along with a drop in temperature of ~50°C relative to the core. As with pyrite from Doyon and the lower-grade Grand Duc veins, a drop in temperature cannot explain the decrease in $\delta^{34}S$ as that would shift $\delta^{34}S$ to heavier compositions. Therefore, other

processes must have occurred that have a greater opposing effect on $\delta^{34}S$ compared to a decrease in temperature.

One possible mechanism to cause the decrease in $\delta^{34}S$ and increasing concentrations of select metals along the pyrite rim is fluid boiling or phase separation (McKibben and Eldridge, 1990; Röman et al., 2018; Schaarschmidt et al., 2021). As explained above, during fluid boiling, H_2 is lost to the vapor phase and causes aqueous H_2S to oxidize to SO_4^{2-}, which preferentially partitions ^{34}S, leaving the aqueous H_2S depleted in ^{34}S and subsequently forming pyrite recording lower $\delta^{34}S$ composition than pyrite formed pre-boiling (McKibben and Eldridge, 1990). Additionally, pyrite precipitated due to fluid boiling is commonly characterized by relatively higher concentrations of As-Cu-Pb-Ag-Au with lower Co and Ni contents and is commonly porous (i.e., sieved textured) with inclusions of other sulfides (e.g., chalcopyrite; Román et al., 2018). Combining the elemental associations, sieved texture, and sulfide inclusions are all characteristic of the pyrite rims in the high-grade Grand Duc vein, combined with the lower $\delta^{34}S$, this would suggest fluid boiling played a role during pyrite formation.

4.6.6 Impact of Consequences of Metamorphism on Sulfide Preservation

Geochemical, isotopic, and microstructural studies have investigated the influence of regional metamorphism and the retention of trace element compositional patterns in pyrite from a wide variety of gold deposits that have experienced varying degrees of regional metamorphism (Au-rich VMS, Pilote et al., 2020, Yergeau et al., 2022b; Orogenic Au, Large et al., 2009, Steadman and Large, 2016, Kresse et al., 2018, Gregory et al., 2019, Large and Maslennikov, 2020, Liu et al., 2021; IOCG, Steadman et al., 2021, King et al., 2024). However, the impact metamorphism has on the trace element content of pyrite depends on metamorphic grade and notably at conditions above mid-greenschists facies, the trace element content of pyrite can be significantly modified

(Gregory et al., 2019). However, many deposits where multiple generations of pyrite have been recognized argue for the preservation of chemically and/or isotopically distinct pyrite generations that preserve pyrite of different origins and importantly the preservation of non-metamorphic pyrite zones (mainly in the core of pyrite; Large et al., 2007, 2009, Steadman and Large, 2016, Kresse et al., 2018, Pilote et al., 2020, Liu et al., 2021). In the Doyon-Bousquet-LaRone mining camp regional metamorphism ranges from mid-greenschist to lower amphibolite facies (Tourigny et al., 1989; Marquis et al., 1990b; Dubé et al., 2007; Mercier-Langevin, 2005; Yergeau et al., 2022a) and the impact of this metamorphism on pyrite trace element and isotopic compositions in the Doyon and Grand Duc deposits must be considered.

Pyrite from the Doyon deposit and the lower-grade veins from the Grand Duc deposit display similar textures with a porous region in the central portion of the grain and a non-porous rim (e.g., Figs. 4.7B and 4.10B). Within the porous region, common composite inclusion of gold + petzite ± calaverite are present. Temperatures recorded by pyrite from both deposits are near (~490°C) or lower (~400°C) than peak metamorphic conditions (450° to 500°C) whereas the maximum temperature provided by telluride inclusions (~300°C; Cabri, 1965) may represent lower end of metamorphism. In addition to gold occurring in porous regions of pyrite, it also occurs along fractures and grain boundaries of sulfides and gangues minerals in both the Doyon deposit (Fig. 4f, g) and the lower-grade veins from the Grand Duc deposit (Fig. 4.3K). In terms of trace metal contents in pyrite, both systems show a depletion in Au in pyrite itself and only display elevated Au in regions where gold inclusions occur (e.g., Figs. 4.7G and 4.10G). Other ore metals such as Ag (not shown in figures) and Te (Fig. 4.7H and 4.10H) are also depleted outside of Au-Ag-Te-rich areas, The combination of these observations would suggest that pyrite in the Doyon deposit and the lower-grade veins from the Grand Duc deposit was modified during regional metamorphism and Au and other ore metals were remobilized from the pyrite structure and resulted

in the precipitation of gold and Au-Ag-Te grains. Additionally, the $\delta^{34}S$ composition of pyrrhotite inclusions in pyrite ranges from 1.03 to 1.18‰. Based on the association of pyrrhotite with Au-Ag-tellurides inclusions, which have a maximum temperature stability of 304° ± 10°C (Cabri, 1965), any pyrite in equilibrium with pyrrhotite would have $\delta^{34}S$ compositions between 1.93 and 2.08‰ (Ohmoto and Rye, 1979). However, the $\delta^{34}S$ composition of pyrite are inconsistent with the constraints from pyrrhotite and tellurides, suggesting that ore mineral precipitation (and pyrrhotite) likely occurred in response to metal remobilization during regional metamorphism. Although the trace element and ore mineral characteristics have been influenced by regional metamorphism, the sulfur isotope compositions and patterns have retained their magmatic signature as $\Delta^{33}S$ is consistent within and between individual pyrite grains, representing a singular sulfur source and with no evidence of a sedimentary $\Delta^{33}S$ signal present. Therefore, the increase in $\delta^{34}S$ seen in pyrite likely reflects a reducing fluid event related to wall-rock sulfidation and is a viable gold precipitation mechanism for the Doyon deposit and the lower-grade veins from the Grand Duc deposit.

In the high-grade vein from the Grand Duc deposit, the influence of metamorphism on pyrite is not as clear. As shown in the pyrite trace element map in Figure 4.9, there is a significant change in dissolved trace element chemistry in the pyrite rim with enrichments in numerous epithermal-related elements (i.e., Au-Ag-As-Te-Bi-Sb-Se) and are not related to accessory mineral inclusions. Doyon and the lower-grade Grand Duc pyrite lack these metal enrichments in the rims. Additionally, the $\delta^{34}S$ composition systematically decreases from the core to rim in pyrite in this high-grade vein with $\Delta^{33}S$ remaining constant, thereby ruling out non-magmatic sulfur sources (Fig. 4.17D). Coinciding with the drop in $\delta^{34}S$ is an enrichment in epithermal-related elements along the rims, suggests pyrite preserves a primary magmatic-hydrothermal fluid boiling event related to gold deposition. This sulfur isotope behaviour is in contrast to Doyon and the lower-

grade Grand Duc pyrite. Although pyrite records a fluid boiling event, it should be noted that pyrrhotite and other base metal sulfides occur post-pyrite and pre- to syn-gold (Fig. 4.5B and C) as well as gold and tellurobismuthite occurring synchronous with chlorite alteration. Based on the $\delta^{34}S$ composition (1.36 to 1.98‰) and temperature (295° to 330°C) of pyrite rims, if pyrrhotite and pyrite were in equilibrium, pyrrhotite should have $\delta^{34}S$ between 0.46 and 1.08‰, which is lower than the true $\delta^{34}S$ composition of pyrrhotite (0.86 to 1.50‰). Furthermore, chlorite is intimately intergrown with gold and tellurides in the chlorite-rich alteration and chlorite is coeval with base metals and gold in the quartz carbonate vein. Utilizing the temperature obtained from chlorite thermometry (~405°C) and the $\delta^{34}S$ composition of pyrrhotite, if pyrite was isotopic equilibrium with pyrrhotite, pyrite would have $\delta^{34}S$ between 1.56 and 2.20‰, which is similar to, but slightly higher than the true rim composition of pyrite. Aside from isotopic constraints, it is clear from textural relationships that pyrrhotite and gold were deposited post-pyrite and therefore gold and tellurides were likely a result of Au remobilization during regional metamorphism.

4.7 CONCLUSIONS

In this study we have combined $\Delta^{33}S$, $\delta^{34}S$, and trace element systematics in multi-stage pyrite to document the history of two Archean intrusion-hosted Au deposits in the Abitibi greenstone belt. Evidence is presented that confirms a magmatic source of sulfur and metals potentially related to the magmatic system that generated the MIC and coeval volcanic assemblages. The $\Delta^{33}S$ signature of pyrite falls within error of the MDF field indicating a magmatic source of sulfur for the Doyon and Grand Duc deposits. The trace metal characteristics and $\delta^{34}S$ composition of pyrite from the high-grade Grand Duc vein are consistent with an epithermal fluid signature (Au-Ag-As-Te-Bi-Sb-Se) related to a rare example of preserved epithermal boiling in

Archean terranes. In contrast to the high-grade Grand Duc vein, mineralization at Doyon and the lower-grade Grand Duc veins regional metamorphism has impacted the pyrite trace metal chemistry (e.g., through leaching of Au-Ag-Te to precipitate secondary ore mineral assemblages), but primary As zoning in pyrite is preserved and is directly related to an increase in $\delta^{34}S$, linked to wall-rock sulfidation. Thus, even though these deposits have been variably modified during regional metamorphism, the combination of methods applied here can discriminate primary magmatic-hydrothermal processes responsible for the development of these Au-rich deposits, linking them to causative magmatism. Future work should apply these methods more broadly across greenstone belts where cryptic magmatic-hydrothermal processes and contributions to Au-rich systems not completely obscured by metamorphism have been overlooked.

4.8 ACKNOWLEDGEMENTS

Financial support for this project came from the Targeted Geoscience Initiative program of the Geological Survey of Canada. The authors thank Y. Liu (University of Toronto), R. Sharpe (University of Manitoba) and B. Boucher (University of New Brunswick) for their valuable contribution to EMPA, SIMS, and LA-ICP-MS analysis of pyrite. Alan Galley and David Yergeau provided valuable assistance in the field during sample collection and discussions about the regional and local geology. The authors are grateful to the geology departments and staff at the Westwood (Iamgold Corporation) and LaRonde Penna (Agnico Eagle Mines Ltd) mines for access to drill core and tours of the properties. K. Neyedley acknowledges scholarship support from the Natural Sciences and Engineering Research Council of Canada and the Nova Scotia Research & Innovation Graduate Scholarship program.

4.9 REFERENCES

Barton, P. B., Jr., and Skinner, B. J., 1979, Sulfide mineral stabilities, in Barnes, H. L., ed., Geochemistry of hydrothermal ore deposits: New York, Wiley Intersci., p. 278-403.

Belkabir, A., and Hubert, C., 1995, Geology and structure of a sulfide-rich gold deposit: an example from the Mouska gold mine, Bousquet district, Canada: Economic Geology, v. 90, p. 1064-1079.

Börner, F., Keith, M., Bücker, J.L., Voudouris, P., Klemd, R., Haase, K., Kutzschbach, and Schiperski, F., 2022, In-situ trace element and S isotope systematics in pyrite from three porphyry-epithermal prospects, Limnos Island, Greece: Frontiers in Earth Science, 10:916107, doi: 10.3389/feart.2022.916107.

Boucher, M.B., Robb, S.J., Hanley, J.J., Kerr, M.J., and Mungall, J.E., 2023, Platinum-group elements (PGE) in the New Afton alkalic Cu-Au porphyry deposit, Canadian Cordillera, I: Relationships between PGE, accessory metals and sulfur isotopes in pyrite: Frontiers in Earth Science: https://doi.org/10.3389/feart.2023.819129

Cabri, L. J., 1965, Phase relations in the Au-Ag-Te system and their mineralogical significance: Economic Geology, v. 60, p.1569-1606.

Cathelineau, M., 1988, Cation site occupancy in chlorites and illites as a function of temperature: Clay Minerals, v. 23, p. 471-485.

Crowe, D.E., and Vaughn, R.G., 1996, Characterization and use of isotopically homogeneous standards for in situ laser microprobe analysis of 34S/32S ratios: American Mineralogist, v. 81, p. 187-193.

Davis, D.W., 2002, U-Pb geochronology of Archean metasedimentary rocks in the Pontiac and Abitibi subprovinces, Quebec, constraints on timing, provenance, and regional tectonics: Precambrian Research, v. 115, p. 97−117.

Ding, T., Valkiers, S., Kipphardt, H., De Bièvre, P., Taylor, P. D. P., Gonfiantini, R., and Krouse, R., 2001, Calibrated sulfur isotope abundance ratios of three IAEA sulfur isotope reference materials and V-CDT with a reassessment of the atomic weight of sulfur: Geochimica et Cosmochimica Acta, v. 65, p, 2433–2437.

Dubé, B., Mercier-Langevin, P., Hannington, M.D., Davis, D.W., and Lafrance, B., 2004, Le gisement de sulfures massifs volcanogènes aurifères LaRonde, Abitibi, Québec: Altération, minéralisations, genèse et implications pour l'exploration: Ministère des Ressources naturelles, de la Faune et des Parcs, Québec Report MB 2004-03, 112 p.

Dubé, B., Mercier-Langevin, P., Hannington, M.D., Lafrance, B., Gosselin, G., and Gosselin, P., 2007, The LaRonde Penna world-class Au-rich volcanogenic massive sulfide deposit, Abitibi, Québec: Mineralogy and Geochemistry of alteration and implications for genesis and exploration: Economic Geology, v. 102, p. 633-666.

Dubé, B., and Mercier-Langevin, P., 2020, Gold deposits of the Archean Abitibi greenstone belt, Canada: Society of Economic Geologists Special Publication 23, p. 669-708.

Farquhar, J., Wing, B.A., 2003, Multiple sulfur isotopes and the evolution of the atmosphere: Earth and Planetary Science Letters, v. 213, p. 1-13.

Farquhar, J., Bao, H., and Thiemens, M.H., 2000, Atmospheric influence of Earth's earliest sulfur Cycle: Science, v. 28, p. 756–758.

Farquhar, J., Wu, N., Canfield, D., and Oduro, H., 2010, Connections between sulfur cycle evolution, sulfur isotopes, sediments, and base metal sulfide deposits: Economic Geology, v. 105, p. 509–533.

Fillion, M., Vallee, M., and Lavoie, C., 1977, Les gisements d'or de la SOQUEM Silverstack, Canton Bousquet, Quebec: CIM Bulletin, v. 70, p. 159−172.

Galley, A.G., and Lafrance, B., 2007, Évolution et métallogénie du pluton de Mooshla: Ministère des Ressources naturelles et de la Faune, ET 2007-02, 31 p.

Galley, A.G., and Lafrance, B., 2014, Setting and evolution of the Archean synvolcanic Mooshla Intrusive Complex, Doyon-Bousquet-LaRonde mining camp, Abitibi greenstone belt: emplacement history, petrogenesis, and implications for Au metallogenesis: Economic Geology, v. 109, p. 205-229.

Galley, A.G., and Mercier-Langevin, P., 2024, Mineralization and alteration at the Doyon deposit, Doyon-Bousquet-LaRonde mining camp, Québec, Canada: Example of an Archean subsea-floor Au(-Cu) porphyry-epithermal-style system: Geological Survey of Canada, Open File xxxx, xx p. In prep.

Gosselin, G., 1998, Veines de quartz aurifères précoces à la zone ouest de la mine Doyon, canton de Bousquet, Preissac, Abitibi: M.Sc. thesis, Université du Québec à Chicoutimi, 125 p.

Gregory, D.D., Cracknell, M.J., Large, R.R., McGoldrick, P., Kuhn, S., Maslennikov, V.V., Baker, M.J., Fox, N., Belousov, I., Figueroa, M.C., Steadman, J.A., Fabris, A.J., and Lyons, T.W., 2019, Distinguishing Ore Deposit Type and Barren Sedimentary Pyrite Using Laser Ablation-Inductively Coupled Plasma-Mass Spectrometry Trace Element Data and Statistical Analysis of Large Data Sets: Economic Geology, v. 114, p. 771-786.

Grundler, P.V., Brugger, J., Etschmann, B.E., Helm, L., Liu, W., Spry, P.G., Tian, Y., Testemale, D., and Pring, A., 2013, Speciation of aqueous tellurium(IV) in hydrothermal solutions and vapors, and the role of oxidized tellurium species in Te transport and gold deposition: Geochimica et Cosmochimica Acta, v.120, p. 298-325.

Guha, J., Gauthier, A., Vallée, M., Descarreaux, J., and Lange-Brard, F., 1982, Gold mineralization at the Doyon mine (Silverstack), Bousquet, Quebec, in Hodder, R.W., and Petruk, W., eds., Geology of Canadian Gold Deposits: Canadian Institute of Mining and Metallurgy, Special Volume 24, p. 50-57.

Gunning, H.C., 1941, Region de Bousquet-Joannes, Quebec: Geological Survey of Canada Memoir 206, 80 p.

Hastie, E.C.G., Kontak, D.J., and Lafrance, B., 2020, Gold Remobilization: Insights from Gold Deposits in the Archean Swayze Greenstone Belt, Abitibi Subprovince, Canada: Economic Geology, v. 115, p. 241-277.

Holliger, P., and Cathelineau, M., 1988, In situ U-Pb age determination by secondary ion mass spectrometry: Chemical Geology, v. 70, p. 173.

Keith, M., Smith, D.J., Jenkin, G.R.T., Holwell, D.A., and Dye, M.D., 2018, A review of Te and Se systematics in hydrothermal pyrite from precious metal deposits: Insights into ore-forming processes: Ore Geology Reviews, v. 269-282.

King, S.A., Cook, N.J., Ciobanu, C.L., Ehrig, K., Campo Rodriguez, Y.T., Basak, A., and Gilbert, S., 2024, Coupled Microstructural EBSD and LA-ICP-MS Trace Element Mapping of Pyrite Constrains the Deformation History of Breccia-Hosted IOCG Ore Systems: Minerals, v. 14, https://doi.org/10.3390/min14020198.

Kresse, C., Lobato, L.M., Hagemann, S.G., Figueiredo e Silva, R.C., 2018, Sulfur isotope and metal variations in sulfides in the BIF-hosted orogenic Cuiabá gold deposit, Brazil: Implications for the hydrothermal fluid evolution: Ore Geology Reviews, v. 98, p. 1-27.

LaFlamme, C., Jamieson, J.W., Fiorentini, M.L., Thébaud, N., Caruso, S., and Selvaraja, V., 2018a, Investigating sulfur pathways through the lithosphere by tracing mass independent fractionation of sulfur to the Lady Bountiful orogenic gold deposit, Yilgarn Craton: Gondwana Research, v. 58, p. 27-38.

LaFlamme, C., Sugiono, D., Thébaud, N., Caruso, S., Fiorentini, M., Selvaraja, V., Jeon, H., Voute, F., and Martin, L., 2018b, Multiple sulfur isotopes monitor fluid evolution of an Archean orogenic gold deposit: Geochimica et Cosmochimica Acta, v. 222, p. 436-446.

Lafrance, B., Moorhead, J., and Davis, D.W., 2003, Cadre géologique du camp minier de Doyon-Bousquet-LaRonde: Ministère des Ressources naturelles, de la Faune et des Parcs, Québec Reports ET 2002-07, 45 p., and ET 2002-07 C001 1:20,000 map sheet.

Lafrance, B., Davis, D.W., Goutier, J., Moorhead, J., Pilote, P., Mercier-Langevin, P., Dubé, B., and Galley, A., 2005, Nouvelles datations isotopiques dans la portion québecoise du Groupe de Blake River et des unités adjacentes: Ministère des Ressources naturelles et de la Faune, Québec Report RP 2005-01, 26 p.

Lang, J.R., and Baker, T., 2001, Intrusion-related gold systems: the present level of understanding: Mineralium Deposita, v. 36, p. 477-489.

Langshur, A., 1990, The geology, geochemistry and structure of the Mooshla intrusion, Bousquet mining centre, Quebec: Unpublished M.Sc. thesis, Ottawa, Canada, University of Ottawa, 172 p.

Large, R.R., and Maslennikov, V.V., 2020, Invisible Gold Paragenesis and Geochemistry in Pyrite from Orogenic and Sediment-Hosted Gold Deposits: Minerals, v. 10, doi:10.3390/min10040339.

Large, R.R., Maslennikov, V.V., Robert, F., Danyushevsky, L.V., and Chang, Z., 2007, Multistage Sedimentary and Metamorphic Origin of Pyrite and Gold in the Giant Sukhoi Log Deposit, Lena Gold Province, Russia: Economic Geology, v. 102, p. 1233-1267.

Large, R.R., Danyushevsky, L., Hollit, C., Maslennikov, V., Meffre, S., Gilbert, S., Bull, S., Scott, R., Emsbo, P., Thomas, H., Singh, B., and Foster, J., 2009, Gold and Trace Element Zonation in Pyrite Using a Laser Imaging Technique: Implications for the Timing of Gold in Orogenic and Carlin-Style Sediment-Hosted Deposits: Economic Geology, v. 104, p. 635-668.

Liu, L., Ireland, T.R., Holden, P., Ávila, J., Vasconcelos, P., and Mavrogenes, J., 2021, Sources of auriferous fluids associated with a Neoarchean BIF-hosted orogenic gold deposit revealed by the multiple sulfur isotopic compositions of zoned pyrites: Contributions to Mineralogy and Petrology, v. 176, https://doi.org/10.1007/s00410-021-01788-3.

Marquis, P., Hubert, Brown, A.C., and Rigg, D.M., 1990a, An evaluation of genetic models for gold deposits of the Bousquet district, Quebec, based on their mineralogical, geochemical and structural characteristics: Canadian Institute of Mining and Metallurgy Special volume 24, p. 383−399.

Marquis, P., Hubert, C., Brown, A.C., and Rigg, D.M., 1990b, Overprinting of early, redistributed Fe and Pb-Zn mineralization by late-stage Au-Ag-Cu deposition at the Dumagami mine, Bousquet district, Abitibi, Québec: Canadian Journal of Earth Sciences, v. 27, p. 1651–1671.

McFarlane, C., Luo, Y., 2012. U–Pb geochronology using 193 nm excimer LA–ICP-MS optimized for in situ accessory mineral dating in thin section. Geoscience Can. 39, 158–172.

McKibben, M.A., and Eldridge, C.S., 1990, Radical sulfur isotope zonation of pyrite accompanying boiling and epithermal gold deposition: a SHRIMP study of the Valles Caldera, New Mexico: Economic Geology, v. 85, p. 1917-1925.

McNicoll, V., Goutier, J., Dubé, B., Mercier-Langevin, P., Ross, P-S., Dion, C., Monecke, T., Legault, M., Percival, J., and Gibson, H., 2014, U-Pb geochronology of the Blake River Group, Abitibi greenstone belt, Quebec, and implications for base metal exploration: Economic Geology, v. 109, p. 27–59.

Mercier-Langevin, P., 2005, Géologie du gisement de sulfures massifs volcanogènes aurifères LaRonde, Abitibi, Québec: Unpublished Ph.D. thesis, Quebec, Canada, Institut National de la Recherche Scientifique, Centre Eau, Terre et Environnement, 689 p.

Mercier-Langevin, P., Dubé, B., Hannington, M.D., Davis, D.W., Lafrance, B., 2004, Contexte geologique et structural des sulfures massifs volcanogenes auriferes du Gisement LaRonde,

Abitibi: Ministere des Ressources naturelles, de la Faune et des Parcs, Quebec, Report ET 2003-03, 47 p.

Mercier-Langevin, P., Dubé, B., Hannington, M.D., Davis, D.W., Lafrance, B., and Gosselin, G., 2007a, The LaRonde Penna Au-rich volcanogenic massive sulfide deposit, Abitibi greenstone belt, Quebec: Part 1. Geology and geochronology: Economic Geology, v. 102, p. 585−609.

Mercier-Langevin, P., Dubé, B., Hannington, M.D., Richer-Laflèche, M., and Gosselin G., 2007b, The LaRonde Penna Au-rich volcanogenic massive sulfide deposit, Abitibi greenstone belt, Quebec: Part 2. Lithogeochemistry and paleotectonic setting: Economic Geology, v. 102, p. 611−631.

Mercier-Langevin, P., Dubé, B., Lafrance, B., Hannington, M., Galley, A., Moorhead, J., and Gosselin, P., 2007c, Metallogeny of the Doyon-Bousquet-LaRonde mining camp, Abitibi greenstone belt, Quebec: Geological Association of Canada, Mineral Deposits Division, Special Publication 5, p. 673−701.

Mercier-Langevin, P., Wright-Holfeld, A., Dubé, B., Bernier, C., Houle, N., Savoie, A., and Simard, P., 2009, Stratigraphic setting of the Westwood-Warrenmac ore zones, Westwood project, Doyon-Bousquet-LaRonde mining camp, Abitibi, Quebec: Geological Survey of Canada Current Research Paper 2009-03, 20 p.

Mercier-Langevin, P., Goutier, J., Ross, P.-S., McNicoll, V., Monecke, T., Dion, C., Dubé, B., Thurston, P., Becu, V., Gibson, H., Hannington, M., and Galley, A., 2011, The Blake River Group

of the Abitibi greenstone belt and its unique VMS and gold-rich VMS endowment: Geological Survey of Canada Open File Report 6869, 61 p.

Mercier-Langevin, P., Dubé, B., Blanchet, F., Pitre, D., and Laberge, A., 2017, The LaRonde Penna Au-rich volcanic-hosted massive sulfide deposit: Reviews in Economic Geology, v. 19, p. 225−245.

Neall, F.B., and Phillips, G.N., 1987, Fluid-wall rock interaction in an Archean hydrothermal gold deposit: a thermodynamic model for the Hunt Mine, Kambalda: Economic Geology, v. 82, p. 1679-1694.

Neumayr, P., Walshe, J., Hagemann, S., Petersen, K., Roache, A., Frikken, P., Horn, L., and Halley, S., 2008, Oxidized and reduced mineral assemblages in greenstone belt rocks of the St. Ives gold camp, Western Australia: vectors to high-grade ore bodies in Archaean gold deposits?: Mineralium Deposita, v. 43, p. 363-371.

Neyedley, K., Hanley, J.,J., Mercier-Langevin, P., Crowley, J. L., Tsay, A., Zajacz, Z., Fayek, M., and Sharpe, R., 2024a, Constraints on the origin and metal fertility of the Archean Mooshla Intrusive Complex (MIC), Doyon-Bousquet-LaRonde mining district, Abitibi greenstone belt, Québec, Canada: Part I: Accessory mineral composition, thermobarometry, and geochronology: Journal of Petrology, accepted January 2024.

Neyedley, K., Mercier-Langevin, P., Tsay, A., Zajacz, Z., Fayek, M., Crowley, J. L., and Hanley, J. J., 2024b, Constraints on the origin and metal fertility of the Mooshla Intrusive Complex (MIC),

Doyon-Bousquet-LaRonde mining district, Abitibi greenstone belt, Quebec, Canada, II: Silicate melt inclusions in magmatic zircon and quartz: Journal of Petrology, in prep, June 2024.

Ohmoto, H., and Rye, R.O., 1979, Isotopes of sulfur and carbon: *In* Geochemistry of Hydrothermal Ore Deposits. Barnes HL (ed) J Wiley and Sons, p. 509-567.

Peterson, E.C., and Mavrogenes, J.A., 2014, Linking high-grade gold mineralization to earthquake-induced fault-valve processes in the Porgera gold deposit, Papua New Guinea: Geology, v. 42, p. 383-386.

Pilote, J-L., Mercier-Langevin, P., Jackson, S.E., Dubé, B., Yang, Z., Lawley, C.J.M., Petts, D.C., Layne, G.D., and Piercey, S.J., 2020, Interrogating the composition and genesis of argillite-hosted pyrite nodules at the LaRonde Penna gold-rich volcanogenic massive sulphide deposit, Abitibi, Quebec: Insights into metallogenic implications: in Targeted Geoscience Initiative 5: Contributions to the Understanding of Canadian Gold Systems, (ed.) P. Mercier-Langevin, C.J.M. Lawley, and S. Castonguay; Geological Survey of Canada, Open File 8712, p. 75–91. https://doi.org/10.4095/323666

Reich, M., Kesler, S.E., Utsunomiya, S., Palenik, C.S., Chyssoulis, S.L., and Ewing, R.C., 2005, Solubility of gold in arsenian pyrite: Geochimica et Cosmochimica Acta, v. 69, p. 2781-2796.

Riciputi, L.R., Paterson, B.A., and Ripperdan, R.L., 1998, Measurement of light stable isotope ratios by SIMS: Matrix effects for oxygen, carbon, and sulfur isotopes in minerals: International Journal of Mass Spectrometry, v. 178, p. 81–112.

Román, N., Reich, M., Leisen, M., Morata, D., Barra, F., and Deditius, A.P., 2019, Geochemical and micro-textural fingerprints of boiling in pyrite: Geochimica et Cosmochimica Acta, v. 246, p. 60-85.

Savoie, A., Trudel, P., Sauve, P., Hoy, L., and Lao, K., 1991, Geologie de la mine Doyon (region de Cadillac): Ministere de l'Energie et des Ressources, Quebec, Report ET 90-05, 80 p.

Schaarschmidt, A., Haase, K.M Klemd, R., Keith, M., Voudouris, P.C., Alfieris, D., Strauss, H., and Wiedenbeck, M., 2021, Boiling effects on trace element and sulfur isotope compositions of sulfides in shallow-marine hydrothermal systems: evidence from Milos Island, Greece: Chemical Geology, v. 583, 120457. https://doi.org/10.1016/j.chemgeo.2021.120457.

Sharman, E.R., 2011, Application of multiple sulfur isotope analysis to Archean ore-forming processes: Unpublished Ph.D. thesis, Montreal, Canada, McGill University, 196 p.

Sharman, E. R., Taylor, B.E., Minarik, W.G., Dubé, B., Wing, B.A., 2015, Sulfur isotope and trace element data from ore sulfides in the Noranda district (Abitibi, Canada): implications for volcanogenic massive sulfide deposit genesis: Mineralium Deposita, v. 50, p. 591-606.

Shunk, F. A., 1969, Constitution of binary alloys: New York, MacGraw-Hill, 720 p.

Steadman, J.A., and Large, R.R., 2016, Synsedimentary, Diagenetic, and Metamorphic Pyrite, Pyrrhotite, and Marcasite at the Homestake BIF-Hosted Gold Deposit, South Dakota, USA:

Insights on Au-As Ore Genesis from Textural and LA-ICP-MS Trace Element Studies: Economic Geology, v. 111, p. 1731-1752.

Steadman, J.A., Large, R.R., Olin, P.H., Danyushevsky, L.V., Meffre, S., Huston, D., Fabris, A., Lisitsin, V., and Wells, T., 2021, Pyrite trace element behavior in magmatic-hydrothermal environments: An LA-ICPMS imaging study: Ore Geology Reviews, v. 128, https://doi.org/10.1016/j.oregeorev.2020.103878.

Stone, W.E., 1990, Archean volcanism and sedimentation in the Bousquet gold district, Abitibi greenstone belt, Quebec: implications for stratigraphy and gold concentration: Geological Society of America Bulletin, v. 102, p. 147-158.

Tanner, D., Henley, R.W., Mavrogenes, J.A., and Holden, P., 2016, Sulfur isotope and trace element systematics of zoned pyrite crystals form the el Indio Au-Cu-Ag deposit, Chile: Contributions to Mineralogy and Petrology, v. 171, https://doi.org/10.1007/s00410-016-1248-6.

Thompson, J.F.H., Sillitoe, R.H., Bakr, T., Lang, J.R., and Mortensen, J.K., 1999, Intrusion-related gold deposits associated with tungsten-tin provinces: Mineralium Deposita, v. 34, p. 323-334.

Trudel, P., Sauve, P., Tourigny, G., Hubert, C., and Hoy, L., 1992, Synthèse des caractéristiques géologiques des gisements de la région de Cadillac (Abitibi): Ministère des Ressources naturelles, Québec, Report MM 91-01, 106 p.

Tourigny, G., Hubert, C., Brown, A.C., and Crépeau, R., 1989, Structural control of gold mineralization at the Bousquet mine, Abitibi, Québec: Canadian Journal of Earth Sciences, v. 26, p. 157–175.

Valiant, R.I., and Hutchinson, R.W., 1982, Stratigraphic distribution and genesis of gold deposits, Bousquet region, northwestern Quebec: Canadian Institute of Mining and Metallurgy Special Volume 24 p. 27−40.

Voute, F., Hagemann, S.G., Evans, N.J., and Villanes, C., 2019, Sulfur isotopes, trace elements, and textural analyses of pyrite, arsenopyrite and base metal sulfides associated with gold mineralization in the Pataz-Parcoy district, Peru: implication for paragenesis, fluid source, and gold deposition mechanisms: Mineralium Deposita, v. 54, p. 1077-1100.

Ward, J., Mavrogenes, J., Murray, A., and Holden, P., 2017, Trace element and sulfur isotopic evidence for redox changes during formation of the Wallaby Gold Deposit, Western Australia: Ore Geology Reviews, v. 82, p. 31-48.

Wilson S.A., Ridley W.I. and Koenig A.E., 2002, Development of sulfide calibration standards for the laser ablation inductively coupled plasma-mass spectrometry technique: Journal of Analytical and Atomic Spectrometry, v. 17, p. 406–409.

Yergeau, D., Mercier-Langevin, P.L., Dubé, B., Malo, M., and Savoie, A., 2022a, The Westwood Deposit, Southern Abitibi Greenstone Belt, Canada: An Archean Au-Rich Polymetallic Magmatic-

Hydrothermal System—Part I. Volcanic Architecture, Deformation, and Metamorphism: Economic Geology, v. 117, p. 545-575.

Yergeau, D., Mercier-Langevin, P.L., Dubé, B., McNicoll, V., Jackson, S.E., Malo, M., and Savoie, A., 2022b, The Westwood Deposit, Southern Abitibi Greenstone Belt, Canada: An Archean Au-Rich Polymetallic Magmatic-Hydrothermal System—Part II. Hydrothermal Alteration, Mineralization, and Geologic Model: Economic Geology, v. 117, p. 577-608.

4.10 TABLES

Table 4.1. Bulk rock geochemistry for mineralized samples from Grand Duc and Doyon West Zone

Sample #	18KN03	18KN07	18KN08	18KN09	18KN11	18KN05	18KN06	
Deposit	Grand Duc	Grand Duc	Grand Duc	Grand Duc	Grand Duc	Doyon	Doyon	
UTM E*	682104	682393	682393	682393	682410	683248	683248	
UTM N*	5347929	5347984	5347984	5347984	5347974	5347798	5347798	
DDH	SGD045-16	SGD011-15	SGD011-15	SGD011-15	SGD025-15	NA	NA	
Depth (m)	395.8	12.3	18.9	21.4	12	NA	NA	Detection Limit
Au[1] (g/t)	297.88					30.45	23.80	0.47
Ag	46.67					23.34	2.92	2.92
Au[2] (ppm)	>100	5.928	0.885	3.936	1.578	37.433	32.258	0.002
Ag	40.87	2.21	0.54	1.65	0.77	38.56	21.05	0.2
As	13	3.5	3.9	3.3	4.6	107.2	34.2	0.7
Bi	596.16	1.72	0.36	2.51	0.76	1.03	2.55	0.02
Cd	1.4	0.07	0.07	0.04	0.05	0.13	0.14	0.02
Co	97.6	34.6	13.8	29.9	22.5	4.2	7.6	0.03
Cu	16840[a]	217	174	126	116	335	807	0.6
In	3.74	0.084	0.033	0.04	0.048	0.692	1.172	0.002
Mo	1.44	0.71	0.78	0.53	0.76	1.55	0.86	0.06
Pb	85.3	5.5	3.1	6.5	6.6	1.6	2.3	0.2
Sb	0.47	0.06	0.08	0.06	0.05	0.05	0.02	0.009
Se	9	2.1	1.1	3.5	1.2	4.6	9.1	0.2
Sn	2.8	0.3	0.6	0.3	0.4	1.6	4.4	0.06
Te	>40	3.13	0.98	4.74	1.91	24.64	29.4	0.02
Tl	0.054	0.015	0.01	0.013	0.013	0.008	0.01	0.0006
Zn	354	9	18	16	10	12	2	2

[1] = Gravimetric Fire Assay; [2] = ICP-MS; [a] = AAS: Atomic Absorption Flame; * UTM zone 17N

Table 4.2: Representative SEM-EDS analyses of ore minerals from the Doyon deposit

Texture	Mineral	Au (at. %)	Ag	Te	Pb
Composite inclusion in Py	Gold	88.8	11.2		
	Ptz	16.4	50.5	33.1	
	Clv	35.6		64.4	
Composite inclusion in Py	Gold	88.5	11.5		
	Ptz	17.5	49.7	32.8	
Composite inclusion in Py	Gold	79.9	19.1		
	Ptz	17.7	49.9	32.5	
	Alt			52.3	47.7
Py fracture	Gold	88.8	11.2		
Py fracture	Gold	87.9	12.1		
Py-qtz boundary	Gold	88.2	11.8		
Inclusion in Py	Gold	82.1	17.9		
Qtz fracture	Gold	82.4	17.6		
Inclusion in Ccp	Gold	82.2	17.8		
Composite inclusion in Py	Ptz	17.4	50.3	32.3	
	Clv	33.4		66.6	
Composite inclusion in Py	Ptz	12.6	53.7	33.7	
	Hs		62.4	37.6	
Composite inclusion in Py	Ptz	17.6	49.4	33	
	Hs		61.8	38.2	
Inclusion in Py	Ptz	17.7	49.5	17.8	
Inclusion in Qtz	Ptz	16.9	50.5	32.6	
Py grain boundary	Ptz	10.3	53.5	36.2	
Composite inclusion in Qtz	Ptz	17.4	50.6	32	
	Hs	66.6	33.4		
Inclusion in Py	Clv	34.1		65.9	
Qtz fracture	Clv	34.7		65.3	
Py fracture	Gold-Ptz	59.7	27.2	13.1	
Py fracture	Gold-Ptz	40.2	56.3	3.5	
Qtz fracture	Gold-Ptz	38.8	47.7	13.5	

Abbreviations: Alt = altaite; Ccp = chalcopyrite; Clv = calaverite; Hs = hessite; Ptz = petzite; Py = pyrite; Qtz = quartz; Gold-Ptz = gold-petzite intergrowth

Table 4.3: Representative SEM-EDS analyses of ore minerals from the Grand Duc deposit

Sample/Grade	Location	Texture	Mineral	Au (at. %)	Ag	Bi	Te	Pb
18KN03/	Patchy Chl Alt	Chl-Ser grain boundary	Gold	85.2	14.8			
High grade	Patchy Chl Alt	Chl-Ser grain boundary	Gold	88.3	11.7			
	Patchy Chl Alt	Composite grain; Chl grain boundaries	Gold	84.5	15.5			
			Alt				52.5	47.5
	Patchy Chl Alt	Composite grain; Po-Chl grain boundary	Gold	88.6	11.4			
			TeBi			44.9	55.1	
	Patchy Chl Alt	Chl-Ser grain boundary	TeBi			39.8	60.2	
	Patchy Chl Alt	Chl grain boundaries	TeBi			41.5	58.5	
	Patchy Chl Alt	Chl grain boundaries	Alt				52.6	47.4
	Patchy Chl Alt	Chl grain boundaries	Ts/Tt			50.1	49.9	
	Patchy Chl Alt	Chl grain boundaries	Ts/Tt			50.3	49.7	
	Vein	Po-Ccp grain boundary	Gold	84.4	15.6			
	Vein	Po-Py grain boundary	Gold	83.4	16.6			
	Vein	Ccp-Py grain boundary	Gold	85.5	14.5			
	Vein	Sph-Py grain boundary	Gold	84.7	15.3			
	Vein	Po-Cal grain boundary	Gold	85.4	14.6			
	Vein	Fracture in Py	Gold	84.4	15.6			
	Vein	Fracture in Py w/ Sph and Ccp	Gold	83.8	16.2			
	Vein	Py-Qtz grain boundary	Gold	85.5	14.5			
	Vein	Void in Py	Gold	87.4	12.6			
	Vein	Fracture in Qtz	Gold	86.7	13.3			
	Vein	Fracture in Qtz	Gold	86.5	13.5			
	Vein	Composite grain; Void in Py	Gold	88.4	11.6			
			TeBi			40.2	59.8	
18KN07/	Vein	Void in Py	Gold	92.2	7.8			
Moderate grade	Vein	Composite grain; Void in Py	Gold	88.8	11.2			
			Clv	35.2			64.8	
	Vein	Void in Py	TeBi			39.6	60.4	
	Vein	Void in Py	Alt				50.9	49.1
	Vein	Py-Py grain boundary	Gold	71.2	28.8			
	Vein	Py-Qtz grain boundary	Gold	73.1	26.9			
18KN09/	Sieved pyrite vein	Void in Py	Gold	93.3	6.7			
Moderate grade	Sieved pyrite vein	Composite grain; Void in Py	Gold	85.1	14.9			
			Ptz	17.8	49.4		32.8	
			TeBi			39.6	60.4	
			Te				100	
	Sieved pyrite vein	Py-Py grain boundary	Gold	74.4	25.6			
	Sieved pyrite vein	Fracture in Qtz	Gold	69.1	30.9			
	Sieved pyrite vein	Composite grain; Void in Py	Voly		25.7	24.9	49.4	
			Hs		67.5		32.5	
	Sieved pyrite vein	Void in Py	TeBi			40.6	59.4	
	Clean pyrite vein	Fracture in pyrite	Gold	71.7	28.3			
	Clean pyrite vein	Py-Py grain boundary	Gold	84.5	15.5			

Abbreviations: Alt = altaite; Cal = calcite; Ccp = chalcopyrite; Chl = chlorite; Clv = calaverite; Hs = hessite; Ptz = petzite; Py = pyrite; Qtz = quartz; Ser = sericite; Sph = sphalerite; Te = native Te; TeBi = tellurobismuthite; Ts/Tt = Tsumoite or Tetradymite Voly = volynskite

Table 4.4: Summary of mineralized vein characteristics at Doyon and Grand Duc

Deposit	Doyon West Zone	Grand Duc		
		High grade	Moderate grade	Low grade
Samples	18KN05, 18KN06	18KN03	18KN07	18KN09
MIC host lithology	Phase E	Phase I	Phase I	Phase I
Major gangue	Quartz	Quartz, Calcite, Chlorite	Quartz	Quartz
Minor gangue	Chlorite, Muscovite	Muscovite	Calcite, Chlorite, Muscovite	Calcite, Chlorite, Muscovite
Major sulphides	Pyrite	Pyrite-Pyrrhotite-Chalcopyrite	Pyrite	Pyrite
Minor sulphides	Chalcopyrite-Pyrrhotite	Sphalerite	Chalcopyrite-Pyrrhotite	Chalcopyrite-Pyrrhotite
Trace minerals	Magnetite, Cassiterite		Magnetite	Magnetite
Ore minerals	Gold, Petzite, Calaverite, Hessite	Gold, Tellurobismuthite, Altaite, Tsumoite or Tetradymite	Gold, Tellurobismuthite, Petzite, Calaverite, Hessite, Altaite	Gold, Petzite, Calaverite, Hessite, Altaite, Tellurobismuthite, Volynskite, Native Te
Gold Au:Ag ratio (At. %)	72:28 to 95:5	75:25 to 91:9	65:35 to 94:6	60:40 to 90:10

Altaite = PbTe; Calaverite = $AuTe_2$; Cassiterite = SnO_2; Hessite = Ag_2Te; Petzite = Ag_3AuTe_2; Tellurobismuthite = Bi_2Te_3; Tetradymite = Bi_2Te_2S; Tsumoite = BiTe; Volynskite = $AgBiTe_2$

4.11 FIGURES

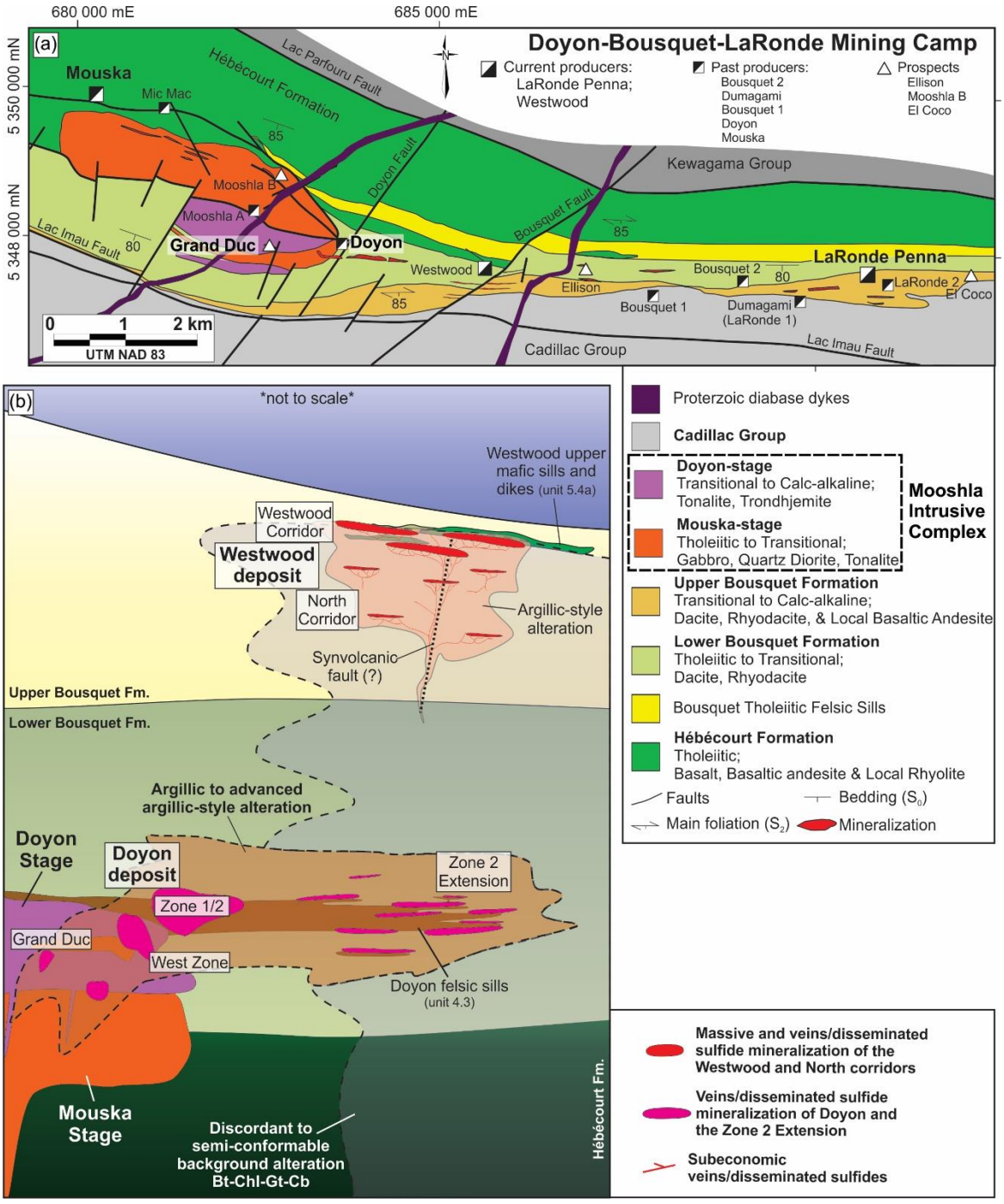
680 000 mE
685 000 mE
5 350 000 mN
5 348 000 mN
(a)
Doyon-Bousquet-LaRonde Mining Camp
Current producers: LaRonde Penna; Westwood
Past producers: Bousquet 2, Dumagami, Bousquet 1, Doyon, Mouska
Prospects: Ellison, Mooshla B, El Coco
Mouska
Mic Mac
Hébécourt Formation
Lac Parfouru Fault
Doyon Fault
Kewagama Group
Mooshla B
Mooshla A
Grand Duc
Doyon
Bousquet Fault
Lac Imau Fault
Westwood
Ellison
Bousquet 2
LaRonde Penna
LaRonde 2
El Coco
Bousquet 1
Dumagami (LaRonde 1)
Cadillac Group
0 1 2 km
UTM NAD 83
(b)
not to scale
Westwood upper mafic sills and dikes (unit 5.4a)
Westwood Corridor
Westwood deposit
North Corridor
Argillic-style alteration
Synvolcanic fault (?)
Upper Bousquet Fm.
Lower Bousquet Fm.
Argillic to advanced argillic-style alteration
Doyon Stage
Doyon deposit
Zone 1/2
Zone 2 Extension
Grand Duc
West Zone
Doyon felsic sills (unit 4.3)
Mouska Stage
Discordant to semi-conformable background alteration Bt-Chl-Gt-Cb
Hébécourt Fm.
Proterzoic diabase dykes
Cadillac Group
Doyon-stage
Transitional to Calc-alkaline; Tonalite, Trondhjemite
Mouska-stage
Tholeiitic to Transitional; Gabbro, Quartz Diorite, Tonalite
Mooshla Intrusive Complex
Upper Bousquet Formation
Transitional to Calc-alkaline; Dacite, Rhyodacite, & Local Basaltic Andesite
Lower Bousquet Formation
Tholeiitic to Transitional; Dacite, Rhyodacite
Bousquet Tholeiitic Felsic Sills
Hébécourt Formation
Tholeiitic; Basalt, Basaltic andesite & Local Rhyolite
Faults
Bedding (S0)
Main foliation (S2)
Mineralization
Massive and veins/disseminated sulfide mineralization of the Westwood and North corridors
Veins/disseminated sulfide mineralization of Doyon and the Zone 2 Extension
Subeconomic veins/disseminated sulfides

Fig. 4.1: (a) Simplified geology map of the Doyon-Bousquet-LaRonde mining camp showing the location of Mooshla intrusive complex and spatial relationship to mines in the area. Modified from Mercier-Langevin (2009). (b) Representative section through the stratigraphy highlighting the spatial relationships and distribution between the Mooshla intrusive complex, intrusion-related deposits (i.e., Doyon and Zone 2 extension) and Au-rich VMS (i.e., Westwood) deposits. The hydrothermal alteration zones associated with each deposit style are also illustrated. Modified from Yergeau et al. (2022b).

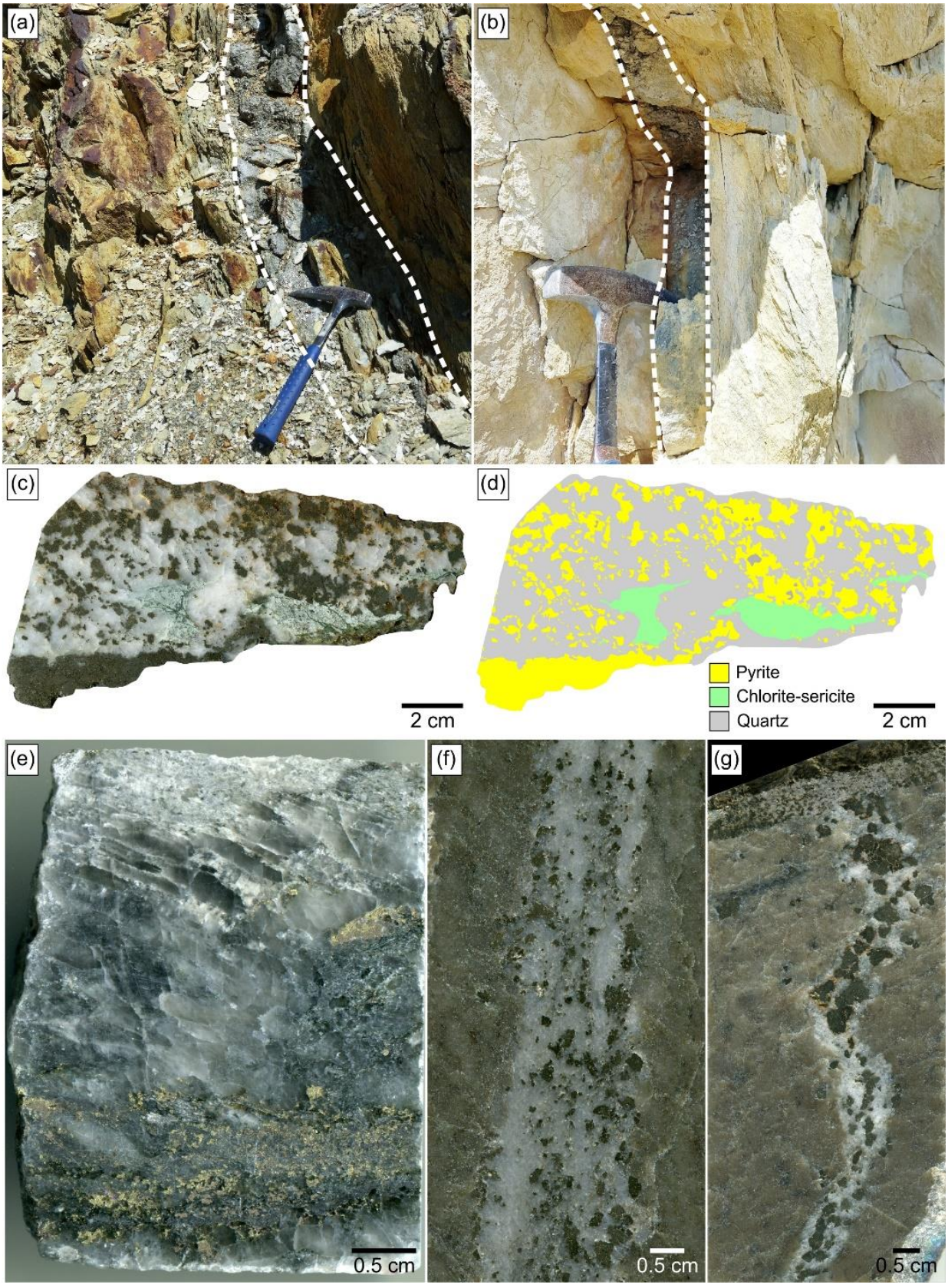
(a)
(b)
(c)
(d)
2 cm
Pyrite
Chlorite-sericite
Quartz
2 cm
(e)
(f)
(g)
0.5 cm
0.5 cm
0.5 cm

Fig. 4.2: Field photographs of the veins sampled from the Doyon West deposit for this study and representative slab scans from the Doyon West deposit and Grand Duc deposit. (a) Mineralized Doyon vein from which sample 18KN05 was taken. (b) Mineralized Doyon vein from which sample 18KN06 was taken. (c) Representative slab from Doyon (sample 18KN05). (d) Outline of the slab in (c) to highlight the distribution of pyrite in the sample. (e) High-grade mineralized vein from Grand Duc (sample 18KN03), note the greater proportion of chalcopyrite compared to Doyon samples (frame c) and other Grand Duc veins (f-g). (f) Moderate-grade mineralized vein from Grand Duc (sample 18KN07). (g) Moderate-grade mineralized vein from Grand Duc (sample 18KN09). White dashed lines in frames (a) and (b) represent the surface exposure of the mineralized vein at surface.

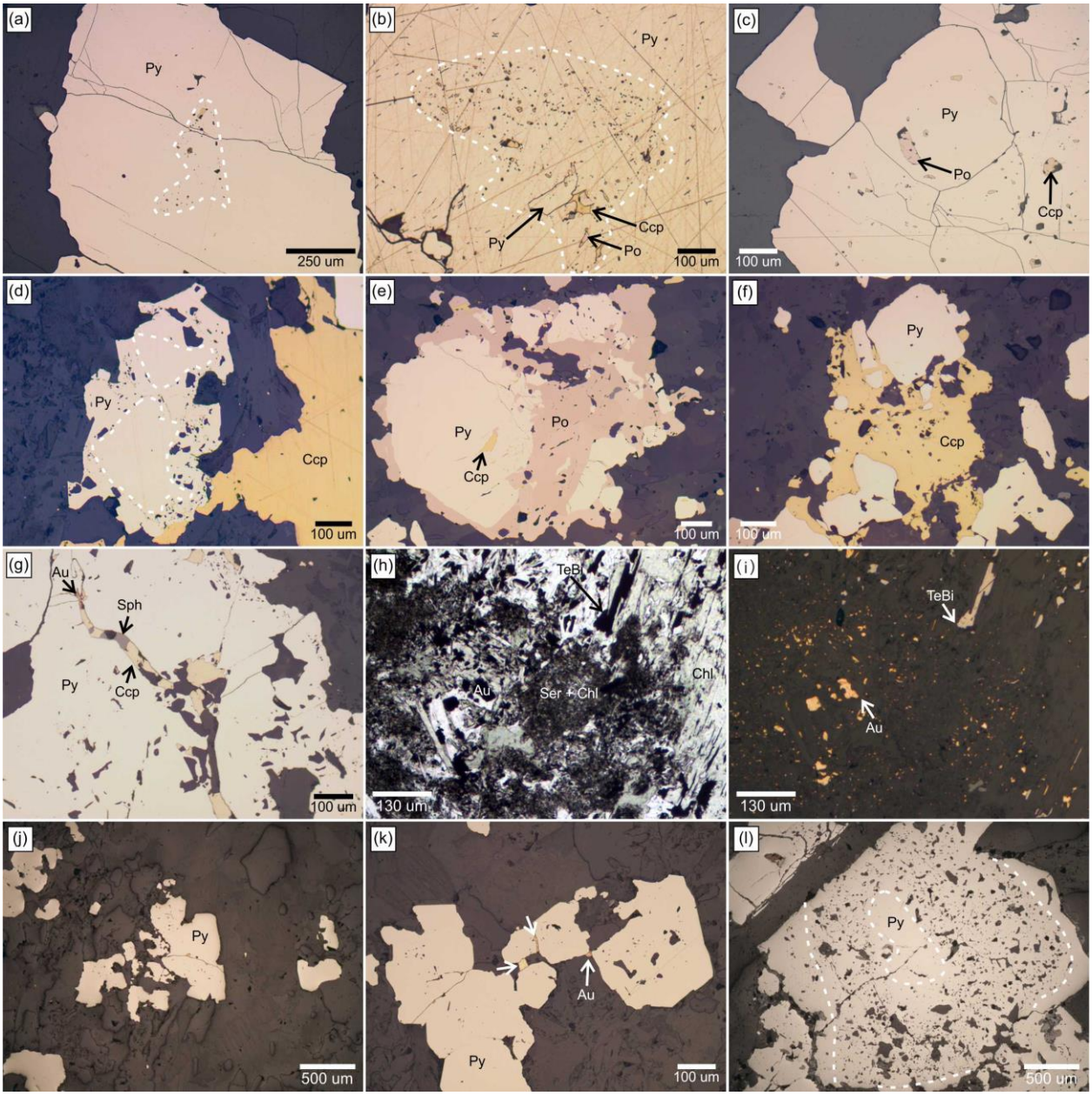
(a)
Py
250 um
(b)
Py
Py
Ccp
Po
100 um
(c)
Py
Po
Ccp
100 um
(d)
Py
Ccp
100 um
(e)
Py
Po
Ccp
100 um
(f)
Py
Ccp
100 um
(g)
Au
Sph
Py
Ccp
100 um
(h)
TeBi
Au
Ser + Chl
Chl
130 um
(i)
TeBi
Au
130 um
(j)
Py
500 um
(k)
Au
Py
100 um
(l)
Py
500 um

Fig. 4.3: Representative sulfide textures from the Doyon West deposit (a-c) and Grand Duc deposit high- (d-h) and moderate- to low-grade veins (j-l). (a) Zoned pyrite grain from Doyon with an inclusion-rich core and an inclusion-free rim (18KN06; reflected light [RL]). (b) Pyrite grain from Doyon that was etched with nitric acid. Note that the etching effected the inclusion-rich core and the inclusion-free rim to the same degree (18KN05; RL). (c) Pyrite grains from Doyon containing multiple pyrrhotite and chalcopyrite inclusions (15KN05; RL). (d) Pyrite from Grand Duc that has an inclusion-free core and a sieved rim (18KN03; RL). (e) Pyrite from Grand Duc that is replaced by pyrrhotite indicated pyrrhotite is forming after pyrite (18KN03; RL). (f) Pyrite from Grand Duc that is replaced by chalcopyrite indicated chalcopyrite is forming after pyrite (18KN03; RL). (g) A fracture in pyrite from Grand Duc that is infilled with chalcopyrite, sphalerite, and gold (18KN03; RL). (h) Representative image of the patchy chlorite alteration from Grand Duc (18KN03; plane polarized light). (i) Same image as in (e) but taken in RL to show the presence of gold and tellurobismuthite. (j) Large, pyrite grains from Grand Duc that are relatively unzoned and only weakly sieved (18KN07; RL). (k) Weakly sieved pyrite from Grand Duc with gold occurring along pyrite grain boundaries and fractures (18KN07; RL). (l) Pyrite with a relatively un-sieved, clean core, a highly sieved middle portion of the grain, and a relatively un-sieved rim (18KN09; RL). Au = gold; Ccp = chalcopyrite; Chl = Chlorite; Py = pyrite; Po = pyrrhotite; Ser = sericite; Sph = sphalerite; TeBi = tellurobismuthite.

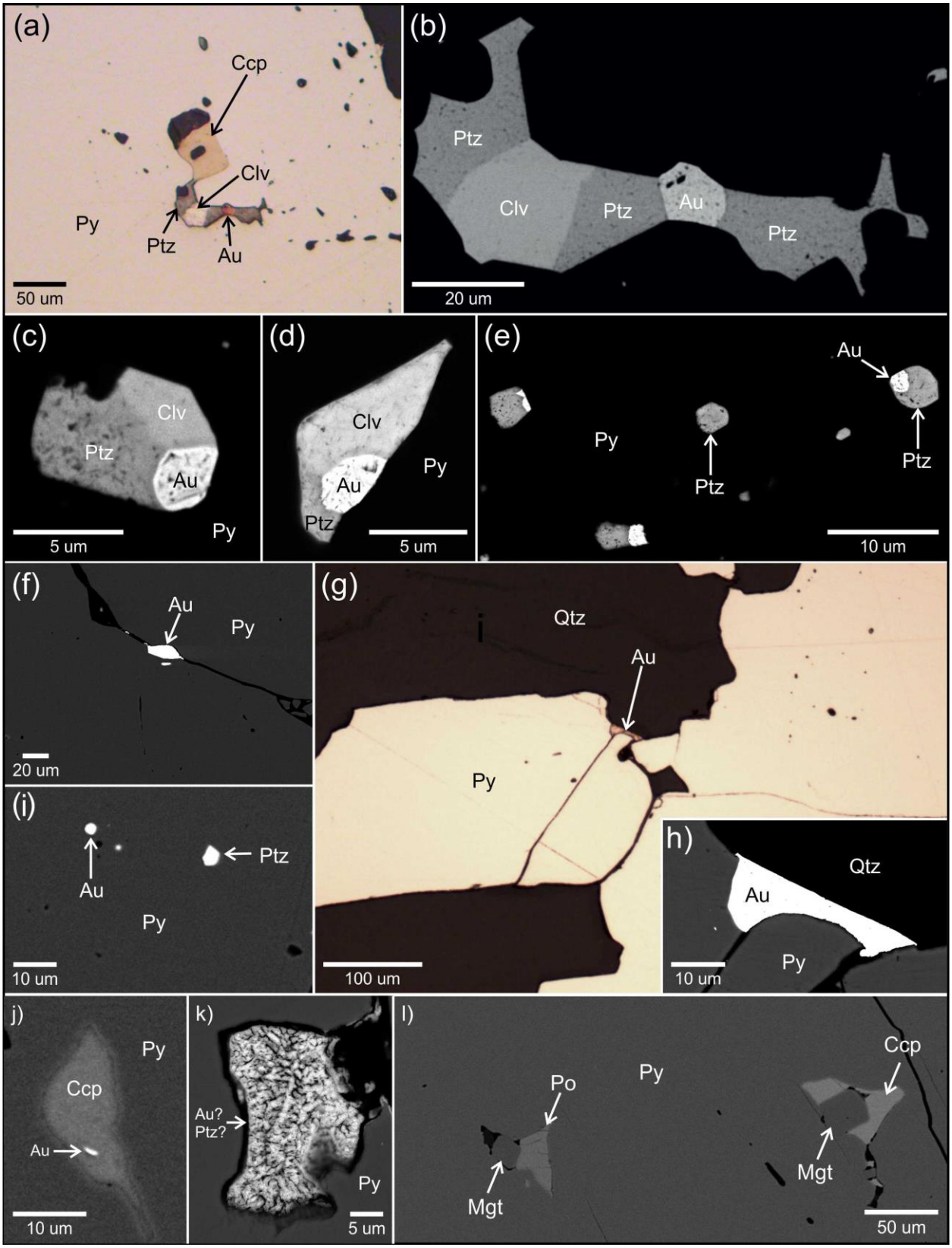
(a)
Ccp
Clv
Py
Ptz
Au
50 um
(b)
Ptz
Clv
Ptz
Au
Ptz
20 um
(c)
Clv
Ptz
Au
Py
5 um
(d)
Clv
Au
Py
Ptz
5 um
(e)
Au
Py
Ptz
Ptz
10 um
(f)
Au
Py
20 um
(g)
Qtz
Au
Py
100 um
(i)
Au
Ptz
Py
10 um
(h)
Qtz
Au
Py
10 um
(j)
Py
Ccp
Au
10 um
(k)
Au?
Ptz?
Py
5 um
(l)
Py
Po
Ccp
Mgt
Mgt
50 um

Fig. 4.4: Representative reflected light and SEM-BSE images of the various textural settings of gold in mineralized veins from the Doyon West deposit. (a-b) Composite inclusion in pyrite composed of gold, petzite, calaverite, and chalcopyrite. Note the planar grain edges formed by the ore minerals suggestive of open space filling. (c-d) Composite inclusions in pyrite composed of gold, petzite, and calaverite. (e) Multiple composite inclusions composed of gold and petzite as well as inclusions of only petzite present in pyrite. (f) Gold present along a fracture running through pyrite. (g-h) Gold present along the grain boundary of quartz and pyrite. (j) Inclusion of chalcopyrite in pyrite that contains a small grain of gold. (k) Ore mineral occurring along a fracture in pyrite that has a composition that is a mixture gold and petzite. (l) Multiple voids in pyrite infilled with pyrrhotite, chalcopyrite, and magnetite. Au = gold; Clv = calaverite; Ccp = chalcopyrite; Mgt = magnetite; Po = pyrrhotite; Py = pyrite; Ptz = petzite; Qtz = quartz.

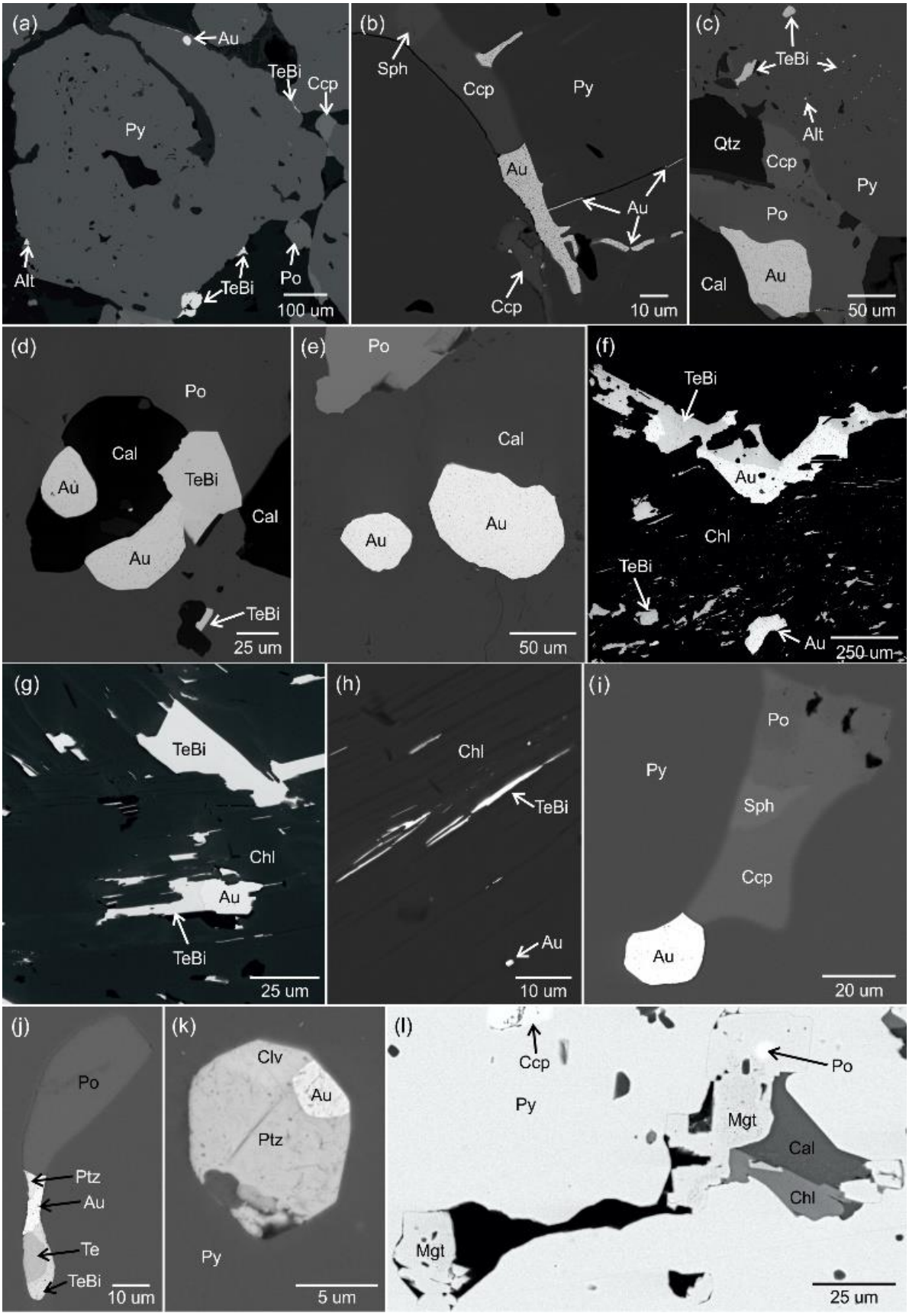
(a)
Au
TeBi
Ccp
Py
Alt
TeBi
Po
100 um
(b)
Sph
Ccp
Py
Au
Au
Ccp
10 um
(c)
TeBi
Alt
Qtz
Ccp
Py
Po
Cal
Au
50 um
(d)
Po
Cal
Au
TeBi
Cal
Au
TeBi
25 um
(e)
Po
Cal
Au
Au
50 um
(f)
TeBi
Au
Chl
TeBi
Au
250 um
(g)
TeBi
Chl
Au
TeBi
25 um
(h)
Chl
TeBi
Au
10 um
(i)
Po
Py
Sph
Ccp
Au
20 um
(j)
Po
Ptz
Au
Te
TeBi
10 um
(k)
Clv
Au
Ptz
Py
5 um
(l)
Ccp
Po
Py
Mgt
Cal
Chl
Mgt
25 um

Fig. 4.5: Representative SEM-BSE images of the various textural settings of ore in mineralized veins from the Grand Duc deposit. (a) Sieved grain of pyrite that contains an inclusion of gold along the outer grain margin. Numerous grains of tellurobismuthite and a grain of altaite occur along the grain margin of pyrite (18KN03). (b) Fracture in pyrite that has been infilled with gold, sphalerite, and chalcopyrite. Note how gold extends into fractures perpendicular to the main fracture (18KN03). (c) Gold occurring along the grain boundaries of pyrrhotite and calcite. Numerous grains of tellurobismuthite and altaite occur as inclusions filling in voids in pyrite (18KN03). (d) Sieved area in pyrrhotite that has been infilled with gold, tellurobismuthite, and calcite (18KN03). (e) Gold occurring along fractures in calcite (18KN03). (f) Composite and individual grains of gold and tellurobismuthite occurring in strong, patchy chlorite alteration (18KN03). (g-h) Grains of gold and tellurobismuthite occurring along grain boundaries of chlorite and sericite (18KN03). (i) Composite inclusion filling in a void in pyrite composed of gold, chalcopyrite, sphalerite, and pyrrhotite (18KN07). (j) Composite inclusion in pyrite composed of pyrrhotite, gold, petzite, tellurobismuthite, and native Te (18KN09). (k) Composite inclusion in pyrite composed of gold, petzite, and calaverite (18KN07). (l) Magnetite, pyrrhotite, chalcopyrite, calcite, and chlorite filling in voids in pyrite (18KN07). Au = gold; Alt = altaite; Cal = calcite; Ccp = chalcopyrite; Chl = Chlorite; Clv = calaverite; Mgt = magnetite; Py = pyrite; Po = pyrrhotite; Ptz = petzite; Qtz = quartz; Sph = sphalerite; Te = native tellurium; TeBi = tellurobismuthite.

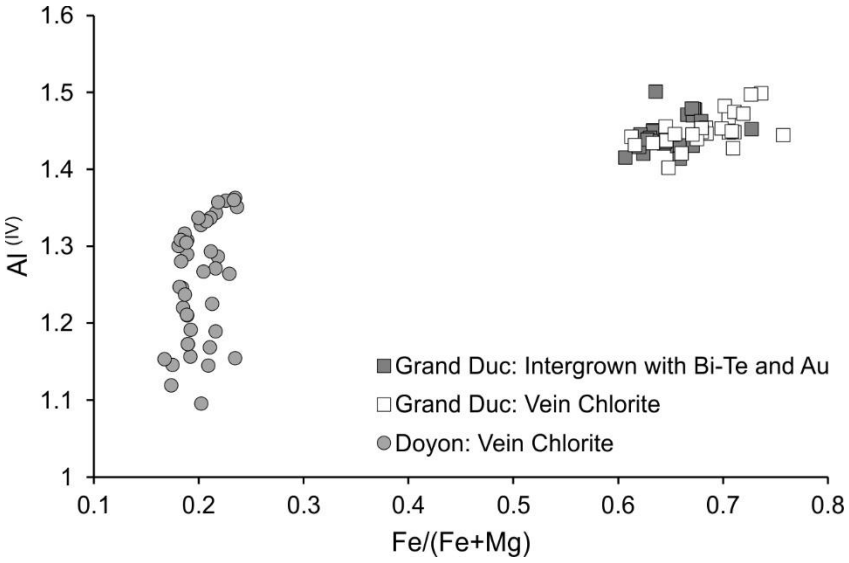

Fig. 4.6: Major element chlorite mineral chemistry data determined by EMPA analysis recalculated to atoms per formula unit.

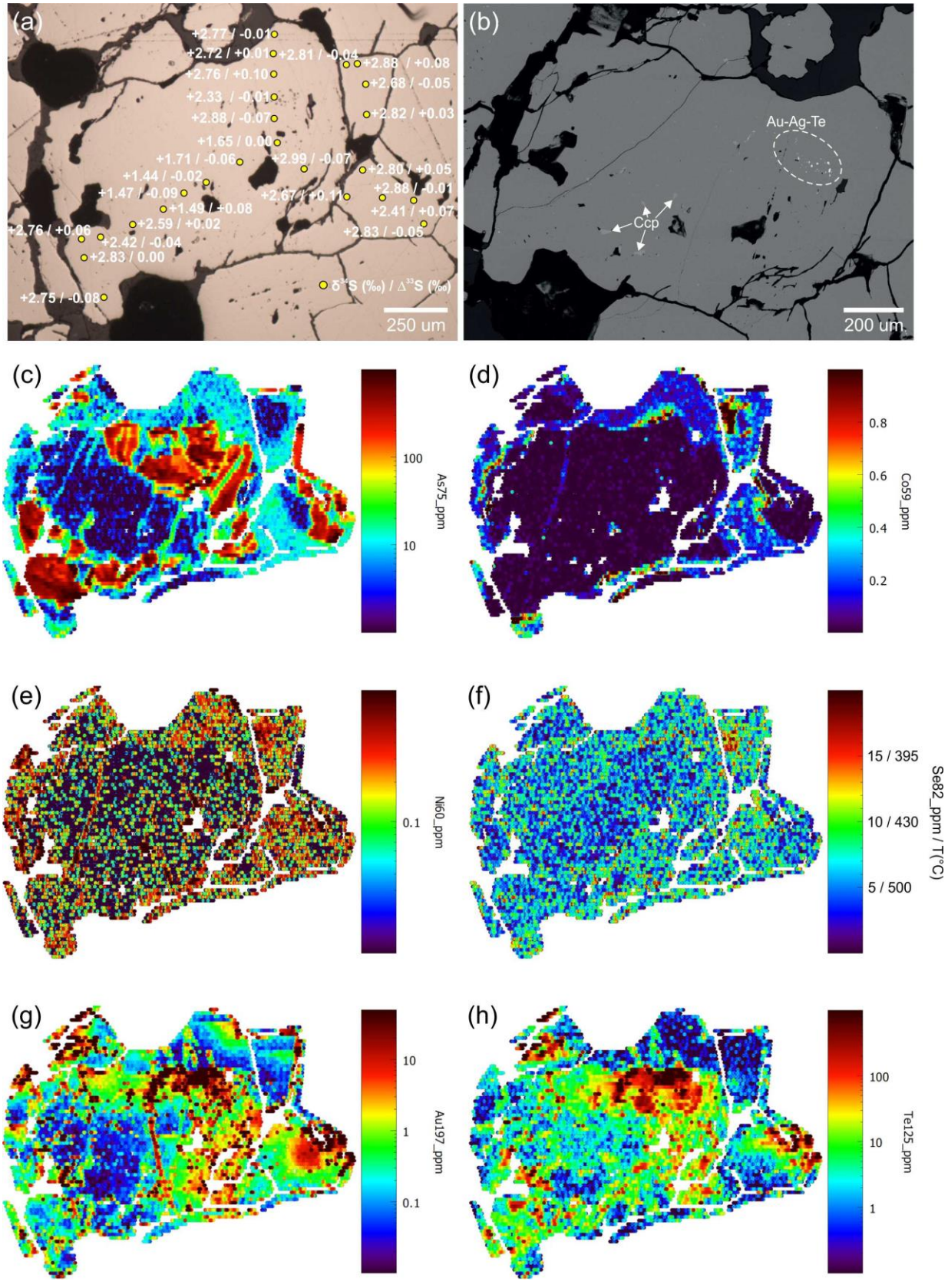
(a)
+2.77 / -0.01
+2.72 / +0.01
+2.81 / -0.04
+2.88 / +0.08
+2.76 / +0.10
+2.68 / -0.05
+2.33 / -0.01
+2.88 / -0.07
+2.82 / +0.03
+1.65 / 0.00
+1.71 / -0.06
+2.99 / -0.07
+2.80 / +0.05
+1.44 / -0.02
+1.47 / -0.09
+2.67 / +0.11
+2.88 / -0.01
+1.49 / +0.08
+2.41 / +0.07
+2.59 / +0.02
+2.76 / +0.06
+2.83 / -0.03
+2.42 / -0.04
+2.83 / 0.00
δ34S (‰) / Δ33S (‰)
+2.75 / -0.08
250 um
(b)
Au-Ag-Te
Ccp
200 um
(c)
100
10
As75_ppm
(d)
0.8
0.6
0.4
0.2
Co59_ppm
(e)
0.1
Ni60_ppm
(f)
15 / 395
10 / 430
5 / 500
Se82_ppm / T(°C)
(g)
10
1
0.1
Au197_ppm
(h)
100
10
1
Te125_ppm

Fig. 4.7: Reflected light (a) and SEM-BSE (b) images of pyrite from the Doyon West deposit (sample18KN05) that was mapped by LA-ICP-MS to determine the trace element distribution patterns (c-h) and analyzed by SIMS to determine the $\delta^{34}S$ and $\Delta^{33}S$ composition for each different trace element zone (a). Temperature calculations in (d) are based on the semi-quantitative Se-in-pyrite thermometer of Keith et al. (2018). Ccp = chalcopyrite; Au-Ag-Te = gold-silver-tellurides.

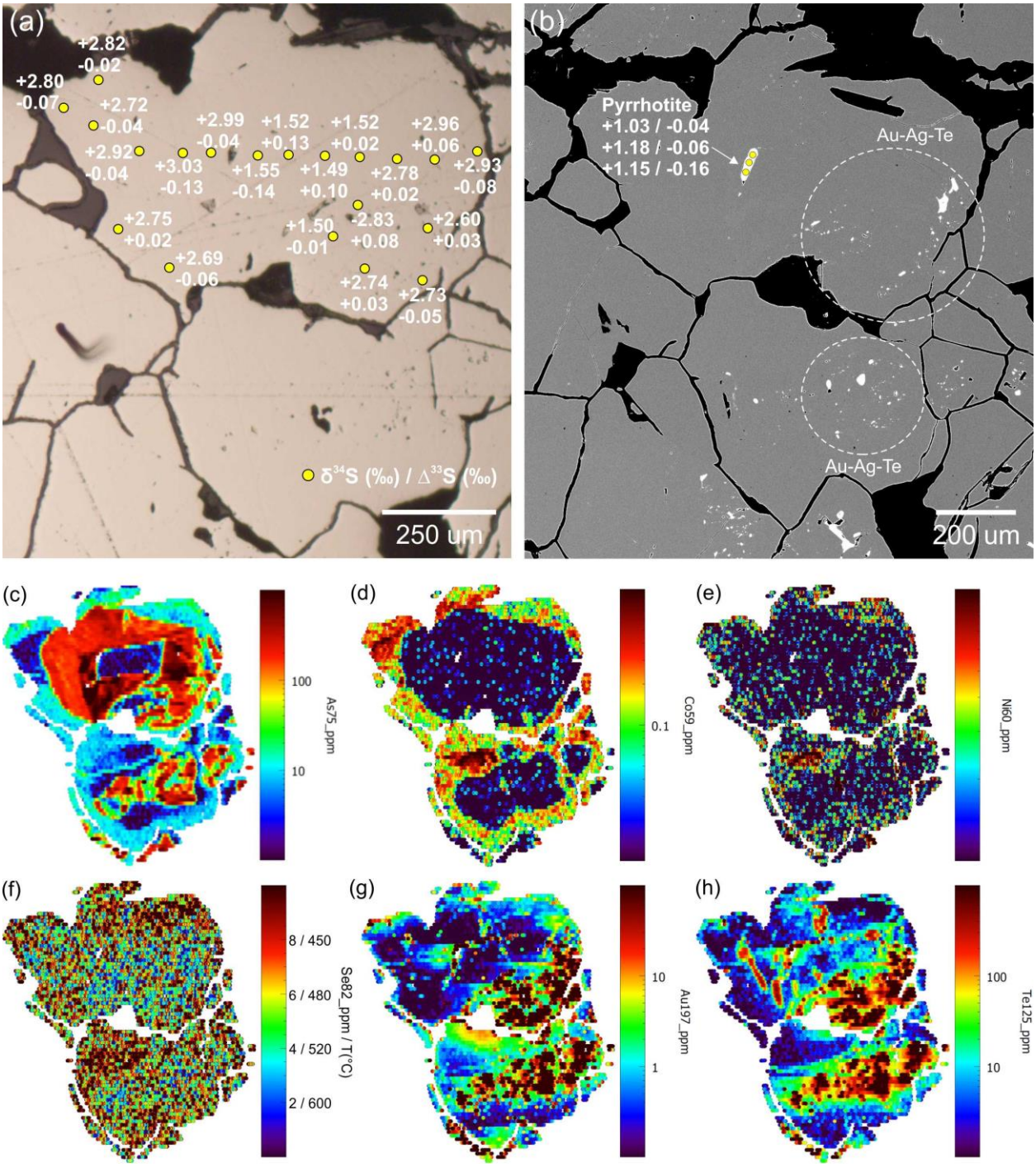
(a)
+2.82
-0.02
+2.80
-0.07
+2.72
-0.04
+2.99
-0.04
+1.52
+0.13
+1.52
+0.02
+2.96
+0.06
+2.92
-0.04
+3.03
-0.13
+1.55
-0.14
+1.49
+0.10
+2.78
+0.02
+2.93
-0.08
+2.75
+0.02
+1.50
-0.01
-2.83
+0.08
+2.60
+0.03
+2.69
-0.06
+2.74
+0.03
+2.73
-0.05
δ34S (‰) / Δ33S (‰)
250 um
(b)
Pyrrhotite
+1.03 / -0.04
+1.18 / -0.06
+1.15 / -0.16
Au-Ag-Te
Au-Ag-Te
200 um
(c)
100
10
As75_ppm
(d)
0.1
Co59_ppm
(e)
Ni60_ppm
(f)
8 / 450
6 / 480
4 / 520
2 / 600
Se82_ppm / T(°C)
(g)
10
1
Au197_ppm
(h)
100
10
Te125_ppm

Fig. 4.8: Reflected light (a) and SEM-BSE images (b) of pyrite from Doyon (18KN05) that was mapped by LA-ICP-MS to determine the trace element distribution patterns (c-h) and analyzed by SIMS to determine the $\delta^{34}S$ and $\Delta^{33}S$ composition for each different trace element zone (a). Temperature calculations in (d) are based on the semi-quantitative Se-in-pyrite thermometer of Keith et al. (2018). Au-Ag-Te = gold-silver-tellurides

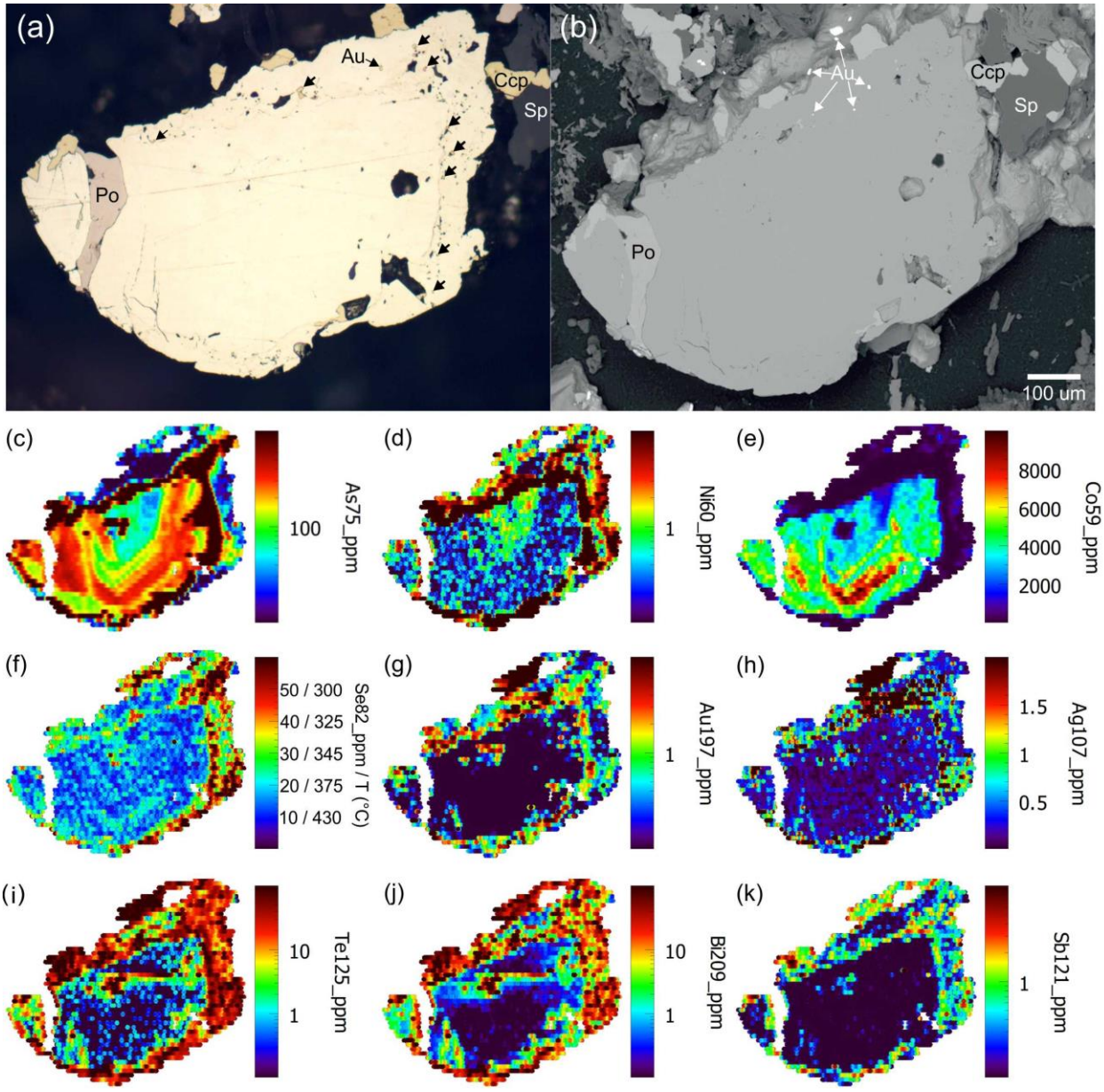
(a)
Au
Ccp
Sp
Po
(b)
Au
Ccp
Sp
Po
100 um
(c)
100
As75_ppm
(d)
1
Ni60_ppm
(e)
8000
6000
4000
2000
Co59_ppm
(f)
50 / 300
40 / 325
30 / 345
20 / 375
10 / 430
Se82_ppm / T (°C)
(g)
1
Au197_ppm
(h)
1.5
1
0.5
Ag107_ppm
(i)
10
1
Te125_ppm
(j)
10
1
Bi209_ppm
(k)
1
Sb121_ppm

Fig. 4.9: Reflected light (a) and SEM-BSE (b) images of pyrite from the high-grade Grand Duc deposit vein (sample 18KN03) that has been acid etched. This grain was also mapped by LA-ICP-MS to determine the trace element distribution patterns (c-k). Note the inclusions of gold (Au) along the rim of pyrite. Black arrows in (a) without a label indicate chalcopyrite inclusions along the rim. Temperature calculations in (d) are based on the semi-quantitative Se-in-pyrite thermometer of Keith et al. (2018). Au = gold; Ccp = chalcopyrite; Po = pyrrhotite; Sp = sphalerite.

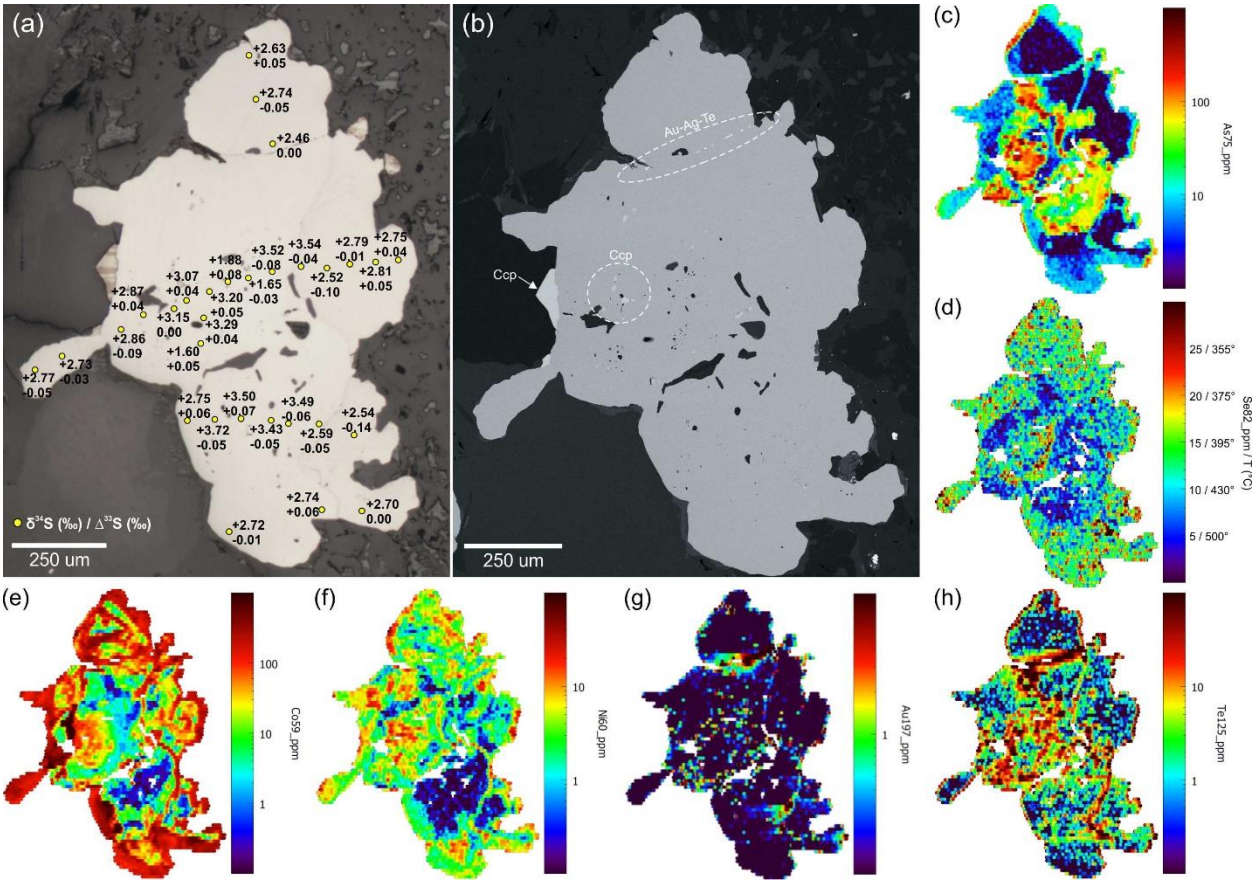

Fig. 4.10: Reflected light (a) and SEM-BSE images (b) of pyrite from the moderate- to low-grade Grand Duc vein (18KN07) that was mapped by LA-ICP-MS to determine the trace element distribution patterns (c-h) and analyzed by SIMS to determine the $\delta^{34}S$ and $\Delta^{33}S$ composition for each different trace element zone (a). Temperature calculations in (d) are based on the semi-quantitative Se-in-pyrite thermometer of Keith et al. (2018). Au-Ag-Te = gold-silver-tellurides; Ccp = chalcopyrite.

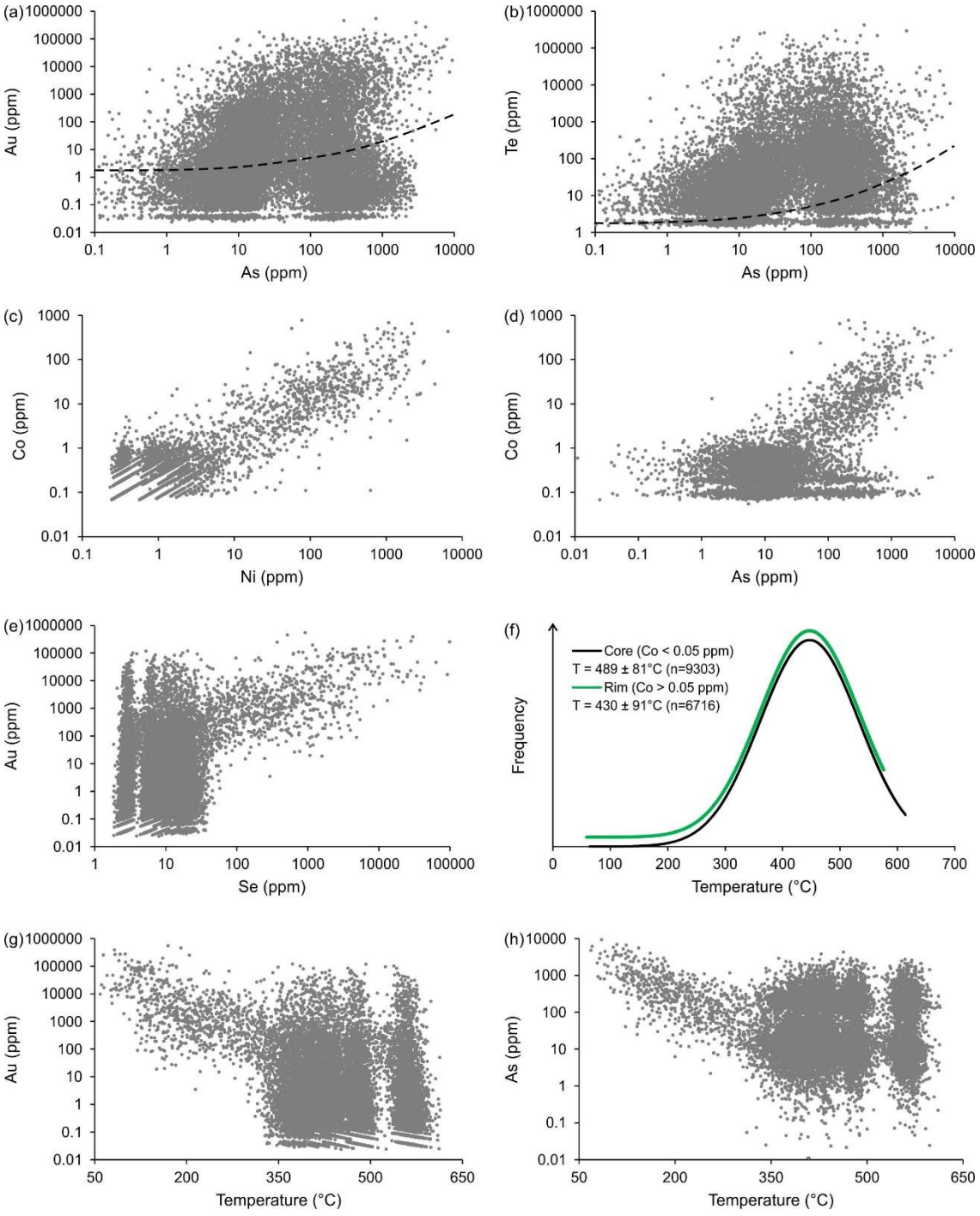
(a)
Au (ppm)
As (ppm)
(b)
Te (ppm)
As (ppm)
(c)
Co (ppm)
Ni (ppm)
(d)
Co (ppm)
As (ppm)
(e)
Au (ppm)
Se (ppm)
(f)
Core (Co < 0.05 ppm)
T = 489 ± 81°C (n=9303)
Rim (Co > 0.05 ppm)
T = 430 ± 91°C (n=6716)
Frequency
Temperature (°C)
(g)
Au (ppm)
Temperature (°C)
(h)
As (ppm)
Temperature (°C)

Fig. 4.11: Scatter plots for selected elements quantified by LA-ICP-MS mapping for pyrite from Doyon shown in Figure 4.8 (n=21, 388). See text for explanation of the compositional variations shown in frames (a-e) and (g-h). Temperatures in frame (f) were calculated using the semiquantitative Se-in-pyrite thermometer of Keith et al., 2018. The black dashed lines in (a) and (b) represent the solubility limit for Au and Te solid solution in pyrite as a function of As (Reich et al., 2005; Keith et al., 2018). Concentrations of Au and Te above the solubility line indicate Au and Te occur in pyrite as inclusions whereas data below the line indicate Au and Te occur in the pyrite lattice.

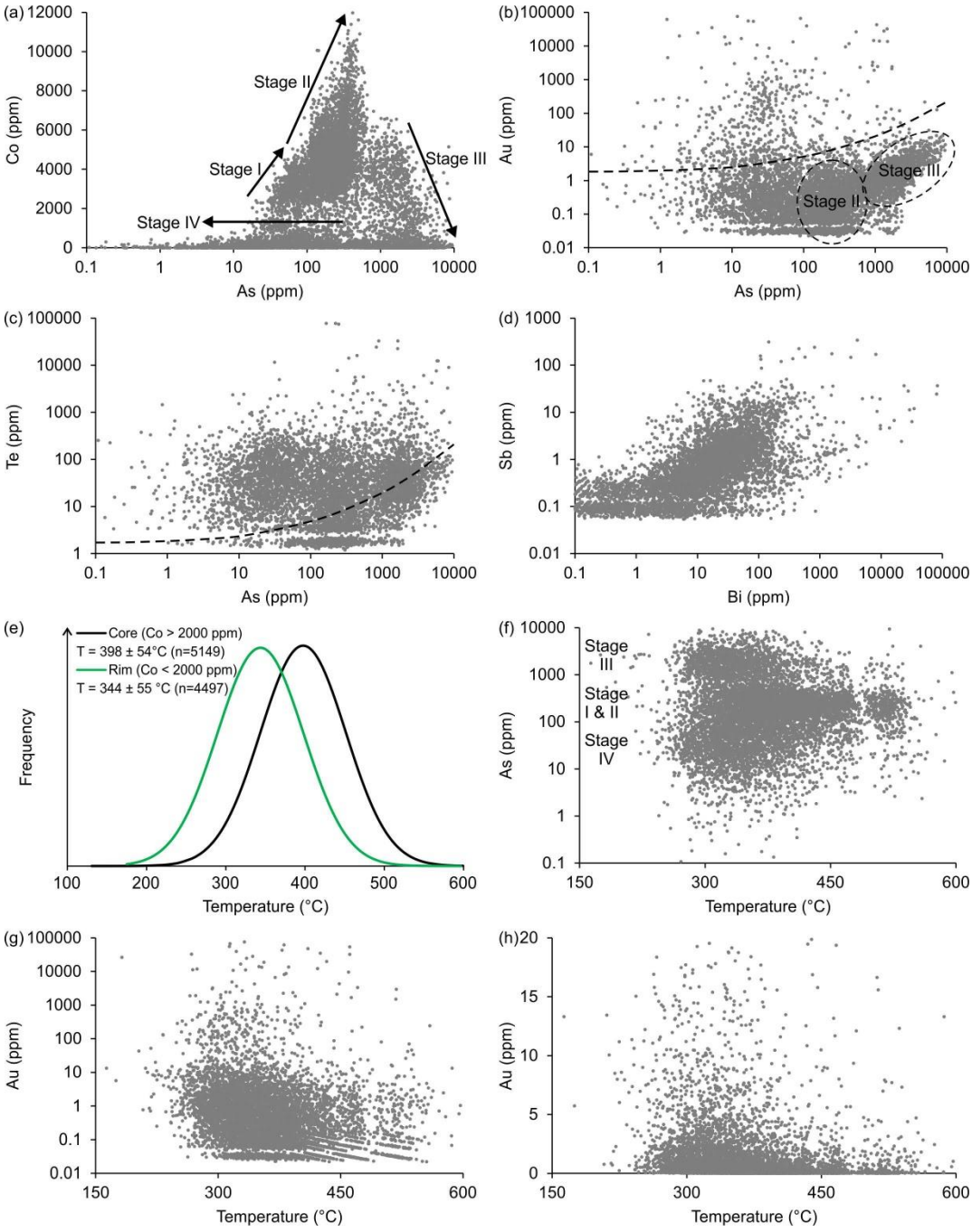
(a)
Co (ppm)
As (ppm)
Stage I
Stage II
Stage III
Stage IV
(b)
Au (ppm)
As (ppm)
Stage II
Stage III
(c)
Te (ppm)
As (ppm)
(d)
Sb (ppm)
Bi (ppm)
(e)
Core (Co > 2000 ppm)
T = 398 ± 54°C (n=5149)
Rim (Co < 2000 ppm)
T = 344 ± 55 °C (n=4497)
Frequency
Temperature (°C)
(f)
As (ppm)
Stage III
Stage I & II
Stage IV
Temperature (°C)
(g)
Au (ppm)
Temperature (°C)
(h)
Au (ppm)
Temperature (°C)

Fig. 4.12: Scatter plots for selected elements quantified by LA-ICP-MS mapping for pyrite from the high-grade vein from Grand Duc shown in Figure 4.9 (n=9, 760). See text for explanation of the compositional variations shown in frames (a-d) and (f-h). Temperatures in frames (e-h) were calculated using the Se-in-pyrite thermometer of Keith et al., 2018. The black dashed lines in (b) and (c) represent the solubility limit for Au and Te solid solution in pyrite as a function of As (Reich et al., 2005; Keith et al., 2018). Concentrations of Au and Te above the solubility line indicate Au and Te occur in pyrite as inclusions whereas data below the line indicate Au and Te occur in the pyrite lattice.

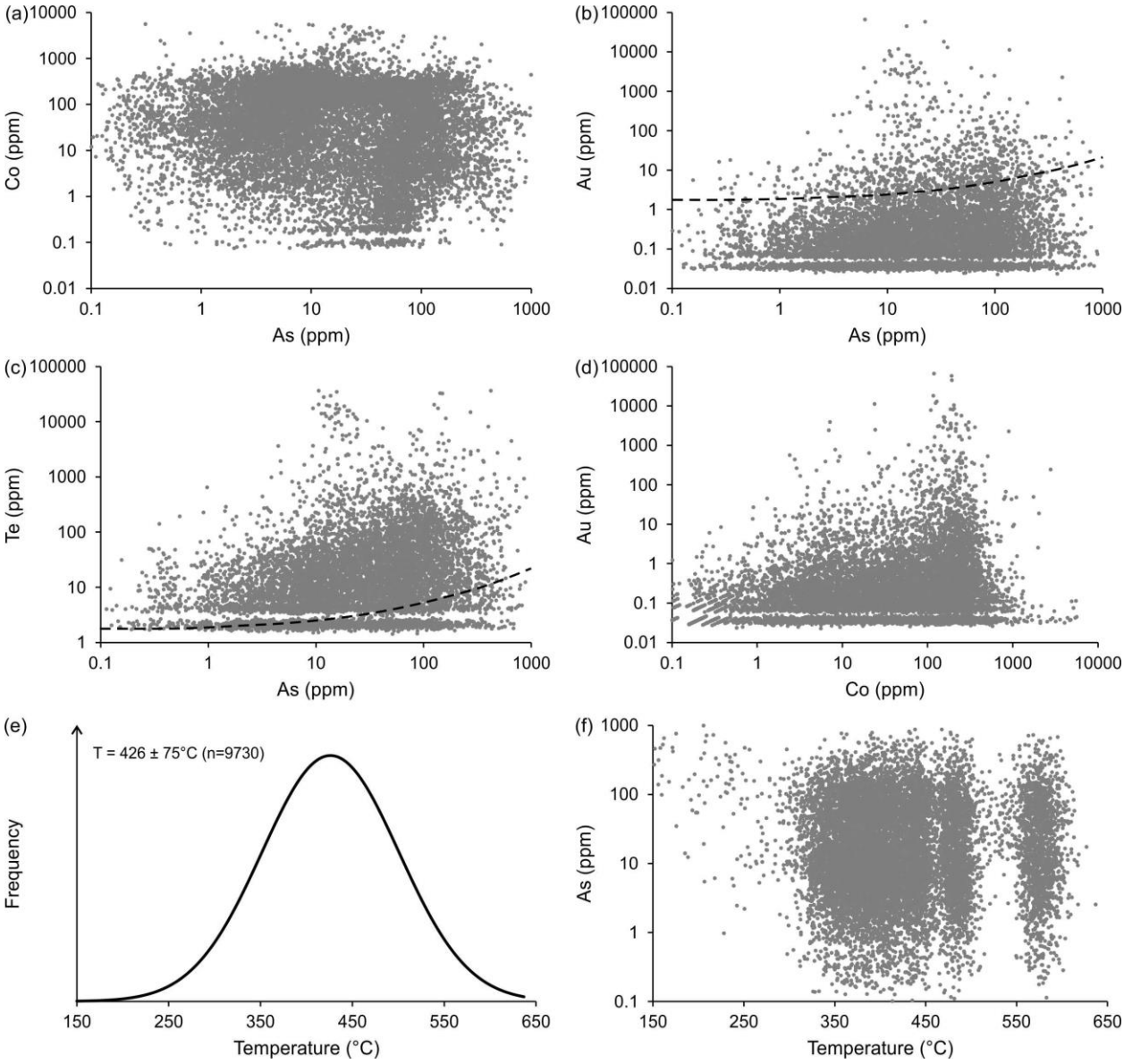
(a)
Co (ppm)
As (ppm)
(b)
Au (ppm)
As (ppm)
(c)
Te (ppm)
As (ppm)
(d)
Au (ppm)
Co (ppm)
(e)
T = 426 ± 75°C (n=9730)
Frequency
Temperature (°C)
(f)
As (ppm)
Temperature (°C)

Fig. 4.13: Scatter plots for selected elements quantified by LA-ICP-MS mapping for pyrite from the moderate- to low-grade vein from Grand Duc shown in Figure 4.10 (n=18, 175). See text for explanation of the compositional variations shown in frames (a-d) and (f). Temperatures in frames (e-f) were calculated using the Se-in-pyrite thermometer of Keith et al., 2018. The black dashed lines in (b) and (c) represent the solubility limit for Au and Te solid solution in pyrite as a function of As (Reich et al., 2005; Keith et al., 2018). Concentrations of Au and Te above the solubility line indicate Au and Te occur in pyrite as inclusions whereas data below the line indicate Au and Te occur in the pyrite lattice.

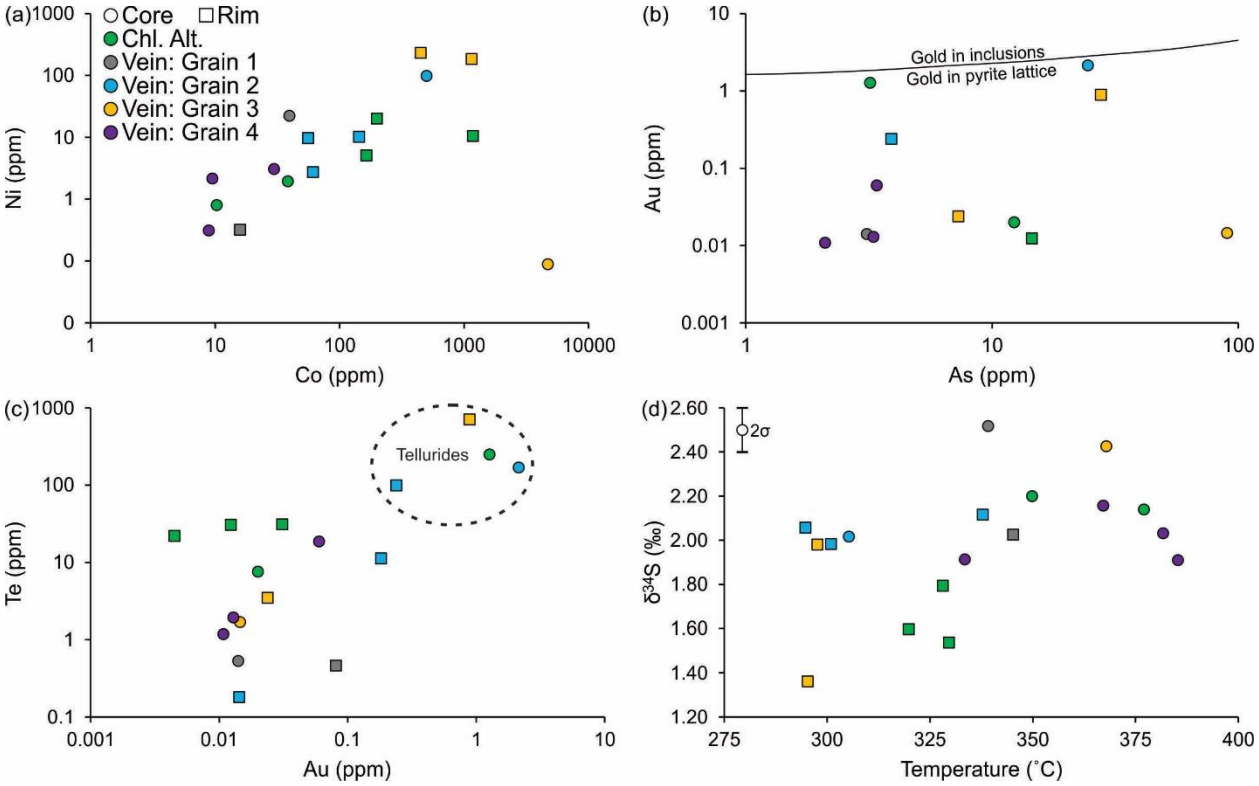

Fig. 4.14: Pyrite LA-ICP-MS point data from the high-grade Grand Duc vein (18KN03). Analyses of pyrite cores are represented by circles and rim analyses by squares. Matching colors represent the same grain for core and rim analyses. (a) Co (ppm) plotted against Ni (ppm). (b) As (ppm) plotted against Au (ppm). The line separating gold in inclusions and gold in pyrite lattice is from Reich et al. (2005). (c) Au (ppm) plotted against Te (ppm). Note the high Au and Te concentrations represent telluride inclusions encountered during ablation. (d) Temperature (°C; Se-in-pyrite thermometer; Keith et al., 2018) plotted against $\delta^{34}S$ (‰) composition determined by SIMS.

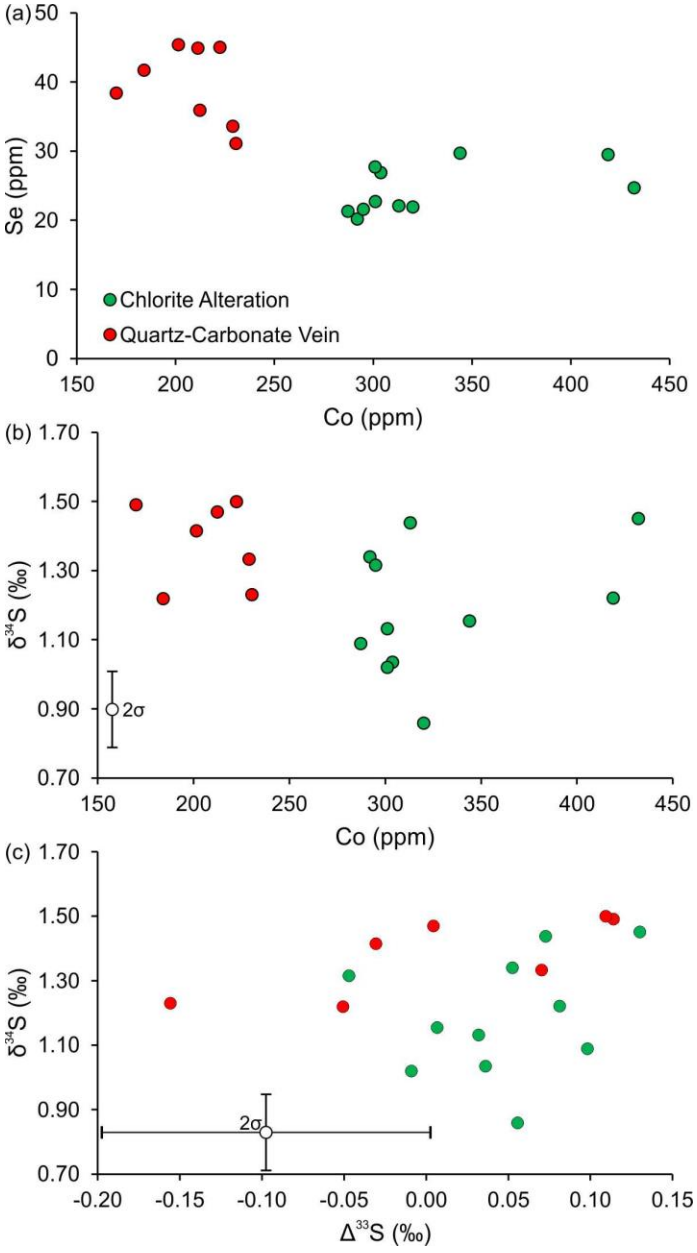

Fig. 4.15: Pyrrhotite LA-ICP-MS point data from the high-grade Grand Duc vein (sample 18KN03). (a) Co (ppm) plotted against Se (ppm). Note the difference in Se and Co concentrations between pyrrhotite occurring in the chlorite alteration compared to pyrrhotite in the quartz-carbonate vein. (b) Co (ppm) plotted against $\delta^{34}S$ (‰). There is no difference in the $\delta^{34}S$ between the chlorite- and vein-hosted pyrrhotite. (c) $\Delta^{33}S$ (‰) plotted against $\delta^{34}S$ (‰).

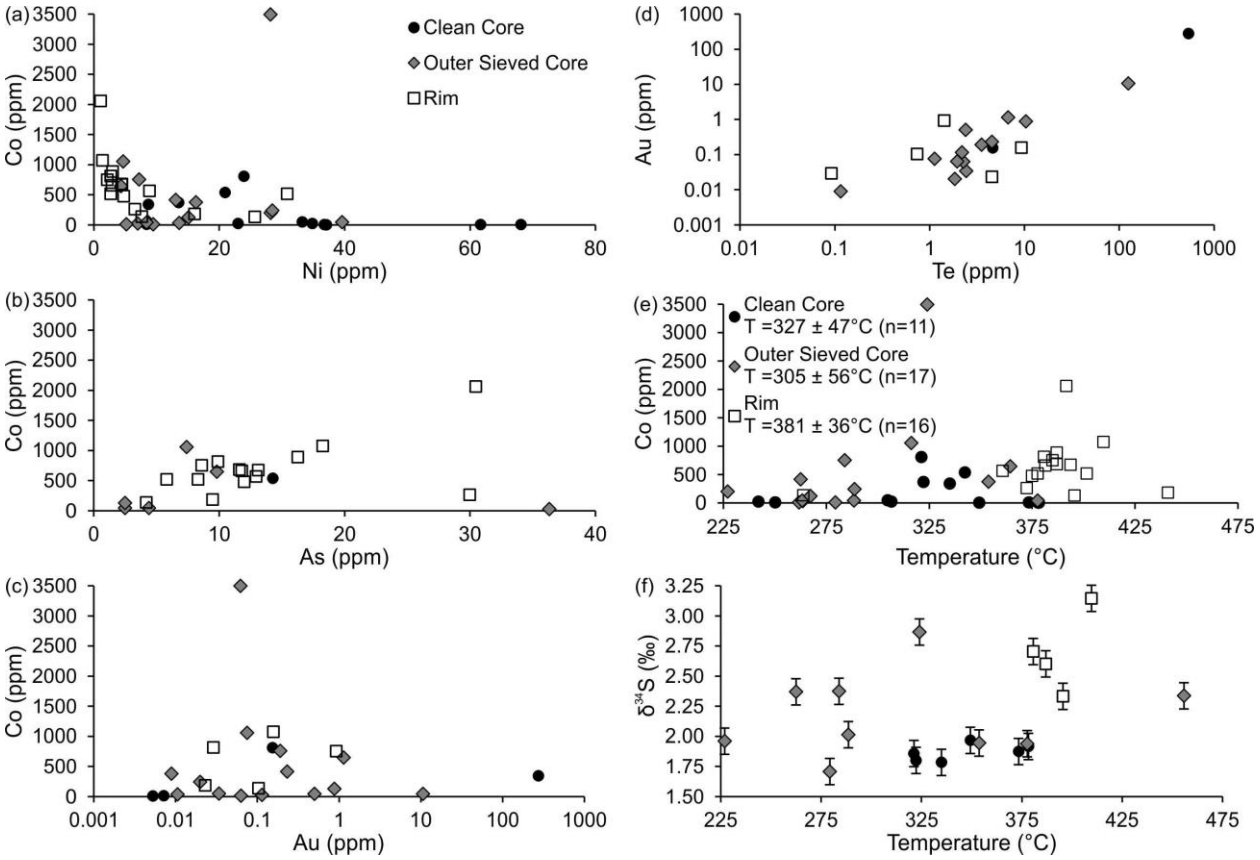

Fig. 4.16: Pyrite LA-ICP-MS point data from the moderate- to low-grade Grand Duc vein (18KN09). (a) Ni (ppm) plotted against Co (ppm). (b) As (ppm) plotted against Co (ppm). (c) Au (ppm) plotted against Co (ppm). (d) Te (ppm) plotted against Au (ppm). (e) Temperature (°C; Se-in-pyrite thermometer; Keith et al., 2018) plotted against Co (ppm). (f) Temperature (°C; Se-in-pyrite thermometer; Keith et al., 2018) plotted against $\delta^{34}S$ (‰) composition determined by SIMS.

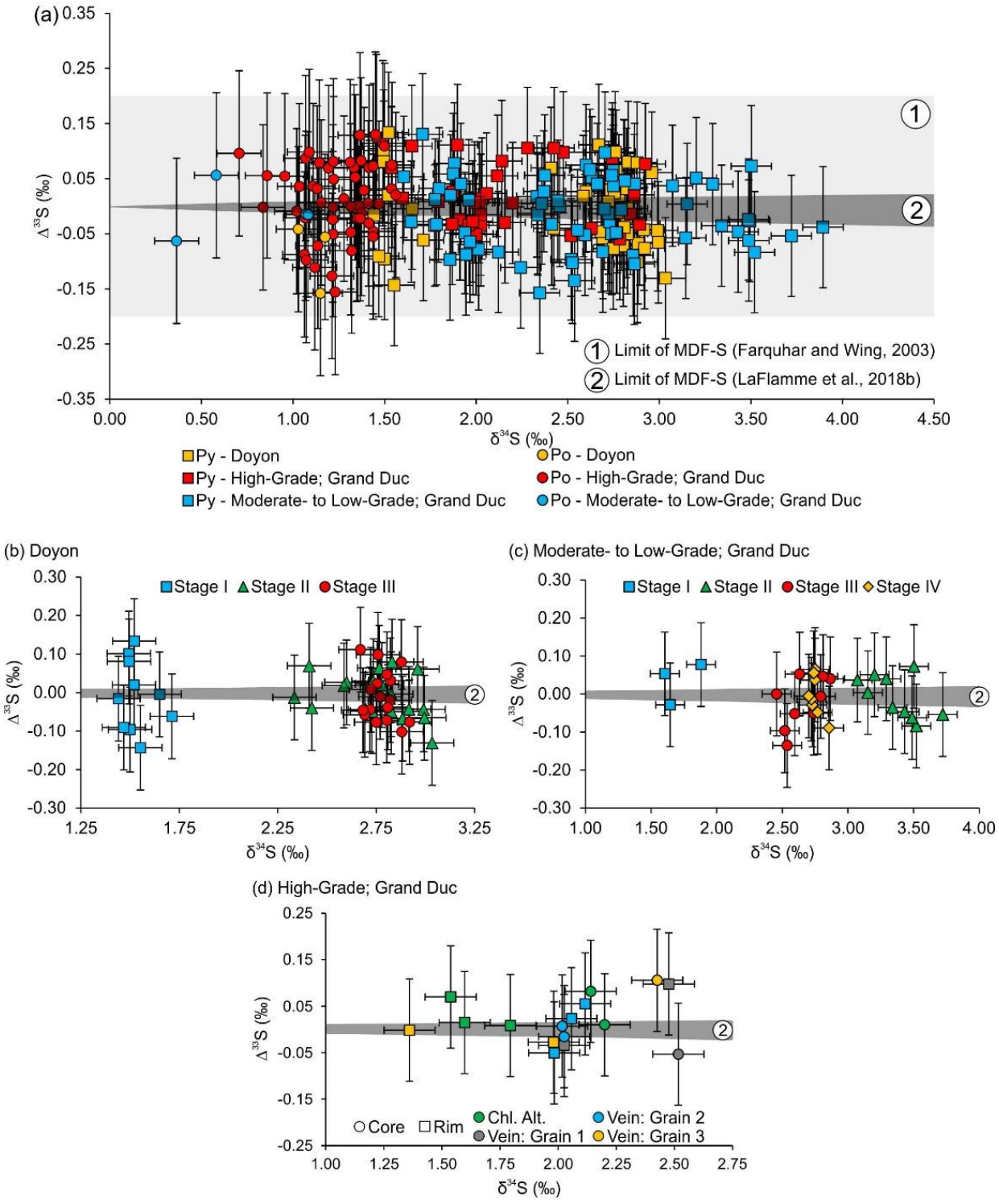
(a)
Δ33S (‰)
δ34S (‰)
① Limit of MDF-S (Farquhar and Wing, 2003)
② Limit of MDF-S (LaFlamme et al., 2018b)
Py - Doyon
Py - High-Grade; Grand Duc
Py - Moderate- to Low-Grade; Grand Duc
Po - Doyon
Po - High-Grade; Grand Duc
Po - Moderate- to Low-Grade; Grand Duc
(b) Doyon
Stage I Stage II Stage III
(c) Moderate- to Low-Grade; Grand Duc
Stage I Stage II Stage III Stage IV
(d) High-Grade; Grand Duc
Core Rim Chl. Alt. Vein: Grain 1 Vein: Grain 2 Vein: Grain 3

Fig. 4.17: Bivariate plots of multiple sulfur isotope data. (a) Sulfur isotope data for pyrite and pyrrhotite from the Doyon West deposit and Grand Duc deposit. Importantly, the $\Delta^{33}S$ values are all within the range and within error of the mass dependant fractionation field (MDF-S field; Farquhar and Wing, 2003; LaFlamme et al., 2018b), implying a magmatic source of sulfur for both Doyon and Grand Duc. (b) $\delta^{34}S$ (‰) plotted against $\Delta^{33}S$ (‰) for Doyon distinguished by the different trace element stages (I, II, III) identified by LA-ICP-MS mapping. (c) $\delta^{34}S$ (‰) plotted against $\Delta^{33}S$ (‰) for the moderate- to low-grade vein from Grand Duc distinguished by the different trace element stages (I, II, III) identified by LA-ICP-MS mapping. Data plotted here is from the grain mapped by LA-ICP-MS presented in Figure 4.10. (d) $\delta^{34}S$ (‰) plotted against $\Delta^{33}S$ (‰) for individual pyrite grains from the high-grade vein from Grand Duc.

Chapter 5: Conclusions and Future Work

5.1: CONCLUSIONS

This thesis documents and characterizes important concepts and processes related to the magmatic evolution of the Mooshla Intrusive Complex relevant to its potential role in the formation of intrusion-related and Au-rich VMS deposits in the Doyon-Bousquet-LaRonde mining district.

Using a combination of petrography, high-precision zircon U-Pb geochronology, accessory mineral thermobarometry, zircon trace element compositions, and quartz- and zircon-hosted silicate and sulfide melt inclusion analytical methods from the different phases that comprise the MIC this chapter provided new constraints on the pressure-temperature-time and compositional evolution of this synvolcanic magmatic system. Silicate and sulfide melt inclusion compositions combined with zircon trace element compositions provide new constraints on deep magmatic processes operating during the evolution of the MIC, linked to Au-rich VMS and other Au-rich magmatic-hydrothermal ore systems in this world class mining district.

The results demonstrate that individual magmatic phases (lithologies) of the MIC crystallized synchronously in distinct magma chambers at deep levels within the crust (~700° to 800°C; ~5 to 1.2 GPa, 16 to 40 km), slightly cooler and shallower than conditions for tonalite-trondhjemite-granodiorite (TTG) magma generation. Zircon trace element compositions associated with each of the individual MIC lithologies implicate multiple, coeval magma chambers. Silicate melt inclusions in quartz and zircon preserve rhyolitic magma compositions in a wide range of lithologies from the MIC, and provide various lines of evidence that help to understand melt evolution at prior to emplacement, while the magmas were fractionating at the conditions constrained by thermobarometry. Low Cs concentrations and normative Rb-Sr-Ba contents in the silicate melt inclusions indicate that the trapped melt was not highly fractionated. Additionally, discriminating ratios (e.g., Al_2O_3 vs SiO_2, Sr/Y, La/Yb) show that melts were of the low-Al TTG

type, that plagioclase (rather than amphibole) fractionation and accumulation was a dominant compositional control on magma composition, and that assimilation of SiO_2-rich material occurred. The requirement of multiple, coeval magma chambers demonstrated by zircon trace element systematics is supported by the silicate melt inclusion compositional record as there is no evolutionary pattern linking one lithology to another through simple fractionation trends.

High resolution zircon U-Pb geochronology shows that the entire intrusive complex formed over a maximum of ~1.44 Ma, with the formation of the compositionally distinct Mouska and Doyon stages occurring within a ~1 Ma window. This indicates a rapid change in tectonic setting from a rift- to arc-dominated environment, early in the magmatic evolution of the MIC magmas. Zircon chemistry records this rapid shift in tectonic affinity. The relatively short time span for the shift from rift- to arc-dominated magmatism is line with timescales for major porphyry Cu-Au systems to evolve from a barren- to mineralized-system (Chiaradia, 2021; Large *et al.*, 2021). The total gold endowment in the Doyon-Bousquet-LaRonde mining camp is similar to the gold endowment in Cu-Au porphyry deposits that have a similar duration of magmatism, in contrast to Au-rich alkaline porphyry systems which have a much shorter magmatic history (Chiaradia, 2021).

Accidentally trapped sulfide present in SMI indicates that early sulfide saturation occurred at depth in multiple crystallizing lithologies. These sulfides have similar ore metal ratios to the Au-rich deposits in the Doyon-Bousquet-LaRonde mining camp suggesting early magmatic sulfides influenced the ore metal tenors of these syn-volcanic and intrusion-hosted deposits, and behaved conservatively, despite indications of a protracted fractionation history (e.g., from zircon chemistry). Zircon oxybarometry indicates that oxygen fugacities were optimal in specific MIC magmas to promote high Au solubility, but also varied widely within the broader MIC magmas as indicated by the presence of magmatic sulfides in some lithologies and magmatic anhydrite in others. Early sulfide saturation implicates sulfides as a temporary storage medium for metals. These

sulfides were destroyed during volatile exsolution at the depth of magma storage, and less likely during ascent. Enrichment of SMI in Au and other metals (e.g., Ag, Cu, Bi) that are typical of porphyry-epithermal environments in arc settings reinforces that consideration must be made for the direct involvement of TTG magmas in providing metals to shallow, ore-forming hydrothermal systems through deep magmatic devolatilization.

For the Doyon West Zone and Grand Duc deposits, evidence is provided that confirms a singular, magmatic source of sulfur and metals likely related to the devolatilizing magmatic system that generated the MIC and coeval volcanic assemblages. The trace metal characteristics and sulfur isotope systematics of pyrite from the high-grade Grand Duc vein are consistent with an epithermal fluid signature (Au-Ag-As-Te-Bi-Sb-Se) related to a rare example of epithermal boiling in Archean terranes.

Overall, this thesis emphasizes that magmatic processes recorded at the level of near-seafloor emplacement in this geological setting (e.g., from field relationships) and bulk rock geochemistry do not fully capture the compositional and geochronological complexity of this magmatic system. The combination of methods utilized here provide evidence of deep crustal magmatic processes directly involved in the magmatic contributions of metals to Au-rich VMS and intrusion-related deposit styles in the Doyon-Bousquet-LaRonde mining camp and likely other similar environments in Archean terranes.

With regards to gold exploration in similar geological environments, some future areas to investigate further would be to identify areas/zones within deposits that have epithermal-like boiling signatures, more detailed high-resolution zircon geochronology combined with trace element compositions to identify a rapid transition from rift- to arc-dominated environments, and identification of metal-depleted silicate melt inclusions suggesting early sulfide saturation has occurrence.

5.2 FUTURE WORK

In Chapter 2 preliminary $\delta^{18}O$ compositions of zircon were determined by SIMS; however, the analytical precision for these analyses is relatively large (± 1.6 ‰; 2σ). To better constrain this, a higher precision SIMS instrument (e.g., Cameca IMS1280; ± 0.2 ‰; 2σ;) than the instrument used in this study (Cameca 7f) should be used to provide tighter constraints on zircon $\delta^{18}O$ composition. The $\delta^{18}O$ composition for individual growth zones in zircon would aid in understanding the nature of any potential sources of contamination in the magmatic system; generally, mantle-derived melts have a $\delta^{18}O$ value of +5.3 ± 0.3‰ (Valley et al., 1998) whereas values >6.5‰ are attributed to melting or assimilation of sedimentary and/or altered volcanic rocks and values <5‰ are attributed to melting of hydrothermally altered material (Valley et al., 2005). In addition to more precise $\delta^{18}O$ analyses on zircon, the Lu-Hf isotopic signature and derived εHf values for zircon are commonly used to trace the source(s) of parental melt. Pairing $\delta^{18}O$ and εHf analyses of zircon would allow for a more thorough understanding of magma source and evolution and determine if there were multiple magma sources and the extent/nature of crustal assimilation involved in the evolution of the Mooshla Intrusive Complex.

To provide a better constraint on the timing of mineralization in the Doyon-Bousquet-LaRonde mining camp, bornite could be analyzed to determine its rhenium–osmium (Re–Os) isotope composition and, potentially, its crystallization age. Bornite is a common mineral in numerous ore zones in Au-rich VMS Bousquet 2-Dumgami deposit (Dubé et al., 2014) and a trace mineral in the North and Westwood Corridors of the Westwood deposit (Yergeau et al., 2022). Determining the age of bornite mineralization may help directly tie the age of mineralization to the Mooshla Intrusive Complex and represents one of the only potentially datable ore minerals present.

Depending on its composition, pyrite can be studied using near-infrared (IR) microscopy, allowing for fluid inclusion microthermometry to be potentially conducted in this mineral (e.g.,

Lüders and Ziemann, 1999). Fluid inclusions are a tool used to understand the fluid source(s) and conditions of precipitation and therefore can be used to understand the fluid history of ore systems in the Doyon-Bousquet-LaRonde mining camp and potentially identify gold precipitation mechanisms (e.g., fluid boiling). Additionally, if fluid inclusions in pyrite can be well imaged and documented, inclusions could be analyzed by LA-ICP-MS to determine their composition. Although some metals will not likely be determined due to their elevated concentrations in the host pyrite, cation (e.g., Na^+, K^+, Ca^+) concentrations could be determined. Additionally, quartz-hosted primary fluid inclusions in mineralized veins can be investigated. Quartz-hosted inclusions can be analyzed by LA-ICP-MS to determine the metal content of magmatic-hydrothermal fluids, potentially identifying the fluid carrying gold.

5.3 REFERENCES

Chiaradia, M., 2021, Magmatic controls on metal endowment of porphyry Cu-Au deposits: Economic Geology Special Publication, v. 24, p. 1-16.

Dubé, B., Mercier-Langevin, P., Kjarsgaard, I., Hannington, M., Bécu, V., Côte, J., Moorhead, J., Legauly, M., and Bédard, N., 2014, The Bousquet 2-Dumagami World-Class Archean Au-Rich Volcanogenic Massive Sulfide Deposit, Abitibi, Quebec: Metamorphosed Submarine Advanced Argillic Alteration Footprint and Genesis: Economic Geology, v. 109, p. 121-166.

Large, S.J.E., Buret, Y., Wotzlaw, J.F., Karakas, O., Guillong, M., von Quadt, A., and Heinrich, C.A., 2021, Copper-mineralised porphyries sample the evolution of a large-volume silicic magma reservoir from rapid assembly to solidification: Earth and Planetary Science Letters, v. 563, https://doi.org/10.1016/j.epsl.2021.116877.

Lüders, V. and Ziemann, M., 1999, Possibilities and limits of infrared light microthermometry applied to studies of pyrite-hosted fluid inclusions: Chemical Geology, v. 154, p. 169-178.

Valley, J.W., Kinny, P.D., Schulze, D.J. and Spicuzza, M.J., 1998, Zircon megacrysts from kimberlite: oxygen isotope variability among mantle melts: Contributions to mineralogy and petrology, v. 133, p. 1-11.

Valley, J.W., Lackey, J.S., Cavosie, A.J., Clechenko, C.C., Spicuzza, M.J., Basei, M.A.S., Bindeman, I.N., Ferreira, V.P., Sial, A.N., King, E.M., and Peck, W.H., 2005, 4.4 billion years of crustal maturation: oxygen isotope ratios of magmatic zircon: Contributions to Mineralogy and Petrology, v. 150, p. 561-580.

Yergeau, D., Mercier-Langevin, P.L., Dubé, B., McNicoll, V., Jackson, S.E., Malo, M., and Savoie, A., 2022b, The Westwood Deposit, Southern Abitibi Greenstone Belt, Canada: An Archean Au-Rich Polymetallic Magmatic-Hydrothermal System—Part II. Hydrothermal Alteration, Mineralization, and Geologic Model: Economic Geology, v. 117, p. 577-608.